Nano Studies

7

2013

Nano Studies

7

2013

Nano Studies, 2013, 7

UDG [53 + 54 + 620.22] (051.2)
N – 21

Nano Studies is a biannual scientific journal published in Georgia.

Nano Studies' topics of interest include Nanoscience and related problems of Physics, Chemistry and Materials Science.

Nano Studies publish following categories of scientific articles: research papers, communications, reviews and discussions.

Nano Studies publish scientific articles in English and also in Georgian and in Russian.

Summaries of all the articles of **Nano Studies** are referred in **Georgian Abstracts Journal** and are accessible in **Tech Inform** (Georgia's Central Institute for Scientific and Technical Information) database: **http://www.tech.caucasus.net**

Full-texts of articles published in **Nano Studies** are free-accessible in **Nano Archive** database: **http://www.nanoarchive.org** and journal's web-site: **www.NanoStudies.org**

Editor & Publisher: **Levan Chkhartishvili**
Editorial Assistant: **Tamar Berberashvili**

Address of Editorial Office: **Department of Physics**
Georgian Technical University
Campus 4, Room 307
77 Merab Kostava Avenue
Tbilisi, 0175, Georgia
www.NanoStudies.org

E-mail: **chkharti2003@yahoo.com**
Phone: **995 322 37 19 42**
Mobile: **995 599 34 07 36**

Publishing House **Nekeri**

ISSN 1987 – 8826

CONTENTS

Proceedings of the International Conference & Exhibition on Advanced & Nano Materials (August 12 – 14, 2013, Quebec-City, Canada)

Contents.

Regular Papers

Science History Pages

Books & Media Reviews

Chronicle

EFFECTS OF SYNTHESIS CONDITIONS ON THE NANOSTRUCTRE OF $Ce_xZr_{1-x}O_2$ MESOPOROUS CERAMICS

A. D. S. Bruno Costa [1], R. Bacani [1],
M. A. Fantini [1], T. S. Martins [2], A. L. M. da Silva [3]

[1] Physics Institute
Cidade Universitária São Paulo
São Paulo, Brazil
antonia_daniele@yahoo.com.br
[2] Instituto de Ciências Ambientais, Químicas e Farmacêuticas
Universidade Federal de São Paulo
São Paulo, Brazil
[3] Eldorado Business
São Paulo, Brazil

Accepted September 19, 2013

1. Introduction

Cerium and zirconium oxides have been widely employed in very different fields like catalysis, ceramics, fuel cell technologies, gas sensors, solid state electrolytes, etc. [1, 2]. It has been reported that the addition of ZrO_2 to CeO_2 leads to improvements in oxygen storage capacity, thermal resistance, and catalytic activity of ceria [3, 4]. In addition, these materials may be used as anode in solid–oxide fuel cells (SOFC) operated with hydrocarbons [5].

Some authors have stated that SBA – 15 (Santa Barbara Amorphous N° 15) ordered mesoporoussilicas, which possesses larger pores, thicker wall, and higher thermal stability could be used, together with Ce – ZrO_2, as promising catalyst support. According to the [6], ordered mesoporous structure improves the oxygen storage capacity and thermal stability. Thus, there is a great interest to synthesize highly ordered nanoporous materials (pore in the range of 2 – 50 nm) [7]. It was pointed out [8] the importance to work with mesoporous materials, because their particle size is not determined by temperature. Actually, it is established that the template, such as hexagonal SBA – 15, prevents grain growth of the embedded material during thermal treatments. Furthermore, the hydrothermal treatments provide a driving force to insert nanoparticles into mesopores [9].

It is required not only to develop mesoporous material, but also to provide a comprehensive characterization with regard to pore size, surface area, porosity,and pore size distributionin order to select and optimize the performance of nanoporous materials [7, 10]. It was also mentioned [11] that ZrO_2 – CeO_2 physical and chemical properties are strongly related to crystal structures, dopant concentration, temperature, and microstructures. Therefore, some authors have studied the influence of synthesis conditions on material properties [1, 3, 12]. In [13], for instance, it has been reported that Ce – ZrO_2 crystal phase and ceria structure is related to the dissolution of zirconium into the ceria due to preparation conditions.

$Ce_xZr_{1-x}O_2$ mesoporous ceramics, with x between 0.5 and 0.9, prepared with different methods of synthesis are analysed in this study. The effect of differences in preparation route in material properties will be evaluated by different techniques like X-ray diffraction (XRD) with Rietveld refinement and nitrogen adsorption / desorption.

2. Materials and methdos

2.1 Materials preparation

In this work two different methods of synthesis were analysed. In both syntheses, crystalline compounds of $Ce_xZr_{1-x}O_2$, with x between 0.5 and 0.9, were prepared with Zr and Ce chloride precursors, using triblock copolymer Pluronic P123 as structure directing agent and HCl (2 mol / L) as the solvent. Synthesis A used 11.4 mL of a NH_4OH solution added at once to the initial mixture, with final pH between 4 and 5. In the synthesis B, NH_4OH was introduced dropwise to adjust different pH values (between 3 and 6). Then, the hydrothermal treatments were made in a teflon autoclave for 48 h at 80 °C. After this treatment, the samples were dried at 60 °C. Finally, these samples were calcinedat 540 °C (1 °C / min) in N_2 atmosphere and kept for 4 h at 540 °C in air. Samples names used in this study are presented in **Table 1**.

Table 1. Samples names.

Samples	Synthesis A	Synthesis B
$Ce_{0.9}Zr_{0.1}O_2$	Ce90A	Ce90B
$Ce_{0.7}Zr_{0.3}O_2$	Ce70A	Ce70B
$Ce_{0.5}Zr_{0.5}O_2$	Ce50A	Ce50B

2.2. XRD analysis

The samples were analysed by XRD using a Rigaku Difractometer, model Ultima Plus, with Cu K_α radiation source (λ = 1.5418 Å). Data in the angular region of 2θ = 10 – 100 ° were collected in a step-scanning mode, with a step of 0.02 ° and a step-counting time of 5 s.

2.3. Rietveld refinement

The Rietveld's powder structure refinement analysiswas performed to extract some information about structural parameters, such as atomic coordinates, lattice parameters, temperature factors, and others [14 – 16]. The Rietveld's software DBWS – 9807a is specially designed to refine the structural parameters through a least-squares method [17]. Peaks shapes were fitted using pseudo-Voigt (pV) function with asymmetry. The background of each pattern was fitted by a polynomial function of degree 5. The least-square minimization of the difference between the observed and simulated powder diffraction pattern could be observed in DMPLOT program [17]. The R's values such as R_p, R_{wp}, R_{exp}, and S_{Gof} (R_{wp} / R_{exp}) were used as numerical criteria of fit, indicating the agreement between the observed and calculated quantities [18]. R_p and R_{wp} indices involves a preliminary data reduction step in which the background was

subtracted from the intensity measured at each step in the pattern. R_{exp} values were a Gaussian statistics which assumes a minimum value for R_{wp} [19].

The Scherrer's equation,

$$D = k\lambda/(\beta\cos\theta), \quad (1)$$

was used to estimate the mean crystallite size after peak´sfitting. The program DBWS allows determining all crystallographic planes using Eq. (1), where λ is the X-ray wavelength, β is the width of the diffraction peak profile at half maximum height resulting from small crystallite size in radians and k is a constant related to crystallite shape, normally taken as 0.9 [20].

A linear behaviour in the Williamson–Hall graphic could be expressed by equation:

$$\beta\cos\theta/\lambda = k/D + (4\varepsilon/\lambda)sen\theta, \quad (2)$$

where β is full width at half maximum, λ is wavelength, and k is the constant, which depends of symmetry reflection, usually with taken as $k = 1$ [21]. Eq. (2) could be approximated to a straight line y, in which the linear coefficient is equal to $1/D$, where D is the average crystallite diameter. The angular coefficient is equal to $4\varepsilon/\lambda$, where ε is the microstrain.

2.4. Nitrogen adsorption isotherms (NAI) analysis

Nitrogen adsorption isotherms were measured with Micromeritics ASAP 2020 volumetric sorption analyser using 99.998 % pure nitrogen. Measurements were performed in liquid nitrogen on samples degassed for 24 h, under reduced pressure at 200 °C. The measurements were taken at 77 K (N_2). The pore size distribution, pore volume and pore radius were calculated using Barret–Joyner–Halenda (BJH) method [22]. The specific surface area was obtained by the Brunauer–Emmet–Teller (BET) method [23]. The pore size distribution (PSD) was calculated using Kruk–Jaroniec–Sayari (KJS) method [24].

3. Results and discussions

3.1. X-Ray diffraction and Rietveld Refinement characterization

The XRD of $Ce_xZr_{1-x}O_2$ for both syntheses A e B are shown in **Figure 1** (y_{obs} – black line). Samples of $Ce_{0.9}Zr_{0.1}O_2$ observed in **Figure 1(a)** present a cubic fluorite structure like ceria, with space group *Fm*–3*m* for both syntheses. In this phase, there are 11 main reflections (111), (200), (220), (311), (222), (400), (331), (420), (422), (511) and (333) planes, which are represented by letters a, c, e, f, g, h, i, j, l, m, and n, respectively, in **Figure 1**. Sample Ce90A does not present a tetragonal phase, while sample Ce90B presents a small percentage of this phase indicated by the letters b, peak (110), and e, peak (200).

Samples Ce70A, Ce70B, Ce50A and Ce50B present both cubic and tetragonal phases. The percentage of all phase is summarized in **Table 2**. It was noticed that synthesis B presents a higher amount of cubic phase. Moreover, it was remarked that there is a decrease in percentage of cubic phase with the decrease of x (amount of ceria content). Synthesis A exhibits ZrO_2 phase, which is not dissolved in CeO_2. This phase is tetragonal with space group $P4_2/nmc$, as indicated in the literature [25, 26]. The percentages of this phase are also presented in **Table 2**. It was observed that higher amounts of zirconia in sample composition result in higher percentage of ZrO_2 phase. Synthesis B does not present ZrO_2 phase.

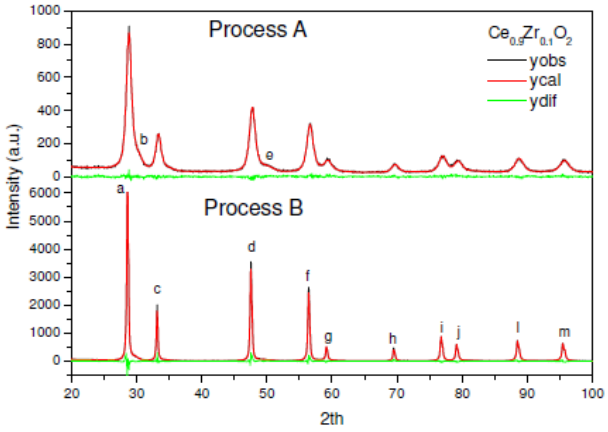

(a)

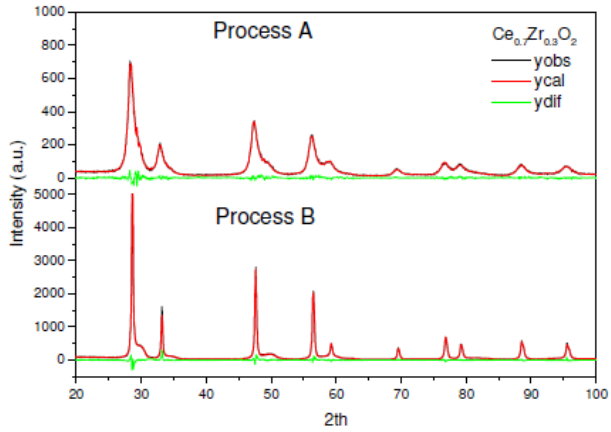

(b)

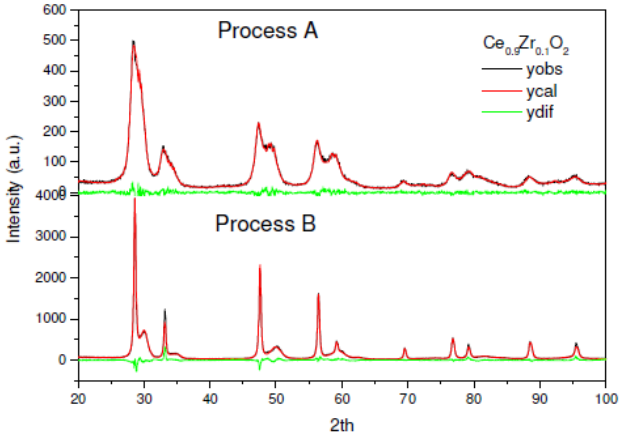

(c)

Figure 1. Diffractograms of $Ce_xZr_{1-x}O_2$, with $x = 0.9$ (a), 0.7 (b) and 0.5 (c), powders prepared through syntheses A and B. Observed and calculated patterns, and difference spectrum are presented (in black and red, and green lines, respectively).

Table 2. Phase quantities (% mass).

Phases	$Ce_{0.9}Zr_{0.1}O_2$		$Ce_{0.7}Zr_{0.3}O_2$		$Ce_{0.5}Zr_{0.5}O_2$	
	Synthesis A	Synthesis B	Synthesis A	Synthesis B	Synthesis A	Synthesis B
Cubic	91.0 %	95.0 %	59.0 %	81.0 %	47.0 %	69.0 %
Tetragonal	–	5.0 %	26.0 %	19.0 %	23.0 %	31.0 %
ZrO_2	9.0 %	–	15.0 %	–	30.0 %	–

In cubic phase, the ceria and zirconia are localized in Wyckoff position 4a, while the oxygen occupies the site 8c. For tetragonal phase, the Wyckoff positions for ceria and zirconia are 2a, whereas the oxygen occupies the site 4d. The Wyckoff positions of ZrO_2 phase are 2b and 4d.

The calculated pattern (y_{cal} – red line) and the difference pattern (y_{dif} – green line) obtained by Rietveld refinement are also presented in **Figures 1(a)**, **(b)** and **(c)** for the two syntheses methodes. These graphs show a good agreement between the calculated and observed patterns. These results could also be confirmed by numerical criteria of fit, such as R_{wp}, R_p and S_{Gof} exhibit in **Table 3**.

Table 3. Numerical criteria of fit.

	Ce90A	Ce90B	Ce70A	Ce70B	Ce50A	Ce50B
R_p, %	4.74	6.76	6.06	6.97	5.51	6.28
R_{wp}, %	6.51	8.53	7.80	9.01	7.12	8.30
R_{exp}, %	11.67	9.18	13.15	8.78	13.12	8.54
S_{Gof}	1.37	0.94	0.59	1.03	0.54	0.97

In Rietveld procedure, a model based on a reference for $Ce_{0.9}Zr_{0.1}O_2$ [27], $Ce_{0.7}Zr_{0.3}O_2$ [5], $Ce_{0.5}Zr_{0.5}O_2$ [28], and ZrO_2 were used. Variations of unit cell parameters are shown in **Table 4** for cubic phase, in **Table 5** for tetragonal phase, and in **Table 6** for ZrO_2 phase. For cubic phase, the cell parameters are higher in synthesis B. On the other hand, tetragonal phases exhibit higher unit cell parameters for synthesis A.

Table 4. Cell parameters of cubic phase.

Parameter	Ce90A	Ce90B	Ce70A	Ce70B	Ce50A	Ce50B
$a = b = c$, Å	5.4056	5.4084	5.4080	5.4084	5.4071	5.4077
$\alpha = \beta = \gamma$, °	90	90	90	90	90	90
Density, g / cm^3	5.837	7.892	5.774	7.484	5.840	7.138

Table 5. Cell parameters of tetragonal phase.

Parameter	Ce90A	Ce90B	Ce70A	Ce70B	Ce50A	Ce50B
$a = b$, Å	–	3.6646	3.7151	3.6573	3.6914	3.6194
c, Å	–	5.2423	5.3080	5.2255	5.2725	5.2469
$\alpha = \beta = \gamma$, °	–	90	90	90	90	90

Table 6. Cell Parameters of ZrO_2.

Parameter	Ce90A	Ce70A	Ce50A
$a = b$, Å	3.6272	3.6545	3.6914
c, Å	5.3015	5.3091	5.2661
$\alpha = \beta = \gamma$, °	90	90	90

The densities, which are calculated by DBWS program in Rietveld analysis, are also presented in **Table 4**. Samples of syntheses A are less dense than samples of syntheses B, as could be noticed in **Figure 2**. This result could be pointed out by a greater amount of cubic phase in synthesis B. In conjunction, these calculated densities decrease with the decrease in the amount of ceria. These results could be explained by a higher molar mass of Ce compared with Zr.

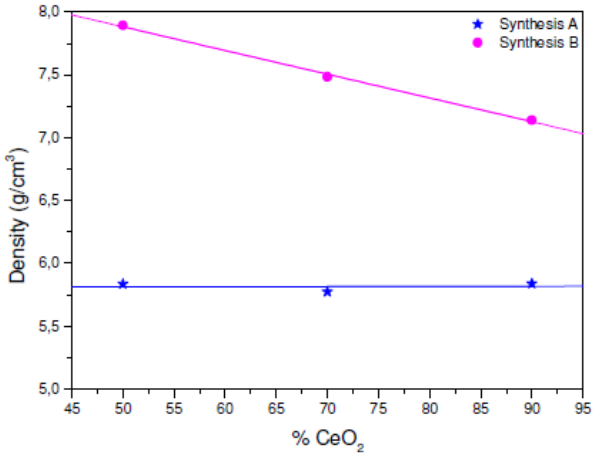

Figure 2. Graphs of density versus cerium percentage for syntheses A and B.

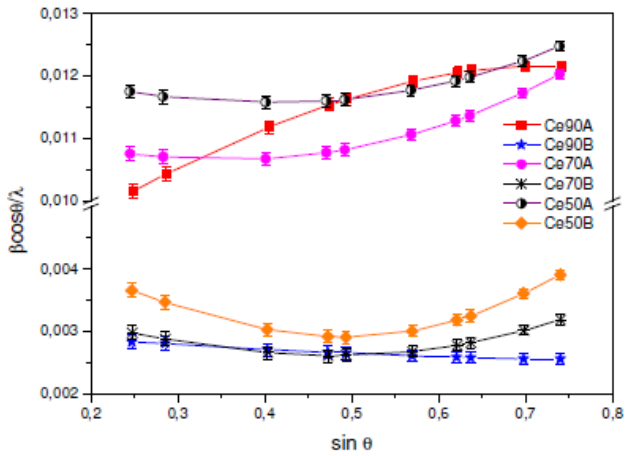

(a)

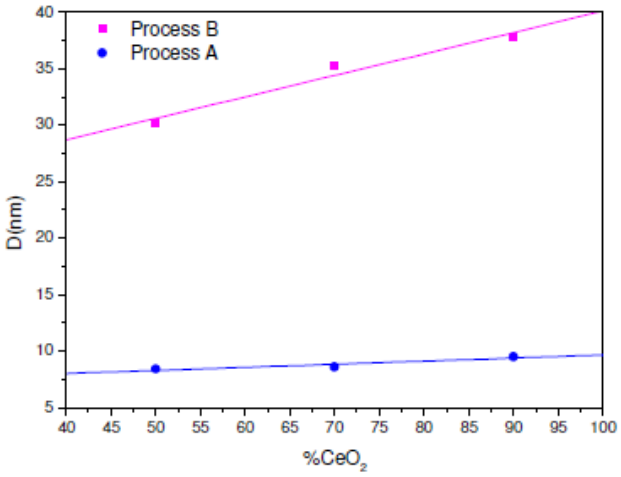

(b)

Figure 3. (a) Williamson–Hall graphs for $Ce_xZr_{1-x}O_2$;
(b) Crystallite size in function of ceria content.

Figure 3(a) presents the Williamson–Hall graphs for $Ce_xZr_{1-x}O_2$ obtained through Rietveld refinement for both syntheses. Syntheses A do not show linear graphs, indicating a non-uniform crystallite size. In a similar way, syntheses B display a non-linear behavior. Nevertheless, sample Ce90B exhibits a good linearity. So, it is possible to state that the crystallite size for this sample is uniform in all planes.

Figure 3(b) illustrates the crystallite size for different amount of ceria for both syntheses. It could be recognized that synthesis B has higher crystallite size values. **Table 7** presents the crystallite sizes, which are calculated by Scherrer equation, and linear regression on Williamson–Hall graphs. The crystallite sizes are between 30 and 40 nm for synthesis B and between 5 and 10 nm for synthesis A. **Table 7** also presents the microstrain results. Sample Ce90B shows negative microstrain, which is visualized by a descending line in **Figure 3(a)**. This result means that the crystalline network is been contracted. The other samples show an ascending line, indicating expansions in crystalline network.

Table 7. Crystallite sizes (nm) and microstrain.

Parameter	Ce90A	Ce90B	Ce70A	Ce70B	Ce50A	Ce50B
Scherrer equation	9.5	37.8	8.6	35.2	8.4	30
Williamson–Hall	10.5	34.8	12.0	40.6	9.1	36
Microstrain, %	0.146	– 0.021	2.430	0.028	0.069	0.040

Figure 4 shows a XRD patterns (y_{obs} with black line) of different pH obtained during preparation of synthesis B. These samples possesses a cubic structure, with space group *Fm*–3*m*, and a tetragonal phase with space group $P4_2/nmc$. All samples present the same main reflections of ones presented in **Figure 1**.

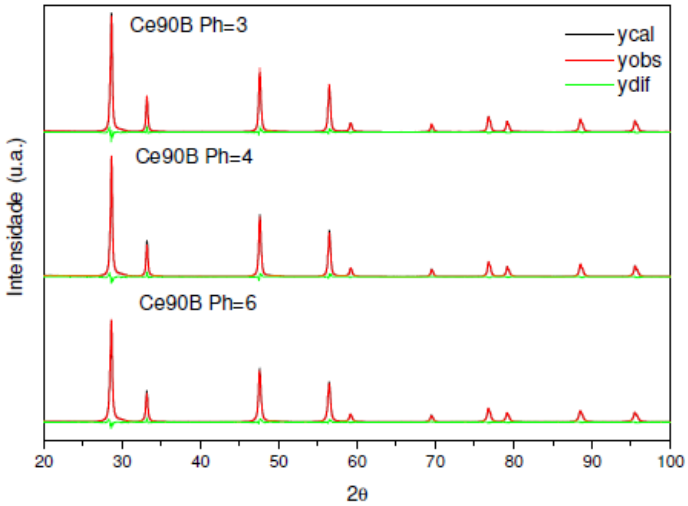

Figure 4. Comparative diffractograms for synthesis B prepared with different pH.

The calculated pattern (y_{cal} – red line) and difference pattern (y_{dif} – green line) obtained by Rietveld refinement are also presented in **Figure 4**. These graphs show a good agreement between the calculated and observed patterns. These results could also be confirmed by numerical criteria of fit, such as R_{wp}, R_p and S_{GOf} exhibited in **Table 8**.

Table 8. Numerical criteria of fit.

Samples	R_p,%	R_{wp},%	R_{exp},%	S_{Gof}
Ce90B pH = 3	6.76	8.53	9.18	0.94
Ce90B pH = 4	6.45	8.24	8.93	0.92
Ce90B pH = 6	5.93	7.54	9.38	0.80

In Rietveld procedure, a previous model adopted in this study was also used. Variations of unit cell parameters for cubic and tetragonal phases are shown in **Table 9**. For cubic phase, the cell parameters are higher for greater pH values. Besides, tetragonal phases exhibit higher unit cell parameters for lower pH values. The densities are also presented in **Table 9**. The densities slightly increase with a decrease in pH values. The percentage of cubic phase decrease on a small scale with increase in pH values, as could be observed in **Table 10**.

Table 9. Cell parameters of cubic phase.

Samples	Cubic phase			Tetragonal phase		
	$a = b = c$, Å	$\alpha = \beta = \gamma$, °	Density, g / cm^3	$a = b$, Å	c, Å	$\alpha = \beta = \gamma$, °
Ce90B pH = 3	5.4087	90	7.892	3.6646	5.2423	90
Ce90B pH = 4	5.4084	90	7.946	3.6561	5.2292	90
Ce90B pH = 6	5.4094	90	7.985	3.6500	5.2226	90

Table 10. Phase quantities (% mass).

Phases	Ce90B pH = 3	Ce90B pH = 4	Ce90 pH = 6
Cubic	95.0 %	94.9 %	94.4 %
Tetragonal	5.0 %	5.1 %	5.6 %

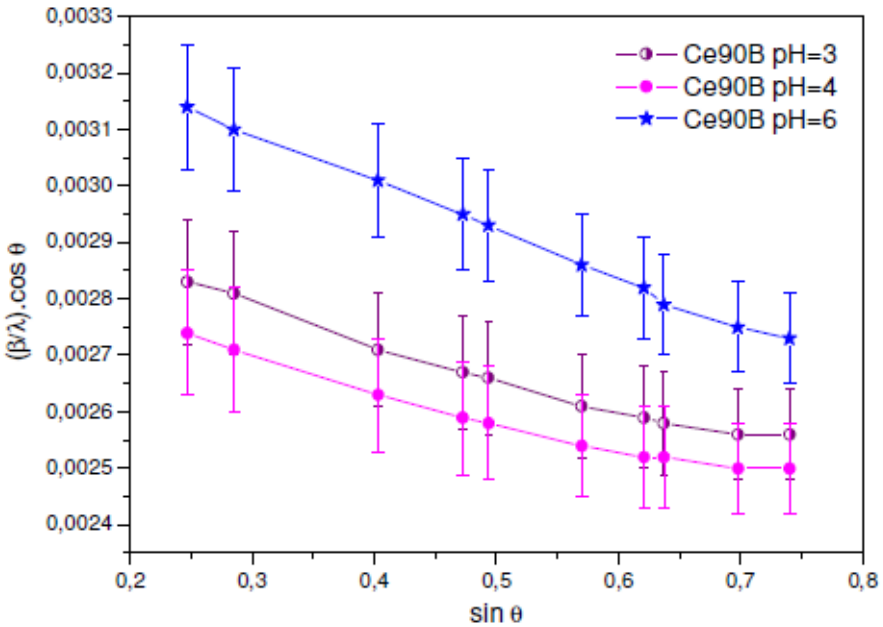

Figure 5. Williamson–Hall graphs for $Ce_xZr_{1-x}O_2$.

Table 11. Crystallite sizes (nm) and microstrain.

Parameter	Ce90B pH = 3	Ce90B pH = 4	Ce90B pH = 6
Scherrer equation	37.8	38.9	34.7
Williamson–Hall	34.8	35.3	29.9
Microstrain, %	– 0.021	– 0.018	– 0.032

Figure 5 presents the Williamson–Hall graphs for $Ce_xZr_{1-x}O_2$ obtained through Rietveld refinement for samples with different pH values. These samples exhibit a good linearity, indicating a uniform distribution of particle size. **Table 11** shows the crystallite sizes calculated by Scherrer equation and linear regression on Williamson–Hall graphs. There is a small change in crystallite size, when the pH values are modified. The crystallite sizes are between 29 and 40 nm. **Table 7** also presents the microstrain results, whose values are negative. These results imply a crystalline network contraction.

3. 2. Nitrogen sorption isotherms

Nitrogen sorption isotherms of syntheses A and B are presented in **Figure 6**. All materials exhibit a type IV isotherm and type H4 of hysteresis loop according to IUPAC classification [29], which represents a mesoporous solid. These syntheses generate a solid with narrow slit-like pores.

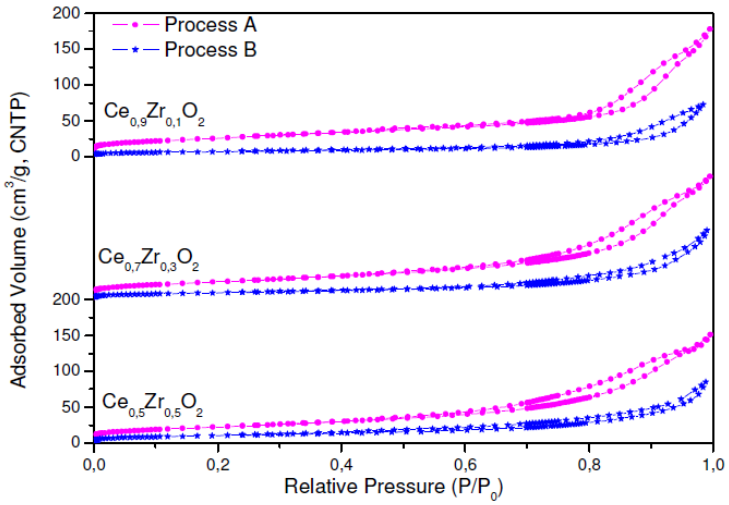

Figure 6. Nitrogen physisorption isotherm for syntheses A and B.

Table 12. Specific surface area (S_{BET}), pore volume and pore diameter.

	Ce90A	Ce90B	Ce70A	Ce70B	Ce50A	Ce50B
S_{BET}, m^2 / g	91.9	24.1	88.3	33.7	80.1	36.2
Pore volume, cm^3 / g	0.2845	0.1164	0.2775	0.1564	0.2482	0.1434
Average pore diameter, nm	12.5	17.3	12.0	15.7	10.9	10.9

The BET specificsurface area S_{BET}, the pore volume, and the average pore diameter are presented in **Table 12**. The S_{BET} were higher for synthesis A, whose values are between 80 and 92 m^2 / g, than for synthesis B (24 – 36 m^2 / g). It is possible to notice a tendency of increase in

surface area with the amount of ceria content for both syntheses, as exposed in **Figure 7(a)**. Syntheses A reveal larger pore volume than syntheses B, as could be observed in **Table 12** and in **Figure 7(b)**.

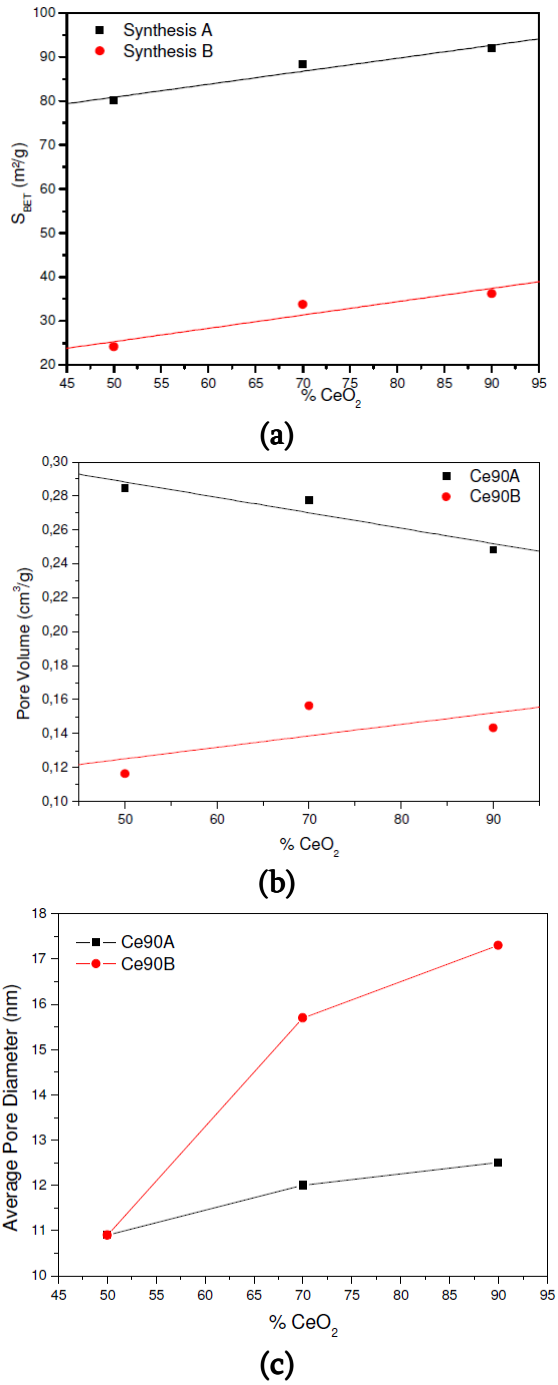

Figure 7. (a) specific surface area (S_{BET}), (b) pore volume, and (c) average pore diameteras a function of cerium amount.

Table 12 also exhibits the average pore diameter for both syntheses. For the two syntheses, there is a trend to increase the average pore diameter with the percentage of ceria in the sample composition. This behaviour is better visualized in **Figure 7(c)**. The higher values of pore diameter were obtained for synthesis B with values between 10 and 18 nm, while synthesis A presents average pore diameters between 10 and 13 nm.

The pore size distribution is shown in **Figure 8**. There is a presence of micropores in all samples. However, the greater amount of pores is in the mesoporous range. In the two syntheses, the concentration of pores increases with the amount of ceria. It could be also noticed that syntheses A have a greater percentage of pores than synthesis B.

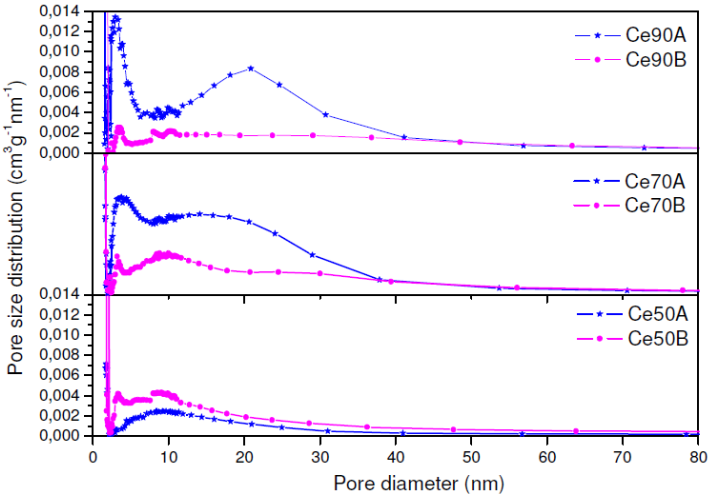

Figure 8. Pore size distribution.

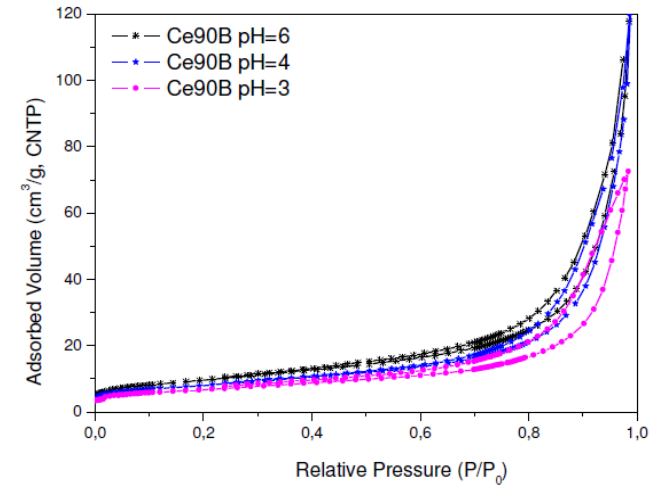

(a)

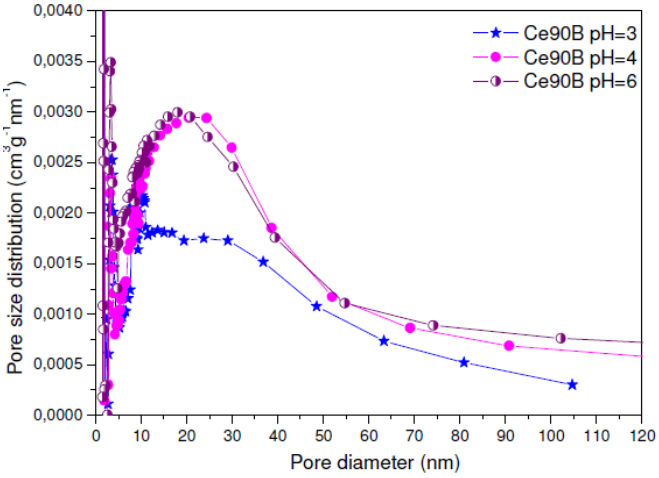

(b)

Figure 9. (a) nitrogen physisorption isotherm for syntheses A and B, and (b) pore size distribution.

Nitrogen sorption isotherm of syntheses with pH values of 3, 4 and 6 is shown in **Figure 9(a)**. All materials exhibit a type IV isotherm and type H4 of hysteresis loop, which represent a mesoporous structure. These syntheses generate a solid with narrow slit like pores. Sample Ce90B with pH = 3 shows the lowest pore volume absorbed.

The pore size distribution is presented in **Figure 9(b)**. There is a presence of micropores in all samples. However, the greater amount of pores is in the mesoporous range. It could be perceived that the concentration of pores is lower for samples prepared with pH = 3.

Table 13. Specific surface area (S_{BET}), pore volume and pore diameter of the samples with different pH values.

	Ce90B pH = 3	Ce90B pH = 4	Ce90B pH = 6
S_{BET}, m^2 / g	24.1	28.5	34.8
Pore volume, cm^3 / g	0.1164	0.1996	0.2208
Average pore diameter, nm	17.3	24.6	21.5

The BET surface area, the pore volume and the average pore diameter are presented in **Table 13**. The BET surface areas increase with the increase in pH values, with values between 24 and 35 m^2 / g. The pore volumes also increase with increase in pH values. The average pore diameters oscillate with pH values, exhibiting pore with diameters between 17 and 25 nm.

4. Conclusions

From XRD results it could be concluded that the two proposed syntheses produce a solid solution of $Ce_xZr_{1-x}O_2$ crystallized in a two phase system: cubic (space group $Fm\bar{3}m$) and tetragonal ($P4_2/nmc$). Synthesis A also generates a non-dissolute phase in ceria (ZrO_2), which is a tetragonal phase with space group $P4_2/nmc$. The synthesis B has a higher density, larger crystallite size and greater amount of cubic phase. The two syntheses present a non-uniform particle size distribution with the exception of sample Ce90B. Notwithstanding different pH values used in syntheses B the crystal phases did not change, but there are other differences in crystal structure like cell parameters, density and crystallite size.

All materials exhibit a type IV isotherm and type H4 of hysteresis loop, indicating a mesoporous structure with narrow slit like pores. Synthesis A possesses a higher specific surface area and a larger pore volume. On the other hand, synthesis B exhibits a larger pore diameter. The BET specificsurface areas and pore volume increase with the increase in pH values. The average pore diameters are affected by pH values. It is possible to notice a tendency of increase specific surface area and pore diameter with increase in the amount of ceria content for both syntheses. Through pore size distribution, all samples have a greater concentration of pore size in mesoporous range. Nevertheless, there is a presence of micropores in all samples.

Acknowledgment

This research was supported by Sao Paulo Research Foundation – FAPESP.

References

1. R. di Monte, J. Kaspar, H. Bradshaw, C. Norman. A rationale for the development of thermally stable nanostructured CeO_2 – ZrO_2-containing mixed oxides. J. Rare Earths 26 (2008) 136-140.
2. Sh. Song, R. O. Fuentes, R. T. Baker. Nanoparticulate ceria–zriconia anode materials for intermediate temperature solid oxide fuel cells using hydrocarbon fuels. J. Mater. Chem. 20 (2010) 9760 -9769.
3. Y. Gu, Sh. Feng, J. Li, X. Gu, M. Wang. Preparation of mesoporous $Ce_{0.5}Zr_{0.5}O_2$ mixed oxide by hydrothermal templating method. J. Rare Earths 25 (2007) 710-714.
4. S. Gopalakrishnan, M. G. Fagab, I. Milettoa, S. Colucciaa, G. Caputoc, S. Sauc, A. Giaconiac, G. Berliera. Unravelling the strucuture and reactivity of supported Ni particles in Ni – $CeZrP_2$ catalysts. Appl. Catal. B 138-139 (2013) 353-361.
5. D. G. Lamas, R. O. Fuentes, I. O. Fábregas, M. E. Fernández de Rapp, G. E. Lascalea, J. R. Casanova, N. E. Walsöe de Reca, A. F. Craievich. Synchrotron X-ray diffraction study of the tetragonal–cubic phase boundary of nanocrystalline ZrO_2 – CeO_2 synthesized by a gel-combustion process. J. Appl. Crystallog. 38 (2005) 867-873.
6. F. Huang, Y. Zheng, Z. Li, Y. Xiao, Y. Zheng, G. Cai, K. Wei. Synthesis of highly dispersed ceria–zirconia supported on ordered mesoporous alumina. Chem. Commun. 47 (2011) 5247-5249.
7. M. Thommes. Physical adsorption characterization of nanoporous materials. Chemie Ingenieur Technik 82 (2010) 1059-1073.
8. S. A. Ghom, T. Andreu, C. Zamani, J. R. Morante. Mesoporous ceria–zirconia solid solutions as oxygen gas sensing material using high temperature hot plates. IEEE Semicond. Conf. 2 (2012) 277-280.
9. H. Yotou. Novel method for insertion of Pt / $CeZrO_2$ nanoparticles into mesoporous SBA–16 using hydrothermal treatment. Appl. Catal. A 458 (2013) 137-144.
10. J. A. Hedstrom, M. F. Toney, E. Huang, H. C. Kim, W. Volksen, T. Magbitang, R. D. Miller. Pore morphologies in disordered nanoporous thin films. Langmuir 20 (2004) 1535-1538.
11. M. Yashima, T. Hirose, S. Katano, Y. Suzuki, M. Kakihana, M. Yoshimura. Structural changes of ZrO_2 – CeO_2 solid solutions around the monoclinic–tetragonal phase boundary. Phys. Rev. B 51 (1995) 8018-8025.
12. C. V. Santilli, V. H. V. Sarmento, K. Dahmouche, S. H. Pulcinelli, A. F. Craievich. Effects of synthesis conditions on the nanostructure of hybrid sols produced by the hydrolytic condensation of (3-methacryloxypropyl) trimethoxysilane. J. Phys. Chemi. C 113 (2009) 14708-14714.
13. K. Hashimoto, N. Toukai, R. Hamada, S. Imamura. Reduction of Rh / CeO_2 – ZrO_2 with hydrogen. Caltal. Lett. 50 (1998) 193-198.
14. H. Rietveld. Line profiles of neutron powder-diffraction peaks for structure refinement. Acta Crystalog. 22 (1967) 151-152.
15. H. Rietveld. A profile refinement method for nuclear and magnetic structures. J. Appl. Crystalog. 2 (1969) 65-71.

16. Ed. R. Young. The Rietveld Method, International Union of Crystallography Monographs on Crystals, 5. 1995, Oxford: Oxford Univ. Press – IUC.
17. R. A. Young, A. Sakthivel, T. S. Moss, C. O. Paiva–Santos. DBWS – An upgrade of the DBWS*. Programs for Rietveld refinement with PC and mainframe computers, J. Appl. Crystalog. 2 (1995) 366-367.
18. E. Jansen, W. Schäfer, G. Will. *R*-values in analysis of powder diffraction data using Rietveld refinement. J. Appl. Cryst. 27 (1994) 492-496.
19. R. J. Hill, R. X. Fischer. Profile Agreement indices in Rietveld and pattern-fitting analysis. J. Appl. Crystalog. 23 (1990) 462-468.
20. A. Monshi, M. Foroughi, M. Monshi. Modified Scherrer equation to estimate more accurately nano-crystallite size using XRD. World J. Nano Sci. & Eng. 2 (2012) 154-160.
21. G. K. Williamson, W. H. Hall. X-ray line broadening from filed aluinium and wolfram. Acta Metllurgica 1 (1953) 22-31.
22. E. P. Barret et al. The determination of pore volume and area distributions in porous substances. I. Computations form nitrogen isotherms. J. Am. Chem. Soc. 73 (1951) 373-380.
23. S. Brunauer, P. H. Emmett, E. Teller. Adsorption of gases in multimolecular layers. J. Am. Chem. Soc. 60 (1938) 309-319.
24. M. Kruk, M. Jaroniec, A. Sayari. Application of large pore MCM – 41 molecular sieves to improve pore size analysis using nitrogen adsorption measurements. Langmuir 13 (1997) 6267-6273.
25. D. A. Clemente, E. Lucchini, S. Meriani, N. Furlan. Crystal structures of $CeO_2 – ZrO_2 – Ta_2O_5$ ternary system studied by Rietveld method. J. Eur. Ceram. Soc. 25 (2005) 1863-1876.
26. P. M. Abdala, M. C. A. Fantini, A. F. Craievich, D. G. Lamas. Crystallite size-dependent phases in nanocrystalline $ZrO_2 – Sc_2O_3$. Phys. Chem. Chem. Phys. 12 (2010) 2822-2829.
27. R. O. Fuentes. Synthesis of nanocrystalline $CeO_2 – ZrO_2$ solid solutions by a citrate complexation route: A thermomechanical and structural study. J. Phys. Chem. 113. (2009) 914-924.
28. S. Meriani, G. Spinolo. Powder data for metastable $Zr_xCe_{1-x}O_2$ ($x = 0.84$ to 0.40) solid solutions with tetragonal symmetry. Powd. Diffrac. 2 (1987) 255-256.
29. K. S. W. Sing. Reporting physisorption data for gas / solid systems with special Reference to the determination of surface area and porosity. Pure & Appl. Chem. 57 (1985) 603-619.

EFFECT OF PROPOLIS EXTRACT TO MORPHOLOGY OF ELECTROSPUN POLYURETHANE NANOFIBERS

R. Erdem [1], İ. Usta [2], E. Sancak [2], D. E. Koçak [2], M. Akalin [2]

[1] Serik Vocational School of Higher Education
Akdeniz University
Antalya, Turkey
erdemramazan@gmail.com
[2] Marmara University
Istanbul, Turkey

Accepted September 19, 2013

1. Introduction

Propolis is an adhesive natural resin collected by honeybees from various plants. It is used as building material for the hives as well as protective barrier against intruders. There are numerous studies reported that propolis is considered to be responsible for the low influence of bacteria and moulds within the hive [1]. Because of its beneficial biological properties such as: antibacterial, antifungal, antioxidant, anti-inflamatory, antitumor, hepato-protective, local anesthetic, immuno-stimulatory, antimutagenic, etc. propolis is widely preferred to be used for pharmaceutical purposes [2].

Recently, research about polymer-based composite materials has been significantly grown. In order to develop such composite materials, there are different techniques applied either by blending different polymers or by incorporating inorganic materials into polymers [3]. Electrospinning is a simple method for fabricating multifunctional nanocomposite materials. Electrospinning is a term used to describe a class of fiber forming in submicron range by applying electrostatic forces. The process is comprised of several operational components: (*i*) charging of the fluid, (*ii*) formation of the cone-jet, (*iii*) thinning of the instable jet in an electric field, and (*iv*) collection of the jet on a suitable collector [4].

Polyurethane (PU) is one of the most widely preferred polymers for the electrospinning processes due to its easy processability, good resistance to chemicals, microorganisms and abrasion, and satisfactory hydrolytic ability [5]. In addition, PU possesses good barrier properties and oxygen permeability. As a result of that it has been extensively studied for developing wound dressing materials [6].

There has been only limited study on antibacterial activity of Turkish propolis [7] (Uzel A. et. al.); furthermore, there was no report about the usage of it in electrospinning applications. The purpose of this study is to investigate the morphological characteristics of polyurethane / propolis blended electrospun nanofibers.

2. Materials and methods

PU which has a molecular weight of 155.000 g / mol was obtained from Nano FMG (Turkey). Ethanolic propolis extract (PRP) was acquired from Kale Natural (Turkey). All polymers and agents were used as received without any additional chemical processing.

2.1. Preparation of solutions

PU (8 % wt.) was dissolved in dimethylformamide (DMF) / tetrahydrofurane (THF) blended (60 / 40 %) solvent at 80 °C for 6 h. After the polymer completely dissolved, 0.05 g NaCl was added to the solution in order to increase the conductivity. Then, PRP extract was added into the PU solution at ratios of 1, 3, 5, and 10 % (w / w). Blended solutions were mixed by laboratory type magnetic stirrer (Stuart, SB 162) for 3 h at room temperature. pH values of each blended homogenous solutions were measured with pH indicator strips (Merck, Germany). The viscosities of the solutions were identified with a Brookfield Digital Viscometer by using s21 type spindle with a rotational speed of 30 rpm. The electrical conductivity of the blended solutions was also measured with a laboratory type conductivity meter (WTW, Cond 3110) under ambient atmosphere.

2.2. Electrospinning process

Electrospinning was performed in the laboratory spinning unit (NS 24, Nano FMG), which was designed in terms of a vertical working principle. Each solution was placed in a 3 ml syringe and sent to the drum collector (covered with aluminum foil) through a 20 gauge nozzle. The power supply (AC) was set up for a positive voltage of 35 kV. The flow rate of the solution was also determined by setting up the syringe pump at 1 – 1.55 ml / h. The rotational speed of the drum collector was 35 rpm and its distance was set to 15 cm (optimum distance based on preliminary tests) away from the nozzle. At the time of the experiments, relative humidity and temperature values ranged from 35 – 42 % RH and 26 – 31 °C.

2.3. SEM analysis of electrospun nanofibers

Electrospun fibers were characterized by Scanning Electron Microscopy (SEM, JSM–5910 LV from JEOL). First of all, fibers coated with a thin gold palladium (20 / 80 %) layer using a sputter coater from Polaron (SC 7620) and the morphology of the nanofibrous membranes were observed by SEM analysis at an accelerating voltage of 20 kV. The fiber diameter distribution was calculated over 50 fibers with the Image J (2011) software from the SEM images obtained at a magnification of 20000 and 50000 ×.

3. Results and discussion

3.1. Solution properties

Table 1 shows the viscosity; conductivity and pH values of PU and / or PRP based solutions. According to the data in the table, viscosity was decreased when the amount of PRP was increased in the solution. It could be attributed to less chain entanglements occurred between the molecules. On the other hand, increasing PRP content caused a significant increase in the solution's conductivity. One of the explanations considered for the increasing conductivity was about the growing activity of NaCl in the solution by introducing more amount of PRP to the solution. It was also recorded that raising the ratio of PRP content to the solutions increased the pH values. Viscosity of the solutions was declined significantly when more amount of propolis added into the solution. We hypothesized that propolis reduced the level of chain entanglements in the polymer solution which decreased the viscosity of the solution.

Table 1. Viscosity, conductivity and pH values of PU and / or PRP based solutions.

Polymer	Blend ratio, %	Viscosity, cP	Conductivity, μS / cm	pH
PU (8 wt. %)	100	393	37.5	7
PU (8 wt. %) / PRP	99 / 1	98	78	8 – 9
PU (8 wt. %) / PRP	99 / 3	62	136	8 – 9
PU (8 wt. %) / PRP	99 / 5	60	247	9
PU (8 wt. %) / PRP	90 / 10	56	420	9

3.2. Morphology of the nanofibers

Figure 1 presents the SEM images of various ratios of PU / PRP (100, 99 / 1, 97 / 3, 95 / 5, 90 / 10 %) based electrospun nanofibers. It can be observed that these randomly oriented electrospun nanofibers exhibited bead-free, smooth surface with almost uniform diameters along their lengths except the nanofibers electrospun from 90 / 10 % (PU / PRP) blend. The solution including 10 % PRP was hardly electrospun and the nanofibers obtained through electrospinning were non-uniform, also there were plenty of beads occurred. This change in morphology can be explained by the low volatility of the propolis extract. So it becomes increasingly difficult for the electrospun material to completely dry before it hits the collector due to the presence of less volatile PRP. Furthermore, the adhesive property of PRP could trigger bead formations as well as providing the connection of fibers to each other at the points where they were crossing [8].

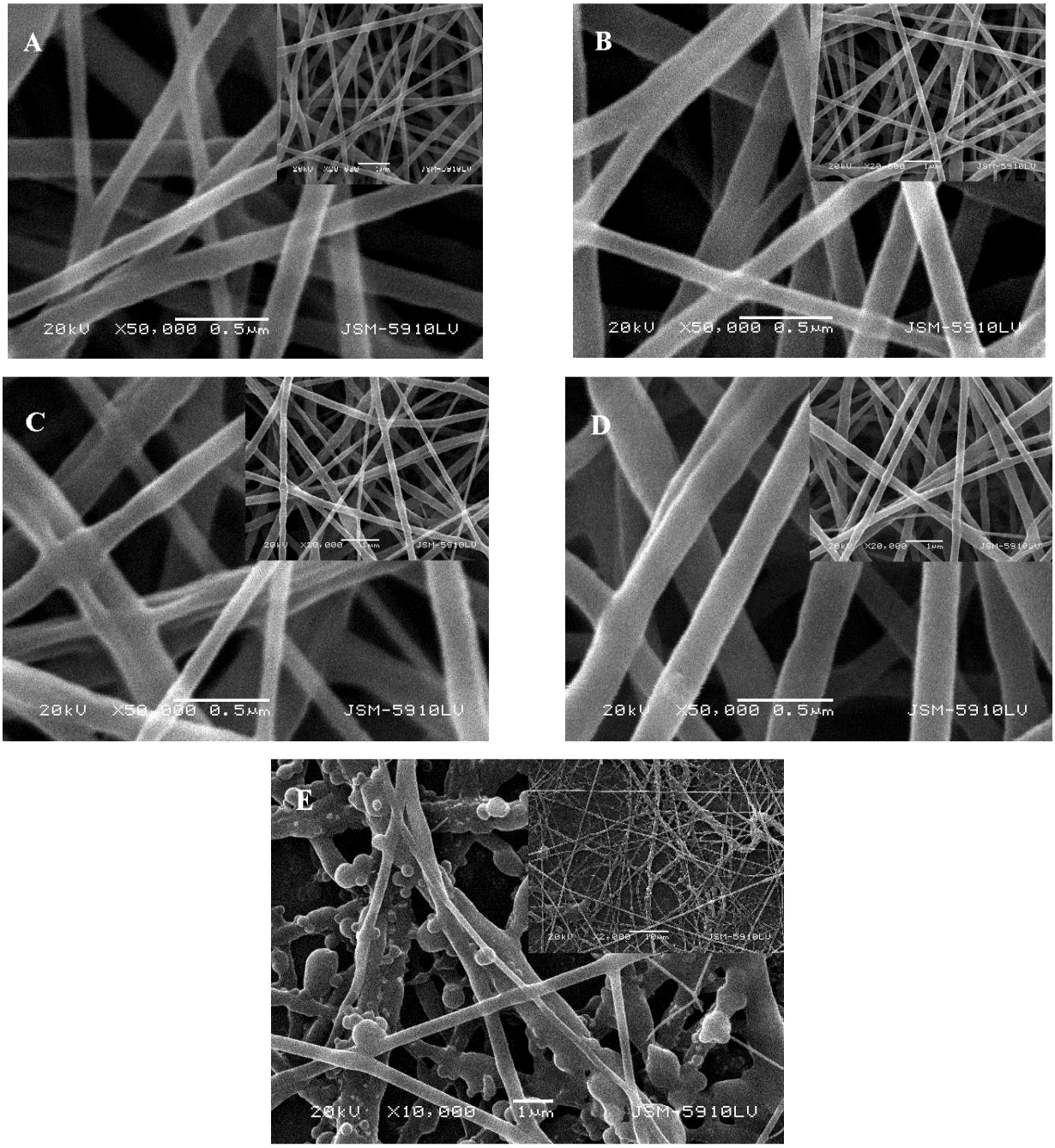

Figure 1. SEM images of various ratios of PU / PRP based electrospun Nanofibers: A – PU (100 %), B – PU / PRP (99 / 1 %), C – PU / PRP (97 / 3 %), D – PU / PRP (95 / 5 %), and E – PU / PRP (90 / 10 %).

The fiber diameters of thenanofibrous membranes were determined to be in the range between 147 ± 48 and 437 ± 249 nm, respectively (**Figure 2**). From the results, it could be stated that solution viscosity and conductivity played an important role to obtain the fiber diameter in a wide range. It is known that increase in solution viscosity also increases the diameter of electrospun nanofibers. Also, increase in solution conductivity decreases the diameter of electrospun nanofibers. Enhancing PRP amount in the blend caused thinner fibers until the PRP content reached to 10 %. Presumably, due to the adhesivity and low volatility of PRP declined the degree of electrospinability of the blended solution and thicker as well as non-uniform fibers were fabricated.

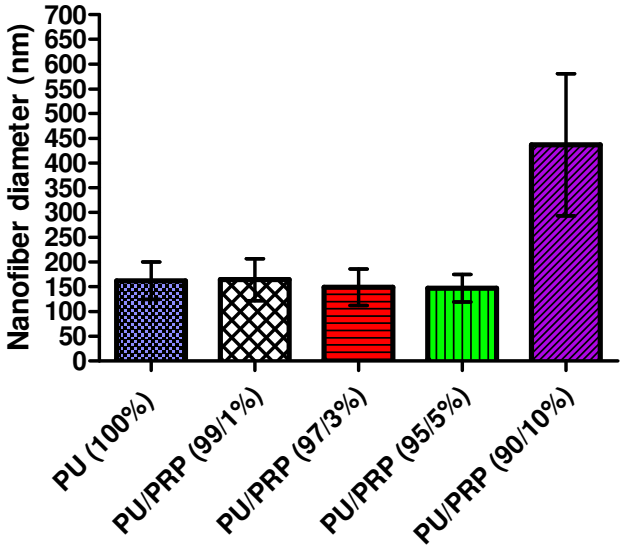

Figure 2. Nanofiber diameters: PU (100 %) – 162 ± 75, PU / PRP (99 / 1 %) – 164 ± 73, PU / PRP (97 / 3 %) – 149 ± 64, PU / PRP (95 / 5 %) – 147 ± 48, and PU / PRP (90 / 10 %) – 437 ± 249 nm.

4. Conclusions

Propolis blended polyurethane based nanofibrous membranes were successfully fabricated by electrospinning technique. Except the blend solution including 10 % wt. propolis, smooth and defect-free nanofibers were fabricated from all blended solutions. The diameters of nanofibers were ranged from 162 ± 75 to 437 ± 249 nm. Our study showed that propolis added polyurethane nanofibrous membranes can be fabricated. By performing further biological evaluations such as; antimicrobial tests, cytotoxicity tests, animal model tests, etc., novel nanofibrous materials could be developed for especially wound dressing applications.

Acknowledgements

The authors acknowledge the financial support of this work by BAPKO (Scientific Research Projects Department of Marmara University, Turkey) with the Project code: FEN–D–100713–0339.

References

1. V. S. Bankova, S. L. de Castro, M. C. Marcucci. Propolis: Recent advances in chemistry and plant origin. Apidologie 31 (2000) 3-15.
2. N. Kalogeropoulos, S. J. Kontelesb, E. Troullidoua, I. Mourtzinosa, V. T. Karathanosa. Chemical composition, antioxidant activity and antimicrobial properties of propolis extracts from Greece and Cyprus. Food Chem. 116 (2009) 452-461.

3. L. D. Tijing, A. Amarjargal, Zh. Jiang, M. T. G. Ruelo, Ch.-H. Park, H. R. Pant, D.-W. Kim, D. H. Lee, Ch. S. Kim. Antibacterial tourmaline nanoparticles / polyurethane hybrid mat decorated with silver nanoparticles prepared by electrospinning and UV photoreduction. Curr. Appl. Phys. 13 (2013) 205-210.
4. G. C. Rutledge, S. V. Fridrikh. Formation of fibers by electrospinning. Adv. Drug Delivery Rev. 59 (2007) 1384-1391.
5. L. D. Tijing, W. Choi, Zh. Jiang, A. Amarjargal, Ch.-H. Park, H. R. Pant, I.-T. Im, Ch. S. Kim. Two-nozzle electrospinning of (MWNT / PU) / PU nanofibrous composite mat with improved mechanical and thermal properties. Curr. Appl. Phys. 13 (2013) 1-9.
6. R. Wynne, M. Botti, H. Stedman, L. Holsworth, M. Harinos, O. Flavell, C. Manterfield. Effect of three wound dressings on infection, healing comfort, and cost in patients with sternotomy wounds: A randomized trial. Chest. 125 (2004) 43-49.
7. A. Uzel, K. Sorkun, Ö. Önçağ, D. Çoğulu, Ö. Gençay, B. Salïh. Chemical compositions and antimicrobial activities of four different Anatolian propolis samples. Microbiol. Res. 160 (2005) 189-195.
8. A. R. Unnithan, P. B. Tirupathi Pichiah, G. Gnanasekaran, K. Seenivasan, N. Barakat, Y.-S. Cha, Ch.-H. Jung. Emu oil-based electrospun nanofibrous scaffolds for wound skin tissue engineering. Colloids Surf. A 415 (2012) 454-460.

Ge- AND In-BASED ONE-DIMENSIONAL NANOSTRUCTURES: SELF-CATALYTIC GROWTH

D. Jishiashvili, L. Chkhartishvili, L. Kiria, Z. Shiolashvili,
N. Makhatadze, A. Jishiashvili, V. Gobronidze

Institute of Cybernetics
Georgian Technical University
Tbilisi, Georgia
d_jishiashvili@gtu.ge

Accepted September 19, 2013

1. Introduction

The development of new technologies for the synthesis of innovative one-dimensional (1D) materials is a key issue for fabricating advanced nanodevices, which in most cases have no macro-sized analogues. Recently we have reported about the growth of InP-nanowires and core-shell nanostructures using the hydrazine (N_2H_4) vapour diluted with 3 mol. % H_2O [1].

Hydrazine is active compound, which finds wide range of applications. It is used as a rocket fuel, airbag inflator, chemical blowing agent, textile dye, pharmaceutical intermediates, etc. [2 – 9]. Recently, hydrazine was used for the control of graphene properties by reducing it from the graphene oxide [10 – 12]. Graphene oxide is a single layer, containing carbon, oxygen, OH and COOH groups. The stack of graphene oxide layers forms the 3-dimensional graphite oxide. To date, the temporal evolution of graphene oxide chemistry during hydrazine reduction remains vague indicating its complicated nature. Besides the nitrogen and oxygen precursors (NH_3, NH_2, NH, N, N_2, and H_2O) the products of hydrazine pyrolysis contain also hydrogen, which serves as a reducing agent in sophisticated chemical processes [13].

The purpose of this study was to investigate the self-catalytic vapor–liquid–solid (VLS) growth of germanium- and indium-based 1D nanomaterials during the annealing process in hydrazine vapour. The choice of Ge and In as model materials for the study of hydrazine annealing effects is based on the fact that the former is the popular group IV semiconductor material with increasing importance in application, while the latter represents the popular group III metal, which forms important nitride and oxide nanostructures with a wide range of applications including ultrasensitive gas sensors [14, 15].

2. Experimental

The nanowires (NWs) were grown in the vertical quartz reactor, which was first evacuated down to $5.3 \cdot 10^{-3}$ Pa and then filled with N_2H_4 vapor, which was containing 3 mol. % H_2O. The reactor was then isolated from the vacuum system and the saturated pressure of N_2H_4 ($\sim 1.3 \cdot 10^3$ Pa) was established in the chamber at the room temperature. The source materials

(unpolished, (111) oriented, 2 mm thick Ge or a piece of metallic In with the mass of ~ 0.8 g) were placed at the flat bottom of the reactor (the hot zone) and the substrates (polished Si, glass and sapphire) were placed on a tubular quartz spacer at 0.5 – 2.0 cm above the source (the cold zone). The external furnace was attached to the bottom of the reactor. The sources were annealed in the temperature range of 400 – 580 °C. The substrate was subsequently heated due to radiative and convective heating from below, and its temperature was determined by the source temperature and the distance from the source. The typical growth process lasted for 40 – 60 min.

The morphology and structure of NWs were studied using FEI Quanta FEG 600 scanning electron microscope (SEM) and Philips CM 200 FEG transmission electron microscope (TEM). XRD data were taken on a Shimadzu XRD–6000 diffractometer.

3. Results and discussion

The growth of nanowires proceeds through the transport of molecules to the growth front and subsequent solidification. In our experiments we used two solid sources: Ge and In. Both materials have negligible vapor pressure in the selected temperature range (460 – 520 °C) and their direct thermal evaporation should be eliminated. As it was mentioned, we used the hydrazine containing 3 mol. % water. After the pyrolysis the ambient contains hydrogen, water and different nitrogen precursors. The hydrides of Ge and In readily dissociate at this temperatures and thus they will not participate in the growth processes. The remaining water plays the key role in the formation of the flux of molecules. If the water forms stoichiomtric oxides (GeO_2 and In_2O_3), then this stable oxides with high melting points (GeO_2 – 1230 °C [16] and In_2O_3 – 1920 °C [17]) will remain on the surface. However, the amount of water in hydrazine is insufficient to produce stoichiometric oxides and the water forms the volatile sub-oxides (GeO and In_2O). The whole mass transport in the growth process was accomplished by these sub-oxide molecules, which readily sublimate in the selected temperature range. In this paper we shall consider the structure and some details of the formation of nanowires, grown by the annealing of Ge and In sources in hydrazine vapor.

The Ge_3N_4 nanowires begin to grow on Ge source at temperatures exceeding 480 °C. **Figures 1a** and **b** represent the SEM images of Ge source, which was annealed during 1 h in the water-diluted hydrazine vapor at 510 °C. The nanowires were growing on the Ge source surface and simultaneously on the Si substrate located on the quartz spacer at 0.5 cm above the source. Near the edge of the Ge source, which was screened by the quartz spacer, the deep triangular etch pits are clearly seen (**Figure 1a**). The etch pits of these shapes are characteristic features of Ge (111) surface etching [18]. The results presented in **Figures 1a** and **b** prove that in our experiments the water molecules are actively eroding Ge, forming the intensive flux of volatile monoxide molecules, which then serve as precursors for the growth of nitride nanowires. A thick mat of nanowires was formed on the source and the length of NWs was in the range of several micrometers.

The TEM images of the same nanowires are presented in **Figures 1c – e**. Selected area electron diffraction pattern is presented in **Figure 1f** and it proves a high crystallinity of Ge_3N_4 NWs. The measured diameters of NWs were ranging from 80 to 7 nm. The catalyst droplets are clearly seen at the nanowire tips, confirming the growth of NWs through the VLS mechanism.

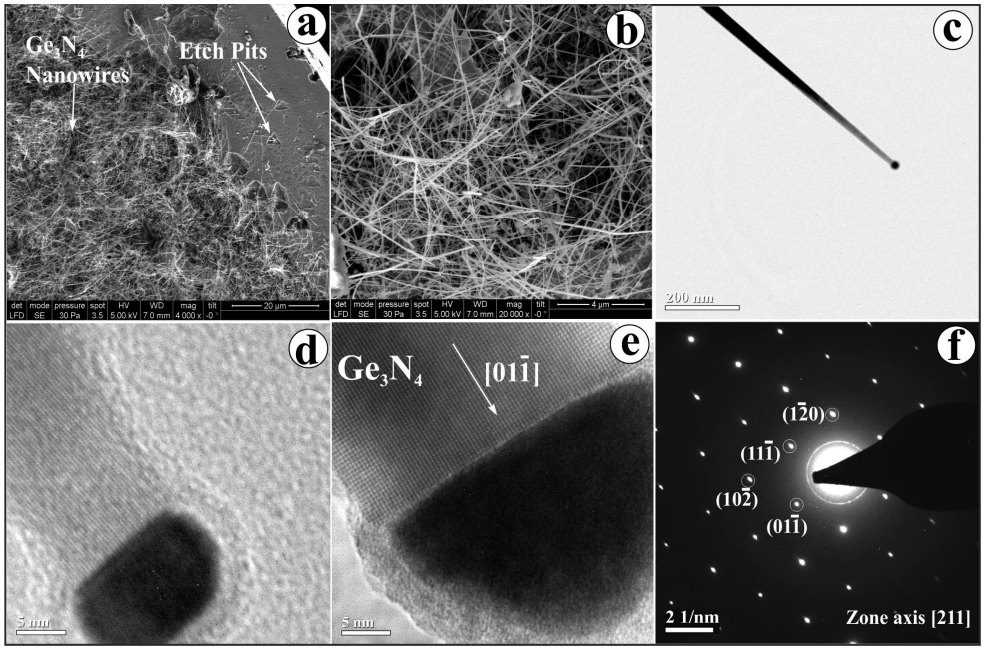

Figure 1. SEM images of Ge_3N_4 NWs grown at 510 °C. The triangular etch pits were formed after erosion of Ge by H_2O molecules (a); the enlarged view of NWs (b); general TEM view of Ge_3N_4 NWs grown by VLS mechanism (c, d); HRTEM image of the catalyst tip and α-Ge_3N_4 nanowire grown in the direction perpendicular to (01–1) plane (e); selected area electron diffraction (SAED) pattern of α-Ge_3N_4 nanowire (f).

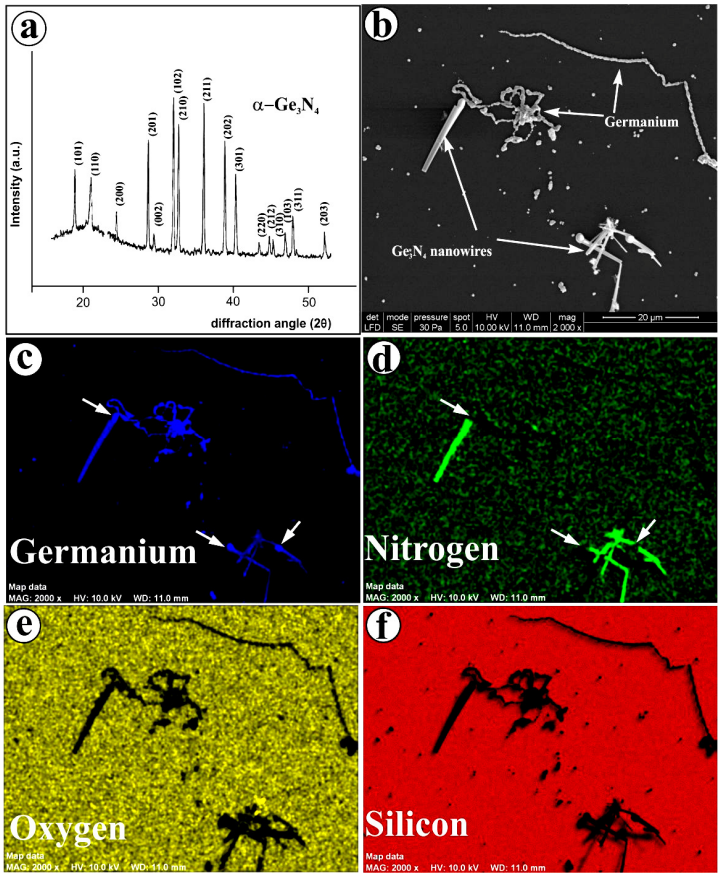

Figure 2. XRD pattern of α-Ge_3N_4 NWs (a); SEM image of nanowires grown on the Si substrate (b); elemental mapping of nanomaterials depicted in **Figure 2b** (c – f).

In **Figure 2c** the plain growth front is clearly defined. The bright shell is seen around the dark catalyst droplet. According to Auger analysis (the Auger spectrum is not presented), the only elements existing on the source surface are germanium, nitrogen and oxygen. We suppose that at the first stage of growth the volatile GeO molecules are formed. A part of them forms small $(GeO)_n$ clusters and re-adsorbs, just as it happens in the well known oxide-assisted growth of Si nanowires [19]. The sub-oxides may have sufficiently low melting temperature [20, 21], and the $(GeO)_n$ clusters may form liquid droplets on the Ge source surface. The $(GeO)_n$ cluster is then enriched with Ge which is formed due to the reaction $2\,GeO = Ge + GeO_2$ ($\Delta G = -218$ kJ / mol at 500 °C). The molten catalyst may be also enriched with Ge, diffusing from the solid source through the liquid-solid interface, or due to the reduction of Ge from GeO_x in the presence of hydrogen atoms. The nitrogen precursors impinging on the Ge droplet are diffusing through it. As a result of this oversaturation the solid Ge_3N_4 begins to precipitate from the catalyst droplet forming the nanowire. We suppose that the catalyst in **Figure 1e** mainly consists of Ge. It also contains oxygen, which is accumulated mainly in the shell. The dark core and bright shell of the catalyst tip in **Figure 1e** represents the so called *z*-contrast indicating that the core consists of the atoms with high atomic number *z* (probably Ge), while the mean atomic number of a shell is low (probably GeO_x) and it appears as a light layer around the dark core. The trunk of NW consists of α-Ge_3N_4 as it is confirmed by TEM and powder XRD analysis presented in **Figure 2a**. It should be noted that more than 30 nanowires were analyzed by TEM method and all NWs exhibited the α-Ge_3N_4 structure. It should be also mentioned that from the available two publications describing the growth of 1D Ge_3N_4 nanomaterials at 850 °C, only α-phase nanowires were synthesized in one case as reported in [22] and α- and β- Ge_3N_4 nanobelts were produced in another case as reported in [23]. These results confirm that the stability of α-Ge_3N_4 nanowires is quite high. The temperatures in our processes were at least by 350-370°C lower compared to those used in [22] and [23].

The nanowires which were growing on the Si substrate located above the Ge source had significantly larger size in spite of the fact that their growth temperature was by 25 °C lower than the Ge source temperature. The diameters of tips vary in the range of micrometers. The length of NWs reaches ~ 17 μm. They are slightly tapered with increased diameters near the catalyst tip. This indicates that the flow GeO molecule to the substrate (which is placed in the cold zone of the reactor) increases with time. It simultaneously increases the size of catalyst droplet and the diameter of the growing nanowire, causing its tapering. Such large NWs cannot be analyzed by TEM because the electron beam will not pass through them. We used the energy dispersive X-ray (EDX) analysis and elemental mapping to study the composition of nanowires.

Figure 2b presents the SEM image of nanomaterials grown on Si substrate. Besides the nanowires with catalyst droplet at the tip, some other chain-like structures and micrometer-sized particles are observed, which are scattered all over the surface The elemental mapping images in **Figures 2c – f** reveal that Ge presents in NWs, their tips and in most of chains and particles (**Figure 2c**). Three tips in this figure are marked with white arrows. **Figure 2d** shows the distribution of nitrogen, which is concentrated only in the trunks of NWs. Three white arrows in this image represent the places where the Ge tips are located in **Figure 2c**. However, these places have the dark color of the background indicating that the tips do not contain nitrogen and consist mainly of Ge. The images representing the distribution of oxygen and Si (**Figures 2e** and **f**) show only the shadows of nanomaterials confirming the absence of these

elements in nanostructures. The pure color of Si surface proves that in spite of a dense flux of GeO molecules arriving on the Si, they do not form any condensed thin film or layer on its surface. It means that adsorbed GeO molecules have enough energy to migrate over the surface, find sites with minimum free energy and incorporate in the growing structure. The partial readsorption of GeO may also take place. The most of the chain-like structures and particles consist solely of Ge indicating that germanium is effectively reduced from its oxides by hydrogen, which is a final stabile product of hydrazine decomposition.

The results of these initial experiments confirmed that in spite of the presence of water molecules (and hence the oxygen precursors) in the hydrazine vapor, the pure α-Ge_3N_4 was produced in both zones i.e. on the Ge source and on the Si substrate.

For producing the In-based nanostructures the same experimental setup was used but the Ge source was substituted with a piece of metallic In. In contrast to Ge_3N_4 nanowires, the In-based nanowires were growing only on the substrate which was placed in the cold zone of a reactor.

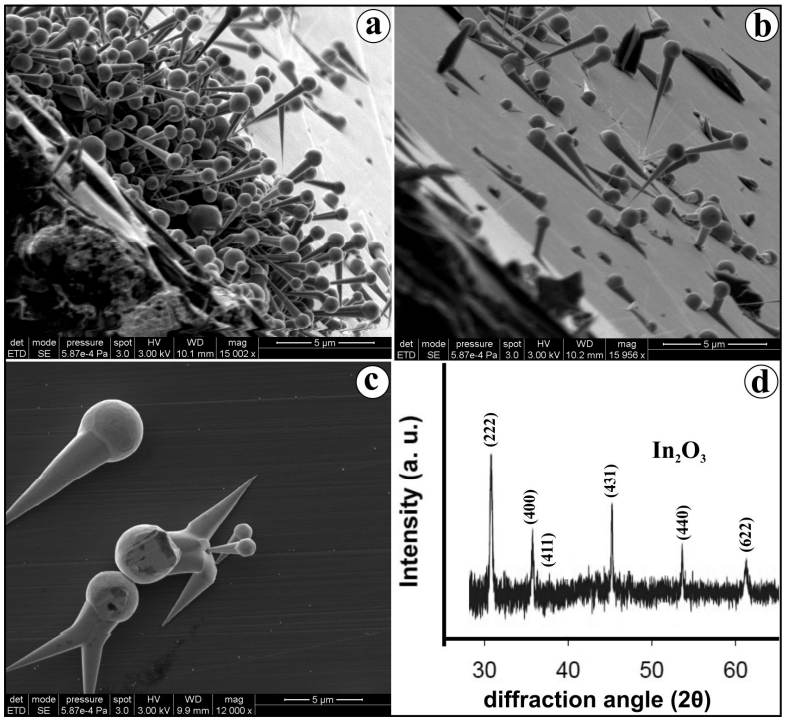

Figure 3. SEM images of In-based nanowires (a – c); XRD pattern of In-based nanowires (d).

The SEM images of In-based nanowires grown on Si substrate at 460 °C are presented in **Figures 3a – c**. The nanowires are tapered with micrometer range diameters near the tip and tens of nanometer near the opposite end. The nanowires have the average length of 5 μm. The catalyst droplets are also very large reaching micrometer sizes. These large tips are considered to be the heavy burden for nanowires which are connected with Si through a thin tapered end with the diameter of ~ 80 nm. Some of the NWs in **Figure 3a** and **b** are still attached to the Si substrate protruding above it. However some of them are broken NWs, which fell on the surface, and their tips are flattened indicating that the nanowire was growing from the liquid catalyst when its thin stem was broken. After hitting the Si surface a part of a catalyst flattens, as it can be seen in **Figures 3a** and **b**.

Figure 3c shows different morphological defects taking place in nanowires grown at slightly elevated temperature (480 °C). The nanowires in the bottom left side of **Figure 3c** were growing side by side. The sizes of their catalysts were also growing with time. At a certain moment the two catalysts merged into one forming the nanowire depicted in **Figure 3c**. The increased temperature leads to the increase in the degree of tapering. This proves that the increase of a flux of molecules cause tapering of NWs, because the increase of a flux of In_2O_3 at elevated temperatures results in a more abrupt tapering of NWs

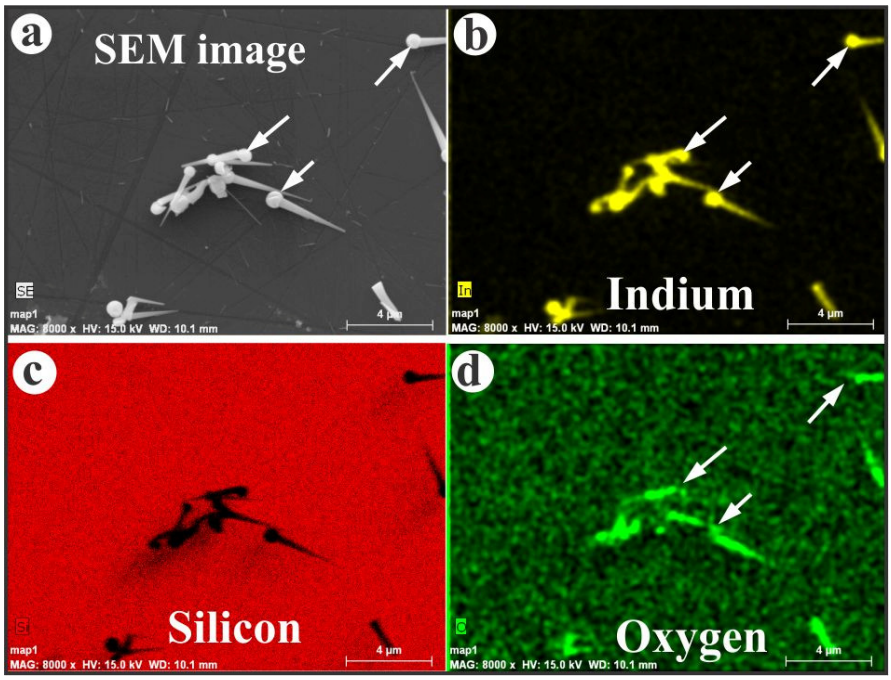

Figure 4. SEM image of VLS grown In_2O_3 nanowires (a);
elemenrtal mapping of nanowires shown in **Figure 4a** (b – d).

The nanowires comprise crystalline In_2O_3 as it is evidenced by the XRD pattern shown in **Figure 3d**. The information on the composition of NWs was obtained also from their elemental maps presented in **Figures 4b – d**. Three arrows in the SEM picture (**Figure 4a**) are indicating the catalyst tips. The tips disappear when the image was obtained in pseudo-colors of oxygen, which exists only in the trunks of NWs. It is clear, that catalyst consists of nearly pure In, while the trunk is formed from the In_2O_3.

To explain the exceptional growth of In_2O_3 nanowires in the presence of active nitrogen precursors we have analyzed the formation of In_2O_3 at 500 °C through the chemical reactions of In_2O with O_2 and H_2O, and compared them with the formation of InN using the most active radicals - NH and NH_2. The maximum negative value of the Gibbs free energy was obtained for the synthesis of InN from NH and NH_2 precursors (– 697 and – 409 kJ / mol, respectively). The formation of In_2O_3 from In_2O using O_2 or H_2O has far less negative energies: 139 and 41 kJ / mol. respectively. This means that the synthesis of InN is energetically favorable. However, the kinetic factors are often more important than thermodynamics in the non-equilibrium systems [24]. We suppose that the high rate of the oxidation reaction in comparison with the rate of InN formation causes the exceptional growth of In_2O_3 nanowires in our experiments. More detailed thermodynamic analysis is needed to clear this subject.

4. Conclusions

We have grown the Ge_3N_4 and In_2O_3 nanowires by annealing Ge and In solid sources in the vapour of hydrazine diluted with 3 mol. % H_2O. The ambient was containing nitrogen precursors and water as a source of oxygen. The whole mass transfer in the growth processes was accomplished through the formation of volatile sub-oxsides (GeO and In_2O). Both nanowires grew through the VLS process using Ge and In self-catalyst droplets. After annealing of Ge source at 490 – 510 °C only crystalline α-Ge_3N_4 NWs were produced on the Ge source and Si substrate surfaces. Beside nitride nanowires the Ge particle and chain-like Ge microstructures were also formed on the substrate, indicating that a part of GeO was reduced by hydrogen. The flux of GeO molecules to the Si substrate was increasing with time, causing the different directions of tapering for Ge_3N_4 nanowires grown on source and Si substrate. When In was annealed in the range of 460 – 480 °C the In_2O_3 NWs were produced only on the surface of Si substrate. They were growing from the In self-catalyst droplets and had lengths of several micrometres. They were strongly tapered and had micrometer range diameters near the catalysts and several tens of nanometres at the opposite end. At elevated temperatures the flux of In_2O molecules was also increased, causing more abrupt tapering of In_2O_3 nanowires.

References

1. G. R. Patzke, R. Kontic, Z. Shiolashvili, N. Makhatadze, D. Jishiashvili. Hydrazine-assisted formation of indium phosphide (InP)-based nanowires and core–shell composites. Materials 6 (2013) 85-100.
2. J. W. Akkerman. Hydrazine monopropellant reciprocating engine development. J. Eng. Ind. 101 (1979) 456-462.
3. S. S. Puranik, H. M. Joshi, S. B. Ogale, K. M. Paknikar. Hydrazine based facile synthesis and ordered assembly of metal nanoparticles (Au, Ag) on a bacterial surface layer protein template. J. Nanosci. & Nanotechnol. 8 (2008) 3565-3569.
4. J. T. Robinson, F. K. Perkins, E. S. Snow, Zh. Wei, P. E. Sheehan. Reduced graphene oxide molecular sensors. Nano Lett. 8 (2008) 3137-3140.
5. L. Y. Zhang, J. Wang, L. M. Wei, P. Liu, H. Wei, Y. F. Zhang. Synthesis of Ni nanowires via a hydrazine reduction route in aqueous ethanol solutions assisted by external magnetic fields. Nano Micro Lett. 1 (2009) 49-52.
6. T. K. Todorov, K. B. Reuter, D. B. Mitzi. High-efficiency solar cell with Earth-abundant liquid-processed absorber. Adv. Mater. 22 (2010) E156-E159.
7. E. Granot, B. Filanovsky, I. Presman, I. Kuras, F. Patolsky. Hydrazine / air direct-liquid fuel cell based on nanostructured copper anodes. J. Power Sources 204 (2012) 116-121.
8. J. T. Han, J. I. Jang, B. H. Jeong, S. Y. Jeong, H. J. Jeong, G.-W. Lee. In-situ synthesis of hydrazine in graphene oxide suspension and stable dispersion of spontaneously reduced graphene oxide assisted by hexamethyldisilazane. Nanotechnol. 1 (2013) 220-223.
9. S. E. F. Kleijn, B. Serrano–Bou, A. I. Yanson, M. T. M. Koper. Influence of hydrazine-induced aggregation on the electrochemical detection of platinum nanoparticles. Langmuir 29 (2013) 2054-2064.

10. S. Park, J. An, J. R. Potts, A. Velamakanni, Sh. M. R. S. Ruoff. Hydrazine-reduction of graphite- and graphene oxide. Carbon 49 (2011) 3019-3023.
11. P. G. Ren, D. X. Yan, X. Ji, T. Chen, Z. M. Li. Temperature dependence of graphene oxide reduced by hydrazine hydrate. Nanotechnol. 22 (2011) 5705-5713.
12. R. Wang, Y. Wang, Ch. Xu, J. Sun, L. Gaoa. Facile one-step hydrazine-assisted solvothermal synthesis of nitrogen-doped reduced graphene oxide: reduction effect and mechanisms. RSC Adv. 3 (2013) 1194-1200.
13. D. Dirtu, L. Odochian, A. Pui, I. Humelnicu. Thermal decomposition of ammonia. N_2H_4 – an intermediate reaction product. Cent. Eur. J. Chem. 4 (2006) 666-673.
14. S. J. Kim, I. S. Hwang, C. Na, I. D. Kim, Y. Kang, J. H. Lee. Ultrasensitive and selective C_2H_5OH sensors using Rh-loaded In_2O_3 hollow spheres. J. Mater. Chem. 21 (2011) 18560-18567.
15. P. Sowti Khiabani, E. Marzbanrad, H. Hassani, B. Raissi. Fast response NO_2 gas sensor based on In_2O_3 nanoparticles. J. Am. Ceram. Soc. 96 (2013) 2493-2498.
16. D. Schmeisser, R. D. Schnell, A. Bogen, F. J. Himpsel, D. Rieger, G. Landgren, J. F. Morar. Surface oxidation states of germanium. Surf. Sci. 177 (1986) 455-465.
17. Zh. W. Pan, Z. R. Dai, Z. L. Wang. Nanobelts of semiconducting oxides. Science 291 (2001) 1947-1949.
18. M. Grundmann. The Physics of Semiconductors: An Introduction Including Nanophysics and Applications. 2010, Berlin –Heidelberg: Springer Verlag.
19. R. Q. Zhang, Y. Lifshitz, S. T. Lee. Oxide-assisted growth of semiconducting nanowires. Adv. Mater. 15 (2003) 635-640.
20. S. N. Noor Mohammad. Analysis of the vapor-liquid-solid mechanism for nanowire growth and a model for this mechanism. Nano Lett. 8 (2008) 1532-1538.
21. G. Xu, Z. Li, J. Baca, J. Wu. Probing nucleation mechanism of self-catalyzed InN nanostructures. Nanoscale Res. Lett. 5 (2009) 7-13.
22. T. Xie, Zh. Jiang, G. Wu, X. Fang, G. Li, L. Zhang. Characterization and growth mechanism of germanium nitride nanowires prepared by an oxide-assisted method. J. Crys. Growth 283 (2005) 286-290.
23. Y. H. Gao, Y. Bando, T. Sato. Nanobelts of the dielectric material Ge_3N_4. Appl. Phys. Lett. 79 (2001) 4565-4567.
24. J. W. Mullin. Crystallization. 2001, Woburn: Reed Edu. & Prof. Publ. Ltd.

JET MILLING AND THERMAL PROCESSING OF ARGENTUM JAROSITE NANOPARTICLES FOR SILVER RECYCLING

V. Leshchynsky [1], H. Weinert [1], J. Chojnacka [1],
T. Wisniewski [1], C. A. Martínez Pérez [2], Sh. Tilvaldyev [2]

[1] Metal Forming Institute
Poznan, Poland
leshchynsky@inop.poznan.pl
[2] University of Juarez
Chihuahua, Mexico

Accepted September 19, 2013

1. Introduction

Large quantities of industrial wastes are accumulating in many countries and cannot be disposed without prior special processing. In particular, waste products from the mining and metal refining industries, sewage sludges and residues from power station and waste incineration plants can contain heavy metals at high concentrations. For this reason, they cannot be disposed into wastewaters plant treatment and must be subjected to special treatments in order to reduce metal contents. Besides, some waste products containing high concentration of strategic metals (copper, zinc, lead, chromium, etc.), may be regarded as a secondary source of metals. European and American countries greatly suffer from necessity of disposal of polymetallic sulfide waste containing gold, silver, and its treatment is of great importance.

Typically, the tailings, which are resulted from the ore processing are waste solids arising from flotation, leaching and bioleaching operations. In flotation process, the raw material (for example, sphalerite concentrate) is calcined and then solubilised into sulphuric acid solution and eventually sequestered from the electrolyte by electrowinning [1]. Silver and gold are part of the ore refinery residue and flotation tailings. Mineralogical results showed that composite tailings are refractory in nature. The main aims of the following operations are decomposition of jarosite minerals by leaching with high productivity and effectiveness. For these reasons the mechanochemical treatment (mechanical activation) is applied [2]. The principles and technology of powder mechanical activation during the powder milling and cold spraying are observed in [3]. Based on these data the main technology approach of enhancing gold and silver recovery from the tailings consists of firstly decomposing the jarosite minerals by mechanical activation (milling nano- and microparticles) [4] and then secondly by thermal oxidation. The mechanical activation and thermal oxidation of residue compounds alleviate and accelerate the following leaching of gold and silver. Additionally it allows to apply thiourea or thiosulphate leaching instead of cyanide one. Thus the aim of this paper is an experimental study of the mechanical activation-thermal oxidation processing of jarosite containing waste to enhance the following Silver leaching process. Usually the various jarosite compound oxidation technologies

such as ozone oxidation [5] are being applied. However some substantial drawbacks of this wet technology are obvious. So, development of thermal oxidation of mechanically activated jarosite compounds is believed to optimize the jarosite recycling technology.

2. Experimental procedure

Jarosite-type waste (from Penoles, Mexico) was characterised using SEM, EDS and XRD analysis. XRD analysis showed the presence of two main phases: Jarosite AM3(OH)6(SO4)2 and gypsum $CaSO_4 \cdot 2\,H_2O$ (**Figure 1a**). SEM–EDAX analysis showed the content of oxygen, iron and sulphur (**Figure 1b**) that are the most important elements for further treatment of this waste.

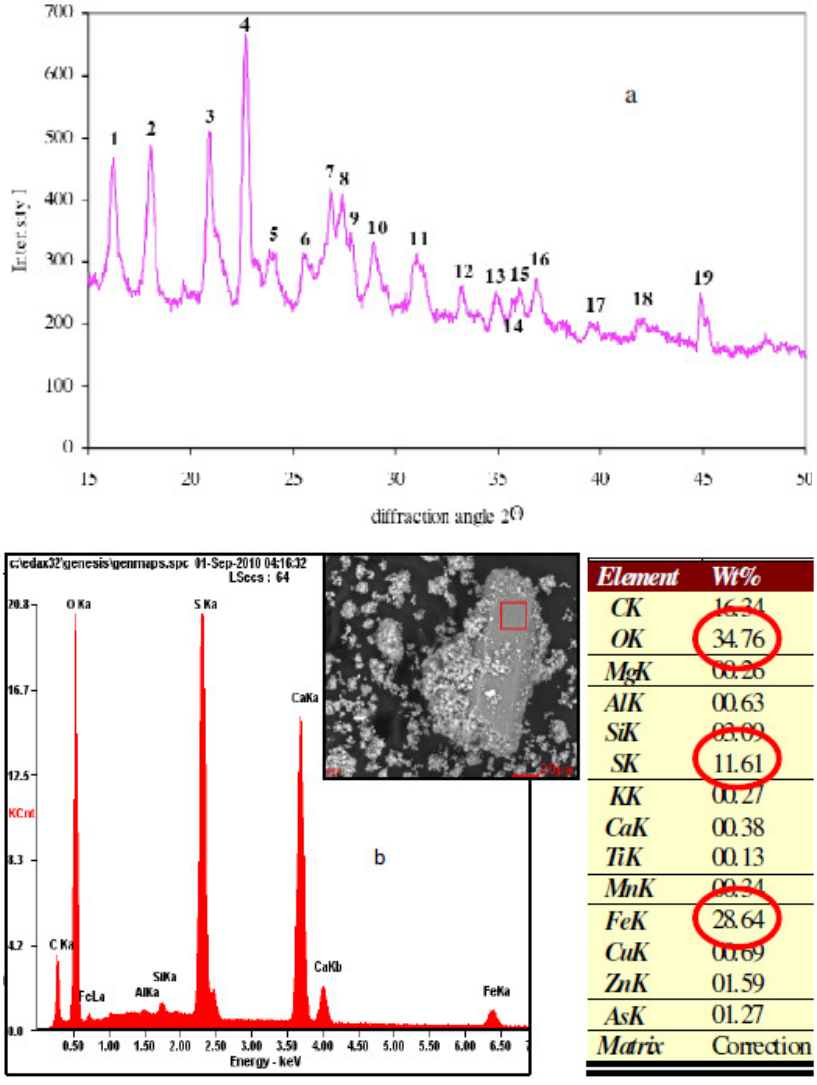

Figure 1. Composition of jarosite-type waste (Penoles, Mexico): (a) XRD results and (b) SEM–EDS.

The oxidation tests at different temperatures (200 – 600 °C) and time (5 – 40 min) were performed with jarosite waste in a laboratory tube furnace and fluidized bed reactor (**Figure 2a**). Materials after oxidation were studied using SEM and chemical analysis (**Figure 2b**). The heating tests were carried out in the microwave oven (1150 W, 120 V) and in the laboratory resistance furnace Thermo Scientific Thermolyne, model # F–47925–80 (1000 W, 120V, 8.3 A).

Elements	I batch	II batch	I batch + grinding + fluidzed	I batch+grinding + fluidzed
O	48,8	47,1	37,3	40,1
Fe	27,1	25,7	34,8	31,6
S	11,6	15,3	10,3	11,8
Ca	1,32	1,05	4,66	4,33
Si	3,45	3,46	3,29	2,86
Pb	2,19	2,23	3,06	2,76
Zn	1,65	1,65	2,01	1,81
Na	0,74	0,71	1,17	1,21
As	0,51	0,68	0,86	0,80
Ag	0,05	0,03	0,06	0,07

Figure 2. Flidized bed reactor (a) and composition of processed jarosite (b).

The variables studied were: incident microwave power and processing time for the Microwave oven and processing time and temperature – for the furnace. 22-times 100 g samples were placed in ceramic boats and oxidized (roasted) inside of the heating camera. The furnace was preheated to the appropriate temperature before the samples were introduced. The oxidation process was performed for the different range of the temperature (200 – 550 °C) with processing time of 5, 10 and 15 minutes for the each range of temperature (**Table 1**).

Table 1. Matrix for the oxidizing process in the furnace (J–0 – the origin (basis) material before the oxidizing process).

Temperature	5 min	10 min	15 min
200 °C	J–1	J–2	J–3
300 °C	J–4	J–5	J–6
350 °C	J–7	J–8	J–9
400 °C	J–10	J–11	J–12
450 °C	J–13	J–14	J–15
500 °C	J–16	J–17	J–18
550 °C	J–19	J–20	J–21

Microwave heating (oxidizing) test were conducted on 6.2 g samples of the jarosite for 5 min for the initial material (J–0 + M), and on several samples of the material, previously oxidised in the furnace for 5 min in different range of the temperature (**Table 2**).

Table 2. Matrix for the oxidizing process in the microwave.

Material previously heated in the furnace for 5 min	Microwave heating	Processing time
200 °C (J–1)	J–1 + M	5 min
300 °C (J–4)	J–4 + M	5 min
350 °C (J–7)	J–7 + M	5 min
400 °C (J–10)	J–10 + M	4 min
450 °C (J–13)	J–13 + M	4 min

Every time, once the desired temperature and processing time of oxidation was reached, the material was taken out of the heating camera to cool to room temperature and eventually sampled for the analysis. X-Ray diffraction patterns were collected using a Philips X'pert PW 3040 wide angle X-ray diffractometer, operating in step scan mode, with Cu K_α radiation (1.54052 Å). Patterns were collected in the range 3 to 90 ° for 2θ with a step size of 0.02 ° and a rate of 30 s per step. Samples were prepared as a finely pressed powder into special glass sample holders. The profile fitting option of the software uses a model that employs twelve intrinsic parameters to describe the profile, the instrumental aberration and wavelength dependent contributions to the profile. Samples also were analyzed by scanning electron microscopy (SEM / EDS) Philips XL 30 with EDS.

3. Results and discussion

Analysis of mining waste treatment by milling/oxidation technologies including analysis of available jet mill systems and oxidation methods (plasma, fluidized bed furnace, microwave, etc.) was carried out. At the first stage it was decided to use commercial jet mill system to evaluate initial ore residuals from Mexico that demonstrates high efficiency to get fine powder fracture in the range 1 – 5 μm. Final product was studied by SEM. Cumulative particle volume (%) versus particle diameter for various jet mill speeds is presented in **Figure 3**. The content of submicron particles in the milled product is about 50 % at jet mill vane velocity 11340 rpm.

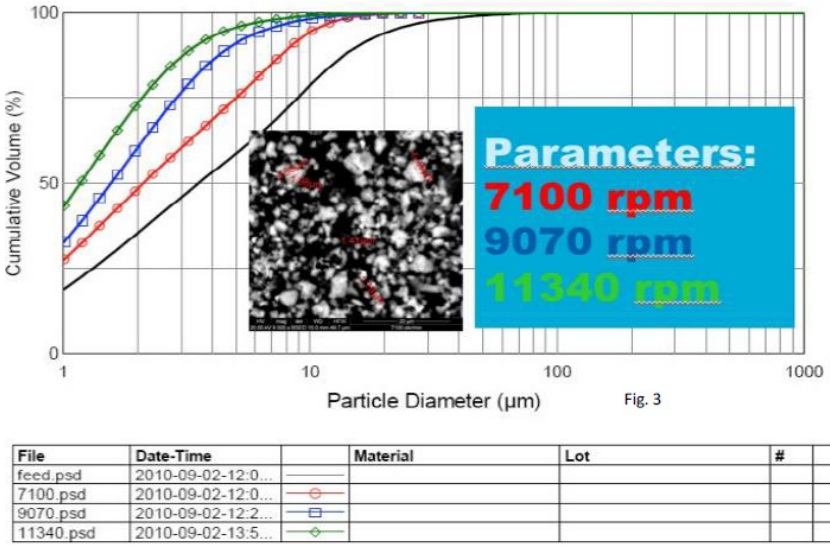

Figure 3. Experimental results of jarosite jet milling during 5 min.

The total results of the decomposition of jarosite by oxidizing in resistant oven are given in **Table 3**, that shows continuous oxidation process with increasing of the heating parameters (temperature and processing time).

Table 3. Amount (%) of the jarosite in the material after oxidized in the furnace.

	5 min	10 min	15 min
200 °C	66	53	46
300 °C	36	26	22
350 °C	22	18.8	15.5
400 °C	16	12	6
450 °C	10	7	0
500 °C	0	0	0
550 °C	0	0	0

Some amount of the jarosite (up to 10 – 15 %) in the heating material decomposes in relatively low temperature – 200 °C with processing time for 5 min. With increasing processing time (10 and 15 min) the amount of decomposed jarosite increases up to 20 and 30 %, respectively, and highly noticeable results are achieve at 450 – 500 °C. Effect of the heating temperature and processing time indicates, that the decomposition of the jarosite increased with an increase in heating time when heating temperature was above 400 °C. The higher the heating temperature, the shorter the heating time needed to decompose jarosite by the oxidizing in the furnace. The mechanisms of thermal oxidation depends on the reaction temperature and processing time, and include removal of residual moisture and jarosite decomposition of $AM_3(OH)_6(SO_4)_2$ and gypsum $CaSO_4 \cdot 2\ H_2O$ and formation of $M_2(SO_4)_n$ at the temperatures about 400 °C. The following processes are defined to be reactions: $Fe_2(SO_4)_3 \rightarrow Fe_2O_3 + 3\ SO_3$, $ZnSO_4 \rightarrow ZnO + SO_3$, and $Ag_2SO_4 \rightarrow Ag_2O + SO_3$.

Analysis shows, that during decomposition of the jarosite by oxidation in conventional oven the weight losses transformations occurs at about 120, 260 and 510 °C in three steps: 1 – moisture loss at ~ 100 °C, 2 – dehydroxylation / deammoniation at ~ 400 °C, and 3 – thermal transformation of sulphates to oxides at ~ 500 °C.

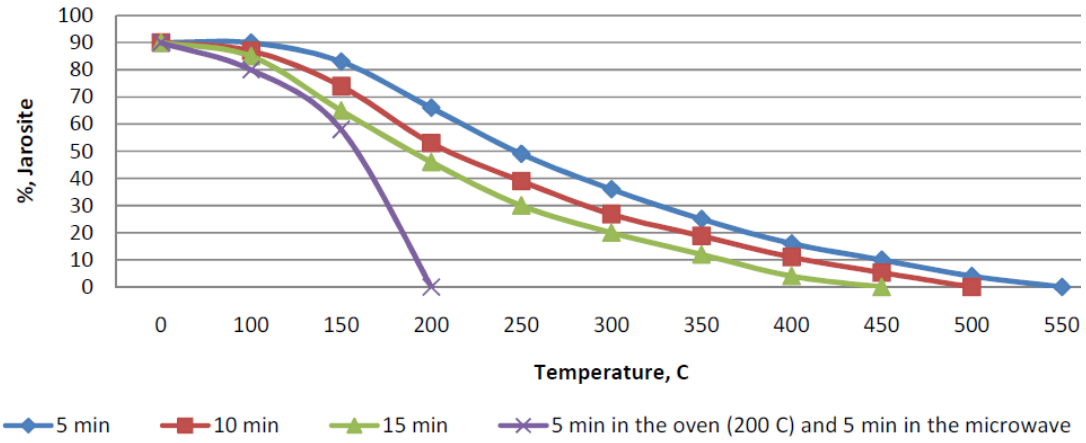

Figure 4. Decomposition of the jarosite by oxidation in the resistance conventional oven and microwave oven.

Decomposition of the jarosite by the heating the material in the microwave oven performed several times by two ways: first – heating the initial (basic or "fresh") material for the different period of time (1 to 5 min), and, second – heating material, that previously was preheated in resistance oven (200 °C) for 5 min. The results shows (**Figure 4**) that microwave heating completely decomposes the silver-jarosite faster if processing material previously preheated.

4. Conclusions

The decomposition of the mechanically activated jarosite by jet milling – oxidation roasting of the material in the furnace and microwave oven has been investigated. It is defined, that the mechanisms of thermal oxidation depend on the reaction temperature and include removal of residual moisture, jarosite decomposition of $AM_3(OH)_6(SO_4)_2$ and gypsum $CaSO_4 \cdot 2\,H_2O$ and formation of $M_2(SO_4)_n$ at the temperatures about 400 – 500 °C. The mechanisms of thermal oxidation depend on the reaction temperature and duration of the process. Effect of the heating temperature and processing time indicates, that the decomposition of the jarosite (by the roasting in the furnace) increased with an increase of heating time, and it completely decomposes when heating temperature was above 400 °C. The results, presented above, show that decomposition of the jarosite by the oxidation roasting in the furnace, started at temperature 200 °C, and total decomposition occurs after heating at 450 °C for 15 min. For the combination of the furnace oxidation (200 °C and processing time 5 min) and microwave roasting (1150 W for 5 min) decomposition rate was higher in shorter period of time, and the specific energy consumption was lower than the corresponding values for conventional roasting.

References

1. H. Kasaini, K. Kasongo, N. Naude, J. Katabua. Enhanced leachability of gold and silver in cyanide media: Effect of alkaline pre-treatment of jarosite minerals. Miner. Eng. 21 (2008) 1075-1082.
2. P. Baláz, E. Dutková. Mechanochemistry of sulphides from minerals to advanced nanocrystalline materials. J. Thermal Anal. & Calorim. 90 (2007) 85-92.
3. R. G. Maev, V. Leshchynsky. Introduction to Low Pressure Gas Dynamic Spray: Physics and Technology. 2007, Weinheim: Wiley-VCH.
4. P. Baláz, E. Dutková. Fine milling in applied mechanochemistry. Miner. Eng. 22 (2009) 681-694.
5. F. Barrida–Ordonez, F. Nava–Alonso, A. Uribe–Salas. Cyanide oxidation by ozone in a steady state flow-bubble column. Miner. Eng.19 (2006) 117-122.

MECHANISMS OF NUCLEATION AND GROWTH OF METASTABLE PHASES IN Mg–Gd AND Mg–Gd–Nd ALLOYS

S. Abd El Majid, M. Bamberger, A. Katsman

Technion
Haifa, Israel
akatsman@technion.ac.il

Accepted September 19, 2013

1. Introduction

Magnesium alloys containing heavy rare earth metals are very attractive candidates for the automotive industry including racing cars and aerospace applications [1 – 4], due to their high strength properties combined with low density. The high solubility of RE element in Mg matrix at high temperature and its rapid decrease with lowering temperature, show remarkable age-hardening response during isothermal aging.

Microstructural characterization of the Mg – RE alloys performed by many researchers [2, 3, 5 – 12] has confirmed a four staged precipitation sequence: α-Mg supersaturated solid solution (S.S.S.S.) → β″ (DO_{19}) → β' (BCO) → β_1 (FCC) → β (FCC) [9, 10], where the later precipitate can coexist with the former. Among the four precipitated phases, the coherent β″ and β' phases are considered to be the primary strengthening phases [9, 10]. The yield strength or hardness usually reaches a maximum, as the materials form a microstructure with fine β' precipitates during aging [6, 9 – 11]. The characterisitics of these precipitates (coherency, shape, size and density) play a significant role in the hardening effect. Among RE elements, Gd and Nd are considered as most promising for achievement of best Mg – RE alloys properties.

In the present work, nucleation and growth of metastable phases and their transformations during aging were investigated in the alloys Mg – 6Gd – 3.7Nd and Mg – 4.7Gd (wt. %) with additions of Zn, Y and Zr. They were investigated by a combination of transmission electron microscopy (TEM), high resolution transmission electron microscopy (HRTEM), energy dispersive X-ray spectrometry (EDS) and JEMS simulation. Microhardness measurements were performed to reveal the effect of precipitation on the mechanical properties of the alloy.

2. Experimental

High purity Mg (99.9 wt. %) was melted in a cemented graphite crucible under a protective atmosphere CO_2 and HFC–134a (CF_3CH_2F), high purity Gd (99.9 wt. %), Nd (99.9 wt. %) "for Mg – Gd – Nd-based alloy", Zn (99.9 wt. %), Mg – 40Y (wt. %) and Mg – 16Zr master alloys were added at a melt temperature of 760 °C, then casted into steel mould. The

chemical composition of the investigated alloys were Mg – 4.7Gd – 0.37Zn – 0.14Y – 0.09Zr and Mg – 6Gd – 3.7Nd – 0.3Zn – 0.18Y – 0.15Zr (wt. %).

Specimens were cut from the cast and encapsulated in quartz ampoules under Ar atmosphere. Solution treated (ST) at 540 °C for 24 h, quenched into water, and then aged at 175 °C in an oil bath for various periods of time up to 125 days, followed by water quenching.

The microhardness of aged specimens was measured by a Vickers hardness tester under a load of 50 g and holding time of 15 s. 20 – 40 indentations were conducted on each specimen.

The combination of HRTEM, TEM with SAED and JEMS simulation was carried out to characterize the nanometer-scale precipitates. The characterization includes crystal structure and composition of the precipitates, precipitation hardening sequence, orientation relationships between precipitates and the matrix and between precipitates themselves, if it exists. Thin foils for TEM characterization were prepared by ion beam thinning, and were examined at the acceleration voltage of 200 kV.

3. Results

3.1. Aging response

The combination of HRTEM, TEM with SAED and JEMS simulation was carried out to characterize the nanometer-scale precipitates. The characterization includes crystal structure and composition of the precipitates, precipitation hardening sequence, orientation relationships between precipitates and the matrix and between precipitates themselves, if it exists.

The age hardening curves of the two investigated alloys, Mg – 6Gd – 3.7Nd and Mg – 5Gd based alloys during aging at 175 °C, are presented in **Figure 1**.

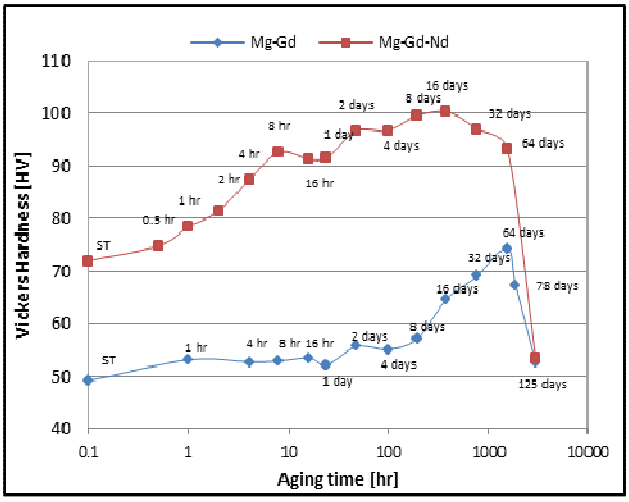

Figure 1. Age hardening curve of the two alloys aged at 175 °C.

The aging of ST samples was performed at 175 °C up to 125 days. Mg – 6Gd – 3.7Nd based alloy displays three peaks: the first after 8 h of aging, the second after 2 days and the third peak, with the maximum value of about 100 HV, after 16 days of aging. The Mg – Gd based alloy displays two-peaks, the first – after 2 days, and the second peak, with the maximum value of about 75 HV, after 64 days of aging. Further aging led to decrease in the microhardness (over aging).

3.2. Microstructure of aged samples

Aging periods of 16 h, 16 and 32 days in Mg – 6Gd – 3.7Nd based alloy; and 16, 64 and 76 days in Mg – 5Gd based alloy were selected for microstructure investigation, which represent under-aged, peak-aged and over-aged conditions.

3.2.1. Under-aged samples

As seen from the TEM image (**Figure 2**), the microstructure of Mg – Gd – Nd alloy aged for 16 h contained very thin platelet-shape precipitates formed on $\{0–110\}_\alpha$ planes and alongated along $[0001]_\alpha$ direction.

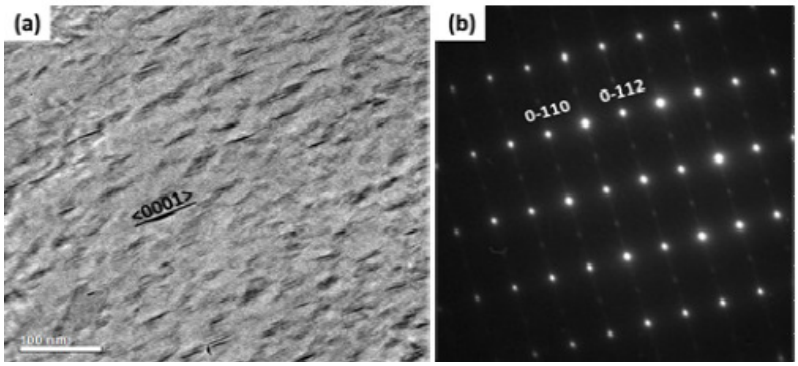

Figure 2. (a) TEM image and (b) corresponding SAED pattern of Mg – Gd – Nd alloy aged for 16 h at 175 °C with Z.A. $[2–1–10]_\alpha$.

From TEM SAED and JEMS simulation, it was found that β″ precipitate have DO_{19} structure with lattice parameters of $a = 2\,a_{\alpha\text{-Mg}}$ and $c = c_{\alpha\text{-Mg}}$, while the composition of β″ is Mg_3RE and are fully coherent with the Mg matrix.

In Mg – Gd based alloy, no precipitates appear in specimen aged for 16 h. TEM image and SAED pattern of Mg – Gd specimen aged for 16 days are presented in Figure 3. As seen from the SAED pattern, the precipitate reflections are from β″ and β' precipitates.

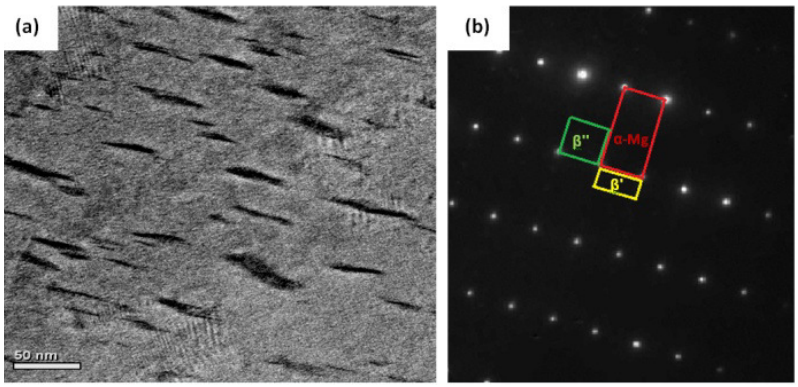

Figure 3. (a) TEM image and (b) corresponding SAED pattern Of Mg – Gd alloy aged for 16 days at 175 °C with Z.A. $[2–1–10]_\alpha$.

It was found that β″ precipitates have the same crystal structure and composition like that found in Mg – Gd – Nd alloy. The composition of β' is Mg_7RE and have BCO structure with lattice parameters $a = 0.64$, $b = 2.22$ and $c = 0.52$ nm.

3.2.2. Peak-aged samples

The HAADF STEM image and SAED pattern typical of microstructure in Mg – Gd – Nd specimen aged for 16 days are presented in Figure 4. As seen from the image, the microstructure contained three kinds of precipitates β', β_1 phases, and very thin precipitates with few tens of nanometer size that are probably β″ precipitates.

The platelets β' and β_1 have $\{10–10\}_\alpha$ habit planes; β' precipitates are extending along $[0001]_\alpha$ direction, while β_1 precipitates are extending along two directions of $<2110>_\alpha$.

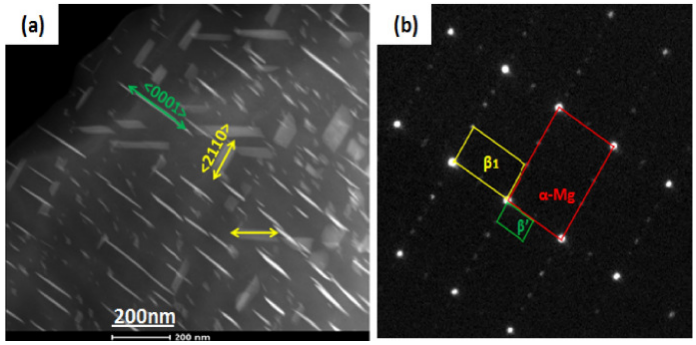

Figure 4. HAADF STEM image and corresponding SAED pattern of Mg – Gd – Nd alloy aged at 175 °C for 16 days with Z.A. $[10–10]_\alpha$ in (a, b) and for 32 days with Z.A. $[2–1–10]_\alpha$ in (c, d).

It was found that β' precipitates have the same crystal structure and composition like that found in Mg – Gd alloy. The β_1 precipitates have FCC crystal structure with the lattice parameter a = 0.74 nm, the composition of β_1 is Mg_3RE.

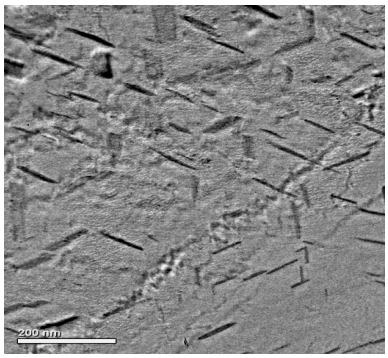

Figure 5. TEM image in Mg – Gd alloy aged for 64 days at 175 °C.

Typical TEM image of the Mg – Gd based alloy specimen aged for 64 days is shown in **Figure 5**. As can be seen, the microstructure contained β', β_1 precipitates and a small amount of β″ precipitate. Crystal structure, composition and orientation relationships of the precipitates are similar to that found in Mg – Gd – Nd based alloy.

3.2.3. Over-aged samples

Typical HAADF STEM image and corresponding SAED pattern of the Mg – Gd – Nd based alloy specimen aged for 32 days are shown in **Figure 6**. As can be seen, the microstructure

contained β' and β_1 precipitates, while β_1 precipetates appear often to be associated with β' precipitate. β' precipitates are elongated along $[0001]_\alpha$ direction while β_1 precipitates are elongated along two directions of $<-2110>_\alpha$. The OR $[100]_{\beta'} \parallel [111]_{\beta 1}$, $(00-2)_{\beta'} \parallel (20-2)_{\beta 1}$ between β' and β_1 precipitates was found (**Figure 6b**).

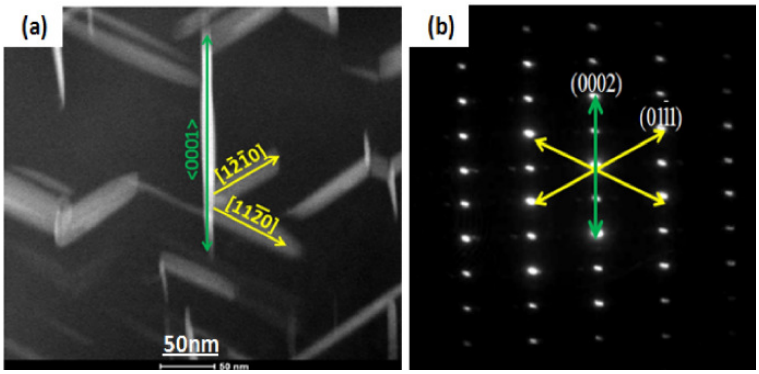

Figure 6. (a) HAADF STEM image and (b) corresponding SAED pattern of Mg – Gd – Nd alloy aged for 32 days at 175 °C; with Z.A. $[2-1-10]_\alpha$.

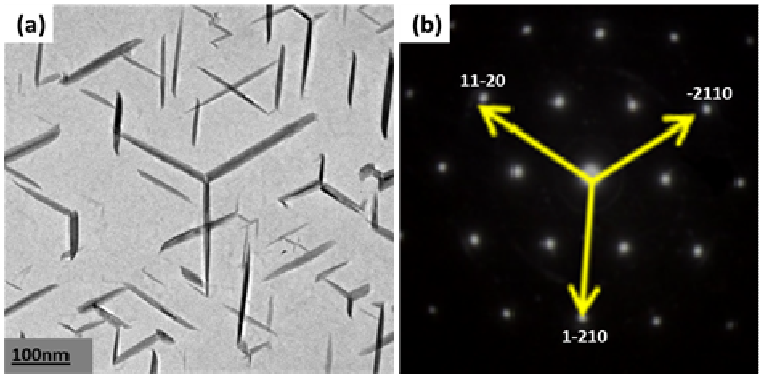

Figure 7. (a) TEM image and (b) corresponding SAED pattern of Mg – Gd – Nd alloy aged for 64 days at 175 °C with Z.A. $[0001_\alpha$.

After aging for 64 days, the β' precipitates almost totally transformed to platalet β_1 precipitates. The typical microstructure (TEM image) and corresponding SAED pattern of Mg – Gd – Nd alloy specimen aged for 64 days (**Figure 7**) show that the platelet β_1 precipitates are elongated along three equivalent directions of $<-21-10>_\alpha$ with habit planes $\{10-10\}_\alpha$.

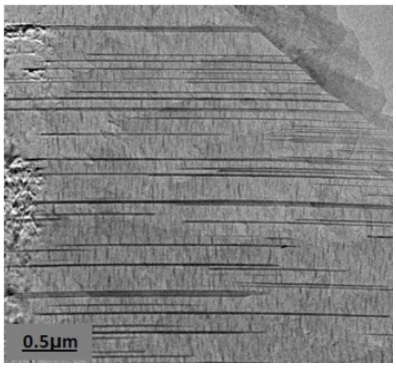

Figure 8. TEM images of Mg – Gd – Nd alloy aged for 125 days at 175 °C showing needle-like β precipitates.

In 175 °C / 125 days aged specimen of the Mg – Gd – Nd based alloy, the microstructure contained long needle-like precipitates much coarser than those observed in 175 °C / 64 days aged specimen (**Figure 8**). These precipitates seem to grow from the eutectic structure as the continuation of its β phase in the process of coarsening when the smaller β_1 and β precipitates presented in the α-Mg matrix are dissolved. The β phase has a crystal lattice with FCC ($a \approx 2.22$ nm) structure and composition of Mg_5RE.

4. Discussion

The precipitation sequence during isothermal aging in Mg – 6Gd – 3.7Nd – 0.3Zn – 0.18Y – 0.15Zr (wt. %) alloy and Mg – 4.7Gd – 0.37Zn – 0.14Y – 0.09Zr (wt. %) alloy is identical to that observed in binary Mg – Gd alloy (reported in [7]). In the first stage the metastable phase β″ (Mg_3RE) with HCP (DO_{19}) structure is precipitated from the α-Mg (S.S.S.S.). One can assume that high supersaturation of matrix by RE elements is resulted in homogeneous nucleation of fully coherent β″ precipitates. The β″ precipitates have a platelet-like shape in habit planes $\{-2110\}_{\alpha\text{-Mg}}$ & $\{0-110\}_{\alpha\text{-Mg}}$ with the following OR: $[0001]_{\beta''} \parallel [0001]_{\alpha}$ and $(01-10)_{\beta''} \parallel (01-10)_{\alpha}$. Nucleation and growth are controlled by diffusion of RE elements in the Mg matrix. Since the diffusion of Nd is faster than that of Gd, the first β″ precipitates have a composition of Mg_3Nd. After intensive β″ (Mg_3Nd) nucleation, the Nd supersaturation of matrix decreases substantially, nucleation is terminated, but the growth of precipitates continues due to Nd diffusion and is accompanied by their coarsening (dissolution of some small Mg_3Nd precipitates in favor of larger precipitates). Apparently, these processes resulted in the first peak of microhardness observed in the Mg – Gd – Nd based alloy after ~ 8 h aging. The following growth of β″ occurs due to Gd diffusion and results in increase of microhardness during ~ 2 days of aging, whereupon the coarsening provides the second peak of the microhardness. In that time the supersaturation of the matrix by RE elements decreases substantially both in Nd and in Gd. It is noteworthy that only the second peak (after 2 days of aging) was observed in the Mg – Gd based alloy (**Figure 1**).

During the second stage β″ precipitates transformed to metastable β' (Mg_7RE) precipitates with BCO structure. The β' precipitates have a platelet-like shape in habit planes $\{0-110\}_{\alpha\text{-Mg}}$ and grew along $<0001>_{\alpha\text{-Mg}}$. The β' precipitates are coherent with the Mg matrix, with the following OR: $[001]_{\beta'} \parallel [0001]_{\alpha}$, and $(110)_{\beta'} \parallel (2-1-10)_{\alpha}$.

Table 1. Summary of composition, structure, lattice parameters, number of atoms per unit cell and volume of the unit cell for β″, β' and β_1 precipitates in Mg – Gd and Mg – Gd – Nd alloys.

Phase	Composition	Structure	Lattice Parameters, nm	Atoms	Volume of unit cell, nm^3
β″	Mg_3RE	DO_{19}	$a = 0.64$ $c = 0.52$	6 Mg 2 RE	0.1843
β'	Mg_7RE	BCO	$a = 0.64$ $b = 2.22$ $c = 0.52$	28 Mg 4 RE	0.7321
β_1	Mg_3RE	FCC	$a = 0.74$	12 Mg 4 RE	0.4052

It is likely that nucleation of β' occurs heterogeneously at the β″ / α-Mg interface. The phase transformation involves additional Mg atoms from the adjacent Mg matrix and transformation of the DO_{19} crystal structure of β″ into the BCO crystal structure of β'. This transformation requires short range diffusion of Mg and RE atoms. It should be noted that the final volume of precipitated phase, β', is substantially larger than that of β″ participating in reaction β″ + α-Mg → β'. The volume of β″ (Mg_3RE, DO_{19}) unit cell (consisting of 2 atoms of RE and of 6 atoms of Mg) is equal to ~ 0.18 nm^3, while the volume of β' (Mg_7RE, BCO) unit cell (consisting of 4 atoms of RE and of 28 atoms of Mg) is equal to ~ 0.73 nm^3 (**Table 1**). It means that the precipitated volume of β' is nearly twice of β″ for the same amount of RE atoms. By these means, the transformation β″ → β' is accompanied by substantial increase of precipitates' size. Additional growth of β' precipitates during aging occurs due to diffusion of RE elements from the Mg matrix. These processes are resulted in the microhardness increase up to 16 days of aging in the Mg – Gd – Nd based alloy and up to 64 days in the Mg – Gd based alloy (**Figure 1**).

Further aging resulted in transformation of all β' precipitates into the β_1 (Mg_3RE) precipitates with FCC structure. The β_1 precipitates have a platelet-like shape in habit planes $\{0–110\}_{\alpha\text{-}Mg}$, grew along three directions of $<1–2–10>_{\alpha\text{-}Mg}$ (**Figure 7**) and are semi-coherent with the Mg matrix, with the following OR: $[110]_{\beta1} \parallel [0001]_{\alpha}$, and $(1–11)_{\beta1} \parallel (11–20)_{\alpha}$.

The nucleation of β_1 was associated with β' precipitates, apparently, due to very small lattice mismach between β' and β_1 precipitates for their OR $[100]_{\beta'} \parallel [111]_{\beta1}$ and $(00–2)_{\beta'} \parallel (20–2)_{\beta1}$. Such heterogeneous nucleation resulted in formation of K-like and V-like particle associations (**Figure 6a**).

Unit cell of the FCC β_1 (Mg_3RE) phase consists of 4 RE atoms and 12 Mg atoms, with the total volume of 0.405 nm^3 (**Table 1**). It means that the transformation β' → β_1 is accompanied by reduction of precipitate volume by ~ 44.5 % due to release of Mg atoms into the Mg matrix. Reduction of precipitates' size, together with a coarsening process resulted in a decrease of microhardness after 16 days of aging of the Mg – Gd – Nd based alloy (64 days aging of the Mg – Gd based alloy). The β_1 precipitates nucleate at the β' / α-Mg interface in a such manner that the lattice mismatch between the new β_1 phase and β' is minimal. However, the growth directions of β_1 $<1–2–10>_{\alpha\text{-}Mg}$ differ from the growth directions of β' $<0001>_{\alpha\text{-}Mg}$. It means that the β' → β_1 transformation should be accompanied by dissolution of the β' precipitate and diffusion of RE atoms from β' to adjacent β_1 precipitate.

In the fourth stage of aging, the β_1 precipitates transformed into a stable incoherent β (Mg_5RE) precipitates with FCC structure as observed in the over aging samples.

5. Conclusions

- The α-Mg (S.S.S.S.) in Mg – Gd – Nd and Mg – Gd alloys decomposes during aging into the following four successive phases: β″ (Mg_3RE, DO_{19}) → β' (Mg_7RE, BCO) → β_1 (Mg_3RE, FCC) → β (Mg_5RE, FCC).
- β″ phase nucleates homogeneously from the supersaturated Mg matrix, while β' nucleates heterogeneously on the β″ phase and involves additional Mg atoms from the adjacent Mg matrix.
- β″ and β' are coherent with the α-Mg matrix, β_1 is semi-coherent with the matrix.

- The nucleation of β_1 was associated with β' precipitates, resulting in formation of K-like and V-like particle associations.
- Transformation $\beta' \rightarrow \beta_1$ occurs with decrease of precipitated volume providing decrease of microhardness.
- The platelets β' and β_1 have $\{0–110\}_{\alpha\text{-Mg}}$ habit planes; β_1 grows along three close packed directions of the matrix $<1–2–10>_{\alpha\text{-Mg}}$, while β' grows along $<0001>_{\alpha\text{-Mg}}$.
- Hardening occurred with three-peaks in the Mg-Gd-Nd alloy and two-peaks in Mg-Gd alloy. Additional first peak was connected with faster diffusion of Nd and β'' (Mg_3Nd) formation.

References

1. B. L. Mordike, T. Ebert. Magnesium: Properties – applications – potential. Mater. Sci. & Eng. A 302 (2001) 37-45.
2. K. Y. Zheng, J. Dong, X. Q. Zeng, W. J. Ding. Effect of pre-deformation on aging characteristics and mechanical properties of Mg – Gd – Nd – Zr alloy. Trans. Nonferrous Met. Soc. China 17 (2007)1164-1168.
3. K. Y. Zheng, J. Dong, X. Q. Zeng, W. J. Ding. Effect of thermo-mechanical treatment on the microstructure and mechanical properties of a Mg – 6Gd – 2Nd – 0.5Zr alloy. Mater. Sci. & Eng. A 454-455 (2007) 314-321.
4. L. Huber, I. Elfimov, J. Rottler, M. Militzer. Ab initio calculations of rare-earth diffusion in magnesium. Phys. Rev. B 85 (2012) 144301 1-7.
5. D. H. Ping, K. Hono, J. F. Nie. Atom probe characterization of plate-like precipitates in a Mg – RE – Zn – Zr casting alloy. Scr. Mater. 48 (2003) 1017-1022.
6. X. Gao, S. M. He, X. Q. Zeng, L. M. Peng, W. J. Ding, J. F. Nie. Microstructure evolution in a Mg – 15Gd – 0.5Zr (wt. %) alloy during isothermal aging at 250 °C. Mater. Sci. & Eng. A 431 (2006) 322-327.
7. M. Nishijima, K. Hiraga, M. Yamasaki, Y. Kawamura. Characterization of β' phase precipitates in an Mg – 5 at. % Gd alloy aged in a peak hardness condition. Mater. Trans. 47 (2006) 2109-2112.
8. D. H. Li, J. Dong, X. Q. Zeng, C. Lu, W. J. Ding. Characterization of β″ precipitate phases in a Mg – Dy – Gd – Nd alloy. Mater. Characterization 58 (2007) 1025-1028.
9. K. Y. Zheng, J. Dong, X. Q. Zeng, W. J. Ding. Precipitation and its effect on the mechanical properties of a cast Mg – Gd – Nd – Zr alloy. Mater. Sci. & Eng. A 489 (2008) 44-54.
10. K. Y. Zheng, X. Q. Zeng, J. Dong, W. J. Ding. Effect of initial temper on the creep behavior of a Mg – Gd – Nd – Zr alloy. Mater. Sci. & Eng. A 492 (2008) 185-190.
11. L. Gao, R. S. Chen, E. H. Han. Microstructure and strengthening mechanisms of a cast Mg – 1.48Gd – 1.13Y – 0.16Zr (at. %) alloy. J. Mater. Sci. 44 (2009) 4443-4454.
12. G. Sha, J. H. Li, W. Xu, K. Xia, W. Q. Jie, S. P. Ringer. Hardening and microstructural reactions in high-temperature equal-channel angular pressed Mg – Nd – Gd – Zn – Zr alloy. Mater. Sci. & Eng. A 527 (2010) 5092-5099.

ROOM TEMPERATURE SYNTHESIS OF MONODISPERSE GOLD NANO-PARTICLES AND NANO-SHARDS WITH CYCLIC AND LINEAR DIKETONES

W. J. Peveler, I. P. Parkin

University College London
London, United Kingdom
william.peveler.11@ucl.ac.uk

Accepted September 19, 2013

1. Introduction

Colloidal gold, first synthesised in a controlled fashion by Faraday in the 19th century, has, in the last 20 years, found applications in many fields due to the surface plasmon resonance (SPR) properties and tuneable shape and size of gold nanoparticles (AuNPs). In-vitro imaging, drug delivery and severalsingle-molecule detection techniques have come to rely on a supply of mono-disperse and stable AuNP suspensions, of the appropriate size and shape [1 – 3].

The most prevalent syntheses of AuNPs commonly utilise methods pioneerd by Turkevich et al. [4] or Brust et al. [5]. These require boiling chloroauric acid ($HAuCl_4$) in the presence of a reducing agent; sodium citrate or sodium hydride respectively. Both methods are reliable, and many advances have been made regarding fine size control and understanding the mechanism [6 – 10].

Recently, however, there has been much focus on the synthesis of so-called "green" AuNPs via plant extract mediated reduction, at a range of temperatures. Shankar et al. [11] pioneered the work, and since then many papers have been focussed on using leaf or fruit extracts to produce both nanoparticles and large nanoplates of gold and silver, for example [12 – 16]. It has now been shown that cyclohexanonehas the ability to reduce chloroauric acid to gold nanoparticles and similar nanoplates, at room temperature, by a mechanism described in [17]. This has been suggested as a plausible mechanism for the reduction occurring with the plant extracts, which could contain similar functional groups. Further to this work, we have recently shown that other cyclic and linear ketones have the ability to reduce chloroauric acid, but not all ketones are capable of stabilising a colloidal suspension of the AuNPs in water [18]. Herein we demonstrate that diketones create an even more interesting set of gold nanostructures, improving on the particles created with mono-ketones with their rapid synthesis and wider range of architectures.

2. Experimental

Reagents were used as supplied from Sigma Aldrich, without further purification. All water used was deionised (> 15 MΩ), and reactions were performed at room temperature (ca. 20 °C).

UV–Vis spectroscopy was performed with a Perkin–Elmer Lamda–25 instrument. Tunneling electron microscopy (TEM) samples were prepared by dropping 2 or 3 drops of undiluted reaction solution onto carbon-coated copper grids and drying in air overnight. TEM micrographs were collected using Jeol 1010 and 2010 instruments, fitted with Gatan Orius digital cameras, at a beam acceleration of 80 and 200 keV, respectively. Images processing and particle counting were performed with Gatan Digital Micrograph and ImageJ software.

An aqueous chloroauric acid ($HAuCl_4$) stock solution was made up to 6 mM with anhydrous $HAuCl_4$ (102 mg, 0.3 mmol) in 50 ml water. The colloidal suspensions were synthesised by mixing an excess of ketone: 1,4-cyclohexanedione (1) (0.5 g, 4.4 mmol); 1,3-cyclohexanedione (2) (0.5 ml, 4.4 mmol); acetylacetone (3) (0.5 ml, 4.8 mmol); 2,5-hexanediketone (4) (0.5 ml, 4.3 mmol) with water (9.5 ml) in a glass vials. $HAuCl_4$ stock solution (0.44 ml, 2.6 μmol) was then rapidly injected and the vial shaken by hand.

3. Results and discussion

3.1. Results with cyclic diketones

The reaction of 1 was followed by UV–Vis spectroscopy. Due to the rapid nature of the reaction, some information from the first 60 s of the reaction was lost, however a characteristic SPR band appeared in the first scan, at around 536 nm, and grew rapidly for 20 min, before stabalising. The reaction went to completion within 30 min (**Figure 1**).

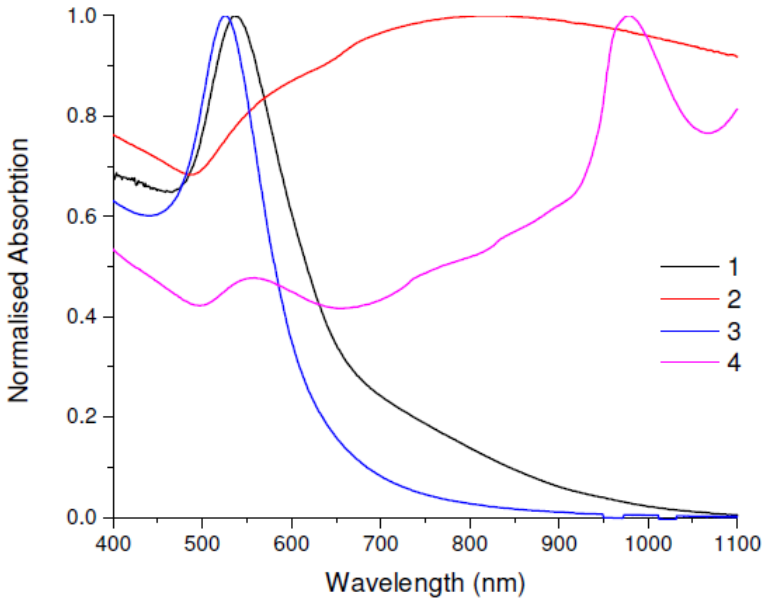

Figure 1. UV–Vis spectra of 4 linear ketones, 1 – 1,4-cyclohexanedione, 2 – 1,3-cyclohexanedione, 3 – acetylacetone and 4 – 2,5-hexanediketone.

On mixing the solution of cyclohexanedione with $HAuCl_4$ a rapid colour change was observed, within several seconds. 1,4-cyclohexanedione (1) took on a purple tingle, rapidly becoming dark mauve after a minute (**Figure 2b**). 1,3-cyclohexanedione (2) started to turn grey on mixing, darkening with time (**Figure 2a**).

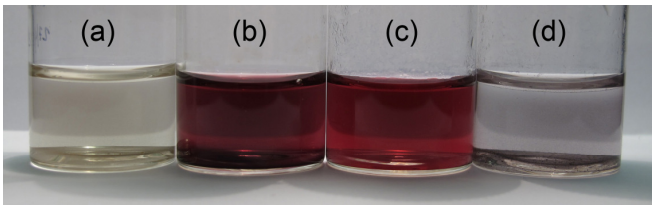

Figure 2. Images of diketone AuNPs after 24 h. (a) 1,3-cyclohexanedione, (b) 1,4-cyclohexanedione, (c) acetylacetone, and (d) 2,5-hexanedikeonte.

Several drops were removed after 5 h and deposited on a TEM grid. The particles proved to be remarkably monodisperse, with a mean size of 20.7 ± 5 nm (**Table 1**). Also of note was the very low number of nanoplates observed, and those that were found were far smaller than the typical sizes seen in samples of cyclohexanone, cyclopentanone or other cyclic ketone or plant extract based gold colloids (**Figure 3b**).

Table 1 TEM particle counting results

Diketone	Shape	N	Average, nm	SD, nm
1,4-cyclohexanedione (1)	spheroidal / prismatic	148	21	5
1,3-cyclohexandione (2)	shard / star like	22	250	–
acetylacetone (3)	Spheroidal / amorphous	95	13	9
2,5-hexanediketone (4)	spheroidal / plate	163	22	7

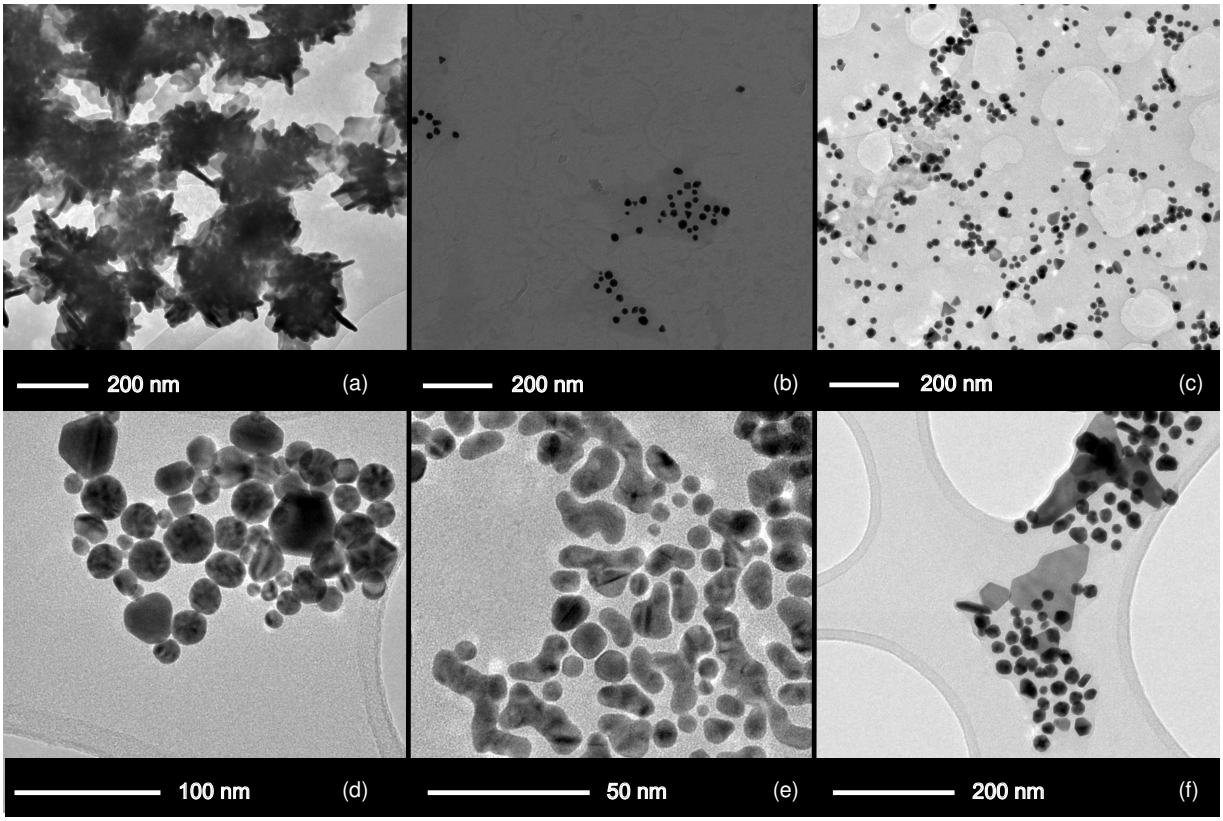

Figure 3. TEM images of AuNPs produced with diketones: (a) 1,3-cyclohexanedione 2; (b) and (c) 1,4-cyclohexanedione after 5 h and 3 months, respectively; (d) and (e) acetyacetonate 3 and (f) 2,5-hexanediketone 4.

A sample was allowed to age for 3 months, and imaged again, and although some enlarge particles were seen, no nanoplates were observed. However the dispersity of the sample had increased. Several large amorphous particles and some nanorods were observed (**Figure 3c**).

The reaction of 2 was also measured by UV–Vis spectroscopy and a very different spectral evolution was observed. Ultimately a shouldered, broad peak was observed with a maximum ca. 800 nm and shoulder at ca. 560 nm (**Figure 1**).

As before, after several hours a TEM sample was prepared, but no conventional nanoparticles were found. Instead a large number of complex shard-like shapes, here christened nano-shards (previously similar structures have also been referred to as nanostars in [19]). These varied in diameter between 200 and 400 nm, and clustered together with some irregular plate type structures and small particle conglomerates (**Figure 3a**).

3.2. Results with linear diketones

Two equivalent linear ketones were also mixed with similar chloroauric acid solutions. Acetylacetone (3) was used as a proxy for 1,3-cyclohexanedione and 2,5-hexanediketone (4) for 1,4-cyclohexanedione. On mixing, however, very different results were obtained for both ketones. On mixing with 3, a bright pink colour immediately developed, darkening slightly over 5 min (**Figure 2c**). On mixing with 4 no immediate change was observed, however after 24 h a grey / purple colour developed, and a precipitate had formed (**Figure 2d**).

The reaction of 3 was again too fast to follow satisfactorily by UV–Vis spectroscopy, however the few scans possible before competition of the reaction showed a rapidly growing peak at 526 nm which reached its maximum after ~ 3 min. With 4 the sample had precipitated over night, and thus a good spectrum was hard to achieve, however small peaks were visible at 555, 761, and 850 nm, with a much larger peak at 978 nm.

Both reaction mixtures were imaged with TEM, and sample micrographs are given in **Figures 3d – f**. Particles produced with **3** were a heterogenous mixture of small spheroids (13 ± 9 nm – **Table 1**) and also a number of small amorphous structures, appearing to consist of several fused spheroidal particles in a branched structure (**Figure 3e**).

Reaction with 4 produced two extremes of particles. A large number of fairly monodisperse spheroidal particles were produced (22 ± 7 nm), but these were mixed with large, amorphous, thin gold plates (**Figure 3f**).

3.3. Discussion of mechanism and ketone effects

It has been previously shown by Uppal et al. [17] and Peveler & Parkin [18] that ketones reduce chloroauric acid via chlorination of the α-position, as demonstrated in **Figure 4**. Further to this, it can be shown that the lower the pK_E of an enol solution (the greater the concentration of enol form over keto) the faster the reaction proceeds.

Although initially the reactions of the linear and cyclic diketones appear very different, there are some similarities to be found. The key similarity is the rapid rate of reaction for 2 and 3. This is attributed to the high reactivity of the α-proton between the two carbonyl groups, raising the enol content, and facilitating rapid reaction via the suggested mechanism of α-chlorination. However the different ligating properties of the two ligands, arising from

differing ketone spacing due to the conformation-changing properties of ring strain, lead to very different shaped and sized nanoparticles (**Figure 5**).

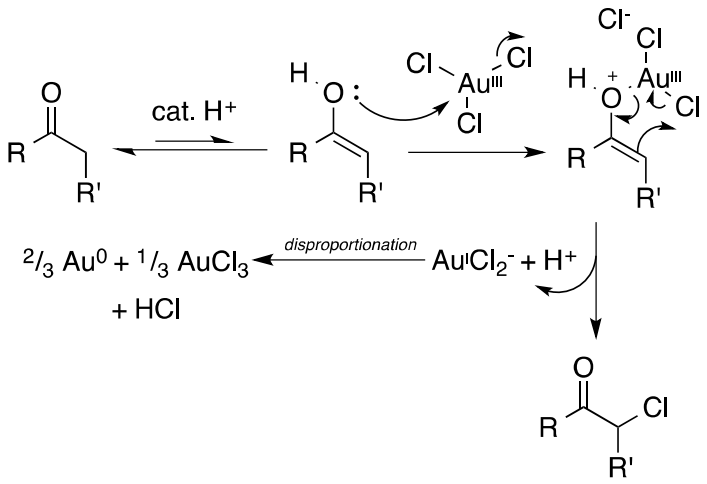

Figure 4. Proposed mechanism for AuNP formation with a generic ketone.

1,3-cyclohexanedione acetylacetone

Figure 5. Different conformations of the ketones in 2 and 3.

Interestingly the linear 1,4-diketone equivalent (4) reacts at a much slower rate than its cyclic counterpart. This is likely to be due to the lower enol content in solution of the linear diketone (**Table 2**).

Table 2. Relationship between ketone Properties and the rate of reaction. pK_E data from [20] and other chemical data sources.

Diketone	Solubility, g / L	pK_E	Reaction time
1,4-cyclohexanedione (1)	soluble	< 6.38	30 min
1,3-cyclohexandione (2)	soluble	5.26	5 min
acetylacetone (3)	160	0.64	3 min
2,5-hexanediketone (4)	100	7.51	24 h

As shown previously, linear mono-ketones show poor particle capping properties, due to their lower solubilities and structural differences, leading to more amorphous particles. However, by increasing the solubility and number of ketone units these properties can be improved, exemplified with ketones 3 and 4 and their improved reaction rate and yield of largely monodisperse particles.As all samples were fully soluble in the dilute chloroauric acid solution, none of the inhomogeneity effects previously observed for cycloheptanone, for example, were seen here. Instead all dispersty arising is attributed to the surface stabilisation properties of the ketones on the AuNPs.

Ketone 4 reacts very differently to it's mono-ketone equivalent, 3-hexanone [18], although at a roughly similar rate. Both have a similar reactivity in terms of pK_E, but the diketone seems to be much better at at-least partially stabilising gold nanostructures, due to it's higher solubility, larger number of reactive sites (twice as many) and better ligating properties.

4. Conclusions

We have demonstrated the incredible versatility of the newly discovered ketone based synthesis for AuNPs at room temperature. Furthermore, we have found that the use of diketones not only speeds the synthesis, by tuning the reactivity of the ketone, but also allows control on the size and shape of particles formed by altering the surface stabilisation properties. As the diketones utilised had good water solubility, none of the effects of poor solution mixing were observed, that had been previously encountered.

We have added to the homologous series of ketones studied, and furthered understanding of how best to control this facile and rapid synthesis of gold nanostrucutres. Of particular interest is the synthesis of nanoshards (or nanostars) and large nanoplates, which have great potential as SERS substrates for single molecule detection.

Acknowledgements

This work was supported by EPSRC Grant no. EP / G037264 / 1 as part of UCL's Security Science Doctoral Training Centre (SECReT). The authors would like to thank the UCL Institute of Opthalmology's Imaging Facility for access to TEM facilities.

References

1. M. Riskin, R. Tel-Vered, O. Lioubashevski, I. Willner. Ultrasensitive surface plasmon resonance detection of trinitrotoluene by a bis-aniline-cross-linked Au nanoparticles composite. J. Am. Chem. Soc., 2009, 131, 21, 7368-7378.
2. S. Kasera, F. Biedermann, J. J. Baumberg, O. A. Scherman, S. Mahajan. Quantitative SERS using the sequestration of small molecules inside precise plasmonic nanoconstructs. Nano Lett., 2012, 12, 11, 5924-5928.

3. S. Kundu. A new route for the formation of Au nanowires and application of shape-selective Au nanoparticles in SERS studies. J. Mater. Chem. C, 2013, 1, 4, 831-842.
4. J. Turkevich, P. C. Stevenson, J. Hillier. A study of the nucleation and growth processes in the synthesis of colloidal gold. Discuss Faraday Soc., 1951, 11, 10, 55-75.
5. M. Brust, M. Walker, D. Bethell, D. J. Schiffrin, R. Whyman. Synthesis of thiol-derivatised gold nanoparticles in a two-phase liquid–liquid system. Chem. Commun., 1994, 7, 801-802.
6. J. Kimling, M. Maier, B. Okenve, V. Kotaidis, H. Ballot, A. Plech. Turkevich method for gold nanoparticle synthesis revisited. J. Phys. Chem. B, 2006, 110, 32, 15700-15707.
7. M. A. Uppal, A. Kafizas, T. H. Lim, I. P. Parkin. The extended time evolution size decrease of gold nanoparticles formed by the Turkevich method. New J. Chem., 2010, 34, 7, 1401-1407.
8. M. A. Uppal, A. Kafizas, M. B. Ewing, I. P. Parkin. The effect of initiation method on the size, monodispersity and shape of gold nanoparticles formed by the Turkevich method. New J. Chem., 2010, 34, 12, 2906-2914.
9. I. Ojea–Jiménez, J. M. Campanera. Molecular modeling of the reduction mechanism in the citrate-mediated synthesis of gold nanoparticles. J. Phys. Chem. C, 2012, 116, 44, 23682-23691.
10. J. Polte, T. T. Ahner, F. Delissen, S. Sokolov, F. Emmerling, A. F. Thünemann, R. Kraehnert. Mechanism of gold nanoparticle formation in the classical citrate synthesis method derived from coupled in situ XANES and SAXS evaluation. J. Am. Chem. Soc., 2013, 132, 4, 1296-1301.
11. S. S. Shankar, A. Rai, B. Ankamwar, A. Singh, A. Ahmad, M. Sastry. Biological synthesis of triangular gold nanoprisms. Nat. Mater., 2004, 3, 7, 482-488.
12. D. Philip. Rapid green synthesis of spherical gold nanoparticles using Mangifera indica leaf. Spectrochim. Acta A, 2010, 77, 4, 807-810.
13. D. Philip, C. Unni, S. A. Aromal, V. K. Vidhu. Murraya Koenigii leaf-assisted rapid green synthesis of silver and gold nanoparticles. Spectrochim. Acta A, 2011, 78, 2, 899-904.
14. L. Christensen, S. Vivekanandhan, M. Misra, A. K. Mohanty. Biosynthesis of silver nanoparticles using murraya koenigii (curry leaf): An investigation on the effect of broth concentration in reduction mechanism and particle size. Adv. Mater. Lett., 2011, 2, 6, 429-434.
15. P. Dauthal, M. Mukhopadhyay. Prunus domestica fruit extract-mediated synthesis of gold nanoparticles and its catalytic activity for 4-nitrophenol reduction. Ind. & Eng. Chem. Res., 2012, 51, 40, 13014-13020.
16. S. Mukherjee, V. Sushma, S. Patra, A. K. Barui, M P. Bhadra, B. Sreedhar, C. R. Patra. Green chemistry approach for the synthesis and stabilization of biocompatible gold nanoparticles and their potential applications in cancer therapy. Nanotechnol., 2012, 23, 455103, 1-5.
17. M. A. Uppal, A. Kafizas, M. B. Ewing, I. P. Parkin. The room temperature formation of gold nanoparticles from the reaction of cyclohexanone and auric acid: A transition from dendritic particles to compact shapes and nanoplates. J. Mater. Chem. A, 2013, 1, 25, 7351-7359.
18. W. J. Peveler, I. P. Parkin. Rapid synthesis of gold nanostructures with cyclic and linear ketones. RSC Adv., 2013 – in press.

19. P. Senthil Kumar, I. Pastoriza–Santos, B. Rodríguez–González, F. Javier García de Abajo, L. M. Liz–Marzán. High-yield synthesis and optical response of gold nanostars. Nanotechnol., 2007, 19, 015606, 1-5.
20. J. R. Keeffe, A. J. Kresge, N. P. Schepp. Keto-enol equilibrium constants of simple monofunctional aldehydes and ketones in aqueous solution. J. Am. Chem. Soc., 1990, 112, 12, 4862–4868.

CHARACTERIZATION OF CALCIUM SILICATE HYDRATE AND CALCIUM HYDROXIDE IN NANOSILICA BINDER COMPOSITES

I. Yakub, N. M. Sutan, C. S. Kiong

University Malaysia Sarawak
Sarawak, Malaysia
yibrahim@feng.unimas.my

Accepted September 19, 2013

1. Introduction

Pozzolanic reaction is the reaction of vitreous silica with calcium hydroxide (C–H), which is formed during the hydration of the ordinary Portland cement (OPC) binder producing additional calcium silicate hydrate (C–S–H) that resembles tobermorite or jennite structure, which is the main constituent for the strength and density in the harden binder paste. The pozzolanic activity includes two parameters; the amount of lime (CaOH) that pozzolan can react with and the rate of reaction. The rate of the pozzolanic activity is related to the surface area of pozzolan particles where higher surface area of pozzolan particle (or finer particle) gives more pozzolanic reactivity [1].

One of the synthetic nanomaterials that has been gaining attention and has been applied in binder material due to its pozzolanic characteristic is nanosilica. This material normally consists of very fine vitreous particles approximately 1000 times smaller than the average binder particles. It is based on silica particles of 5 – 50 nm and is much smaller than those of silica fume (microsilica) which contains particles of 0.1 – 1 μm. Previous studies have shown that due to the very high specific surface area (~ 1000 m^2 / g) and the spherical shape of silica particles, it can potentially enhance the performance of binder mainly due to its reaction with C–H to develop more of the strength-carrying compound in binder structure: C–S–H [2 – 4].

The factor that affects nanosilica reactivity in binder is its high surface area where the precipitation of C–S–H gel works in the nucleation. Besides, it has been found in several studies that if nanosilica particles are uniformly dispersed in the binder paste it will accelerate the hydration rate due to its high activity [5 – 9]. Previous studies have shown that the pozzolanic activity of the nanosilica is higher than the silica fume [10 – 13]. The addition of nanosilica to binder (cement) based materials can control the degradation of C–S–H reaction caused by calcium leaching in water, block water penetration, increase the compressive strength and reduce the overall permeability of hardened concrete which results in finer hydrated phases of C–S–H gel and densified microstructure [1].

To date there are limited knowledge on the effects of nanosilica as a binder replacement on the pozzolanic reaction. Therefore this study aimed to investigate the extents of pozzolanic reaction of nanosilica binder composites (nSBC) by the characterization of calcium silicate hydrate gel (C–S–H) and calcium hydroxide (C–H) crystal using X-ray diffraction technique (XRD) and scanning electron microscopy / energy dispersive X-ray spectroscopy (SEM/EDX).

2. Materials and method

2.1. Materials

Nanosilica used in this study was Aldrich silicon dioxide nanopowder of 10 – 20 nm particle size with 99.5 % silica. Binder used was ordinary Portland cement (OPC) (ASTM Type 1 recognized by ASTM C150) manufactured by Cahaya Mata Sarawak Cement Sdn. Bhd (CMS) and it exceeded the quality requirements specified in the Malaysian Standard MS 522: Part 1: 1989 Specifications for OPC. The information for chemical and mineralogical characteristics of the OPC binder was obtained from CMS and is simplified in **Table 1**.

Table 1. Chemical and mineralogical composition of OPC.

Component	CaO	SiO_2	Al_2O_3	Fe_2O_3	SO_3	MgO	Na_2O	K_2O	Others	LOI
Value, % (Composition / percentage)	63.00	21.69	5.75	3.25	2.35	1.97	0.50	0.28	0.11	1.00

In order to investigate the extents of pozzolanic reaction of nSBC, characterization of C–S–H and C–H using X-ray diffraction technique (XRD) and scanning electron microscopy (SEM) / (EDX) were performed. nSBC paste samples were prepared with water-binder ratio of 0.50 and 2, 3 and 5 % by weight nanosilica binder replacement which were designated as nSBC – 2 %, nSBC – 3 % and nSBC – 5 % respectively. Control sample without nanosilica was labelled as OPC. All specimens were casted into Universal Container 30 ml, 28 × 85 mm and dry-cured at room temperature (32 °C) and average relative humidity of 90 %.

2.2. Characterization by XRD and SEM / EDX

The fine powder samples (passing 75 μm) and polished small samples were prepared and analysed using XRD at day 28, 60 and 90 and SEM / EDX at day 28. Acetone was used to stop the hydration process of these samples. XRD analysis for all prepared samples was performed using PAN analytical equipment with Cu K_α radiation and λ of 0.1546 nm. The specifications were: count step 4 s / step; step size 0.02 degree; and range 50 – 650 2Theta angle. SEM / EDX images for all prepared samples were captured by scanning electron microscope and energy dispersive X-ray spectroscopy (JSM–6701F) supplied by JEOL Company Ltd, Japan that followed the ASTM C 1723–10 (2010) code of practice. The specimens were that of Karnovsky's fixative and were then taken through a graded alcohol dehydration series. Once dehydrated, the coated and polished specimens of control mortar and modified mortar were viewed on the SEM.

3. Results and discussion

Figure 1 shows the SEM images of the four samples (OPC, nSBC – 2 %, nSBC – 3 % and nSBC – 5 %) after 28 days. C–H that has plate-like morphology can be seen present on all samples except for poor view on nSBC – 5 % (**Figure 1d**). For OPC sample, reticulated or lace-

like morphology that implied C–S–H produced at early hydration stage can also be seen on nSBC – 3 % and more obvious on nSBC – 5 % sample. C–S–H of middle-stage hydration products that look like needles radiating from grain can be seen in all samples though at different density. Meanwhile, spherical agglomerates that can be observed on the C–H structure in OPC, nSBC – 3 % and nSBC – 5 % samples were attributed to C–S–H that was formed during late stage of hydration process [10].

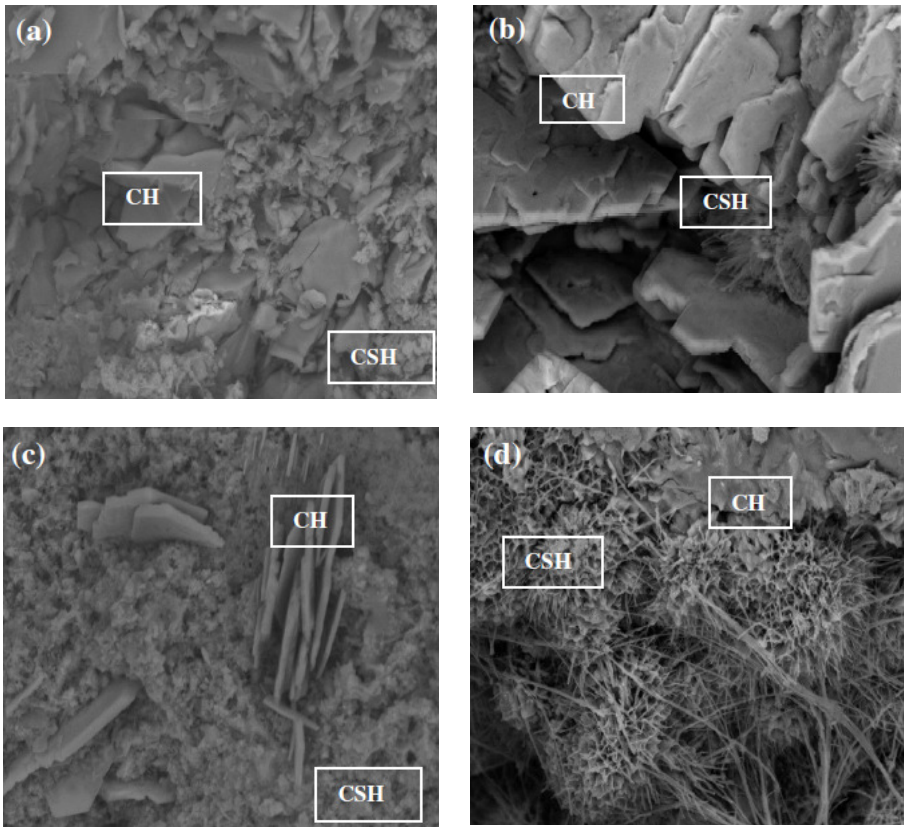

Figure 1. SEM images of: (a) OPC, (b) nSBC – 2 %, (c) nSBC – 3 % and (d) nSBC – 5 % at day 28.

The higher density of C–S–H compared to C–H when the composition of nanosilica had been increased indicates that the progress of pozzolanic reaction increased alongside the increase in nanosilica content. Besides, the C–S–H that was formed at early stage can be found more on nSBC – 5 % compared to control sample after 28 days showing the escalation of pozzolanic reaction mostly due to increase in available pozzolan particles at early contact with water and C–H in the mortar sample. The characteristic of C–S–H produced can be further investigated through its Ca / Si ratio which can be estimated using EDX shown in **Figure 2**.

The Ca / Si ratio of C–S–H in OPC, nSBC – 2 %, nSBC – 3 % and nSBC – 5 % samples had been calculated as 0.276, 8.812, 3.014 and 2.756 respectively. According to [14], the Ca / Si ratio for Tobermorite and Jennite are 0.83 and 1.5 respectively. Besides, ratio of more than that means C–S–H is of more amorphous structure and ratio near 2 resembles C–S–H with Tobermorite and Jennite structure in mixture. The former can be applied here to describe that OPC, nSBC – 2 % and nSBC – 3 % possessed C–S–H structure far more amorphous than Tobermorite while the latter explained the structure of C–S–H in nSBC – 5 % can be approximated to Tobermorite–Jennite mixture.

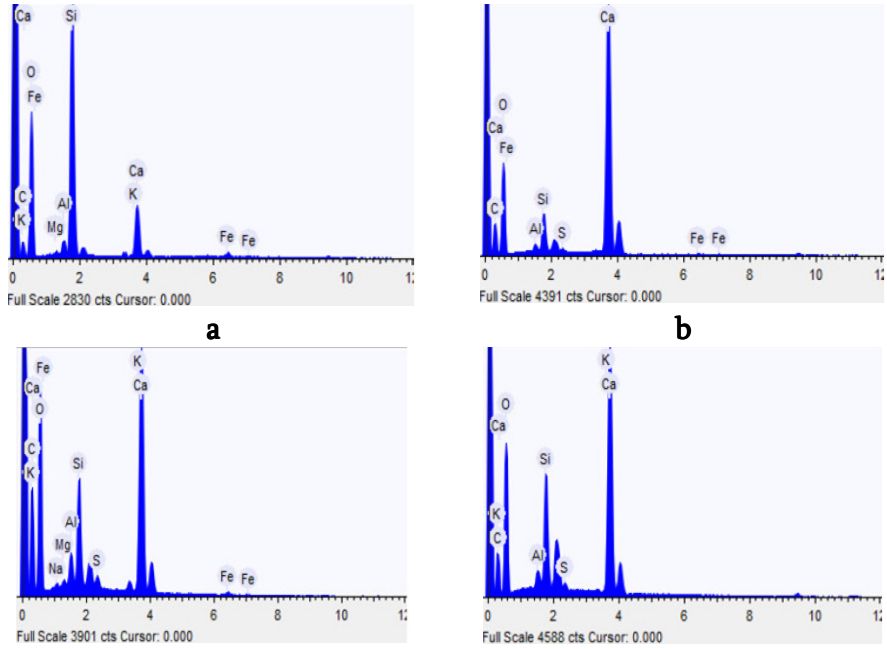

Figure 2. EDX pattern (Cu K_α radiation) of: (a) OPC, (b) nSBC – 2%, (c) nSBC – 3%, and (d) nSBC – 5% at day 28.

As SEM–EDX results showed positive appearance of C–S–H, it is central to demonstrate the analysis of the sample structure using XRD. **Figure 3** shows X-ray diffractograms for OPC, nSBC – 2 %, nSBC – 3 % and nSBC – 5 % at day 28. Crystalline C–H appeared on all samples at peaks around 18.07, 34.17 and 47.19 while amorphous C–S–H can be analysed at peak around 29.54. In the same figure, significant intensity of C–S–H can be found on sample nSBC –3 %.

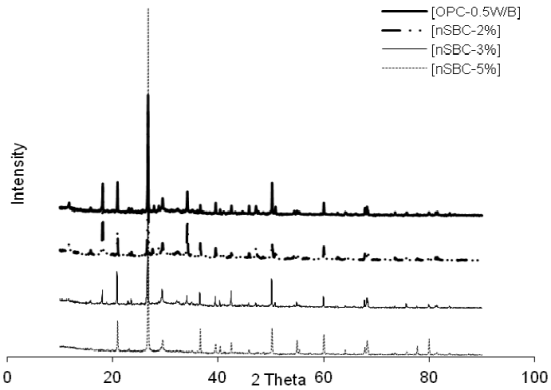

Figure 3. XRD pattern (Cu K_α radiation) of OPC (control) and nSBC at day 28.

Figure 4 shows the XRD patterns for OPC and nSBC for 28, 60 and 90 days. From 28 to 90 days, the intensity of C–H peaks increased in OPC sample and decreased in other samples. Furthermore after 60 days, it can be seen that the intensity for peaks of C–H decreased the most for nSBC – 2 % compared to other samples but average intensity in nSBC – 5 % slightly increased. However after 90 days, nSBC – 5 % sample also showed a reduction in C–H intensity. Overall, the C–H peaks decreased the most in nSBC – 2 % followed by nSBC – 3 % and nSBC – 5 %. As for C–S–H, the intensity increased after 60 days for nSBC – 2 % and nSBC – 5 % but decreased afterward. For nSBC – 3 %, the intensity of C–S–H was detected to decrease from day 28 until after 90 days.

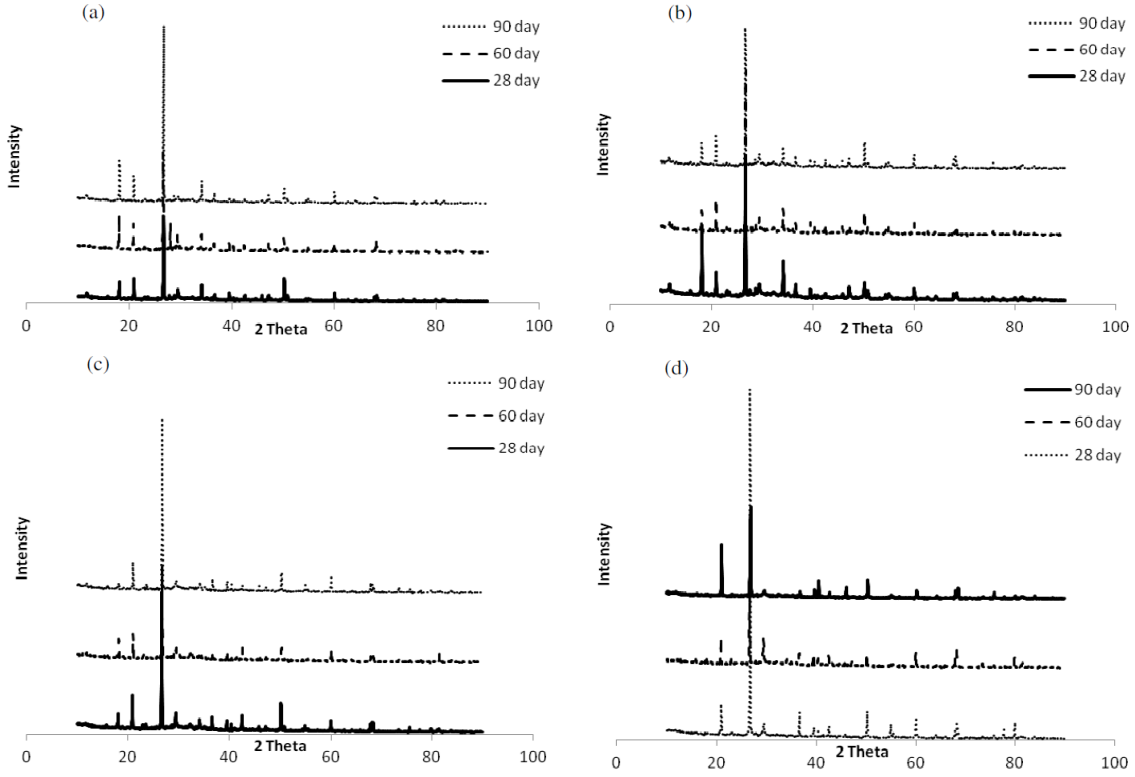

Figure 4. XRD pattern (Cu *Kα* radiation) of: (a) OPC, (b) nSBCS – 2 %, (c) nSBC – 3 %, and (d) nSBC – 5 %.

As C–H kept on increasing in OPC sample but decreasing in nSBC samples, it shows that the formation of Portlandite in OPC sample has continued until after 90 days but consumed in samples that contained nSBC due to pozzolanic reaction with silica. nSBC – 2 % showed the most reduction of C–H but the intensity of C–S–H fluctuated where it increased after 60 days but decreased after 90 days. This is mainly due to the change in chemical structure of C–S–H into another form [14] which was not detectable at peak around 29.54. nSBC – 3 % showed the reduction of both C–H and C–S–H after 28 days until after 90 days because after pozzolanic reaction, the alteration in structure (as that happened to nSBC – 2 %) occurred earlier compared to nSBC – 2 %. Whilst for nSBC – 5 %, both the C–H and C–S–H intensity increased after 60 days also showing pozzolanic activity (due to increasing formation of C–S–H) and increased in hydration process in the same time. After 90 days, C–H intensity decreased because of the consumption in pozzolanic reaction while C–S–H decreased because of change in molecular structure to amorphous phase.

4. Conclusions

C–H and C–S–H had been characterized in OPC and nSBC samples using SEM / EDX and XRD to investigate the progress of pozzolanic reaction. SEM images showed presence of both C–H and C–S–H morphologies at different density for all samples while EDX had been used to determine Ca/Si ratio of C–S–H structure. Besides, the intensity of C–H and C–S–H presence after 28, 60 and 90 days had been observed from XRD pattern. Both hydration and pozzolanic processes can be seen occurring simultaneously in all samples but nSBC – 2 % and nSBC – 3 % showed dominant activity of pozzolanic reaction though C–S–H intensity decreased after

60 days due to change of structure to a more amorphous phase. Between nSBC – 2% and nSBC – 3 %, the former was more amorphous at day 28 but the latter changed in structure to become more amorphous earlier which was the result of decreasing C–S–H intensity after 28 days. As a conclusion, nanosilica promotes pozzolanic reaction at different progression level when used at different composition as replacement in the binder, and XRD as well as SEM / EDX are applicable in observing this progress qualitatively. However, further study should be performed to quantify the extent of pozzolanic reaction so the optimum pozzolan dosage can be obtained.

Acknowledgements

The authors wish to acknowledge University Malaysia Sarawak for supporting this work under SGS / 03(S113) / 894 / 2012(26) grant and Prof. Dr. Sinin Hamdan from Faculty of Engineering, UNIMAS, Malaysia for proof-reading this paper.

References

1. V. M. Malhotra, P. K. Mehta. Pozzolanic and Cementitious Materials. 2004, London: Taylor & Francis.
2. K. Sobolev, M. Ferrara. How nanotechnology can change the concrete word. Am. Ceram. Bull. 84 (2005) 15-17.
3. Q. Ye. Influence of nano-SiO_2 addition on properties of hardened cement paste as compared with silica fume. Constr. & Amp. Building Mater. 21(2007) 539-545.
4. V. Ershadi, T. Ebadi, A. R. Rabani, L. Ershadi, H. Soltanian. The effect of nanosilica on cement matrix permeability in oil well to decrease the pollution of receptive environment. Int. J. Environ. Sci. & Dev. 2 (2011) 128-132.
5. Q. Yu, K. Sawayama, S. Sugita, M. Shoya, Y. Isojima. The reaction between rice husk ash and $Ca(OH)_2$ solution and the nature of this product. Cement & Concrete Res. 29 (1999) 37-43.
6. J. J. Gaitero, I. Campillo, P. Mondal, P. Shah. Small changes can make a great difference. Trans. Res. Record, 2142 (2010) 1-5.
7. M. Khanzadi, M. Tadayon, H. Sepehri, M. Sepehri. Influence of nano-silica particles on mechanical properties and permeability of concrete. In: Proc. 2nd Int. Conf. on Sustainable Construction Mater. & Technol., 2010.
8. J. I. Tobon, O. J. Restrepo, J. Paya. Comparative Analysis of performance of Portland cement blended with hanosilica and silica fume. Dyna 163 (2010) 37-46.
9. M. R. Arefi, M. R. Javaheri, E. Mollaahmadi, H. Zare, B. Abdollahi Nejand, M. Eskandari. Silica nanoparticles size effect on mechanical properties and microstructure of cement mortar. J. Am. Sci. 7 (2011) 231-238.
10. E. M. Gartner, J. M. Gaidis, J. M. Mater. Ch. 3: Hydration of Portland cement. In: Topics in the Structure and Performance of Cements (Eds. J. Bensted, P. Barnes), 2002, London: Spon Press.
11. H. Li, H.-G. Xiao, J. Yuan, J. Ou. Microstructure of cement mortar with nano-particles. Composites B 35 (2004) 185-189.
12. S. Mann. Nanotechnology and Construction European Nanotechnology Gateway. 2006, Report.
13. A. F. Sadrmomtazi, A. Fasihi, F. Balalaei, A. K. Haghi. Investigation of mechanical and physical properties of mortars containing silica fume and nano-SiO_2. In: Proc. 3rd Int. Conf. Concrete & Dev. 2009, 1153-1161.
14. J. J. Chen. (2002) Solubility and structure of calcium silicate hydrate. 10th February 2013. http://www.civil.northwestern.edu/people/thomas/pdf/Chen_SolStruc_CCR_sub.pdf.

AN INVESTIGATION ELECTROMAGNETIC SHIELDING AND MECHANICAL PROPERTIES OF CONDUCTIVE FIBER REINFORCED COMPOSITES

E. Sancak, Z. Yıldız, M. Yuksek, N. Demirel, E. D. Kocak

Marmara University
Istanbul, Turkey
myuksek@marmara.edu.tr

Accepted September 19, 2013

Introduction

The usage and the number of electrical and electronic devices have grown rapidly as a result of developing technology, modern life conditions and growing income. Many devices such as AC motors, digital computers, calculators, televisions, radios, cell phones, wireless modem and telephones, electronic typewriters, transmission line, digital circuitry, electronic home devices are capable of emitting electromagnetic waves that will result in some electromagnetic interference problems [1].

With the development of science and technology, people enjoy the convenience brought by various electrical and electronic devices but at the same time they are also exposed to the pollution of electromagnetic radiation. When a high frequency electromagnetic wave enters a human body, it vibrates molecules to give out heat. The network of veins within high-risk organs such as the eyes could be weakened because this heat cannot be easily dissipated. Moreover, it could increase the possibility of leukemia and other cancers. Biologists have reported that even a short-term exposure to low-density electromagnetic radiation could result in temporary sterility [2 – 4]. Therefore, a great deal of effort is needed to further the development of electromagnetic shielding materials.

Electromagnetic wave consists of an electrical component and magnetic component perpendicular to each other and propagates at right angles to the plane. The waves are produced by the motion of electrically charged particles. These waves are also called “electromagnetic radiation” because they radiate from the electrically charged particles. They travel through empty space as well as through air and other substances. This is difficult to visualize, however the waveform has similar characteristics of other types of waves [5].

Although they seem different, radio waves, microwaves, X-rays, and even visible light are all electromagnetic waves. They are part of the electromagnetic spectrum, and each has a different range of wavelengths, which cause they waves to affect matter differently.

The range of wavelengths for electromagnetic waves from the very long to the very short is called the Electromagnetic Spectrum [6]. When you listen to the radio, watch TV, or cook dinner in a microwave oven, you are using electromagnetic waves. Radio waves, television waves, and microwaves are all types of electromagnetic waves. They differ from each other in wavelength. Wavelength is the distance between one wave crest to the next.

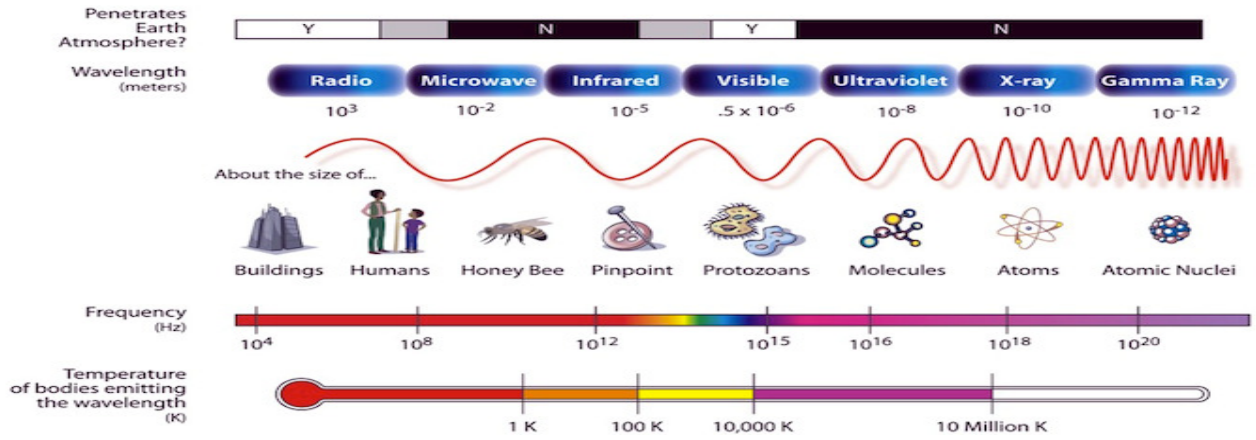

Figure 1. Electromagnetic Spectrum.

Waves in the electromagnetic spectrum vary in size from very long radio waves the size of buildings, to very short gamma rays smaller than the size of the nucleus of an atom (**Figure 1**). The antennae on your television set receive the signal, in the form of electromagnetic waves that is broadcasted from the television station. It is displayed on your television screen. Cable companies have antennae or dishes, which receive waves broadcasted from your local TV stations. The signal is then sent through a cable to your house. Cellular phones also use radio waves to transmit information. These waves are much smaller that TV and FM radio waves.

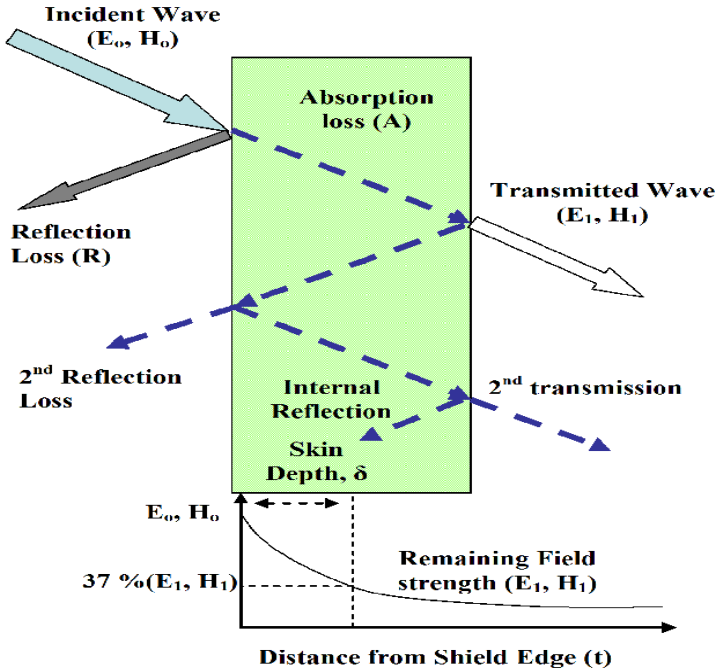

Figure 2. Graphical representation of EMI shielding.

Shielding Effectiveness

Shielding can be specified in the terms of reduction in magnetic (and electric) field or plane-wave strength caused by shielding. The effectiveness of a shield and its resulting EMI attenuation are based on the frequency, the distance of the shield from the source, the thickness of the shield and the shield material. Shielding effectiveness (SE) is normally expressed in

decibels (dB) as a function of the logarithm of the ratio of the incident and exit electric (E), magnetic (H), or plane-wave field intensities (F):

$$SE\ (dB) = 20 \log (E_0 / E_1),$$

$$SE\ (dB) = 20 \log (H_0 / H_1),$$

or

$$SE\ (dB) = 20 \log (F_0 / F_1),$$

respectively. With any kind of electromagnetic interference, there are three mechanisms contributing to the effectiveness of a shield. Part of the incident radiation is reflected from the front surface of the shield, part is absorbed within the shield material and part is reflected from the shield rear surface to the front where it can aid or hinder the effectiveness of the shield depending on its phase relationship with the incident wave, as shown in **Figure 2** [7].

Experimental materials

Stainless and carbon fibers

In the study, the staple stainless steel, carbon and glass fibreswere used. The filament stainless steel fibres were provided by Bekaert Company. The filament carbon fibres were produced by AKSA in Turkey. The filament glass fibres were providedby CAM ELYAF in Turkey. The filament fibers were cut 10 mm length to produce composites.

Thermoset resins

Matrix resin which is thermoset polyester (Polipol 347) manufactured by Poliya (Turkey) were used to fabricate composite structures. Thermoset polyester resin was chosen to fabricate composite because of its low price. Properties of thermoset resin are given in **Table 1**.

Table 1. Properties of thermoset resin.

Test	Value
Flexural strength	117 MPa
Flexural modulus	3546 MPa
Elongation at break	3.86 %
Tensile strenght	52 MPa
Modulus of elasticity in tensile	2800 MPa
Elongation at break	2.12 %
Charpy impact strength	7 KgJ/m^2

Manufacturing of composite structures

Thermosetting polyester was applied as a resin. There are several major manufacturing methods in fiber-reinforced polymer industry. Thermosetting polyester laminates were manufactured via BMC moulding. In this article, BMC samples were studied in term of amount changes and pressure evolution in the moulding cavity during the crosslinking. The BMC is composed of thermoset polyester (195 g), hardener (5 g), short glass fibers (100, 95, 90 or 80 g), calcite (150 g) and short conductive fibers (10, 20 or 30 g). The composites were BMC molded for 30 s at 10 bar and 140 °C. The properties of composite are given in **Table 2**.

Table 2. Properties of reinforced composites.

Sample code	Thermoset resin, g	Hardener, g	Calcite, g	Glass fiber, g	Carbon fiber, g	Stainless steel fiber, g	Thickness, mm
Co–Sa	195	5	150	100		0	3
C–10	195	5	150	95		10	3
C–20	195	5	150	90		20	3
C–30	195	5	150	80		30	3
SS–10	195	5	150	95	10		3
SS–20	195	5	150	90	20		3
SS–30	195	5	150	80	30		3

SS: stainless steel, C: carbon, Co–Sa: control sample

Methods

EM shielding Eeffectiveness (EMSE) measurement

A coaxial transmission line method specified in ASTM D4935–10 was used to test the EMSE of the conductive textile composites. The specimen is prepared with the standard test size of various thicknesses as shown in **Figure 3**. The specimen dimension is 133 mm in diameter of the outer ring. It's needed to prepared two specimens for test, one for reference and another for load testing. Various researchers have described the detailed set-up and testing procedure using a plane-wave electromagnetic field in the frequency range of 15 MHz – 3GHz. The spectrum analyzer and shielding effectiveness test fixture (Electro-Metrics, Inc., EM–2107A) were used to measure the EMSE, which is measured in decibels (dB) in this investigation [8, 9].

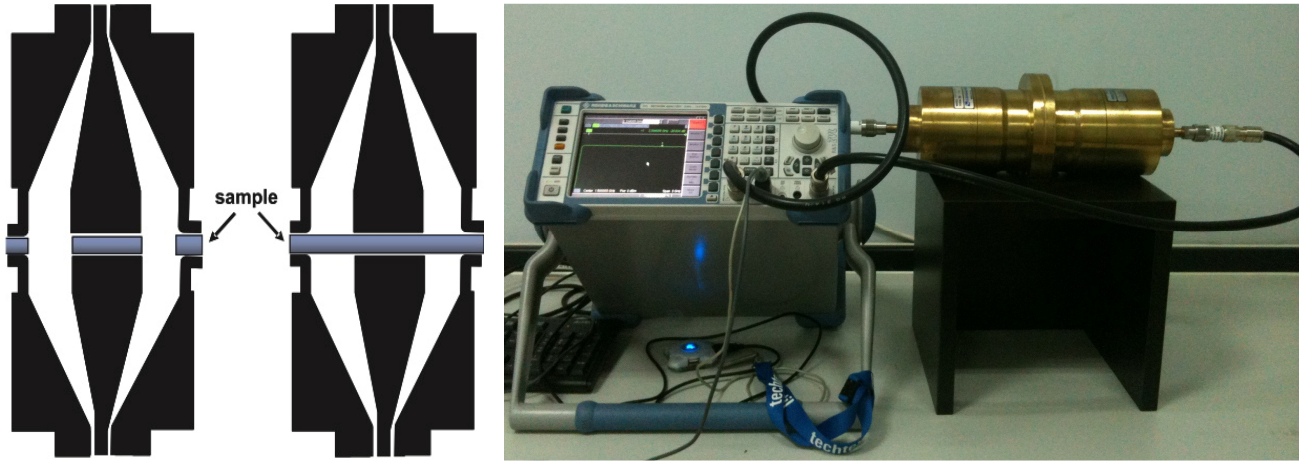

Figure 3. A cross-section of the shielding effectiveness test fixture (a) and set up of EMSE testing apparatus (b).

Table 3. Professional use.

Grade	5 Excellent	4 Very Good	3 Good	2 Moderate	1 Fair
Percentage of electromagnetic shielding	ES > 99.99999 %	99.9999 % ≥ ES > 99.999 %	99.999 % ≥ ES > 99.99 %	99.99 % ≥ ES > 99.9 %	99.9 % ≥ ES > 99.0 %
Shielding effectiveness	SE ≥ 60 dB	60 dB ≥ SE > 50 dB	50 dB ≥ SE> 40 dB	40 dB ≥ SE > 30 dB	30 dB ≥ SE > 20 dB

SE: shielding effectiveness (dB); ES: Percentage of electromagnetic shielding (%) [10].

Table 4. General use.

Grade	5 Excellent	4 Very Good	3 Good	2 Moderate	1 Fair
Percentage of electromagnetic shielding	ES > 99.9 %	99.9 % ≥ ES > 99.0 %	99.0 % ≥ ES > 90 %	90 % ≥ ES > 80 %	80 % ≥ ES > 70 %
Shielding effectiveness	SE ≥ 30 dB	30 dB ≥ SE > 20 dB	20 dB ≥ SE> 10 dB	10 dB ≥ SE > 7 dB	7 dB ≥ SE > 5 dB

SE: shielding effectiveness (dB); ES: Percentage of electromagnetic shielding (%) [10].

Mechanical property characterization

Tensile test technique, ASTM D3039 / 3039M–07 [11] was used to determine the tensile strength of the composite laminates. The tensile strengths were tested using Devotrans Universal test machine at a crosshead speed of 10 mm / min. The charpy impact strengths were tested using Zwick BS 1315 test machine. At least five specimens for each composition were tested. Impact strength was checked by means of charpy impact resistance [12, 13] based on ISO 179–1 standard [14].

Results and discussions

Electromagnetic shielding effectiveness of fiber reinforced composites

The fiber-reinforced composites were scanned with electromagnetic frequencies ranging from 15 to 3000 MHz and the EMSE values were recorded. The values obtained using measurement techniques in above have been graphically investigated in below. In these investigations, EMSE of the composite structures have been considered in terms of kind of conductive fibers.

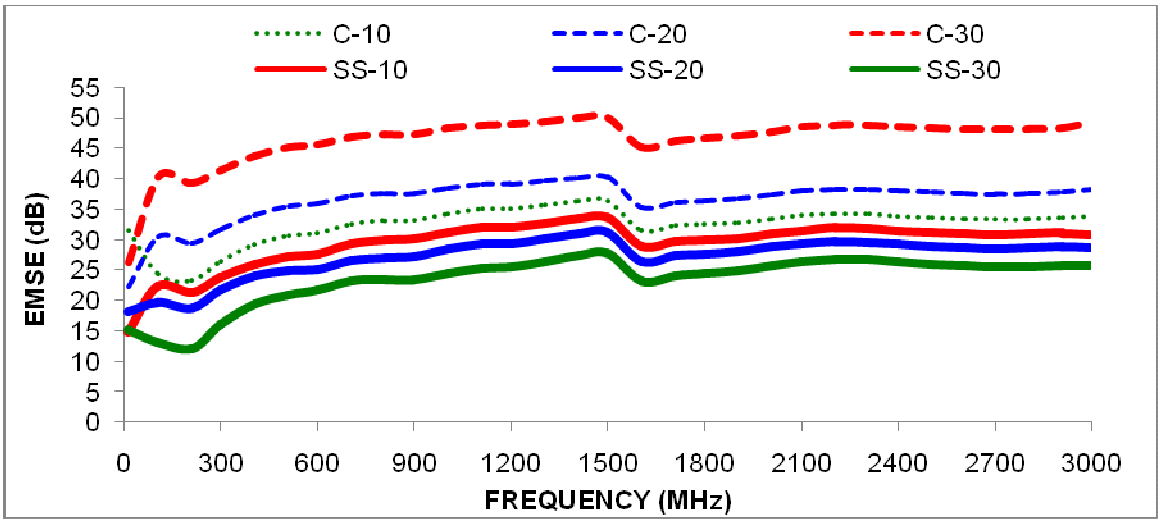

Figure 4. The Effect of amount and rind of conductive fibers on electromagnetic shielding effectiveness (EMSE).

Figure 4 shows the shielding effectiveness of fiber-reinforced composites in the frequencies range of 15 – 3000 MHz. In the frequencies range of 15 – 3000 MHz, fiber reinforced composites produced with different ratios stainless steel and carbon fiber have shown EMSE values behaviour different. It is understood that as the frequency value increases, EMSE value of the with stainless steel and carbon fiber content of 10, 20 and 30 % ratios increase continuously. In the frequencies range of 15 – 300 MHz, it is seen that as the amount of the stainless steel and carbon fiber used in the composite increases, EMSE values also increase. The composite with 30 % carbon fibres have obtained the best EMSE value in the frequencies range of 15 – 3000 MHz. It was found that the EMSE values obtained from composite with carbon fibers is higher than composite with stainless steel fibers.

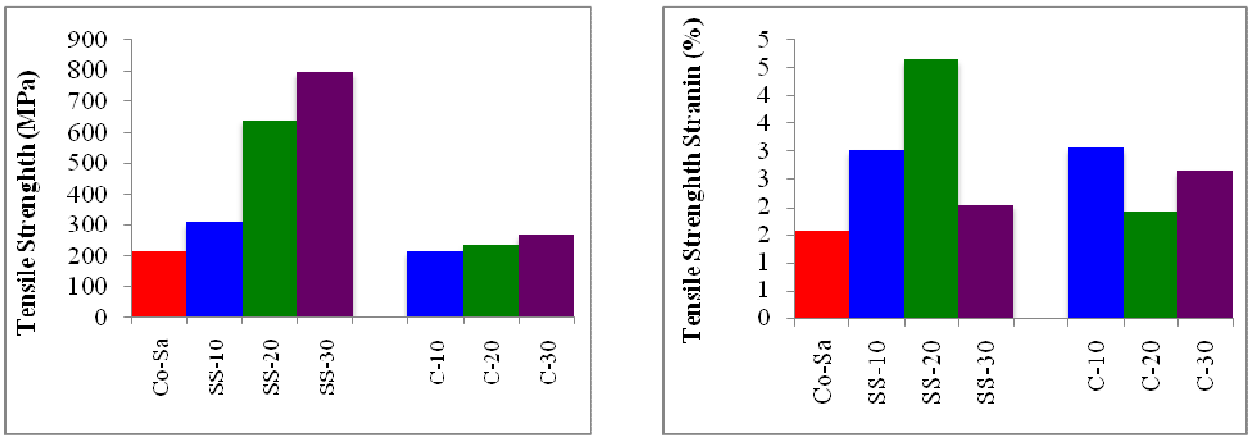

Figure 5. Tensile strength (a) and strain (b) of fiber reinforced composites.

Mechanical properties of fiber reinforced composites

Mechanical tests were conducted for each sample in one direction and experiments were repeated as specified in the standards. Tensile strength and impact strength tests were applied to the composite materials. Results of the mechanical tests were compared in the graphics. Tensile strength and strain of composites were evaluated in the **Figure 5**. When graphics are examined,

it is observed that, when considering the type of conductive materials, the fiberreinforced composite (SS–30) displays higher tensile strength than the others and the fiber reinforced composite (SS–20) displays higher tensile strength strain than the others as well. It is understood that as the stainless steel and carbon fiber content of 10, 20 and 30 % ratios increase, The tensile strengthand tensile strength strain value increases. Among all the composites, when comparing the amount of stainless and carbon fibers in composite, the fiber reinforced composite that is composed of stainless steel fiber displays higher tensile strength and tensile strength strain than the carbon fibers.

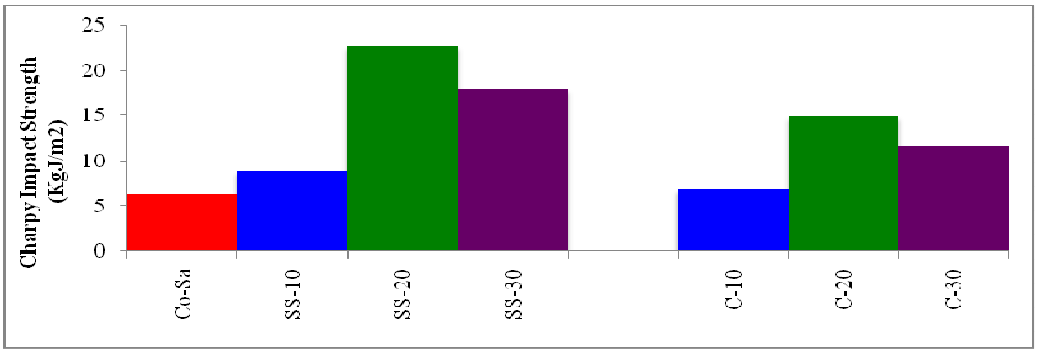

Figure 6. Charpy impact strength of knitted fabric reinforced composites.

Charpy impact strength of composites was evaluated in the **Figure 6**. When graphic is examined, it is observed that, when considering the type of conductive materials, the fiber reinforced composite (SS–20) displays charpy impact strength than the others. It is understood that as the stainless steel and carbon fiber content of 10, 20 and 30 % ratios increase, the impact strength value increases.Among all the composites, when comparing the amount of stainless and carbon fibers in composite, the fiber reinforced composite that is composed of stainless steel fiber displays higher impact strengththan the carbon fibers.

Conclusions

In this study, the properties of the electromagnetic shielding and mechanical of the composite with stainless steel and carbon fibers were investigated. The Mechanical and EMSE values were obtained and presented in figures.

It was observed that as the stainless steel and carbon fiber ratio used at the composite increases, the effectiveness of the electromagnetic shielding (EMSE) also increases at all frequencies. As a result, it can be seen that the isotropic oriented stainless steel and carbon conductive fibers in composite structure make more effectives electromagnetic shielding. It was found that as the frequency increases, the effectiveness of the electromagnetic shielding of the composite structures increase depending on stainless steel and carbon fibres used in the structure. the EMSE values obtained from composite with carbon fibers is higher than composite with stainless steel fibers. It is evident that the conductivity of the composite structure depends on ratios of stainless steel and carbon fibres used in the composite. As the effectiveness of electromagnetic shielding values were evaluated from **Tables 3** and **4**, it was found that the electromagnetic waves by composite were shielded about 99 % at 15 – 3000 MHz frequency ranges.

The fiber reinforced composite (SS–20) displays the best charpy impact strength. The fiber reinforced composite (SS–30) displays the best tensile strength. One of the most important factors affecting the mechanical properties of the composites is fiberproperty and the other important factor is amount of fibers.

Acknowledgements

This work was supported by the Scientific Research Project Unit (BAPKO) of the Marmara University (Project number FEN–D–100713–0337).

References

1. A. Das, V. K. Kothari, A. Kothari, A. Kumar, S. K. Tuli. Effect of various parameters on electromagnetic shielding effectiveness of textile fabrics. Indian J. Fibre & Textile 34 (2009) 144-148.
2. H. E. Leverkusen. Metallized fibers and textile fabrics. Melliand Textiberichte (Eng. ed.) 10 (1981) 366-369.
3. P. W. French, R. Penny, J. A. Laurence, D. R. mc Kenzie. Mobile phones heat shock proteins and cancer. Differentiation 67 (2000) 93-97.
4. K. Lai, R.-J. Sun, M.-Y. Chen, H. Wu, A.-X. Zha. Electromagnetic shielding effectiveness of fabrics with metallized polyester filaments. Textile Res. J. 77 (2007) 242-246.
5. M. Štefečka, M. Kando, H. Matsuo, Y. Nakashima, M. Koyanagi, T. Kamiya, M. Černák. Electromagnetic shielding efficiency of plasma treated and electroless metal plated polypropylene nonwoven fabrics. J. Mater. Sci. 39 (2004) 2215-2217.
6. S. Palamutcu, N. Dağ. Fonksiyonel Tekstiller 1: Elektromanyetik Kalkanlama Amaçlı Tekstil Yüzeyleri. E-J. Textile Technol. 3 (2009) 87-101.
7. C. T. Xingcun. Advanced Materials and Design for Electromagnetic Interference Shielding. 2009, CRC Press – Taylor & Francis Group, 44-45.
8. H. C. Chen, K. C. Lee, J. H. Lin, M. Koch. Comparison of electromagnetic shielding effectiveness properties of diverse conductive textiles via various measurement techniques. J. Mater. Proc. Technol. 192 (2007) 549-554.
9. Standard Test Method for Measuring the Electromagnetic Shielding Effectiveness of Planar Materials. D4935–10 (2010) ASTM.
10. Test Method of Specified Requirements of Electromagnetic Shielding Textiles. FTTS–FA–003 (2003) 1-4.
11. Standart Test Method for Tensile Properties of Polymer Matrix Composite Materials. ASTM D 303.
12. E. Bozkurt, E. Kaya, M. Tanoglu. Mechanical and thermal behavior of non-crimp glass fiber reinforced layered clay/epoxy nanocomposites. Composites Sci. & Technol. 67 (2007) 3394-3403.
13. G. W. Du, F. Ko. Analysis of multiaxial Warp–Knit performs for composite reinforcement. Composites Sci. & Technol. 56 (1996) 253-260.
14. ISO 179–1. Plastics –- Determination of Charpy Impact Properties. Part 1: Non-instrumented impact test.

TEMPERATURE DEPENDENCE OF THE ELECTRICAL TRANSPORT PROPERTIES OF MULTIPLAYER GRAPHENE

E. S. Sadki [1], H. Okazaki [2], T. Watanabe [2], T. Yamaguchi [2], Y. Takano [2]

[1] UAE University,
Abu Dhabi, United Arab Emirats
e_sadki@uaeu.ac.ae
[2] National Institute for Materials Science
Tsukuba, Japan

Accepted September 19, 2013

1. Introduction

Graphene has very interesting fundamental properties and promising applications [1]. Consequently, this material also re-generated an interest in studying its multilayer systems, ranging from few to large numbers of graphene materials (i.e. graphite) [2]. However, the low temperature properties, and superconductivity in particular, have not been sufficiently investigated in graphene and few-layer graphene systems. This is despite the several experimental demonstrations of superconductivity in intercalated graphite (e.g. [3]), and few theoretical predictions on superconductivity in graphene and few-layer graphene (e.g. [4]). Some groups have reported superconductivity in multilayer graphene induced by electrical gating [5] and potassium doping [6]. However, these results have not been confirmed by others so far. In this work, multilayer graphene (MLG) systems with different numbers of graphene layers are fabricated, and their electrical transport properties are measured at low temperatures to explore some of the above theoretical and experimental reports.

2. Experimental

The MLG thin films samples are prepared by scotch tape method of kish graphite onto a 300 nm thermally grown silicon oxide on silicon wafer (SiO_2 / Si) [7]). The MLGs of interest are initially located under an optical microscope, patterned by electron beam lithography, followed by gold / titanium (50 nm / 5 nm) evaporation, and finally lifted-off, to form electrodes configuration for electrical transport characterization. **Figures 1a** and **b** show an example of six metal terminals deposited on an MLG sample. An atomic force microscope (AFM) (Nanocute, SII NanoTechnology) is operated in AC-mode to measure the thickness of the MLG samples.

Figure 1c shows an AFM topography image of an MLG sample, with its measured thickness. Raman spectroscopy (RAMAN–11, Nanophoton), equipped with a laser of 532 nm in wavelength, is used to estimate the number of layers in the MLG samples. The electrical resistance measurements of the samples are conducted in a four-terminal configuration from room temperature down to 2 K, using a physical properties measurement system (PPMS, Quantum Design) with a constant current of typically 100 nA. For comparison, the same electrical measurements were also conducted using an AC lock-in amplifier technique.

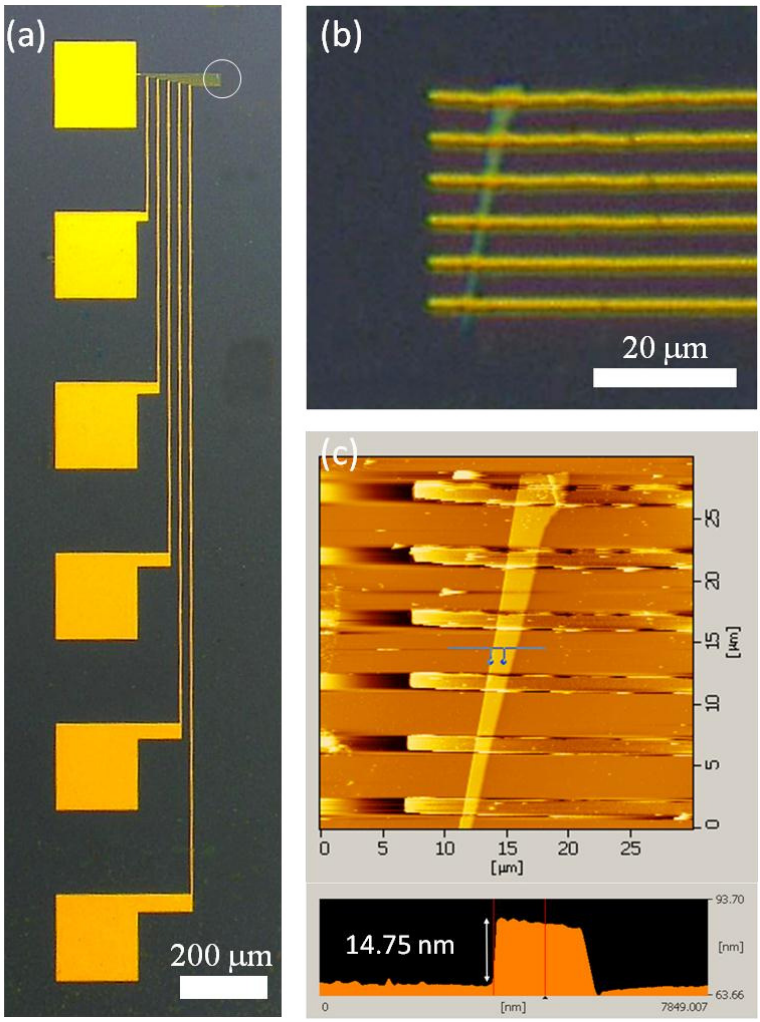

Figure 1. Optical microscopy photographs of (a) the fabricated gold electrodes configuration, with a MLG sample located in the area within the circular indicator, and (b) a close-up on MLG1 sample under the gold terminals; (c) an atomic force microscopy (AFM) topography image of MLG1, with the inset below showing the measured thickness of the sample.

2. Results and discussion

The AFM-measured thickness of three samples MLG1, MLG2, and MLG3, are 14.75, 3.93, and 3.37 nm, respectively. Assuming a thickness of 0.345 nm for a single layer graphene, the estimated number of graphene layers is 42, 8, and 3, for MLG1, MLG2, and MLG3, respectively. These figures are compared with Raman spectroscopy data below.

Figure 2 shows the Raman spectrum of the samples. The G-band and 2D-band peaks are clearly observed (2D-band was not measured for MLG1). These peaks are used to obtain many structural and physical properties of monolayer graphene and MLGs [8]. In particular, these peaks were used to estimate the number of graphene layers in MLGs [9]. For example, the number of graphene layers was correlated to both the intensities of the G-band peak and 2D-band peak, as well as to their positions [10 – 12].

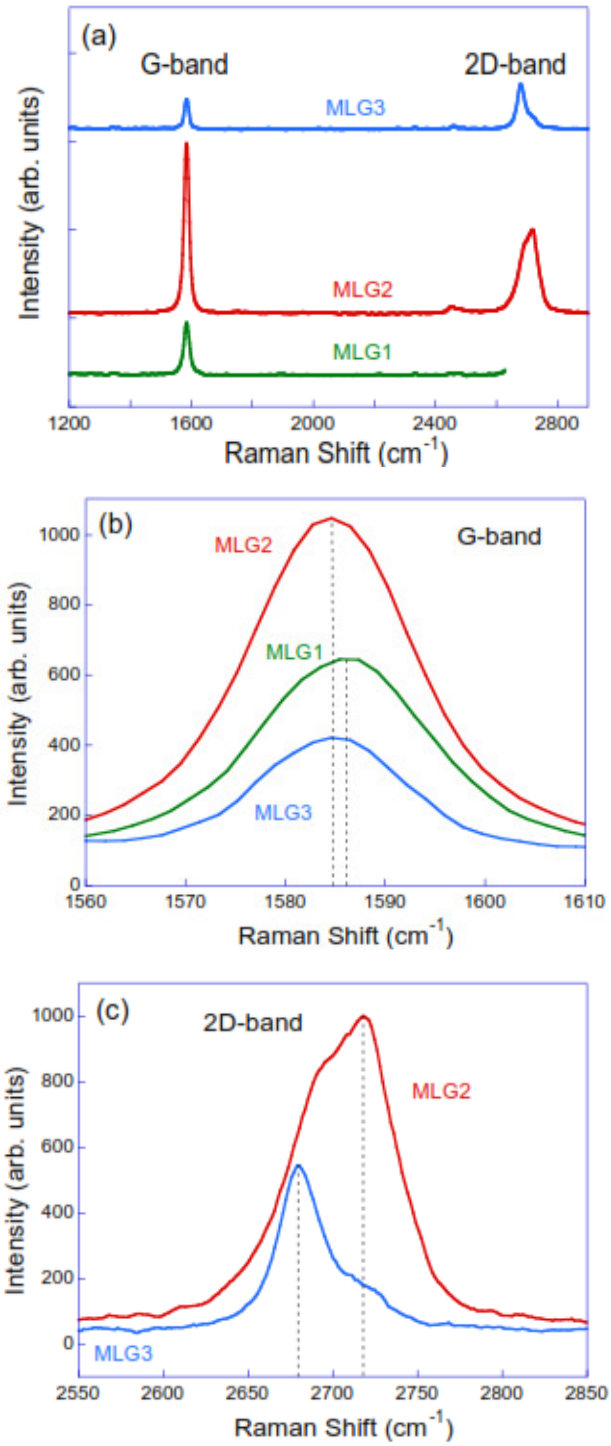

Figure 2. (a) Raman spectrum of the MLG samples excited by a 532 nm laser. Raman spectrum (b) around the G-band, and (c) the 2D-band. Dotted vertical lines show the positions of the respective peaks.

As shown in **Figure 2b**, the G-band peaks of sample MLG1 is located at 1586.4 cm^{-1}, and that of both MLG2 and MLG3 coincide at the same position 1584.6 cm^{-1}. In general the frequency is expected to shift lower with increasing the number of layers [8]. However, for MLGs with less than around 10 layers, the change is not systematic [11, 12]. Therefore, the peaks positions of the G-band of our samples cannot be used to accurately determine the number of layers. The ratio of the intensities of the G-band peaks of MLG2 on MLG3 is about 2.3 (see **Table 1**). This value is in good agreement with the data from [11, 12] that corresponds

to a number of layers of 7 and 3 for MLG2 and MLG3, respectively. This is in good agreement with the AFM data. However, errors are expected in AFM measurements on MLGs due to their dependence on the operating conditions [13], and hence, Raman data is preferable for this calculation as the difference in G-band peak intensities significantly changes with the number of layers. It is noted that the intensity of the G-band peak of MLG1 is lower than that of MLG2. This is expected for graphene layers of more than about 7 to 9 [11, 12].

Table 1. Summary of samples properties.

Sample	AFM thickness, nm	G-band position, cm^{-1}	G-band peak intensity, a.u.	2D-band position, cm^{-1}	2D-band peak intensity, a.u.	Number of graphene layers
MLG1	14.75	1586.4	566	–	–	42
MLG2	2.93	1584.6	789	2718	924	7
MLG3	1.28	1584.6	335	2680	505	3

The 2D-band peaks for MLG2 and MLG3 are shown in **Figure 2c**. The peaks positions are located at 2718 and 268 cm^{-1} for MLG2 and MLG3, respectively. This shift of the 2-band peak to higher frequencies with increasing number of graphene layers is in agreement with both experiments and theoretical predictions [8]. By comparison with the data from [12], the general shape of our peaks corresponds indeed to the 3 and 7 layers graphene systems. All the above data is summarized in **Table 1**. **Figure 3** presents the electrical resistance versus temperature results. With decreasing temperature, all MLG samples show first an increase in the resistance up to a maximum point, then a decrease, and finally a small increase at the lowest temperatures. The increase in the resistance up to the maximum point was more dramatic with increasing the number of graphene layers in the samples, with normalized resistance to the 300 K value (i.e. $R / R_{300\,K}$) of 1.8, 1.2, and 1.1, for MLG1, MLG2, and MLG3, respectively. The position of the maximum value of the resistance is located at 19, 50, and 39 K, respectively.

The above results are quite different from that of bulk graphite that shows a monotonic decrease in the resistance with decreasing temperature, i.e. metallic-like behavior [14]. However, similar qualitative effects to our data were observed when the thickness of the graphite samples was reduced to below 20 mm [15, 16]. The thinnest measured samples from these groups were 12 [15] and 13 nm [16]. The thickness of these samples correspond roughly to our MLG1, and indeed the value of the normalized resistance at the peak value (~ 1.3), and its position (~ 50 K) from [15] are in reasonable agreement with our data for MLG1. However, for the 13 nm thickness sample from [16], no peak was observed. Nevertheless, the same group [16] observed a peak with $R / R_{300\,K} \sim 1.5$ at 35 K for a 20 nm thick sample, which is strikingly very similar to MLG1. This peak was explained by competing contributions between a semiconducting-like behaviour of the intrinsic graphene layers and metallic-like behaviour originating from interfaces or defects between these layers [16], or by assuming the simple two band model (STB) of overlapping between the electrons and holes bands around the Fermi level of graphite [15].

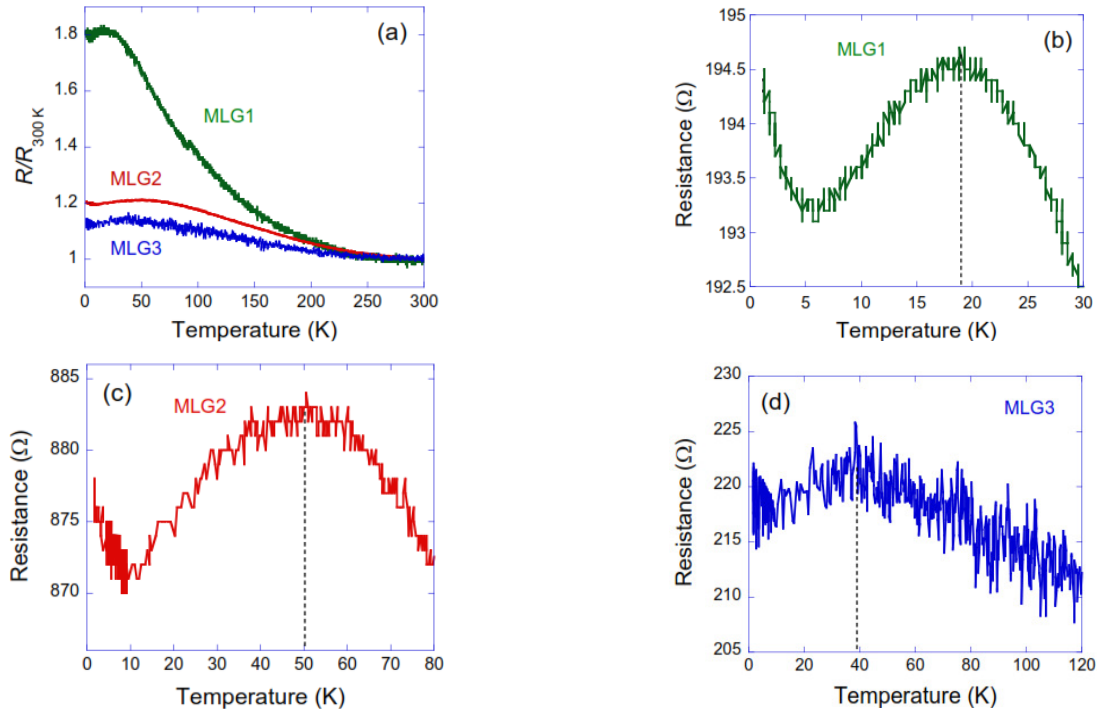

Figure 3. (a) Normalized resistance (R / $R_{300\,K}$) of the MLG samples measured from 300 down to 1.5 K. The resistance versus temperature of the samples (b) MLG1, (c) MLG2, and (d) MLG3, measured before the maximum resistance and down to 1.5 K. The dotted lines show the location of the onset of the observed down-turn of the resistance.

The peaks in the resistances of MLG2 and MLG3 observed are less pronounced than that of MLG1, with values of about 20 and 10 % above $R_{300\,K}$, for MLG2 and MLG3, respectively. This is inconsistent with the experimental data from [15] and [16] that predict that the maximum normalized resistance should increase with reducing the number of graphene layers. However, these groups never measured MLG samples as thin as ours. It is also noted that the signal to noise ratio decreases with decreasing the number of graphene layers. This could be explained by increased sensitivity to the environment for thinner samples, especially MLG3.

In order, to explore all the above theories and others, further structural analysis on defects / interfaces in our samples, as well as electrical transport measurements under magnetic fields are required, which is beyond the scope of this paper. Finally, it is noted that superconductivity, which is characterized by a dramatic drop of the electrical resistance to zero, is not observed in our MLG samples. A way to explore this possibility is by controlling the electronic carrier concentration by electronic gating [5], ionic-liquid doping [17], or intercalation [3]. These could be very interesting paths to explore in the future.

Conclusion

In conclusion, different multilayer graphene (MLG) samples were fabricated, and the number of their graphene layers were determined from both Atomic Force Microscopy (AFM) and Raman Spectroscopy analysis. The electrical resistance is measured from room temperature down to 2 K. The measured electrical resistance of the MLGs shows an increase with decreasing temperature, and then a downturn decrease at lower temperatures. The increase in the resistance up to the maximum point was more dramatic with increasing the number of graphene layers in the samples. Superconductivity is not observed in these samples.

References

1. A. K. Geim, K. S. Novoselov. The rise of graphene. Nat. Mater. 6 (2007) 183-191.
2. X. Huang, Z. Yin, S. Wu, X. Qi, Q. He, Q. Zhang, Q. Yan, F. Boey, H. Zhang. Graphene-based materials: Synthesis, characterization, properties, and applications. Small 7 (2011) 1876-1902.
3. T. E. Weller, M. Ellerby, S. S. Saxena, R. P. Smith, N. T. Skipper. Superconductivity in the intercalated graphite compounds C_6Yb and C_6Ca. Nat. Phys. 1 (2005) 39-41.
4. G. Profeta, M. Calandra, F. Mauri. Phonon-mediated superconductivity in graphene by lithium deposition. Nat. Phys. 8 (2012) 131-134.
5. A. Ballestar, J. Barzola–Quiquia, S. Dusari, P. Esquinazi, R. R. Silva, Y. Kopelevich. Electric field induced superconductivity in multigraphene, 2012. http://arxiv.org/abs/1202.3327.
6. M. Xue, G. Chen, H. Yang, Y. Zhu, D. Wang, J. He, T. Cao. Superconductivity in potassium-doped few-layer graphene. J. Am. Chem. Soc. 134 (2012) 6536-6539.
7. K. S. Novoselov, A. K. Geim, S. V. Morozov, D. Jiang, Y. Zhang, S. V. Dubonos, I. V. Grigorieva, A. A. Firsov. Electric field effect in atomically thin carbon films. Science 306 (2004) 666-669.
8. A. C. Ferrari, D. M. Basko. Raman spectroscopy as a versatile tool for studying the properties of graphene. Nat. Nanotechnol. 8 (2013) 235-246.
9. D. Graf, F. Molitor, K. Ensslin, C. Stampfer, A. Jungen, C. Hierold, L. Wirtz. Spatially resolved Raman spectroscopy of sSingle- and few-layer graphene. Nano Lett. 7 (2007) 238-242.
10. I. Calizo, A. A. Balandin, W. Bao, F. Miao, C. N. Lau. Temperature dependence of the Raman spectra of graphene and graphene multilayers. Nano Lett. 7 (2007) 2645-2649.
11. Y. Y. Wang, Z. H. Ni, Z. X. Shen, H. M. Wang, Y. H. Wu. Interference enhancement of Raman signal of graphene. Appl. Phys. Lett. 92 (2008) 043121 1-3.
12. D. Yoon, H. Moon, H. Cheong, J. S. Choi, J. A. Choi, B. H. Park. Variations in the Raman spectrum as a function of the number of graphene layers. J. Korean Phys. Soc. 55 (2009) 1299-1303.
13. P. Nemes–Incze, Z. Osvath, K. Kamaras, L. P. Biro. Anomalies in thickness measurements of graphene and few layer graphite crystals by tapping mode atomic force microscopy. Carbon 46 (2008) 1435-1442.
14. I. L. Spain. Electronic transport properties of graphite, carbons, and related materials. In: Chemistry and Physics of Carbon. 1981, New York: P.A. Marcel Dekker, 119-304.
15. Y. Zhang, J. P. Small, W. V. Pontius, P. Kim. Fabrication and electric-field-dependent transport measurements of mesoscopic graphite devices. Appl. Phys. Lett. 86 (2005) 073104 1-3.
16. N. García, P. Esquinazi, J. Barzola–Quiquia, S. Dusari. Evidence for semiconducting behavior with a narrow band gap of Bernal graphite. New J. Phys. 14 (2012) 053015 1-14.
17. K. Ueno, S. Nakamura, H. Shimotani, A. Ohtomo, N. Kimura, T. Nojima, H. Aoki, Y. Iwasa, M. Kawasaki. Electric-field-induced superconductivity in an insulator. Nat. Mater. 7 (2008) 855-858.

A STUDY OF THE EFFECT OF CARBON NANOTUBES DISPERSION ON THE PROPERTIES OF POLYMER COMPOSITE NANOFIBERS

X. Barbosa, S. Rosa, V. Capel, F. Martínez, R. Quiñones, W. Cuadrado, I. Ramos, J. Sotero–Esteva

University of Puerto Rico at Humacao
Humacao, Puerto Rico
idalia.ramos@upr.edu

Accepted September 19, 2013

1. Introduction

Carbon nanotubes (CNTs) have a unique combination of mechanical, electrical, optical, and thermal properties that make them excellent candidates for the fabrication of multifunctional polymer nanocomposites. The use of carbon nanotubes to enhance the properties of nanocomposite materials has important important applications in the development of technological applications for chemical sensing, photoemission, structural materials, energy storage, among others [1, 2].

The distribution and alignment of carbon nanotubes and their adhesion to the polymer matrix are critical to improve the processability, electrical, magnetic, and optical properties of polymer nanocomposites [3, 4]. Many efforts have been dedicated to find effective methods to overcome the van der Waals attractions that maintain the tubes aggregated. The challenge is to separate the CNTs from the bundles and stabilize them in the polymer matrix to prevent secondary agglomeration. The dispersion processes for CNTs include mechanical methods, as well as chemical and physical functionalization [5]. The dispersion of carbon nanotubes in aqueous and organic media is caused by non-covalent adsorption of surfactants and polymers. The physical absorption of surfactants on the CNT surface lowers the surface tension of the nanotubes preventing the formation of aggregates and overcoming the van der Waals attraction by electrostatic / steric repulsive forces. The efficiency of the surfactant depends on the properties of the surfactant and its medium. CNTs dispersion is promoted by cationic surfactants in water-soluble polymers and by non-ionic surfactant in water-insoluble polymers [6]. In the presence of polymers, the suspension of CNTs leads to non-covalent functionalization of the nanotubes due to the wrapping of polymers around the tubes. The polymer wrapping process is achieved through the van der Waals interactions and $\pi - \pi$ stacking between CNTs and polymer chains containing aromatic rings [5].

The techniques based on pre-dispersion of CNTs in a solvent, followed by mixing with a polymer, have proven to be effective to obtain uniform dispersion of tubes in nanocomposites. Our work integrates several of the techniques described above to prepare a CNT / polymer precursor solution to produce composite nanofibers using the technique of electrospinning. Electrospinning is a simple and economical to produce long and continuous nanocomposites in the shape of fibers [7, 8]. In this method, an electrically charged polymer solution is fed through

a small hole or needle. As a result, a jet of solution emerges from the needle towards a collecting plate, producing long fibers with micro and nanometric diameters. Studies of CNT / polymer nanofibers produced using electrospinning show that the process induces the alignment of the CNTs along the fibers [9]. The incorporation of carbon nanotubes into electrospun fibers with large surface areas is important for the development of chemical and biological sensors and electromechanical actuators [1, 10].

In this work, the interactions between CNTs, surfactants, solvents and polymer are studied with the goal of enhancing the properties of electrospun CNT / polymer composite nanofibers. In the experimental part of this research, single wall carbon nanotubes (SWCNTs) are dispersed in chloroform ($CHCl_3$) using sonication, with and without the addition of the ionic surfactants sodium dodecyl sulfate (SDS) and sodium dodecylbenzenesulfonate (SDBS). After dispersion, the CNTs are added to a polymeric solution of polyvinylpyrrolidone (PVP) and poly(methylmethacrylate) (PMMA) in $CHCl_3$. The resultant SWCNT / polymer solution is used as the precursor for electrospinning.

UV–Vis absorption measurements are used to study the dispersion of carbon nanotubes. The absorption spectra provides information about the effectiveness of a surfactant for dispersing carbon and the diameter distributions of the samples [11, 12]. Individual CNTs are active in the UV–Vis in opposition to bundles of CNTs that are hardly active. The last behaviour is attributed to charge transfer via tunnelling between the respective nanotubes [13]. As a result, the intensity of the absorption spectrum of a solution is directly related to the amount of individually dispersed.

The electrical conductivity of carbon nanotubes is also related to the dispersion. The use of surfactants alters the state of aggregation of the CNTs and produces variations in conductivity. In addition, as a result of the dispersion processes, individual CNTs are expected to create pathways for the current to flow [14].

In the preparation of the CNT / polymer precursor for electrospinning process there are two crucial junctions: when surfactants and solvent are added to the bundled CNTs in order to disperse them, and when the dispersed CNTs are mixed with the polymer. The questions addressed in the computational part of this paper are: what is the product of the CNT dispersion processes, and how the polymer conforms about that product?

Molecular dynamics simulations represent the dynamics of matter as represented in computationally simulation techniques. The elementary entities in these simulations can be sub atomic particles, atoms or sets of atoms (such as monomers in polymers or peptides in proteins). When the elementary entities are atoms and the dynamics is simulated by iterative integration of Newton's equations, as it is the case in this work, the technique is called classical molecular dynamics (CMD). The forces in a CMD system are defined by means of a set of potential functions with parameters that depend on the different atom types in the system. In this work we use the potential function,

$$\sum_{bounds} K_b (b - b_0)^2 + \sum_{angles} K_\phi (\phi - \phi_0)^2 + \sum_{dihedrals} K_\theta (1 + \cos(n\theta - \delta) +$$

$$+ \sum_{nonbonded} \left[\frac{q_i q_j}{4\pi D r_{ij}} \varepsilon_{ij} \left[\left(\frac{R_{\min\, i,j}}{r_{ij}} \right)^{12} - 2 \left(\frac{R_{\min\, i,j}}{r_{ij}} \right)^{6} \right] \right], \qquad (1)$$

that represents Van der Waals, Coulomb, bond, angle and torsion interactions. The coefficients in formula (1) are often selected based on experimental techniques or by sub atomic MD simulations. Their validity is always dependent on their demonstrated closeness to experimental values.

Literature shows many successful simulations of systems involving different combinations of carbon allotrope, polymers, surfactants and solvents. Of particular relevance to this work are carbon nanotubes (CNT) – polymer systems [15] and CNT / surfactant simulations [16]. Simulating the combination of materials in this work requires, however, the combinations of both.

In this paper, MD simulations and experimental results will be used to study the interactions between SWCNTs, surfactants (SDS and SDBS), solvent ($CHCl_3$), and polymer (PMMA) in the precursor solution for electrospinning and the characteristics of the electropun SWCNT / PMMA nanofibers.

2. Computational methods

The effectiveness of the sonication method used to disperse CNT in water in the presence of surfactants has being experimentally studied before [16]. Experimental observations for the end-product, that is, what is the conformation of surfactants around the CNTs is not conclusive but CMD simulations suggest that for high concentrations of SDS in water the surfactant forms a cylindrical micelle around the nanotube. Based on those results, the initial positions of the CNT and the surfactants for the CMD simulations in his work are set in a cylindrical micelle conformation. as shown in **Figure 2a**. Then periodic boundary conditions are set defining a box with a width that is 3.14 Å larger than the CNT. The other two dimensions are set large enough to accommodate the surfactant (SDS or SDBS) micelle around the CNT, plus additional 15 Å for the solvent. Since the CNT atoms are being kept fixed throughout the simulation, this set-up simulates an infinite nanotube with a tubular surfactant micelle. Then, the solvent ($CHCl_3$) is added and equilibrated with an energy minimization and a 500 K step dynamics simulation in which only the solvent is free to move. Then all molecules but the CNT are set loose for a 10 K step equilibration. Finally, nose–hoover pressure control at 1.0132 bar is set, the system is transferred to a GNU-equipped server, and the production simulation is run for at least 10 ns of simulated time. Langevin temperature control at 300 K is used in all simulations.

For the study of the conformation of the polymer about the CNTs, two simulations are prepared by adding the combination of PMMA to the initial CNT / SDS and CNT / SDBS setups described above and solvating with chloroform. **Figure 1** shows the initial setup for CNT / SDS. The one for CNT / SDBS is similar. The preparation of the production run follows the same protocol as described above.

The setup of the simulations is made using Wolffia 1.0 [17], a graphical user interface that set-up such simulations, on a laptop computer with and Intel Core i7–3630QM processor. The production simulation runs were performed using the general-purpose CMD simulator NAMD 2.9 multi core and CUDA version for LINUX [18] on a system equipped with a Intel Xeon CPU E5-2665 processor and four Nvidia Tesla C2050 GPU units.

Force field parameters for the CNT and SDS parameters were adapted from the ones used by are those used in [15] and [19], respectively. A four-atom chloroform model was used as described in [20] and the TIP3P was used for water. SDBS parameters were adapted from the CHARMM 27 force field and the charges of the atoms from [21]. Other relevant settings used include 12 A cut-off for non-bonded neighbor lists, 1 fs time step, 1 – 2 exclusions for simulations with SDS, 1 – 3 with fixed bond length for the ones with SDBS.

3. Experimental methods

The experimental analysis was done using single-walled carbon nanotubes (90 % CNTS, 50 % SWNTs, 1 – 2 nm diameter, 5 – 15 μm length, nanostructured & amorphous materials).

3.1. CNTs dispersion

The dispersion solutions were prepared using the solvent Choroform ($CHCl_3$, ≥ 99.8 %, Sigma Aldrich) with and without the addition of surfactants Dodecyl sodium sulfate (SDS, $CH_3(CH_2)_{11}OSO_3Na$, ≥ 98.5%, Sigma Aldrich) and Sodium dodecylbenzene-sulfonate (SDBS, $CH_3(CH_2)_{11}C_6H_4SO_3Na$, Sigma Aldrich). Three dispersion solutions were prepared using $CHCl_3$, SDS / $CHCl_3$, and SDBS / $CHCl_3$. The dispersion solutions were made at 1 wt % of the surfactant in the solvents. The weight ratio of the surfactant to SWCNTs is 10. The SWCNTs in the dispersion solutions were sonicated using a Brandson Model 1510 at 40 kHz for 1 h.

3.2. Precursor solutions

The precursor solutions for electrospinning were prepared by adding the SWCNTs in their dispersion solutions to a polymeric solution composed of poly(methyl methacrylate) (PMMA, M_w ~ 996 000, Sigma Aldrich) in $CHCl_3$ (22 wt %).

3.3. UV–Visible spectroscopy

An Agilent 8453 UV–Vis spectrometer was used to measure the absorbance in the region of 1100 to 200 nm, for the SWCNTs in the dispersion solutions and the precursor solution for electrospinning.

3.4. Electrospinning

In electrospinning, a high voltage is used to create an electrically charged jet of polymer solution, which dries or solidifies to leave a polymeric fiber. The electrospinning setup consists of a syringe, a syringe pump, a power supply, and a grounded collecting plate and has been described previously [22]. The electrospinning was done at room temperature with a voltage of approximately 10 kV. The fibers were collected on quartz slides.

3.5. Electrical measurements

Current–voltage measurements were conducted on strips of single mats of electrospun fibers, of approximately 0.1 mm × 0.25 mm, deposited on Si / SiO_2 wafers. The metallic contacts were prepared using Pelco colloidal silver liquid. A Keithley 6517 was used to measure the electrical current through the mats as the voltage was swept from –1 to +1 V.

4. Results and discussion

4.1. Computational results

4.1.1. Dispersed nanotubes with different surfactants and solvents

The simulation of the dispersed CNT in water serves in this work for validating the methods by comparing the results with available results in literature. Results of our simulations using water as solvent, show how both SDS and SDBS aggregate around the nanotube as cylindrical and hemispherical micelles respectively (**Figure 1**). The results are consistent with recent results [23].

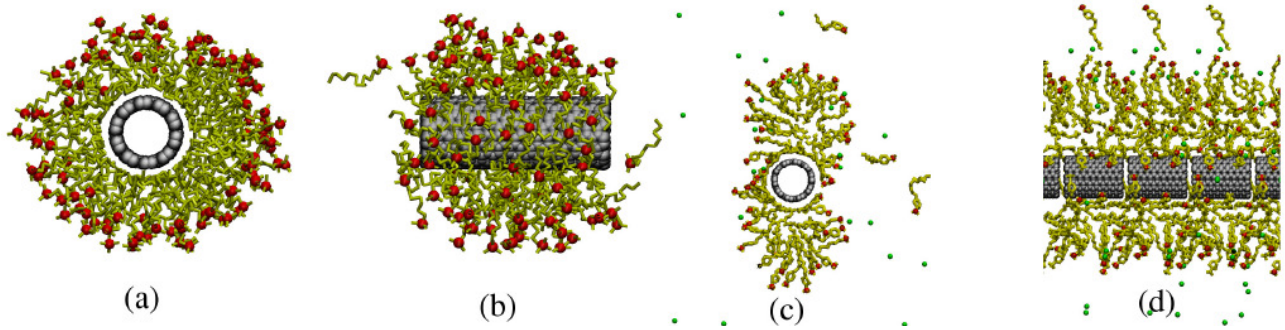

Figure 1. (a, b) SDS and (c, d) SDBS micelles around the CNT in water. Surfactants are in yellow with red spheres at the sulphate end and Sodium in green, CNT in grey. Hydrogen and solvent are hidden for clarity. These results are presented for validation of the method.

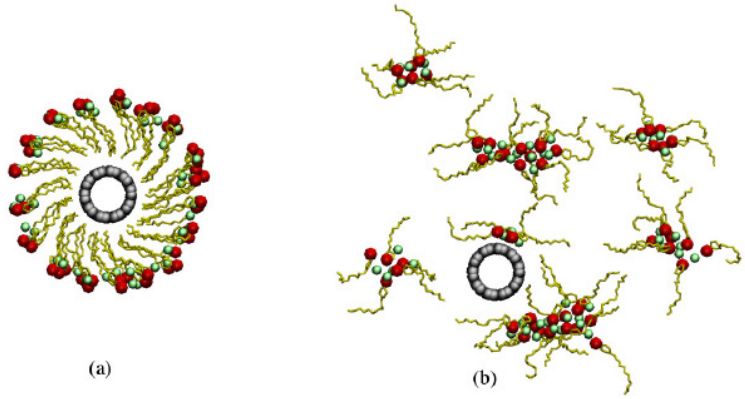

Figure 2. Initial (a) and final (b) positions of the CNT–SDBS system in chloroform. SDBS is in yellow with red spheres at the sulphate end and sodium in green, CNT in grey. Hydrogen and solvent are hidden for clarity.

When using chloroform as a solvent the end-result noticeably changed (**Figure 2**). Both surfactants, initially placed around the CNT, detached from the nanotube and formed dendrimer-like structures where the sulphate parts concentrate at the centers and the dodecyl chains, its non polar part, branching outward. This is consistent with the use of a non-polar solvent. It could be further observed that many of those structures remain completely detached from the CNT. A detailed investigation of this behavior would require quantitative measurements, such as potential mean force, which are out of the scope of this publication.

4.1.2. PMMA in the presence of a CNT–chloroform–surfactant system

Figure 3 shows the initial and final conformation of PMMA about the CNT / SDS system using chloroform as a solvent. Since the nanotube has been kept in a fixed position throughout the simulation, it serves as a reference point to infer how the rest of the molecules have moved. The polymer and surfactant are drawn to each other with the polar end of SDS attaching to the PMMA strands. The dodecyl tails of the SDS face outward even for the surfactant molecules that migrated to the outside of the system suggesting that in a larger timescale they would aggregate in this form around the polymer. Results of the PMMA / CNT / SDBS simulation are similar to this one. Two simulations smaller in size, of 20 ns simulated time, with three strands of PMMA and SDS or SDBS surfactants in chloroform, confirm that this aggregation around the polymer occurs. A detailed investigation of the preferred affinity of the surfactants to the polymer compared to the CNT would require quantitative measurements as well.

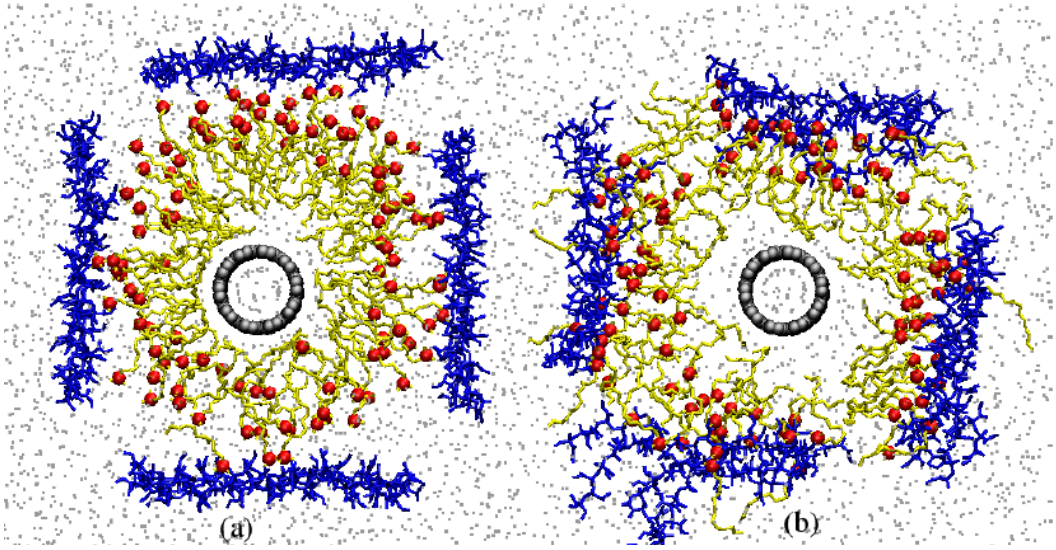

Figure 3. Initial (a) and final (b) positions of the system PMMA–SDS. PMMA is in blue, SDS in yellow with red spheres at the polar end, CNT in grey, and $CHCl_3$ (grey dots). Hydrogen and Sodium hidden for clarity. Image rendered with VMD.3.

4.2. Experimental results

4.2.1. UV –Visible spectroscopy

Figure 4 shows the UV–Vis spectra of the SWCNTs dispersion solutions in $CHCl_3$ after sonication for 1 h. The absorbance curves show a maximum between 200 and 300 nm, the UV–Vis active area for individual CNTs. The surfactants, SDS and SDBS are not soluble in $CHCl_3$.

During the preparation of the samples, the dispersion solutions with SDS and SDBS had a white cloudy color in opposition to the clear non-surfactant solutions, that shows a higher absorption in **Figure 4**. However, after mixing with the PMMA, all the precursor appear to have uniform distribution and produced good quality (uniform and long) electrospun fibers. The addition of surfactants has also being used to facilitate the integration of the CNTs into the polymer matrix [4]. **Figure 5** shows the UV–Vis spectra of the precursor solutions with the SDBS precursor suggesting a better dispersion of nanotubes and possibly a better integration to the polymer.

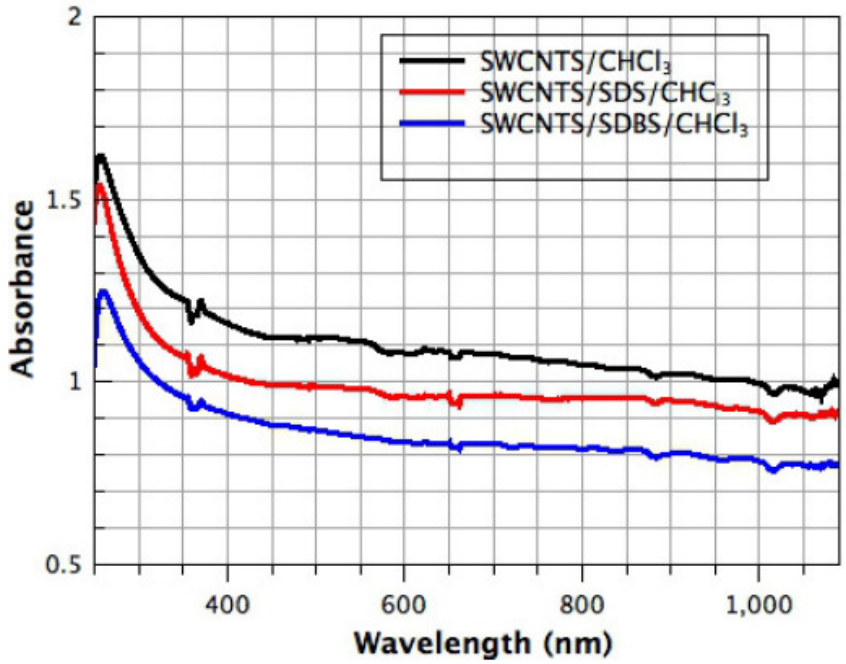

Figure 4. UV–Vis spectra of SWCNT dispersion solutions.

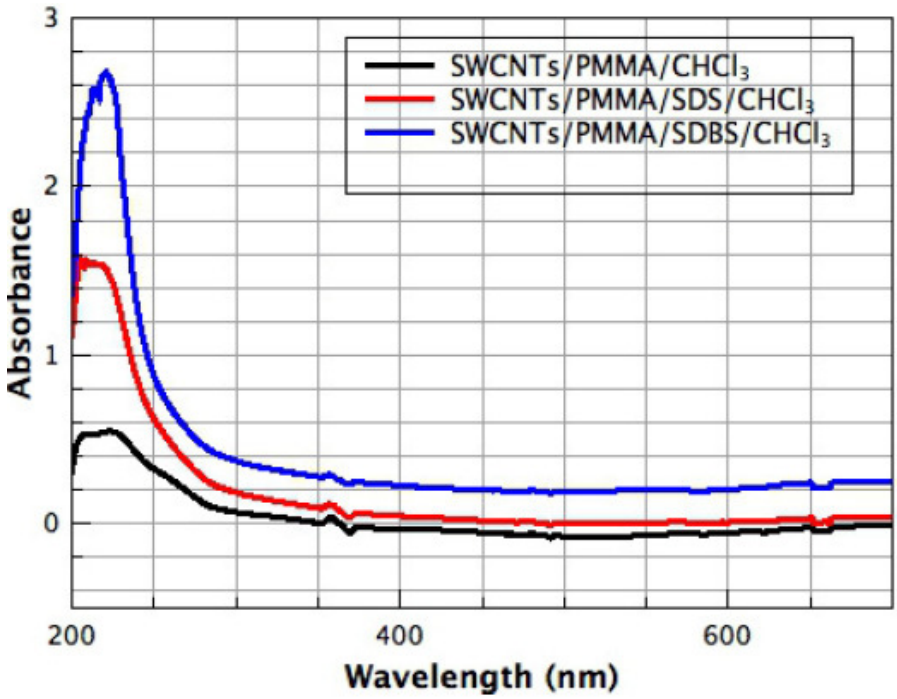

Figure 5. UV–Vis spectra of SWCNTs / PMMA precursor solutions.

4.2.2. Electrical characterization

Figure 6 shows the current–voltage characteristics on mats of SWCNT / PMMA fibers. The fibers with the carbon nanotubes dispersed in SDBS have the highest current and the least conductive are those dispersed without a surfactant. This can be attributed to a better dispersion of the nanotubes that promotes the interaction of the single CNTs creating a path for the electrical current [14]. More electrical measurements on single fibers with enhanced metallic contact are needed to understand the electronic transport properties of the composite fibers.

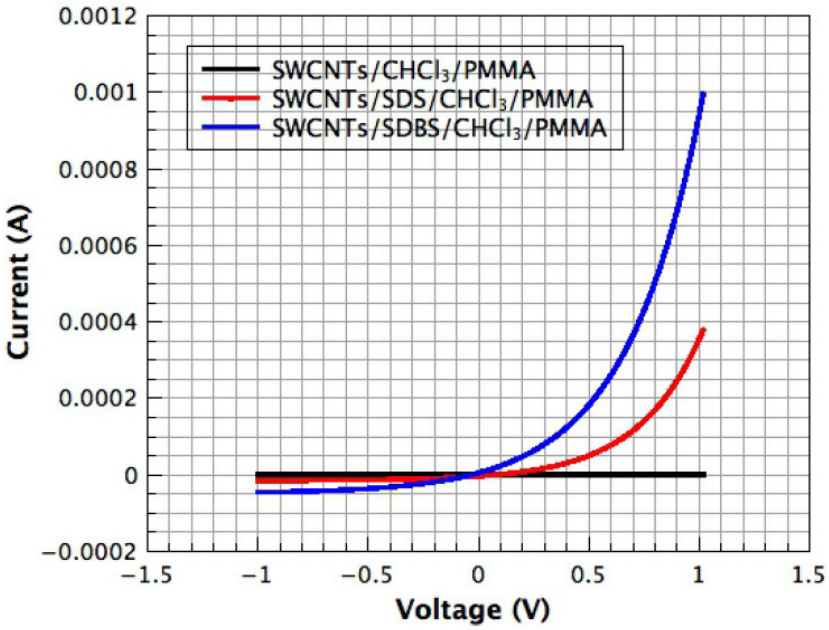

Figure 6. Current–voltage characteristics of SWCNT / PMMA electrospun fibers.

5. Conclusions and future work

The interactions between SWCNTs, cloroform, SDS, SDBS, and PMMA in precursor solutions and electrospun nanofibers were studied using MD Simulations, UV-spectroscopy, and current-voltage measurements. Results suggest that even though the surfactants are not soluble in chloroform, the sonication of SWCNTs in SDBS / cloroform and their addition to PMMA produces a precursor solution with well-dispersed nanotubes. This precursor allows the formation of uniform, continuous, and conductive nanofibers. More quantitive measurements are necessary to understand the interactions between CNTs / surfactans and choroform and the preferred affinity of the surfactants to the polymer compared to the CNTs. The electrical characterization of single nanofibers will provide more information about the electrospun fibers properties.

Acknowledgement

This research was sponsored by the National Science Foundation under grant NSF–DMR–0934195, PENN–UPRH Partnership for Research and Education in Materials (PREM).

References

1. L. Qu, Q. Peng, L. Dai, G. M. Spinks, G. G. Wallace, R. H. Baughman. Carbon nanotube electroactive polymer materials: Opportunities and challenges. MRS Bull. 33 (2008) 215-224.
2. M. Scarselli, P. Castrucci, M. de Crescenzi. Electronic and optoelectronic nano-devices based on carbon nanotube. J. Phys. Cond. Matter 24 (2012) 313202 1-13.
3. X.-L. Xie, Y.-W. Mai, X.-P. Zhou. Dispersion and alignment of carbon nanotubes in polymer matrix: A review. Mater. Sci. Eng. R 49 (2005) 89-112.
4. N. G. Sahoo, S. Rana, J. W. Cho, L. Li, S. H. Chan. Polymer nanocomposites based on functionalized carbon nanotubes. Prog. Polym. Sci. 35 (2010) 837-867.
5. P.-C. Ma, N. A. Siddiqui, G. Marom, J.-K. Kim. Dispersion and functionalization of carbon nanotubes for polymer-based nanocomposites: A review. Composites A 41 (2010) 1345-1367.
6. L. Vaisman, H. D. Wagner, G. Marom. The role of surfactants in the dispersion of carbon nanotubes. Adv. Colloid Interface Sci. 128-130 (2006) 37-46.
7. A. Formhals. Process and apparatus for preparing artificial threads. Patent # 1975504 (1934).
8. S. Ramakrishna, K. Fujihara, W.-E. Teo, T.-Ch. Lin, Z. Ma. An Introduction to Electrospinning and Nanofibers. 2005, World Sci. Publ. Co.
9. J. Gao, A. Yu, M. E. Itkis, E. Bekyarova, B. Zhao, S. Niyogi, R. C. Haddon. Large-scale fabrication of aligned single-walled carbon nanotube array and hierarchical single-walled carbon nanotube assembly. J. Am. Chem. Soc. 126 (2004) 16698-16699.
10. S. M. Rosa, J. P. Crespo, A. Meléndez, J. J. Santiago–Avilés, I. Ramos, E. M. Campo. CNT dispersion and precursor synthesis for electrospinning of polymer-CNT composites. Proc. SPIE 8107 (2011) 1-6.
11. L. Jiang, L. Gao, J. Sun. Production of aqueous colloidal dispersions of carbon nanotubes. J. Colloid Interface Sci. 260 (2003) 89-94.
12. J. A. Fagan, B. J. Bauer, E. K. Hobbie, M. L. Becker, A. R. Hight Walker, J. R. Simpson, J. Chun, J. Obrzut, V. Bajpai, F. R. Phelan, D. Simien, J. Y. Huh, K. B. Migler. Carbon nanotubes: Measuring dispersion and length. Adv. Mater. 23 (2011) 338-348.
13. J. Yu, N. Grossiord, C. E. Koning, J. Loos. Controlling the dispersion of multi-wall carbon nanotubes in aqueous surfactant solution. Carbon 45 (2007) 618-623.
14. Q. Y. Tang, I. Shafiq, Y. C. Chan, N. B. Wong, R. Cheung. Study of the dispersion and electrical properties of carbon nanotubes treated by surfactants in dimethylacetamide. J. Nanosci. & Nanotechnol. 10 (2010) 4967-4974.
15. R. R. Johnson, A. T. Charlie Johnson, M. L. Klein. The nature of DNA-base–carbon-nanotube interactions. Small 6 (2010) 31-34.
16. M. F. Islam, E. Rojas, D. M. Bergey, A. T. Johnson, A. G. Yodh. High weight fraction surfactant solubilization of single-wall carbon nanotubes in water. Nano Lett. 3 (2003) 269-273.
17. M. Medina–Cuadrado. Wolffia: An environment with a graphical user interface to prepare and monitor classical molecular dynamics simulations, 2013 – in press.

18. J. C. Phillips, R. Braun, W. Wang, J. Gumbart, E. Tajkhorshid, E. Villa, Ch. Chipot, R. D. Skeel, L. Kalé, K. Schulten. Scalable molecular dynamics with NAMD. J. Comput. Chem. 26 (2005) 1781-1802.
19. T. Cheng, Q. Chen, F. Li, H. Sun. Classic force field for predicting surface tension and interfacial properties of sodium dodecyl sulfate. J. Phys. Chem. B 114 (2010) 13736-13744.
20. A. Lukyanov, A. Malafeev, V. Ivanov, H.-L. Chen, K. Kremer, D. Andrienko. Solvated poly-(phenylene vinylene) derivatives: conformational structure and aggregation behavior. J. Mater. Chem. 20 (2010) 10475-10485.
21. F. Palazzesi, M. Calvaresi, F. Zerbetto. A molecular dynamics investigation of structure and dynamics of SDS and SDBS micelles. Soft Matter 7 (2011) 9148-9156.
22. Y. Wang. Diversity of nanofibers from electrospinning: From graphitic carbons to ternary oxides. In: Nanofibers (Ed. A. Kumar), 2010.
23. N. R. Tummala, B. H. Morrow, D. E. Resasco, A. Striolo. Nanotube dispersions using surfactants: Insights from molecular dynamics simulations. ACS Nano 4 (2010) 7193-7204.

INTERACTION OF CARBON NANOTUBES WITH MINERAL NUTRIENTS FOR THE PROMOTION OF GROWTH OF TOMATO SEEDLINGS

D. K. Tiwari [1], N. Dasgupta–Schubert [1], L. M. Villaseñor [1], Dh. Tripathi [2], J. Villegas [1]

[1] Universidad Michoacana de San Nicolás de Hidalgo
Morelia, México
dkt@ifm.umich.mx
[2] Banaras Hindu University
Varanasi, India

Accepted September 19, 2013

1. Introduction

Carbon nanotubes (CNTs) are molecular-scale tubes of graphitic carbon with outstanding electrical, mechanical and thermal properties, which have attracted a major interest in their exploitation for diverse applications. Some carbon nanotubes can be extremely efficient conductors of electricity and heat, some act as semiconductors, depending on their configurations. Most studies of CNTs in bioscience have focused on their influences in animal and human cells but relatively scant attention has focused on the role of CNT in the agrosciences. Indeed, the study on the effects of CNTs in plant science is a newly emerging area of research [1, 2] where of late, several studies have focussed on their interaction with plant cells and their dramatic effects plant growth [3, 4]. At present, many different studies are being performed all over the world to elucidate the contribution of CNT in agricultural and environmental applications. The most popular studies in this area are the production of biofuel, glucose oxides, hydroxyapatite and in plant growth. The draw-backs to CNT are where they directly enter the human body such as by ingestion or inhalation because of their toxicity [1, 5, 6]. As far as the latter is concerned, a recent study in our laboratory has shown the impact of CNTs on germinating maize plant organs and their role in the delivery of water and nutrients for the growth of maize seedlings [7].

Seed-coats however, are considerably thicker than plant cell walls or membranes, making their penetration by the CNTs difficult, if not unlikely. A study [8] purports to show the penetration of the seed-coat by the MWCNT, but this work has not been adequately corroborated. The interaction of the CNT with the seed-coat occurs in such a manner as to accelerate seed germination in a way that varies with seed-type and the specific physiology of the germinating plant as well as the degree of CNT purity and its concentration [9]. A recent study in our laboratory [7] has shown that MWCNTs alter the surface topography of the seed-coat of maize seeds by perforative scarification. Such alterations would facilitate the delivery of water to accelerate seed imbibition and thus germination [10]. The large aspect ratios of CNTs could possibly affect water conduction since molecular dynamic calculations have shown the CNTs act as molecular channels for enhanced water transport [11, 12]. The results of our

previous experiments on maize plants [7] show that germination in the presence of MWCNT was rapid with the radicle emerging after 48 h whereas for the control (non-MWCNT treated) seeds, the radicle emerged only after 72 h. Water content was also enhanced in the MWCNT treated seeds. In contrast to water imbibition however, the germinating seed in the initial stages has little need for external nutrients since the embryo contains sufficient nutrients. It is in the latter stages after the emergence of true leaves and shoot elongation that higher nutrient supply would be expected to benefit the growing plant. The question of how the CNT affects nutrient acquisition by the plant in the later stages of growth has not been adequately addressed.

Consolidation these various aspects together, the objectives of the present work were the following: (1) the germination and growth of tomato seedlings as a function of the concentration of pristine MWCNT and dMWCNT in the 3 growth periods of 7, 14 and 27 days to see the effect of de-aggregation and CNT concentration in the different growth periods (2) the macro- and micro-nutrient element concentrations in the plant at different growth stages for the aforesaid 2 types of MWCNT treatments as a function of their different concentrations and when growth is conducted in plain agar and in agar fortified with 1–MS basal nutrient medium.

2. Experimental

2.1. Materials

Standard Murashige & Skoog (MS) medium (M5519) and pristine MWCNT (purity > 95 %, OD 6 – 9 nm, L 5 μm) were purchased from Sigma–Aldrich®, St. Louis, MO, USA. Bacteriological agar (BA) (Bioxon®) was purchased from Becton–Dickinson (BD de Mexico, Mexico City, Mexico), which contains a certain level of mineral nutrients as ionic or polar species [13]. Tomato seeds were purchased from a local seed supplier (Hortaflor, Rancho Los Molinos SA de CV, Mexico).

2.2. Medium preparation and plant growth

a) Plain medium, with and without MWCNT

The first experimental set consisted of tomato seedlings grown in bacteriological agar (BA) gel medium spiked with different concentrations of MWCNT. The appropriate masses of weighed MWCNT were mechanically mixed with deionized (DI) water for different concentration of mediums mentioned in **Table 1**.

Weighed BA powder for concentration of 15 g / l was added at a very slow rate to the aqueous phase MWCNT and finally autoclaved at 120 °C for 20 min. The BA solutions containing the different concentrations of the MWCNT were then poured into replicate sterile petridishes to set as the gel substrate for seed growth. Tomato seeds were cleaned by magnetic stirring in a 70 % ethanol solution for 2 min and washed with DI water. They were then surface sterilized in a 1 % v / v solution of sodium hypochlorite by gentle stirring for 10 min, then washed several times with DI water. The seeds were blotted dry in sterile paper towels and implanted into the gel substrates described previously. The petridishes were covered and appropriately labeled. These operations were done in the laminar flow-hood. The petridishes were then transferred to a climate-controlled chamber (temperature 23 – 25 °C, Relative

humidity (RH) ~ 71.5 %, photoperiod 16 h light – 8 h dark) and the seeds were allowed to germinate for 7 days. The total number of seedlings was 78 with each case listed in **Table 1** containing 13 seedlings.

Table 1. Sample description of tomato plants germinated in BA medium assisted with and without MWCNT.

Sample name	Growth medium and time	MWCNT concentration, µg / ml
C0	7 days germinated plants in BA growth medium with and without MWCNT **(C)**	0 (standard)
C5		5
C10		10
C20		20
C40		40
C60		60

b) Plant growth in medium with nutrient and dMWCNT

The second experimental set concerned the tomato plant growth using MWCNT ultrasonically dispersed in 1–MS medium of pH 5.75 for 2 h. First, a stock solution of 1–MS basal nutritive medium solution of pH 5.75 was made. Then the appropriate masses of the MWCNT were mixed in 100 ml of 1–MS medium solution and ultrasonicated for 2 h. After dispersion, this 100 ml solution was used to prepare the bacteriological agar medium solution of concentration 8 g / l (**Table 2**).

Tables 2. Sample description of tomato plantsgerminated in nutrient added and dMWCNT introduced BA growth medium.

Sample name	Growth medium and time	dMWCNT concentration, µg / ml
T0	14 days germinated plants in nutritive (1–MS) BA medium with and without dMWCNT **(T)**	0 (control)
T5		5
T10		10
T'0	27 days germinated plants in nutritive (1–MS) BA medium with and without dMWCNT**(T')**	0 (control)
T'5		5
T'10		10

Other processes were identical to the first set of experiment as mentioned in Subsection 2.2a. The total numbers of seedlings were 60 with each case listed in table 2 containing 10 seedlings, and the ambient condition was same as in the previous experiment (Subsection 2.2a).

2.3. Elemental analysis of the seedling tissue by polarized energy dispersive X-ray fluorescence analysis (pEDXRF)

pEDXRF spectrometry were applied for the analysis of macro and micro nutrient elements in the germinated tomato plants. The operating principle of pEDXRF is based on the

cancellation of the Bremmstrahlung background by the double polarization of the initial x-ray beam. The advantages of pEDXRF lie in its non-destructive, multi-elemental and rapid trace analysis capabilities.

Dry plant parts were milled in a grinder for 5 – 10 min till the entire mass appeared as a fine powder. The elemental analysis of the powders was carried out by the pEDXRF spectrometer SpectroXepos III (Spectro Analytical Instruments GmbH, Kleve, Germany) using the TurboQuant™ analytical routine. It is important to remember that for the low sample dry mass yields as in the present work, the quantity of interest is the relative magnitude of the element's concentration corresponding to the different treatments.

3.4. Fourier transform infra red (FTIR) spectroscopy

FTIRscans were run at resolution of 4 cm^{-1} between 40 – 4000 cm^{-1} range using Bruker tensor 27 FTIR spectrometer. Powder samples of whole seedlings (germinated plants) corresponding to the different experimental conditions (Subsection 2.2) were used.

2.4. Data analysis

Averages and standard errors were computed over 10 sets of replicates for each case listed in the tables 1 and 2 with the number of seedlings for each set as cited previously. The softwares;GraphPad Prism, Excel, and Origin were used for data reduction and analysis.

3. Results and discussion

3.1. Germination without MS nutrients and undispersed MWCNT growth medium

Figure 1 shows the effect of pristine MWCNT on tomato seedlingsof 7 days. We placed the sterile tomato seeds in without nutrient BA medium with different concentration of MWCNT. The medium without MWCNT (0 µg / ml) germinated plants were used as standard germinated medium compared with MWCNT treated systems. In this experiment we have used the various concentration of MWCNT to know, the effect of various concentration on germination and what will happen if exceeds the availability of MWCNTs in growth medium. The root and shoot length statistics of 7 days germinated plant seedlings are shown in Figure 1a with respect to MWCNT presented medium. The root length shows that there is no statistical variation with presence of MWCNT-germinated plants compared with standard medium germinated plants. The medium containing MWCNT of concentration 20 and 60 µg / ml have decrease in the root length than other media systems. Since MWCNT added without dispersion and there is not any clear information about homogeneous distribution of MWCNT in the medium. Sometimes MWCNTs are elongated in the medium and much availability of MWCNT causes the toxic effect in the medium, which is already explained in our previous work [7]. Shoot length distribution with respect to MWCNT concentration (**Figure 1a**) shows that, even without nutrients in the germinated medium MWCNT affects the growth more compared with standard medium germinated plants. From **Figure 1a**, we can see that there is better germination at concentration of 40 and 60 µg / ml of MWCNT. The root and shoot lengths are decreasing, this is because of the high availability of MWCNT.

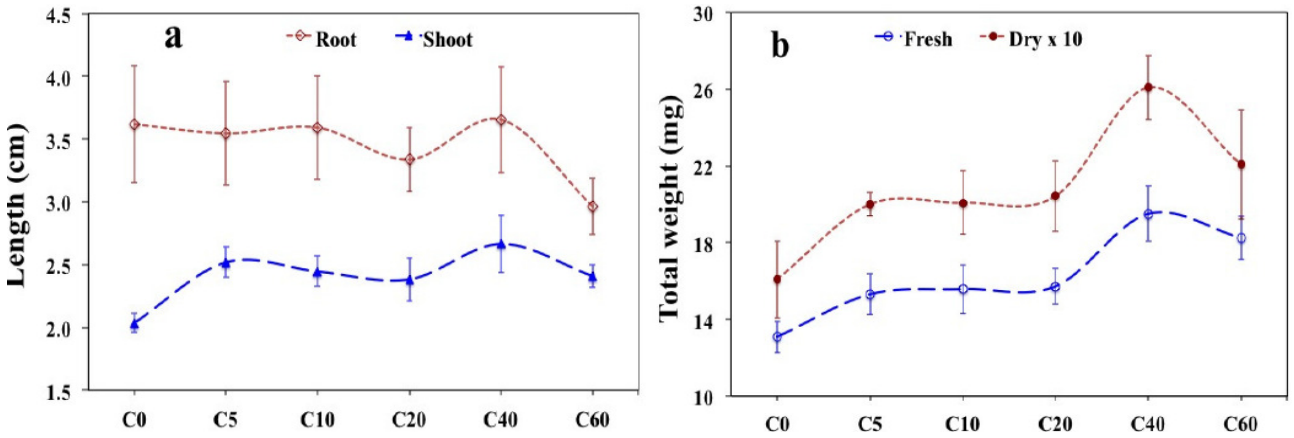

Figure 1. Effect of pristine MWCNT on 7 days tomato seedlings (**Table 1**).
a) Length of root and shoot growth on a medium with and without MWCNT.
b) Total fresh and dry × 10 weightmeasurement with respect to MWCNT concentration.

Figure 1b shows the total fresh and dry biomass measurement with MWCNT concentration, the dry weight data with respect to MWCNT concentrations are shown with their respective concentration multiplied by 10, its because to plot fresh and dry weight measured data on same plot. Total fresh and dry weight a measurement shows that, presence of MWCNT not only affects the growth of tomato seedlings but also affects the biomass than standard medium. From **Figure 1** we find that the best germination (length) and biomass (fresh and dry weight) find at MWCNT, 40 μg / ml present germination medium.

3.2. Seedling growth in MS nutrient and dMWCNT

Figure 2 shows the tomato germination in presence of nutrient medium for longer days. **Figure 2a**, shows the germination of tomato plants in full nutritive medium with and without dMWCNT. The presence of dMWCNTshows the better germination than respective control system. The root and shoot length is better in dMWCNT assisted growth medium of concentration 5 and 10 μg / ml than without dmwcnt but there is not any significant difference between 5 and 10 μg / ml concentration for root system while for shoot these two concentrations affects the germination for 14 and 27 days of seedlings.

If we compare, the rate of germination for 27 days of seedling, growth of different concentrations of dMWCNT than their respective concentration of 14 days seedlings; we can see that the rate of germination is lower as explained earlier. **Figure 2b** shows the root and shoot length statistics for 14 and 27 days of seedlings with respect to their % water availability, which shows that the root length follows the better linear trend with % water content, while in case of shoots the trend is not very fit. The linear fit of root and shoot length variation with respect to % water content is given as: root, $y = 3.69\,x - 29.04$, $R^2 = 0.75$, shoot; $y = -0.93\,x + 81.47$, $R^2 = 0.19$, of 14 days germinated plants and root, $y = 0.39\,x + 5.12$, $R^2 = 0.70$, shoot; $y = -0.06\,x + 13.50$, $R^2 = 0.03$, for 27 days germinated plants. The R^2 vale of linear fit for shoot shows that, in early days (14 days) follow better trend than that of 27 days, this is because all the germination done in closed circular magenta boxes of controlled photo-condition (16 h light, 8 h dark) and for longer days of germination, it is not only depends on the nutrient and water transport, there might happen photosynthesis too.

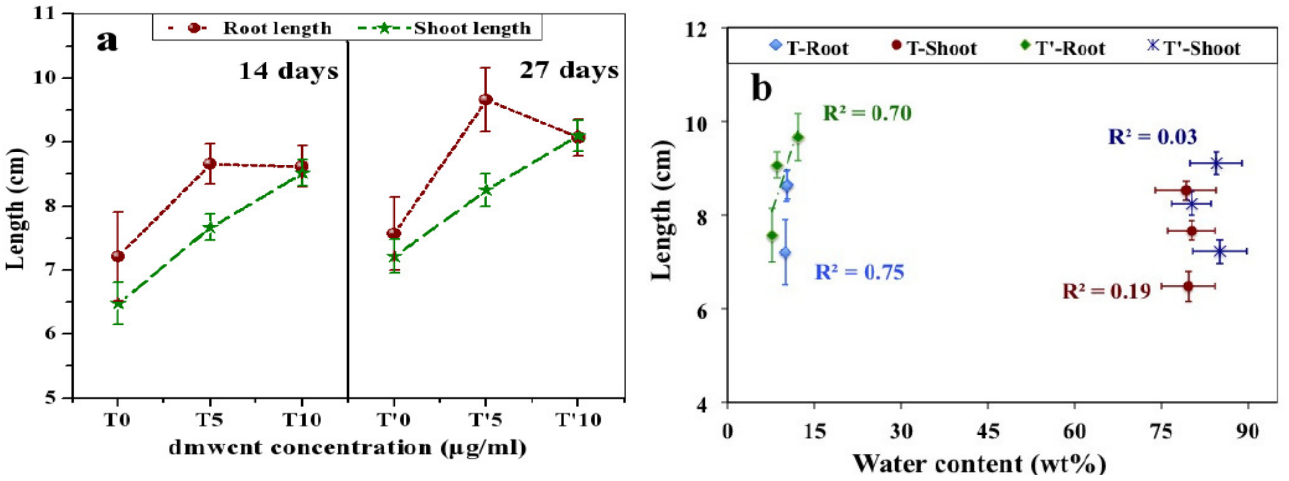

Figure 2. Tomato seedling growthin the presence of dMWCNT of 14 and 27 days (**Table 2**). a) Root and shoot length measurement. b) Root and shoot length variation with respect to % water content. Results are shown average ± SE of 10 plants per each treatment.

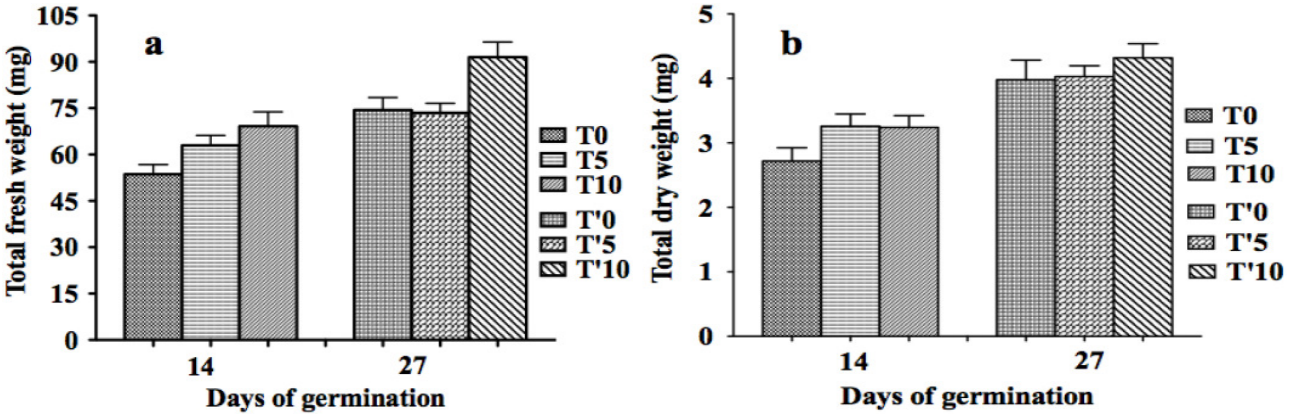

Figure 3. Effect of dMWCNT on growth and development of tomato plants of 14 & 27 days (**Table 2**) seedlings. a) Total fresh weight. b) Total dry weight. Results are shown average ± SE of 10 plants per each treatment.

Total fresh and dry weight measurements of root and shoots are shown in **Figure 3**. For lower days, dMWCNT shows high fresh weight than their respective control medium while for longer days, higher concentration of dMWCNT is more effective to gain biomass (**Figure 3a**). If we compare the growth of 27 days seedlings with their respective of 14 days, we can see that the control medium germinated plants gain weight in better ratio than that of dMWCNT, 5 µg / ml, while higher concentration (10 µg / ml) have better response. Dry weight measurement of total seedlings (**Figure 3b**) shows that, for longer days of germination the dMWCNT is beneficial for growth rate and also in biomass.

3.3. % elemental concentration analysis

The availability of nutrient elements in the germinated plants as explained in Subsections 2.2a and b (**Tables 1** and **2**) were analyzed using pEDXRF spectrometer shown in **Figure 4**. Since plants get carbon, hydrogenand oxygen from the air and water, considered as a non-mineral nutrient, except all these nutrients, there are certain minerals nutrients are very

important for plants to grow and develop which they get from the soil medium. The measured macro and Micro nutrient elements are K, Ca, Mn, Fe, Cu and Zn, whichplays very crucial role in the plants life. The detailed description of these nutrients and their availability in nutrient and MWCNT assisted growth medium is explained below.

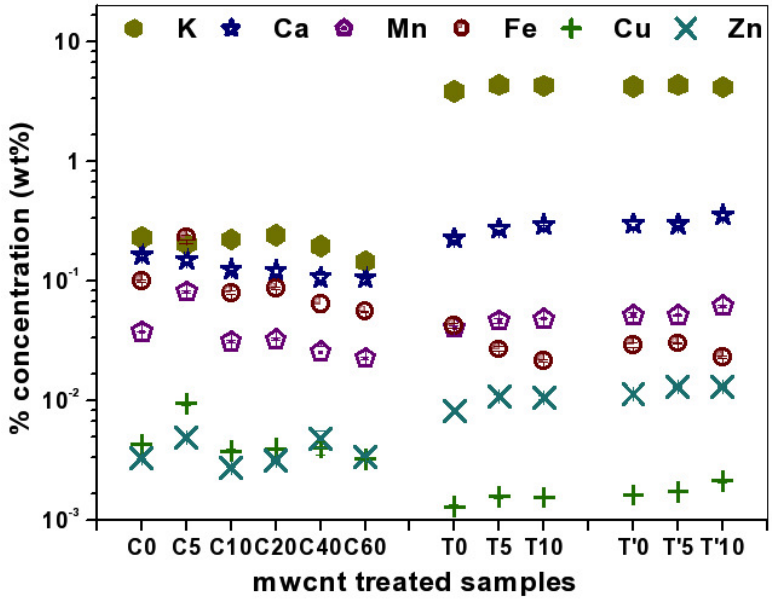

Figure 4. Percentage concentration of nutrient elements present in germinated tomato plants. C0 – 60 shows the samples germinated for 7 days with varying MWCNT concentration from 0 to 60 μg / ml and without using any additional nutrient in the growth medium (**Table 1**).T0 – 10 are the sample germinated for 14 days in presence of 1–MS nutrient in growth mediumand dMWCNT concentration 0 – 10 μg / ml (**Table 2**). T'0 – 10 are the samples of 27 days germinated plants in presence of 1–MS nutrient and dMWCNT 0–10 μg / ml concentration in the growth medium (**Table 2**).

Potassium (K): K is primary macronutrient very important for plants to help, building protein, photosynthesis and reduction of disease. K also plays a key role in maintenance of plant water balance and a vast array of physiology process vital for plant growth. Figure 4 shows clearly that plant germinated with nutrient growth medium contains high concentration (4 – 5 %) while without nutrient medium have much lower concentration (0.25 %) of K. Presence of MWCNT concentration in nutrient growth medium shows higher percentage than respective control, while plants grown without nutrients have high concentration at 20 μg / ml. The K deficiency to tomato plants exhibits uneven fruit ripening, poor texture and soft fruits.

Calcium (Ca): Ca is an important secondary nutrient essential for plants to provide the expansion of cell walls. It also helps to transport and retention of other elements as well as strength. Ca concentration of plants, germinated without nutrient medium decreases with increase of MWCNT concentration (**Figure 4**) while for nutrient media germinated plants Ca concentration increases with increase of dMWCNT concentration. That shows dMWCNT not only affects the germination but also promotes the nutrient elements (Ca) during germination.

Iron (Fe): Fe is a micronutrient, essential to plant growth, formation of chlorophyll and acts as an oxygen career. From **Figure 4**, Fe concentration decreases with introduction of MWCNT and dMWCNT except MWCNT 5 μg / ml.

Manganese (Mn): Mn functions with enzyme system involved in breakdown of carbohydrates and nitrogen metabolism. Mn concentration follows the same trend as Fe with presence of MWCNT concentration, while in nutrient germinated plants dMWCNT increase the transportation rate than without dMWCNT treated system. This means dMWCNT support the delivery of Mn element same as Ca.

Copper (Cu): Cu concentration in the germinated plants are random and their delivery and presence is not highly affected by MWCNT or dMWCNT. Only the MWCNT with concentration of 5 µg / ml shows high availability of Cu while in other cases it is decreasing and almost close to the plants germinated without MWCNT, and in dMWCNT it is slightly higher % ratio than their respective control. From **Figure 4**, we notice that in the nutritive medium the Cu concentration is much lower than that of without nutritive medium of early days of germination, that means this Cu concentration is not because of the nutrient availability but because of the presence in the cell matrix of seeds. While the seeds are start germination there availability in seed cell matrix is high while the plants start growing this Cu nutrient transported by natural transport statistics of seed cell process to make plants strong and availability getting less.

Zinc (Zn): The Zn concentration varying with the growth medium, with the MWCNT concentration of 5 and 20 µg / ml (C), the Zn concentration increases relatively then other growth medium. While the plants grown in MS nutritive medium and dMWCNT the concentration of Zn is highly differ from those germinated with MS medium and with the presence of dMWCNT the concentration increasing compared with their control germinated plants. This shows clearly that dMWCNT promotes the Zn availability within plants in higher ratio than that of without dMWCNT. Another aspect of this is, if we compare only the control system germinated plants of C0 (without nutrient), T0 (MS germinated plants of 14 days) and T'0 (MS germinated plants of 27 days), the concentration on Zn increasing with time and also the presence of nutrients promotes the transport of Zn elements itself my seeds without any promoter like MWCNT but while medium is introduced by MWCNT or dMWCNT the promotion of Zn elements is higher.

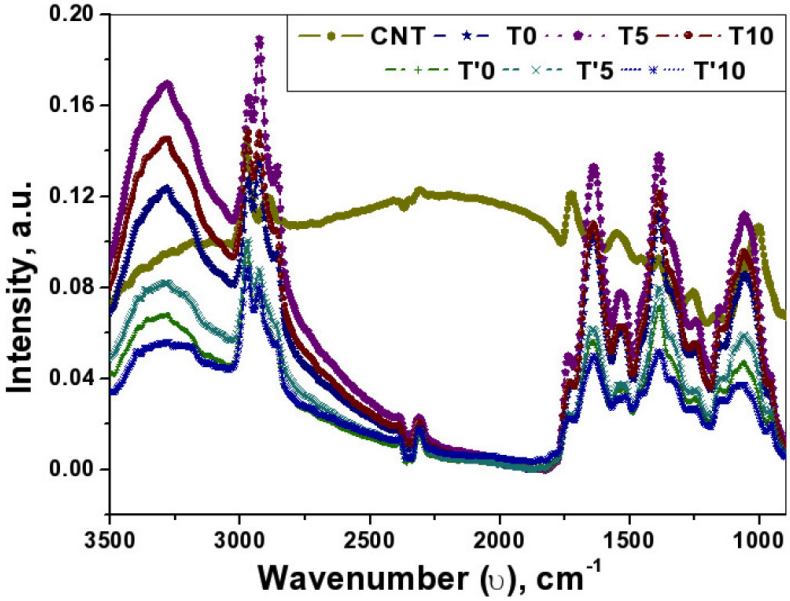

Figure 5. Detection of MWCNT in14 and 27 days
(**Table 2**) tomato seedlings using infrared spectrometer.

3.4. FTIR Analysis

The results of FTIR of germinated plants are shown in **Figure 5**. We can see that the peaks obtained for the germinated plants are different from the peaks of MWCNT (solid dark yellow trace). The FTIR measurements were made of whole germinated plants have 14 and 27 days (**Table 2**) and there is not any presence of MWCNT. This result is consistent with the recent observations made in by Miralles et al. [14], who also detected practically no presence of MWCNTs in their plant tissue.

4. Conclusion

Our result demonstrates that MWCNT and dMWCNT both promotes the tomato plant germination. The plants grow with MWCNT and without any addition nutrient growth medium are beneficial but the rate of germination is lower in comparison to those containing nutrient growth medium and ultrasonically dispersed MWCNT (dMWCNT). The promotion of nutrient elements is depends on the there status in periodic table and ionic interaction. To early days of germination (7 day) the MWCNT of 40 μg / ml concentration is more beneficial for biomass gain as well as shoot growth, when we using the dMWCNT and standard nutrients growth medium the rate of germination is higher comparatively with MWCNT and without nutrient medium. We see that carbon nanotubes (MWCNT & dMWCNT) are highly effective to tomato seed germination and their development than control medium also promotes the nutrients in germinated plants. For longer days of germination higher concentration of dMWCNT is more effective then lower concentration and promotes germination, biomass and some nutrient elements.

Acknowledgements

This work is supported by CONACYT, Mexico, providing doctoral fellowship to D. K. Tiwari (No. 229122). Authours are also thankful to Dr. Salomon Eduardo Borjas Garcia (IFM–UMSNH) and M.C. Maria Remedios Cisneros Magaña (IIM–UMSNH) for their help to pEDXRF and FTIR analysis.

References

1. C. M. Rico. Interaction of nanoparticles with edible plants and their possible implications in the food chain. J. Agricult. & Food Chem. 59 (2011) 3485-3498.
2. A. Ditta. How helpful is nanotechnology in agriculture? Adv. Nat. Sci. Nanosci. & Nanotechnol. 3 (2012) 033002 1-10.
3. S. Morla, C. S. V. Ramachandra Rao, R. Chakrapani. Factors affecting seed germination and seedling growth of tomato plants cultured in vitro conditions. J. Chem. Bio. Phys. Sci. B 1 (2011) 328-334.

4. A. Mondal, R. Basu, S. Das, P. Nandy. Beneficial role of carbon nanotubes on mustard plant growth: An agricultural prospect. J. Nanopart. Res. 13 (2011) 4519-4528.
5. S. Agnihotri, M. Rostam–Abadi, M. J. Rood, R. Chang. Energy and environmental applications of carbon nanotubes. Fuel Chem. Division Preprints 47 (2002) 474-475.
6. R. Nair, S. Hanna Varghese, B. G. Nair, T. Maekawa, Y. Yoshida, D. S. Kumar. Nanoparticulate material delivery to plants. Plant Sci. 179 (2010) 154-163.
7. D. K. Tiwari, N. Dasgupta–Schubert, L. M. Villaseñor–Cendejas, J. Villegas, L. Carreto–Montoya, S. E. Borjas–García. Interfacing carbon nanotubes (CNT) with plants: Enhancement of growth, water and ionic nutrient uptake in maize (Zea Mays) and Implications for nanoagriculture. Appl. Nanosci. (On-line: June 2013.) – DOI 10.1007/s13204-013-0236-7.
8. M. Khodakovskaya, E. Dervishi, M. Mahmood, Y. Xu, Zh. Li, F. Watanabe, A. S. Biris. Carbon nanotubes are able to penetrate plant seed-coat and dramatically affect seed germination and plant growth. ACS Nano 3 (2009) 3221-3227. Retraction see in:
8′. M. Khodakovskaya, E. Dervishi, M. Mahmood, Y. Xu, Zh. Li, F. Watanabe, A. S. Biris. Retraction notice for “Carbon nanotubes are able to penetrate plant seed-coat and dramatically affect seed germination and plant growth”. ACS Nano 6 (2012) 7541-7541.
9. H. Villagarcia, E. Dervishi, K. de Silva, A. S. Biris, M. V. Khodakovskaya. Surface chemistry of carbon nanotubes impacts the growth and expression of water channel protein in tomato plants. Small 8 (2012) 2328-2334.
10. M. B. mac Donald. Physiology of Seed Germination. Columbus: The Ohio State Univ. (2007).
11. F. Zhu, K. Schulten, Water and proton conduction through carbon nanotubes as models for biological channels. Biophys. J. 85 (2003) 236-244.
12. Z. I. Miskovic. Interactions of ions with carbon nano-structures. J. Phys. Conf. Ser. 133 (2008) 012011 1-11.
13. Difco™ and BBLTM Manual, 2nd Ed. http://www.bd.com/europe/regulatory/Assets/ IFU /Difco_BBL/281230.pdf.
14. P. Miralles, E. Johnson, T. L. Church, A. T. Harris. Multiwalled carbon nanotubes in alfaalfa and wheat: Toxicology and uptake. J. Royal Soc. Interface 9 (2012) 3514-3527.

DEVELOPMENT OF HIGH PRODUCTIVITY MECHANICAL CLEAVAGE TECHNOLOGY OF GRAPHENE-LIKE NANOPARTICLES MANUFACTURING

H. Weinert, V. Leshchynsky

Metal Forming Institute
Poznan, Poland
leshchynsky@inop.poznan.pl

Accepted September 19, 2013

1. Introduction

Solid lubricant nanoparticles is being produced now by various technology routes, and its application as an oil additives have been proved [1]. From the view of chemistry of lubrication, several factors affect the interactions occurring between the moving surfaces and the lubricant between them. The application of solid lubricant particles and particularly inorganic fullerene-like (IF) WS_2 and MoS_2 nano materials first synthesized by solid–gas reactions at a fairly high temperature (i.e., 1000 °C) [2, 3] is quite effective as shown by Rapoport et al. using hollow nanoparticles of WS_2 mixed with oil [1]. Usually the superior tribological performance of IF solid lubricant nanoparticles is attributed to the chemical inertness and round-shaped hollow cage structures of inorganic fullerenes. From the other side thin films of IF-MoS_2 nanoparticles exhibited ultra-low friction (friction coefficient about 0.008) and wear [4] when they were deposited by an arc discharge method. Those exceptional properties were attributed to the presence of curved S–Mo–S planes that prevent oxidation and preserve the layered structure. However, the real mechanisms of the ultra-low friction when the IF nanoparticles are placed on an interface or are embedded in a solid matrix are not completely clear and need to be further examined.

Recently, the exceptional friction properties of graphene-like MoS_2 and carbon platelets were found in [5]. Graphene, which is a two dimensional network of sp^2-hybridized carbon atoms has created a great sensation in the last few years because of the unique properties and phenomena exhibited by it. Graphene is fascinating not only academically but also promises numerous applications. A natural extension of the study of graphene would be to synthesize graphene analogues of other layered inorganic solid lubricant materials, the obvious candidates being WS_2, MoS_2 and BN.

MoS_2 and WS_2 are quasi-two-dimensional compounds in which the atoms in the layer are bound by strong covalent forces, while van der Waals forces hold the layers together just as in graphite. Intercalation of alkali metals in layered metal dichalcogenides is one of the widely spread exfoliation methods reported some time ago. A graphene-like two-dimensional structure of WS_2 have been obtained [6] by lithium intercalation and exfoliation. Rao et al. [7] have successfully carried out the reported the synthesis of few-layer MoS_2 and WS_2 by employing multiple chemical routes followed by unambiguous characterization involving different

experimental techniques, including atomic force microscopy (AFM) and high-resolution transmission electron microscopy. Graphene analogues of MoS_2 and WS_2 can be synthesized by employing different chemical methods [7, 8]. However, there is an urgent need to develop a large-scale method to manufacture graphene reliably for various promising applications being developed [9 – 11]. These applications rely largely on the unique properties of graphene [12, 13] and the properties are strongly affected by the method of synthesis [14]. While several laboratory methods to synthesize graphene have been developed and reported, the suitability of these methods to large-scale manufacturing remains to be proven.

Mechanical cleavage by scotch tape was the first method that successfully prepared free-standing graphene [9, 15] and has been proven to work on other layered materials, such as hBN_7 and MoS_2. During mechanical cleavage, the pulling force can easily break the weak van der Waals interaction between graphene layers and leave the strongly sp^2 bonded in plane structure intact. A shear force can have a similar effect. In pencil writing, very thin graphite sheets, mainly produced by shearing, are left on the paper. The mechanically peeled 2D sheets have fewer defects than those produced by chemical methods. However, mechanical cleavage by scotch tape has extremely low yield. If a mechanical process can be developed to treat tens of thousands of particles in one run and to peel each particle hundreds of times, a large number of high-quality nanosheets can be harvested for studies and practical applications. Ball milling may be used for thickness reduction of layered materials [16, 17] and even for graphene production [18, 19]. However, most ball milling treatments are violent processes which destroy or disorder the crystal structure and introduce a great number of defects. The works [11, 20] demonstrated that a fully controlled milling process can mechanically peel hBN particles into BN nanosheets with little damage to the in-plane crystal structure. In contrast to the low-yield of mechanical cleavage by scotch tape, the controlled ball milling process can produce a large amount of BN nanosheets at one time. The controlled ball milling could be a process to supply a large quantity of high-quality BN nanosheets. It seems that similar technology may be developed for layered solid lubricant nanoplatelets production on the base of careful controlling milling parameters.

The main conclusions of state-of-art of graphene-like nanoparticles manufacturing are the followings:

- large scale mechanical exfoliation methods of solid lubricant graphene-like nanoparticles production seems to be promising technique due to small amount of defects;
- there is a need of carefully controlling mechanical exfoliation parameters to achieve peeling of nanosheets similar as those shown on **Figure 1**;
- the usual ball milling technique scheme needs to be modified on the base of stress state analysis at the contact interface.

Thus, the aim of the paper is to develop the mechanical exfoliation technology of MoS2 graphene-like nanoparticles manufacturing with carefully controlling exfoliation parameters, and to make the first characterization of nanoparticle-microparticle mixture obtained by this technology.

2. Experimental set up and procedure

The rolling cleavage device to produce the nano- and microparticle mixtures is shown on **Figure 1**. The low energy ball milling regime is being achieved due to deformation of the

particulate medium (located in the powder cavity, **Figure 1**) with low velocity which is controlled by rotation speed. From other side the normal load is carefully controlled to optimize regime of the particle exfoliation.

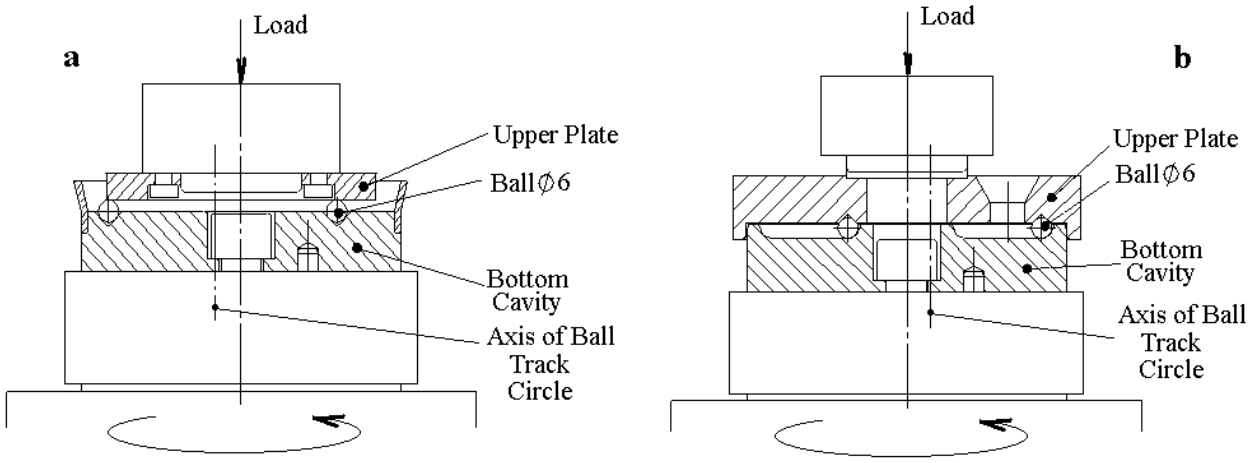

Figure 1. Schematic of rolling cleavage device for particle exfoliation.

The particle cleavage process was realized due to rolling and sliding movement of the balls which are located in the track circle (**Figures 1a** and **b**). The sliding movement of the ball is achieved due to eccentricity of an axis of the track circle. Two technology schemes are chosen for experiment. In the first option a groove of the track circle serves as a powder cavity, and the milling / exfoliation process is realized both in the groove and at the contact of the ball with an upper plate (**Figure 1a**). At the second option the milling / exfoliation process is being made directly in the bottom cavity. The main task is to compare the effectiveness of these devices, and to choose the better option. The processing regimes of are the followings: normal load 100 kg; rotation speed 200 rpm; number of the balls in the track 5; processing time 1.5, 2 and 3.5 h.

The particle characterization techniques applied are scanning electron microscopy made with SEM FEI, and atomic force microscopy (AFM). AFM (SPM) has so far been the main method for directly identifying and confirming the thickness and roughness of single- and few-layer graphene. It played a vital role in the discovery of graphene [9]. Scanning probe microscope (SPM) platform is designed for the study of properties of the surface at nanometer scale. It allows visualizing and perform quantitative measurements of mechanical properties of the sample working with sizes from several microns to angstrom. Femto Scan microscope SPM FSM 0307 produced by Advanced Technologies Centre was chosen.

3. Contact analysis

The main objective of the present analysis may therefore be stated as the investigation of the effect of rolling parameters on the normal and shear contact stress variation in the powder layer. The geometry of the plane rolling contact problem is depicted in Figure 2. The substrate is subjected to the tractive rolling of a rigid ball of radius R and solid lubricant powder layer. The ball rolls over the surface of the substrate with a constant velocity, V, in the negative Ox direction. It is assumed that the elastic modulus and the Poisson's ratio are retained as a

constant. The rolling contact problem of the solid lubricant powder layer (film) / substrate system will be analyzed on the base of approach developed by Guler et al. [21] to estimate the stresses in the layered particle during loading and unloading.

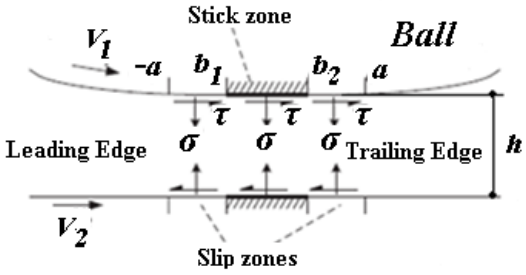

Figure 2. Schematic of the ball-flat contact zone and the related parameter definitions in accordance with [21].

The shear modulus of the homogeneous substrate is constant and represented by G_2 whereas the shear modulus of the lubricant layer is approved G_0. Let's define the shear modulus ratio as

$$\Gamma = \mu_2 / \mu_0, \quad (1)$$

where Γ is the stiffness ratio. Γ plays an important role in the stress state as well as in the material architecture. It is also assumed that the value of the Poisson's ratio, v, is the same for both the powder layer and the substrate. The equations the governing equations associated with the contact problem of a coating / substrate system of were set up and solved in [21] for various friction conditions. **Figure 3** [21] examines the effect of friction coefficient f on the normal and shear stresses in dimensionless coordinates taking into account the parameters of the contact: $v = 0.3$, $a/h = 0.5$, $R/h = 100$, $Q/fP = 0.75$. The results reveal variation of the normal and shear stresses for different values of the friction coefficient. It can be seen that as value of f increases the normal stress becomes more compressive within leading edge slip zone and increases within trailing edge slip zone. Furthermore, the normal stress is tensile at the trailing edge point of the contact zone, $x = a$. When the friction coefficient increases, the tensile stress peak observed at the trailing edge of the contact increases as well. One has to note that the tensile peak can be alleviated by reducing the stiffness ratio Γ.

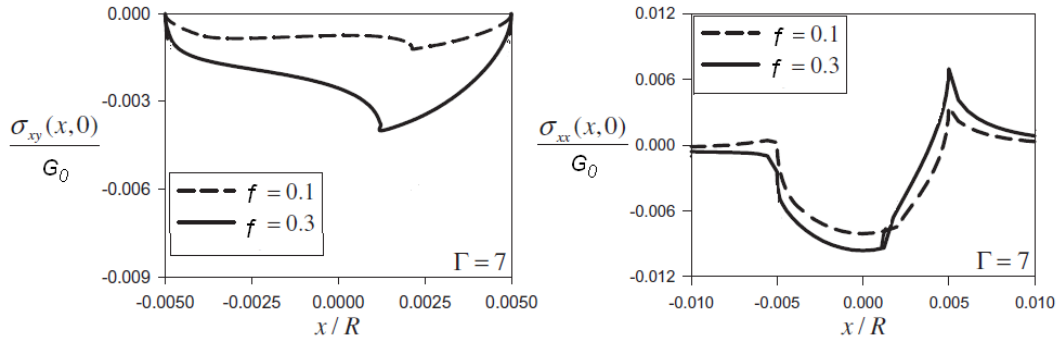

Figure 3. Stress distribution in the contact zone. Modeling results [21]. (a) – shear stress; (b) – normal stress.

The stress component calculation results based on our parameters of experiment for different stiffness ratios are shown on **Figure 4**. The shear modulus of MoS_2 is known to be

about $G_0 = 4$ GPa [22], and G of the steel substrate is of 79 GPa. Thus, the higher values of Γ (Γ = 20) leads to tensile normal stress σ of about 40 MPa, and shear stress τ is about 180 MPa in the MoS_2 particles. Taking into account the chosen contact parameters of the second option of rolling cleavage device (**Figure 1b**) $a / h = 0.5$, $R / h = 100$ (powder layer thickness is of about 30 μm) we may conclude that the solid lubricant particles have a big tension and shear stresses at the area of trailing edge which may result in their exfoliation.

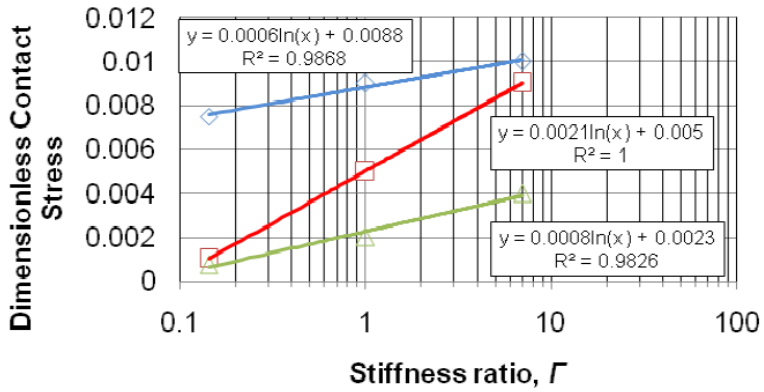

Figure 4. The stress component calculation results for different stiffness ratios Γ. Blue – normal stress σ / G_0 at leading edge; red – normal stress σ / G_0 at trailing edge; green – shear stress τ / G_0.

4. Experimental results and discussion

It is crucial for assessing the method to confirm the state of the exfoliated MoS_2 and WS_2 particles. The pristine material used here is common natural MoS_2 and WS_2 particles, whose typical SEM image is shown in **Figure 5**. SEM images on **Figure 6** characterize the particles after the rolling cleavage treatment for various times. The lateral size of flakes in the powder mixture varies in the range of 0.2 – 1.2 μm, while the thickness is far below 1 μm, indicating that the original material is mainly exfoliated into considerably thinner flakes. Thereby, it is reasonable to infer that the thinner flakes which we hunt certainly exist in the powder mixture.

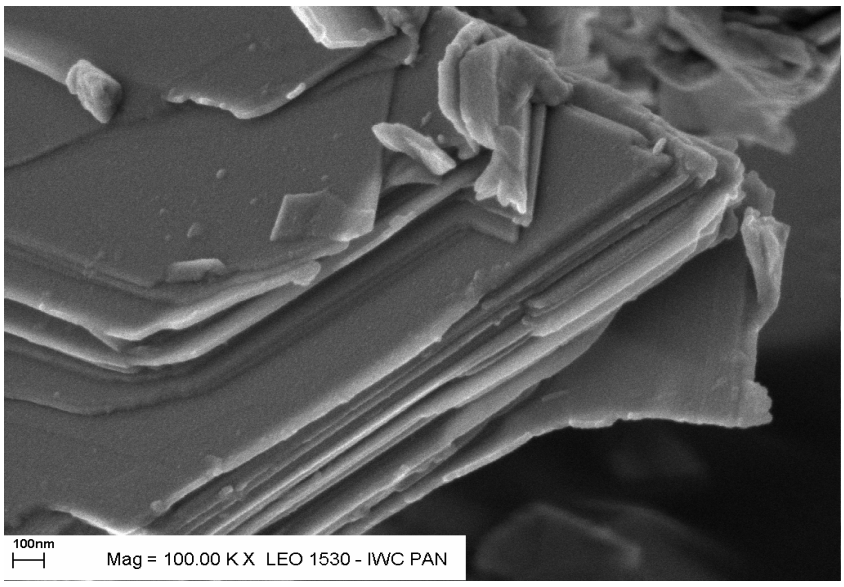

Figure 5. SEM of pristine natural MoS_2 particle.

The images (**Figures 6d – f**) clearly shows the thin flakes obtained by the exfoliation due to favorable combination of normal and shear stresses at the trailing edge of the milling balls. One should note that the milling time of 3.5 h appears to be optimal. Then we need to use AFM and TEM to further characterize and analyze the thinner flakes in the powder mixture.

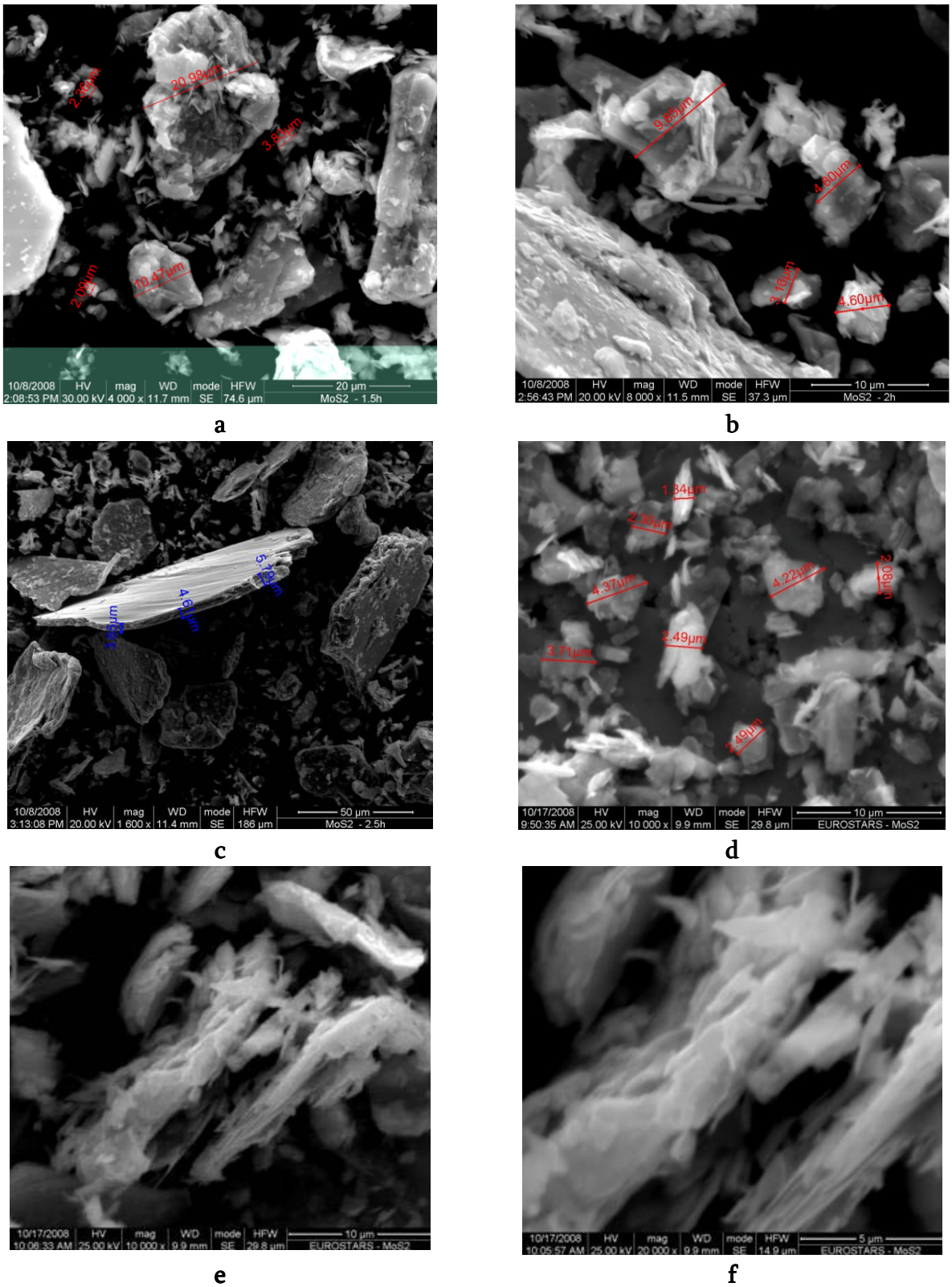

Figure 6. SEM images of MoS_2 particles after rolling cleavage during 1.5 (a), 2.0 (b), 2.5 (c), and 3.5 h (d, e, f).

To study individual MoS_2 particle with AFM the special method for sample preparation was applied. Chemically pure water was used to prepare suspension of particles. This suspension was deposited on the mica surface. After drying the mica individual was well fixed on it's surface. The fixation strength was enough in order to avoid displacement of particle by cantilever in contact and friction modes. Typical images of individual nanoparticles of MoS_2 are shown in **Figure 7**. **Figure 8** illustrates typical dimensions of individual micro-particle: length 1857 nm, thickness 70 – 330 nm. Layered structure is clear observed on the image. The results of examination show that mechanical method allows to produce MoS_2 flakes with graphene-like layered structure.

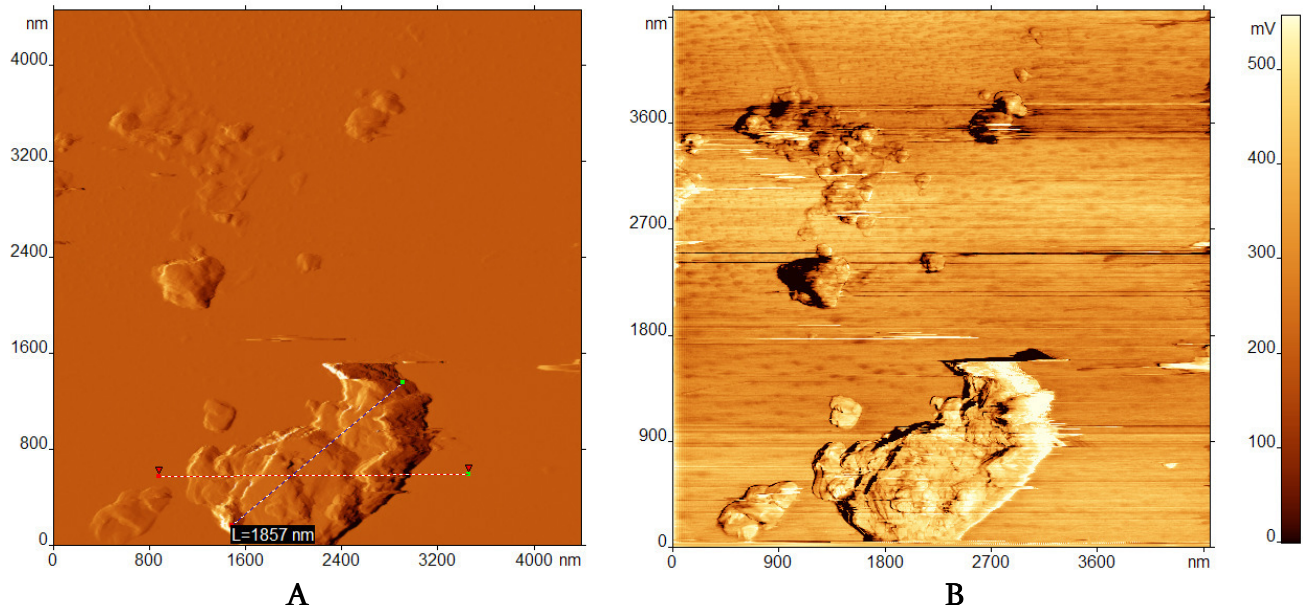

Figure 7. General view (A-contact mode with back illumination and B-friction modes) of individual micro-flake of MoS_2 on mica surface.

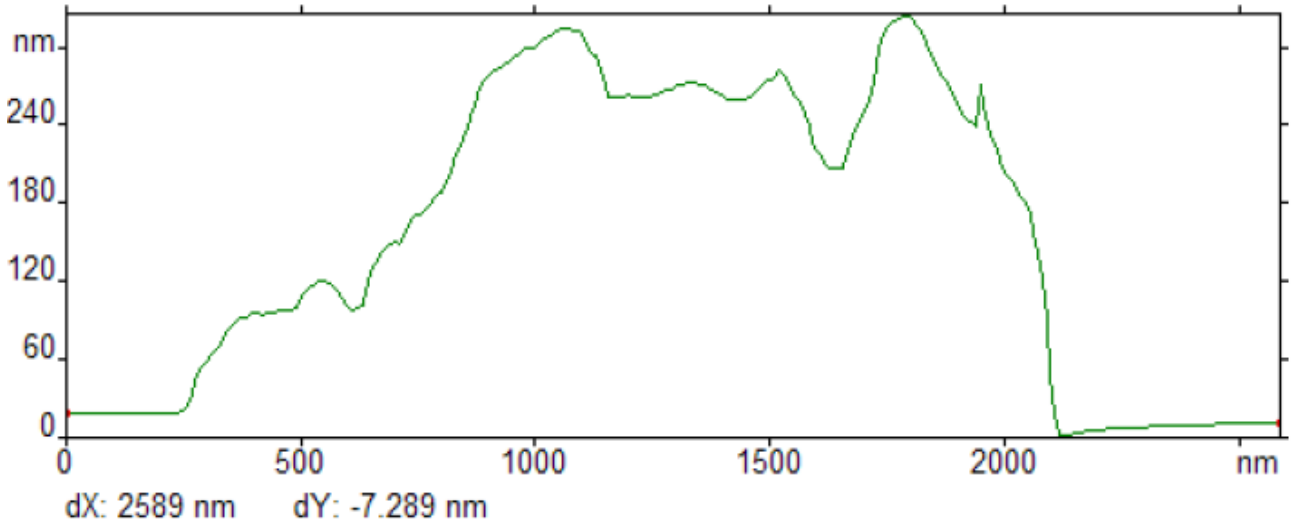

Figure 8. Typical height variations for individual micro-particle of MoS_2 on mica surface.

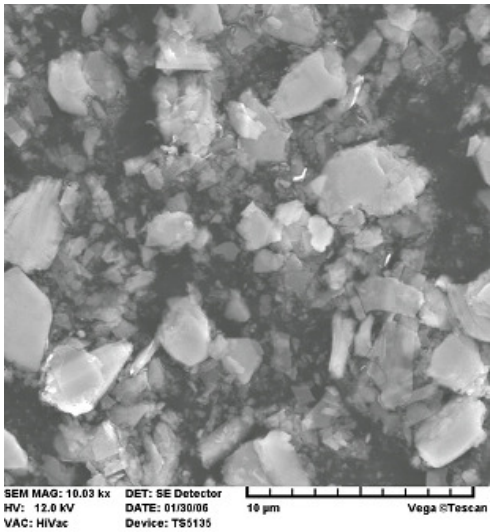

a

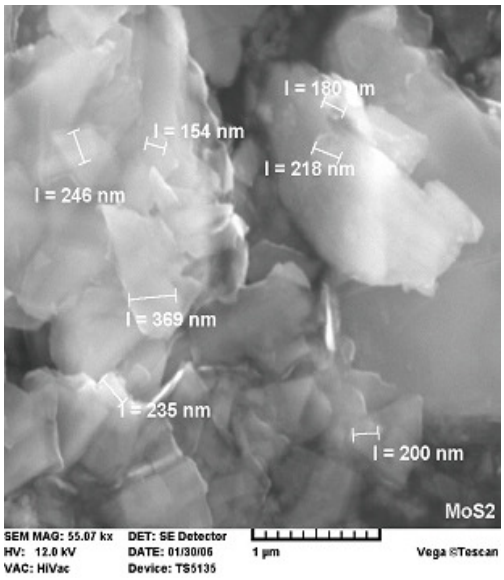

b

Figure 9. The thin platelets of obtained by rolling cleavage of MoS_2 particles: (a) magnification 10 000 × and (b) magnification 55 000 ×.

The main conclusion of SPM examination of milled and annealed MoS_2 particles is that the rolling cleavage technique has a good potential of large scale manufacturing of MoS_2 platelets as the solid lubricants. **Figure 9** illustrate the presence of thin flakes of 200 – 500 nm size. Some of them looks transparent that means the thickness of these platelets is less 15 nm.

5. Conclusions

- The rolling cleavage technique has a good potential of large scale manufacturing of MoS2 platelets as the solid lubricants.
- The contact parameters of the rolling cleavage technique allows to obtain in solid lubricant particles the big tension and shear stresses at the area of trailing edge which may result in their exfoliation.
- A careful control of the rolling cleavage technology parameters allow to achieve a stable exfoliation process.

References

1. L. Rapoport, Yu. Bilik, Y. Feldman, M. Homyonfer, S. R. Cohen, R. Tenne. Hollow nanoparticles of WS_2 as potential solid-state lubricants. Nature 387 (1997) 791-793.
2. R. Tenne, L. Margulis, M. Genut, G. Hodes. Polyhedral and cylindrical structures of tungsten disulphide. Nature 360 (1992) 444-446.
3. D. J. Srolovitz, S. A. Safran, M. Homyonfer, R. Tenne. Morphology of nested fullerenes. Phys. Rev. Lett. 74 (1995) 1779-1781.
4. M. Chhowalla, G. A. J. Amaratunga. Thin films of fullerene-like MoS_2 nanoparticles with ultra-low friction and wear. Nature 407 (2000) 164-167.
5. T. Filleter, R. Bennewitz. Structural and frictional properties of graphene films on SiC (0001) studied by atomic force microscopy. Phys. Rev. B 81 (2010) 155412 1-7.
6. D. Yang, R. F. Frindt. Li-intercalation and exfoliation of WS_2. J. Phys. Chem. Solids 57 (1996) 1113-1116.
7. H. S. S. R. Matte, A. Gomathi, A. K. Manna, D. J. Late, R. Datta, S. K. Pati, C. N. R. Rao. MoS_2 and WS_2 analogues of graphene. Angew. Chem. Int. Ed. 49 (2010) 4059-4062.
8. C. N. R. Rao, A. Nag. Inorganic analogues of graphene. Eur. J. Inorg. Chem. 27 (2010) 4244-4250.
9. S. Stankovich, D. A. Dikin, G. H. B. Dommett, K. M. Kohlhaas, E. J. Zimney, E. A. Stach, R. D. Piner, S. T. Nquyen, R. S. Ruoff. Graphene-based composite materials. Nature 442 (2006) 282-286.
10. A. Danelska, M. Szafran. Surface properties of nanoceramic powders. Arch. Metall. & Mater. 56 (2011) 1077-1081.
11. D. Michalik, M. Sopicka–Lizer, J. Plewa, T. Pawlik. Application of mechanochemical processing to synthesis of YAG: Ce garnet powder. Arch. Metall. & Mater. 56 (2011) 1257-1264.
12. S. Park, R. S. Ruoff. Chemical methods for the production of graphenes. Nat. Nanotechnol. 4 (2009) 217-224.
13. Zh. Ni, Y. Wang, T. Yu, Z. Shen. Raman spectroscopy and imaging of graphene. Nano Res. 1 (2008) 273-291.
14. M. J. Allen, V. C. Tung, R. B. Kaner. Honeycomb carbon: A review of graphene. Chem. Rev. 110 (2009) 132-145.
15. J. C. Meyer, A. K. Geim, M. I. Katsnelson, K. S. Novoselov, T. J. Booth, S. Roth. The structure of suspended graphene sheets. Nature 446 (2007) 60-63.
16. M. Jin, H.-K. Jeong, T.-H. Kim, K. P. So, Y. Cui1, W. J. Yu, E. J. Ra, Y. H. Lee. Synthesis and systematic characterization of functionalized graphene sheets generated by thermal exfoliation at low temperature. J. Phys D 43 (2010) 275402 1-7.
17. N. W. Pu, Y. Sung, Y. M. Liu, M. D. Ger. Production of few-layer graphene by supercritical CO_2 exfoliation of graphite. Mater. Lett. 63 (2009) 3-18.
18. K. S. Novoselov, A. K. Geim, S. V. Morozov, Y. Jiang, S. V. Dubonos, I. V. Grigirieva, A. A. Firsov. Electric field effect in atomically thin carbon films; Science 306 (2004) 666-669.
19. B. Jayasena, S. Subbiah. A novel mechanical cleavage method for synthesizing few-layer graphenes. Nanoscale Res. Lett. 6 (2011) 95-101.

20. L. H. Li, Y. Chen, G. Behan, H. Zhang, M. Petravic, A. M. Glushenkov. Large-scale mechanical peeling of boron nitride nanosheets by low-energy ball milling, J. Mater. Chem. 21 (2011) 11862-11866.
21. M. A. Guler, S. Adibnazari, Y. Alinia. Tractive rolling contact mechanics of graded coatings, Int. J. Solids & Str. 49 (2012) 929-945
22. I. Kaplan–Ashiri, S. R. Cohen, N. Apter, Y. Wang, G. Seifert, H. D. Wagner, R. Tenne. Microscopic investigation of shear in multiwalled nanotube deformation, J. Phys. Chem. C 111 (2007) 8432-8436.

BROADENING THE CONCEPTS OF EFFICIENT LIGATION AND FUNCTIONALIZATION USING AZIDE-ALKYNE 1,3-DIPOLAR CYCLOADDITIONS FOR DEVELOPMENT OF NEOTERICPOLYMERIZED IONIC LIQUIDS

B. P. Mudraboyina, M. Obadia, R. Sood, I. Allaoua,
P. Cassagnau, E. Espuche, A. Serghei, E. Drockenmuller

Université Claude Bernard Lyon 1
Villeurbanne, France
eric.drockenmuller@univ-lyon1.fr

Accepted September 19, 2013

1. Introduction

Polymerized ionic liquids (PILs) are unique polyelectrolytes with cationic and anionic groups included in the repeating unit of a polymer chain [1, 2]. They are extremely attractive in the field of materials science as they combine the characteristic properties of ionic liquids (high ionic conductivity, thermal and chemical stabilities) with those of polymers (mechanical stability, processing and tunable macromolecular design). PILs can be synthesized by either direct polymerization of IL monomers or by chemical modification of existing polymers. Many examples have demonstrated their potential in applications such as dye sensitized solar cells, fuel cells, lithium batteries, actuators, field effect transistors, light-emitting electrochemical cells, electrochromic devices, switchable surfaces, sensors, thermo-responsive nanostructured assemblies, permselective membranes for CO_2 recovery or catalysis [3 – 6]. In all these applications, imidazolium-based PILs are by far the most widespread and investigated materials. Thus, the design of new PILs using simple synthetic procedures is of outmost importance to develop innovative materials with enhanced properties as required by emerging technologies.

2. Experimental

Diisopropylethylamine (DIPEA, 99 %), iodomethane (CH_3I, 99 %), copper (I) iodide triethylphosphite ($CuIP(OEt)_3$, 97 %) and chloroform ($CHCl_3$, 98 %) were purchased from Aldrich and used as received. α-azide-ω-alkyne monomer, was synthesized as described previously. ^1H NMR (400 MHz) spectra were recorded on a Bruker DRX 400 Spectrometer in $CDCl_3$ or DMF–d_7. Differential scanning calorimetry (DSC) measurements were performed under nitrogen using a DSC 2920 (TA Instruments) at a heating rate of 20 °C / min. T_g values were measured during the second heating cycle. Thermogravimetric analysis (TGA) was performed under nitrogen using a TGA 2950 (TA Instruments) at a heating rate of 10 °C / min. The dielectric measurements were performed by means of broadband dielectric spectroscopy, using a high-resolution Alpha-analyzer assisted by a Quatro temperature controller (Novocontrol GmbH). The sample was prepared by placing the polymer between two freshly

polished brass electrodes followed by a heating procedure at 120 °C in a pure nitrogen atmosphere. The thickness of the sample cell was controlled by employing glass fibers (50 μm in diameter) as spacers. The dielectric spectra were measuredbetween 0.1 Hz and 10 MHz by applying a sinusoidal voltage of 0.1 V. The temperature was controlled by heating the sample under flow of pure nitrogen, which leads to a negligible humidity in the measurement chamber. The thermal stability was set to be better than 0.1 K in absolute values with relative variations less than 0.2 K / min.

General procedure for CuAAC *step growth polymerization*

A 2 M solution of α-azide-ω-alkyne (1.3 g, 5.0 mmol), $CuIP(OEt)_3$ (18 mg, $50 \cdot 10^{-3}$ mmol) and DIPEA (0.65 g, 5.0 mmol) in $CHCl_3$ (2.5 mL) was stirred in the dark for 24 h at 60 °C. The reaction mixture was diluted with $CHCl_3$ and the polymer was precipitated twice in diethyl ether before being dried under vacuum to yield poly(1,2,3-triazole) **2** as a white powder (1.1 g, 86 %, M_n = 75 kDa, D = 1.7, $CHCl_3$, PS calibration). ^{1}H NMR ($CDCl_3$): δ = 7.52 (s, $OCH_2C=CH$), 4.62 (s, $OCH_2C=CH$), 4.33 (t, NCH_2CH_2), 3.51 (t, CH_2CH_2O), 1.89 (s, NCH_2CH_2), 1.59 (s, CH_2CH_2O), 1.26 (s, $NCH_2CH_2(CH_2)_7$).

General procedure for the poly(3-*methyl*-1,2,3-*triazolium iodide*)*s – synthesis of* 1

A solution of poly(1,2,3-triazole) **2** (0.5 g, 2.0 mmol of triazole groups) and CH_3I (1.25 mL, 20 mmol) in $CHCl_3$ (20 mL) was stirred for 16 h at 45 °C. Crude compound **1** was recovered from the biphasic reaction mixture, extracted with $CHCl_3$ and dried under vacuum to yield pure **1** as an orange glassy material (0.78 g, 100 %). ^{1}H NMR (DMF–d_7): δ = 9.16 (s, $OCH_2C=CH$), 4.98 (s, $OCH_2C=CH$), 4.79 (t, NCH_2CH_2), 4.45 (s, NCH_3), 3.61 (t, CH_2CH_2O), 2.03 (m, NCH_2CH_2), 1.60 (m, CH_2CH_2O), 1.28 (s, $NCH_2CH_2(CH_2)_7$).

3. Results and discussion

Ever since the outstanding development of the copper-catalyzed azide-alkyne cycloaddition (CuAAC) modular ligation [7], a large variety of macromolecular materials containing1,2,3-triazolegroups have been reported [8 – 13]. Recently, several 1,4-disubstituted-1,2,3-triazolium ionic liquids have been developed [14 – 20], and their potential as efficient reaction media [21], anion-templated formation of rotaxanes [22], receptors for anion recognition [23], stereoselective organocatalysts [24], ligands for ruthenium-catalyzed olefin metathesis [25], as well as precursors of *N*-heterocyclic carbene ligands for palladium-catalyzed Suzuki coupling have been established [26]. We have recently pioneered the synthesis of 1,2,3-triazolium-based PILs [27]. Formation of poly(3-methyl-1,2,3-triazolium iodide) **1**as a glassy orange amorphous material (with a T_g of 5 °C) having good film-forming properties, was achieved by CuAAC polyaddition and further quaternization of the 1,2,3-triazole ring using methyl iodide. Ionic conductivity of 1 ($\kappa_0 = 8 \cdot 10^{-8}$ S / m at 30 °C) (**Figure 1**) was found comparable to other PILs having iodide as counter anion [2, 28 – 30]. However, T_g of 1 is found to be significantly lower than that of analogous imidazolium PILs. The obtained conductivity values for the best VFT fitting parameters (κ_∞ = 0.32 S / cm, B = 1230 K and T_0 = 228 K) are in good accordance with those generally obtained for dialkyl-imidazolium derivatives having comparable anion obtained by step growth polymerization [31 – 33].

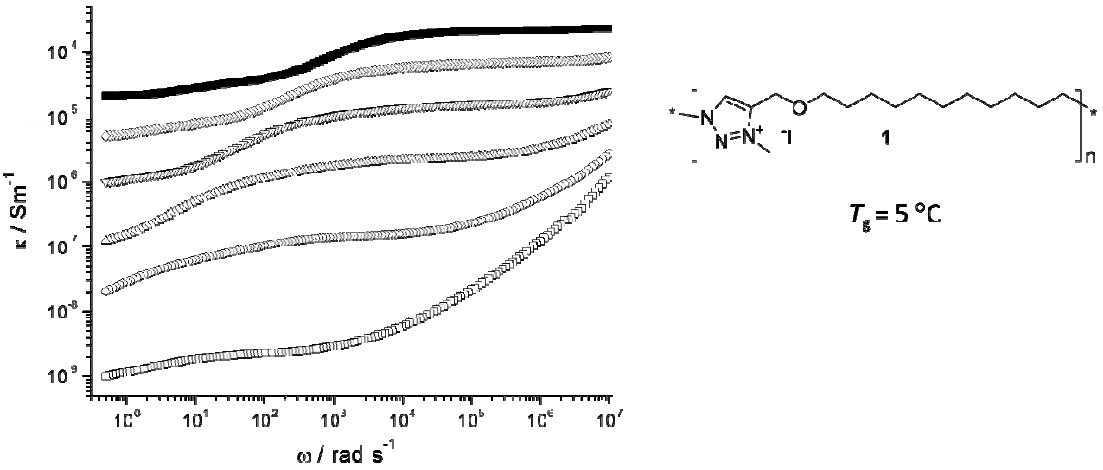

Figure 1. Conductivity of PIL 1, κ, versus frequency, ω, at 20 (□), 40 (○), 60 (△), 80 (▽), 100 (◇), and 120 °C (■).

Furthermore, the synthetic design leaves a scope for anion exchange which leads to display of varied conductivity and mechanical properties of the derivatives. The tuning of structural parameters of the monomer, the quaternizing group and the counter-anion is expected to have a tremendous effect on ionic conductivity and thermal stability, crucial properties in most applications of PILs. The scope of this communication is to demonstrate the unprecedented synthesis of a broad range of 1,2,3-triazolium-based PILs and their potential as new ion conducting materials.

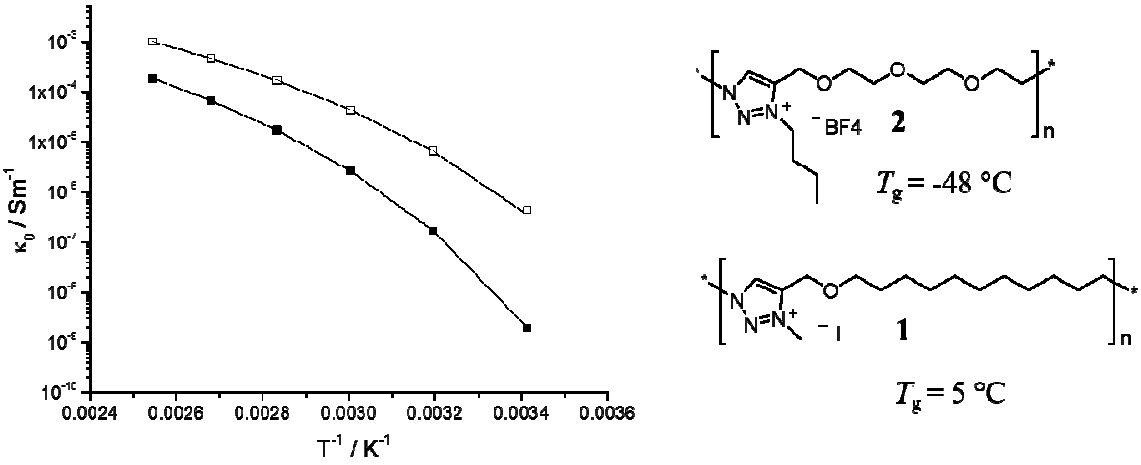

Figure 2. Direct current conductivity, κ_0, versus inverse temperature for poly(3-methyl-1,2,3-triazolium iodide (■)) **1**andpoly(3-butyl-1,2,3-triazolium tetrafluoroborate (□)) 2. The solid lines represent the best VFT fit of experimental data with κ_∞ = 0.32 S / cm, B = 1230 K and T_0 = 228 K for 1, and κ_∞ = 0.48 S / cm, B = 1120 K and T_0 = 212 K for 2.

In the line of these developments, a neoteric trimethylene glycol, (TEG) based 1,2,3-triazolium PIL **2 (**is a low T_g semi-crystalline polymer (T_g = – 48 °C) has been synthesized and subjected to temperature dependence of ionic conductivity studies by BDS (**Figure 2**). The initial studies at room temperature demonstrated an increase of three orders of magnitude in conductivity when compared to that of 1 **(**is a low T_g amorphous material (T_g = 5 °C). The counter anion, tetrafluoroborate is also known to be a more compatible anion for conductivity

over halide anions.Although introduction of TEG on main chain resulting in a more hydrophilic and hygroscopic character, TEG segments have favoured ionic conduction [34]. The results are promising, displaying such magnanimous increases in terms of conductivity with mere changing of anion and so very promising that fine tuning of the properties of PILs can lead to to development of conducting materials. Further investigation is on-going to improve the conductivity properties. Also permeability studies are currently conducted to explore the permittivity of CO_2 over H_2 and other gases. These materials also will be tested for more applicability as the research proceeds. It is most likely that these can be used in many applications where the conductivity and permeability is the main issue.

Considering the easy formation and the abundance of macromolecular structures carrying 1,2,3-triazole units [9], and their versatile conversion to 1,2,3-triazolium analogues, a spectacular development of this new class of PILs is envisioned. Indeed, with the immense library of polymer architectures accessible combining CuAAC and macromolecular engineering methods to obtain main chain or side chain 1,2,3-triazoliums (**Figure 3**) together with the broad variety of anion exchange reaction accessible, such materials might play a major role in the field of PILs.

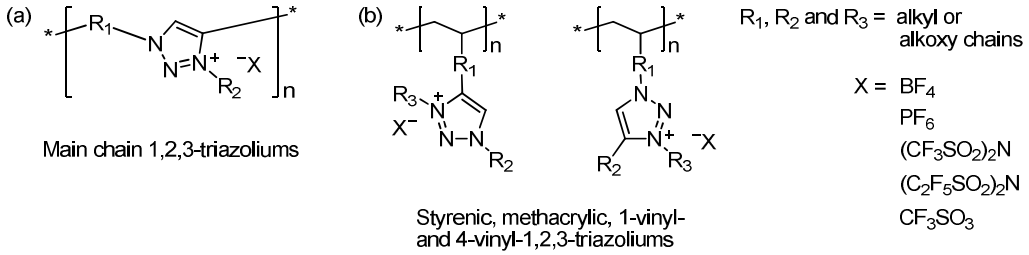

Figure 3. Two different class of triazoliums *viz*, (a) main chain 1,2,3-triazoliums and (b) side chain styrenic or methacrylic 1-vinyl- and 4-vinyl-1,2,3-triazoliums that are under current investigations.

4. Conclusions

The first generation TPILs not only demonstrates ionic conduction similar to that of PILs with comparable structure, pendant substituent and anion, but their synthesis also benefits from the robust and orthogonal nature of CuAAC. Here, in this communication, the undergoing synthesis and application of other 1,2,3-triazolium-based PILs with different counter-anions obtained either by step growth or chain growth polymerization methods will be discussed in details. The potential of 1,2,3-triazolium chemistry to tackle new synthetic challenges using unexplored approaches competent to broaden the current structural variety of PILs with properties such as thermal stability and conductivity will be discussed. The scope to further development of neoteric PILs is promising with our latest developments and understanding of the nature of substituents used in synthetic methods.

Acknowledgements

Authors gratefully acknowledge the financial support from the Agence Nationale de la Recherche (ANR) under contract ANR–10–BLAN–0932–01 (MATMAC). E. Drockenmuller gratefully acknowledges the financial support from the Institut Universitaire de France (IUF).

References

1. O. Green, S. Grubjesic, S. Lee, M. A. Firestone. The design of polymeric ionic liquids for the preparation of functional materials. J. Macromol. Sci. C, 2009, 49, 4, 339-360.
2. A. S. Shaplov, E. I. Lozinskaya, Ya. S. Vygodskii. Polymer ionic liquids (PILs): Synthesis, design and application in electrochemistry as ion conducting materials. In: Electrochemical Properties and Applications of Ionic Liquids. 2011, New York: Nova Sci. Publ., Ch. 9: 203-298.
3. E. B. Anderson, T. E. Long. Imidazole- and imidazolium-containing polymers for biology and material science applications. Polymer, 2010, 51, 12, 2447-2454.
4. D. Mecerreyes. Polymeric ionic liquids: Broadening the properties and applications of polyelectrolytes. Prog. Polymer Sci., 2011, 36, 12, 1629-1648.
5. J. Yuan, M. Antonietti. Poly(ionic liquid)s: Polymers expanding classical property profiles. Polymer, 2011, 52, 7, 1469-1482.
6. C. Detrembleur, A. Debuigne, M. Hurtgen, C. Jerome, J. Pinaud, M. Fevre, P. Coupillaud, J. Vignolle, D. Taton. Synthesis of 1-vinyl-3-ethylimidazolium-based ionic liquid (co)polymers by cobalt-mediated radical polymerization. Macromol., 2011, 44, 16, 6397-6404.
7. H. C. Kolb, M. G. Finn, K. B. Sharpless. Click chemistry: Diverse chemical function from a few good reactions. Angew. Chem. Int. Ed., 2001, 40, 11, 2004-2021.
8. M. Meldal. Polymer "clicking" by CuAAC reactions. Macromol. Rapid Commun., 2008, 29, 12-13, 1016-1051.
9. R. K. Iha, K. L. Wooley, A. M. Nyström, D. J. Burke, M. J. Kade,C. J. Hawker. Applications of orthogonal "click" chemistries in the synthesis of functional soft materials. Chem. Rev., 2009, 109, 11, 5620-5686.
10. S. Beghdadi, I. A. Miladi, D. Addis, H. Ben Romdhane, J. Bernard, E. Drockenmuller. Synthesis and polymerization of C-vinyl- and N-vinyl-1,2,3-triazoles. Polym. Chem., 2012, 3, 7, 1680-1692.
11. Zh. Chen, D. R. Dreyer, Z.-Q. Wu, K. M. Wiggins, Zh. Jiang, Ch. W. Bielawski. Synthesis of main-chain poly(carbazole)s via CuAAC. J. Polym. Sci. A, 2011, 49, 6, 1421-1426.
12. E. D. Pressly, R. J. Amir, C. J. Hawker Rapid synthesis of block and cyclic copolymers via click chemistry in the presence of copper nanoparticles. J. Polym. Sci. A, 2011, 49, 3, 814-819.
13. M. lo Conte, M. J. Robb, Y. Hed, A. Marra, M. Malkoch, C. J. Hawker, A. Dondoni. Exhaustive glycosylation, pegylation, and glutathionylation of a [G4]-ene$_{48}$ dendrimer via photoinduced thiol-ene coupling. J. Polym. Sci. A, 2011, 49, 20, 4468-4475.
14. Y. Zekarias, L. Jürgen. 1,2,3-triazolium salts as a versatile new class of ionic liquids. In: Ionic Liquids – Classes and Properties, 2011.
http://www. intechopen.com/books/ionic-liquids-classes-and-properties/1-2-3-triazolium-salts-as-a-versatile-new-class-of-ionic-liquids.
15. J. T. Fletcher, M. E. Keeney, S. E. Walz. 1-allyl- and 1-benzyl-3-methyl-1,2,3-triazolium salts via tandem click transformations. Synthesis, 2010, 19, 10, 3339-3345.
16. J. M. Aizpurua, M. Sagartzazu–Aizpurua, Z. Monasterio, I. Azcune, C. Mendicute, J. I. Miranda, E. García–Lecina, A. Altube, R. M. Fratila. Introducing axial chirality into mesoionic 4,4′-bis(1,2,3-triazole) dicarbenes. Org. Lett., 2012, 14, 7, 1866-1868.
17. H. B. Nulwala, Ch. N. Tang, B. W. Kail, K. Damodaran, P. Kaur, Sh. Wickramanayake, W. Shi, D. R. Luebke. Probing the structure-property relationship of regioisomeric ionic liquids with click chemistry. Green Chem., 2011, 13, 12, 3345-3349.
18. Y. Yoshida, Sh. Takizawa, H. Sasai. Synthesis of spiro bis(1,2,3-triazolium) salts as chiral ionic liquids. Tetrahedron Lett., 2011, 52, 51, 6877-6879.

19. C. Caumes, O. Roy, S. Faure, C. Taillefumier. The click triazolium peptoid side chain: A strong cis-amide inducer enabling chemical diversity. J. Am. Chem. Soc., 2012, 134, 23, 9553-9556.
20. S. Sanghi, E. Willett, C. Versek, M. Tuominen, E. B. Coughlin. Physicochemical properties of 1,2,3-triazolium ionic liquids. RSC Adv., 2012, 2, 3, 848-853.
21. M.-C. Tseng, H. T. Cheng, M. J. Shen, Y. H. Chu. Bicyclic 1,2,3-triazolium ionic liquids: Synthesis, characterization, and application to rutaecarpine synthesis. Org. Lett., 2011, 13, 16, 4434-4437.
22. K. M. Mullen, J. Mercurio, Ch. J. Serpell, P. D. Beer. Exploiting the 1,2,3-triazolium motif in anion-templated formation of a bromide-selective rotaxane host assembly. Angew. Chem. Int. Ed., 2009, 48, 26, 4781-4784.
23. R. K. Chhatra, A. Kumar, P. S. Pandey. Synthesis of a bile acid-based click-macrocycle and its qpplication in selective recognition of chloride ion. J. Org. Chem., 2011, 76, 21, 9086-9089.
24. S. S. Khan, J. Shah, J. Liebscher. Synthesis of new ionic-liquid-tagged organocatalysts and their application in stereoselective direct aldol reactions. Tetrahedron, 2010, 66, 27-28, 5082-5088.
25. J. Bouffard, B. K. Keitz, R. Tonner, V. Lavallo, G. Guisado–Barrios, G. Frenking, R. H. Grubbs, G. Bertrand. Synthesis of highly stable 1,3-diaryl-1H-1,2,3-triazol-5-ylidenes and their applications in ruthenium-catalyzed olefin metathesis. Organomet., 2011, 30, 9, 2617-2627.
26. T. Karthikeyan, S. Sankararaman. Palladium complexes with abnormal N-heterocyclic carbene ligands derived from 1,2,3-triazolium ions and their application in Suzuki coupling. Tetrahedron Lett., 2009, 50, 42, 5834-5837.
27. P. Dimitrov–Raytchev, S. Beghdadi, A. Serghei, E. Drockenmuller. Main-chain 1,2,3-triazolium-based poly(ionic liquid)s issued from AB + AB click chemistry polyaddition. J. Polymer Sci. A, 2013, 51, 1, 34-38.
28. E. Azaceta, R. Marcilla, A. Sanchez–Diaz, E. Palomares, D. Mecerreyes. Synthesis and characterization of poly(1-vinyl-3-alkylimidazolium) iodide polymers for quasi-solid electrolytes in dye sensitized solar cells. Electrochim. Acta, 2010, 56, 1, 42-46.
29. P. K. Singh, B. Bhattacharya, R. K. Nagarale, S. P. Pandey, K. W. Kim, H. W. Rhee. Ionic liquid doped poly(N-methyl 4-vinylpyridine iodide) solid polymer electrolyte for dye-sensitized solar cell. Synth. Met., 2010, 160, 9-10, 950-954.
30. G. Wang, Sh. Zhuo, L. Wang, Sh. Fang, Y. Lin. Mono-ion transport electrolyte based on ionic liquid polymer for all-solid-state dye-sensitized solar cells. Solar Energy, 2012, 86, 5, 1546-1551.
31. M. Lee, U. H. Choi, R. H. Colby, H. W. Gibson. Ion conduction in imidazolium acrylate ionic liquids and their polymers. Chem. Mater., 2010, 22, 21, 5814-5822.
32. M. Green, J.-H. Choi, K. Winey, T. Long. Synthesis of imidazolium-containing ABA triblock copolymers: role of charge placement, charge density, and ionic liquid incorporation. Macromol., 2012, 45, 11, 4749-4757.
33. U. H. Choi, M. Lee, Sh. Wang, W. Liu, K. I. Winey, H. W. Gibson, R. H. Colby. Ionic conduction and dielectric response of poly(imidazolium acrylate) ionomers. Macromol., 2012, 45, 9, 3974-3985.
34. S. Binauld, C. J. Hawker, E. Fleury, E. Drockenmuller. A modular approach to functionalized and expanded crown ether based macrocycles using click chemistry. Angew. Chem. Int. Ed., 2009, 48, 36, 6654-6658.

EFFECT OF PREPARATION CONDITIONS ON THE MORPHOLOGY AND MECHANICAL BEHAVIOR OF POLYETHYLENE VINYL ACETATE – CLAY NANOCOMPOSITES

A. A. Abdel Hafiz, A. R. Ramadan, A. M. K. Esawi

The American University in Cairo
Cairo, Egypt
ali.abdelhafiz@gmail.com

Accepted September 19, 2013

1. Introduction

Polymer layered silicate nanocomposites (PLSNs) exhibit synergistic properties encompassing improvement in mechanical, thermal, and barrier properties, leading to a wide range of applications in fuel cells [1], packaging, filtration, timing belt, engine cover and seats of cars [2]. Montmorillonite (MMT) is one group of layered silicates which is widely used in the preparation of polymer-clay nanocomposites. Intercalated and/or exfoliated structures are obtained, where clay layers maintain their repetitive structure with the polymer chains penetrating in the interlayer spacings for the former, or the clay layers separate from each other and disperse within the polymer matrix for the latter [3]. The interlayer spacing in the pristine clay structure has a bearing on the formation of the nanocomposites: a small spacing makes it difficult for polymeric chains to penetrate through and hinders the intercalation and exfoliation processes [3].

Different preparation methods have been used for the preparation of PLSNs. The most common method is melt compounding, where mechanical shearing forces, applied during extrusion or injection molding, lead to the increase in the interlayer spacing of the silicate layers, thus allowing the polymeric chains to intercalate them. This method can also lead to the exfoliation of the clay layers. Successful attempts to produce PLSNs with intercalated/exfoliated clay particles have been reported by many research groups [4]. However, the change in melt properties, such as viscosity, upon the addition of the clay particles has been found to lead to polymer degradation under conditions of high shear rates so careful selection of process parameters is important [5]. Nevertheless, the speed and simplicity of melt compounding, as well as its compatibility with standard industrial techniques, makes it a very attractive technique for the preparation of PLSNs.

Solution compounding is another approach for the preparation of PLSNs. The process entails the dispersion of clay layers in a solvent, which often results in swelling, and then mixing this dispersion with a solution of the polymer. This leads to polymer chains displacing the solvent in the clay inter-layers leading to intercalation [3]. Solvent removal is typically carried out by evaporation, and the removal of the solvent is crucial to the success of the process since any solvent residue can lead to polymer degradation during further processing. One of the advantages of solution compounding is that the agitation of the clay dispersion prior

to mixing with the polymer solution facilitates the separation of the clay layers leading to an improved structure in the final composite. In this respect, the process can produce intercalated, as well as exfoliated, structures for clays and polymers suffering fromlimited compatibility [2].

Clay is hydrophilic in nature while most synthetic polymers are hydrophobic in nature, which results in an immiscible structure due to the poor interaction between them. Modification of clay by intercalating organic ligands through the inter-gallery spacing is one of the successful ways to overcome this problem and improve the interaction between the clay and the polymer. For example, according to Bezhad and Vahidused different chemical processes to modify MMT clay with hexadecyl-trimethyl-ammonium after realizing it is not compatible with ABS in its natural form [6]. The same concept was followed by other researchers [7 – 11]. This was not only limited to chemical routes. For example, Yoon et al. added polar co-monomers to aid melt intercalation when mixing polystyrene with clays [12]. These studies indicate the possibility of different chemical speciessuccessfully intercalatingthe clay structure. Processing conditions affect the extent of intercalation. Burgentzle et al. studied the dispersion of organophilic MMT clays into different organic solvents. Results showed that organophilic clays exhibited a high tendency to swell, incorporating solvents in their inter-layer spacing [13].

Polyethylene co-vinyl acetate (EVA) is a thermoplastic polymer, which is close to the elastomers family due to its flexibility and softness. EVA is well known for its barrier properties and crack propagation resistance. Polarity of EVA is a function of the amount of acetatein the chain: increasing the acetate content increases the polarity, but reduces EVA's crystallinity and deteriorates the mechanical behavior as reportedby [14]. A limited number of studies investigated EVA-MMT clays especially using natural or unmodified [15 – 17].

The present work investigates the effect of different preparation processes, namely solution compounding, sonication and extrusion on the structure and morphology of the nanocomposite of EVA and 5 wt. % non-modified Na^+-montmorillonite clay (cloisite Na^+). An investigation of the mechanical behavior was also conducted and related to the observed morphologies.

2. Experimental

2.1. Sample preparation

10 wt. % of EVA polymer (polyethylene co-vinyl acetate containing 18 wt. % acetate, Sigma Aldrich) were completely dissolved in Tetrahydrofuran (THF) (Scharlu, HPLC grade) at 50 °C. 5 wt. %, a filler amount commonly used in different investigations of polymer-clay nanocomposites, of sodium montmorillonite (Na^+ MMT) (Southern Clays Products) was added to the solution using two different approaches. The first approach entailed directly adding the clay to the EVA–THF solution, then leaving this to dry to constant weight at room temperature to give sample "EVA–Na^+–D". The second approach entailedpre-dispersion of the clay inthe THF solvent for 30 min. Pre-dispersion of clay fillers is a widely usedapproach in composite preparation when good filler dispersion is sought. Neat clay was added to THF solution and was mixed by magnetic stirring at 50 °C, before adding it to the polymer solution. The resulting composite solution waseither left to dry to constant weight at room temperature, or was sonicated for 30 min before drying, leading to composite samples "EVA–Na^+–P" and "EVA–Na^+–

PS", respectively. All resulting composites were then subjected to hot compaction at 140 °C for 3 min, to obtain the desired shape for testing. XRD samples were of a disc shape with 25 mm diameter and 2 mm thickness, while tensile testing specimens were of dog-bone shape with gauge length of 20 mm and square cross section of 9 mm^2. Samples EVA-Na^+-P and EVA-Na^+-PS were further processed by melt compoundingusing XTS-19 twin screw counter-rotating extruder,at 280 rpm and 10 min residence time,yielding samples "EVA–Na^+–PE" and "EVA–Na^+–PSE", respectively. Reference samples of neat EVA were processed under the same previous conditions. To compare with wet mixed samples, neat EVA was dissolved into THF at 50 °C, and then left to dry by solvent evaporation to constant weight at room temperature. This resulted in sample EVA–W. To compare with extruded composites, another reference sample was prepared by solution compounding, followed by extrusion at 280 rpm, resulting in sample EVA–E. Both Neat EVA reference samples were hot compacted under the same previous conditions to obtain the same shape of specimens as the nanocomposites ones.

2.2. Structural and mechanical characterization

X-ray diffraction (XRD) investigations were carried outusing a D8 Bruker powder diffractometer operated at 40 kV and 30 mA using copper K_α ($\lambda = 0.1542$ nm) radiation. Transmission electron microscopy (TEM) images were takenusing a JEOL 2010 analytical TEM. Samples were dipped in liquid nitrogen then milled with cryo-microtome into thin layers for imaging. Tensile tests were conducted on an Instron Universal Testing machine. Samples which wereeither compression molded into dog-bone shapes with 20 mm gauge length and cross section of 3×3 mm or obtained from extrusion in the form of wires with 2 – 3 mm diameter and 100 – 150 mm length were tested using a crosshead speed of 20 mm / min.

3. Results

3.1. XRD

Figure 1 compares XRD spectra of EVA–Na^+–D to that of pristine Na^+ and shows that the distinctive base reflection peak of Na^+ MMT was shifted to alower 2θ value of 4.85 °, with peak broadening, corresponding to an inter-gallery spacing of 18.0 Å (compared to an initial inter-gallery spacing for pristine Na^+ of 12.0 Å at 2θ of 7.35 °) indicating significant intercalation.

XRD results in **Figure 2** show that for the pre-dispersed samples EVA–Na^+–P (non-sonicated) and EVA–Na^+–PS (sonicated) the Na^+ MMT basal reflection wasslightly shifted to lower 2θ angles relative to pristine Na^+ MMT, indicating an increase in the inter-gallery spacing between the clay layers. This shift was largerfor the EVA–Na^+–PS and is believed to be due to increased intercalation of EVA chains within the inter-layer spacing as a result of sonication. Calculations indicated an inter-gallery spacing of 12.6 Å and 13.1 Å for EVA–Na^+–P and EVA–Na^+–PS respectively, compared to 12.0 Å for pristine clay.

As for the pre-dispersed nanocomposite samples which were subjected to extrusion, **Figure 3** shows the spectra of EVA–Na^+–PE compared to the pristine Na^+ MMT and the EVA–Na^+–P samples. The distinctive peak of Na^+ remained in the same position of EVA–Na^+–P with no alteration after extrusion. However, the peak intensity increased significantly indicating a significant increase in the order of clay particles in the sample.

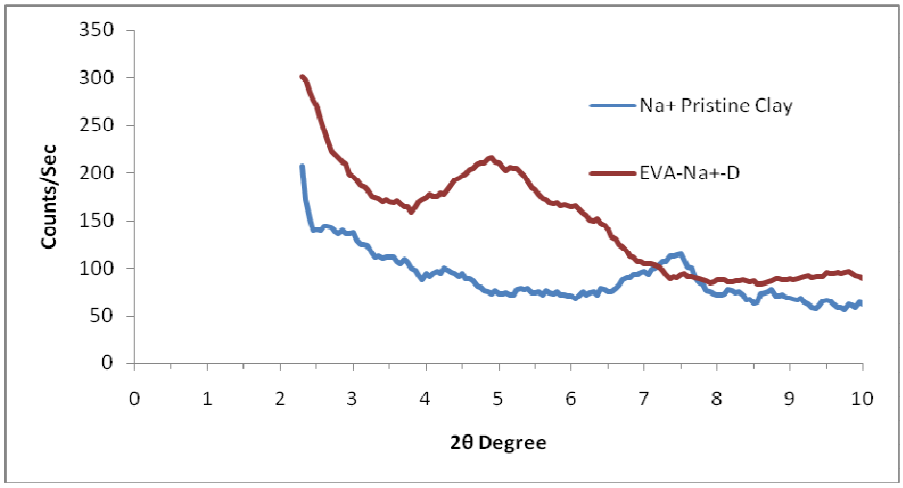

Figure 1. XRD spectra of EVA–Na^+–D andpristine Na^+ MMT.

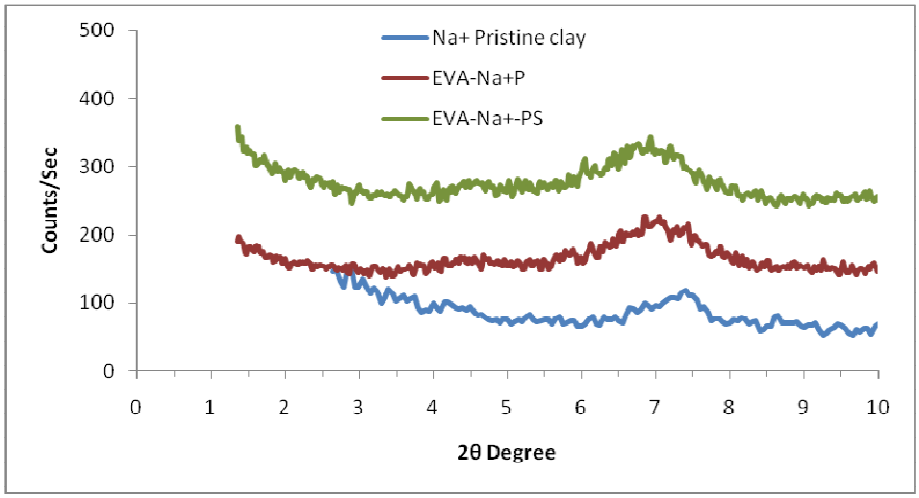

Figure 2. XRD spectra of pre-dispersed EVA–Na^+ nanocomposites and pristine Na^+ MMT.

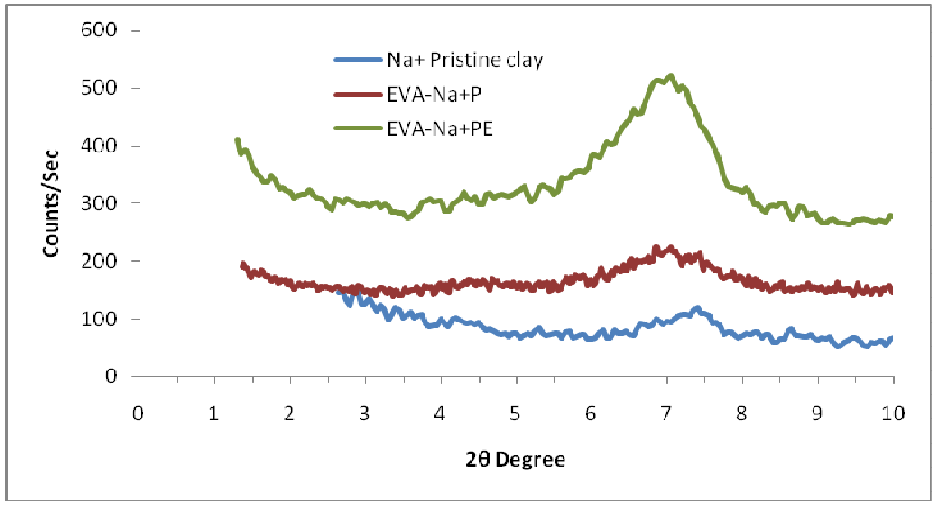

Figure 3. XRD spectra for EVA–Na^+ extruded nanocomposites and pristine Na^+ MMT.

No XRD data are presented for the EVA–Na^+–PSE sample (pre-dispersed, sonicated and extruded) because of its degradation during extrusion. In order to elucidate the reasons behind this degradation, pristine Na^+ MMT was subjected to the same dispersion conditions used in the preparation of the composite samples, but with no EVA added. As received clay, was dispersed

in THF for 30 min at 50 °C with the aid of magnetic stirring. Another Na^+ MMT sample was dispersed following the same previous conditions but was followed by sonication for another 30 min at 50 °C. These two clay samples were then dried to constant weight by solvent evaporation at room temperature. XRD spectra of these samples were collected and are shown in **Figure 4**, where the basal reflections of the dispersed clays were seen shifted to lower 2θ values (6.85 and 6.80 °, respectively) corresponding to inter-layer spacing of 12.9 and 13.0 Å, respectively compared to pristine Na^+ at 2θ of 7.35 ° and inter-gallery spacing of 12 Å. More importantly, the sonicated sample exhibited the appearance of a second XRD reflection at much lower 2θ angles of 3.6 ° with inter-gallery spacing of 24.5 Å, reflecting a significant increase in the interlayer spacing. This second peak is believed to be due to the intercalation of THF molecules in the clay in a different orientation and/or as multilayers.

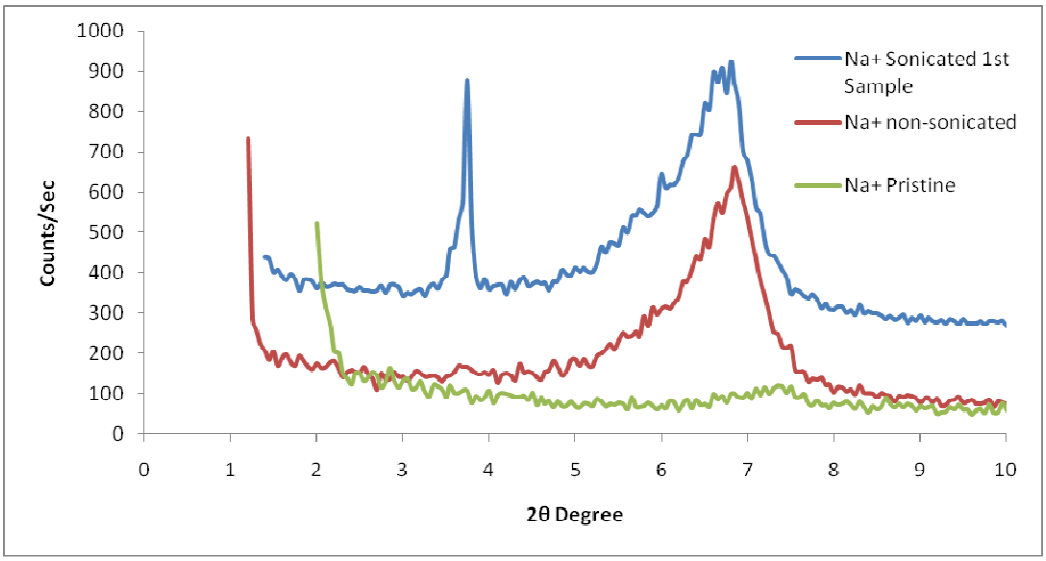

Figure 4. XRD for Na^+ clays, pre-dispersed in THF.

This observation could be explained as follows: THF exhibits low polarity under normal temperature and pressure conditions. However, increasing the temperaturecloser to its boiling point, increasesTHF polarity. This occursduring sonication, resulting in THF interacting more significantly, through its lone pair of electrons, with the positive cation exchange cloud in the polar Na^+ clay. This would lead to THF intercalation in a different orientation and / or possibly as multilayers and the observed significant increaseof the peak intensityfor some of the Na^+ MMT clay particles. The above structureshave led to a degradation of the composite sample during extrusion. As a result of the high shear forces and elevated temperature of 140 °C during extrusion which are believed to have led to the extraction of the THF from the clay particles into the surrounding polymer matrix, causing the degradation.

3.2. TEM

Figure 5 represents TEM images of non-sonicated (EVA–Na^+–P) samples showing areas with a large number of clay particles and / or layers and other areas free of clay, indicating poor dispersion of Na^+ MMT in the EVA matrix. On the other hand, composite samples prepared with pre-dispersed and sonicated clay, exhibited improved dispersion, with lower disparity between sample areas (**Figure 6**).

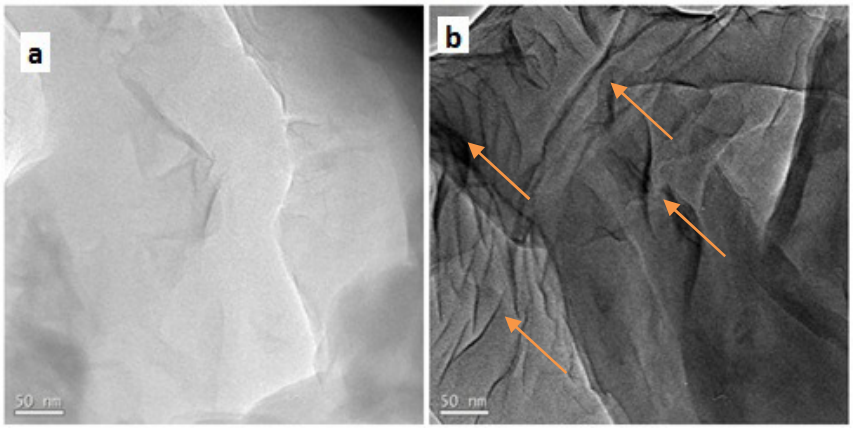

Figure 5. TEM image of EVA-Na^+–P: a) an area free of clay; b) an area with condensed clay particles.

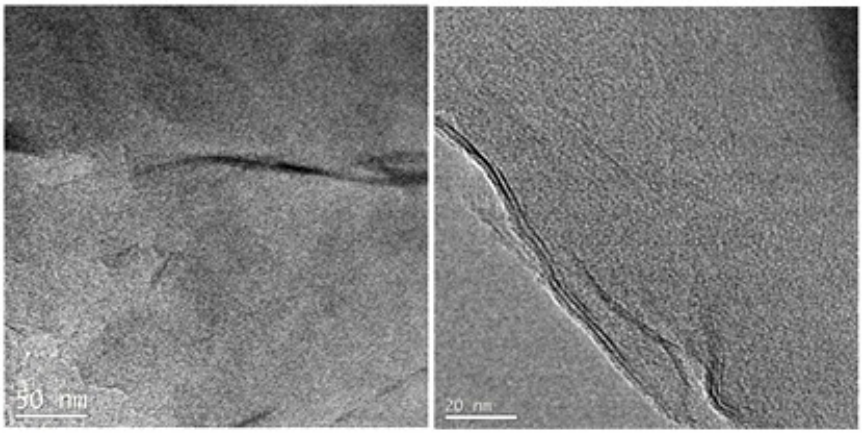

Figure 6. TEM images of EVA–Na^+–PS pre-dispersed and sonicated composite at two magnifications.

For composite samples subjected to further processing by melt blending, TEM images show that although some particles remained intact, extrusion helped in improving exfoliation of the clay particles and the dispersion of the clay layers within the polymer matrix. **Figure 7a** shows an intact clay particle, while **Figures 7b** and **c** show exfoliated structures with individual clay layers. These images confirm that the obtained structure is mixed, comprising exfoliated, intercalated and immiscible regions. No TEM images for sample EVA–Na^+–PSE could be obtained due to sample degradation upon extrusion, as explained earlier.

3.3. Tensile strength

Figure 8 presents the tensile test results for the different EVA–Na^+ composites. As noted from the results, EVA–Na^+–D composites displayed tensile strength valueswith largevariations, which can be attributed to the poor dispersion of clay particles. The composite had regions with a limited number of clay particles and others with many agglomerates. The average tensile strength was found to be 12.1 MPa. On the other hand, pre-dispersed composites EVA–Na^+–P and EVA–Na^+–PS recorded tensile strengths of 9.90 and 10.25 MPa, respectively, with more uniformity among tested specimens and with lower variations. The results of extruded samples are presented at 200 % strain in **Figure 9** (no strength values at break were reported for

extruded samples because the span length of the testing machine was not long enough to allow the sample to extend up to fracture which can be beyond 800 % strain) and show that the extruded composite EVA–Na^+–PE recorded the highest tensile strength of 3.35 MPa, which is in agreement with the significant enhancement in clay dispersion and layers delamination. Hence, extrusion played a positive effect in enhancing the strength of EVA–Na^+–P by allowing more EVA chains to intercalate through clay layers and increasing the amount of delaminated clay layers, as confirmed by TEM analysis presented earlier.

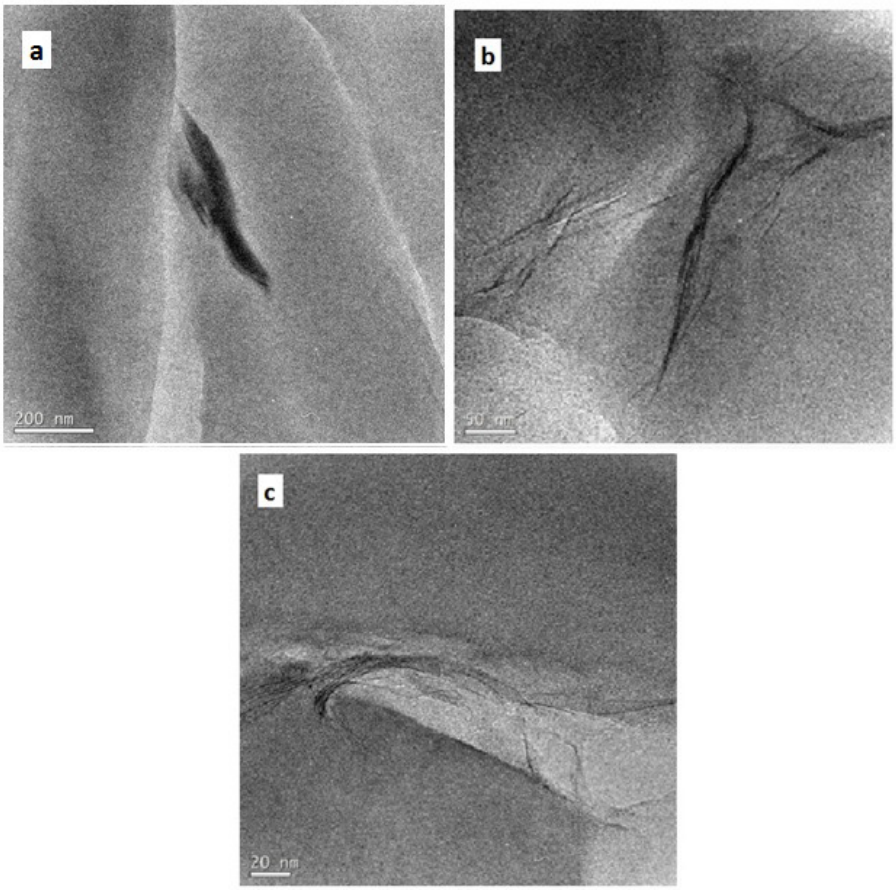

Figure 7. TEM images of EVA–Na^+–PE: (a) large clay agglomerate; (b) individual delaminated clay layers; (c) intercalated clay layers.

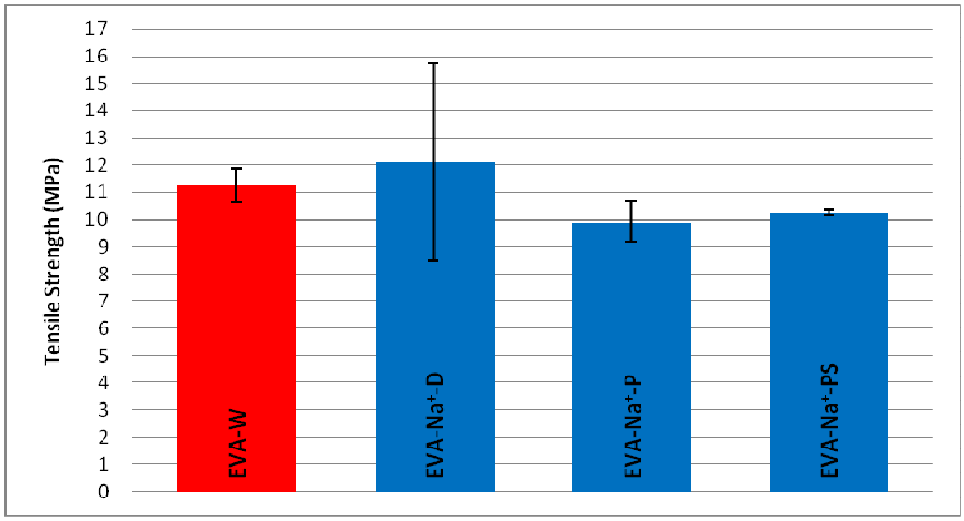

Figure 8. Tensile strength results for EVA–Na^+ wet mixed composites.

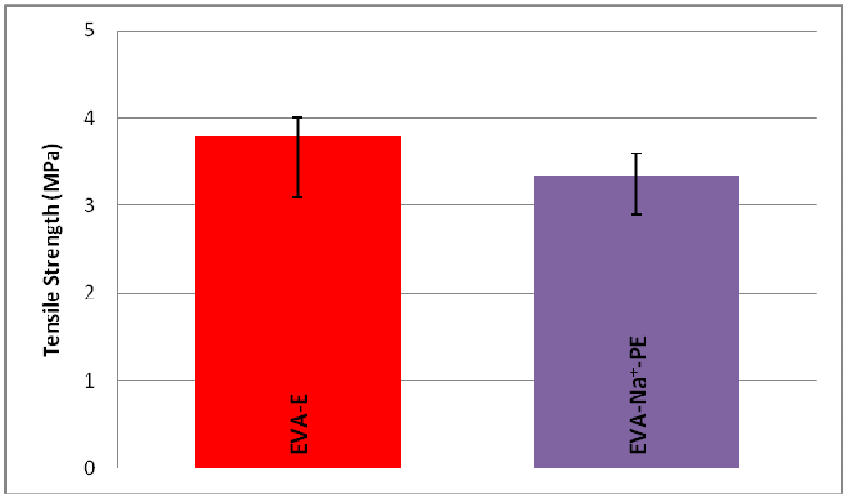

Figure 9. Tensile stress for EVA–Na⁺–PEcompared to neat EVA processed under the same conditions and EVA–Na⁺–P sample.

3.4. Stiffness

Figure 10 shows the stiffness behavior for all EVA–Na⁺ composites. The effect of poor dispersion in the EVA–Na⁺–D also resulted in variations in the observed tensile modulus values. Nonetheless, the average value of 20 MPa constitutes a significant enhancement in tensile modulus over neat EVA, which can be attributed to the obstruction of EVA chains from movement by clay particles. For EVA–Na⁺–PS and EVA–Na–P, the values of stiffness were 7.8 and 7.0 MPa, respectively. The samples displayed less variation, as sonication dispersed the clay particles more uniformly. Sonication and pre-dispersion of clay layers, contributed to better clay dispersion, but isexpected to have altered the aspect ratio of the clay layersthus resulting in the lower stiffness values compared to the EVA–Na⁺–D. This needs further future studies as no reports were found in the literature regarding this issue. Extruded EVA–Na⁺–PE recorded a very uniform behavior with an average stiffness of 20 MPa, which again agrees with the XRD and the TEM results discussed earlier.

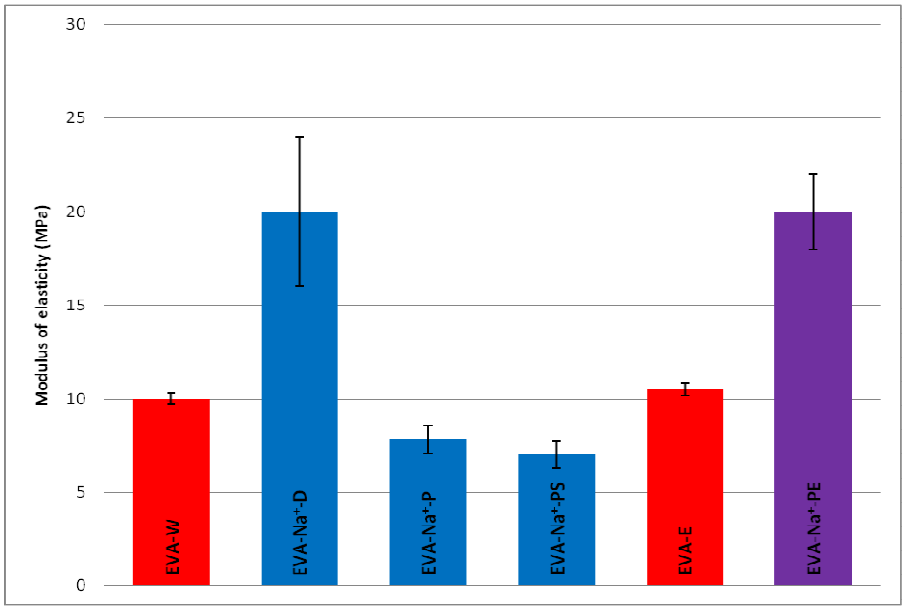

Figure 10. Stiffness of EVA–Na⁺ composites.

4. Discussion

Only a limited number of studies investigated the morphology and structure of EVA-Cloisite clays and among those, only one study was concerned with the unmodified Na^+ clay. Their TEM images of Anilkumar et al. for EVA–Na^+ composite showed very poor dispersion of clay particles with large agglomerates [17]. The observed poor intercalation and the presence of some immiscible clay particles and tactoids in the structure of the nanocomposites prepared in the current study confirmed the poor compatibility between Na^+ and EVA especially when using clays which have not been pre-dispersed. However, it was also observed that pre-dispersion of clays into THF and sonication contributes to better dispersion of the clay layers. In addition, extrusion contributed to improved dispersion and enhanced delamination of clay layers. With the exception of the composite with the Na^+ that has not been pre-dispersed, all other composite samples recorded tensile strength values lower than those of the neat EVA at each of the processing conditions. This is probably due to the fact that Na^+ is different in nature from EVA. Although EVA contains polar acetate groups, their amount is relatively low. In consequence, EVA's polarity is relatively low, resulting in poor compatibility between the EVA matrix and Na^+ filler. Na^+ particles were difficult to disperse into EVA matrix when added with no prior pre-dispersion. Pre-dispersion of clays and sonication enhanced the uniformity of the clay dispersion, but might have altered the aspect ratio of the clay particles. This is thought to be the reason behind the lower values of stiffness. Extrusion enhanced the stiffness and strength due to the good dispersion of clay particles and the better delamination of the clay layers, which resulted in more enhancement in stiffness compared to the neat EVA. The co-rotating extruder used in the present study provides a high shear force at the interface between the two screws, which enhanced the delamination of clay layers. Such an increase in the number of exfoliated clay layers within the polymer melt enhanced the stiffness.

5. Conclusion

The effect of different preparation processes, namely solution compounding, sonication and extrusion on the structure and morphology of the nanocomposite of EVA and 5 wt. % non-modified Na^+-montmorillonite clay was studied. Mechanical behavior was investigated and related to the observed morphology. More advancement towards delamination of clay layers and random dispersion of clay particles was observedafter extrusion of the samples. Extrusion was found to enhance the stiffness of the material by 100 %.The present study has confirmed that controlled removal of the solvent is crucial as solvent residue can lead to polymer degradation during further processing. In particular, the study has revealed that sonication can make solvent removal more difficult. It was found that sonication led to increased intercalation of solvent in the clay structures, which led to sample degradation during extrusion.

References

1. J. Jaafar, A. F. Ismail, T. Matsuura. Preparation and barrier properties of SPEEK / cloisite 15A® / TAP nanocomposite membrane for DMFC application. J. Membrane Sci. 345 (2009) 119-127.

2. S. S. Ray, M. Okamoto. Polymer / layered silicate nanocomposites: A review from preparation to processing. Prog. Polymer Sci. 28 (2003) 1539-1641.
3. S. Pavlidou, C. D. Papaspyrides. A review on polymer–layered silicate nanocomposites. Prog. Polymer Sci. 33 (2008) 1119-1198.
4. M. Alexandre, P. Dubois. Polymer-layered silicate nanocomposites: Preparation, properties and uses of a new class of materials. Mater. Sci. & Eng. R 28 (2000) 1-63.
5. H. R. Dennis, D. L. Hunter, D. Chang, S. Kim, J. L. White, J. W. Cho, D. R. Paul. Effect of melt processing conditions on the extent of exfoliation in organoclay-based nanocomposites. Polymer 42 (2001) 9513-9522.
6. P. Bezhad, R. Vahid. Preparation of ABS / montmorillonite nanocomposite using a solvent / non-solvent method. Polymer 46 (2005) 5533-5540.
7. R. Ishii, H. Wada, K. Ooi. A comparison of supercritical carbon dioxide and organic solvents for the intercalation of 4-phynelazoaniline into a pillared clay mineral. J. Colloid & Interface Sci. 254 (2002) 250-256.
8. S. William–Daryn, R. K. Thomas. The intercalation of a vermiculite by cationic surfactants and its subsequent swelling with organic solvent. J. Colloid & Interface Sci. 255 (2002) 303-311.
9. N. Sibold, Ch. Dufour, F. Gourbilleau, M.-N. Metzner, Ch. Lagrève, L. le Pluart, P.-J. Madec, Th.-Nh. Pham. Montmorillonite for clay – polymer nanocomposites: Intercalation of tailored compounds based on succinic anhydride, acid and acid salts derivatives – A review. Appl. Clay Sci. 38 (2007) 130-138.
10. P. H. Massinga Jr, W. W. Focke, Ph. L. de Vaal, M. Atanasova. Alkyl ammonium intercalation of Mozambican bentonite. Appl. Clay Sci. 49 (2010) 142-148.
11. Y. Liang, H. Ding, Y. Wang, N. Liang, G. Wang. Intercalation of cetyltrimethyl ammonium ion into sercitie in the solvent of dimethyl sulfoxide. Appl. Clay Sci. 74 (2013) 109-114.
12. J. T. Yoon, W. H. Jo, M. S. Lee, M. B. Ko. Effect of comonomers and shear on the melt intercalation of styrenics / clay nanocomposites. Polymer 42 (2001) 329-336.
13. D. Burgentlzlé, J. Duchet, J. F. Gérard, A. Jupin, B. Fillon. Solvent-based nanocomposite coatings. I. Disperison of organophilic montmorillonite in organic solvent. J. Colloid & Interface Sci. 278 (2004) 26-39.
14. D. S. Chaudhary, R. Prasad, R. K. Gupta, S. N. Bhattacharya. Clay intercalation and influence on crystallinity of EVA-based clay nanocomposites. Thermochim. Acta 433 (2005) 187-195.
15. S. Peeterbroeck, M. Alexandre, R. Jérôme, Ph. Dubois. Poly(ethylene-co-vinyl acetate) / clay nanocomposites: Effect of clay nature and organic modifiers on morphology, mechanical and thermal properties. Polymer Degrad. & Stab. 90 (2005) 288-294.
16. C. Lili. Morphology and properties of nanocomposites formed from ethylene-vinyl acetate copolymers and organoclays. Polymer 48 (2007) 6325-6339.
17. S. Anilkumar, M. G. Kumaran, S. Thomas. Characterization of EVA / clay nanocomposite membranes and its pervaporation performance. J. Phys. Chem. B 112 (2008) 4009-4015.

CONDUCTIVE POLYMER / C_{60} COMPOSITE FILM

M. Onoda

Graduate School of Engineering
University of Hyogo
Himeji, Japan
ss-syu02@eng.u-hyogo.ac.jp

Accepted September 19, 2013

1. Introduction

A number of studies have been devoted not only to unveil the properties of conductive polymers but to develop polymer-based functional devices such as light-emitting devices, photovoltaic devices, and transistors. Because of the solubility of conductive polymers with rather longer alkyl chains, apparently cost-effective deposition technologies based on polymer solutions, such as spin-coating and ink-jet printing, have been widely used to make them. Although facilities for spin-coating are rather cheap, this method consume excess of polymer solutions, most of which is blown away during spinning, to obtain high quality films. In addition to the lack of the compatibility with patterning, this is one of most important shortcomings of this method. The ink-jet technology principally draws the pattern as line-to-line manner, and seems to have some problem in production speed. Recently,we have reported a simple procedure to obtain colloidal suspension of a conductive polymer poly(3-octadecylthiophene), as well as the electrophoretic deposition of the polymer from the suspension [1]. In contrast to the films prepared by solution-based techniques such as spin-coating, the film has nanostructured morphology. In the electrophoretic deposition, the materials are solidified as colloidal particles in a non-solvent liquid, and then they are collected by electrophoretic force to form a nanostructured film. Drying of the film is also carried out in non-solvent atmosphere so that the nanostructure is reserved. Because of the large surface area, the nanostructured film is a promising material for sensor and electrochemical applications. Apart from this, a light-emission has been found in a device simply fabricated by vacuum metallization of the electrophoretically deposited poly(3-octadecylthiophene) film, indicating that the absence of macroscopic pin-hole in the film [2, 3]. Therefore, the electrophoretic deposition can be used also in thin-film sandwich-type devices such as light-emitting device and photovoltaic devices. It is well known that using the donor–acceptor composite improves the photon/electron conversion performance of photocells with conductive polymer [4 – 6]. If both components are incorporated more than percolation threshold concentration in the film to make interpenetrating network, both electron and hole can be transported to and collected by the electrodes [7]. Since most of the conductive polymers have p-type or donor nature, much effort has been devoted to synthesize acceptor material with high solubility [8 – 10]. In this paper, we propose different approach to make donor-acceptor composite, employing the electrophoretic deposition.

2. Experimental procedure

We have tried to make the nanocomposite of poly(2-methoxy, 5-(2'-ethylhexyloxy)-1,4-phenylene vinylene), MEH-PPV, and C_{60}, MEH-PPV and C_{60} were the products of Aldrich and MTR, respectively. The procedure of the preparation of suspensions and the electrophoretic deposition are found in our previous paper [2, 3]. A unit of toluene solution of MEH-PPV was injected into four units of acetonitrile, to obtain five units of suspension. The suspension of C_{60} can be obtained through the same method [7]. After mixing the two suspensions with appropriate ratio, the electrophoretic deposition was carried out by applying 250 V for 10 s, between two glass plates coated with indium tin oxide (ITO) 5 mm apart. In contrast to the case of poly(3-octadecylthiophene), both MEH-PPV and C_{60} are deposited on positively biased electrode, indicating the negative surface charge of colloidal particles.

The optical absorption and photoluminescence spectra were measured by a Hitachi U–3410 spectrophotometer and a Hitachi F–2500 fluorescent spectrophotometer, respectively. For liquid samples, a glass cell of 1 mm in optical path was used. The atomic force microscope images were taken by a Burleigh Metris–2000 system.

3. Results and discussion

3.1. MEH-PPV / C_{60} nanocomposite

The idea to obtain nanocomposites of MEH-PPV and C_{60} used in this study is illustrated in **Figure 1**. A suspension containing both MEH-PPV and C_{60} colloids can be obtained by mixing the individual suspensions of them. Since both colloids can be collected on the positively biased electrode. The nanocomposite of MEH-PPV and C_{60} can be obtained.

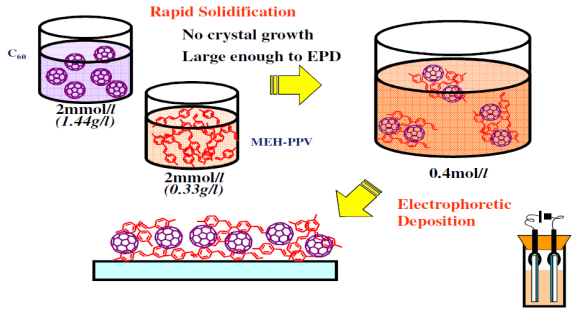

Fugure 1. Procedure to obtain donor–acceptor nanocomposite film by electrophoretic deposition.

3.1.1. Optical absorption and photoluminescence spectra of MEH-PPV colloidal suspension

Figure 2 shows the optical absorption spectra of toluene solution and the suspension of MEH-PPV. The absorption edge shows a drastic red-shift, which is noticeable by naked eye. As shown in **Figure 3**, the photoluminescence of the MEH-PPV suspension is weakened and is red-shifted from that of the toluene solution. These results indicate that the MEH-PPV is suggested to be solid particles in the suspension. However, it is evident that the suspension is a transparent liquid, from the lack of absorption tail at NIR region.

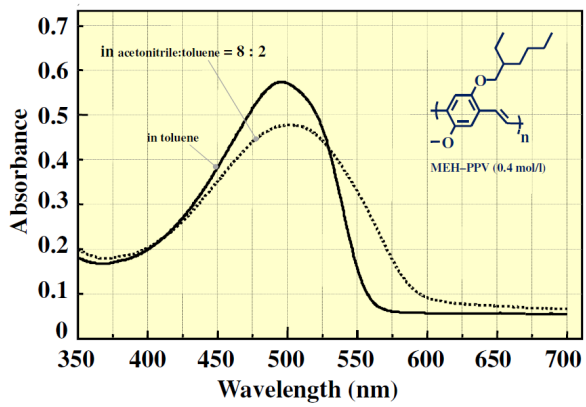

Figure 2. Optical absorption spectra of MEH-PPV in toluene and acetonitrile / toluene (= 4 / 1) mixture. The concentration is 0.066 g / l corresponding to 0.4 mmol / l.

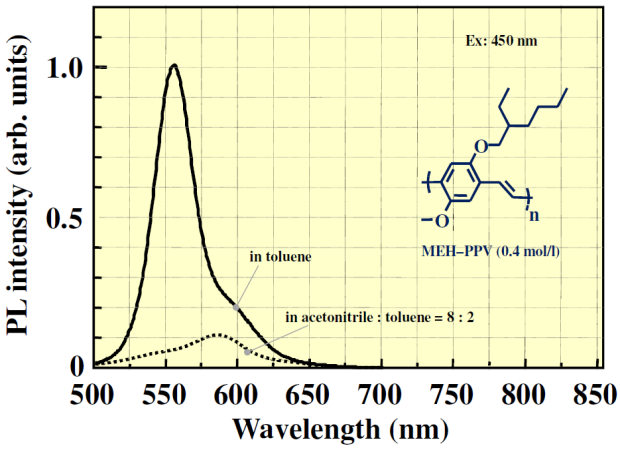

Figure 3. Photolu,inescence spectra of MEH-PPV in toluene and acetonitrile / toluene (= 4 / 1) mixture. The concentration is 0.066 g / l corresponding to 0.4 mmol / l.

3.1.2. Optical absorption spectra of C_{60} colloidal suspension

Figure 4 shows the optical absorption spectra of the toluene solution and the suspension of C_{60}. The solution is clear violet liquid while the suspension is an opaque brown liquid. This result indicates the solidification of C_{60} in the suspension. The opaqueness of the suspension suggests the colloidal size is close or exceeds the wavelength of visible light. However, both suspensions of C_{60} and MEH-PPV do not show notable precipitation for more than a week.

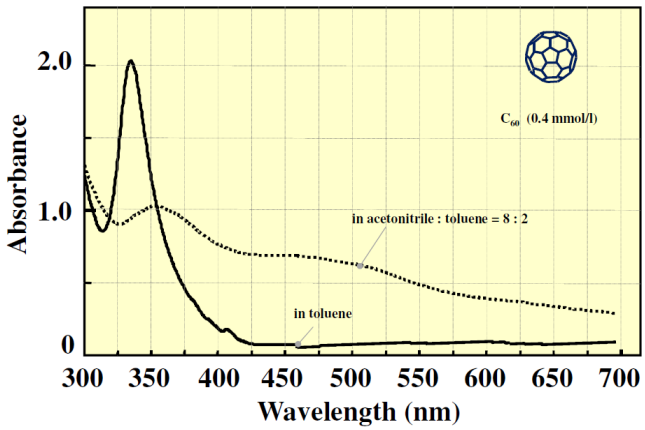

Figure 4. Optical absorption spectra of C_{60} in toluene and acetonitrile/toluene (= 4 / 1) mixture. The concentration is 0.29 g / l corresponding to 0.4 mmol / l.

3.1.3. Optical absorption spectra of MEH-PPV / C_{60} composite films prepared by electrophoretic deposition

The optical absorption spectra of mixtures of MEH-PPV suspension and C_{60} suspension spectra shown in **Figure 5** could be understood as simple superposition of spectra shown in **Figures 2** and **4**. The electrophoretic deposition from the mixture of suspension was carried out by applying 250 V for 1 – 3 s between two ITO electrodes of 5 mm apart soaked in the suspensions. **Figure 6** shows the optical absorption spectra of the composite films of MEH-PPV / C_{60} prepared by electrophoretic deposition. As mentoned in Section 2 (Experimental procedure), the film is deposited on the positively biased electrode. The shapes of the spectra are almost same as those of parent suspensions, indicating that both components are efficiently collected on the ITO electrode.

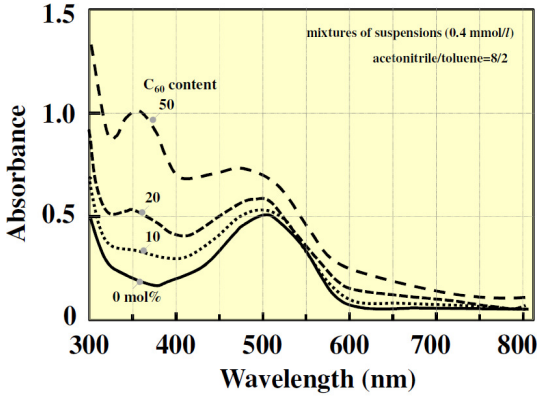

Figure 5. Optical absorption spectra of mixtures of separate suspensions of MEH-PPV and C_{60}.

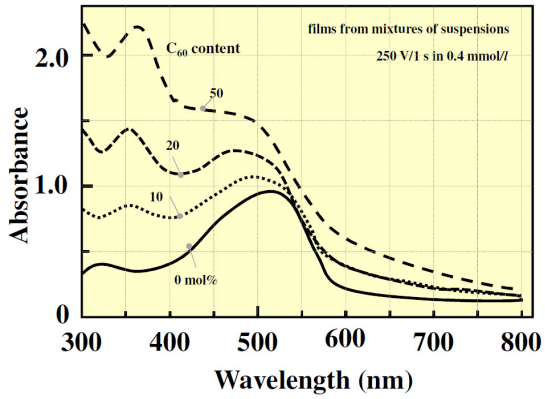

Figure 6. Optical absorption spectra of the MEH-PPV/C_{60} composite film.

3.1.4. AFM images of the MEH-PPV / C_{60} composite filme containing 10 mol. % of C_{60}

As illustrated in **Figure 1**, the donor (MEH-PPV)–acceptor (C_{60}) composites made through the electrophoretic deposition in the mixture suspensions are expected not as molecularly mixture composites but as mixture of nanoparticles of individual components. The atomic force microscope (AFM) image of the film, which is shown in **Figure 7**, also suggests that the C_{60} particle is embedded in rather continuum MEH-PPV film.

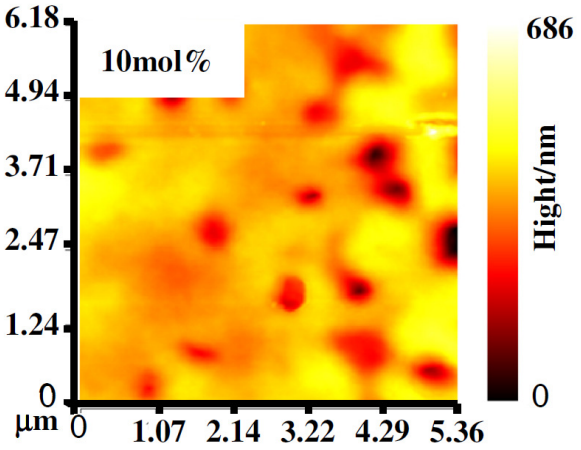

Figure 7. AFM images of the MEH-PPV / C_{60} composite film containing 10 mol. % of C_{60}.

3.1.5. Photoluminescence of the MEH-PPV / C_{60} composite films

However, we observed a drastic quenching of photoluminescence from MEH-PPV by introduction of C_{60} nanoparticles, as shown in **Figure 8**. This clearly indicates that the photoinduced charge transfer between MEH-PPV and C_{60} nanoparticle. Therefore, we can conclude that the donor–acceptor nanocomposite obtained through the electrophoretically deposition in the mixture of suspensions is a promising material for organic photocells.

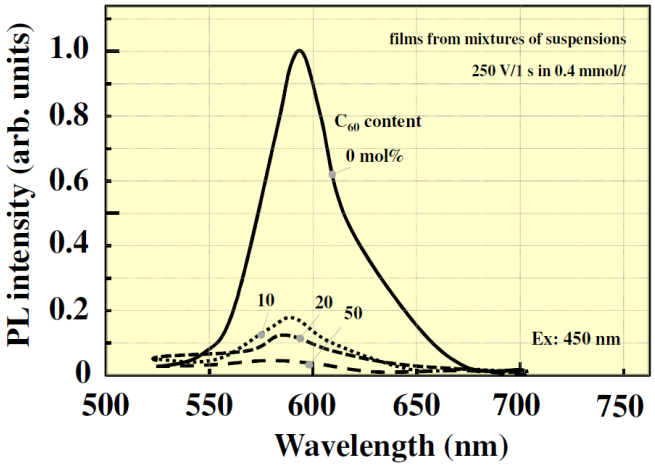

Figure 8. Photoluminescence spectra of the MEH-PPV / C_{60} composite film.

3.1.6. Current–voltage characteristics of a MEH-PPV / C_{60} composite device

Figure 9 shows current–voltage characteristics of a device made from a suspension containing 1 part MEH-PPV and 3 parts C_{60}, which showed the best performance in the present study. The short-circuit current and open-circuit voltage under AM 1.5G 1 sun illumination were 58.6 μA / cm^2 and 0.7 V, respectively, and the power conversion efficiency was approximately $8.6 \cdot 10^{-3}$ %. For this device, electrophoretic deposition was carried out using 1 mm-thick cell to obtain 200 nm-thick films, which are more favorable for photovoltaic devices than 400 nm-thick films produced in 2 mm-thick cell.

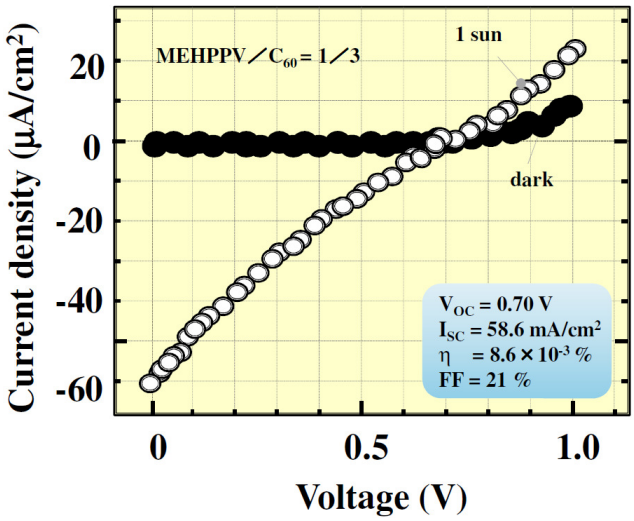

Figure 9. Current–voltage characteristics of the device with a composite film deposited from suspension containing 1 part MEH-PPV as well as 3 parts C_{60}.

3.1.7. Short-circuit current and power conversion efficiency of a MEH-PPV / C_{60} composite device

The relationship short-circuit current as well as power conversion efficiency and C_{60} content is summarized in **Figure 10**. Short-circuit current as well as the power conversion efficiency shows a sharp peak at 3 parts C_{60} regardless of the film thickness. The dependence shown in **Figure 10** is similar to that reported for the composite films consisting of other poly(p-phenylenevinylene) derivative and [6,6]-Phenyl-C_{61}-Butyric Acid Methyl Ester, PCBM [11]. That is, it shows a relatively sharp peak. When the concentration of C_{60} in the composite films is too low, the electron transport path is not formed throughtout the composite, resulting in low power conversion efficiency. On the other hand, too much C_{60} disturbs the hole transport path. Although power conversion efficiencies of the devices are poor in comparison with these from other studies, this paper is intended just to demonstrate the applicability of a new deposition technique with high material efficiency to make MEH-PPV/C_{60} composite films that show photovoltaic effect, and optimization of the device parameter is beyond its scope.

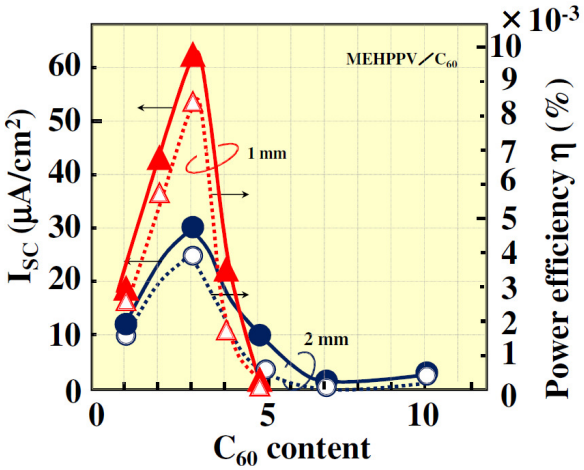

Figure 10. Relationship between the short-circuit current (I_{sc}) as well as power conversion efficiency and C_{60} content in suspensions. 1 and 2 mm-thick cells, respectively. (Triangular and circular symbols correspond to the devices with the films deposited in 1 and 2 mm-thick cells.

4. Conclusions

A novel route to obtain donor-acceptor nanocomposite by using electrophoretic deposition has been proposed. Suspensions containing MEH-PPV and C_{60} nanoparticles are made by mixing suspensions of individual components. The film obtained by the electrophoretic deposition in the suspension shows notable quenching of photoluminescence, indicating the photoinduced charge transfer between donor MEH-PPV and acceptor C_{60}. This results suggests that the donor-acceptor nanocomposite obtained through the electrophoretic deposition in mixture of suspensions is a promising material for organic photocells.

Composite films of a conductive polymer MEH-PPV and neat C_{60} with various C_{60} contents have been obtained by means of electrophoretic deposition from dilute suspensions. It has been observed that deposition from suspensions containing both components results in pinhole-free films, which are applicable to photovoltaic devices, while inhomogeneous films are formed from the suspensions containing only one of the components. The applicability of electrophoretic deposition to photovoltaic devices with polymer/C_{60} composites has been successfully demonstrated, although the power conversion efficiency is on the order of just 10^{-3}% at the present stage.

References

1. K. Tada, M. Onoda. Nanostructured conjugated polymer films by electrophoretic deposition. Adv. Func. Mater., 2002, 12, 6-7, 420-424.
2. K. Tada, M. Onoda. Preparation and application of nanostructured conjugated polymer film by electrophoretic deposition. Thin Solid Films, 2003, 438-439, 365-368.
3. K. Tada, M. Onoda. Polymer light-emitting devices for artificial fingerprints. Jpn. J. Appl. Phys., 2003, 42, 9A / B, L1093-L1095.
4. S. Morita, A. A. Zakhidov, K. Yoshino. Doping effect of Buckminsterfullerene in conducting polymer: Change of absorption spectrum and quenching of luminescence. Solid State Commun., 1992, 82, 4, 249-252.
5. N. S. Sariciftci, L. Smilowitz, A. J. Heeger, F. Wudl. Photoinduced electron transfer from a conducting polymer to Buckminsterfullerene. Science, 1992, 258, 5087, 1474-1476.
6. K. Yoshino, K. Tada, A. Fujii, E. M. Conwell, A. A. Zakhidov. Novel photovoltaic devices baed on donor–acceptor molecular and conducting polymer systems. IEEE Trans. Electron Dev., 1997, 44, 8, 1315-1324.
7. S. Barazzouk, S. Hotchandani, P. V. Kamat. Nanostructured fullerene films. Adv. Mater., 2001, 13, 21, 1614-1617.
8. J. J. M. Halls, C. A. Walsh, N. C. Greenham, E. A. Marseglia, R. H. Friend, S. C. Moratti, A. B. Holmes. Efficient photodiodes from interpenetrating polymer networks. Nature, 1995, 376, 6540, 498-500.
9. G. Yu, J. Gao, J. C. Hummelen, F. Wudl, A. J. Heeger. Polymer photovoltaic cells: Enhanced efficiences via a network of internal donor–acceptor heterojunctions. Science, 1995, 270, 5243, 1789-1791.

10. K. Tada, K. Hosoda, M. Hirohata, R. Hidayat, T. Kawai, M. Onoda, M. Teraguchi, T. Masuda, A. A. Zakhidov, K. Yoshino. Donor polymer (PAT6)-acceptor polymer (CNPPV) fractal network photocells. Synth. Met., 1997, 85, 1-3, 1305-1306.
11. J. K. J. van Duren, X. Yang, J. Loos, C. W. Bulle–Lieuwma, A. B. Sieval, J. C. Hummelen, R. A. J. Janssen. Relating the morphology of poly(p-phenylenevinylene) / methanofullerene blend to solar-cell performance. Adv. Func. Mater., 2004, 14, 5, 425-434.

STUDIES ON SURFACE PROPERTIES OF ORGANIC POLYMER COATINGS MODIFIED WITH SILICONE–ACRYLIC NANOPOWDERS

I. Ofat, J. Kozakiewicz

Industrial Chemistry Research Institute
Warsaw, Poland
izabela.ofat@ichp.pl

Accepted September 19, 2013

1. Introduction

Powder coatings (PC) are commonly used in the automotive industry as well as in the production of various tools and appliances to protect metal, plastic and other surfaces from mechanical and weather-related damage. Basic recipe of powder coating (PC) consists of polymer resins, curing agents, colorants and other additives [1] and can be designed to obtain the desired coating properties. Recent development of research on nanoparticles resulted in wide application of such nanoadditives in coating manufacturing process to improve coating durability as well as its appearance [2 – 5]. PC modification with core–shell structured silicone-methacrylic nanoparticles (SMNP) developed in the Industrial Chemistry Research Institute led to PC characterized by distinctly higher elasticity and impact resistance than unmodified products [6, 7]. The idea of applying SMNP as an effective PC modifier, patented first by Wacker [8] was based on the assumption that using the core-shell nanoparticles where silicone resin of low glass transition temperature (T_g) constitutes the core and methacrylic polymer of high T_g constitutes the shell would allow to achieve good distribution of the former in the coating matrix thus leading to excellent ability of the coating to absorb high mechanical stresses created by impact forces. The well known specific characteristics of polysiloxanes [9] predispose siloxane polymers not only to act as suitable impact modifiers in polymer-based composite materials, but also to change their surface properties significantly [10 – 14]. In this paper the results of our studies on the effect of chemical composition of silicone resin (i.e. the polysilioxane core of our SMNP modifier) on surface properties of epoxy–polyester and polyester PC are presented.

2. Experimental

2.1. Materials

(a) *for synthesis of silicone resin i.e. polysiloxane core of SMNP*: octamethylcyclotetrasiloxane (D4) – from Momentive, methyltrimethoxysilane (METMS) and methacryloyltrimethoxysilane (MATMS) – both from Acros Organics, dodecylbenzenesulphonic acid (DBSA) from Aldrich, sodium hydrogen carbonate from POCH, Acticide MBS from Thor;

(b) *for synthesis of poly(methyl methacrylate) shell of SMNP*: methyl methacrylate (MM) from HEKO, potassium persulphate – from POCH, DBSA and Acticide MBS – as above;

(c) *for preparation of PC*: Carboxylated polyester resin (Policen 3000 T) acid value – 33 from PPG Polifarb Cieszyn Poland, Epoxy resin (Epidian 012) from Chemical Company Organika–Sarzyna Poland, Primid XL 552 (from EMS–Chemie AG) – used as hydroxyalkylamide crosslinker for polyester coatings, TiO_2 (rutile from Chemical Company Police Poland) – used as pigment Benzoin from DSM and Resiflow PV 88 from Worlee Chemie GmbH – used as standard additives for powder coating.

2.2. SMNP and coatings preparation

All SMNPs were obtained in a three-step process:

Step I: Core synthesis. In this step aqueous dispersion of silicone resin nanoparticles of ca. 80 nm size were synthesized through emulsion polymerization of silicone monomers in water according to method proposed by Weyenberg et al. [15]. DBSA was used as both catalyst and surfactant. Molar ratios of silicone monomers are collected in **Table 1** and their chemical structures are presented at **Figure 1**. To remove methanol that was formed in hydrolysis of alkoxysilane group, vacuum distillation had to be applied. After the process was completed acticide MBS was added as microbiological preservative.

Table 1. Molar ratios of silicone monomers composition used in preparation of SMNP samples.

Monomer	SMNP–295	SMNP–301
MATMS, mole %	0	15.97
METMS, mole %	22.9	10.84
D4, mole %	77.1	73.19

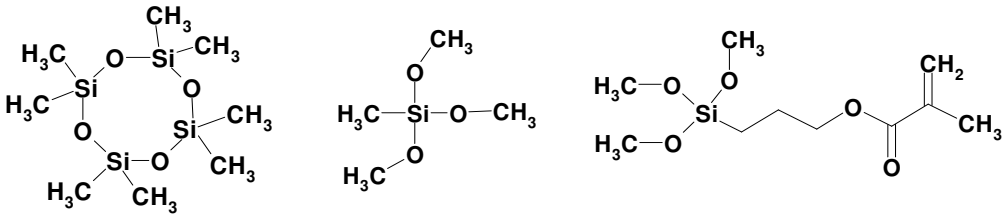

Figure 1. Monomers used to prepare silicone resin.

Step II: Shell synthesis. In this step emulsion polymerization of methyl methacrylate in silicone resin dispersion derived in Step I was carried out as presented in Polish Patent [16] leading to aqueous dispersion of core–shell structured SMNP nanoparticles.

Step III: Preparation of SMNP in agglomerated form. In this step drying of core–shell aqueous dispersion obtained in Step II was conducted using Buchi spray dryer. In this process "nanopowder" agglomerates of the SMNP spherical nanoparticles of grain size from 1 to 20 μm were obtained – see **Figure 2**.

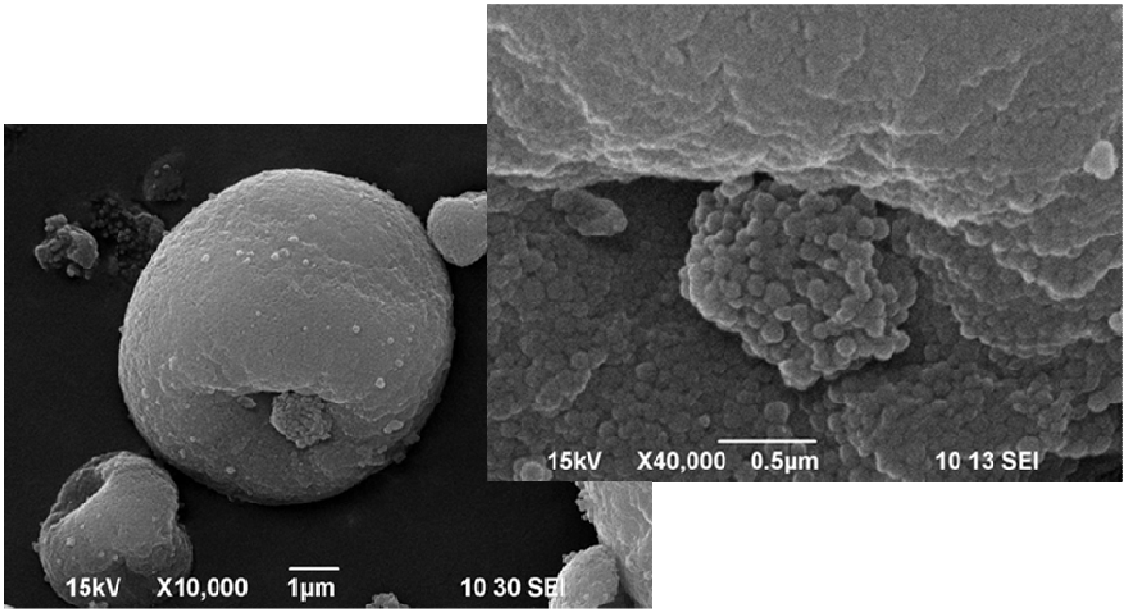

Figure 2. SMNP nanoparticles agglomerated in the "nanopowder" particle.

PC preparation. In order to verify effectiveness of SMNP as PC modifier and to learn how silicone resin composition affects coating surface properties two types of PC were prepared: polyester PC and epoxy–polyester PC. PCs were produced in a standard process which involved the following stages: pre-mixing of components (compositions are presented in **Table 2**), extruding (temperature 80 – 100 °C), crushing, pulverizing, sieving and electrostatic spraying on metallic substrates. In our earlier studies we found [6] that increasing the content of nanopowder in PC from 1 to 5 % resulted in significant changes in surface properties of the cured coating. In the same studies it was proved that modification with just 3 % of nanopowder led to distinct improvement of substantial PC properties (impact resistance, elasticity) while not deteriorating the other coating features (hardness, abrasion resistance). Therefore, we decided to study the effect of silicone resin composition on surface properties of the PC containing only that specific optimum amount of SMNP. Coatings were cured for 15 min at 180 °C.

Table 2. PC composition.

Ingredient	Polyester PC	Epoxy–polyester PC
Epoxy resin	–	22.21
Carboxylic polyester hardener	–	51.83
Polyester resin	56.05	–
Hardener	2.95	–
TiO_2	37.0	22.21
Standard additives	1.0	0.74
SMNP nanopowder*	3.0	3.0

* *applicable only to modified samples.*

Table 3 shows the obtained samples with their designations.

Table 3. PC.

SMNP modifier	Polyester PC	Epoxy–polyester PC
None	P–0	H–0
Modified with SMNP–295	P–295	H–295
Modified with SMNP–301	P–301	H–301

2.3. Characterization of cured coatings

Thickness of cured coatings was measured with PosiTector 200 ultrasonic thickness gage, the tests conformed with ISO 2808. For comparative studies coatings with similar thickness (60 – 90 μm) were chosen. Surface elemental composition was determined by an energy dispersive spectrometry (SEM–EDS) using Jeol JSM–6490 LV microscope and by X-ray photoelectron spectroscopy (XPS) using ESCALAB–210 apparatus. Coatings surface appearance was tested by atomic force microscopy (AFM) using the Multimode NS3D microscope and by optical microscopy using optical microscope NIKON ECLIPSE MA 200. Contact angle (CA) of water and diiodomethane on cured coatings was examined using Kruss DSA 100E goniometer and surface free energy (SFE) values, including its polar and dispersive parts, were calculated based on the CA data.

2.4. Results and discussion

Results of SEM–EDS and XPS studies conducted for the epoxy-polyester PC are presented in **Figures 3** and **4**, respectively.

Based on the SEM EDS results shown in **Figure 3** it can be noted that for the epoxy–polyester PC modification with 3 % of SMNP resulted in the apparent change of elemental composition of coating surfaces. Results of EDS investigations presented in **Figure 3a** proved that concentration of O and Si elements was much higher and concentration of C element was lower on the surface of PC modified with SMNP than on the surface of unmodified sample. Si EDS maps showed that Si was not uniformly distributed on modified samples surfaces which could result from poor miscibility of silicones within the polymer matrix. This observation is also reflected in EDS spectra (**Figures 3c** and **d**). The presence of Ti on the PC surface is obvious since TiO_2 was the component of coating recipe.

According to XPS results, shown in **Figure 4**, silicone resin migration to surfaces of PC samples modified with SMNP could be observed. The content of Si (correlated with C content) at a very close distance to the surface was much higher than few nanometers deeper in the bulk of coating while even that value, specifically for H–295 sample, was very much higher (**Table 4**) than the value representing the average Si content in the modified coating recipe (0.4 %). For unmodified sample Si was not detected by XPS.

Quite significant difference between Si concentration on the surface observed for H–295 and H–301 samples can be explained by difference in silicone resin structure in both cases. In case of H–295 the silicone resin had more hydrophobic and less polar character due to absence of less hydrophobic and more polar silicone monomer (MATMS) in starting composition of silicone monomers what resulted in lower compatibility of silicone resin with the polymer matrix of PC and eventually led to easier migration of the resin to the coating surface.

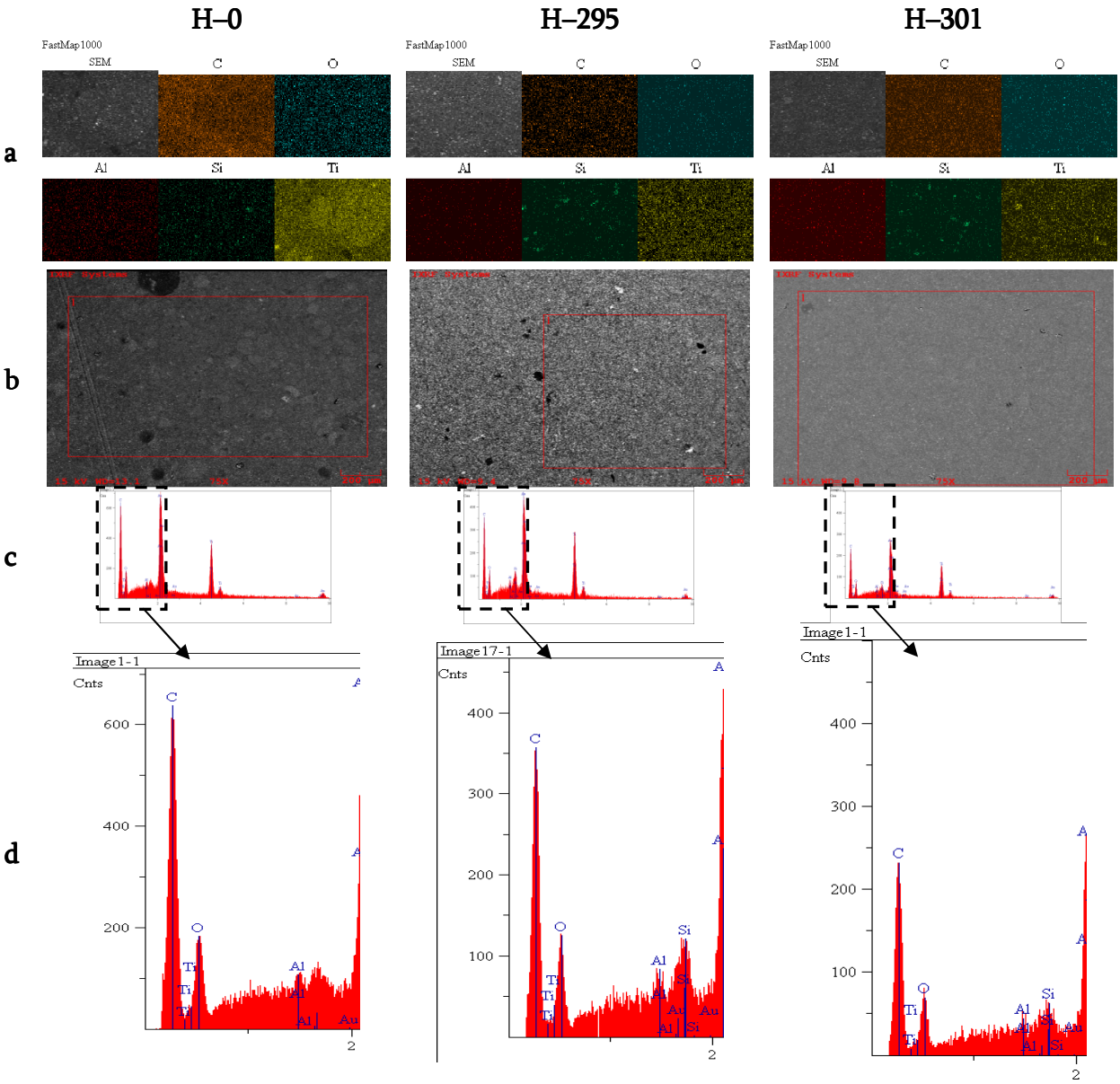

Figure 3. Elemental composition of surfaces of modified and unmodified epoxy–polyester PC assessed by SEM–EDS: a – elements distribution images – magnification 1000 ×, b – SEM images, c – EDS spectra – magnification applied 75 ×, and d – relevant details of EDS spectra.

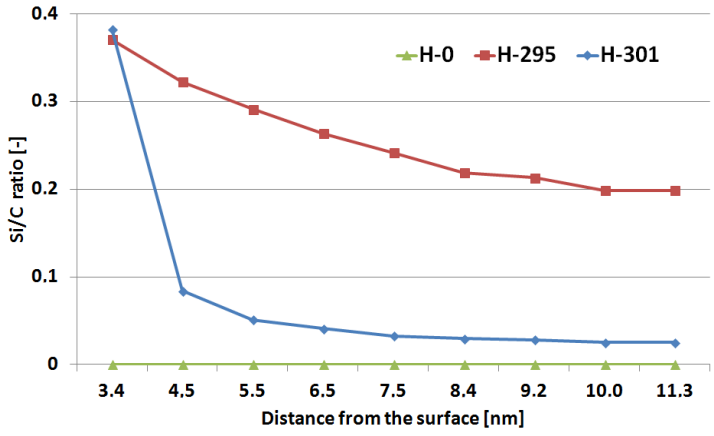

Figure 4. Change of silicon to carbon (Si / C) ratio with diminishing distance from the surface for epoxy–polyester PC, as determined by XPS.

Table 4. Concentration of Si at the different distance from the surface for H–295 sample.

Distance from surface, nm	Si content, %
3.4	22.3
4.5	19.7
5.5	18.0
6.5	16.3
7.5	15.0
8.4	13.8
9.2	13.4
10.0	12.7
11.3	12.5

Results of SEM–EDS and XPS studies conducted for polyester PC are presented in **Figures 5** and **6**, respectively.

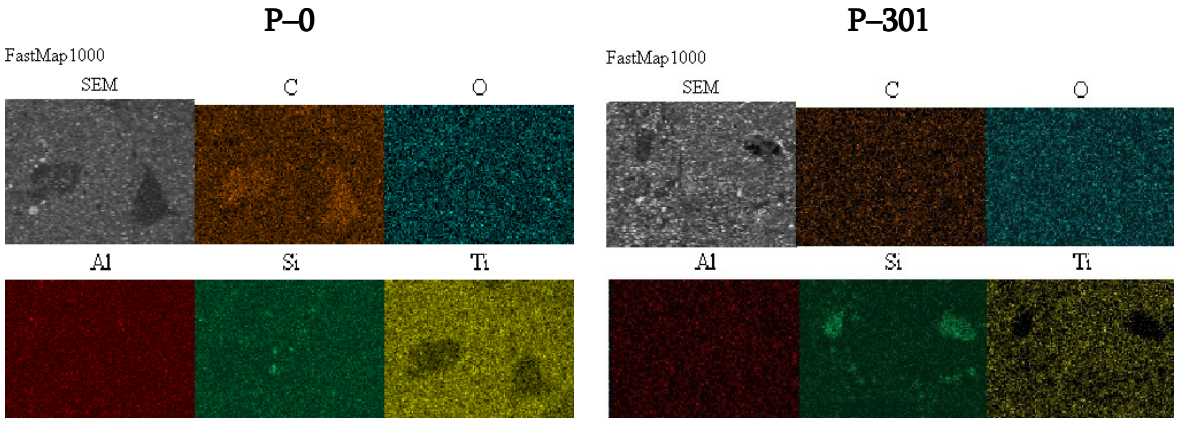

Figure 5. Elemental composition of surfaces of polyester PC assessed by SEM–EDS: elements distribution images – magnification 1000 ×.

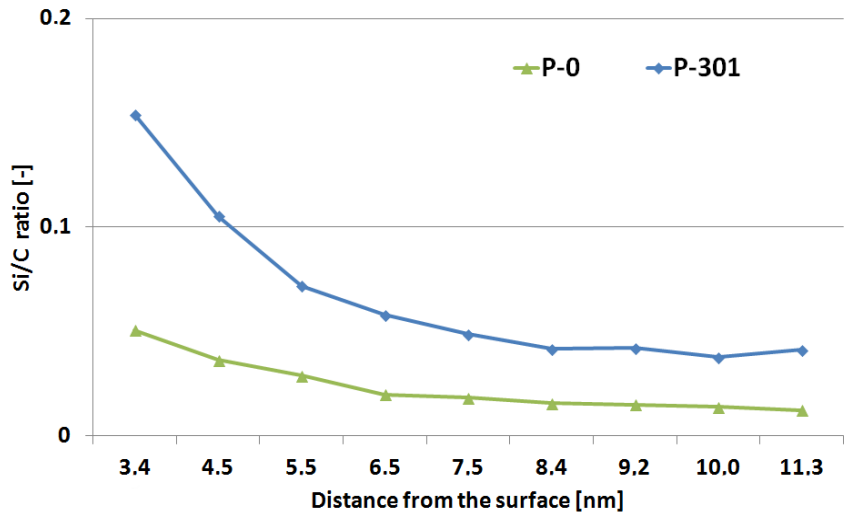

Figure 6. Change of silicon to carbon (Si / C) ratio with diminishing distance from the surface for polyester PC, as determined by XPS.

Similarly as in the case of epoxy-polyester coatings, surfaces of polyester coatings modified with SMNP differ from surfaces of concentration of Si and O elements as compared is much higher for P–301 (modified) sample than for P–0 (unmodified) sample. XPS studies (**Figure 6**) confirmed that Si content (correlated with amount of C) decreased with increasing distance from surface.

Morphologies of the surfaces of modified and unmodified PC were observed using inverted optical microscope with applied 5 × objective lens and polarized light. In **Figures 7a – c**, **e** and **f**) the relevant 3D maps are shown. For better determination of surfaces appearance micrometre scale topographic profiles were generated, they were taken along the line marked on the 3D maps. Those profiles are presented in **Figures 7d** and **g**.

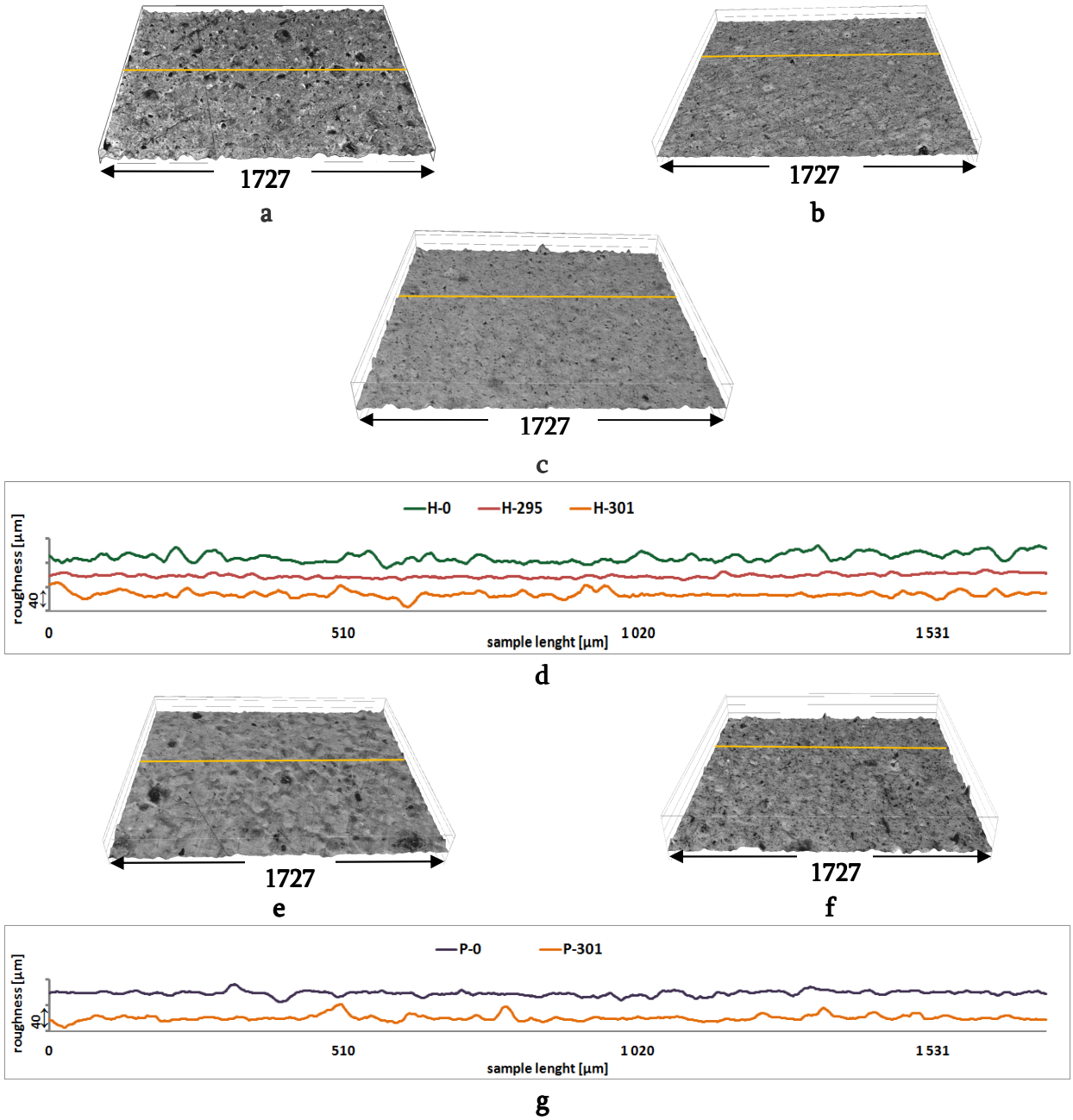

Figure 7. Inverted optical microscope 3D images of epoxy–polyester PC. a – unmodified epoxy–polyester PC, b – epoxy–polyester PC modified with 3 wt. % SMNP–295, c – epoxy–polyester PC modified with 3 wt. % SMNP–301, e – unmodified polyester PC , f – polyester PC modified with 3 wt. % SMNP–301, d and g – comparison of PC topography profiles.

From the results shown in **Figure 7** it seems clear that modification with SMNP significantly affected the structure of PC surfaces, especially in case of epoxy–polyester PC, making the surface more smooth. Surface structure of unmodified sample is shaped in the form of many hills and valleys with wider diameter then in the case of modified samples. For H–295 sample the surface is much smoother (distance from the lowest to the highest point around 15 μm) than for other hybrid coatings where that distance is around 40 μm. It can also be noted that the surface profile is much smoother for H–295 sample than for H–301 sample what can be the result of higher content of silicone resin on the surface of H–295.

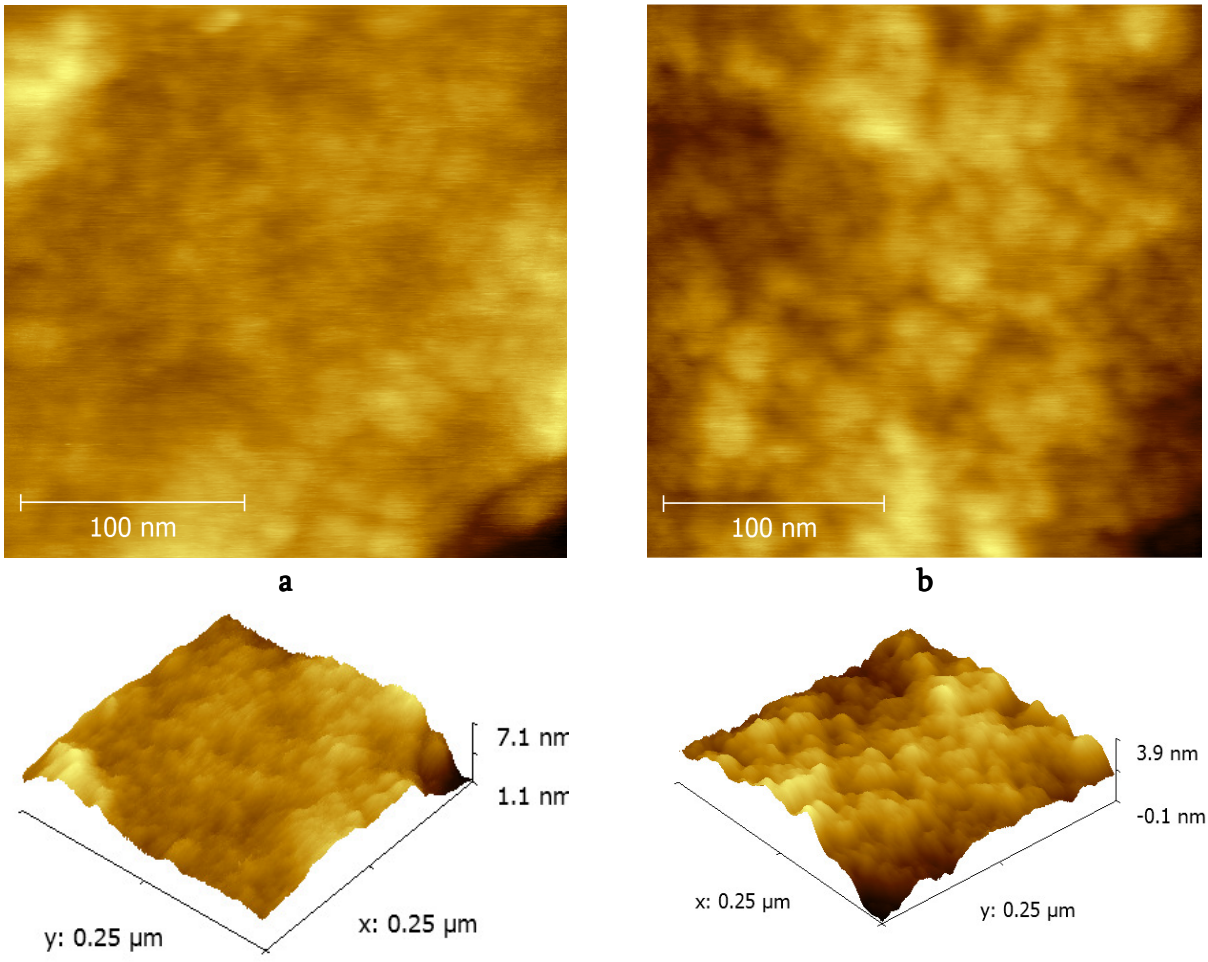

Figure 8. AFM images for unmodified epoxy–polyester PC (a, c) and for epoxy–polyester PC modified with 3 wt. % SMNP–295 (b, d).

The nanostructure of coating surface was studied by AFM (**Figure 8**). The nanostructure of H–0 (**Figures 8a** and **c**) and H–295 (**Figures 8b** and **d**) looks quite similar. Taking into account different z-scale of topography profiles it is apparent that for sample modified with SMNP, i.e. H–295 the bulges are more discrete, peak-to-peak distance between asperities seems to be greater than for H–0 (i.e. unmodified) sample.

Finally, the contact angle of the modified and unmodified PC was determined at ambient temperature using sessile drop method for 2 liquids – water and diiodomethane, surface free energy (γ_s) with its parts (polar γ_p and dispersive γ_d) was calculated using Owens–Wendt method. Results are shown in **Table 4**.

Table 4. Contact angle and surface free energy results.

	H–0	H–295	H–301	P–0	P–295	P–301
Contact angle, deg						
H_2O	88.2	99.2	87.8	86.5	98.5	88.4
CH_2I_2	27.6	45.8	30.5	28.3	43.9	31.3
SFE, mJ / m^2						
γ_s	45.47	37.67	44.20	45.04	38.68	43.88
γ_d	44.68	37.60	43.21	43.89	38.60	42.97
γ_p	0.79	0.07	0.99	1.15	0.08	0.91

As it can be concluded from the results presented in **Table 4**, modification of PC with highly hydrophobic and low-polar silicone resin which migrated easily to the coating surface resulted in very significantly increased CA value and decreased SFE value observed for H–295 sample. For PC modified with more polar and less hydrophobic silicone resin those differences were much less distinct.

3. Conclusions

Modification of epoxy–polyester and polyester powder coatings with silicone–polymethacrylic core–shell nanopowders (SMNP) was performed. It was found through SEM–EDS and XPS studies that such modification led to change in chemical composition of coating surfaces what indicated that silicone resin migrated to the surface. That effect was much more significant for the coatings modified with SMNP containing more hydrophobic and less polar silicone resin. Similar observations were made with regard to the results of studies on the effect of modification of the coatings with SMNP on surface profiles and contact angles.

Acknowledgements

The authors wish to thank The Polish National Centre for Research and Development for providing financial support for the studies described in this paper that were conducted under the project NR 08–0004 10.

The authors wish to acknowledge the assistance of Ms. Joanna Trzaskowska in preparation of SMNP samples, Ms. Helena Kuczynska in preparation of PC samples, Ms. Sylwia Kowalska and Ms. Aneta Lukomska in SEM–EDS surfaces determination and Dr. Janusz W. Sobczak and Ms. Justyna Jakubowska in XPS / AFM and optical microscopy investigations, respectively.

References

1. I. Wheeler. Ch. 14: Powder coatings. In: Metallic Pigments in Polymer. 1999, Smithers Rapra Technology Ltd.

2. F. Bauer, H.-J. Gläsel, U. Decker, H. Ernst, A. Freyer, E. Hartmann, V. Sauerland, R. Mehnert. Trialkoxysilane grafting onto nanoparticles for the preparation of clear coat polyacrylate systems with excellent scratch performance. Prog. Org. Coat., 2003, 47, 2, 147-153.
3. Ed. R. H. Fernando, L.P. Sung. Ch. 1: Nanocomposite and nanostructured coatings: Recent advancements. In: Nanotechnology Applications in Coatings. ACS Symp. Ser., 2009, 1008.
4. M. Špírková, A. Strachota, L. Brozova. The influence of nanoadditives on surface, permeability and mechanical properties of self-organized organic–inorganic nanocomposite coatings. J. Coat. Technol. & Res., 2010, 7, 2, 219-228.
5. M. J. Hanus, A. T. Harris. Nanotechnology innovations for the construction industry. Prog. Mater. Sci., 2013, 58, 7, 1056-1102.
6. J. Kozakiewicz, H. Kuczyńska, T. Jesionowski, R. Nowakowski, J. W. Sobczak, A. Koncka–Foland. Zastosowanie nanocząstek o zaprojektowanej budowie jako modyfikatorów farb proszkowych. Inżynieria Materiałowa, 2007, 28, 5, 863-866.
7. J. Kozakiewicz. In: Proc. Waterborne Symp. 2012, New Orleans, 386-389.
8. K. Mautner, B. Deubzer. Elastomeric graft copolymers having a core / shell structure. US Patent # 5223586 (1993).
9. J. Chojnowski, M. Cypryk. Ch. 1: Synthesis of linear polysiloxanes. In: Silicon-Containing Polymers. The Science and Technology of Their Synthesis and Applications. 2000, Dordrecht: Kluwer Acad. Publ.
10. Y. Wu, H. Duan, Y. Yu, Ch. Zhang. Preparation and performance in paper coating of silicone-modified styrene–butyl acrylate copolymer latex. J. Appl. Polymer Sci., 2001, 79, 2, 333-336.
11. K. Mequanint, R. Sanderson. Self-assembling metal coatings from phosphated and siloxane-modified polyurethane dispersions: An analysis of the coating–air interface. J. Appl. Polymer Sci., 2003, 88, 4, 893-899.
12. R. Rodríguez, C. de las H. Alarcón, P. Ekanayake, P. J. mc Donald, J. L. Keddie, M. J. Barandiaran, J. M. Asua. Correlation of silicone incorporation into hybrid acrylic coatings with the resulting hydrophobic and thermal properties. Macromol., 2008, 41, 22, 8537-8546.
13. S. Sobhani, A. Jannesari*, S. Bastani. Effect of molecular weight and content of PDMS on morphology and properties of silicone-modified epoxy resin. J. Appl. Polymer Sci., 2012, 123, 1, 162-178.
14. B. Pilch–Pitera. Surface properties of polyurethane powder lacquers modified with polysiloxane–methacrylic core–shell nanoparticles. J. Appl. Polymer Sci., 2012, 123, 2, 807-814.
15. D. R. Weyenberg, D. E. Findlay, J. Cekada Jr., A. E. Bey. Anionic emulsion polymerization of siloxanes. J. Polymer Sci. C, 1969, 27, 1, 27-34.
16. J. Kozakiewicz, J. Skarżyński, W. Domanowski, A. Koncka–Foland, A. Grott. Sposób wytwarzania wodnych dyspersji polimerycznych nanocząstek typu "rdzeń–otoczka". Polish Patent # 210583, 2011.

POLYMERIC BIOCOMPOSITES WITH NANOCELLULOSE

A. Masek, M. Zaborski

Institute of Polymer and Dye Technology
Technical University of Lodz
Lodz, Poland
anna.masek@p.lodz.pl

Accepted September 19, 2013

1. Introduction

The use of elastomers is currently increasing. Environmentally friendly materials that rapidly decompose are being researched [1]. Traditional elastomers are cross-linked with peroxides or sulfur; therefore, they are not biodegradable [2]. New, environmentally friendly cross-linking agents need to be discovered. The presence of an oxirane ring in natural rubber allows for the use of different compounds for cross-linking, such as amines, acids, or anhydrides. These compounds can also be used for epoxide resins [3]. Similarly, the amine functional group, $–NH_2$, and the acidic carboxyl group, –COOH, in amino acids allow for a number of chemical reactions [2, 4]. Therefore, amino acids may actively promote cross-linking in elastomers that contain an oxirane group.

2. Materials and methods of experimental investigation

2.1. Chemicals

The materials used in this study were as follows: epoxidized natural rubber (ENR(50), Epoxyprene 50; manufacturer: Kumpulan Guthrie Berhad, Malaysia); Aerosil 380 silica (Degussa), which were used as fillers; and Arbocel ultrafine cellulose (UFC 100, Rettenmaier Polska Sp. z.o.o.), which were used as cross-linking agents along with the following new cross-linking agents (3 phr):

– L-lysine (≥ 98.0 %) – Fluka Chemie AG
– L-glutamine (99 %) – Aldrich Chemical Company
– L-glutamate (99 %) – Aldrich Chemical Company
– L-glycine (98 %) – Aldrich Chemical Company
– L-asparagine (≥ 99.0 %) – Fluka Chemie AG

2.2. Measurement methods

Rubber blends were prepared by means of a laboratory mixing mill with rolls of the following dimensions: length L = 330 mm, diameter D = 140 mm. The speed of rotation of the front roll was V_p = 20 rpm, friction 1.1, the average temperature of rolls was about 40 °C.

The vulcanization of rubber blends was carried out with the use of steel vulcanization molds placed between the shelves of electrically heated hydraulic press. A teflon film was used as spacers preventing the adherence of blends to the press plates. Samples were vulcanized at a temperature of 160 °C, under a pressure of 15 MPa for 30 min.

The density of crosslinks in the vulcanisates network was determined by the method of equilibrium swelling. The vulcanizates were subjected to equilibrium swelling in toluene for 48 h at room temperature. The swollen samples were then weighed on a torsion balance and dried in a dryer at a temperature of 60 °C to a constant weight and after 48 h they were reweighed. The cross-linking density was determined on the basis of Flory–Rehner's equation:

$$\theta_e = -\frac{\ln(1-V_r)+V_r+\mu V_r^2}{V_0\left(V_r^{1/3}-V_r/2\right)} \quad (1)$$

for the elastomer-solvent interactions amounting to $\mu = 0.238 + 0.786\ V_r$, where V_r is the volume fraction of the elastomer in the swollen gel.

The tensile strength of vulcanizates was tested according to standard PN–ISO 37:1998 by means of a ZWICK tester, model 1435, for dumbbell w–3.

3. Results and discussion

Amines promote the cross-linking of elastomers. It appears that silica can also influence the crosslinking reaction (**Table 1**). Silica increases the cross-linking density. Under these conditions, the elastomer most likely reacts with SiO_2, which is demonstrated by the increased decomposition rate of the lattice points proportional to the increase in the concentration of SiO_2, as observed in the infrared spectrum of the ENR mixture with silica before and after firing.

Table 1. Influence of amino acids on cross-link density of natural rubber ENR (50) vulcanisates.

Amino acids	ν_t, 10^{-5} mole / cm^3	$\Delta\nu_{NH_3}$, 10^{-5} mole / cm^3	$\Delta\nu_{NH_3} / \nu_t$, %
Lysine	7.22	0.61	8.45
Glutamine	7.90	1.90	12.66
Glutamine	13.29	3.51	26.41
Glutamate	15.39	1.40	9.09
Glycine	11.36	3.60	31.69
Asparagine	13.11	0.60	3.39

ν_t – cross-link density calculated with the use of the equilibrium swelling test in toluene.

$\Delta\nu_{NH_3}$, $\Delta\nu_{NH_3} / \nu_t$ – concentration and proportion of lattice points decomposing under the influence of ammonia vapours.

Optimal properties were obtained for the vulcanizate that contained 30 parts by weight of silica and cross-linked with glutamine (**Table 2**). The TS value was 6.20 MPa after elongation by 559 %.

Using amino acids to develop biodegradable polymers appears to be an interesting approach that allows vulcanizates to be obtained that contains easily hydrolyzed amide or ester bonds instead of sulfur bridges.

Table 2. Mechanical properties of natural rubber ENR(50) vulcanizates cross-linked using different amino acids.

Amino acids	SE_{100}, %	SE_{200}, %	SE_{300}, %	TSb, MPa	E_b, %
Lysine	0.51	0.73	1.04	2.40	514
Glutamine	0.55	0.68	0.78	1.06	497
Glutamine	1.66	2.31	3.20	6.20	559
Glutamate	2.36	3.31	4.21	5.40	493
Glycine	2.05	2.81	3.69	5.13	478
Asparagine	0.96	1.18	1.39	1.68	576

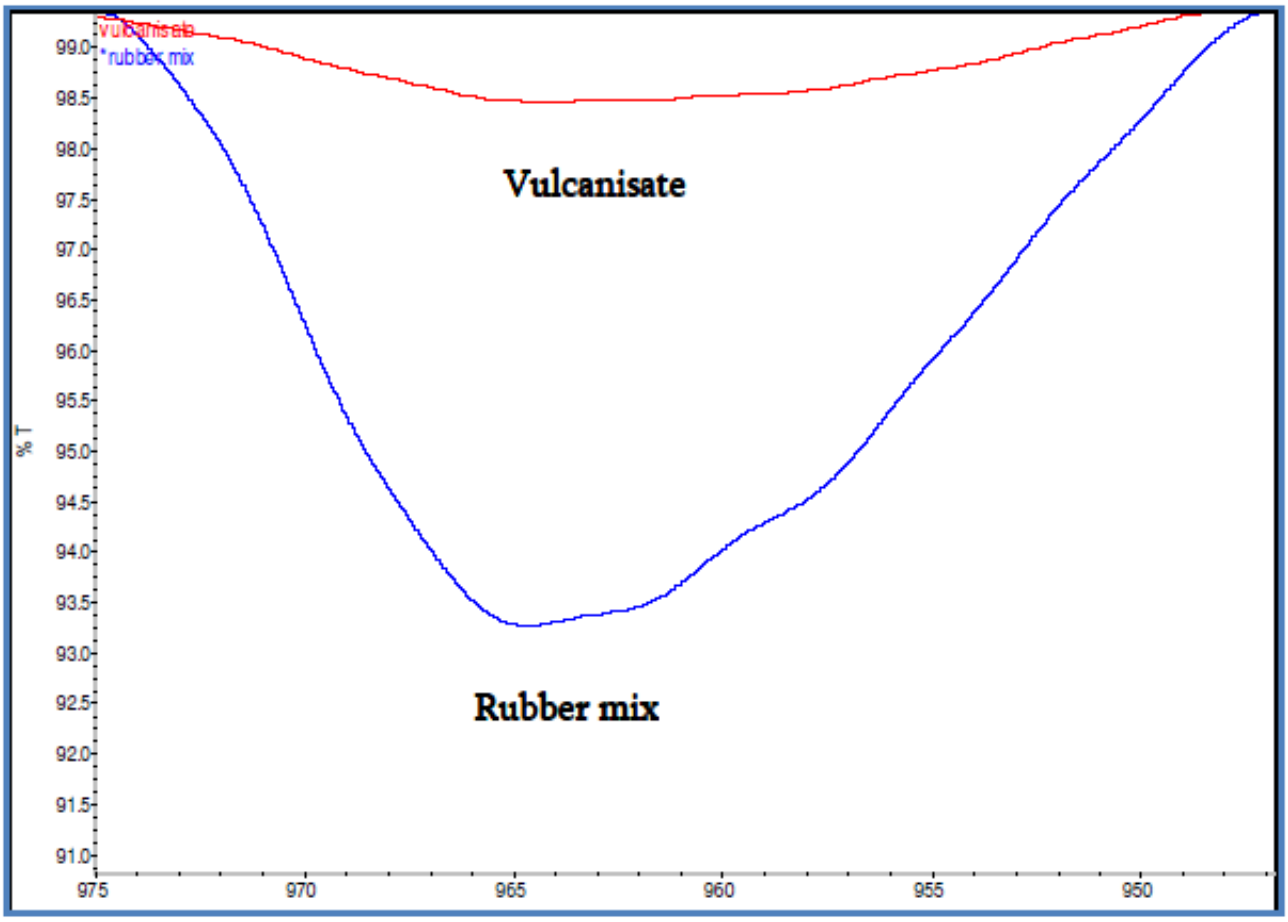

Figure 1. FT–IR spectrum of rubber and vulcanizate ENR(50) mixture.

The infrared spectrum of the ENR vulcanizate (**Figure 1**) exhibits an epoxy group band (~ 960 cm^{-1}) with decreased intensity compared to that of the unvulcanized ENR rubber mixture, which indicates that the OH groups from silica react with the epoxy groups present in ENR.

4. Conclusions

The investigated amino acids are appropriate cross-linking agents for epoxidized natural rubber (ENR). However, the vulcanizate properties are not satisfactory. The idea of using natural substances to cross-link elastomers is an entirely new and pro-ecological approach. Another approach may be to use mixtures of different amino acids, which may increase the probability of interaction with the elastomer. Further research of this issue will be conducted.

Acknowledgement

This study was supported by Ministry of Science of Higher Education: Project number IP 2011 03417.

References

1. U. Edlund, A.-C. Albertsson. Polyesters based on diacid monomers. Adv. Drug Deliv. Rev. 55 (2003) 586.
2. P. Matzinos, V. Tserki, A. Kontoyiannis, C. Panayiotou. Processing and characterization of starch / polycaprolactone products. Polym. Degrad. & Stab. 77 (2002) 17.
3. T. Semba, K. Kitagawa, U. S. Ishiaku, H. Hamada. The effect of crosslinking on the mechanical properties of polylactic acid / polycaprolactone blends. J. Appl. Polym. Sci. 101 (2006) 1816.
4. R. Wang, Sh. Wang, Y. Zhang, Ch. Wan, P. Ma. Toughening modification of PLLA / PBS blends via in situ compatibilization. Polym. Eng. & Sci. 49 (2009) 26-33.

INFLUENCE OF R AND R′ ALKYL GROUPS (– CH_3 OR – C_2H_5) ON THE PROPERTIES OF AEROGELS SYNTHESIZED FROM $RSi(OR')_3$ PRECURSORS

T. Matias [1], M. Ochoa [1, 2], A. Portugal [1], L. Durães [1]

[1] University of Coimbra
Coimbra, Portugal
luisa@eq.uc.pt
[2] Instituto Pedro Nunes
Coimbra, Portugal

Accepted September 19, 2013

1. Introduction

Sol–gel is one of the most important bottom-up strategies for synthesis of tailored nanostructured materials. It's being used for more than two centuries, but only in the eighties, the scientific and commercial interest in sol-gel technology gained a new moment with the generalized use of supercritical fluids to dry the gels (reported by Kistler already in 1932). In this way, highly porous and monolithic materials are generated and called aerogels [1, 2].

Sol–gel technology offers several advantages when compared to the traditional processing of ceramics, namely: i) high homogeneity and purity of the products, due to the use of controlled precursors and concentrations in liquid medium; ii) low processing temperatures, which enable energy savings, the reduction of crystallization and phase separation phenomena, and the possibility of combination of ceramics with organic materials; iii) chemical manipulation of the system at the molecular level from the sol stage, allowing the synthesis of new phases and / or materials with tailored shape and properties. In fact, when operating at this scale, small changes in the synthesis conditions can produce surprising modifications on the product properties. However, high sensitivity can also be a problem, since uncontrolled conditions / effects can lead to undesirable changes and to an increase in the variance of the product properties. Thus, it is crucial to know each chemical reacting system in detail in order to identify the most critical factors.

In general, the sol–gel technology involves at least three stages: preparation of a gel, ageing in the mother liquor and drying the gel. In the first stage, the precursor is diluted / dissolved in a solvent, and a sufficient amount of water equivalents is added to promote hydrolysis. Then, condensation reactions occur from hydrolyzed species, producing colloidal condensed entities – sol formation. The use of a catalyst favours polycondensation reactions and, consequently, the growth of a solid three-dimensional network of colloidal particles occurs resulting in a gel with the container shape – gelation process. The precursor, solvent and catalyst(s) can be mixed all in one pot or in separate moments if a fine control of each type of reaction is needed.

The ageing is normally used to increase the cohesion / strength of the solid network of the gel in order to prevent, as far as possible, cracks in the drying stage. This strengthening

occurs through the thickening of the cross-linking necks and the filling of small pores by further condensation and dissolution–reprecipitation mechanisms.

For the removal of the liquid that fills the pores of the solid structure of the gel, three main drying methods are used, as described below:

1) Ambient Pressure Drying (APD) – The solvent is evaporated (evaporative drying) at ambient pressure by promoting the crossing of the liquid-gas equilibrium line, i.e. heating the gel up to the evaporation temperature of the solvent. In this case, and if the liquid wets the solid, pore collapse and shrinkage of the solid network usually occurs due to capillary stresses that develop in the smaller pores during the evaporation process. The produced materials are called xerogels and are denser than aerogels.
2) Supercritical Fluids Drying (SFD) – The liquid is removed from the solid network in supercritical conditions, bypassing the critical point. Since there are no liquid–gas interfaces (menisci), the surface tensions typical of the evaporative drying are avoided as well as the shrinkage of the structure. The resulting materials, named aerogels, are highly porous and lightweight materials. There is the option to bring the solvent to a supercritical state, which is a methodology denominated by High Temperature Supercritical Drying, since it requires temperatures above the critical temperature of the solvent, normally between 200 and 300 °C for the simplest alcohols; alternatively, the solvent may be removed / extracted in cold conditions (40 – 50 °C), by dissolving it in a flow of supercritical CO_2, being this methodology designated by Low Temperature Supercritical Drying.
3) Freeze Drying (FD) – The triple point is bypassed by using negative temperatures to freeze the liquid inside the gel and then conditions for sublimation of the frozen liquid. This type of drying also prevents the formation of the liquid–vapour interfaces, however its use is limited to solvents where the triple point is easy to reach, for example water, and has not yet proved to produce good monoliths. The materials dried with this method are called cryogels.

Although the chemical structure of the material does not change significantly after the ageing, the drying stage is of crucial importance to keep the porous structure of the gel in the final material. Concerning this point, the supercritical fluids drying is the best option to produce highly porous and monolithic material. However, it requires expensive, complex and hazardous equipment.

The reactions rates in the gel preparation are particularly dependent on pH, concentrations of the intervenient compounds and temperature, and these factors are often used to control the process and the product properties. In the case of sol-gel chemistry of Si alkoxides, as the silicon has low positive partial charge, the global gelation kinetics is very slow, and the hydrolysis and condensation reactions can be catalysed separately by acids and bases respectively (two-step catalysed sol–gel chemistry), allowing a better control of the process; in addition, since the Si forms bonds 50 % covalent – 50 % ionic, a wide distribution of the bond angles in the group Si–O–Si is possible and, consequently, the produced solid networks may be branched and random, which facilitates the formation of monoliths [3].

The tetramethyl and tetraethyl orthosilicates (TMOS and TEOS) are the most studied Si alkoxide precursors. The obtained silica native aerogels, although highly porous (bulk density of 100 – 350 kg m^{-3}; specific surface area of 500 – 1000 $m^2 g^{-1}$) and transparent, are very brittle (rigid) and hydrophilic, which lead to their extensive deterioration when subjected to handling

and environmental moisture [4, 5]. The presence of a non-hydrolysable alkyl group in trialkoxysilanes solves the referred degradation problem, since it remains in the 3D-solid network of the aerogels (**Figure 1**) conferring them hydrophobicity. The R group, in the case of one methyl moiety, causes a decrease on the degree of the cross linking and an increase of the degree of disorder in the structure (**Figure 1**), giving more porosity and flexibility to the material [6, 7]. Although, the type of R and R′ groups of $RSi(OR')_3$ precursors influence the rates of hydrolysis and condensation reactions, the growth of the inorganic solid network, the microstructure and the physical properties of the final materials, and other reactions may appear such as reesterification, depolymerisation and transesterification, due to the presence of all the compounds in solution [8].

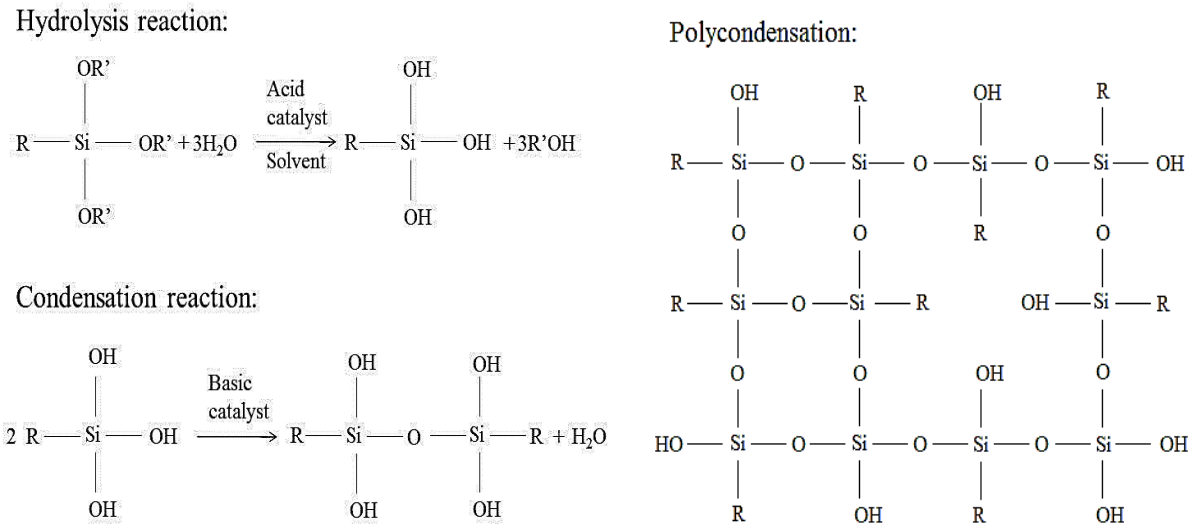

Figure 1. Sol–gel reactions for $RSi(OR')_3$ precursors (R, R′ = CH_3 or CH_2CH_3).

In this work, the literature information about organically modified silica aerogels/xerogels prepared from $RSi(OR')_3$ precursors, focusing on R, R′ = methyl and ethyl, is summarized, in order to draw conclusions about the effect of changing R and R′ groups on the sol–gel synthesis process and product properties. In addition, our own results were added to be compared and discussed along with the ones in the literature.

2. Experimental

MTMS ($CH_3Si(OCH_3)_3$, 98 %, Aldrich), ETMS ($CH_3CH_2Si(OCH_3)_3$, 97 %, Aldrich), MTES ($CH_3Si(OCH_2CH_3)_3$, 99 %, Aldrich), ETES ($CH_3CH_2Si(OCH_2CH_3)_3$, 97 %, Fluka) were used as precursors, preferentially alone, but in some cases the addition of TMOS ($Si(OCH_3)_4$, 98 %, Fluka) or TEOS ($Si(OCH_2CH_3)_4$, 98 %, Aldrich) was necessary to promote the gelation. Methanol (MeOH; CH_3OH, 99.8 %, Aldrich) and ethanol (EtOH; CH_3CH_2OH, Fisher Scientific) were used as solvents. Oxalic acid ($C_2H_2O_4$, 99 %, Fluka) and ammonium hydroxide (NH_4OH, 25 % in water, Fluka) were the acid and basic catalysts, respectively, in the form of aqueous solutions.

The organically modified silica aerogels and xerogels were prepared from the trialkoxysilanes following the two-step acid-base catalysed sol–gel synthesis, ageing and drying procedures already described in an earlier work for MTMS [9] (see drying conditions for aero-b

and xero-a samples for reference). The general methodology starts with the mixing of the precursor, solvent and the acid catalyst solution – hydrolysis step. After one day, the basic catalyst solution is added to promote condensation of the hydrolysed species – gelation step. The obtained gels are aged for two days at 27 °C, and then dried in supercritical conditions of the methanol in an autoclave (260 °C, 100 bar), to obtain aerogels, or in an oven at ambient pressure with several temperature steps (60, 100, 150 and 200 °C), to produce xerogels. More specific synthesis conditions will be presented in the next section along with the introduction of results. The chemical, physical and structural properties of the resultant materials were evaluated using the techniques and procedures described below.

1 – Fourier transform infrared spectroscopy (FT / IR–4200, Jasco) – The samples were milled and mixed with KBr in a mass ratio of 1 : 200 and the resultant mixtures were pressed to obtain thin circular pellets. A wave number range of 400 – 4000 cm^{-1} was used to collect the spectra for analysis of chemical structure.

2 – Contact angle technique (OCA 20, Dataphysics) – Water drops were dropped on a flat surface of the sample. The angle between the baseline and a tangent to the drop contour at the three phase point (solid–liquid–gas) was evaluated (wetting angle) to assess the hydrophobicity of the samples.

3 – Bulk density measurement – The weight and size of regular pieces of material were measured accurately to calculate the bulk density.

4 – He picnometry (Accupyc 1330, Micromeritics) – This pycnometer was used to measure the skeletal density of the samples and, by combining this information with the bulk density, the porosity of the samples was evaluated.

5 – N_2 gas adsorption (ASAP 2000, Micromeritics) – The specific surface area and the pore size distribution of the materials were assessed, applying the BET and BJH-desorption models, respectively, to data of adsorption-desorption isotherms.

6 – Scanning electron microscopy (JMS–5310, JOEL) – The microstructure of the materials was observed by SEM. Due to the low electrical conductivity of the samples, an Au film was deposited on their surface, using the physical vapour deposition technique during 20 s.

7 – Thermal constants measurement (thermal constants analyzer TPS 2500 S, hot disk) – The analyses of the thermal conductivity of the samples were carried out at 20 °C. The used equipment has reproducibility better than 1 % and accuracy better than 5 %.

8 – Compression test (AG 100 kN, Shimadzu) – The flexible materials were submitted to uniaxial compression, being the load and the sample length simultaneously measured. The Young's modulus was evaluated from the slope of the linear fit in the elastic region.

3. Synthesis and properties of Polysilsesquioxanes obtained from trialkoxysilanes: Literature and authors results

3.1. Methyltrimethoxysilane – MTMS

Methyltrimethoxysilane is the most common precursor from the four studied in this work, since it allows the production of aerogels / xerogels with fascinating properties in terms of flexibility, density and hydrophobicity. Bhagat et al., Durães et al., Hegde et al., Nadargi et al.

and Rao et al. [6, 7, 9, 10 – 17] prepared xerogels and aerogels using the MTMS precursor and a procedure similar to that described in Section 2.

In general, the MTMS / MeOH / H_2O molar ratios that provide lower densities and good monolithicity were 1 : 35 : 8, excepted in an old work [10], where the optimal properties were obtained for MTMS : MeOH : H_2O : NH_4OH molar ratios of 1 : 14 : 4 : $1.7 \cdot 10^{-1}$, and in [11], where the used MTMS : MeOH : acid H_2O : basic H_2O molar ratios were 1 : 35 : 6.25 : 6.25. The properties obtained for the best xerogels and aerogels of each work are presented in **Table 1**. In current work, we used MTMS : MeOH : acid H_2O : basic H_2O molar ratios of 1 : 35 : 4 : 4, and the concentrations of the basic and acid catalysts solutions were 0.01 and 10 M, respectively.

Table 1. Properties of aerogels and xerogels obtained from MTMS.

Source	Density, kg m^{-3}	Porosity, %	Surface area, m^2 g^{-1}	Pore size, Å	Thermal conductivity, W m^{-1} K^{-1}	Contact angle, °	Young's modulus, Pa
Aerogels							
[10]	120	–	–	–	0.086	159	–
[6]	40	–	–	–	0.057	164	$3.0 \cdot 10^4$
[12]	37	98	–	–	0.057	149	$1.1 \cdot 10^4$
[11]	51	97	–	–	0.057	160	–
[13]	55	–	363 ± 7	30	–	135	–
[14 – 16]	42	99	–	–	0.057	–	–
[17]	103 ± 14	92	412 ± 7	34	–	151 ± 4	–
[18]	220	–	623	30	–	–	–
[9]	54 ± 6	95	512 ± 11	44	–	147 ± 3	–
Current work	50 ± 3	97	271 ± 6	37	0.036	149 ± 2	$5.2 \cdot 10^3$
Xerogels							
[7]	62	–	520	45	–	152	–
[13]	80	–	386 ± 7	32	–	141	–
[17]	88 ± 5	93	409 ± 10	38	–	148 ± 2	–
[9]	78 ± 11	93	427 ± 11	36	–	136 ± 5	–
Current work	80 ± 2	93	579 ± 14	24	0.040	146 ± 2	$2.9 \cdot 10^4$

MTMS was also combined with the surfactant pluronic F127 to obtain aerogels and xerogels with controlled pores morphology, as studied by Kanamori et al. [18] – see **Table 1**. In their synthesis procedure, diluted acetic acid, urea and F127 (0 – 1 g) were mixed and, then, the MTMS precursor was added. The resultant mixture was placed in a closed vessel and aged in an oven at 60 °C. After 5 days of condensation / ageing, the gels were washed with methanol (3 ×), to remove the surfactant and unreacted species. Finally, the gels were dried by supercritical fluids extraction with CO_2 at 80 °C and 140 bar. Higher shrinkage and densities were observed for small quantities of F127, because of a pronounced phase separation due to the occurrence of local condensations even after gelation. For 0.4 g of F127 the phase separation was significantly reduced and macropores became smaller. In fact, the morphology of the pores became finer with an increasing of F127 amount, making the aerogels move from opaque to transparent above 0.6 g of the F127. The macropores formation and the size / volume of the mesopores can

be controlled by the F127 concentration, but the mesopores characteristics were mainly defined by the amount of solvent.

The obtained materials have very promising properties for super thermal and acoustic insulation, and can particularly be used in space applications [13, 17], due to their very low density and thermal conductivity, and high contact angle, surface area and porosity. These aerogels / xerogels are also highly flexible.

Comparing the aerogels properties with those of xerogels, it is observed that the seconds present only slightly inferior properties but their production requires less complex and hazardous drying technology, as already concluded in [9]. This is due to the highly hydrophobic nature of the solid network of these gels, which minimizes the capillary stresses and originates the known spring-back effect during evaporative drying of the alcoholic solvent, making possible to produce aerogel-like materials [2].

3.2. Ethyltrimethoxysilane – ETMS

The ETMS precursor was used in sol–gel works in an attempt to synthesize organically modified silica materials with suitable properties for certain applications, namely for insulators, catalyst supports, molecular separation membranes, dielectric or optical materials and sensors [19 – 21]. These literature works are summarized below.

Ochoa et al. [21] tested ETMS alone and in combination with MTMS using a ETMS / MeOH molar ratio of 20 to obtain xerogels. The used procedure was similar to that described in Section 2. When ETMS was used alone and in equimolar ETMS / MTMS mixtures, no gel formation took place, due to phase segregation, and a resin-like precipitate was obtained leading to compact tablets after drying. For these materials, the obtained densities were high, and the specific surface areas were very low (**Table 2**). For higher amounts of MTMS in the system, the properties of the obtained materials were closer to those indicated in the last section for xerogels synthesized from MTMS, and a good hydrophobic behaviour was achieved (**Table 2**). It was concluded that ETMS contributes to a preferential growth of the solid structure in one direction, resulting in a packed and organized structure. Thus, the ETMS precursor was not considered appropriate for the production of xerogels for space thermal insulation purposes; however, when used with MTMS, materials with very high contact angles could be obtained.

In this work, a similar study to the one conducted by Ochoa et al. [21] was performed, but with TMOS co-precursor. The silanes : MeOH : H_2O molar ratio were 1 : 12 : 6. Interesting results were obtained when a mixture of 50 % of ETMS and 50 % of TMOS was used, since the resulting material was monolithic and presented high surface area. However, the density was very high and the xerogel very rigid (**Table 2**).

Harreld et al. [20] and Anderson et al. [22] also combined ETMS with TMOS to synthesize hydrophobic aerogels. Anderson et al. [22] synthesized the gels using a one step experimental procedure (basic) and the drying process consisted in a new method called RSCE (rapid supercritical extraction). For the synthesis, the silanes : MeOH : H_2O : NH_4OH molar ratios were 1 : 12 : 4 : $7.4 \cdot 10^{-3}$. Through this drying method, they could obtain aerogels from TMOS / ETMS precursors with very low density, high porosity, low thermal conductivity and high contact angle – **Table 2**. The used method allowed the fabrication of aerogels in 7 – 15 h, much faster than with conventional methods, where the required time for gelation / ageing / drying is normally 4 – 5 days.

Harreld et al. [20] synthesized organically modified silica gels and washed them with various solvents – *n*-pentane, acetone, acetone / *n*-pentane, hexanes, ethanol, *n*-propanol, *n*-butanol and *n*-pentanol, in order to control the capillary stresses and limit the shrinkage during the evaporative drying. In the synthesis, the used silanes : H_2O : HCl molar ratios were $1 : 2 : 4.5 \cdot 10^{-6}$ and the pH was increased to 6.5 by the addition of a methanol-buffer solution (80 % methanol and 20 % sodium acetate / acetic acid). After gelation, the gel was aged during one week and subsequently washed with a solvent, through three washing cycles, to remove water, alcohol and unreacted silanols. After the solvent exchange, the gels were dried in ambient air but limiting the solvent evaporation rate by an aperture. Thus, the average pore size of the xerogels could be modified through drying with *n*-alcohols with various alkyl-lengths (2 – 5 carbons). Also, the pore size distributions could be controlled by using mixtures of *n*-alkanes and acetone. The xerogels synthesized from 60 % TMOS and 40 % ETMS and dried with *n*-pentane had the largest specific surface area – 830 $m^2 g^{-1}$, but no other properties were reported.

Table 2. Properties of aerogels and xerogels obtained from ETMS.

Source	Molar % of precursor(s)	Density, kg m^{-3}	Porosity, %	Thermal conductivity, W m^{-1} K^{-1}	Contact Angle (°)
Aerogels					
[22]	75 % TMOS and 25 % ETMS	68	96	0.031	151
	50 % TMOS and 50 % ETMS	64	96	0.034	153
Xerogels					
Source	Molar % of precursor(s)	Density kg m^{-3}	Surface area, m^2 g^{-1}	Pore size, Å	Contact angle, °
[21]	100 % ETMS	794 – 1089	1.7 ± 0.1	43	126 ± 4
	50 % ETMS and 50 % MTMS	46 – 870	2.9 ± 0.3	45	140 ± 4
	25 % ETMS and 75 % MTMS	104 – 234	21.2 ± 1.1	20	142 ± 5
	100 % MTMS	89 – 125	416 ± 9.0	42	129 ± 2
Current work	50 % ETMS and 50 % TMOS	1318.0	628.8 ± 6.2	24	–

Newalker et al. [19] also used the co-precursor approach to produce organically modified silica xerogels, with high surface area, from ETMS, but combining this precursor with sodium silicate. The experimental procedure consisted in two-steps and several solvents were tested, like acetone, acetonitrile, ethanol and methanol. Acetone and acetonitrile solvents led to higher specific surface areas (357 and 691 $m^2 g^{-1}$, respectively) and increased the microporosity and, on the other hand, methanol and ethanol solvents led to improved hydrophobicity of the xerogels.

3.3. Methyltriethoxysilane – MTES

The early stage of the hydrolysis of the MTES precursor was studied by Brunet [23] through ^{29}Si NMR. To prepare the samples, the MTES was dissolved in ethanol and, then, an HCl solution was added to the mixture to catalyse the reaction. It was concluded that the hydrolysis rate is dependent on the water amount and the H^+ concentration. With a substoichiometric H_2O / Si ratio, the hydrolysis was incomplete and the condensation was slow.

When the water was in excess, the hydrolysis was faster and complete and the condensation started earlier.

The rates of the hydrolysis and condensation of MTES were studied by FTIR, for acid and alkaline conditions, by Jiang et al. [24, 25]. In the preparation of the samples, several solvents were used, namely methanol, ethanol, 1,4-dioxane (DOX), dimetilformamide (DMF) and acetone, and different temperatures were tested. When the system was acid-catalysed, for high temperature values (36 – 52 °C), the hydrolysis rate of MTES was higher and similar for methanol, ethanol and DOX solvents. With DMF, the hydrolysis rate was very low when compared with the obtained for the other solvents. When the system was base-catalysed, the condensation rate was very high, being the hydrolysis the rate-limiting step of the overall reaction.

Nadargi et al. [14 – 16] produced organically modified silica aerogels using MTES as precursor. They studied several molar ratios of methanol / MTES (6.5 – 19.4) and H_2O / MTES (0.7 – 6.4), and different molarities of the oxalic acid (0.0001 – 1 M) and ammonium hydroxide (2 – 13.4 M) solutions. The aerogels were synthesized by an experimental procedure similar to the one described in Section 2. More flexible, hydrophobic and less dense aerogels were obtained for MTES / MeOH / H_2O molar ratios of 1 : 19.4 : 3.6 and two days of ageing. The properties of the materials obtained in these conditions are presented in **Table 3**.

Table 3. Properties of aerogels and xerogels obtained from MTES.

Source	Density, kg m^{-3}	Porosity, %	Surface area, m^2 g^{-1}	Pore size, Å	Thermal conductivity, W m^{-1} K^{-1}	Contact angle, °	Young's modulus, Pa
Aerogels							
[14]	50	–	–	–	–	141	$3.95 \cdot 10^4$
[15, 16]	52	97	–	–	0.056	150	–
[17]	101 ± 3	92	362 ± 20	27	–	145 ± 2	–
Current work	49 ± 4	97	245 ± 7	45	0.035	147 ± 8	–
Xerogels							
[26]	120	95	727	80	–	–	–
[17]	151 ± 12	87	41 ± 1	33	–	155 ± 5	–
Current work	104 ± 8	94	449 ± 6	37	0.040	154 ± 5	$1.82 \cdot 10^4$

Durães et al. [17] also synthesized aerogels and xerogels with MTES, but tested a different solvent, ethanol, besides methanol. The aerogels / xerogels obtained with ethanol exhibited higher densities (304 – 429 kg m^{-3}), lower surface areas (113 – 191 m^2 g^{-1}), high contact angles (140 – 141 °) and low porosities (67 – 76 %) when compared with the aerogels / xerogels synthesized with methanol. It was concluded that ethanol was not an appropriate solvent for the synthesis of insulation materials for space. On the other hand, when methanol was used with MTES (MTES : MeOH : H_2O = 1 : 35 : 8; acid catalyst concentration = 0.001 M; basic catalyst concentration = 10 M), the resulting materials presented interesting properties for space applications. The results obtained for methanol are presented in **Table 3**.

In this work, aerogels and xerogels with globally better properties than those found in the works described in the literature were obtained by the procedure described in Section 2.

The MTES : MeOH : H_2O molar ratios were 1 : 35 : 8, and the acid and base catalysts concentrations were equal to 0.1 and 10 M, respectively. Their properties are shown in **Table 3**.

Aravind & Soraru [26] synthesized xerogels using MTES as precursor, isopropanol as solvent (solvent / MTES = 80 %), HCl (3 M) as the acid catalyst and NH_4OH (13.4 M) as basic catalyst. The MTES was diluted in methanol and the acid solution was added under stirring. After 1 h of hydrolysis, the basic solution was added, while stirring. The resulting solution was placed in an oven at 50 °C for gelation and ageing during 7 days, the solvent being exchanged with isopropanol three times each 24 h. The gels were slowly dried, during 15 days, at ambient pressure and 50 °C.

The aerogels / xerogels obtained from MTES have low density and thermal conductivity and high contact angle, surface area and porosity, which make them very good thermal and acoustic insulators. The observed differences in the properties of aerogels and xerogels are higher in this case than for the case of the gels made from MTMS.

3.4. Ethyltriethoxysilane – ETES

The ETES precursor has also been used for synthesis of hydrophobic organically modified silica aerogels, but always using TEOS in the chemical processing stage to compensate, in some way, for the low hydrolysis and condensation rates of ETES.

The works found with ETES are all from Rao and co-workers [4, 11. In 2004, Rao et al. used two different methods to synthesize the gels: co-precursor and derivatization methods. In the co-precursor method, the experimental procedure was the same as described in Section 2 and the TEOS : ETES : EtOH : acid H_2O molar ratios were 1 : 0.1 – 0.6 : 5 : 7. The concentration of the oxalic acid solution was 0.001 M. In the derivatization method, ETES was added only after gelation. The sols were transferred to circular moulds and, after gelation, the formed gels were carefully removed from the moulds and kept 24 h in a chemical bath containing 20 % (vol.) of ETES in methanol, at 45 °C in an oven. This bath was then exchanged by pure ethanol for three times in intervals of 6 h, at the same temperature, to remove the unreacted ETES, water or catalyst. The aerogels obtained with the co-precursor method had a contact angle of 128 ° and their hydrophobicity could be maintained up to 309 °C. When the derivatization method was used, the contact angle was 120 ° and the hydrophobicity could be maintained up to 282 °C. In addition, the aerogels produced using the co-precursor method were less transparent than the derivatized aerogels, since the latter did not undergo any structural changes.

The impermeability of organically modified silica aerogels was studied by Rao et al. [11], in 2007, using several precursors (MTMS, TEOS with ETES, and PTMS), solvents (methanol, ethanol and acetone) and acid catalysts (hydrochloric acid, nitric acid, oxalic acid and sulphuric acid). This study was motivated by the potential use of these aerogels as coatings for anticorrosive applications on metallic surfaces and for protection of sculptures and statues, preventing their deterioration. Rao et al. prepared the aerogels by a two-step sol–gel process similar to the one described in Section 2, with TEOS : MeOH : ETES : acid H_2O : basic H_2O molar ratios equal to 1 : 33 : 1 : 6.25 : 6.25, and acid and basic catalysts solutions concentrations of 0.001 and 1 M, respectively. The obtained results for the sample composed by 50 % ETMS and 50 % TEOS are presented in **Table 4**.

Table 4. Properties of aerogels and xerogels obtained from ETES and TEOS.

Source / Sample composition	Density, kg m^{-3}	Porosity, %	Surface area, m^2 g^{-1}	Pore size, Å	Thermal conductivity, W m^{-1} K^{-1}	Contact angle, °
Aerogels						
[11]	148	93	–	–	0.073	151
Current work – MeOH (50 % ETES and 50 % TEOS)	213	89	744 ± 8	51	–	–
Current work – EtOH (33 % ETES and 67 % TEOS)	209	88	808 ± 8	75	–	–
Xerogels						
25 % ETES and 75 % MTMS	109 ± 11	81	13 ± 0.4	154	0.0441	142 ± 4

In the current work, the precursor ETES was also studied. It was combined with TEOS and MTMS precursors. The adopted synthesis procedure is described in Section 2. For the TEOS / ETES system, when the used solvent was methanol, the silanes : solvent : H_2O molar ratios were 1 : 33 : 7, whereas for ethanol these ratios were equal to 1 : 5 : 7; the concentrations of the acid and basic catalysts solutions for both cases were 0.001 and 1 M, respectively. The drying of the samples composed by TEOS / ETES was performed by two different methods, ambient pressure drying (APD) and supercritical fluid drying (SFD). In all cases, no monolithic structures were obtained, what somehow limited the materials characterization. The obtained results for SFD are presented in **Table 4**. For APD, the densities were very high: 702 and 1140 kg m^{-3} when methanol and ethanol were used, respectively. When SFD was applied, the densities decreased drastically to ≈ 210 kg m^{-3}, independently of the solvent used (**Table 4**). Despite of the relatively high densities for aerogels, these materials presented a very high specific surface area (740 – 810 m^2 g^{-1}) and porosity (88 – 89 %), making them potential good adsorbents.

In the combination ETES / MTMS, several synthesis conditions were tested, namely two different molar percentages of MTMS precursor, 50 and 75 %, two silanes / MeOH molar ratios, 20 and 35, and two acid catalyst concentrations, 0.1 and 0.01 M. These materials were synthesized and dried at ambient pressure by the procedures described in Section 2. Gel formation occurred when only 25 % of ETES was used, similarly to what happened for the ETMS precursor. In **Table 4**, the best results in terms of monolithicity and low shrinkage are presented. They were obtained with silanes : MeOH : H_2O molar ratios of 1 : 20 :8 and the acid and basic catalysts solutions concentrations of 0.01 and 10 M, respectively. With the same precursor / solvent molar ratio, but with an acid concentration of 0.1 M, the obtained material had a monolithic structure but was denser (150 kg m^{-3}). When the used precursor / solvent molar ratio was 35, the gelation did not occur in the overall volume of the solution.

From **Table 4** it is clear that MTMS is a better co-precursor than TEOS to be used with ETES, if the density and thermal conductivity must be kept low, but the specific surface area obtained with MTMS / ETES system is very low.

3.5. Chemical and microstructural characteristics of aerogels / xerogels obtained from the studied $RSi(OR')_3$ precursors

In this section, a comparison between the physicochemical structure of the aerogels / xerogels obtained from MTMS, ETMS, MTES and ETES is done in **Figures 2 – 4**, but only based on results obtained in our work, in order to keep synthesis / drying conditions similar. However, even with the materials synthesized in the current work, the conditions to achieve gelation are very dependent on the chemical system. The main synthesis / drying conditions applied for the materials used in this comparison and the designation of the samples are as follows:

i) MTMS–aerogel (synthesis MTMS : MeOH : H_2O = 1 : 35 : 8, [$C_2H_2O_4$] = 0.01 M, [NH_4OH] = 10 M; gelation 5 h; drying SFD);

ii) ETMS / TMOS–xerogel (synthesis ETMS / TMOS = 1, silanes : MeOH : H_2O = 1 : 12 : 6, [HCl] = 0.2 M, [NH_4OH] = 0.5 M; gelation 5 h; drying APD); in the current work, only xerogels were produced for the system ETMS / TMOS, so in this case we used a xerogel for comparison;

iii) MTES–aerogel (synthesis MTES : MeOH : H_2O = 1 : 35 : 8, [$C_2H_2O_4$] = 0.1 M, [NH_4OH] = 10 M; gelation 8 h; drying SFD);

iv) ETES / TEOS–aerogel (synthesis ETES / TEOS = 1, silanes: MeOH : H_2O = 1 : 33 : 7, [$C_2H_2O_4$] = 0.001 M, [NH_4OH] = 1 M; gelation 8 h; drying SFD).

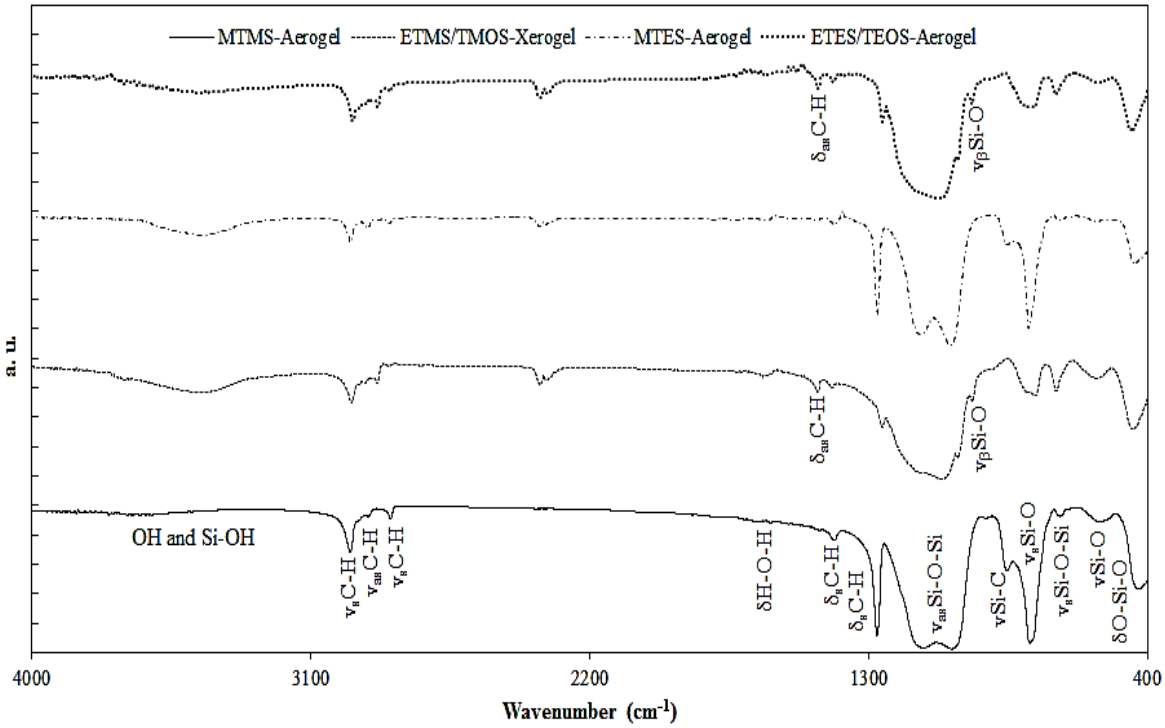

Figure 2. FTIR spectra for the materials obtained with MTMS, ETMS, MTES and ETES (ν stretching vibration, ν_s symmetric stretching vibration, ν_{as}, antisymmetric stretching vibration, δ deformation vibration, δ_s symmetric deformation vibration, δ_{as} antisymmetric deformation vibration (bending), ν_β, in plane-stretching vibration).

The chemical structure of all materials is composed by a solid network of organically modified silica (see **Figure 1**), with Si–O–Si bonds, and organic groups – CH_3 (from MTMS and MTES) and – CH_2CH_3 (from ETMS and ETES) linked to each Si, giving hydrophobic materials. The MTMS and MTES FTIR spectra are very similar (**Figure 2**), as expected, since the final

structure of these materials is the same. The main difference for the MTMS and MTES precursors stems from the fact that in the hydrolysis reaction, methanol is released in the case of MTMS and ethanol when MTES is used. However, the solvent is absent from the final product and this difference does not show in the spectra. Comparing the FTIR spectra of the systems obtained from ETMS and ETES, they are also very similar (**Figure 2**), for the same reasons. However, when the spectra of MTMS and MTES-derived aerogels are compared with the ETMS / TMOS and ETES / TEOS-derived materials, the bands due to antisymmetric stretching vibration of C–H (ν_{as} C–H) in CH_2 groups appear more in the later between 2900 and 2950 cm^{-1} and not only in the range 2850 – 2900 cm^{-1}. This stretching vibration is also visible at ~ 1400 cm^{-1} in the systems with ETMS and ETES.

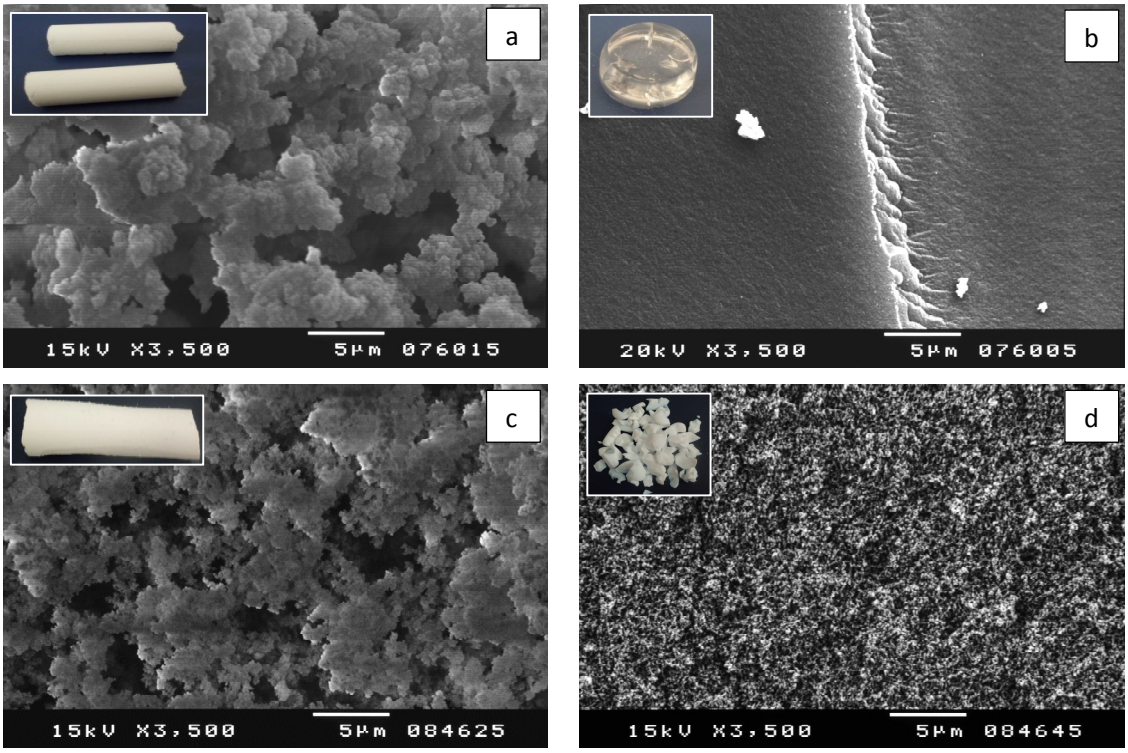

Figure 3. SEM micrographs and typical aspect (insets) of the materials synthesized in the current work: a) MTMS-derived aerogel, b) xerogel obtained from 50 % ETMS and 50 % TMOS, c) MTES-derived aerogel and d) aerogel obtained from 50 % ETES and 50 % TEOS using MeOH as solvent.

In **Figure 3**, the aspect (figure insets) and the microstructure of the materials obtained with MTMS, ETMS, MTES and ETES precursors can be observed. The MTMS and MTES-derived aerogels are similar. These materials are composed by a very open and random three-dimensional network, with pores in all size ranges, which is consistent with their low values of density (50 kg m^{-3}) and high porosity (97 %). The structural units (primary particles) of these two aerogels are very small, with a size much less than 1 µm. ETMS and ETES precursors generate materials with closed, organized and homogeneous structure, without large pores and with very small structural units. This is very clear in the case of xerogels (**Figure 3b**) and not so much in the case of aerogels (**Figure 3d**), as expected due to pore collapse during APD. This is also in line with the higher density and brittleness that these materials exhibit when compared to the MTMS and MTES-derived aerogels (see **Tables 1 – 4**).

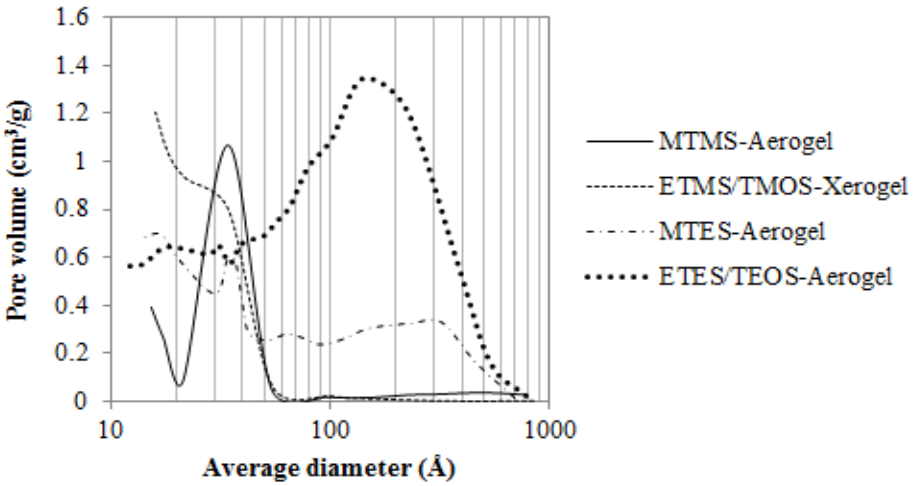

Figure 4. Pore size distributions of materials obtained from MTMS, ETMS, MTES and ETES.

The pores sizes of all materials are broadly in between 2 and 50 nm – mesopores, except for the ETMS / TMOS-derived xerogel, where a large quantity of pores are below 2 nm, i.e. micropores (**Figure 4**). Accordingly, the obtained isotherms for all the materials are of type IV, typical of mesoporous materials. The pore structures of the MTES and ETES / TEOS-derived aerogels display a wider distribution of mesopores than the MTMS-derived aerogel, presenting a multimodal profile that is typical of less homogeneous gelation medium.

4. Discussion

The effect of the R' alkoxy group (methoxy or ethoxy) in the gelation process and on the properties of the final materials can be analysed based on MTMS and MTES-derived aerogels, as the R derivative group has a much higher effect that can mask the R′ effect.

From data given for the synthesis details in the last section, it is notorious that the ethoxy group leads to higher gelation time than the methoxy group (8 h with MTES versus 5 h for MTMS). This retardation is due to slow hydrolysis and condensation reactions, which can be explained by the steric effect caused by a larger alkoxy group [1, 27], but also by the release of ethanol in the process. The effect on gelation of having ethanol as a solvent instead of methanol was already discussed in [17]. In the current work, the solvent chosen for the comparisons was always methanol, but some amount of ethanol is released during the hydrolysis in the case of MTES. Thus, the overall reactions rate will decrease slightly in the presence of some ethanol, and this can have several causes, namely: i) the lower charge activity of the catalysts, caused by the smaller dielectric constant of ethanol; ii) the higher steric effects and more complex hydrogen bonding structures with water and silicic acid, which decrease the mobility of the species [17].

However, as the condensation pursues in a basic medium and there are not so significant retardation effects due to low concentration of ethanol, condensation reactions still occur faster than the hydrolysis reactions and the produced polymers are very ramified. Therefore, apparently, the change of the alkoxy group between methoxy and ethoxy groups does not cause a marked change in the macroscopic properties of the obtained aerogels, but produces some changes in the properties of the xerogels, possibly due to the more significant capillary stresses

that develop in the presence of a longer chain alcohol. This explains why the xerogels and aerogels obtained with MTES have not so close densities as in the case of MTMS. The change operated in the alkoxy group seems to have also an effect in the pore size distributions, giving more heterogeneity in the pore structure when the ethoxy goup is used.

Regarding the effect of the R derivative group (methyl or ethyl), it is stated by Loy et al. [28] that, during the sol stage, the length and weight of this group promotes the phase separation of the Si species from the less dense alcoholic phase, forming oily or resinous oligomers in the bottom of the container. When this separation occurs, as already discussed in [21], the condensation does not occur in the overall volume of the solution due to the concentration of the hydrolysed species in the bottom of the container, which leads to localized polycondensation and formation of an oil or a resin-like phase that originates a compact material after drying. This phase separation was observed in the current work for ETMS and ETES precursors when not combined with TMOS, TEOS or MTMS. The addition of tetraalkylorthosilicates allows the quick formation of silanols in the medium and the starting of the condensation reaction, entrapping the hydrolysed ETMS and ETES species and preventing their sedimentation / segregation.

5. Conclusions

MTMS and MTES precursors lead to aerogels with high contact angle (140 – 165 °), porosity (97 – 99 %) and surface area (~ 300 – 500 $m^2 g^{-1}$), and very low density (37 – 55 kg m^{-3}) and thermal conductivity (35 – 57 mW $m^{-1} K^{-1}$), making these materials very good insulators for space applications or other insulation purposes. Only a small effect of increasing the gelation time and the pore structure disorder was observed with the change from a methoxy to an ethoxy group, being the overall properties of MTMS and MTES-derived aerogels very similar. ETMS and ETES precursors only produce gels when combined with TMOS, TEOS or MTMS, because the size and weight of the R group (ethyl) cause significant additional steric hindrance and segregation in the reacting medium, thus the growth of the solid network is more difficult and occurs in a more organized way and confined volume. All the precursors lead to highly hydrophobic materials due to the presence of the non-hydrolysable alkyl substituent group.

Acknowledgements

This work is funded by FEDER funds through the Operational Programme for Competitiveness Factors – COMPETE and National Funds, through FCT – Foundation for Science and Technology under the project PTDC / EQU–EPR / 099998 / 2008 – GelSpace – Silica Based Aerogels for Insulation of Spatial Devices.

References

1. L. Hench, R. Orefice. Sol–gel technology. In: Kirk–Othmer Encyclopedia of Chemical Technology, 22. 1997, New York: John Wiley & Sons, 497-527.
2. M. A. Aegerter, N. Leventis, M. M. Koebel. Aerogels Handbook. 2011, New York: Springer.

3. A. Pierre, G. Pajonk. Chemistry of aerogels and their applications. Chem. Rev. 102 (2002) 4243-4265.
4. A. Rao, R. Kalesh. Organic surface modification of TEOS based silica aerogels synthesized by co-precursor and derivatization methods. J. Sol–Gel Sci. & Technol. 30 (2004) 141-147.
5. A. Dorcheh, M. Abbasi. Silica aerogel; synthesis, properties and characterization. J. Mater. Proc. Technol. 199 (2008) 10-26.
6. A. Rao, S. Bhagat, H. Hirashima, G. Pajonk. Synthesis of flexible silica aerogels using methyltrimethoxysilane (MTMS) precursor. J. Colloid Interface Sci. 300 (2006) 279-285.
7. S. Bhagat, C. Oh, Y. Kim, Y. Ahn, J. Yeo. Methyltrimethoxysilane based monolithic silica aerogels via ambient pressure drying. Microporous Mesoporous Mater. 100 (2007) 350-355.
8. A. Jitianu, A. Britchi, C. Deleanu, V. Badescu, M. Zaharescu. Comparative study of the sol–gel processes starting with different substituted Si-alkoxides. J. Non-Cryst. Solids 319 (2003) 263-269.
9. L. Durães, M. Ochoa, N. Rocha, R. Patrício, N. Duarte, V. Redondo, A. Portugal. Effect of the drying conditions on the microstructure of sílica based xerogels and aerogels. J. Nanosci. & Nanotechnol. 12 (2012) 6828-6834.
10. A. Rao, M. Kulkarni, D. Amalnerkar, T. Seth. Superhydrophobic silica aerogels based on methyltrimethoxysilane precursor. J. Non-Cryst. Solids 330 (2003) 187-195.
11. A. Rao, D. Hegde, P. Shewale. Imperviousness of the hydrophobic silica aerogels against various solvents and acids. Appl. Surf. Sci. 253 (2007) 4137-4141.
12. N. Hegde, A. Rao. Physical properties of methyltrimethoxysilane based elastic silica aerogels prepared by the two-stage sol–gel process. J. Mater. Sci. 42 (2007) 6965-6971.
13. L. Durães, S. Nogueira, A. Santos, C. Preciso, J. Hernandez, A. Portugal. Flexible silica based xerogels and aerogels for spatial applications. In: Proc. 10th Int. Chem. Biol. Eng. Conf. (Eds. E. Ferreira, M. Mota). 2008, Braga: University of Minho, 563-563.
14. D. Nadargi, A. Rao. Methyltriethoxysilane: New precursor for synthesizing silica aerogels. J. Alloys & Comp. 467 (2009) 397-404.
15. D. Nadargi, S. Latthe, A. Rao. Effect of post-treatment (gel aging) on the properties of methyltrimethoxysilane based silica aerogels prepared by two-step sol–gel process. J. Sol–Gel Sci. Technol. 49 (2009) 53-59.
16. D. Nadargi, S. Latthe, H. Hirashima, A. Rao. Studies on rheological properties of methyltriethoxysilane (MTES) based flexible superhydrophobic silica aerogels. Microporous Mesoporous Mater. 117 (2009) 617-626.
17. L. Durães, M. Ochoa, A. Portugal, N. Duarte, J. Dias, N. Rocha, J. Hernandez. Tailored silica based xerogels and aerogels for insulation in space environments. Adv. Sci. Technol. 63 (2010) 41-46.
18. K. Kanamori, Y. Kodera, G. Hayase, K. Nakanishi, T. Hanada. Transition from transparent aerogels to hierarchically porous monoliths in polymethylsesquioxane sol-gel system. J. Colloid Interface Sci. 357 (2011) 336-344.
19. Newalker, B. L. and Komarneni, S. (2000) Synthesis and characterization of microporous silica prepared with sodium silicate and organosilane compounds. J. Sol–Gel Sci. & Technol. 18, 191-198.

20. J. Harreld, T. Ebina, N. Tsubo, G. Stucky. Manipulation of pore size distributions in silica and ormosil gels dried under ambient pressure conditions. J. Non-Cryst. Solids 298 (2002) 241-251.
21. M. Ochoa, L. Durães, A. Beja, A. Portugal. Study of the suitability of silica based xerogels synthesized using ethyltrimethoxysilane and / or methyltrimethoxysilane precursors for aerospace applications. J. Sol–Gel Sci. & Technol. 61 (2012) 151-160.
22. A. Anderson, M. Carrol, E. Green, J. Melville, M. Bono. Hydrophobic silica aerogels prepared via rapid supercritical extraction. J. Sol–Gel Sci. & Technol. 53 (2010) 199-207.
23. F. Brunet. Polymerization reactions in methyltriethoxysilane studied through ^{29}Si NMR with polarization transfer. J. Non-Cryst. Solids 231 (1998) 58-77.
24. H. Jiang, Z. Zheng, Z. Li, X. Wang. Effects of temperature and solvent on the hydrolysis of alkoxysilane under alkaline conditions. Ind. Eng. Chem. Res. 45 (2006) 8617-8622.
25. H. Jiang, Z. Zheng, X. Wang. Kinetic study of methyltriethoxysilane (MTES) hydrolysis by FTIR spectroscopy under different temperatures and solvents. Vib. Spectrosc. 46 (2008) 1-7.
26. P. Aravind, G. Soraru. High surface area methyltriethoxysilane-derived aerogels by ambient pressure drying. J. Porous Mater. 18 (2011), 159-165.
27. C. J. Brinker, G. W. Scherer. Sol–Gel Science. 1990.Boston: Academic Press.
28. D. Loy, B. Baugher, C. Baugher, D. Schneider, K. Rahimain. Substituent effects on the sol–gel chemistry of organotrialkoxysilanes. Chem. Mater. 12 (2000) 3624-3632.

PRESS FORMING OF CHICKEN FEATHER FIBRE (CFF) REINFORCED BIO-COMPOSITES: EFFECTS OF CFF VOLUME ON MECHANICAL AND THERMAL PROPERTIES

M. S. Ozen, M. Yüksek, M. Uzun, E. Sancak, İ. Usta, O. Atak

Marmara University
Istanbul, Turkey
m.uzun@marmara.edu.tr

Accepted September 19, 2013

1. Introduction

With the rising environmental concerns, much research has focused on the development of sustainable bio-composite materials since the last decade [1]. Bio-composites are composite materials consisting of at least one phase from a biological origin. In terms of the fibres, the bio-composites are typically reinforced with plant fibres [2, 3] such as flax, bamboo, hemp; or animal fibres, such as feathers [4, 5]. In recent years, the use of waste materials as composite reinforcement has been also widely studied. The development of the use of the chicken feather fibres as composite reinforcement has become popular and these fibres have potential to get scientific and commercial attractions. Chicken feather are primarily composed of keratin. Chicken feather are hollow fibre structure and strong in nature due to the 91 % keratin content. Chicken feather fibres have the similar properties to the other fibres and especially to wool fibres because of keratin structure. Chicken feather fibres are six or eight times stronger than cellulosic fibres. The fibres have superior properties compared to cotton and wool fibres at some specific applications. The most remarkable properties of chicken feather fibres are fibre fineness and higher liquid take-up capacity. Chicken feather fibres have larger surface areas because of smaller fibre diameter. The usage of wettable reinforcing material at composite production is vital important to obtain higher mechanical properties.

The chicken feather fibres (CFF) are usually described as a waste by-product and they are contributing to globally environmental pollution due to the disposal problems. There are two main types of chicken feather disposal methods exist, the first one is “burning” and the second one is “burying”. Both of them have negative effect on the environment. The burning pollutes the air and the burying contaminates the ground. There are some studies on the poultry wastes, for instance some studies were carried out the use of CFF as provender which is currently found that it is risky for the human health. Recent studies on the chicken feather waste demonstrated that the waste can be employed as a composite reinforcement. The composite reinforcement application of the CFF offers much more effective way to solve environmental concerns as compared to the traditional disposal methods. It is also important to mention that the use of CFF as composite reinforcement offers a number of advantages such as inexpensive, renewable, and abundantly available. The CFF as a composite reinforcement also provides desirable properties including, lightweight, high thermal insulation, excellent acoustic properties, non-abrasive behaviour and excellent hydrophobic properties. The CFF has the

lowest density value in comparison with the all natural and synthetic fibres [6 – 10]. Hernandez et al. found that the CFF keratin biofibres allows an even distribution within and adherence to polymers due to their hydrophobic nature and they reported that CFF reinforced composites have good thermal stability and low energy dissipation [11]. In a previous study by the author has found that the CFF reinforced composite have potential applications due to its improved impact behaviour [12].

The main objective of this study was to develop and characterise novel CFF containing bio-composites. The study mainly focused on the development and application of CFF in the composite structures. It is also aimed to combine CFF and glass fibres as composite reinforcement.

2. Experimental

2.1. Materials

2.1.1. Matrix

The polyester resin (Polipol™ 347) was procured from Poliya® Polyester Industry and Trade Ltd. Co. (Istanbul, Turkey). The mechanical properties of resin are given in **Table 1**. The hardener (Akperox CH80) manufactured and supplied by AKPA, EmsalBoya A.Ş. (Istanbul, Turkey). The main properties of the hardener are shown in **Table 2**.

Table 1. Mechanical properties of cured resin.

Test	Method	Value
Flexural strength	ISO 0178	117 MPa
Flexural modulus	ISO 0178	3546 MPa
Elongation at break	ISO 0178	3.86 %
Tensile strength	ISO 0527	52 MPa
Modulus of elasticity in tensile	ISO 0527	2800 MPa
Elongation at break	ISO 0527	2.12 %
Izod impact strength	ISO 0180	7 kJ / m^2

Table 2. Hardener properties.

Product code	AKPEROX CH80
Product description	Di-methyl ftalat solution with MEKP blend
Density	1.17 g / cm^3
Viscosity	25 mPa
Solvent	DMP
Active oxygen content	9.9 – 10.0 %
Peroxite content	50 %
SADT Temperature	60 °C
CAS No	1338–23–4, 131–11–3, 78–93–3

2.1.2. Reinforcements

The chicken feathers were kindly supplied by SekerPilic A.Ş., Bolu, Turkey. They were washed by using a lab dyeing machine at 60 ° with a polar solvent (ethanol). After the washing process the chicken features were rinsed and left to dry for 24 h at room temperatures. After 24 h of conditioning, the body part (quilt) of the CFF was removed by manually to make homogeneous fibre structures (**Figure 1**). The chicken feather fibre properties are given in **Table 2**. It was found that the chicken feather fibre does not have constant linear density. BMC1 type glass fibre (E-Glass) was obtained from Cam Elyaf AS, Turkey. The length of the glass fibres is 20 mm and the diameter of the glass fibres are 13 μm.

Table 3. Mechanical properties of chicken feature fibres (CFF).

	CFF
Linear density (Tex)	45 – 85
Fibre length, cm)	1 – 5
Elongation, %	10.85
Breaking tensile, kg	0.75

Figure 1. Chicken feather fibres.

2.2. Preparation of composites

The composites were fabricated with four different CFF fibre loadings (0, 5, 10 and 20 %). The composites were manufactured by using bulk moulding compound (BMC). The matrix materials were prepared in portions as given in **Table 4**. Initially, polyester resin and hardener were mixed in a mixer for 2 min to prepare BMC paste. The chopped glass fibres were spread into mould and were mixed for 5 min. After five minutes mixing, the CFF fibres were also added into the paste and the BMC paste was mixed another 5 min. Finally, calcite (**Figure 2**) was added and the BMC paste prepared. Then, the composite structures were prepared by making use of a hydraulic press (60 tonne capacity), Hidromak A.Ş. (Bursa, Turkey). The mould was heated up to 140 ° during moulding process. The BMC paste was cured and converted to composite structures at 30 s under 10 bars press. After the curing, the test specimens were cut by using a standard saw cutter and prepared in accordance with the used test methods.

Table 4. Sample preparation.

	Resin, g	Hardener, g	Calcite, g	Glass fibre, g	CFF, g
Control Sample (CN)	195	5	150	100	0
CFK–5	195	5	150	95	5
CFK–10	195	5	150	90	10
CFK–20	195	5	150	80	20

Figure 2. Calcite powder.

2.3. Test methods

2.3.1. Thermal conductivity

Thermal conductivity measurements of developed composites were done in a heat conduction apparatus in accordance with TS 4512 standard (TS 4512: Determination of Thermal Transmittance of Textiles, 1985).

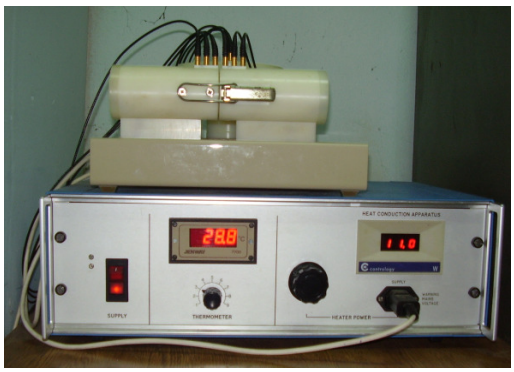

Figure 3. Thermal conductivity test equipment.

2.3.2. Mechanical Properties

The control and the CFF reinforced composites were evaluated in accordance with ASTM D3039 (Tensile Properties of Polymer Matrix Composite Materials), EN ISO 14125 (Fibre-reinforced plastic composites – Determination of flexural properties), and EN ISO 179–1 (Determination of Charpy impact properties). Charpy impact properties were determined by using a Zwick BS Type–2 (**Figure 4**). The dimensional properties of test specimens are given in **Table 5**.

Table 5. Dimensional properties of Charpy test specimens.

Dimension	Values, mm
Length	62.5
Width	10
Thickness	2.5
Distance between gauges	50

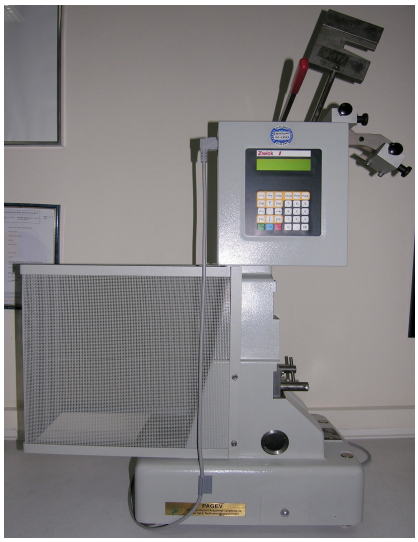

Figure 4. Charpy impact test equipment.

3. Results and discussion

The mechanical and thermal properties of developed composites are given in **Table 6**. It was found that, upon loadings of the CFF reinforcement, the tested mechanical properties of the composites changed quite appreciably over time, similar results were obtained for thermal properties; however, the thermal properties did not changed as much as mechanical properties changed. The lowest tensile strength values were found with the control composite (0 %). The CFF reinforcements have a positive effect on the tensile properties of composites; in most of the cases, they increased the tensile strength of the composites appreciably. The 20 % CFF reinforcement reduced the tensile strength value as compared to 10 % CFF reinforced composites. It could be because of the inhomogeneous mixing of high amount (20 %) of CFF fibres. This study has illustrated that the tensile strength of composites can be enhanced by using CFF as reinforcement up to certain level. The increase in the CFF loadings needs to be optimised in order to maximise the effectiveness of the CFF reinforcement.

The breaking elongation of the reinforced composites was increased about 100 %. The increased in the breaking elongation have been observed all CFF reinforced composites. 10 % CFF reinforced had superior breaking elongation as compared to the tested composites.

It is interesting to observe from **Figure 5** that the Young modulus of the composites was reduced when they were reinforced with glass and CFF fibres. The Young modulus of the control (0 %) composite was found to be significantly lower in comparison with the reinforced composites. The non-uniformity and / or non-homogeneous structure of reinforced composites

can probably influence the Young modulus values. It is obvious from the Charpy impact values that the impact values increase with the CFF loading percentages. A previous study by the author has also confirmed these results [12]. The Charpy impact values increases with the CFF loading percentage. The 20 % CFF loaded composites have enhanced impact values in comparison with the other composites tested.

Table 6. Mechanical and thermal properties of chicken feature fibre (CFF) reinforced composites.

	0 %	5 %	10 %	20 %
Tensile strength, MPa	217.1	533.2	623.6	582.3
Elongation at break, %	2.03	4.06	4.65	4.08
Young modulus, MPa	3681.7	1205.5	2934.0	1789.3
Charpy impact, kg J / mm^2	6.33	12.73	14.73	17.13
Thermal conductivity *k*, W / m K	1.20	1.13	1.09	1.04

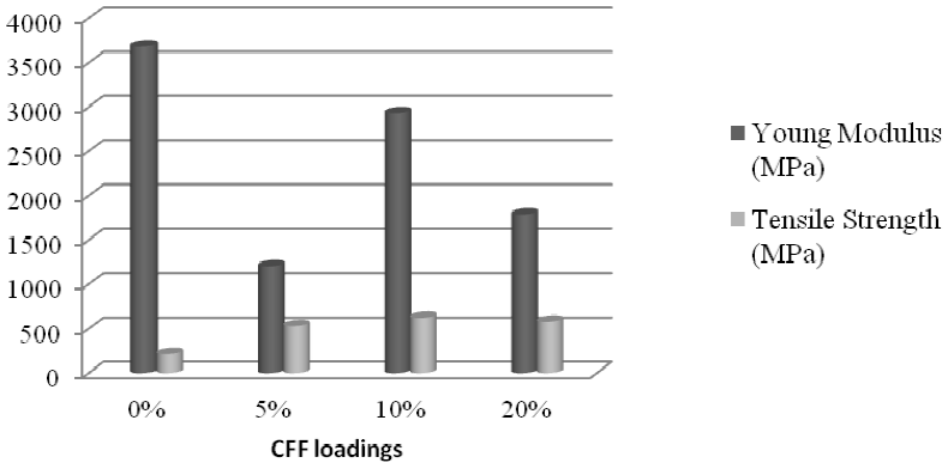

Figure 5. Young modulus and tensile strength vs. CFF loading.

The thermal conductivity results are presented in **Table 6**. The thermal conductivity *k* ranged from 1.09 to 1.20 W / m K in the dry state. The control composite obtained had the highest thermal conductivity values as compared to all test combinations. It has been clearly seen that the presence of CFF and glass fibres within the composites decreases the thermal conductivity of structures. Data from **Table 6** which shows that there was a direct relationship between the fibre loadings and the thermal conductivity of the composites tested. It seems possible that these results are due to the CFF fibre properties. The thermal conductivity of composites is found to be depending on the fibres into the structure.

4. Conclusions

The findings from this study make several contributions to the current literature. First of all, the possible use of CFF fibre as a composite reinforcement has been highlighted. Secondly, the developed composites have been analysed and compared based on the findings in terms of mechanical and thermal conductivity properties. In this research paper, four composite

structures were produced, tested and compared. The comparison in terms of dimensional properties indicates that developed composites have similar dimensional properties which are extensively important for the evaluation of the tested properties. It is important to demonstrate that the CFF could be an alternative reinforcement material to bio-composites. It could possibly reduce the pollution which the CFF causes. There are some studies on physical properties of CFF reinforced composites; however, there is currently no published information on CFF composites which is produced by bulk moulding compound (BMC) method. The combination of moulding compound is also novel. It was considered that the developing and analysing main properties of CFF reinforced composites would be useful to extend the existing literature.

The results demonstrate that the difference between the unreinforced and reinforced is significantly important in terms of the tested parameters. The CFF reinforcement of the composites was found to provide better tensile strength and Charpy impact properties as compared to the control composite. Surprisingly, the 10% CFF loaded composite was found to have notably higher tensile strength value than the other tested counterparts. The CFF fibre reinforced composites have enhanced Charpy impact properties in comparison with the control composite. The control composites had higher thermal conductivity than the fibre reinforced composites. The loading percentages also influence the thermal conductivity of composites drastically.

Acknowledgement

This work was supported by the Scientific Research Project Unit (BAPKO) of the Marmara University (FEN–A–100713–0328).

References

1. K.-T. Lau, K. H.-Y. Cheung, D. Hui. Natural fibre composites preface. Composites B 40 (2009) 591-593.
2. A. K. Bledzki, S. Reihmane, J. Gassan. Properties and modification methods for vegetable fibres for natural fibre composites. J. Appl. Polymer Sci. 59 (1996) 1329-1336.
3. H. Kinoshita, K. Kaizu, M. Fukuda, H. Tokunaga, K. Koga, K. Ikeda. Development of green composite consists of woodchips, bamboo fibres and biodegradable adhesive. Composites B 40 (2009) 607-612.
4. M. Zhan, R. P. Wool. Bio-composites from chicken feathers and plant oils for printed circuit boards. In: 13th Ann. Green Chem. & Eng. Conf. 2009, College Park: MD.
5. C. K. Hong, R. P. Wool. Development of a bio-based composite material from soybean oil and keratin fibres. J. Appl. Polym. Sci. 95 (2005) 1524-1538.
6. J. R. Barone, W. F. Schmidt, Ch. F. E. Liebner. Compounding and moulding of polyethylene composites reinforced with keratin feather fibre. Composites Sci. & Technol. 65 (2005) 683-692.
7. T. A. Bullions, D. Hoffman, R. A. Gillespie, J. Price–o'Brien, A. C. Loos. Contributions of feather fibres and various cellulose fibres to the mechanical properties of polypropylene matrix composites. Composite Sci. & Technol. 66 (2006) 102-114.

8. N. Reddy, Y. Yang. Structure and properties of chicken feather barbs as natural protein fibres. J. Polym. & Environ. 15 (2007) 81-87.
9. S. Huda, Y. Yang. Composites from ground chicken quill and polypropylene. Composites Sci. & Technol. 68 (2008) 790-798.
10. M. Zhan, R. P. Wool, J. Q. Xiao. Electrical properties of chicken feather fibre reinforced epoxy composites. Composites A 42 (2011) 229-233.
11. A. L. Martinez –Hernandez, C. Velasco –Santos, M. de-Icaza, V. M. Castano. Dynamical-mechanical and thermal analysis of polymeric composites reinforced with keratin biofibers from chicken feathers. Composites B 38 (2010) 405-410.
12. M. Uzun E. Sancak, I. Patel, I. Usta, M Akalin, M. Yuksek. Mechanical behaviour of chicken quills and chicken feather fibres reinforced polymeric composites. Arch. Mater. Sci. & Eng. 52 (2011) 82-86.

INFLUENCE OF HEXAGONAL BORON NITRIDE NANOCRYSTALS ON WEAR PROCESSES IN BRASS

L. Chkhartishvili, M. Darchiashvili, A. Gachechiladze,
B. Margiev, L. Rukhadze, O. Tsagareishvili

F. Tavadze Institute of Metallurgy & Materials Science
Tbilisi, Georgia
chkharti2003@yahoo.com

Accepted September 19, 2013

1. Introduction

Wear is a common problem for different types of surfaces of engineering components subjected to dynamic loadings. In the industry, a number of lubricants are used in order to reduce friction and wear in machines and engines with moving parts. Typically, lubricants utilized are in the form of liquids or greases. But, materials of such consistency does not to meet all the requirements for heavy-loaded friction pairs operating under extreme conditions – extremely high or extremely low temperatures, in ultra-high vacuum, under extreme contact pressures, at high or low sliding speeds, etc.

Currently, this problem is solved by the preparation of liquid lubricants containing solid additives of layered crystalline materials. However, widely used additives, e.g. molybdenum disulfide (MoS_2) and graphite, contain heavy metals, sulfur, carbon, etc. and then are environmental pollutants. They can be successfully replaced by promising "green" boron-based lubricants [1] or boriding the rubbing surfaces [2]. In particular, the addition of even ~ 1wt. % hexagonal boron nitride (h-BN) powder in oil, a grease or fuel provides excellent tribological properties.

For the first time, Kimura et al. had conducted [3] a series of detailed sliding experiments, which reveals the behavior of h-BN when added to the lubricating oil. In the case of sliding of bearing steel vs. itself, h-BN slightly increases the coefficient of friction, but dramatically decreases wear; and boron is found to remain on rubbing surfaces in form of non-stoichiometric oxide. However, when bearing steel is sliding against cast iron powdered h-BN decreases the coefficient of friction and the remnant is mostly BN. There is suggested a number of recent results confirming that h-BN is effective in reducing wear if used as a liquid lubricant additive – see citations in [4].

The increase in dispersion of h-BN suppresses the sedimentation processes in a liquid lubricant that improves its performance. This is particularly important in the metalwork, when the cutting or grinding processes are accompanied by the significant heat-releasing. A graphite-like lamellar structure of h-BN predetermines its tribological properties: intra-layer bonds are strongly covalent with a deal of ionicity, whereas weak van der Waals polarization-forces are responsible for the inter-layers interaction. Therefore, layers of h-BN are easily moving relative to each other. In the process of rubbing, the single-crystalline h-BN particles are spontaneously

aligned so that their basal planes are parallel to the rubbing metal surfaces. Thus, the friction between metal surfaces is replaced by the internal friction between BN-hexagonal layers. Sometimes in nanoscale junctions containing h-BN, the effect of super-lubricity occurs, which means the almost frictionless tribological state.

From the friction experiments conducted with h-BN in sliding contacts with various metals, this material is known as solid lubricant as well [5]. An alternative way to reduce the wear and friction is the production of self-lubricating materials by the introducing h-BN particulates in the surface layer or in the bulk of rubbing metallic materials. Such approach has been a major topic of interest in the last decade. It has been successfully examined in different Fe-based alloys – low-carbon [6], austenitic [7], stainless [8], high-Cr [9], CrMo- [10], TiC-steels [11], and distaloy [12], as well as in certain Cu-based pseudoalloys [13]. This issue is closely related to the processes of growth of h-BN layers on Fe- [14 – 18] or Cu-surfaces [19 – 26] and vice versa – formation of Fe- [27 – 29] and Cu-coatings [30, 31] onto the h-BN basal plane.

Here we propose a new self-lubricating composite material containing the brass-matrix and particulates of h-BN.

2. Experimental

We have investigated the tribological properties of composite materials based on commercially available powdered (~ 300 nm) brass composed of 68.5 wt. % Cu and 31.5 wt.% Zn, and containing trace impurities of < 0.1 wt. % Fe, < 0.03 wt. % Pb, < 0.02 wt. % Bi, < 0.01 wt. % P and < 0.005 wt. % Sb. Thus, Cu is main component of the alloy, while Fe is the main impurity. As the anti-friction component it is used nanosized h-BN powder produced by the specially developed technology [32]. As a precursor in synthesis of h-BN, it is used the mixture of boric acid (H_3BO_3) and urea (CH_4ON_2). Process is conducted under the ammonia (NH_3) atmosphere in the temperature range of 1000 – 1100 °C. The resulting product is the slightly textured nanocrystalline h-BN with the specific gravity of ~ 2.1 g / cm^3.

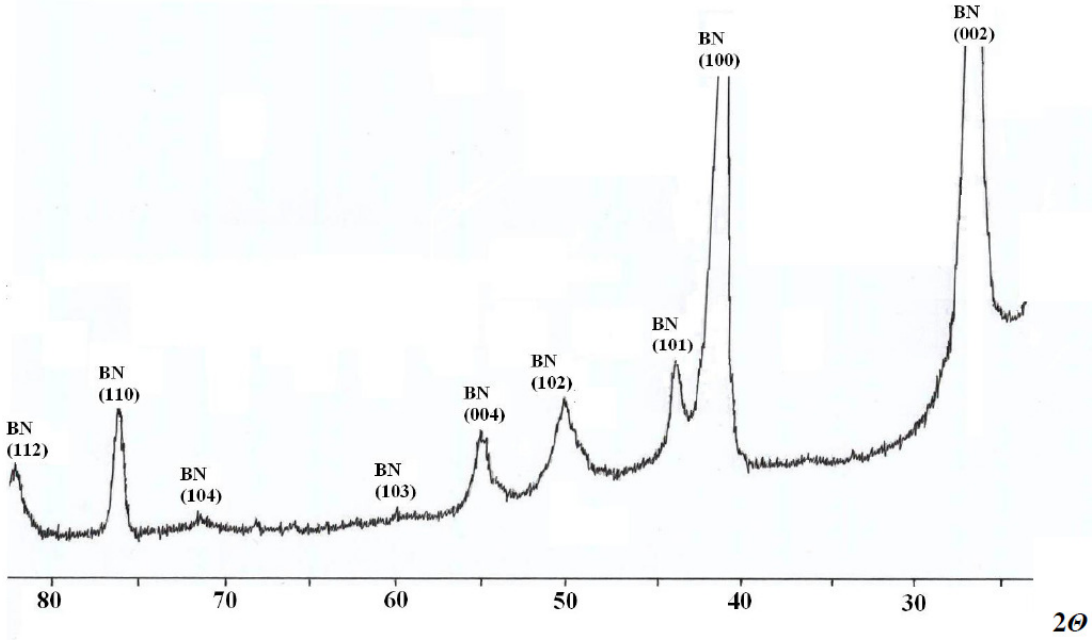

Figure 1. XRD spectrum of boron nitride powder synthesized from mixture of boric acid and urea under the ammonia atmosphere at high temperatures.

From the X-rays diffraction spectrum presented in **Figure 1**, it can be concluded that the obtained BN crystallites possess the layered hexagonal lattice structure. The presence of differently broadened diffraction peaks indicates their non-spherical shape. According to the relevant morphological model [33, 34], particles of this powder should be disk-shaped.

The sizes of these particles have been evaluated by Selyakov–Scherer method [35]. Based on the measured broadening in XRD peaks and utilizing the formula $\Delta(2\Theta) = K\lambda / (D_{hkl} \cos\Theta)$ — $\Delta(2\Theta)$ is the half-width of a diffraction maximum (in rad), K is the form-factor of a crystallite (its value may range from 0.98 to 1.39) assumed to be of 1.20 for h-BN, λ is the wavelength (for the Cu K_α radiation used, it equals to 0.1539 nm), D_{hkl} is the grain size along the normal to the (hkl) plane, and Θ is the Bragg angle — it is estimated the mean sizes of crystallites. Peaks' total broadening includes both broadenings caused by the small grain size, and so-called apparatus broadening related to deformation and defects of various types. Our evaluation of grain sizes has been carried out based on maxima (004) and (100), for which apparatus broadenings are of ≈ 0.5 and ≈ 0.3 °, respectively. Neglecting the broadening caused by the deformation and different defects, we find that the mean thickness of the disc-like h-BN particles is ≈ 25 nm, while their mean diameter is ≈ 240 nm.

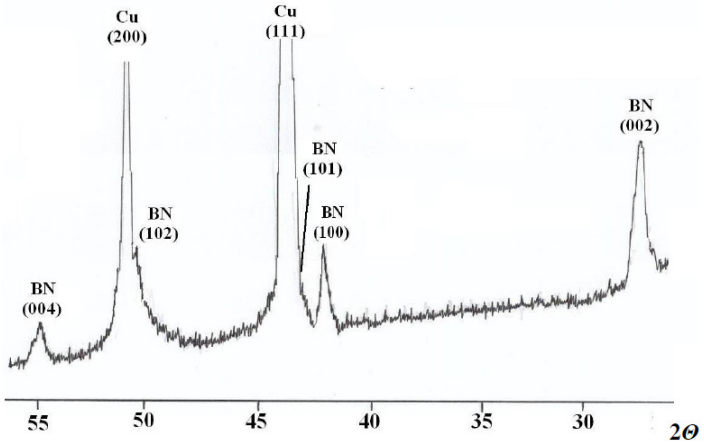

Figure 2. XRD spectrum of the Cu-plated h-BN powder.

In order to improve adhesion between brass matrix and introduced h-BN particles, these particles have been chemically plated by copper. XRD spectrum of the copper-plated powdered h-BN is shown in **Figure 2**. Plated nanocrystalline h-BN has been introduced directly into the matrix melt. The microstructure of the obtained composite material is shown in **Figure 3**.

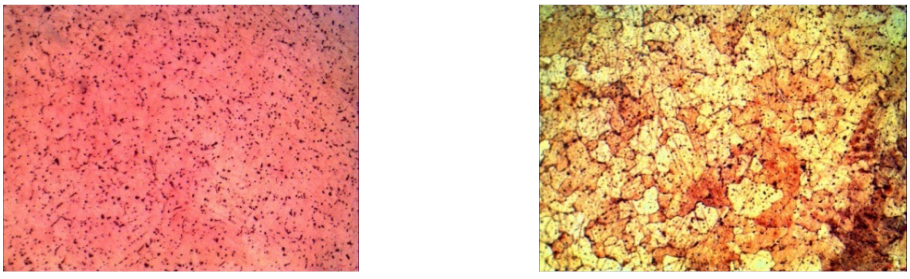

(a) (b)

Figure 3. Microstructure (× 400) of brass + 1 wt. % h-BN composite samples polished: (a) mechanically and (b) chemically.

The anti-friction additive of h-BN is found to be almost uniformly distributed within the matrix, i.e. without preferential accumulation at the grain boundaries or other structural defects.

3. Results

As is known, the stabilization of the geometry is an important factor of the proper operation of friction pairs working in extreme conditions. In order to determine the achieving of such stabilization, temperature-dependences of the thermal expansion coefficient α have been measured both for the brass matrix without additions and for the obtained composite. From **Figure 4**, one can see that the introducing of the h-BN friction modifier insignificantly affects the α values. This fact demonstrates the stabilization of the geometry of friction pairs made from the composite brass + 1 wt. % h-BN.

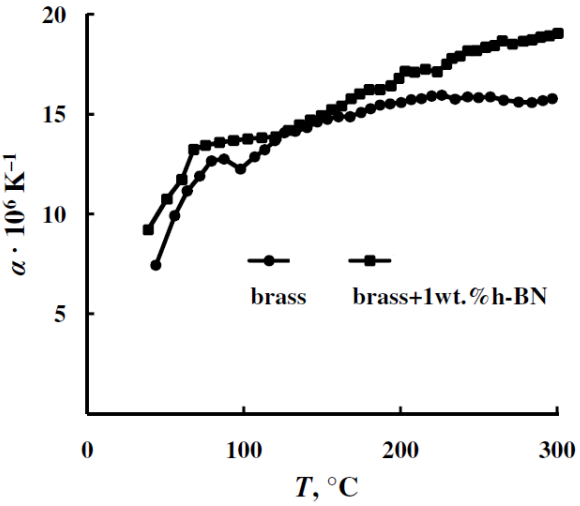

Figure 4. Temperature-dependences of the thermal expansion coefficient for brass and composite brass + 1 wt. % h-BN.

The introducing of 5 wt. % h-BN in the brass matrix significantly increases the room temperature thermal conductivity of the material: from 25 to 50 $W / m \cdot K$. The increase in thermal conductivity indicates an intensification of heat exchange processes in overloaded friction pairs with higher h-BN content (brass + 5 wt. % h-BN).

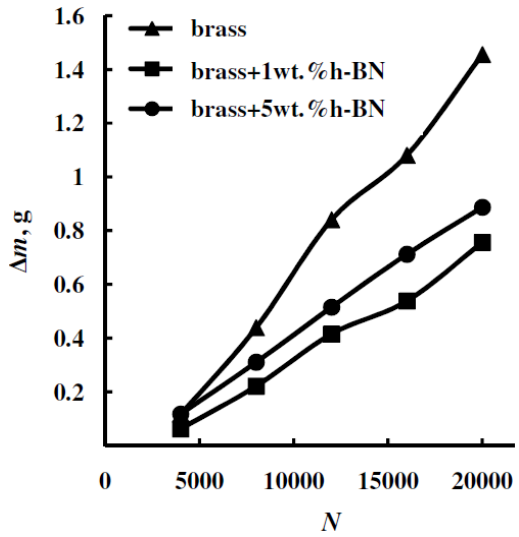

Figure 5. Dependence of the wear on the content of friction modifier and the number of rotations.

The tribological properties of the obtained material have been investigated by the "disk-drive" method. The diameter of the samples is 50 mm, the thickness of the reference sample is 12 mm, and that of the testing samples is 10mm. Speed of sliding is 0.9m/s at the slipping coefficient of ~ 10 %. **Figure 5** shows the wear vs. the content of friction modifier and the number of rotations. The normal loading is of 225 N. From the **Figure 5**, it can be seen that the introducing of friction modifier – h-BN significantly reduces mass-losses of the sample of composition brass + 1 wt. % h-BN, apparently changing the wear mechanism if compared to the original sample.

Radical changes also are seen in morphology and the linear sizes of the wear particles (**Figure 6**). However, the further increase in the h-BN content, up to 5 wt. %, increases mass-losses during friction, what is probably due to a decrease in the shear modulus and also the structural loosening of the composite.

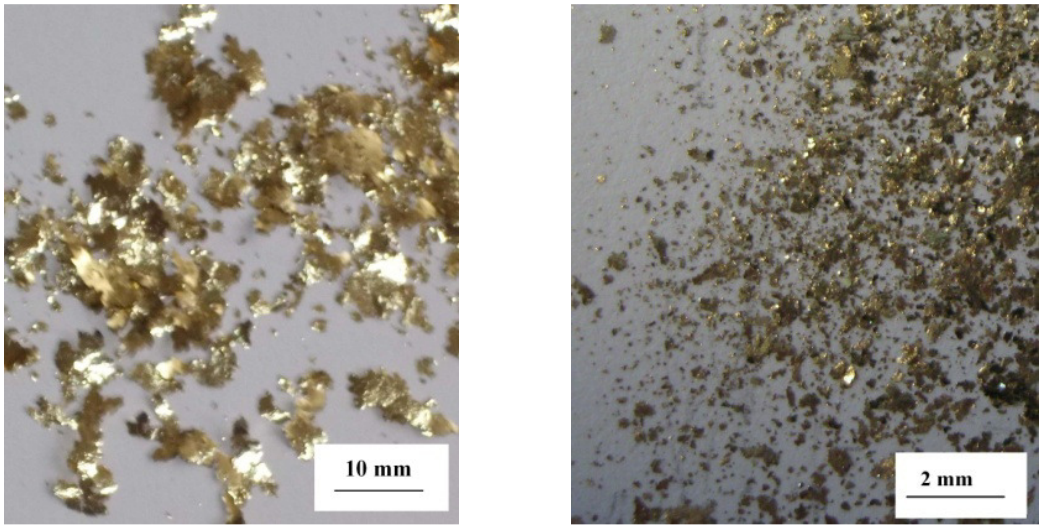

Figure 6. Wear products of (a) brass and (b) brass + 1 wt. % h-BN

Figure 7 shows the dependence of the wear of the samples on the sliding speed at different normal loadings.

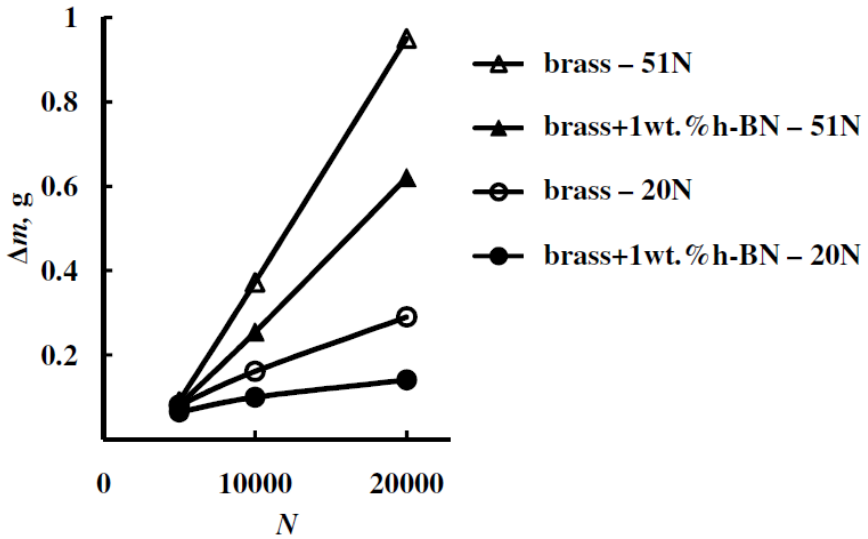

Figure 7. Dependence of wear on sliding speed at different normal loadings.

In the **Table 1**, there are presented the values of the linear rate of wear k at 12500 rotations and normal loadings of 117 N. D_0 and D are, respectively, the initial and final diameters of the disc-shaped testing sample, and s is the total sliding distance (in mm).

Table 1. Linear wear of brass and composite brass + 1 wt. % h-BN.

Samples	D_0, mm	D, mm	$\Delta d = (D_0 - D)/2$, mm	$k = \Delta d / s$
brass	49.76	49.63	0.065	$0.21 \cdot 10^{-7}$
brass + 1wt.% h-BN	50.33	50.24	0.045	$0.14 \cdot 10^{-7}$

From the above obtained data, we can state that the introducing of friction modifier in form h-BN in the matrix made from metallic alloy (brass) substantially reduces wear changing the wear mechanism in matrix. The optimal amount of the modifier is estimated as a few wt. %.

4. Conclusions

In summary, a method for preparing of the composite anti-frictional material based on brass (containing 68.5 wt. % Cu and 31.3 wt. % Zn) has been developed. The nanocrystalline hexagonal boron nitride obtained by low-temperature chemical synthesis has been used as the friction modifier. Morphology and size of h-BN nanoparticles has been determined by broadening of the X-ray diffraction maxima. They are found to have the disc-shapes with thy mean diameter of 240 nm and mean thickness of 25 nm. To obtain composite alloy brass + 1 wt. % h-BN, the chemically copper-plated h-BN nanoparticles should be directly introduced into the brass-melt.

Measurements of the thermal expansion coefficient of the composite material brass + 1 wt. % h-BN showed that friction modifier insignificantly affects its value what means the stabilization of the geometry of friction pairs made from this material. Alongside with this, the increase in the room temperature thermal conductivity as compared with that of matrix indicates the possibility to intensify the heat exchange processes at the friction surfaces at high loadings in the high-temperature range of operation. This will ensure the stability of the friction pairs at high temperatures and loadings. Studying the tribological properties shows that h-BN as the friction modifier radically changes the wear mechanism. It is evidenced by changes in the morphologies and the linear sizes of the wear particles at “catastrophic” loadings (225 N). Tribological measurements conducted at lower loadings (20 and 51 N) confirm the positive influence of h-BN on the tribological properties of this newly developed anti-frictional material. The optimal amount of friction modifier is estimated to be a few wt. % of h-BN.

References

1. A. Erdemir. Advances in boron-based lubricants and lubricant additives. In: Proc. 4th Int. Boron Symp. 2009, Eskişehir: Osmangazi Univ. Press, 3-9.
2. A. Greco, K. Mistry, V. Sista, O. Eryilmaz, A. Erdemir. Friction and wear behavior of boron based surface treatment and nanoparticles lubricant additives for wind turbine gearbox applications. Wear, 2011, 271, 9-10, 1754-1760.

3. Y. Kimura, T. Wakabayashi, K. Okada, T. Wada, H. Nishikawa. Boron nitride as a lubricant additive. Wear, 1999, 232, 2,199-206.
4. L. Chkhartishvili. Correlation between surface specific area and particles average size: Hexagonal boron nitride nano-powders. Nano Studies, 2012, 6, 1, 65-76.
5. D. H. Buckley. Friction and transfer behavior of pyrolytic boron nitride in contact with various metals. ASLE Trans., 1978, 21, 2, 118-124.
6. Sh. Chatterjee, J. D. Majumdar, S. M. Shariff, G. Padmanabham, A. R. Choudhury. Effect of laser post-treatment on Al_2O_3 – TiB_2 – TiN composite coating with free hBN. Int. J. Adv. Manuf. Technol., 2012, 61, 5-8, 559-567.
7. S. Emura, M. Kawajiri, X. Min, S. Yamamoto, K. Sakuraya, K. Tsuzaki. Machinability improvement and its mechanism in SUS304 aAustenitic stainless steel by h-BN addition. J. Iron & Steel Inst. Jpn., 2012, 98, 7, 358-367.
8. S. Mahathanabodee, T. Palathai, S. Raadnui, R. Tongsri, N. Sombatsompo. Effects of hexagonal boron nitride and sintering temperature on mechanical and tribological properties of SS316L / h-BN composites. Mater. & Design, 2013, 46, 1, 588-597.
9. K. Sakuraya, H. Okada, F. Abe. BN type inclusions formed in high Cr ferritic heat resistant steel. Energy Mater., 2006, 1, 3, 158-166.
10. Y.-N. Wang, Y.-P. Bao, M. Wang, L.-C. Zhang. Precipitation behavior of BN type inclusions in 42CrMo Steel. Int. J. Min. Metall. & Mater., 2013, 20, 1, 28-36.
11. S. Mridha, N.I. Taib, A. N. Idriss. Composite coating on steel surfaces by adding TiC and h-BN particulates under TIG torch melting. Adv. Mater. Res., 2012, 576, 1, 463-466.
12. J. Karwan–Baczewska, M. Rosso. Effect of boron on microstructure and mechanical properties of PM sintered and nitrided steels. Powd. Metall., 2001), 44, 3, 221-227.
13. V. V. Garbuz, L. I. Kostenetskaya, V. Ya. Petrishchev, M. M. Churakov. Interaction between boron nitride and molybdenum in the conditions of formation of pseudoalloys. Powd. Metall. & Met. Ceram., 1991, 30, 1, 73-75.
14. T. Takahashi, H. Itoh, A. Takeuchi. Chemical vapor deposition of hexagonal boron nitride thick film on iron. J. Cryst. Growth, 1979, 47, 2, 245-250.
15. T. E. Warner, D. J. Fray. Nitriding of iron boride to hexagonal boron nitride. J. Mater. Sci., 2000, 35, 21, 5341-5345.
16. D. Babonneau, F. Pailloux, J.-P. Eymery, M.-F. Denanot, Ph. Guérin, E. Fonda, O. Lyon. Spontaneous organization of columnar nanoparticles in Fe – BN nanocomposite films. Phys. Rev. B, 2005, 71, 035430, 1-11.
17. A. Essafti, A. Abouelaoualim, J. L. G. Fierro, E. Ech-Chamikh. Structural and optical properties of amorphous oxygenated iron boron nitride thin films produced by reactive cosputtering. Thin Solid Films, 2009, 517, 15, 4281-4285.
18. N. A. Vinogradov, A. A. Zakharov, M. L. Ng, A. Mikkelsen, E. Lundgren, N. Martensson, A. B. Preobrajenski. One-dimensional corrugation of the h-BN monolayer on Fe (110). Langmuir, 2012, 28, 3, 1775-1781.
19. M. Hubáček, T. Sató. The effect of copper on the crystallization of hexagonal boron nitride. J. Mater. Sci., 1997, 32, 12, 3293-3297.
20. Sh. Chatterjee, Zh. Luo, M. Acerce, D. M. Yates, A. T. Ch. Johnson, L. G. Sneddon. Chemical vapor deposition of boron nitride nanosheets on metallic substrates via decaborane / ammoniar. Chem. Mater., 2011, 23, 2, 4414-4416.

21. N. Guo, J. Wei, L. Fan, Y. Jia, D. Liang, H. Zhu, K. Wang, D. Wu. Controllable growth of triangular hexagonal boron nitride domains on copper foils by an improved low-pressure chemicalv deposition method. Nanotechnol., 2012, 23, 415605, 1-4.
22. S. Joshi, D. Ecija, R. Koitz, M. Iannuzzi, A. P. Seitsonen, J. Hutter, H. Sachdev, S. Vijayaraghavan, F. Bischoff, K. Seufert, J. V. Barth, W. Auwärter. Boron nitride on Cu (111): An electronically corrugated monolayer. Nano Lett., 2012, 12, 11, 5821-5828.
23. K. K. Kim, A. Hsu, X. Jia, S. M. Kim, Y. Shi, M. Hofmann, D. Nezich, J. F. Rodriguez–Nieva, M. Dresselhaus, T. Palacios, J. Kong. Synthesis of monolayer hexagonal boron nitride on Cu foil using chemical vapor deposition. Nano Lett., 2012, 12, 1, 161-166.
24. S. Suzuki, H. Hibino. Chemical vapor deposition of hexagonal boron nitride. e-J. Surf. Sci. & Nanotechnol., 2012, 10, 1, 133-138.
25. J. Gómez Díaz, Y. Ding, R. Koitz, A. P. Seitsonen, M. Iannuzzi, J. Hutter. Hexagonal boron nitride on transition metal surfaces. Theo. Chem. Acc., 2013, 132, 4, 1-17.
26. S. Roth, F. Matsui, Th. Greber, J. Osterwalder. Chemical vapor deposition and characterization of aligned and incommensurate graphene / hexagonal boron nitride heterostack on Cu (111). Nano Lett., 2013, 13, 6, 2668-2675.
27. F. D. Natterer, F. Patthey, H. Brune. Ring state for single transition metal atoms on boron nitride on Rh (111). Phys. Rev. Lett., 2012, 109, 066101, 1-4.
28. F. D. Natterer, F. Patthey, H. Brune. Erratum: Ring state for single transition metal atoms on boron nitride on Rh (111) (Physical Review Letters (2012) 109 (066101)). Phys. Rev. Lett., 2012, 109, 089901, 1-1.
29, H. Yan, A. H. Wang, X. L. Zhang, Z. W. Huang, W. Y. Wang, J. P. Xie. Nd : YAG laser cladding Ni base alloy / nano-h-BN self-lubricating composite coatings. Mater. Sci. & Technol., 2010, 26, 4, 461-468.
30. V. M. Perevertajlo, O. B. Loginova, I. A. Petrusha, A. A. Svirid. Wettability of pyrolytical boron nitride by the metallic melts. Superhard Mater., 1996, 2, 1, 12-16.
31. D. Sen, R. Thapa, K. Bhattacharjee, K. K. Chattopadhyay. Site dependent metal adsorption on (3×3) h-BN monolayer: Stability, magnetic and optical properties. Comput. Mater. Sci., 2012, 51, 1, 165-171.
32. B. G. Margiev, R. V. Chedia, A. A. Gachechiladze, L. S. Chkhartishvili, I. L. Kupreishvili, A. G. Mikeladze, D. L. Gabunia, O. A. Tsagareishvili. Production of nanocrystalline boron nitride by chemical synthesis. In: Abs. 3rd Int. Samsonov Memorial Conf. Mater. Sci. Ref. Comp. 2012, Kiev: IPMS–KPI, 204-204.
33. L. Chkhartishvili. Morphology model for nano-powdered boron nitride lubricants. In: Cont. 2nd Int. Conf. Nanotechnol. 2012, Tbilisi: Nekeri, 86-99.
34. L. Chkhartishvili, T. Matcharashvili, R. Esiava, O. Tsagareishvili, D. Gabunia, B. Margiev, A. Gachechiladze. Powdered hexagonal boron nitride reducing nano-scale wear. In: Phys., Chem. & Appl. Nanostr. 2013, Singapore: World Scientific, 438-440.
35. Ya. S. Usmanskij, Yu. A. Skakov, A. N. Ivanov. L. N. Rastorguev. Crystallography, X-ray and electron microscopies. 1982, Moscow: Metallurgy.

FLUORESCENT NANOPARTICLES OF ANTHRACENE AND bis-MSB

M. Kakuichi [1], K. Kasatani [1], Y. Morita [1], H. Okamoto [1], J. Kawamata [2]

[1] Graduate School of Science & Engineering
Yamaguchi University
Ube, Japan
kasatani@yamaguchi-u.ac.jp
[2] Graduate School of Medicine
Yamaguchi University
Yamaguchi, Japan

Accepted September19, 2013

1. Introduction

Nanoparticles are very attractive materials. Nanoparticles of metals and semiconductors have properties different from crystals or atoms. Energy of electrons in a metal or semiconductor nanoparticle depends significantly on the particle size due to quantum effects. On the other hand, properties of organic nanoparticles have not yet been fully clarified.

Nanoparticles of organic compounds are expected to be durable against strong laser light because of their short lifetimes of excited states. During the past twenty years, fine particles of organic compounds were prepared by reprecipitation method, and their optical properties have been studied [1 – 4]. Recently organic phosphorescent nanoparticles were reported [5].

Luminescent semiconductor nanoparticles have been used for bioimaging [6]. However, they contain heavy metals or toxic elements. Development of luminescent organic nanoparticles is strongly expected for bioimaging application, because organic nanoparticles will be much less toxic than semiconductor ones.

We have already reported two-photon absorption cross sections of nanoparticles of naphthalocyanine derivatives [7], third-order nonlinear optical properties of several organic nanoparticles [8], and fluorescence behavior of organic nanoparticles, mainly of anthracene nanoparticles [9]. In this study, we measured UV/visible absorption spectra, fluorescence spectra, fluorescence quantum yields, and fluorescence lifetimes, of nanoparticles of anthracene and 1,4-bis(2-methylstyryl)benzene (bis-MSB). Fluorescence quantum yields of both anthracene nanoparticles doped with naphthacene and anthracene nanoparticles doped with perylene were as high as 0.75.

2. Experimental

Figure 1 shows structural formulas of organic compounds studied. Anthracene and bis-MSB were used as nanoparticles, and naphthacene and perylene were used as dopants. These compounds were purified several times by recrystalization. Transparent organic nanoparticles

dispersed in water were prepared by reprecipitation method. The typical condition for preparing anthracene nanoparticles was as follows: 1 ml of acetone solution of anthracence (ca. $2 \cdot 10^{-d3}$ M) was injected using a syringe into 100 ml of water stirred vigorously at ca. 10 °C. A dopant (naphthacene or perylene) was added in acetone solutions at a very low concentration. Poly(vinyl alcohol) (PVA, 100 ppm) was added to the water to stabilize nanoparticles in water.

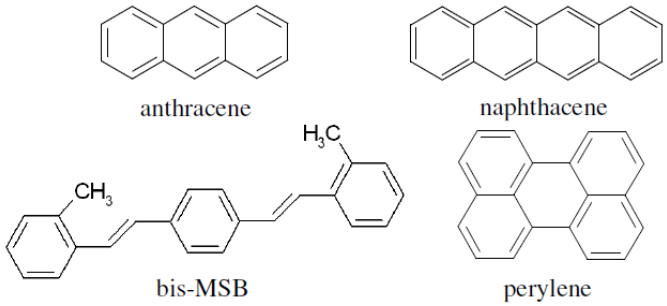

Figure 1. Structural formulas of organic compounds studied.

Fluorescence spectra and fluorescence quantum yields were measured by an absolute PL quantum yield measurement system (Hamamatsu Photonics, C9920–03G). Fluorescence lifetimes were measured with a combination of a femtosecond Ti:sapphire laser and a streak camera. In order to analyze the fluorescence decay curves, they were simulated. The observed fluorescence decay curve, $I(t)$, is assumed to be expressed by the following convolution integral

$$I(t) = \int_0^t L(t')R(t-t')\,dt', \quad (1)$$

where $L(t)$ is the temporal profile of the laser pulse, and $R(t)$ is the response of the sample irradiated by a laser with an ideal delta function shape pulse. $R(t)$ is assumed to be a single exponential function. Sometimes $R(t)$ is assumed to be a double exponential function

$$R(t) = a_1\exp(-t/t_1) + a_2\exp(-t/t_2). \quad (2)$$

All the parameters in equation (2) and the time difference between the experimental and simulated fluorescence decay curves, Δt, were determined using a nonlinear, least-squares iterative convolution method based on the Marquardt algorithm [10, 11]. Scattered light of a laser pulse is recorded as $L(t)$.

3. Results and discussion

Figures 2 and **3** show the UV/visible absorption spectra of anthracene nanoparticles and those of bis-MSB nanoparticles, respectively. A very small amount of dopant gave no influence on the absorption spectra of both matrixes. Doping anthracene nanoparticles with naphthacene does not change UV/visible absorption spectra because of the very low concentration of the dopant.

Figure 4 shows fluorescence spectra of anthracene nanoparticles doped with naphthacene. Exciting wavelength was 375 nm. The fluorescence spectrum of anthracene nanoparticles without dopant shows fluorescence longer than ca. 400 nm with a weak vibronic structure. Doping of naphthacene decreased fluorescence of anthracene nanoparticles and strong fluorescence of naphthacene appeared. Fluorescence of anthracene nanoparticles almost disappeared at a doping concentration of as low as 0.1 mol%.

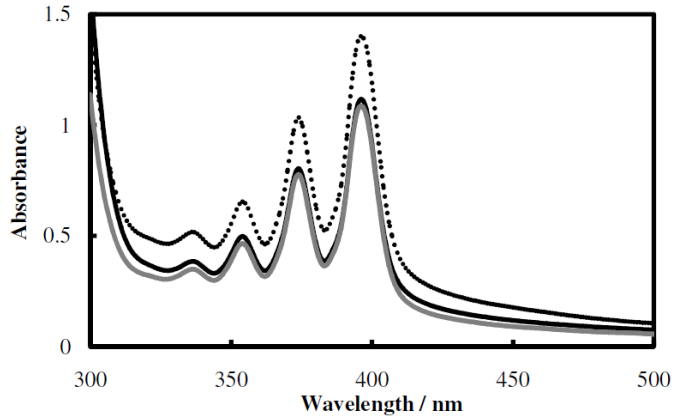

Figure 2. Ultraviolet/visible absorption spectrum of anthracene nanoparticles (black solid line), that of anthracene nanoparticles doped with perylene (black dotted line), and that of anthracene nanoparticles doped with naphthacene (gray solid line).

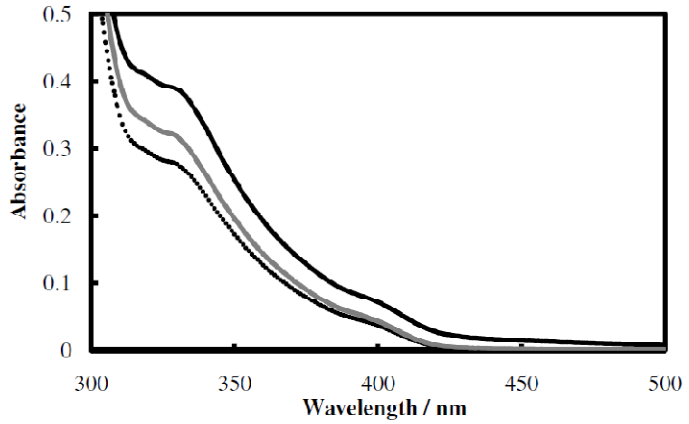

Figure 3. Ultraviolet/visible absorption spectrum of bis-MSB nanoparticles (black solid line), that of bis-MSB nanoparticles doped with perylene (black dotted line), and that of bis-MSB nanoparticles doped with naphthacene (gray solid line).

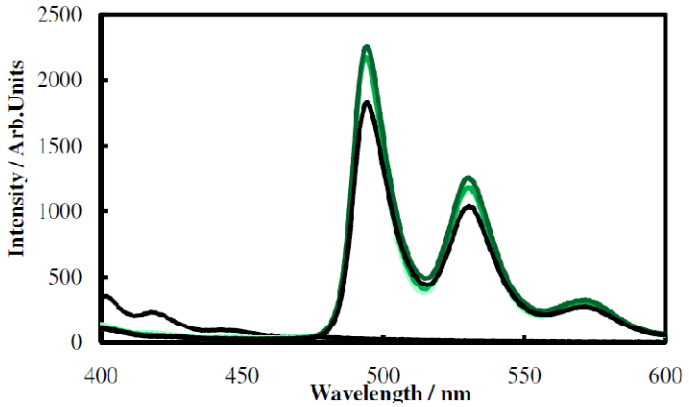

Figure 4. Fluorescence spectra of anthracene nanoparticles and anthracene nanoparticles doped with naphthacene. Concentration of naphthacene: 0 (black dotted line), 0.1 (lightt green solid line), 0.3 (green solid line), 0.5 (dark green line), and 0.7 mol. % (black solid line).

Figure 5 shows fluorescence spectra of anthracene nanoparticles doped with perylene. Exciting wavelength was 375 nm. Doping of perylene decreased fluorescence of anthracene nanoparticles and strong fluorescence of perylene appeared. Fluorescence of anthracene nanoparticles almost disappeared at a doping concentration of 0.1 mol. %.

Figure 6 shows fluorescence spectra of bis-MSB nanoparticles doped with naphthacene. Exciting wavelength was 375 nm. The fluorescence spectrum of bis-MSB nanoparticles without dopant shows fluorescence longer than 420 nm. Doping of naphthacene decreased fluorescence of bis-MSB nanoparticles and strong fluorescence of naphthacene appeared. Fluorescence of bis-MSB nanoparticles almost disappeared at a doping concentration of 4 mol. %.

Figure 7 shows fluorescence spectra of bis-MSB nanoparticles doped with perylene. Exciting wavelength was 375 nm. Doping of perylene decreased fluorescence of bis-MSB nanoparticles and strong fluorescence of perylene appeared. Fluorescence of bis-MSB nanoparticles almost disappeared at a doping concentration of 0.5 mol. %.

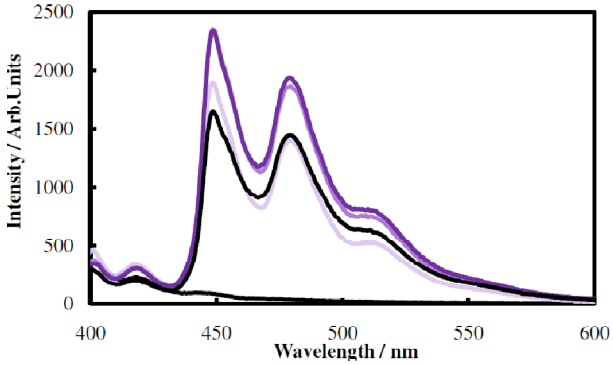

Figure 5. Fluorescence spectra of anthracene nanoparticles and anthracene nanoparticles doped with perylene. Concentration of perylene: 0 (black dotted line), 0.1 (light purple dotted line), 0.3 (purple solid line), 0.5 (dark purple solid line), and 0.7 mol. % (black solid line).

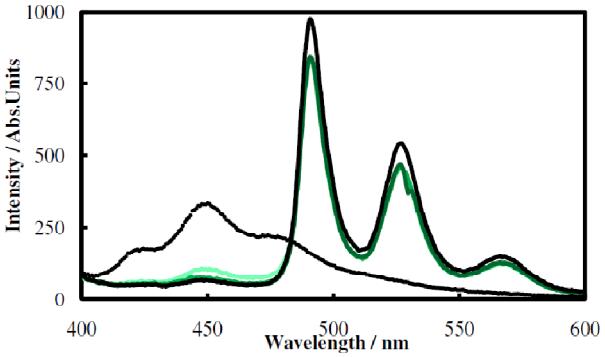

Figure 6. Fluorescence spectra of bis-MSB nanoparticles and bis-MSB nanoparticles doped with naphthacene. Concentration of naphthacene: 0 (black dotted line), 4 (light green line), 6 (green solid line), 8 (darkt green solid line), and 10 mol. % (black solid line).

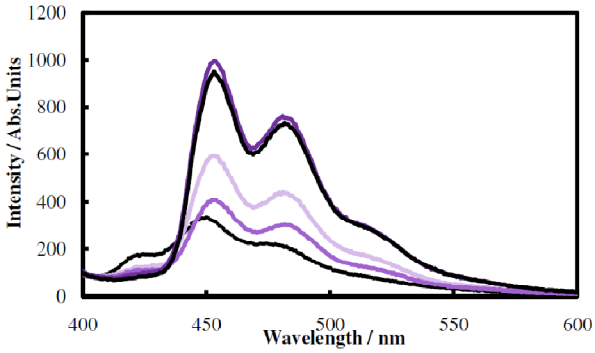

Figure 7. Fluorescence spectra of bis-MSB nanoparticles and bis-MSB nanoparticles doped with perylene. Concentration of perylene: 0 (black dotted line), 0.5 (the lightest purple dotted line), 1.0 (purple solid line), 1.5 (dark purple solid line), and 2.0 mol. % (black solid line).

Figures 8 and **9** show the dependences of fluorescence quantum yield on doping concentration for anthracene nanoparticles doped with naphthacene and anthracene nanoparticles doped with perylene, respectively. Fluorescence quantum yield of anthracene nanoparticles increased drastically from 0.10 by doping. The largest value of fluorescence quantum yield of anthracene nanoparticles doped with naphthacene was as high as 0.75 at a naphthacene concentration of 0.5 mol. %. The largest value of fluorescence quantum yield of anthracene nanoparticles doped with perylene was also as high as 0.75 at a perylene concentration of 0.25 mol. %.

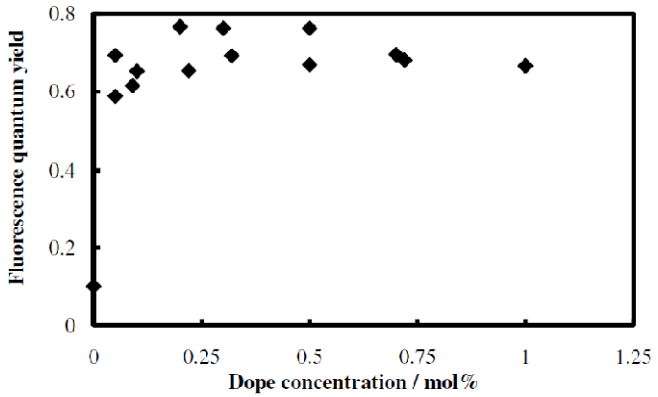

Figure 8. The dependence of fluorescence quantum yield of anthracene nanopariticles doped with naphthacene on dopant concentration.

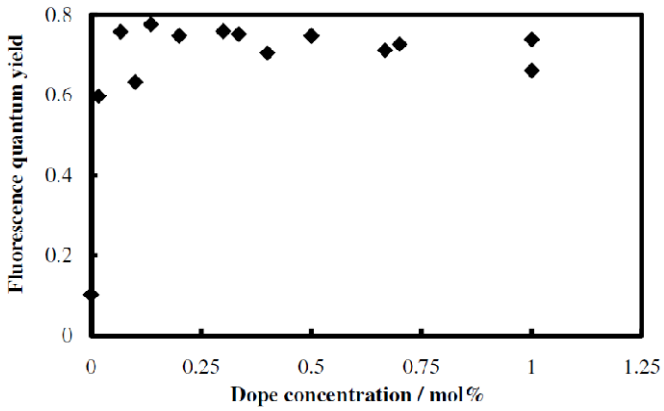

Figure 9. The dependence of fluorescence quantum yield of anthracene nanopariticles doped with perylene on dopant concentration.

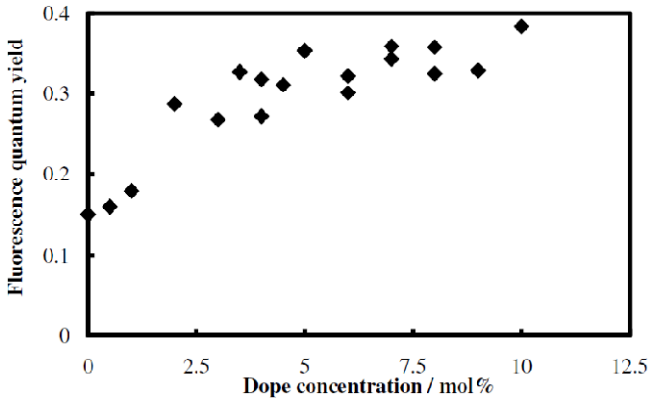

Figure 10. The dependence of fluorescence quantum yield of bis-MSB nanopariticles doped with naphthacene on dopant concentration.

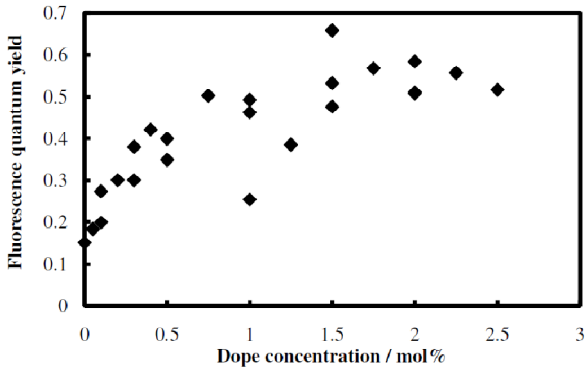

Figure 11. The dependence of fluorescence quantum yield of bis-MSB nanopariticles doped with perylene on dopant concentration.

Figures 10 and **11** show the dependences of fluorescence quantum yield on doping concentration for bis-MSB nanoparticles doped with naphthacene and bis-MSB nanoparticles doped with perylene, respectively. Fluorescence quantum yield of bis-MSB nanoparticles increased from 0.15 by doping. The largest value of fluorescence quantum yield of bis-MSB nanoparticles doped with naphthacene was about 0.35 at a naphthacene concentration of 7.5 mol. %. The largest value of fluorescence quantum yield of bis-MSB nanoparticles doped with perylene was about 0.55 at a perylene concentration of 2.0 mol. %.

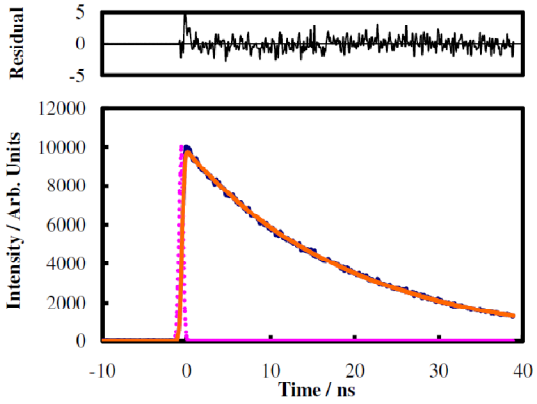

Figure 12. Fluorescence decay curve of anthracene nanoparticles doped with naphthacene and its simulation. The dope concentration of naphthacene: 0.5 mol. %. Fluorescence intensity (dark blue solid line), laser (pink dotted line), simulation (orange solid line).

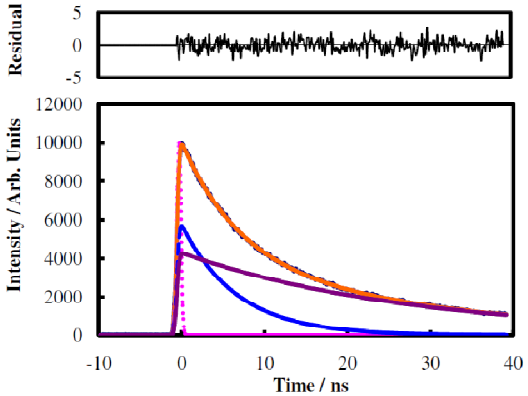

Figure 13. Fluorescence decay curve of anthracene nanoparticles doped with peylene and its simulation. The dope concentration of perylene: 0.5 mol. %. Fluorescence intensity (dark blue solid line), laser (pink dotted line), simulation (orange solid line), first exponential (blue dotted line), second exponential (dark red broken line).

Fluorescence decay curve of anthracene nanoparticles doped with naphthacene was single exponential (see **Figure 12**). On the other hand, fluorescence decay curve of anthracene nanoparticles doped with perylene was not single exponential (see **Figure 13**).We assumed double exponential response for the fluorescence of these nanoparticles. The results of all lifetime measurements are summarized in **Tables 1 – 4**.

Table 1. Fluorescence lifetimes of anthracene nanoparticles doped with naphthacene.

Concentration of naphthacene, mol. %	Fluorescence lifetime, ns	
	Fast(weight)	Slow(weight)
0	1.83 (94.1 %)	15.3 (5.9 %)
0.25	21.1(–)	– (–)
0.50	19.3(–)	– (–)
1.00	0.44 (15.8 %)	17.3 (84.2 %)

Table 2. Fluorescence lifetimes of anthracene nanoparticles doped with perylene.

Concentration of perylene,mol. %	Fluorescence lifetime, ns	
	Fast(weight)	Slow(weight)
0	1.83 (94.1 %)	15.3 (5.9 %)
0.25	8.71 (61.8 %)	33.7 (38.2 %)
0.50	6.68 (58.7 %)	28.0 (41.3 %)
1.00	5.77 (56.8 %)	22.2 (43.2 %)

Table 3. Fluorescence lifetimes of bis-MSB nanoparticles doped with naphthacene.

Concentration of perylene, mol. %	Fluorescence lifetime, ns	
	Fast(weight)	Slow(weight)
0	1.23 (81.9 %)	5.72 (18.1 %)
2.00	1.01 (25.3 %)	17.5 (74.7 %)
5.00	3.87 (16.4 %)	17.6 (83.6 %)
8.00	3.55 (18.6 %)	17.0 (81.4 %)

Table 4. Fluorescence lifetimes of bis-MSB nanoparticles doped with perylene.

Concentration of naphthacene, mol. %	Fluorescence lifetime, ns	
	Fast(weight)	Slow(weight)
0	1.23 (81.9 %)	5.72 (18.1 %)
0.10	3.49 (56.1 %)	11.1 (43.9 %)
1.00	3.07 (57.9 %)	10.5 (42.1 %)
2.00	3.79 (58.4 %)	11.7 (41.6 %)

On comparison between the results of anthracene nanoparticles doped with naphthacene and those of bis-MSB nanoparticles doped with naphthacene, we concluded that anthracene nanoparticles are good matrices for naphthacene; fluorescence quantum yields were higher and fluorescence lifetimes were longer in anthracene nanoparticles than in bis-MSB nanoparticles. Doping efficiency of naphthacene into bis-MSB nanoparticles seems very poor; probably high percentage of naphthacene cannot be doped into bis-MSB nanoparticles. For perylene, anthracene nanoparticles are also better matrices than bis-MSB nanoparticles.

However, high doping concentration into anthracene nanoparticles induced concentration quenching; dimer formation in a nanoparticle may have reduced fluorescence quantum yield at high dope concentration. In all four kinds of doped nanoparticles, energy transfer from a nanoparticle to a dopant molecule seems to be very fast and effective.

4. Conclusions

Fluorescence spectra, fluorescence quantum yields, and fluorescence lifetimes of anthracene nanoparticles doped with perylene, anthracene nanoparticles doped with naphthacene, bis-MSB nanoparticles doped with perylene, and bis-MSB nanoparticles doped with naphthacene, were measured. When doping nanoparticles with a dopant, fluorescence of nanoparticles was quenched and strong fluorescence of dopant was observed. Energy transfer from a nanoparticle to a dopant molecule was fast and efficient. Fluorescence quantum yields of both anthracene nanoparticles doped with naphthacene and anthracene nanoparticles doped with perylene were as high as 0.75 Fluorescence quantum yields of bis-MSB nanoparticles doped with naphthacene and that of bis-MSB nanoparticles doped with perylene were about 0.35 and about 0.55, respectively.

Acknowledgments

The authors thank Messrs. Okuzono, Yamamoto, and Maeda of Yamaguchi University for their experimental help.

References

1. H. Kasai, H. S. Nalwa, H. Oikawa, Sh. Okada, H. Matsuda, N. Minami, A. Kakuta, K. Ono, A. Mukoh, H. Nakanishi. A novel preparation method of organic microcrystals. Jpn. J. Appl. Phys.31(1992) L1132.
2. X.-M. Duan, T. Kimura, Sh. Okada, H. Oikawa, H. Matsuda, M. Kato, H. Nakanishi. Second-order hyperpolarizabilities of aromatic carboxylates without visible absorption.Jpn. J. Appl. Phys.34(1995) L1161.
3. H. Kasai, H. Kamatani, Sh. Okada, H. Oikawa, H. Matsuda, H. Nakanishi.Size-dependent colors and luminescence of organic microcrystals. Jpn. J. Appl. Phys.35(1996) L221.
4. H. Katagi, H. Kasai, Sh. Okada, H. Oikawa, K. Komatsu, H. Matsuda, Zh. Liu, H. Nakanishi. Size control of polydiacetylene microcrystals. Jpn. J. Appl. Phys.35(1996) L1364.
5. Y. Miyashita, Sh. Horino, H. Kasai, H. Oikawa, H. Nakanishi. Preparation and luminescence properties of organic phosphorescent nanoparticles. Jpn. J. Appl. Phys. 51(2012) 025002 1-5.
6. http://www.evidenttech.com/technology.
7. K. Takemura, K. Kasatani, Y. Morita, H. Okamoto, J. Kawamata. Two-photon absorption cross sections of phthalocyanine nanoparticles. Trans. Mater. Res.Soc. Jpn.33(2008) 931.
8. K. Kasatani.Third-order optical nonlinearities of organic nanoparticles.Trans. Mater. Res. Soc. Jpn.34(2009) 451.
9. K. Kasatani.Fluorescent organic nanoparticles. Trans. Mater. Res. Soc. Jpn.36(2011)421.
10. D. W. Marquardt.An algorithm for least-squares estimation of nonlinear parameters. J. Soc. Ind. Appl. Math.11(1963) 431.
11. D. V. o'Connor, W. R. Ware, J. C. Andre. Deconvolution of fluorescence decay curves. A critical comparison of techniques. J. Phys. Chem.83(1979) 1333.

ლურჯ-მწვანე წყალმცენარის *Spirulina platensis* ზოგიერთი თვისების შესწავლა

ნ. კუჭავა

ე. ანდრონიკაშვილის ფიზიკის ინსტიტუტი
ი. ჯავახიშვილის სახ. თბილისის სახელმწიფო უნივერსიტეტი
თბილისი, საქართველო
e.kuchava@mail.ru

მიღებულია 2013 წლის 24 იანვარს

ცნობილია, რომ ყველა სახის ცოცხალი ორგანიზმი თავის შემადგენლობაში შეიცავს ელემენტთა პერიოდული სისტემის თითქმის ყველა ელემენტს მიკრო- და მაკრორაოდენობით, რომლებიც გარკვეულ მონაწილეობას იღებს მათში მიმდინარე ფიზიოლოგიურ პროცესებში. ცნობილია, აგრეთვე, რომ როგორც სხვადასხვა ცოცხალი ორგანიზმის, ასევე მათი შემადგენელი ნაწილების ელემენტური შემადგენლობა და რაოდენობრივი შემცველობა ერთმანეთისაგან განსხვავდება. აღნიშნული საკითხი შესწავლილია ბევრ სამეცნიერო ნაშრომში, რომლებშიც ნაჩვენებია, რომ სიცოცხლისათვის აუცილებელ მიკროელემენტებს დღეისათვის წარმოადგენს Cr, Co, Cu, Fe, Zn, F, I, Mn, Mo, Ni, Se, Si, Sn და V. ქიმიურ ელემენტთა ფიზიოლოგიური როლის დადგენისათვის მეტად მნიშვნელოვანია ამა თუ იმ ბიოსისტემის თვისებებისა და მათში ქიმიური ელემენტების რაოდენობრივი შემცველობის გამოკვლევა. ამ მხრივ ყურადღებას იმსახურებს წყალმცენარეთა თვისებების შესწავლის საკითხი, კერძოდ, ჩვენი ინტერესების სფეროს განეკუთვნება ციანობაქტერია ლურჯ-მწვანე წყალმცენარის Spirulina-ის ერთერთი სახეობა Spirulina Platensis.

Spirulina platensis წარმოადგენს თანამედროვე ბიოტექნოლოგიის ერთ-ერთ მნიშვნელოვან ობიექტს. მას ამჟამად მსოფლიოში განსაკუთრებული ყურადღება ექცევა როგორც საკვების, სამკურნალო საშუალებების და დიეტური პროდუქტების ბიოლოგიურად აქტიურ დანამატს. მისი ათვისება ადვილად ხდება ადამიანისა და ცხოველთა ორგანიზმის მიერ, ამიტომ მან ფართო გამოყენება მოიპოვა მედიცინასა, ფარმაკოლოგიასა და სოფლის მეურნეობაში. Spirulina platensis მდიდარია ცილებით, ცხიმებით, ვიტამინებით, მაკრო- და მიკროელემენტებით. იგი კარგად იზრდება დედამიწის სუბტროპიკული და ტროპიკული ზონების ტუტოვან ტბებში. Spirulina platensis მრავალმხრივი გამოყენება განაპირობებს მისი დეტალურად შესწავლის საჭიროებას.

ე. ანდრონიკაშვილის ფიზიკის ინსტიტუტში აღნიშნულ წყალმცენარეზე გამოკვლევები ჩატარდა IPPAS B–265 ტიპის Spirulina platensis ბიომასის საშუალებით, რომელიც მიღებულ იქნა რუსეთის მეცნიერებათა აკადემიის კ. ტიმირიაზევის სახელობის მცენარეთა ფიზიოლოგიის ინსტიტუტიდან. აღნიშნული წყალმცენარის კულტივირება წარმოებს Zaroukh მკვებავ გარემოში (pH > 8), მუდმივი განათებისას (3500 ლუქსი), 30 – 34 °C ტემპერატურის დროს. ხდება უწყვეტი ბარბატირება და pH-ის კონტროლი. გახანგრძლივებულ ექსპერიმენტში pH-ის ცვლილებას ვაკონტროლებდით

თითქმის ყოველი დღის განმავლობაში. ექსპერიმენტის დასაწყისს ვთვლით ნულოვან დღედ. მეათე დღე არის დაკვირვების ბოლო დღე. მიღებული შედეგები წარმოდგენილია **ცხრილში 1**.

ცხრილი 1. pH-ის ცვლილება Spirulina platensis ბიომასის ზრდის მიხედვით .

დღე	0	3	4	5	6	7	8	10
pH-ის ცვლილება	8.87	9.96	10.03	10.17	10.33	10.79	10.93	11.10

როგორც **ცხრილიდან 1** ჩანს, Spirulina platensis ბიომასის ზრდის დროს მეოთხე – მერვე დღეების შუალედში pH მცირედ იცვლება, ხოლო მე-10 დღეს მისი მნიშვნელობაა 11.10. Spirulina platensis ბიომასის ზრდის 5 – 6 დღის შემდეგ, როცა წყალმცენარის ბიომასა მიაღწევს თავის მაქსიმალურ მნიშვნელობას, წარმოებს ბიომასის ცენტრიფუგირება 20 წთ-ის განმავლობაში 14000 *g*-ის დროს. მიღებული ბიომასა რამოდენიმეჯერ ირეცხება დისტილირებული წყლით და ილექება იგივე პირობებში. გასუფთავებული ბიომასის გამოშრობა ხდება ლიოფილიზაციის მეთოდით АКЛ-ტიპის დანადგარის მეშვეობით.

ცნობილია, რომ Zaroukh გარემო შეიცავს შემდეგ მაკრო- და მიკროელემენტებს: Na, Cl, N, Fe, K, S, Mg, C, P, Mn, Zn, Cu, Mo, Cr, Ni, W, Ti, Co, Ca, V, O, H. Spirulina platensis უჯრედების ზრდის პროცესში აღნიშნული წყალმცენარე მკვებავი გარემოდან ითვისებს მისთვის საჭირო ელემენტებს გარკვეული რაოდენობით, ამიტომ ერთ-ერთი მნიშვნელოვანი როლი ენიჭება წყალმცენარის ელემენტური შემადგენლობის შესწავლას. აღნიშნული საკითხის გარკვევაში აქტიურად მონაწილეობს სხვადასხვა ქვეყნის ბევრი სამეცნიერო-ტექნიკური ლაბორატორია. დიდი მნიშვნელობა აქვს შერჩეული საანალიზო მეთოდის მგრძნობიარობას, სიზუსტეს, აგრეთვე, საანალიზო ნიმუშში ერთდროულად რამოდენიმე ქიმიური ელემენტის რაოდენობრივი განსაზღვრის შესაძლებლობას.

მკვებავ გარემოში Spirulina platensis უჯრედების ზრდის პროცესში ქიმიური ელემენტების აკუმულაციის საკითხი შესწავლილია მრავალ სამეცნიერო შრომაში. მოკლედ შევეხებით ზოგიერთ მათგანს.

დამტკიცებულია, რომ Spirulina platensis გააჩნია მძიმე მეტალების აკუმულირების უნარი. მის მიერ Cd-ის იონების აკუმულაცია და ადსორბცია შესწავლილია [1] შრომაში. [2] შრომის ავტორებს შესაძლებლად მიაჩნიათ Spirulina platensis-ის გამოყენება კადმიუმით, ტყვიითა და ვერცხლისწყლით დაჭუჭყიანებული ჩამდინარე წყლების გასუფთავებისათვის. [3] სამუშაოში აღნიშნულია, რომ Spirulina platensis-ის უჯრედები წარმოადგენს ზოგიერთი დღეგრძელი რადიონუკლიდის (ცეზიუმი-137 და სტრონციუმი-90) ნატურალურ სორბენტს.

ჩატარებულია სპეციალური გამოკვლევა მკვებავ Zaroukh გარემოში სელენის, იოდის და ვერცხლისწყლის სხვადასხვა რაოდენობით დამატების დროს წყალმცენარის ბიომასის მიერ მათი აკუმულირების საკითხის შესასწავლად. დასაბუთებულია ზოგი

სამედიცინო პრეპარატის დამზადების შესაძლებლობა სელენით და იოდით გამდიდრებული Spirulina platensis-ის გამოყენებით [4].

Spirulina platensis-ის უჯრედების მკვებავ გარემოში ზრდის დინამიკაში ელემენტების – სელენი (IV) და ქრომი (III) – მოქმედება ცალკ-ცალკე და ერთდროულად, შესწავლილია [5] სამუშაოში. გამოვლენილია სელენისა (IV) და ქრომის (III) ანტაგონისტური ხასიათი მათი ერთდროული მოქმედებისას, რაც გამოიხატა სელენის (IY) აკუმულაციის პროცესის დათრგუნვით. აღნიშნული სამუშაო შესრულებულია ეპითერმალური ინსტრუმენტალური ნეიტრონული აქტივაციური ანალიზის მეთოდის საშუალებით IBR–2 ტიპის რეაქტორზე ქ. დუბნაში. [6 – 10] სამუშაოებში ატომურ-აბსორბციული სპექტრომეტრიისა (აას) და ინსტრუმენტალური ნეიტრონული აქტივაციური ანალიზის (ინაა) მეთოდების გამოყენებით Spirulina platensis-ის უჯრედების ლიოფილურად გამომშრალ ბიომასაში განსაზღვრულია Co, Ag, Cd, Cr, Ni, Cu, Pb, Mn, Zn, Fe, Mg და Na-ის კონცენტრაცია, აგრეთვე, Spirulina platensis-ის უჯრედების ზრდის დინამიკის დამოკიდებულება მკვებავ გარემოში შეყვანილი მისი რაოდენობისაგან. [11] შრომაში, სხვა საკითხებთან ერთად, განხილულია ქრომის სხვადასხვა ფორმის – ქრომი (III) და ქრომი (VI) – ურთიერთქმედება Spirulina platensis-ის უჯრედებთან ქრომის შესაბამისი ნაერთებით მკვებავი გარემოს დატვირთვისას. დადგენილ იქნა, რომ მისი უჯრედები მკვებავი გარემოდან ახდენს უპირატესად სიცოცხლისათვის აუცილებელი ქრომის (III) აკუმულირებას მის ტოქსიკურ ფორმასთან – ქრომი (VI) – შედარებით. შესაძლებელია, რომ ქრომი (III)-ის ადვილად ათვისება განპირობებული იყოს იმით, რომ ის იმყოფება ორგანულ ნივთიერებასთან (ძმარმჟავა) ნაერთში. [12] შრომაში გაკეთებულია დასკვნა, რომ ქრომის (III) და (VI) კონცენტრაციები Spirulina platensis-ის ბიომასაში არის მკვებავ გარემოში მათი კონცენტრაციების პროპორციული სიდიდე. სპეციალურად შემუშავებული მეთოდიკების საშუალებით [13] შრომაში განხილულია Spirulina platensis-ის ბიომასაში სიცოცხლისათვის ისეთი აუცილებელი ქიმიური ელემენტების აკუმულირების შესაძლებლობის საკითხი, როგორიცაა სელენი, ქრომი და იოდი.

ჩვენს მიზანს შეადგენს Spirulina platensis-ის უჯრედოვანი ზრდის პროცესში მკვებავი გარემოდან ბიომასის მიერ ბიოგენური და ტოქსიკური ელემენტების აკუმულაციის საკითხის შესწავლა, რისთვისაც ჩატარებულ იქნა ორი სახის ექსპერიმენტი. ორივე შემთხვევაში შერჩეულ იქნა ჩასატვირთ ელემენტთა გარკვეული რაოდენობა, რომელიც უზრუნველყოფს ამ ელემენტთა აკუმულაციას Spirulina platensis-ის ბიომასის ზრდით და მისი ხარისხის შენარჩუნებით. ყველა შემთხვევაში Spirulina platensis-ის სუსპენზიის ნიმუშების ყოველდღიურმა მიკროსკოპულმა კონტროლმა გვიჩვენა, რომ აღნიშნულ ექსპერიმენტებში Spirulina platensis-ის უჯრედები ციტოლოგიურად არ განსხვავდება საკონტროლოსაგან. მხედველობაში უნდა იქნეს მიღებული ის გარემოება, რომ წყალმცენარეთა მიერ მეტალთა აკუმულაციის პროცესი შეიძლება წარიმართოს სხვადასხვანაირად, რასაც განაპირობებს ამ პროცესების მექანიზმი. აქედან გამომდინარე, ჩვენი ყველა ექსპერიმენტის შემთხვევაში დაცულ იყო ერთნაირი სტანდარტული პირობები (განათება, ტემპერატურა და სხვ.).

ორივე ექსპერიმენტში ბიოგენური და ტოქსიკური ელემენტების კონცენტრაცია მკვებავ გარემოში მათ ჩატვირთვამდე და ჩატვირთვის შემდეგ შეფასებულ იქნა აას მეთოდის საშუალებით. ბიოგენური ელემენტებიდან ჩვენს მიერ შერჩეულ იქნა შემდეგი ელემენტების: Co, Cu, Zn, Ni, Mn და Fe, გარკვეული კონცენტრაცია. Spirulina platensis-ის

ბიომასის ზრდის დინამიკაში მკვებავ გარემოში ბიოგენური ელემენტების კონცენტრაცია ჩატვირთვამდე და ჩატვირთვის შემდეგ წარმოდგენილია **ცხრილში 2**.

ცხრილი 2. ბიოგენურ ელემენტთა კონცენტრაცია Spirulina platensis-ის ბიომასაში ზრდის დინამიკაში მკვებავ გარემოში მათ ჩატვირთვამდე და ჩატვირთვის შემდეგ (მკგ / გ მშრალი წონა).

ზრდის დღეები *	ელემენტთა კონცენტრაცია (მკგ / გ მშრალი წონა)					
	Co	Cu	Zn	Ni	Mn	Fe
0	0.64	3.93	15	17	23	1237
1	0.92	4.80	16	17	22	1232
2	0.81	5.80	12	14	24	1178
3	0.86	6.20	8	16	24	1214
4	0.89	6.06	9	16	24	1217
7	0.97	8.50	7	17	27	1282
ცდომილება, %	20	10	10	20	15	10

* 0 – ელემენტთა კონცენტრაცია მკვებავ გარემოში ჩატვირთვამდე.

როგორც **ცხრილიდან 2** ჩანს, ექსპერიმენტის მე-7 დღეს Co-ის შემცველობა ცოტათი მომატებულია, ხოლო Cu-ის თითქმის 2-ჯერაა გაზრდილი. Zn-ის რაოდენობა კი ამდენჯერვეა შემცირებული. რაც შეეხება Ni, Mn და Fe-ს მათი შემცველობა თითქმის ისეთივეა, როგორიც მკვებავ გარემოში ელემენტების ჩატვირთვამდე იყო.

ტოქსიკური ელემენტების – Ag, Cd, Cr და Pb-ის – განაწილების საკითხი Spirulina platensis-ის ბიომასაში უჯრედული ზრდის დინამიკაში მკვებავ გარემოში ტოქსიკური

ელემენტების ჩატვირთვამდე და ჩატვირთვის შემდეგ შესწავლილია **ცხრილში 3** მოცემული მნიშვნელობების მიხედვით.

ცხრილი 3. ტოქსიკურ ელემენტთა კონცენტრაცია Spirulina platensis-ის ბიომასაში ზრდის დინამიკაში მკვებავ გარემოში მათ ჩატვირთვამდე და ჩატვირთვის შემდეგ (მკგ / გ მშრალი წონა).

ზრდის დღეები *	ელემენტთა კონცენტრაცია (მკგ / გ მშრალი წონა)			
	Ag	Cd	Cr	Pb
0	0.8	0.95	2.4	21
1	1.5	0.91	2.6	95
2	1.8	0.57	9.0	157
3	1.8	0.55	21	183
4	2.0	0.57	21	193
ცდომილება, %	20	20	20	20

* 0 – ელემენტთა კონცენტრაცია მკვებავ გარემოში ჩატვირთვამდე.

როგორც **ცხრილიდან 3** ჩანს, აღნიშნული ტოქსიკური ელემენტების მკვებავ გარემოში ჩატვირთვამ გამოიწვია Cr-ისა და Pb-ის რაოდენობის ზრდა თითქმის 9-ჯერ, Ag-ისა – მცირედ (2.5–ჯერ), ხოლო Cd–ის შემცველობა ცოტათი შემცირდა (1.7–ჯერ).

შესწავლილ იქნა, აგრეთვე, Cu, Mn, Zn, Mg და Na–ის კონცენტრაცია Spirulina platensis-ის ბიომასაში ზრდის დინამიკის მე-5 დღეს ინაა-ის ფარდობითი მეთოდის გამოყენებით, რომელიც საშუალებას გვაძლევს გამოვიკვლიოთ ქიმიურ ელემენტთა შემცველობა ნიმუშის დაუშლელად, რის გამოც შესაძლებელია აღნიშნული ნიმუშის გამოყენება მრავალჯერადი დასხივებისათვის. აღნიშნული საგრძნობლად ამცირებს ანალიზისათვის საჭირო მასალის რაოდენობას. Spirulina platensis-ის ლიოფილურად გამომშრალი ბიომასის ნეიტრონებით დასხივებისათვის გამოყენებულ იქნა

ე. ანდრონიკაშვილის ფიზიკის ინსტიტუტის ნეიტრონული გამამრავლებელი ПС–=1. ნეიტრონების მაქსიმალური ნაკადი აღნიშნული გამამრავლებლის ვერტიკალურ არხში, სადაც სხივდება საანალიზო ნიმუში, შეადგენს $2.3 \cdot 10^6$ ნ / სმ^2 · წმ–ს. უნდა აღინიშნოს, რომ ნეიტრონების გამამრავლებელში უზრუნველყოფილია ნეიტრონების ნაკადის სტაბილურობა. სისტემის მუშაობის პროცესში დასხივებული ნიმუშების ტემპერატურა არ აღემატება ოთახის ტემპერატურას, განსხვავებით ბირთვული რეაქტორის არხებისაგან, რომლებშიც დასხივებისას ბიოლოგიური ნიმუში განიცდის რამოდენიმე ათეული გრადუსი ტემპერატურის ზემოქმედებას. ნეიტრონებით დასხივებისათვის Spirulina platensis-ის გარკვეული რაოდენობის ბიომასა მოთავსებულ იქნა პოლიეთილენისაგან დამზადებულ მჟავებითა და დისტილატით რამდენიმეჯერ დამუშავებულ სპეციალურ კონტეინერებში. ასეთივე სახით მომზადდა აღნიშნულ ელემენტთა შესადარებელი ეტალონებიც. ელემენტთა კონცენტრაცია შეფასებულ იქნა მათი შედარებით დღემოკლე რადიონუკლიდების: Cu-64, Mn-56, Zn-69m, Mg-27 და Na-24-ის საშუალებით. მიღებული შედეგები წარმოდგენილია **ცხრილში 4**.

ცხრილი 4. ქიმიურ ელემენტთა კონცენტრაცია
Spirulina platensis-ის ბიომასაში (მკგ / გ მშრალი წონა).

ელემენტი	Cu	Mn	Zn	Mg	Na
კონცენტრაცია	18	30	32	2500	18300
ცდომილება, %	20	7	12	15	7

როგორც **ცხრილიდან 4** ჩანს, Spirulina platensis-ის ბიომასაში ჩვენს მიერ ამჯერად განსაზღვრული ელემენტებისაგან Cu არის ყველაზე მცირე რაოდენობით, Mn-ისა და Zn-ის შემცველობა თითქმის ერთნაირია, ხოლო აღსანიშნავია Mg-ისა და Na-ის მაკრორაოდენობები.

ლურჯ-მწვანე წყალმცენარის Spirulina platensis სხვა თვისებებთან ერთად საჭიროდ ვთვლით უაღრესად მოკლედ შევეხოთ მის მიერ ნანონაწილაკების წარმოქმნის უნარს.

ნანონაწილაკების სინთეზი მეცნიერებისა და ტექნიკისათვის წარმოადგენს შედარებით ახალ სფეროს. ამ მიზნით ინტერესის საგანს წარმოადგენს მიკროორგანიზმები, რომელთაც ახასიათებს გარემოში არსებულ არაორგანულ იონებზე ზემოქმედების უნარი. დღეისათვის ცნობილი ნანონაწილაკების წარმომქმნელი მიკროორგანიზმების რაოდენობა მცირეა. შეიძლება დასახელდეს მხოლოდ რამოდენიმე მათგანი, რომელთა საშუალებით შეიძლება მიღებულ იქნეს ქიმიური ელემენტების ვერცხლის, ოქროს, კადმიუმის, ცირკონიუმის, ტიტანის და ნიკელის ნანონაწილაკები.

გარკვეული ქიმიური შემადგენლობისა და ზომის ნანონაწილაკების სინთეზი დამოკიდებულია არა მხოლოდ ორგანიზმის სახეობაზე (მაგალითად, ბაქტერიის

სახეობა), არამედ ექსპერიმენტის პირობებზეც (მაგალითად, ბაქტერიის შემადგენლობა, მეტალების ბაქტერიასთან ინკუბაციის პირობები და სხვ.).

აღმოჩნდა, რომ ნანონაწილაკების მისაღებად საინტერესო მიკროორგანიზმს წარმოადგენს Spirulina platensis, რომელსაც გააჩნია ვერცხლისა და ოქროს ნანონაწილაკების წარმოქმნის უნარი. დადგენილ იქნა, რომ Spirulina platensis-ის ბიომასაში აკუმულირებული ვერცხლის კონცენტრაცია მცირდება მასზე ვერცხლის იონების მოქმედების დროის გაზრდით. შეიძლება ჩაითვალოს, რომ ნანონაწილაკების მიღება ხდება უჯრედებს გარეთ [14, 15].

[16] სამუშაოში Spirulina platensis-ის ბიომასა გამოყენებულ იქნა ოქროს ნანონაწილაკების მისაღებად. შერჩეულ იქნა $HAuCl_4$-ის სხვადასხვა დოზა და დროის სხვადასხვა ინტერვალი. დადგენილ იქნა, რომ 1.5 – 2 დღის შემდეგ წარმოქნილ იქნა ოქროს სფერული ფორმის ნანონაწილაკები ზომით 8 – 40 ნმ (საშუალოდ 20 – 30 ნმ). გაკეთებულია დასკვნა, რომ ოქროს ნანონაწილაკებით გაჯერებული Spirulina platensis-ისs ბიომასა შეიძლება გამოყენებულ იქნეს სამედიცინო, ფარმაცევტული და ტექნოლოგიური მიზნებისათვის. დამტკიცდა, რომ Spirulina platensis-ის მიერ აკუმულირებული ოქროს ნანონაწილაკების კონცენტრაცია რამოდენიმე დღის განმავლობაში სწრაფად გაიზარდა. სხვა ბაქტერიებთან ერთად, Spirulina platensis გამოყენებულია ოქროსა და ვერცხლის ნანონაწილაკების მიკრობული სინთეზის ბიოტექნოლოგიის სრულყოფისათვის [17]. შესწავლილია, აგრეთვე, ბაქტერიებისა და მიკროწყალმცენარეების საშუალებით მიღებული ოქროსა და ვერცხლის ნანონაწილაკების მიკრობული სინთეზის მედიცინაში გამოყენების საკითხები [18].

ჩვენი გამოკვლევები ზემოთ აღნიშნული მიმართულებით გრძელდება. იმედი გვაქვს, რომ მიღებულ იქნება სასურველი პარამეტრების ნანონაწილაკები, თუ შექმნილი იქნება სათანადო სამეცნიერო და ტექნიკური ბაზა [14, 15].

შეიძლება დავასკვნათ, რომ შესწავლილ იქნა თანამედროვე ბიოტექნოლოგიის ერთ-ერთი საინტერესო ლურჯ-მწვანე წყალმცენარის Spirulina platensis ზოგიერთი თვისება, კერძოდ, წყალმცენარის უჯრედული ზრდის პროცესში მკვებავი გარემოდან ბიოგენური და ტოქსიკური ქიმიური ელემენტების აკუმულირების უნარი, აგრეთვე, Spirulina platensis-ის ლიოფილურად გამომშრალ ბიომასაში სპილენძის, მარგანეცის, თუთიის, მაგნიუმის და ნატრიუმის შემცველობა. მოკლედ იქნა განხილული Spirulina platensis-ის მიერ ვერცხლისა და ოქროს ნანონაწილაკების წარმოქმნის შესაძლებლობა.

ავტორი თავის სასიამოვნო მოვალეობად თვლის მადლობა გადაუხადოს ა. ბელოკობილსკის, ე. გინტურსა და ა. ხიზანიშვილს ექსპერიმენტებში მონაწილეობისათვის, ხოლო ა. რჩეულიშვილს – აას-ის მეთოდით ზემოთაღნიშნულ წყალმცენარეში ზოგიერთი ქიმიური ელემენტის შემცველობის განსაზღვრისათვის.

მითითებები

1. A. Khizanishvili, A. Belokobilsky, E. Ginturi, N. Kuchava, A. Rcheulishvili. In: Workbook of the 8th Int. Conf. Pharmacy & Appl. Physical Chem. 2004, Monte Verita: Stefano Franscini, PO 24.
2. P. Jonson, A. Shubert. Nutr. Rep. Int., 1986, 34, 6, 1063-1071.
3. L. Loseva, Y. Dardinskaya. In: Res. Inst. Rad. Med. (6th Int. Cong. Appl. Algology). 1993, Czech Republic.

4. L. M. Mosulishvili, E. I. Kirkesali, A. I. Belokobilsky, A. I. Khizanishvili, M. V. Frontasyeva, S. S. Pavlov, S. P. Gundorina. J. Pharmac. & Biomed. Anal., 2002, 30, 1, 87-97.
5. A. I. Belokobilsky, E. N. Ginturi, N. E. Kuchava, E. I. Kirkesali, L. M. Mosulishvili, M. V. Frontasyeva, S. S. Pavlov, N. G. Aksenova. J. Radioanal. & Nucl. Chem., 2004, 259, 1, 65-68.
6. N. E. Kuchava, A. I. Belokobilsky, V. Ya. Kintsurashvili, E. N. Ginturi, L. M. Mosulishvili. Radiation Studies, 2000, 9, 80-86.
7. N. Kuchava, E. Ginturi,V. Kintsurashvili. Bull. Georg. Acad. Sci., 2003, 168, 2, 36-39.
8. N. Kuchava. Bull. Georg. Acad. of Sci., 2004, 169, 3, 490-492.
9. N. Kuchava, E. Ginturi. Bull. Georg. Acad. Sci., 2006, 173, 1, 73-75.
10. N. Kuchava, E. Ginturi, E. Gelagutashvili, N. Bagdavadze, N. Sapozhnikova. Proc. Georg. Acad. Sci. (Biol. Ser.), 2008, 34, 5-6, 321-325.
11. Л. М. Мосулишвили, А. И. Белокобильский, Е. И. Киркесали, А. И. Хизанишвили, Э. Н. Гинтури, Н. Е. Кучава, М. В. Фронтасьева, С. С. Павлов, Н. Г. Аксенова. В кн.: Препринт П–18–2008–8. 2008, Дубна: ОИЯИ, 11.
12. M. V. Frontasyeva, S. S. Pavlov, N. G. Aksenova, L. M. Mosulishvili, A. I. Belokobilsky, E. I. Kirkesali, E. N. Ginturi, N. E. Kuchava. J. Anal. Chem., 2009, 64, 7, 746-749.
13. M. V. Frontasyeva, S. S. Pavlov, L. M. Mosulishvili, E. I. Kirkesali, E. N. Ginturi, N. E. Kuchava. Ecolog. Chem. & Eng., 2009, 16, 53, 3-8.
14. ნ. წიბახაშვილი, ა. რჩეულიშვილი, ე. გინტური, ნ. კუჭავა, ნ. ბაღდავაძე, ვ. გაბუნია. კრებულში: 1-ლი საერთ. კონფ. "ნანოქიმია – ნანოტექნოლოგიები" თეზისები. 2010, თბილისი: წმ. ანდრია პირველწოდებულის სახ. ქართ. უნივ., 37-38.
15. N. Tsibakhashvili, T. Kalabegishvili, V. Gabunia, E. Ginturi, N. Kuchava, N. Bagdavadze, D. Pataraya, M. Gurielidze, D. Gvardjaladze, L. Lomidze. Nano Studies, 2010, 2, 179-182.
16. T. Kalabegishvili, I. Murusidze, E. Kirkesali, A. Rcheylisvili, E. Ginturi, E. Gelagutashvili, N. Kuchava, N. Bagdavadze, D. Pataraya, M. Gurielidze, G. Tsersvadze, V. Gabunia. Nano Studies, 2012, 5, 127-136.
17. T. Kalabegishvili, I. Murusidze, E. Kirkesali, A. Rcheylisvili, E. Ginturi, E. Gelagutashvili, N. Kuchava, N. Bagdavadze, D. Pataraya, M. Gurielidze, L. Lomidze, D. Gvardjaladze. In: Abs. Int. Sci. Sem. "Neuroplatility: Neuros Substrates for Health and Disease. Nev Approches for Research". 2012, Tbilisi: ISTS, 29-30.
18. T. L. Kalabegishvili, I. G. Murusidze, E. I. Kirkesali, A. N. Rcheylisvili, E. N. Ginturi, E. S. Gelagutashvili, N. E. Kuchava, N. B. Bagdavadze, D. T. Pataraya, M. A. Gurielidze, M. V. Frontasyeva, I. I. Zinicovskaia, S. S. Pavlov, V. T. Gristina. J. Life Sci. – has been submitted.

EFFECT OF CHROMATE ON DNA OF *Arthrobacter globiformis*

O. Rcheulishvili [1, 2], N. Datukishvili [1, 3], I. Gabriadze [3],
T. Kutateladze [3], D. Pataraya [4], M. Gurielidze [4], N. Metreveli [1]

[1] Ilia State University
Tbilisi, Georgia
olia.rcheulishvilili.1@iliauni.edu.ge
[2] E. Andronikashvili Institute of Physics
I. Javakhishvili Tbilisi State University
Tbilisi, Georgia
[3] I. Beritashvili Center of Experimental Biomedicine
Tbilisi, Georgia
[3] S. Durmishidze Institute of Biochemistry and Biotechnology
Agricultural University of Georgia
Tbilisi, Georgia

Accepted April 10, 2013

1. Introduction

The environmental contamination with chromium is a worldwide problem. The toxicity of chromium is a function of oxidation state. The hexavalent form of chromium, Cr (VI), which typically exists as the oxyanion chromate (CrO_4^{2-}), has a high solubility and toxicity. In contrast, the reduced form of chromium, trivalent Cr (III), is less toxic and less harmful [1]. Indigenous bacteria can be successfully used to reduce Cr (VI) to Cr (III) [2, 3]. Today, a number of these bacteria have been studied and a molecular understanding of this important microbial process has been gained for some of them. The molecular analysis of chromate resistance determinants in chromate-tolerant bacteria has revealed significant variability and inconsistency of determinant location in genome, in particular: bacterial chromate resistance is generally associated with plasmids, but it can also be related to found on chromosomal DNA, or it could be related to both [4 – 7]. The particular resistance determinant appears to be specific for geographical sites [8].

In last years, several strains of *Arthrobacter* genera isolated from polluted basalts from Georgia were examined for their ability to reduce and detoxify Cr (VI) under aerobic conditions [9 – 12]. Our experiments showed that surface biomolecules (especially diol-rich polysacharides) of these gram-positive bacteria are very important for the chromium biomineralization process [10]. It was also demonstrated that chromate stimulates significant changes in the bacterial cell wall and cell capsule [12]. However the genetic basis of these processes has not been evaluated yet. Here we report the effect of chromate on the DNA of *Arthrobacter globiformis* – one of those basalt-inhabiting bacteria that are tolerant to very high

concentrations of Cr (VI) (more than 1000 mg / l). Recently, we have established that the formation of Cr (III) complexes and uptake of chromium in *Arthrobacter globiformis* is dose-dependent [13].

2. Experimental Procedures

2.1. Chemicals, bacterial growth conditions and sample preparation

All chemicals were ACS-reagent grade and purchased from Sigma (St. Louis, MO, USA).

The bacterial cells were grown aerobically in 250 ml Erlenmayer flasks at 21 °C. The cells were grown with constant shaking in a liquid medium (at a speed of 100 rpm), as described previously [13]: 10 g of glucose, 10 g of peptone, 1 g of yeast extract, 2 g of caseic acid hydrolysate, 6 g of NaCl and 1 l of distilled water.

Arthrobacter globiformis cells were grown in the medium without Cr (VI) (control bacterium) and with different concentrations of Cr (VI) (50, 100, 200 mg / l). Cr (VI) (as K_2CrO_4) was added into the cell culture at different phases of growth. Prior to the measurements, these bacterial cells were harvested at various time points (14, 22, 38, 62 h) by centrifugation (10 000 rpm, 15 min, 4 °C). The growth of bacteria was assessed spectrophotometrically at 600 nm. A subsequent dilution method was used to determine quantitatively of chromium (VI)-resistant live cells [14, 15].

2.2. DNA extraction

Genomic DNA was extracted using a modified phenol-chloroform method as follows: 5.4 ml bacterial cells were harvested by centrifugation at 12 000 *g* for 5 min. The cell pellet was resuspended in 570 µl of TE buffer (10 mM Tris-HCl, pH 7.0, 1 mM Na_2 EDTA), then 30 µl of 10 % SDS and 3 µl of Proteinase K (20 mg / ml) was added and incubated at 37 °C for 2 h to remove the protein component.

After incubation, 100 µl of 5 M NaCl and the equal volume of chloroform was added and centrifuged. After centrifugation, the supernatant was extracted with an equal volume of phenol / chloroform (1 : 1). DNA was precipitated by 0.6 V of isopropanol and centrifuged at 16 000 *g* for 30 min. The pellet was washed by 70 % ethanol, dried and dissolved in 200 µl of 10 mM Tris-HCl, pH 7.0.

Plasmid DNA was isolated from 100 ml cell suspension by modified alkaline lysis according to Brandsch & Decker [14] or from 3 ml cell suspension by QIA prep Spin Miniprep Kit (Qiagen).

2.3. Agarose gel electrophoresis

Both the genomic and plasmid DNA were analyzed by agarose gel electrophoresis using 1.0 % of agarose (Promega) gels. Electrophoresis was performed in 1 × TBE (Tris-Borate EDTA) buffer containing 1 µg / ml of Ethidium Bromide (EtBr). After electrophoresis the DNA bands were visualized and photographed by digital still camera (DSC–S600, Sony).

3. Results and discussion

It is worth mentioning that, despite the prevalence of *Arthrobacter* in the environment, little is known about their plasmids [7]. Earlier the plasmids of circular and linear forms and different sizes were found in different *Arthrobacter* species [7, 16]. The plasmid DNA was identified in some strains of *Arthrobacter globiformis* [17, 18], however no plasmid DNA was found in one of the strains of *Arthrobacter globiformis* from the D.S.M. Culture Collection (Gottingen, FRG) [16].

At the first stage of our experiments, a search for the presence of plasmid DNA in *Arthrobacter globiformis* 151 B was performed. For this purpose, we used the alkaline lysis method according to Brandsch & Decker, which allows isolating high molecular weight plasmids from *Arthrobacter* species [16]. Additionaly, we applied QIA prep Spin Miniprep Kit for checking the obtained results. Both methods allowed us to isolate the plasmid DNA in reasonable yield from *Arthrobacter globiformis* 151 B control cells, but the alkaline lysis resulted in a larger amount of DNA (**Figure 1 A**). Agarose gel electrophoresis of the plasmid and genomic DNA extracts from *Arthrobacter globiformis* 151 B together with DNA of bacteriophage λ exhibited that the molecular mass of plasmid DNA is less than both genomic DNA and λ DNA in size of 48.5 kb (**Figure 1 B**). Existance of one DNA bend in all plasmid DNA extracts indicates about linear form of plasmid (**Figure 1** – *lane 3*).

Figure 1. (A) Plasmid DNA extracted from *Arthrobacter globiformis* 151 B, grown in the medium without Cr (VI) for 14 h, by *lane 1* alkaline lysis (5 µl from 200 µl extract) and *lane 2* QIA prep Spin Miniprep Kit (5 µl from 50 µl extract). (B) Plasmid and genomic DNA extracted from *Arthrobacter globiformis* 151 B grown in the medium without Cr (VI) for 14 h *lane 1* DNA of bacteriophage λ, *lane 2* plasmid DNA and *lane 3* genomic DNA.

Partial characterization by restriction digestion clearly demonstrated differences in restrituion profiles of the plasmid and genomic DNA for all of the three endonucleases used in this study: Eco R 1, Bam H 1, and Hind III (**Figure 2**). The results obtained indicate that *Arthrobacter globiformis* 151 B harbors a linear plasmid with molecular size less than 48.5 kb. However further investigation is needed for comprehensive characterization of the plasmid molecule.

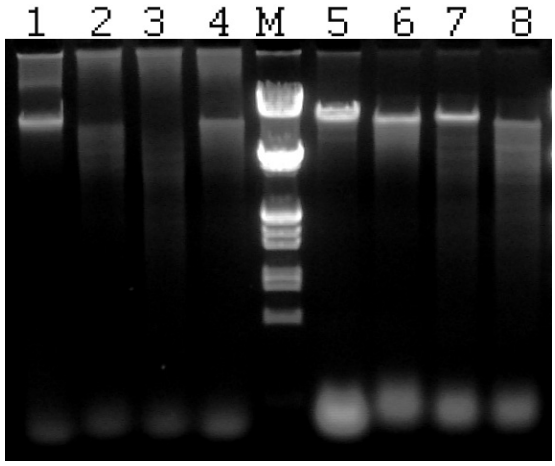

Figure 2. Restriction digestion of plasmid (*lanes 2 – 4*) and genomic (*lanes 6 – 8*) DNA from *Arthrobacter globiformis* 151 B. *lane 1* intacts plasmid DNA; *lane 5* intacts genomic DNA. DNA digected by restriction endonucleases: *lanes 2*, *6* Eco R 1; *lanes 3*, *7* Bam H 1; *lanes 4, 8* Hind III. M – molecular weight marker: 21, 5, 4, 3.5, 2, 1.9, 1.6, 1.4, 0.9, 0.8, 0.5 kb.

In the second set of experiments, the effect of chromate on the extraction of the plasmid DNA of *Arthrobacter globiformis* was investigated (**Figure 3**). **Figure 3 A** represents the picture of agarose gel electrophoresis of plasmid DNAs isolated from the cells grown in the mediums with different concentration of Cr: 0, 50, 100, and 200 mg / l. The electrophoregram shown in **Figure 3 A** demonstrates that the plasmid DNA was missed after exposing the cells even to 50 mg / l of Cr (VI) for 14 h (**Figure 3 A**, *lane 2*).

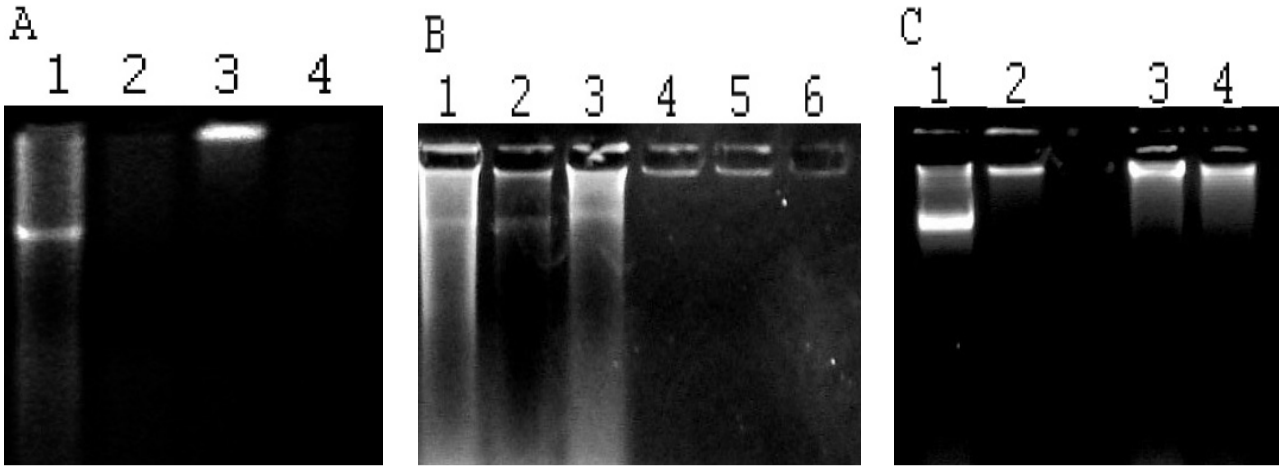

Figure 3. The Influence of chromate concentration, Cr (VI) exposure time and the time of Cr (VI) addition on the plasmid DNA from *Arthrobacter globiformis* 151 B. The plasmid DNA (10 μl from 200 μl extract) from the cells grown. (A) For 14 h with Cr (VI) concentration: *lane 1* – 0 (control), *lane 2* – 50, *lane 3* – 100, *lane 4* – 200 mg / l. (B) Without Cr (VI): *lane 1* – 14, *lane 2* – 38, *lane 3* – 62 h; and exposed to Cr (VI) (50 mg / l): *lane 4* – 14, *lane 5* – 38, *lane 6* – 62 h. (C) 62 h: *lane 1* – without Cr (VI) and with Cr (50 mg / l) added at different stages of growth: *lane 2* – 6, *lane 3* – 12, *lane 4* – 24 h.

In further experiments, we examined Cr (VI) exposure of different duration (from 14 to 62 h) (**Figure 3 B**). Besides, Cr (VI) was added to the bacterial cells at different phases of their growth (exponential and stationary phases of growth) (**Figure 3 C**). In each set of experiments control bacteria were grown without chromate for the same time. However no plasmid was detected in the bacterial cells treated with chromate. It is worth mentioning that, the number of bacterial cells hardly decreased after exposing to chromate (within the range of 50 – 200 mg / l of Cr (VI) (**Figurees 4** and **5**). All the results obtained were justified for the plasmid DNA extracts obtained by both methods applied.

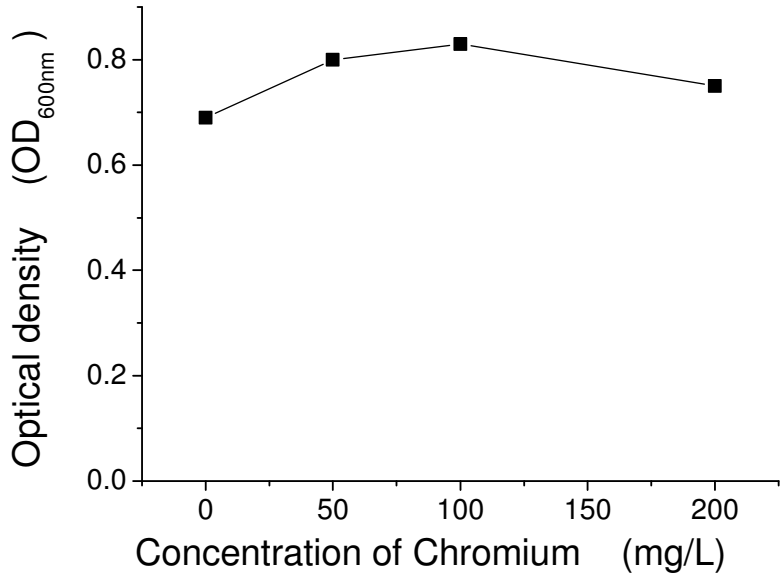

Figure 4. The Influence of chromate concentration on the *Arthrobacter* cell growth. The cells of *Arthrobacter globiformis* were grown in the 100 ml mediums with different concentration of Cr: 0, 50, 100, and 200 mg / l. The bacterial growth was estimated spectrophotometrically at 600 nm.

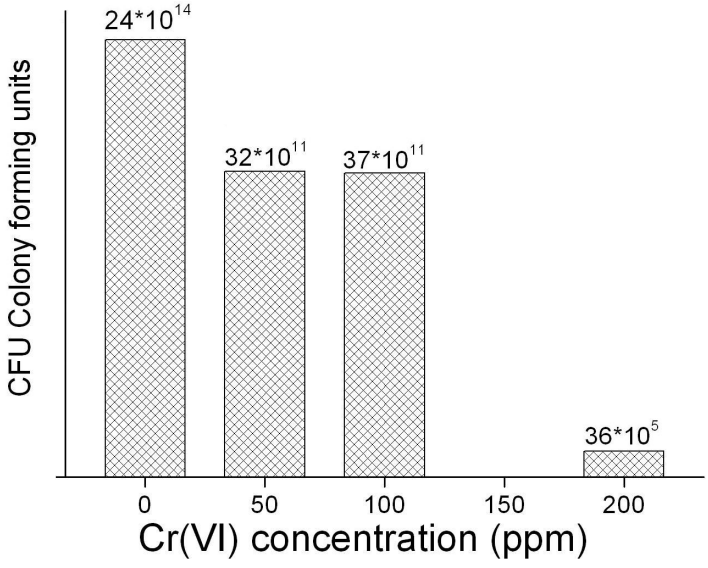

Figure 5. The Influence of chromate concentration on the *Arthrobacter* cell growth.

The study of the extracted genomic DNA by agarose gel electrophoresis also revealed that the increasing chromate concentration in the medium adversely affected the yield of the genomic DNA (**Figure 6**).

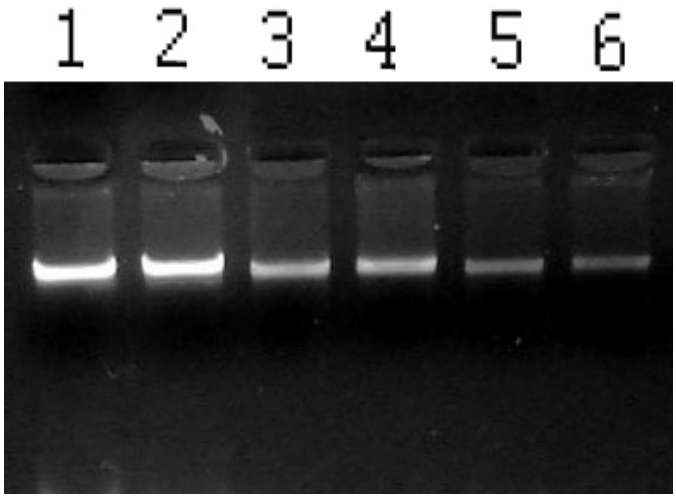

Figure 6. The influence of chromate concentration on the genomic DNA from *Arthrobacter globiformis* 151 B. The genomic DNA (5 μl from 200 μl extract) from the cells grown: *lanes 1 – 2* without Cr, *lanes 3 – 4* with Cr (50 mg / l), *lanes 5 – 6* with Cr (100 mg / l).

Thus, our results demonstrate that chromate is a critical factor influencing the extraction of both genomic and plasmid DNA from chromate-tolerant bacterium *Arthrobacter globiformis* 151 B. At present we cannot say whether the plasmid found is responsible for the Cr (VI) resistance of *Arthrobacter globiformis* 151 B. These experiments are underway.

A subsequent dilution method was used to determine quantitatively of chromium (VI)-resistant cells. In control dishes (bacterial growth without chromium) possibility of counting Colony Forming Units (CFU) was possible on 13th dilution and it was 241×10^{13}. By the concentration 50 mg / l Cr (VI) viable bacterial CFU number was 340×10^{10}. 100 mg / l Cr (VI) – 372×10^{10} CFU, 200 mg / l Cr (VI) – 358×10^{4} CFU. By the higher concentrations of chromium in growth medium, number of bacterial cells is decreased significantly.

Acknowledgments

This study was supported by GNSF (Grant GNSF / PRES 08 / 6-342) and STCU / GNSF (Grant 4330 / 131).

References

1. R. Codd, C. T. Dillon, A. Levina, P. A. Lay. Studies on the genotoxicity of chromium: From test tube to the cell. Coord Chem Rev., 2001, 216-217, 537-582.
2. J. M. Chen, O. J. Hao. Microbial chromium (VI) reduction. Crit. Rev. Environ. Sci. &Technol., 1998, 28, 219-251.
3. D. H. Nies. Microbial heavy-metal resistance. Appl. Microbiol. Biotechnol., 1999, 51, 730-750.
4. C. Viti, A. Pace, L. Giovannetti. Characterization of Cr (VI)-resistant bacteria isolated from chromium-contaminated soil by tannery activity. Current Microbiology, 2003, 46, 1-5.
5. S. Juhnke, N. Peitzsch, N. Hübener, C. Grosse, D. H. Nies. New genes involved in chromate resistance in Ralstonia metallidurans strain CH34. Arch. Microbiol., 2002, 179, 15-25.
6. S. L. Rivera, E. Vargas, M. I. Ramírez–Díaz, J. Campos–García, C. Cervantes. Genes related to chromate resistance by Pseudomonas aeruginosa PAO1. Antonie van Leeuwenhoek, 2008, 94, 299-305.
7. K. Jerke, C. H. Nakatsu, F. Beasley F. A. Konopka. Comparative analysis of eight *Arthrobacter* plasmids. Plasmid, 2008, 59, 73-85.
8. A. Konopka, C. Nakatsu. Ecological interactions between metals and microbes that impact bioremediation. Part 2. In: Annual NABIR PI Meeting, 2004, Warrenton, VA: http://esd.lbl.gov/research/projects/ersp/generalinfo/pi_meetings/PI_mtg_04/04_PI_Meeting_pdf/posters/Konopka_poster04b.pdf.
9. N. Ya. Tsibakhashvili, I. M. Mosulishvili, T. L. Kalabegishvili, D. T. Pataraya, M. A. Gurielidze, G. S. Nadareishvili, H.-Y. N. Holman. Chromate–resistant and reducing microorganisms in Georgia basalts: Their distribution and characterization. Fresenius Environ. Bull., 2002, 11, 352-361.
10. T. L. Kalabegishvili, N. Ya. Tsibakhashvili, H.-Y. N. Holman. Electron spin resonance (ESR) study of chromium (V) formation and decomposition by basalt-inhabiting bacteria. Environ. Sci. & Technol., 2003, 37, 4678-4684.
11. T. Kalabegishvili, A. Rcheulishvili, I. Murusidze, D. Pataraya, M. Gurielidze, H.-Y. Holman. Detoxification of Cr (VI) by basalt-inhabiting bacteria. In: Proc. 8th Int. Conf. Prot. & Restor. Environ. (Eds. E. Gidarakos et al.),2006, Chania, 115-116.
12. Z. Lin, Y. Zhu, T. Kalabegishvili, N. Tsibakhashvili, H-Y. Holman. Effect of chromate action on morphology of basalt-inhabiting bacteria. Mater. Sci. & Eng. C, 2006, 26, 610-612.
13. N. Tsibakhashvili, L. Mosulishvili, T. Kalabegishvili, E. Kirkesali, I. Murusidze, S. Kerkenjia, M. Frontasyeva, H-Y. Holman. Biotechnology of Cr (VI) transformation into Cr (III) complexes. J. Radioanal. & Nucl. Chem., 2008, 278, 565-569.
14. N. A. Krassilnikov. Method of Soil Microorganisms and Their Metabolites Study. 1966, Moscow: Moscow Univ. Press, 7-46.
15. T. V. Aristovskaya, M. E. Vladimirskaya. Isolation and culture of microorganisms. In: Large Practicum in Microbiology. 1962, Moscow: Visshaya shkola, 88-120.

16. R. Brandsch, K. Decker. Isolation and partial characterization of plasmid DNA from *Arthrobacter oxidans*. Arch. Microbiol., 1984, 138, 15-17.
17. P. E. Kolenbrander, M. Weinberger. 2-hydroxypyridine metabolism and pigment formation in three *Arthrobacter* species. J. Bacteriology, 1977, 132, 51-59.
18. G. A. Turnbull, M. Ousley, A. Walker, E. Shaw, J. A. Morgan. Degradation of substituted phenylurea herbicides by Arthrobacter globiformis strain D 47 and characterization of a plasmid-associated hydrolase gene puh A, Appl. Environ. Microbiol., 2001, 67, 2270-2275.

SCALING FEATURES OF AMBIENT NOISE AT DIFFERENT LEVELS OF LOCAL SEISMIC ACTIVITY

T. Chelidze, T. Matcharashvili, N. Zhukova, A. Sborshchikovi

M. Nodia Institute of Geophysics
Tbilisi, Georgia
matcharashvili@gtu.ge
rossoneri08@yandex.ru

Accepted April 18, 2013

Introduction

It is well known, that relative motion of the faults bordering tectonic plates leads to the fast emission of energy propagating over long distances in the form of elastic seismic waves [1]. These seismic waves can be detected by seismographs in the form of vibrations of the Earth's surface.

Seismic signals, contributing to the ambient noise, are regarded as having more regular dynamical structure comparing to random noises [2, 3]. This is quite logical in the light of established for the last decades presence of nonrandom, though high dimensional dynamical structure in the seismic process – the source of seismic signals (see e.g. [2 – 6]). Presence of nonrandom dynamical structure in the earthquake generation process, and seismic waves accordingly, physically is related to the processes accompanying stress accumulation and the breakdown of a disordered solid together with concomitant stick-slip movement. These complex processes involving cascades of transitions (changes) in wide spatial, temporal and energetic scales generally are, or can be, in principle detectable. Some of these transitions – precursory changes, preceding or accompanying breakdown and stick-slip movement in a disordered solid rocks, have already been observed both at the laboratory and the geophysical scales [2, 7, 8]. It is also understandable, that because of complexity of seismic process, such changes might be of different forms, related to variations in mechanical, chemical, hydrological, electromagnetic, etc. processes in the seismic source or peculiarities of wave propagation in rocks, e.g. acoustic, electromagnetic emissions [9, 10].

In the present research we focus on the statistical and fluctuation features of the ambient seismic noise time series using similar concepts. The main goal of this research was to carry out comparative analysis of scaling features of ambient noise time series in the time periods of increased as well as relatively low local seismic activity on the example of seismic data recorded at Oni seismic station in Georgia. Targeted, problem is of general interest and has a great scientific significance, being related to the recognition of changes in apparently similar signals with different physical origins. The recognition of changes caused by arrival of seismic signals in the background random noise is of prime importance from scientific and practical points of views. Such analysis of seismic data often are the subject of vivid interests for different

purposes, including earthquake forecasting, and numerous methods of data analysis are used [1, 11].

In order to accomplish targeted research for selected seismic noise data sets we applied methods often used for time series scaling features analysis.

Used data and methods of analysis

The data used in this study are digital seismograms recorded by broad-band permanent station located in Great Caucasus mountains near town Oni (42.5905 N, 43.4525 E), Georgia (**Figure 1 a**). We investigated all three components of vibrations of Earth's surface, but mainly focused on time series of fluctuations of the Earth's vertical velocity, V_z (see typical 4 day recording in **Figure 1 b**). The data were recorded at sampling frequency of 100 Hz with a dynamic range over 140 dB. Station has a flat velocity response from 0.01 to 100 Hz frequency band. The seismograms are corrected for instrument response before analysis so as to get the ground velocity. Seismic station Oni, where analyzed waveforms were recorded, is part of seismic network operated by the Ilia State University, Seismic Monitoring Centre of Georgia.

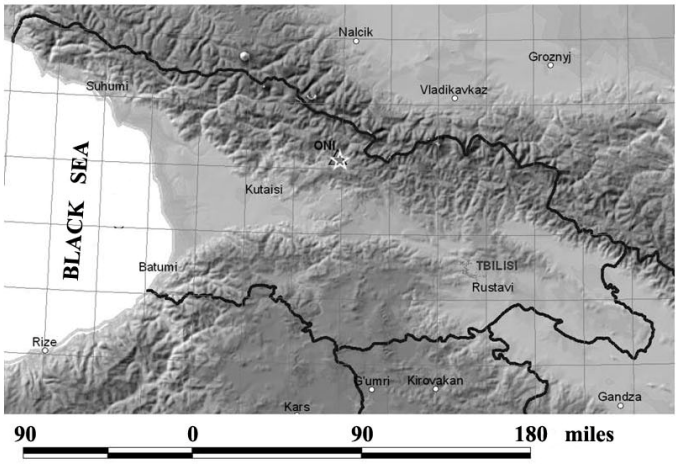

a)

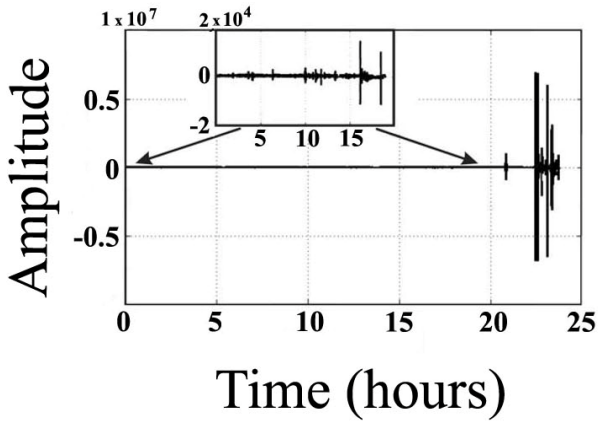

b)

Figure 1. (a) Map of location of Oni seismic station. By the star epicenter of Racha M 6.0 is shown; (b) The data for the M 6.1 Racha earthquake.

In general, complex systems time series, like ambient noise, exhibit fluctuations on a wide range of time scales are often accompanied by the broad distributions of the values. Such fluctuations usually follow scaling laws, which allow characterization of the data and the generating complex system by fractal (or multifractal) scaling exponents. Knowledge of these scaling exponents is very important because they provide unique information on systems behavior and may serve as characteristic fingerprints for comparison with other systems and models.

In this research in order to quantify scaling features of ambient noise we used method for the time series analysis – detrended fluctuation (DFA).

In order to quantify long-range time-correlations in the investigated ambient noise data sets we used method of DFA [12, 13]. DFA was conceived as a method for detrending local variability in a sequence of events, which provides insight into long-term variation features in the complex data sets. This scaling analysis technique provides a simple quantitative parameter (DFA scaling exponent) representing the correlation properties of a time series. As it was already mentioned the very important practical advantage of DFA over many other scaling techniques is that it enables the detection of long-range correlations embedded in time series. Moreover DFA helps to avoid the spurious detection of apparent long-range correlations that are an artifact of non-stationarity.

In practice DFA method consists of three steps [13, 14]. First initial time series $x(k)$ (of length N), is integrated and "profile" $Y(i)$ is determined. After this the resulting series $Y(i)$ is divided into boxes of size n. In each box of length n, local trend, $Y_n(i)$ is calculated. Next, the line points are subtracted from the integrated series $Y(i)$, in each box. The root mean square fluctuation of the integrated and detrended series is calculated:

$$F(n) = \sqrt{\frac{1}{N}\sum_{i=1}^{N}\left[Y(i) - Y_n(i)\right]^2}.$$

This process is repeated for different scales (box sizes) to obtain a power law behavior between $F(n)$ and n. When the signal follows scaling law, a power law behavior for the function $F(n)$ is observed:

$$F(n) \sim n^{\alpha}.$$

The scaling exponent α gives the information about the long-range power law correlation properties of the signal. Scaling exponent $\alpha = 0.5$ corresponds to white noise (noncorrelated signal), when $\alpha < 0.5$ the correlation in the signal is anti-persistent, if $\alpha > 0.5$ the correlation in the signal is persistent. $\alpha = 1$ means uniform power law behavior of $1/f$ noise and $\alpha = 1.5$ represents a Brownian motion. The value $\alpha > 1.5$ corresponds to long-range correlations that may be related to both stochastic and deterministic correlations [7]. It may often happen, that the correlations of recorded data do not follow the same scaling law for all considered n time scales. In such cases the function $F(n)$ displays different power-law behaviors and in double logarithmic plots of the DFA fluctuation function, one or more crossovers between different scaling regimes are observed. These crossover (time) scales separate regimes with different scaling exponents. In practice, the crossover region is defined by the values of n where the function $F(n)$ changes its behavior. The relationship between spectral exponent β and α is given by the formula $\alpha = (1+\beta)/2$.

One of the effective methods to study multi-fractality in non-stationary signals is multifractal MF–DFA algorithm [14].

MF–DFA procedure presumes introduction of two additional steps to the standard DFA [12]. Namely, at first we average over all n segments to obtain the q th order fluctuation function,

$$F_q(n) = \left[\frac{1}{N} \sum_{i=1}^{N} \left[Y(i) - Y_n(i) \right]^q \right]^{1/q}$$

where, in general, the index variable q can take any real nonzero value. For $q = 2$, the standard DFA procedure is retrieved. As far as we are interested in how the generalized q dependent fluctuation functions $F_q(n)$ depend on the time scale n, for different values of q, calculation should be repeated for different time scales.

MDFA approach has been proposed to study multifractality in nonstationary signals when they are long-range power-law correlated

$$F_q(n) \sim n^{\alpha(q)},$$

where $\alpha(q)$ is the generalized scaling exponent. For monofractal time series, $\alpha(q)$ is independent of q, and only if small and large fluctuations scale differently, there will be a significant dependence for multifractal data sets.

Results and discussions

Total length of considered in our research ambient noise time series was in the range from 10 to 35 millions. We used MF–DFA analysis technique [14] to assess multifractal features of ambient noise time series. This approach is based on the identification of scaling of q th order moment depending on signal segment length. It is quiet logical that in **Figure 2**, where the results of MF–DFA are presented, we see typical for multifractal sets, $H(q)$ vs. q dependence for data sets from both seismically active and relatively quiet periods. At the same time, multifractal pattern is more pronounced in the case of locally quiet time period before arrival of seismic waves from Japan earthquake in March of 2011 (dark triangles in Figurte 2).

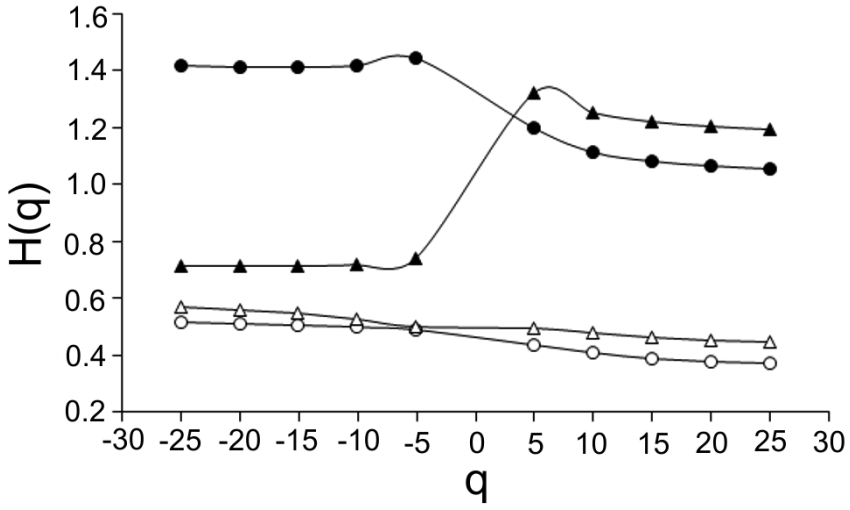

Figure 2. The generalized Hurst exponent $H(q)$ versus q calculated for the seismic noise Z component time series. Filed circles and triangles correspond to the period before M 6.0 Racha earthquake (2009) and period preceding arrival of waveforms of Japan M 9.0 earthquake (2011) accordingly. Open circles correspond to shuffled data sets.

As follows from the results presented in **Figire 2**, shuffling procedure destroys correlation structure of ambient noise data sets in both considered cases, at increased (open circles) and decreased (open triangles) local seismic activity around Oni seismic station. $H(q)$ values calculated for shuffled series are concentrated in the vicinity to 0.5 exhibiting non multi-fractal scaling [14, 15].

Thus, though, at increased seismic activity the dynamics of ambient noise fluctuations looks somehow closer to mono-fractality, there are more arguments to conclude, that in both considered cases we deal with process characterized by multifractal scaling.

Conclusions

On the example of seismic noise data sets recorded at Oni seismic station, we have shown that, in general for wide time scale, ambient noise data sets are characterized by long range correlations. At the same time, on several smaller time scales ambient noise may contain a mixture of different stochastic structures demonstrating different scaling behavior, including both types of persistence, random walk, Brownian behavior, etc.

In periods of both increased or decreased seismic activity, ambient noise reveals multifractal properties. At the same time character of multifractality is different for different levels of local seismic activity. By comparing the second moment exponent of original time series with the shuffled one's, we have found that the largest contribution to multifractality is due to correlations in noise data sets.

References

1. A. Caserta, G. Consolini, P. de Michelis. Statistical features of the seismic noise-field. Studia Geophys. Geod. 51 (2007) 255-266.
2. P. Manshour, S. Saberi, M. Sahimi, J. Peinke, A. F. Pacheco, M. R. R. Tabar. Turbulent-like behavior of seismic time series. Phys. Rev. Lett. 102 (2009) 014101.
3. S. Padhy. Rescaled range fractal analysis of a seismogram for identification of signals from an earthquake. Curr. Sci. 87 (2004) 637-641.
4. V. Lapenna, M. Macchiato, L. Telesca. $1/f^{\beta}$ fluctuations and self-similarity in earthquake dynamics: Observational evidences in Southern Italy. Phys. Earth & Planetary Interiors, 106 (1998) 115-127.
5. T. Matcharashvili, T. Chelidze, Z. Javakhishvili. Nonlinear analysis of magnitude and interevent time interval sequences for earthquakes of Caucasian region. Nonlinear Proc .Geophys. 7 (2000) 9-19.
6. J. B. Rundle, D. L. Turcotte, W. Klein. GeoComplexity and the Physics of Earthquakes. In: AGU Monograph, 120 (Eds. J. B. Rundle, D. L. Turcotte, W. Klein). 2000), Washington: Am. Geophys. Union, 1-3.
7. P. G. Kapiris, K. A. Eftaxias, K. D. Nomikos, J. Polygiannakis, E. Dologlou, G. T. Balasis, N. G. Bogris, A. S. Peratzakis, V. E. Hadjicontis. Evolving towards a critical point: A possible electromagnetic way in which the critical regime is reached as the rupture approaches. Nonlinear Proc. Geophys. 10 (2003) 511-524.

8. P. Manshour, F. Ghasemi, T. Matsumoto, J. Gómez, M. Sahimi, J. Peinke, A. F. Pacheco, M. R. R. Tabar. Anomalous fluctuations of vertical velocity of Earth and their possible implications for earthquakes. Phys. Rev. E. 82 (2010) 036105.
9. K. Karamanos, D. Dakopoulos, K. Aloupis, A. Peratzakis, L. Athanasopoulou, S. Nikolopoulos, P. Kapiris, K. Eftaxias. Preseismic electromagnetic signals in terms of complexity. Phys. Rev. E. 74 (2006) 016104.
10. M. R. R. Tabar, M. Sahimi, F. Ghasemi, K. Kaviani, M. Allamehzadeh, J. Peinke, M. Mokhtari, M. Vesaghi, M. D. Niry, A. Bahraminasab. Short-term prediction of medium and large-size earthquakes based on Markov and extended self-similarity analysis of seismic data. In: Modelling Critical and Catastrophic Phenomena in Geoscience – Lecture Notes in Physics, 705 (2006) 281-301.
11. R. Yulmetyev, P. Hanggi, F. Gafarov, D. G. Yulmetyeva. Non-stationary time correlation in discrete complex systems: Applications in cardiology and seismology. Nonlinear Phen. Complex Syst. 6 (2003) 791-799.
12. C. Goltz. Fractal and Chaotic Properties of Earthquakes – Lecture Notes in Earth Sciences, 77. 1997, Berlin: Springer.
13. H. Kanamori, E. E. Brodsky. The physics of earthquakes. Physics Today 54 (2001) 34-40.
14. J. W. Kantelhardt, S. A. Zschiegner, A. Bunde, S. Havlin, E. Koscielny–Bunde, H. E. Stanley. Multifractal detrended fluctuation analysis of nonstationary time series. Physica A 316 (2002) 87-114.
15. T. Chelidze, T. Matcharashvili. Complexity of seismic process; measuring and applications – A review. Tectonophys. 431 (2007) 49-60.

ПОРОМЕТРИЯ ЦЕОЛИТОВ С ТРЕХМЕРНОЙ СЕТКОЙ КАНАЛОВ

А. А. Капанадзе, Г. В. Ртвелиашвили, Г. Д. Табатадзе

Грузинский технический университет
Тбилиси, Грузия
a.kapanadze@gtu.ge

Принята 23 апреля 2013 года

В качестве матриц с трехмерной сеткой каналов нами использовались промышленно выпускаемые синтетические цеолиты типов NaX, NaA, NaY, CaX и CaA. Кристаллы этих цеолитов имели размеры 1 – 5 мкм.

Несмотря на очевидные преимущества исследования отдельных кристалликов, практически это оказалось невозможным. Поэтому из кристаллов цеолита спрессовывались таблетки нужного объема, которые и использовались в дальнейших опытах. Давление, при котором прессовались таблетки, было выбрано экспериментальным путем. При этом мы исходили из того, что спрессованный образец цеолита должен иметь плотность, по возможности приближающуюся к плотности моно-кристалла, но его структура при этом не должна быть разрушена. Такая высокая плотность спрессованного образца требуется потому, что при последующем заполнении металлом полостей кристаллов будут заполняться и пустоты между кристаллами, образуя т.н. металлическую обмазку. При исследовании различных свойств мелкодисперсного металла (металл внутри кристаллов) обмазка вносит дополнительные трудности, поэтому уменьшение количества обмазки весьма важно. Эта цель достигается уменьшением объема межкристаллических пустот за счет высокой плотности прессуемого образца.

На всех спрессованных таблетках цеолита был проведен рентгеноструктурный анализ, который показал, что до 12 кбар (конец участка быстрого нарастания плотности) никаких структурных изменений в цеолите, по-видимому, не происходит. При более высоких давлениях некоторая часть кристаллов цеолита начинает разрушаться (дробиться на более мелкие). На это указывает аморфное галло, появляющееся на рентгенограмме. По-видимому, разрушаются кристаллы, имеющие несовершенства в своей структуре. Аморфная часть (разрушенные кристаллы), однако, незначительна, и при 28 кбар достигает величины < 10 %. Была также сделана попытка полностью разрушить кристаллы цеолита. Поскольку половину объема кристаллов занимают пустоты в виде каналов и полостей, при давлении, разрушающем структуру кристаллов, можно ожидать резкое (пятидесятипроцентное) уменьшение объема – скачок объема. Цеолиты оказались весьма прочными объектами. До давления 45 кбар скачок объема не наблюдался. Из проведенных опытов следует, что при приготовлении таблеток цеолита для исключения даже незначительных разрушений цеолита следует применять давления прессования до 12 кбар. В последующих экспериментах мы использовали таблетки цеолита, спрессованные давлением 10 кбар с плотностью 1.5 г / см^3.

В нормальном состоянии полости в кристаллах цеолитов заполнены адсорбированной водой. Для цеолитов NaX, CaX и NaY, имеющих структуру, подобную фожазиту, содержание воды составляет 0.51 $см^3 / см^3$ кристалла. В цеолитах NaA и CaA, относящихся к молекулярным ситам Линде типа А объем пустот, заполненных водой, меньше – 0.46 $см^3 / см^3$. Для заполнения внутрикристаллических пустот металлом, необходимо удаление находящейся в них воды (обезвоживание). Режим обезвоживания всех упомянутых цеолитов примерно одинаков. Полное удаление воды из кристаллов происходит при 350 °C в вакууме 10^{-6} мм рт. ст. в течение 8 ч [1], либо при нагревании на воздухе при температуре порядка 500 °C в течение 6 ч. Однако, как видно из **рисунка 1** (кривая *a*), основная масса воды удаляется уже при 200 °C даже в инертной атмосфере. На этом же рисунке (кривая *b*) представлена дериватограмма образца цеолита NaX (зависимость веса образца от температуры), полученная для аналогичных условий. Она почти полностью совпадает с зависимостью, приведенной в работе [2].

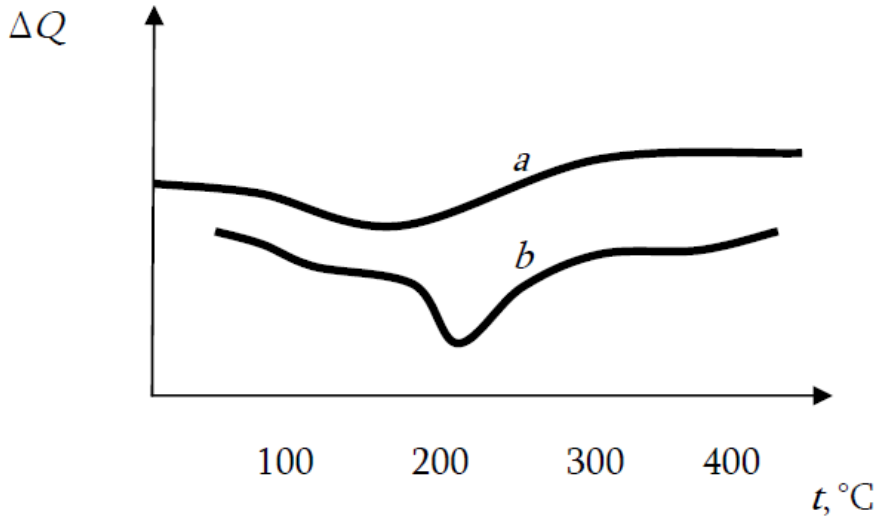

Рисунок 1. Дифференциальная кривая нагревания синтетического фожазита. Кривая *a* построена по данным, приведенным в [3], кривая *b* – по нашим данным.

Основная массопотеря воды у образцов цеолита NaX происходит при температуре 225 °C и почти полностью заканчивается при 460 °C. В вакууме потеря воды происходит быстрее. Согласно [4], вода в указанных цеолитах связана неодинаковыми силами для всех 32 молекул. Так, теплота адсорбции ~ 18 ккал / г · моль для 4 молекул воды и порядка 15 ккал / г · моль для остальных 28 молекул. Авторы предполагают, что это объясняется наличием в цеолитах двух сортов центров адсорбции, отличающихся своим положением в полостях. Мы считаем, что две энергии адсорбции объясняются просто – адсорбируется 27 молекул воды в большой полости и 5 молекул в малой (их объемы, соответственно, 822 и 150 $Å^3$), причем пятая молекула в малой полости либо сомнительна, либо не попадает на центры адсорбирующей стенки. Во всяком случае, в малой полости радиус кривизны стенки, «смачиваемой» волой, в два раза меньше, чем для большой полости. К этому можно добавить, что цеолиты с каналами меньшего диаметра обычно обезвоживаются при более высоких температурах. Подчеркнем и то обстоятельство, что количество воды в цеолите, условия его обезвоживания, завтсят в пределах 10 – 20 % от сорта цеолита (вида его катионов).

Вопрос о состоянии воды в цеолите, ее количестве, положения в плоскостях и поведении при обезвоживании до сих пор обсуждаются в специальной литературе и установившейся точки зрения на него пока нет. Тем не менее, для нас это скорее технологический вопрос и он не имеет самостоятельного значения, поскольку в данном случае нас устраивает даже полуколичественный подход. В дальнейших расчетах мы использовали следующие величины: объем больших полостей, заполненных водой – 0.43 $см^3$ / $см^3$ кристалла, объем малых полостей – 0.07 $см^3$ / $см^3$ кристалла. Эти данные хорошо согласуются с работой [5], где рассматривается геометрическая структура цеолитов типа А и Х.

Для образцов упомянутых цеолитов был выбран следующий режим обезвоживания: температура – 350 °С, вакуум – 10^{-1} мм рт. ст., время обезвоживания – 3 ч. Во избежание растрескивания образцов температура повышалась достаточно медленно (порядка 6 °С в минуту), а затем уже поддерживалась постоянной при заданном вакууме в течение двух часов. Контрольные измерения веса показали, что при этом теряется около 85 % имеющейся в цеолите воды. По-видимому, этот результат говорит о том, что большие полости почти полностью обезвожены, а так как металлом заполняются только они, то выбранный режим является вполне приемлемым для наших целей. Каркас цеолитов при этом режиме обезвоживания не разрушается, что также установлено нами на основании рентгеноструктурного анализа.

Обезвоженный цеолит выбранного нами типа помещался в специальный контейнер, заливался на воздухе жидким металлом и закрывался крышкой. Так как цеолит обладает большой адсорбционной способностью, он помещался в контейнер еще не остывшим (температура цеолита – 250 – 300 °С). Все операции проводились достаточно быстро, чтобы цеолит не успел остыть до того момента, пока он не будет залит металлом. Закрытый контейнер помещался в камеру высокого давления. По мере увеличения давления объем находящейся в контейнере системы цеолит–металл уменьшается. При определенном давлении, критическом для данной системы (P_c), металл проникает внутрь кристаллов цеолита. Происходит резкое изменение сжимаемого объема – скачок.

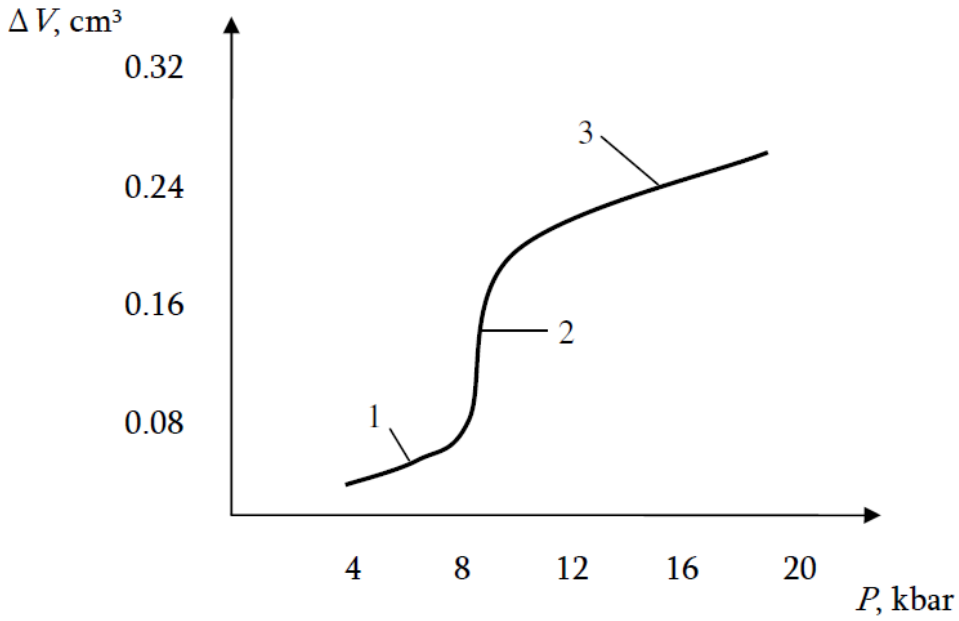

Рисунок 2. Зависимость изменения объема системы NaX – Bi от давления.

На **рисунке 2** изображена порограмма системы NaX – Bi. На этой порограмме можно различить три характерных участка, имеющихся и на других порограммах. Участок 1 представляет собой наклонную прямую, характеризующую изменение сжимаемого объема до критического давления, подчиняющуюся закону Гука для всесторонне сжимаемых тел. Участок 2 фиксирует резкое изменение объема сжимаемой системы – скачок объема из-за проникновения металла внутрь полостей и каналов цеолита. Скачок несколько размыт – начинается при давлении 8.5 кбар и заканчивается при давлении 10 кбар. Это, видимо, происходит из-за наличия трения в системе камера–контейнер–поршень. Участок 3 также представляет собой наклонную прямую, соответствующую закону Гука для всестороннего сжатия (основной вклад в сжимаемость дает жидкий металл). В наших опытах использовались различные типы цеолитов, имеющие отличия в структуре, а также в максимальных диаметрах полостей и каналов. В цеолиты вводились различные металлы, имеющие разные поверхностные нятяжения. Давления, при которых металл входит внутрь полости, величины скачков объема в пересчете на 1 $см^3$ цеолита, а также процент заполнения пустот кристаллов приведены в **таблице 1**.

Таблица 1. Сводные результаты экспериментов по заполнению полостей цеолитов с трехмерной сеткой каналов различными металлами.

Тип цеолита	Вводимый металл	Диаметр больших полостей, Å	P_c, кбар (расчетное)	P_c, кбар (экспериментальное)	P_c (расчетное) / P_c (экспериментальное)	Объем больших полостей, $см^3$ / $см^3$	Величина скачка кристалла, $см^3$ / $см^3$	Заполнение металлом больших полостей, %	Количество атомов на большую полость при $P > P_c$
NaX	Bi	12.0	12.5	11.5	1.09	0.43	0.25	58	14
NaX	Hg	12.0	15.0	12.5	1.20	0.43	0.24	56	18
NaX	Sn	12.0	17.5	15.0	1.17	0.43	0.15	35	10
NaX	Pb	12.0	14.8	14.7	1.01	0.43	0.17	40	10
NaX	In	12.0	20.0	17.0	1.18	0.43	0.19	44	14
NaX	Ga	12.0	24.0	21.5	1.15	0.43	0.19	44	18
NaY	Hg	12.0	15.0	12.5	1.20	0.43	0.22	51	16
NaY	Ga	12.0	24.0	21.5	1.12	0.43	0.19	44	18
CaX	Hg	12.0	15.0	12.7	1.18	0.43	0.22	51	16
CaX	Ga	12.0	24.0	21.0	1.14	0.43	0.19	44	18
CaA	Hd	11,4	15.8	14.7	1.17	0.42	0.17	40	12
NaA	Bi	11.4	13.2	14.5	0.91	0.42	0.16	38	9
NaA	Hg	11.4	16.3	15.0	1.19	0.42	0.16	38	11
NaA	Sn	11.4	18.5	15.4	1.20	0.42	0.16	38	10
NaA	Pb	11.4	15.5	15.1	1.03	0.42	0.16	38	9
NaA	In	11.4	21.0	18.4	1.14	0.42	0.13	31	9
NaA	Ga	11.4	25.5	24.0	1.06	0.42	0.14	33	13

Нетрудно получить соотношение, связывающее критическое давление, при котором жидкий металл проникает в каналы цеолита, с величиной поверхностного натяжения металла и диаметром каналов. Как известно, поверхностное натяжение измеряется энергией, необходимой для увеличения поверхности на единицу площади, или силой, приложенной к единице длины линии, вдоль которой происходит соприкосновение жидкости со стенками канала. Эта сила F может быть легко найдена;

$$F = 10^{-8}\pi\sigma d\cos\beta, \quad (1)$$

где σ – поверхностное натяжение в дин / см, d – диаметр канала в ангстремах, β – краевой угол, равный для несмачивающей жидкости 180 °. С другой стороны сила, необходимая для вдавливания жидкого металла в канал диаметром d, равна

$$F = P_c S = 10^{-7} P_c \frac{\pi d^2}{4}, \quad (2)$$

где P_c – давление в кбар; d, как и выше, измеряется в ангстремах. Схематическое изображение сил, действующих при вдавливании жидкости в канал, приведено ниже на **рисунке 3**.

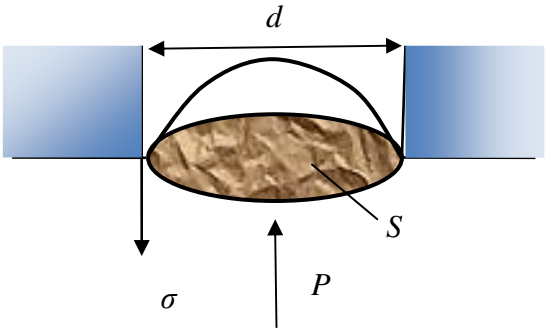

Рисунок 3. Схематическое изображение сил,
Действующих при вдавливании жидкости в канал

Поскольку силы, определяемые соотношениями (1) и (2), взаимно уравновешены, получим:

$$P_c = \frac{0.4\sigma}{d}. \quad (3)$$

Это соотношение носит название порометрической формулы. Она чисто феноменологическая.

В **таблице 1** приведены расчетные значения P_c, получающиеся при использовании формулы (3), в которую подставлены диаметры каналов цеолитов. Как оказалось, расчетные значения P_c наиболее хорошо согласуются с экспериментальными, если в формулу (3) подставлять максимальные значения диаметров каналов. Для всех цеолитов с трехмерной сеткой каналов это максимальные диаметры полостей, а не разделяющих их диафрагм. Полученные таким образом значения P_c совпадают с экспериментальными с точностью до 15 %, как это видно из таблицы, хотя поверхностное натяжение использованных металлов изменяется от 376 для висмута до 730 дин / см для галлия.

Цеолиты NaX, NaY и CaX отличаются только содержанием различных катионов и незначительным разбросом размеров полостей и ведущих в них каналов. Диаметр

больших полостей у цеолита NaX ≈ 12 Å, диаметр канала или диафрагмы, ведущей в большую полость ~ 8 Å [3]. Если бы главную роль при введении металла в цеолит играли диафрагмы, то критическое давление, вычисленное из порометрической формулы, например для ртути, достигало бы величины

$$P_c = \frac{180}{8} = 22.5 \text{ кбар.}$$

Экспериментально же мы получили (см. **таблицу 1**) $P_c = 10.5$ кбар. Высокая проницаемость диафрагм наиболее отчетливо проявляется при введении металлов в цеолит (диаметр больших полостей – 11.4 Å, а диаметр диафрагм – 4.2 Å). Экспериментально полученное P_c для ртути в этом случае составляет 15 кбар. Если бы главную роль играли диафрагмы, то P_c было бы равно 180 / 4.2 ≈ 43 кбар. По-видимому, узкие диафрагмы не оказывают заметного сопротивления атомам жидкости под высоким давлением из-за их малой протяженности по длине канала.

Если мы возьмем данные **таблицы 1** и сравним экспериментально полученные критические давления для различных металлов с рассчитанными по формуле (3), то увидим, что разность между этими значениями не превышает 15 %. Указанные небольшие, в пределах ошибки эксперимента, расхождения между экспериментальными и расчетными значениями получаются, если в формулу (3) подставить максимальный диаметр канала. Так, для цеолита NaX расчетное критическое давление для ртути 15 кбар, а экспериментальное – 12.5 кбар. Отличие 15 %. При вдавливании ртути в цеолит NaA, имеющий, как известно, другие размеры полостей (11.4 Å), это отличие еще меньше. Так, P_c экспериментальное равно 15 кбар (см. **таблицу 1**), а P_c расчетное – 16 кбар. Отличие не более 7 %. Несмотря на то, что повыерхностные натяжения использованных металлов отличаются почти в два раза (376 для висмута и 730 дин / см для галлия), формула (3) хорошо применима.

Ссылки

1. М. Дубинин. Изв. АН СССР (Хим. науки), 5 (1962) 760.
2. R. M. Barrer, W. Maier. Trans. Faraday Soc., 54 (1958) 1074.
3. Э. Э. Сендеров, Н. И. Хитаров. Цеолиты, их синтез и условия образования в природе. 1970, Москва: Наука.
4. O. M. Drbibit, A. V. Kiselev. Trans. Faraday Soc., 67 (1971) 458.
5. А. В. Киселев, А. А. Лопаткин. Кинетика и катализ, 4 (1963) 786.

РЕЗУЛЬТАТЫ ПОВЕРХНОСТНО-ВОЛНОВОЙ ТОМОГРАФИИ ЗЕМНОЙ КОРЫ МАЛОГО КАВКАЗА ПО ДАННЫМ РЕЛЕЕВСКИХ ВОЛН

Т. Гегечкори, Н. Жукова, Е. Мепаридзе, А. Гвенцадзе, А. Сборщикови

Институт геофизики им. М. Нодия
Тбилиси, Грузия
tengeg@gmail.com
rossoneri08@yandex.ru

Принята 24 апреля 2013 года

1. Введение

В последние годы для изучения горизонтальных неоднородностей строения земной коры и верхней мантии Земли все более широко используется данные поверхностных волн. Основной метод исследования – это двумерная томографическая реконструкция латеральных вариаций групповых или фазовых скоростей для набора периодов, построение по этим данным локально-сглаженных дисперсионных кривых, и восстановление вертикальных скоростных разрезов в разных точках исследуемого региона или в выделенных тектоничесикх зонах.

Термин “томография” означает реконструирование изображений объекта по его проекциям. Проекции представляют собой некоторые функционалы физических характеристик объекта. В зависимости от того, какие данные используются, сейсмическая томография подразделяется на лучевую и дифракционную. Лучевая томография основывается на данных о волнах, длины которых много меньше, чем характерные размеры исследуемых неоднородностей, так что для вычисления характеристик волнового поля может быть использован лучевой метод. Дифракционная томография основана на длинноволновом приближении (размеры неоднородностей много меньше длины волны). Методы лучевой томографии к настоящему времени значительно лучше развиты, и они уже достаточно широко применяются для исследования трехмерных скоростных неоднородностей в Земле. В представленной статье томографические расчеты проводились в рамках лучевой томографии.

С помощью двумерной томографии определяются латеральные вариации этих скоростей по данным о скоростях вдоль разных трасс, соответствующих одному и тому же периоду. Набор таких данных для разных периодов позволяет строить локальные дисперсионные кривые, а по ним и скоростные разрезы в отдельных точках, и в конечном итоге получать трехмерные скоростные разрезы. Такой подход имеет то преимущество, что исходные данные практически не подвержены влянию ошибок в определении параметров очагов.

После получения скоростных распределений каждая точка площади характеризуется рядом значений скорости для соответствующего ряда значений периода колебаний в волне, т.е. дисперсионной кривой. Решая обратную задачу по данному

отрезку дисперсионной кривой, получим скоростную колонку в данной точке. Значение скорости в слоях колонки соответствуют поперечной волне, потому что скорость релеевской волны определяется в основном скоростью волны поперечной, и среди других параметров разреза наибольшее влияние на изменение дисперсии ее скоростей оказывают вариации скорости поперечной волны в разных слоях. Совокупность рассчитанных скоростей колонок позволяет определить геологическое строение под изучаемой площадью.

В отличие от медицинской томографии, где объект может просвечиваться по любым направлениям, в сейсмической томографии всегда приходится иметь дело с ограниченным набором данных, который определяется фиксированным расположением станций и локализацией очагов землетрясений. Это приводит к тому, что одни области пересекаются волновыми трассями, ориентированными преимущественно в каком-то одном направлении, а другие – не пересекаются вообще. При решении такого рода задач необходимо использовать априорные представления о характере распределения скорости, причем эти представления должны носить самый общий характер. Очевидно и то, что разрешающая способность таких данных будет различной в разных областях в завимости от расположения трасс. Этим условиям отвечает метод Бэйкуса–Гильберта: количество данных ограничено, их разрешающая способность определяется сглаживающим ядром (или его эффективной "шириной"), различным в разных интервалах, и может быть оценена в рамках данного метода [1 – 3].

2. Результаты томографических расчетов и их обсуждение

Для проведения томорасчетов мы располагали архивными данными – записями поверхностных волн, накопленными в прошлом в Институте геофизики АН Грузии. Это были сейсмограммы сейсмических станций Грузии и копии сейсмограмм станций Армении и Азербайджана, полученные за период с 1961 года по 1985 год. Всего имелось около 800 сейсмограмм, записанных на 21 сейсмостанций Закавказья. На первом этапе проводилась классификация по качеству сейсмограмм и регионам, в которых происходили землетрясения. Помимо качества сейсмических записей, основным критерием их отбора было условие, взаимного пересечения различных трасс эпицентр–сейсмостанция. Это условие лежит в основе метода поверхностно-волновой томографии. На основе изучения сейсмической активности в те годы, основными регионами для проведения томографических расчетов были выбраны восток Турции, Юго-Восточная часть территории Ирана и Средняя Азия. В этом случае условие взаимного пересечения трасс соблюдалось.

На **Рис. 1** приведена схема сейсмостанций Закавказья, данные которых использовались для расчетов.

Дисперсионные кривые групповых скоростей для различных трасс, являющиеся исходным материалом для томорасчетов, строились вручную и с применением, специально составленной программы полуручного метода построения. Наиболее качественные записи поверхностных волн оцифровывались и затем с помощью программы спектрально-временного анализа (FTAN) получали дисперсионные кривые.

Томографические расчеты были проведены в два этапа по мере отбора сейсмограмм. На первом этапе, с целью опробования программы томографических построений были

проведены тестовые расчеты для волн Релея и Лява [4, 5]. На втором этапе были построены томографические модели для 30 отобранных землетрясений Турции и Ирана. Для этого расчета было отобрано 59 трасс эпицентр–сейсмостанция.

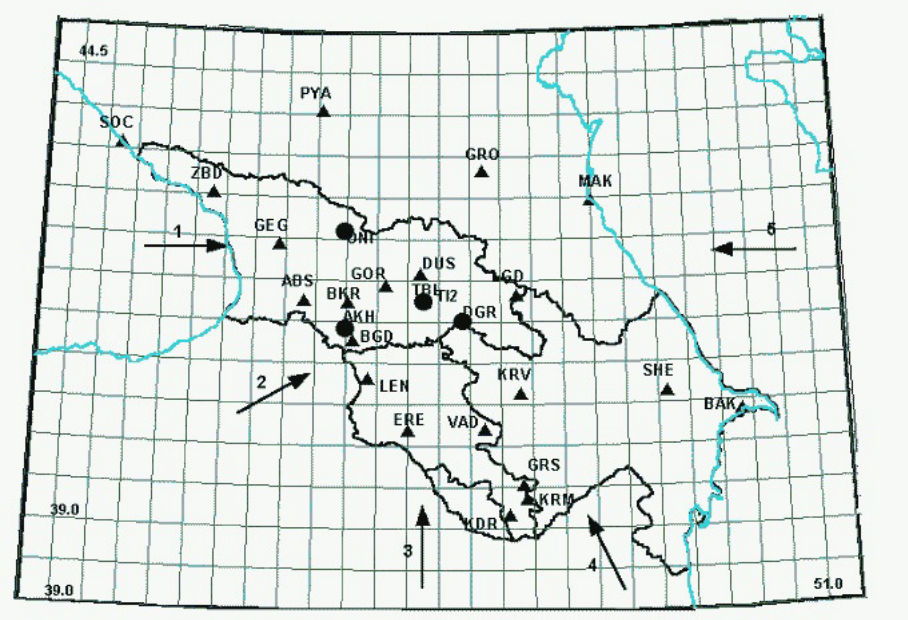

Рисунок 1. Сеть широкополосных сейсмических станций Кавказа 1981 года.
▲ – сейсмические станции;
→ – направление прихода волн;
● – сейсмическая обсерватория.

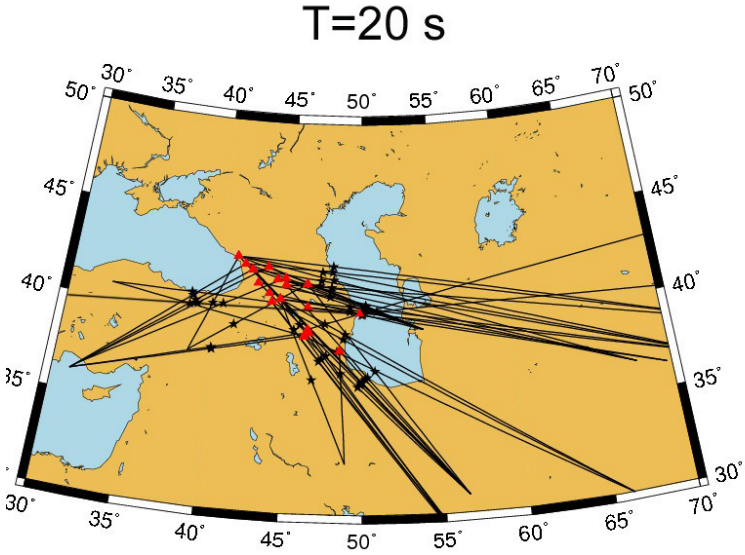

Рисунок 2. Схема трасс сейсмических волн для периода T = 20 сек.

На **Рис. 2** показаны трассы, использованные при расчетах для периодов T = 20 сек. После классификации и отбора сейсмических записей выяснилось, что представительными оказались данные о дисперсии для интервала периодов от T = 10 сек

до T = 22 сек. Верхний интервал периодов естественным образом определялся амплитудно-частотной характеристикой сейсмометров, с помощью которых были получены, использованные нами сейсмограммы.

Можно приблизительно считать, что основная доля энергии поверхностной волны распространяется в слое толщиной порядка половины длины волны, Что соответственно дает информацию о строении именно до таких глубин [6]. Таким образом глубины "просвечивания" земной коры определяются по формуле $\lambda = C\,T / 2$, где λ – длина волны, C – фазовая скорость, T – период волны. Следовательно, проведенные нами томографические расчеты дают представление о горизонтально-неоднородном строении до глубин примерно 40 км.

Томографические расчеты проводились по трем направлениям: 1) полуручной метод, 2) программа для взаимнопересекающих трасс и 3) программа для удаленных землетрясений (более 2000 км). При построении решения для латерального распределения скорости одновременно оценивалось разрешение, которое характеризуется размером (радиусом) эффективной области сглаживания для периодов T = 10 – 20 сек. Решение считалось приемлемым, если радиус области сглаживания не превышал 200 км.

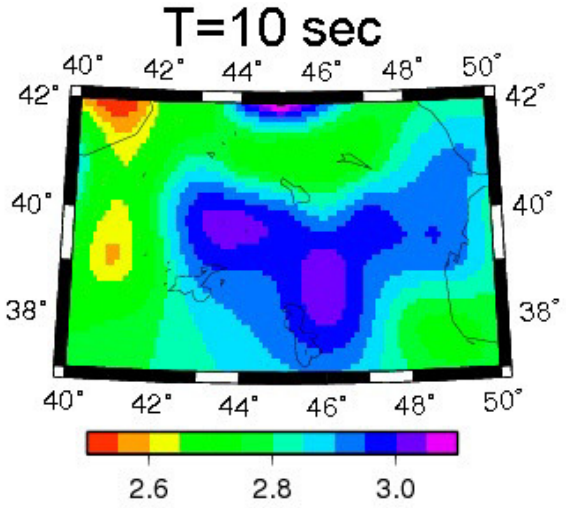

Рисунок 3. Томографическая модель до глубин H = 15 км (T = 10 сек).

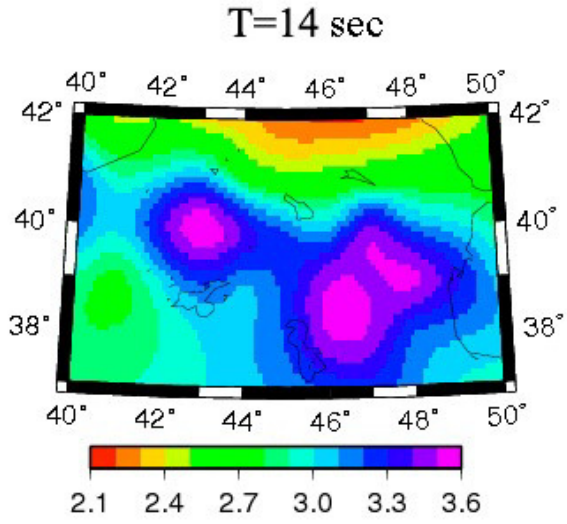

Рисунок 4. Томографическая модель до глубины H = 24 км (T = 14 сек).

Основное свойство поверхностной волны это наличие свободной поверхности Земли. Поэтому в результате томографических построений для каждого конкретного периода мы получаем осредненную модель горизонтально-неоднородного строения от поверхности Земли до глубин равных половине длине волны для этого периода. На **Рис. 3 – 7** приведены, полученные томографические модели латерального строения земной коры региона от свободной поверхности Земли до различных глубин. Сравним полученные томопостроения с имеющимися данными о строении земной коры и тектонических особенностях региона.

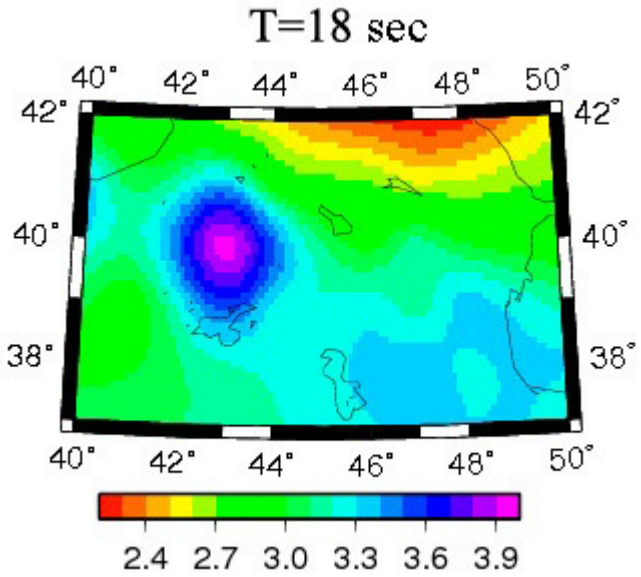

Рисунок 5. Томографическая модель до глубины H = 32 км (T = 18 сек).

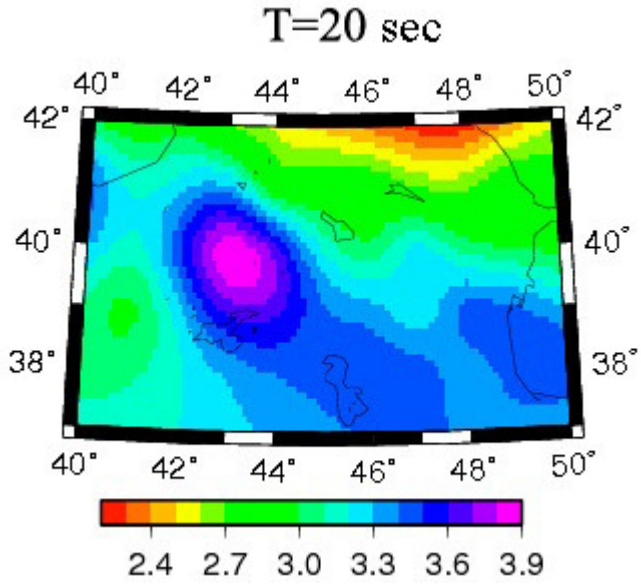

Рисунок 6. Томографическая модель до глубины H = 37 км (T = 20 сек).

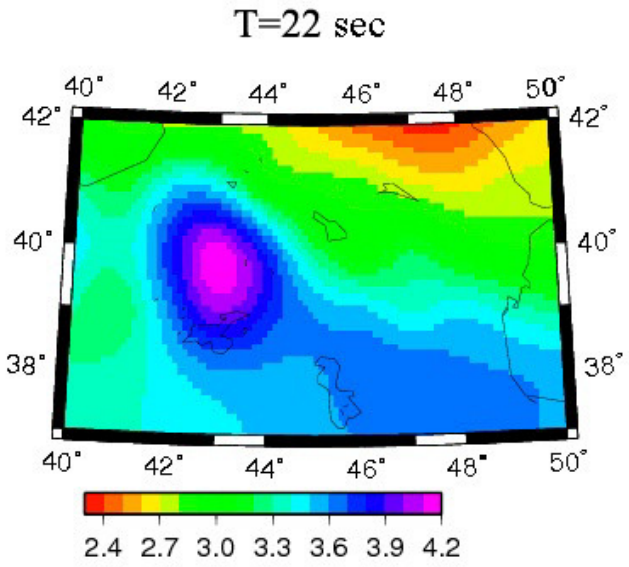

Рисунок 7. Томографическая модель до глубины H = 40 км (T = 22 сек).

Высокоскоростное включение в юго-западной части региона связано с продолжением в сторону Малого Кавказа мегаантиклинория гор Загрос в Иране, которое находит отражение в крупных линеаментных зонах: Ереванского–Мегрийского и Нахичевано–Арагацкой.

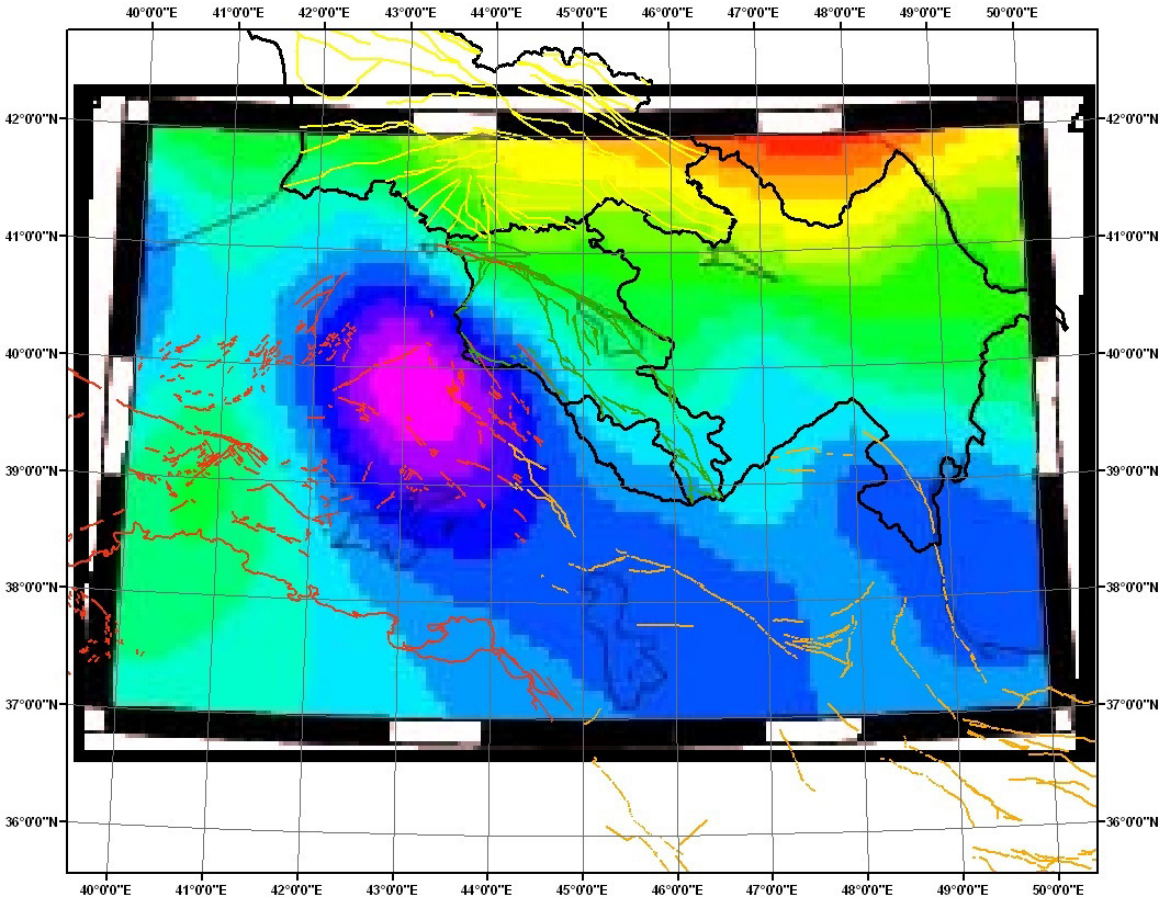

Рисунок 8. Сравненение сетки глубинных и региональных разломов с томографической моделью для T = 20 сек.

Прослеживаемое на **Рис. 4** и **5** на широте 40 °, в восточной части карт, высокоскоростное включение. связано с Джавахетским нагорьем юга Грузии, которое прослеживается и на территории северо-запада Армении. Это – район активной вулканической деятельности в прошлом и в его глубинном строении преобладают горные породы вулканического происхождения. Наличие обширного в юго-западной части региона для глубин 24 – 37 км к высокоскоростного включения с фазовыми скоростями поверхностных волн от 3.4 до 3.7 км / с, приводит к заключению, что данные о мощности земной коры в этом районе, требуют уточнения. Свидетельством надежности, полученных для больших глубин томографических построений может быть тот факт, что модели для периодов T = 20 и 22 сек (**Рис. 6** и **7**) практически совпадают. Сложнее обстоит дело с расчетами для меньших глубин. Земная кора в исследемом регионе значительно отличается от горизонтально-слоистой модели и имеет блоковый характер. Но для повышения разрешающей способности метода удаленность между станциями должна быть 50 – 100 км.

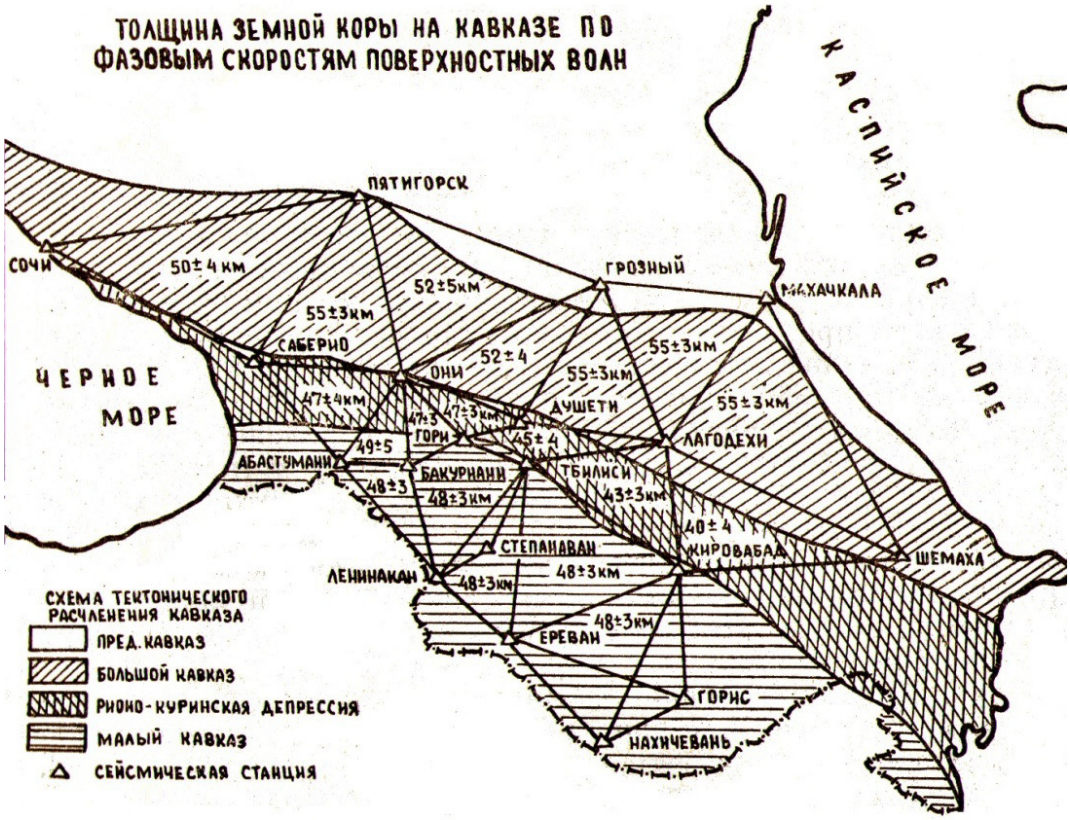

Рисунок 9. Толщина земной коры региона по данным фазовых скоростей поверхностных волн.

На **Рис. 8** приведено сравнение томографических построений для периодов T = 20 сек с имеющимися данными космической фотосъемки о глубинных и региональных разломах с различным проникновением в земную кору [7]. **Рис. 9.** позазывает толщину земной коры региона по данным фазовых скоростей поверхностных волн.

Для более детального томографического исследования верхних слоев горизонтов земной коры необходимо повышать разрешающую способность поверхностно-волновой томографии. Это может быть достигнуто только путем увеличения количества

широкополосных цифровых сейсмостанций. Цифровые записи позволяют снизить нижний уровень регитрируемых периодов до T = 4 сек. В этом случае разрешающая способность метода составит около 10 км. Это позволит исследовать латеральной строение нижних горизонтов осадочного бассейна, т.е. прогнозировать месторождение нефти, газа и полезных ископаемых, а также проводить работы по исследованию долгосрочных предвестников сильных землетрясений.

Необходимость увеличения объема исходных данных и, соответственно, количества пересекающих трасс следует из того факта, что выделенная в центральной, зона повышенных скоростей для периодов T = 18 сек смещена на 1 ° по долготе к востоку. Использование записей широкополосных цифровых сейсмостанций позволит также значительно расширить частотный диапазон в сторону больших периодов T =30 – 80 сек, и получить информацию о горизонтально-неоднородном строении горизонтов земной коры и верхних слоях мантии Земли.

3. Заключение

Метод томографического исследования строения среды является самым эффективным в современной сейсмологии. В предлагаемой работе приведены впервые для региона Малого Кавказа результаты определения латерального строения литосферы методом томографии по данным поверхностных релеевских сейсмических волн. Описана методология томографических расчетов, основанных на использовании данных о временах пробега поверхностных сейсмических волн. Впервые в сейсмологической практике для региона Малого Кавказа и Закавказья получены томографические модели горизонтально-неоднородного строения земной коры до глубины 40 км. Расчеты проведены с использованием данных для релеевских поверхностных волн в интервале периодов от 10 до 22 сек. Проведена геологическая интерпретация полученных томорасчетов.

Данные исследования были проведены в рамках проекта МНТЦ Евросоюза G–1303 – "Исследование структуры литосферы Кавказа методами поверхностно-волновой томографии и трехмерного моделирования".

Ссылки

1. V. K. Borok, T. Yanovskaya. Geophys. J. Roy. Astron. Soc. 13 (1967) 223.
2. G. Backus, F. Gilbert. Phil. Trans. Roy. Soc. A 266 (1969) 123.
3. G. Backus, F. Gilbert. Geophys. J. Roy. Astron. Soc. 16 (1968) 169.
4. T. Gegechkori, N. Tutberidze, S. Gogmachadze. Bull. Georg. Natl. Acd. Sci., 174 (2006) 3.
5. T. Gegechkori, N. Tutberidze, V. Gotsiridze, N. Goguadze, I. Shengelia. J. Georg. Geophys. Soc. (Phys. Solid Earth) A (2007), 12.
6. А. Левшин, М. Ритсволлер. Вычисл. сеймология 32 (2001) 27.
7. Г. Михеев, М. Макаров. Иссл. Земли из космоса 2 (1985) 59.

THERMAL CONDUCTIVITY OF β-RHOMBOHEDRAL BORON DOPED WITH METALS IN NANO-SIZED INTERSTITIALS

L. Chkhartishvili [1], I. Murusidze [2]

[1] Georgian Technical University
Tbilisi, Georgia
chkharti2003@yahoo.com
[2] Ilia State University
Tbilisi, Georgia
miv@iliuni.edu.ge

Accepted April 28, 2013

1. Introduction

Doped β-rhombohedral boron (β-B) is a promising high-temperature semiconductor useful especially as an effective thermoelectric [1]. In β-B it is possible to realize a mechanism of doping different from the conventional one because the crystalline structure of β-B characterized by nano-sized interstitials accommodating metal M atoms. From available experimental studies of influence of the introduced metals on β-B structural, ground-state and electronic properties, one can make the conclusion that metal atoms usually fill interstitials A, D and E (their descriptions see in [2]). The theoretical investigation focused on the binding energy of metallic impurities in β-B lattice and their electron levels is presented by us elsewhere [3]. However, metal impurities being introduced at high concentrations in β-B crystal also serve as effective scattering centers for heat-carrying phonons reducing significantly thermal conductivity of the material and improving in this way its thermoelectric figure-of-merit. Present work is an attempt to analyze the mentioned problem.

2. Vibration frequencies

The values of the vibration frequencies for the 17 dopant metals, which were found in A-, D- and E-type interstitials have been calculated by a quasi-classical-type method developed earlier by us [4]. Used values of quasi-classical parameters of B and dopant M atoms have been pre-calculated and tabulated in [5]. Obtained vibrational frequencies are collected in **Table 1**.

According to the optical data [6], in the β-B phonon spectrum there are bands placed at 150 – 650 and 650 – 1050 cm^{-1} (and also the peak at 1250 cm^{-1} indicating vibrations of the unit cell central atom). All of the vibration frequencies of impurity atoms calculated by us lie above these two bands, within the range 1080 – 4380 cm^{-1}, and, therefore, they should be attributed to localized vibrational modes. The only experimental report [7] on the localized mode definitely identified as the vibration of Ta impurity atoms accommodated in interstitials of β-B crystal is 2200cm^{-1}. Its placement is well-consistent with the frequency 2260 cm^{-1} obtained by us for Ta atoms localized in D-interstitials.

Table 1. Vibrational frequencies.

M	ω_M, cm^{-1}		
	A	D	E
Li	1150	1240	1290
Mg	3080	3330	3450
Al	3150	3400	3520
Sc	2260	3760	3890
Ti	3450	3730	3860
V	3440	3710	3840
Cr	3500	3780	3910
Mn	3490	3770	3900
Fe	3540	3820	3960
Co	3540	3820	3950
Ni	3610	3900	4040
Cu	3920	4230	4380
Zr	3930	2310	1080
Nb	3960	3030	1640
Hf	4020	1920	1820
Ta	4030	2260	2450
Re	3620	1360	1670

3. Thermal conductivity

A more detailed comparison can be realized based on the thermal conductivity measurements in doped β-B samples. Let the concentration of M impurities in interstitials equals to A_M, ω_M is the frequency of the localized vibrations, and ω_0 is the frequency parameter, which characterizes the decay process of atomic displacements. For the physical case, $\omega_0/\omega_M << 1$, the momentum relaxation time τ_M of heat-carrying phonons scattered by localized vibrations is [8]:

$$\tau_M \sim \frac{\left(\exp\left(\frac{\hbar\omega_M}{kT}\right)-1\right)\left(1-\exp\left(-\left(1-\frac{\omega}{\omega_M}\right)\frac{\hbar\omega_M}{kT}\right)\right)}{A_M\omega_M\left(1-\frac{\omega}{\omega_M}\right)^2\left(1+4\left(\ln\left(1+\left(1-\frac{\omega}{\omega_M}\right)\frac{\omega}{\omega_0}\right)-\left(1-\frac{\omega}{\omega_M}\right)\right)\frac{\omega}{\omega_M}\right)}.$$

Here ω denotes the frequency of a scattered phonon, while T is the sample's temperature. We can significantly simplify this relation taking into account that: (*i*) $\omega_0/\omega_M << 1$; (*ii*) $\omega/\omega_M << 1$ for the characteristic value of phonon frequency; and (*iii*) at room temperature, 300K, in β-B $\hbar\omega_M/kT >> 1$. Thus,

$$\tau_M \sim \frac{1}{A_M\omega_M}\exp\left(\frac{\hbar\omega_M}{kT}\right).$$

The thermal conductivity κ_0 of undoped β-B is determined by the cumulative effect of all mechanisms of scattering except for the scattering by localized vibrations. If the thermal conductivity κ_M of doped β-B is calculated according to the Matthiessen's rule we can write down

$$\frac{\kappa_0}{\kappa_M} \approx 1 + \frac{\hbar\omega_M A_M}{kT} \exp\left(\frac{\varepsilon - \hbar\omega_M}{kT}\right).$$

By solving this equation with respect to the parameter ε, we obtain

$$\varepsilon \approx \hbar\omega_M + kT \ln\left(\frac{kT}{\hbar\omega_M A_M}\left(\frac{\kappa_0}{\kappa_M} - 1\right)\right).$$

Using the experimental data concerning the β-B heat-conductivity (see references in [1]) and above obtained ω_M frequencies, we have estimated ε for M-atoms in different interstitials (**Table 2**). In most cases ε has almost identical values, 0.5 – 0.6 eV, which can be interpreted in such a way that all of the impurities occupying nano-sized interstitials effectively scatter phonons.

Table 2. Parameters of scattering of heat-carriers.

M	A_M	κ_M, W / cm · K	ε, eV		
			A	D	E
V	0.011	0.058	0.5	0.5	0.5
Fe	0.010	0.125	0.5	0.5	0.5
Fe	0.020	0.092	0.5	0.5	0.5
Co	0.010	0.040	0.5	0.6	0.6
Co	0.010	0.020	0.5	0.6	0.6
Ni	0.006	0.160	0.5	0.5	0.5
Ni	0.010	0.110	0.5	0.5	0.6
Ni	0.010	0.063	0.5	0.6	0.6
Cu	0.010	0.038	0.6	0.6	0.6
Zr	0.005	0.069	0.6	0.4	0.3
Zr	0.010	0.060	0.6	0.4	0.2
Zr	0.010	0.055	0.6	0.4	0.2
Zr	0.010	0.050	0.6	0.4	0.2
Zr	0.020	0.035	0.6	0.4	0.2
Hf	0.005	0.091	0.6	0.3	0.3
Hf	0.010	0.062	0.6	0.3	0.3
Hf	0.020	0.025	0.6	0.3	0.3
Hf	0.020	0.025	0.6	0.3	0.3

If the doping effects of a given M for interstitials of any type can be described by almost the same ε, we can assume that those atoms in all possible positions act as almost identical scattering centers. The last is true for relatively light elements – V, Fe, Co, Ni and Cu – due to the proximity of frequencies.

However, for heavy elements Zr and Hf accommodated in D- and E-type interstitials, we obtain lower ε: 0.2 – 0.4 eV. It should be associated with noticeable differences in frequencies of localized vibrations of heavy atoms when they are located in the interstitials of various types. Note that the thermal conductivity in Zr- and Hf-doped β-B can be explained by the same ε if we assume that these impurities are predominantly concentrated in the A-type voids.

It is interesting to note that structural studies (see [1]) of the measured samples doped with Zr and Hf indicate the high, low and middle occupancies of interstitials of type A, D and E, respectively, that is consistent with our interpretation. As for the relatively light elements, particularly Fe and Cu, for them the detected occupancies are quite different: low – high – very low and low – high – high, respectively. But in such cases, the distribution of impurities between interstitials not has a significant effect on the thermal conductivity.

4. Conclusion

We have theoretically determined vibration frequencies of 17 metal atoms introduced in nano-sized interstitials of type A, D and E existing in β-B crystals. The comparison with experiment has been implemented for thermal conductivity of β-B doped with metals such as V, Fe, Co, Ni, Cu, Zr and Hf. It has been demonstrated that the decrease in thermal conductivity in these samples can be consistently explained by the scattering of heat-carrying phonons by localized vibrations of impurity atoms. Thus, the metal-doping of β-B in nano-sized interstitials improve its thermoelectric figure-of-merit, not only due to the increase in its conductivity, but also by reducing its thermal conductivity.

References

1. D. L. Gabunia, O. A. Tsagareishvili, L. S. Chkhartishvili, G. F. Tavadze. In: Perspective Mater. & Nanomater. 2007, Kharkov: KhPTI – Contrast, 211.
2. G. V. Tsagareishvili, M. E. Antadze, F. N. Tavadze. Producing and Structure of Boron. 1991, Tbilisi: Metsniereba.
3. L. Chkhartishvili, I. Murusidze, M. Darchiashvili, O. Tsagareishvili, D. Gabunia. Solid State Sci., 2012, 14, 1673.
4. L. Chkhartishvili. Quasi-Classical Theory of Substance Ground-State. 2004, Tbilisi: Tech. Univ. Press.
5. L. Chkhartishvili, T. Berberashvili. J. Electro Magn. Anal. & Appl., 2010, 2, 205.
6. U. Kohlmann, H. Werheit, T. Dose, T. Lundström, In: Proc. 9th Int. Symp. Boron, Borides & Rel. Comp. 1987, Duisburg: UDG, 340.
7. O. A. Golikova, G. V. Tsagareishvili, M. M. Usmanova, T. Khomidov, D. L. Gabunia, A. S. Umarov, Z. Mirzazhonov. Bull. Acad. Sci. Uzb. SSR (Ser. Phys. & Math.), 1981, 5, 88.
8. B. M. Mogilevskij, A. F. Chudnovskij. Thermal Conductivity of Semiconductors. 1972, Moscow: Nauka.

LINEARIZATION OF THE SOLUTION OF LANGEVIN'S EQUATION IN MAGNETIC LIQUIDS

K. V. Kotetishvili, G. G. Chikhladze

Georgian Technical University
Tbilisi, Georgia
ketinooo@hotmail.com

Accepted May 12, 2013

Usually in the Magnetic Resonance Imaging (MRI) three types of magnetic flux density are used, namely:

1. *Strong, homogeneous B_0 field in z direction;*
2. *Transversal, radio-frequency field B_1; and*
3. *Space-coded fields or gradients G in z direction as well.*

B_0 field (nearly 1.5 T) is induced by polarization of nuclear spins. Relatively low is B_1 field (0.01 mT) used for transfer of the induced magnetization in the transversal component of the image and the gradients (nearly 10 mT) used during the relaxation time of space coding of the transversal magnetization in the regime of rest (~ 10 ms). For high B_0 at the ordinary MRI it shows that for magnetic ferro-liquids based on the water the equilibrium of the magnetization will be saturated and the nano-particles of the liquid will be in the strict coincidence with B_0, i.e. will be aligned in B_0 direction.

At low fields in MRI, the MRI scanner operates usually within the interval of 0.1 – 0.35 T and we observe in the article just this interval. For such low B_0 the saturation of the magnetic liquid is not complete, thus it is possible to rotate of physical nano-particles in additional rotating magnetic field. In our case we receive the image for ω speed of the spin of the liquid induced by the field component B_e. This B_e is the precession made field rotating in *xOy* plane and manifests itself as the transversal magnetization vector. B_1 field rotates with Larmor's frequency and is proportional to B_0 with gyro-magnetic constant γ being the proportionality coefficient for them. Thus

$$f_0 = \frac{\gamma}{2\pi} B_0. \quad (1)$$

In the paper, the wide range of rotation frequencies is considered for B_e, including the typical f_0 for the ordinary MRI. Larmor's frequency is 8.5 MHz at ~ 0.2 T and rises up to 14.9 MHz at ~ 0.35 T. The amplitude of B_e is located within 1 – 10 % for B_0, which is relatively wider, than the amplitude of the typical B_1, although it is of the same order that is the magnetic field created by nano-particles. Interaction with transversal magnetization is reached by selection of the frequency of excitement for $B_e(\omega)$, being of the same order that is the inverse τ time of substance relaxation. For typical magnetic nano-particles in bio-medical works its value (approximately one microsecond) is given.

Linearization of the equation

Langevin's equation is related to the ratio of densities of the magnetic and heat energies in magnetic liquids and is given as follows:

$$\vec{M}_{equ} = \vec{M}_{sat} L(\alpha) = \vec{M}_{sat} \left[\coth(\alpha) - \frac{1}{\alpha} \right], \quad (2)$$

here $L(\alpha)$ shows the sequence of magnetic nano-particles for given magnetic fields of $|\vec{H}|$ magnitude. Langevin's parameter α is the function of $|\vec{H}|$ magnitude of the magnetic field and is given by

$$\alpha = \frac{M_l V \mu_0 |\vec{H}|}{kT}, \quad (3)$$

M_l being the linear magnetization of the particles, while V – the magnetic volume of the particles.

The saturation magnetization of M_{sat} of the magnetic liquid is related to M_l by so-called solid magnetic volume of the liquid (φ)

$$M_{sat} = \varphi M_l, \quad (4)$$

Linearization of Langevin's equation may be carried out by means of DC depending on the magnetic field intensity H_0. It presents the magnetic field of the wide DC, typical for MRI. Assume that the long signals i_x and i_y of DC along *Ox*- and *Oy*-axes are absent, as to H_0 itself is directed along i_z, i.e., along *Oz*-axis. Change of sick signal by magnetization around the basic points along t_x, t_y and i_z for h_x, h_y, h_z, respectively, is given as follows:

$$\vec{H} = h_x \vec{i}_x + h_y \vec{i}_y + (H_0 + h_z)\vec{i}_z. \quad (5)$$

Magnetization vector of total equilibrium of the liquid is $\vec{M}_{equ}$, where the magnetization component along i_x, i_y, i_z displacements disappears and becomes m_x, m_y, m_z, respectively.

$$\vec{M}_{equ} = m_x \vec{i}_x + m_y \vec{i}_y + (M_0 + m_z)\vec{i}_z. \quad (6)$$

When $\vec{M}_{equ}$ and $\vec{H}$ become collinear the equation (6) (taking into account the (5)) will be written down as follows:

$$\vec{M}_{equ} = \vec{M}_{sat} L(\alpha) \frac{h_x \vec{i}_x + h_y \vec{i}_y + (H_0 + h_z)\vec{i}_z}{\sqrt{(h_x)^2 + \left(h_y\right)^2 + (H_0 + h_z)^2}}. \quad (7)$$

Further analysis in first is related to the change in small widths of magnetic field h_x, h_y, h_z components and to the role of depending on them magnetization m_x, m_y, m_z components and to the H_0 component of the field of the equilibrium DC in *Oz* direction, which is associated with the magnetization M_0 component of the DC in *Oz* direction as well, given by (2), will become linear for the change of the sick signal of the magnetic field and we get the linearity of the first order for m_x, m_y, m_z.

The terminal summarized magnetization related to the presence of nano-particles in the liquid consists of M_0 component of the DC along *Oz*-axis and the changes of sick signal m_x, m_y, m_z in *x*, *y* and *z* direction respectively.

Taking into account the decomposition of the first order in the denominator of (7), expression for $\vec{M}_{equ}$ may be overwritten as follows:

$$\vec{M}_{equ} \approx \vec{M}_{sat} L(\alpha) \frac{h_x \vec{i}_x + h_y \vec{i}_y + (H_0 + h_z)\vec{i}_z}{H_0} \left(1 - \frac{h_z}{H_0}\right) \approx \vec{M}_{sat} L(\alpha) \frac{h_x \vec{i}_x + h_y \vec{i}_y + H_0 \vec{i}_z}{H_0}. \quad (8)$$

Here all terms of the second order, say $h_x h_z$ and $h_y h_z$, are ignored. It should be noted that there is no any change in Langevin's magnetization component in *Oz* direction, its α parameter is the sum of corrections in Langevin's function in the area of given point (summarized point), denoted by α_0 and changes in the sick signal – α', so

$$\alpha = \alpha_0 + \alpha'. \tag{9}$$

$$\alpha = \frac{M_l V \mu_0}{kT}\sqrt{(h_x)^2 + \left(h_y\right)^2 + (H_0 + h_z)^2} \approx \frac{M_l V \mu_0}{kT} H_0 \left(1 - \frac{h_z}{H_0}\right). \tag{10}$$

It follows then that

$$\alpha_0 = \frac{M_l V \mu_0}{kT} H_0, \tag{11}$$

while

$$\alpha' = \alpha_0 \frac{h_z}{H_0}, \tag{12}$$

and Langevin's equation will be given as follows:

$$L(\alpha) = coth(\alpha_0 + \alpha') - \frac{1}{\alpha_0 + \alpha'}, \tag{13}$$

Let us carry out the linearization of this equation by Taylor's series of the first order:

$$L(\alpha) \approx L(\alpha_0) + \left.\frac{dL(\alpha)}{d\alpha}\right|_{\alpha=\alpha_0} \cdot \alpha', \tag{14}$$

$$L(\alpha) = coth(\alpha_0) - \frac{1}{\alpha_0} - \frac{\alpha'}{sin^2\alpha_0} + \frac{\alpha'}{\alpha_0^2}, \tag{15}$$

$$m_x = M_{sat}\left[coth(\alpha_0) - \frac{1}{\alpha_0} - \frac{\alpha'}{sin^2\alpha_0} + \frac{\alpha'}{\alpha_0^2}\right]\frac{h_x}{H_0}, \tag{16}$$

$$m_y = M_{sat}\left[coth(\alpha_0) - \frac{1}{\alpha_0} - \frac{\alpha'}{sin^2\alpha_0} + \frac{\alpha'}{\alpha_0^2}\right]\frac{h_y}{H_0}, \tag{17}$$

$$M_{equ,z} \approx m_z + M_0 \approx M_{sat}\left[coth(\alpha_0) - \frac{1}{\alpha_0} - \frac{\alpha'}{sin^2\alpha_0} + \frac{\alpha'}{\alpha_0^2}\right]. \tag{18}$$

Inserting $L(\alpha)$ into (8), as it is given by (16) and (17), it becomes possible to apply the magnetization to the components of M_{equ} (see (6)), where H_0 component of the DC disappears, only in *Oz* direction:

$$m_x = M_{sat} L(\alpha)\frac{h_x}{H_0} \approx \frac{M_0}{H_0} h_x, \tag{19}$$

$$m_y = M_{sat} L(\alpha)\frac{h_y}{H_0} \approx \frac{M_0}{H_0} h_y, \tag{20}$$

$$m_z \approx M_{sat}\left(\frac{1}{\alpha_0} - \frac{\alpha'}{sin^2\alpha_0}\right)\frac{h_z}{H_0} \approx \frac{dM_0}{dH_0} h_z, \tag{21}$$

$$M_0 = M_{sat} L(\alpha_0). \tag{22}$$

Here the sick signals of the first order of magnetization m_x, m_y, m_z may be replaced by α', while the terms of the second order will be ignored.

Expressions (19 – 22) show that at the changes in *Oz* directions the ratio of the sick signals of the magnetic field to the terminal magnetization disappears for the given point of DC in Langevin's equation and

$$H_0 = \frac{B_0}{\mu_0} - M_0.$$

When displacements take place from x to y direction, the sick signals of the magnetic field h_x, h_y and the summarized magnetizations m_x, m_y are dependent as M_0 / H_0.

Therefore, in the paper the sick disturbances in the magnetic field signals along i_x and i_y were considered, gradually transferring into $\pi/2$ space (rotates) and creating the rotating field in transversal xOy plane. Change in rather big signals is considered along i_z ($h_z = 0$). For the field of DC we got the enclosure (0.1 – 0.35 T) in the results, where the nano-particles of 4 nm radius of the magnetic nuclei (being the contrast agents of the ordinary MRI) are saturated up to 90 %. At $B_0 = 0.35$ T, $L(\alpha_0) = 0.9$.

References

1. J. Popplewell, R. Rosensweig, R. J. Johnston. Magnetic field induced rotations in ferrofluids. IEEE Trans. Mag. 26 (1990) 1852-1854.
2. G. K. Batchelor. An Introduction to Fluid Dynamics. 2000, Cambridge: Cambridge Univ. Press.
3. K. V. Kotetishvili, K. G. Kapanadze, G. G. Chikhladze. Phase coding in low intensity magnetic fields for MRI applications. J. Appl. Electromag. 14 (2012) 33-39.

ТЕХНОЛОГИЯ ПРИГОТОВЛЕНИЯ ТОНКИХ ПЛЕНОК Tm_2S_3 ДИСКРЕТНЫМ ИСПАРЕНИЕМ

М. Тетелошвили, З. Джабуа, А. Гигинейшвили

Грузинский технический университет
Тбилиси, Грузия
Z.Jabua@hotmail.com

Принята 17 мая 2013 года

Развитие тонкопленочной электроники и других областей новой техники требуют разработку технологии приготовления тонкопленочных объектов. Решение этой задачи связано с изучением физических свойств тонких конденсированных слоев в зависимости от их фазового и химического состава, кристалличности и совершенства кристаллической решетки.

В настоящее время большое внимание уделяется сульфидам редкоземельных элементов (РЗЭ), в частности полуторным сульфидам [1 – 10]. Они являются материалами с эффективными термоэлектрическими, оптическими и магнитными свойствами и представляют интерес в различных размерных состояниях: порошки субмикронного и наноразмеров, поликристаллы, полученные прессованием порошков и кристаллизацией расплавов, монокристаллы и тонкие пленки. Полуторные сульфиды РЗЭ в том числе Tm_3S_2 являются перспективными материалами для создания керамики специальных свойств [10], поэтому актуальной является разработка технологии приготовления тонких, однофазных, кристаллических пленок полуторного сульфида тулия с совершенной кристалической решеткой.

В работе [10] тонкие пленки Tm_3S_2 были получены методом вакуумно-термического испарения из двух независимых источников компонентов. Задачей данной работы являлась разработка технологии приготовления планок Tm_3S_2 методом дискретного-термического испарения предварительно синтезированного объемного материала Tm_3S_2.

Пленки приготовлялись на подложках прямоугольной формы размерами $15 \times 5 \times 1$ мм изготовленных из ситалла, лейкосапфира и монокристаллического кремния. Перед напылением проводили травление подложек в растворе 20 % NaOH, с последующей промывкой дистиллированной водой. Затем их опять травили в смеси 30 % HCl + 60% HNO_3 + 10 % H_2O и опять промывали дистиллированной водой. Концентрация соляной и азотной кислот составляла 99.8 %. После указанной обработки подложки переносили в вакуумную напылительную камеру и непосредственно перед напылением проводили их отжиг в течение 30 – 45 мин при температуре 600 – 1000 °C в вакууме ~ 10^{-6} мм рт. ст.

Многочисленными опытами установлены закономерности приготовления пленок полуторного сульфида тулия методом дискретного вакуумного испарения. Приготовление пленок проводили в вакуумной камере при вакууме ~ 10^{-6} мм рт. ст.

Порошок Tm_3S_2 из бункера шнеком подавался на вольфрамовую лодочку, откуда испарившись материал конденсировался на подложку. Этот метод позволяет получать пленки высокого качества. Основными параметрами, которые влияют на качество приготовленных пленок являются дисперсность порошка, температура подложки и испарителя, скорость испарения, расстояние от испарителя до подложки, природа подложки. Нужно отметить, что все эти параметры взаимосвязаны.

Экспериментально установлено, что для получения пленок высокого качества оптимальной дисперсностью является 100 – 150 мкм. Если дисперсность меньше 100 мкм, то происходит слипание частиц порошка, что вызывает неравномерную подачу материала на испаритель и, как следствие, увеличение времени напыления и загрязнение штока, через которого материал подается на испаритель. Кроме этого восходящий поток таких мелких частиц может препятствовать поступлению материала на испаритель, что увеличивает расход материала. Если дисперсность выше 130 мкм, при постоянной скорости подачи материала частицы порошка не успевают испарятся с поверхности испарителя и соответственно изменяется стехиометрия пара и пленки.

Чистота исходного материала составляла 99.99 %. Температура подложки при напылении равнялась 870 – 920 К. только при этом достигается хорошая адгезия между подложкой и пленкой. Более низкая температура препятствует равномерному распределению адсорбированных атомов, происходит их группирование в виде «островков» разной толщины, между которыми связи часто нарушены. Если температура недостаточно высока, происходит отслаивание пленки от поверхности. Очень высокая температура подложки вызывает реиспарение атомов осажденных на подложке.

Оптимальной температурой испарителя для полуторного тулия является ~ 2800 К: при более низких температурах в условиях постоянства скорости подачи материала частицы порошка не успевают испаряться, что вызывает изменение стехиометрии как пара, так полученной пленки. При более высокой температуре испарителя, энергия испарившегося материала настолько высока, что происходит его «разбрызгивание». Высокая температура испарителя также резко уменьшает срок службы испарителя.

Оптимальное расстояние от испарителя до подложки равно 55 мм, скорость напыления ~ 90 – 105 Å / с. Толщина пленок составляла 0.6 – 2.5 мкм.

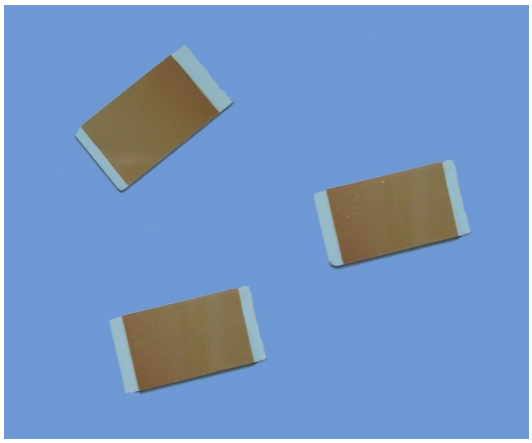

Рисунок 1. Фотография пленки Tm_3S_2 (материал подложки – ситалл).

Приготовленные пленки имели темно коричневую окраску (**рисунок 1**). Фазовый состав приготовленных пленок изучали ренгеновским методом. Рентгенограммы снимали

со скоростью 0.5 – 1 град / мин при излучении Cu K_α с никелевым фильтром в режиме непрерывной записи. Типичная рентгенодифрактограмма представлена на **рисунке 2**.

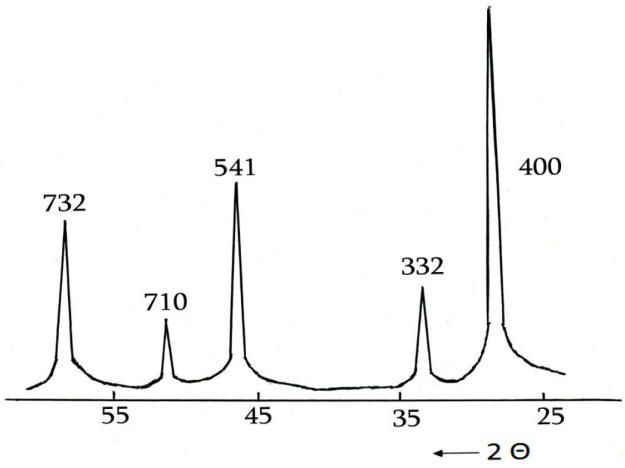

Рисунок 2. Рентгенограмма пленки Tm_3S_2 (материал подложки – ситалл, толщина пленки – 1.6 мкм).

Следует отметит, что максимумы на рентгенограммах пленок Tm_3S_2, приготовленных методом дискретного вакуумного испарения, более острые, их высота больше, а ширина меньше, чем у соответствующих пиков пленок Tm_3S_2, приготовленных методом вакуумно-термического испарения из двух независимых источников [11], что вероятно, говорит о том, что кристаллическая решетка пленок, приготовленных дискретным испарением, более совершенна, чем решетка пленок, приготовленных методом вакуумно-термического испарения из двух независимых источников компонентов.

Анализ рентгенограмм показал, что полученные пленки соответствуют θ форме Tm_3S_2 (кубическая сингония, пространственная группа $I-43d$, структурный тип – Tl_2O_3). Постоянная решетки 12.47 Å, вычисленная из рентгеновских данных, хорошо согласуется с данными работы [12]. Рентгеновским микроанализом установлено, что пленки содержат 40.1 ат. % Tm и 59.9 ат. % S.

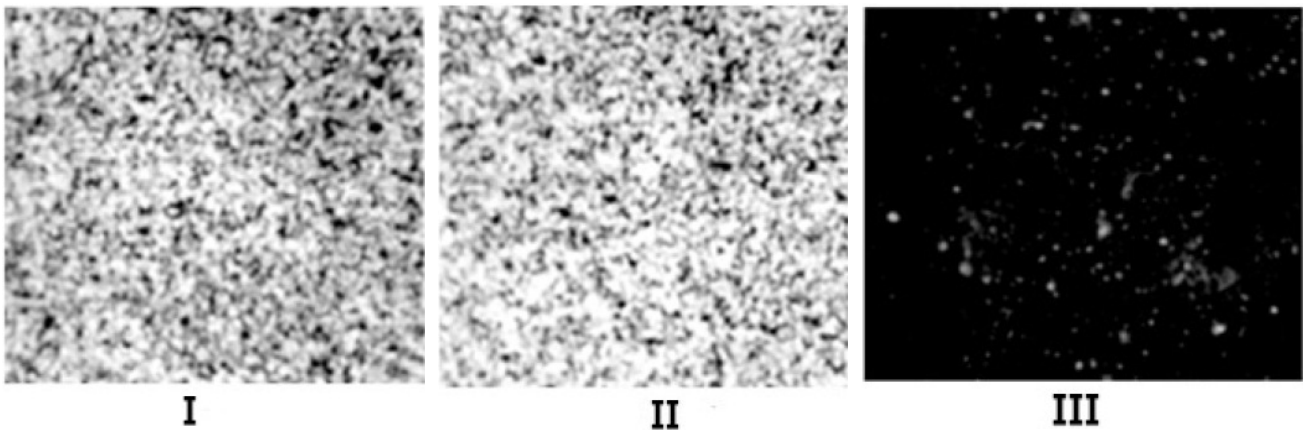

Рисунок 3. Изображение распределения тулия (I), серы (II) на поверхности пленки Tm_3S_2 во вторичных рентгеновских лучах (× 400) и микрофотография поверхности пленки (III).

Во вторичных рентгеновских лучах снята картина распределения компонентов на поверхности пленок. Как видно из **рисунка 3**, компоненты на поверхности пленок распределены довольно равномерно.

Ссылки

1. M. Samiee, K. Garre, M. Cahay, B. Kosel, S. Fairchitd, J. W. Fraser, D. J. Lockvood. Field emission characteristics of a lanthanum monosulfide cold cathode array fabricated using microelectromechanical systems technology. J. Vac. Sci. & Technol. B, 2008, 26, 2, 764-769.
2. S. Fairchitd, J. Jones, M. Cahay, K. Garre, P. Draviam, P. Booichard, X. Wu, D. J. Lockvood. Pulsed laser deposition of lanthanum monosulfide thin films on silicon substrates. J. Vac. Sci. & Technol. B, 2005, 23, 1, 318-321.
3. C. Linton, A. G. Read. Laser spectroscopy of holmium monosulfide. J. Mol. Spectrosc., 2006, 240, 7, 133-138.
4. A. S. Verna. Electronic and optical properties of rare-earth chalcogenides and pnictides. African Phys. Rev., 2009, 3, 1, 11-29.
5. S. M. Luguev, N. V. Lugueva, V. V. Sokolov. Effect of cation vacancies on the thermal conductivity of GdS_x solid solutions. Inorg. Mater., 2008, 44, 8, 796-799.
6. M. Ohta, S. Hirai, H. Kato, V. Sokolov, V. Bakovets. Thermal Decomposition of NH_4SCN for preparation of Ln_2S_3 (Ln = La and Gd). Mater. Trans., 2009, 50, 7, 1885-1889.
7. M. Ohta, S. Hirai, T. Mori, T. Nishimura, K. Shimakage. Thermoelectric properties of Th_3P_4-type rare-earth sulfides Ln_2S_3 (Ln = Gd, Tb) prepared by reaction of their oxides with CS_2. J. Alloys & Comp., 2007, 451, 1-2, 627-631.
8. M. Ohta, S. Hirai, H. Kato, T. Nishimura, Y. Uemura. Termoelectric properties of lantanium sesquisulfides with Ti additive. Appl. Phys. Lett., 2005, 87, 042106, 1-3.
9. H. Yuan, J. Zhage, R. Yu. Synthesis of rare earth sulfides and their UV-vis absorption spectra. J. Rare Earths, 2009, 27, 2, 308-311.
10. А. В. Кертман. Оптическая сульфидная керамика. Соросовский образов. жур. (Химия), 2000, 1-6.
11. З. У. Джабуа, Т. С. Лочошвили, М. Г. Тетелошвили, К. Д. Давитадзе, Г. А. Мазмишили, Л. Н. Глурджидзе. Приготовление тонких пленок триантимонида тулия. Сообщ. АН Грузии, 1994, 150, 1, 106-107.
12. Г. М. Кузмичева, Е. И. Старина, С. Ю. Хлюстова, В. В. Чернышев. Кристаллическая структура θ-Tm_3S_2. Жур. неорг. химии, 1990, 35, 4., 869-873.

MODIFICATION OF THE PROPERTIES OF LEAD SELENIDE LAYERS AT THEIR NANOTHICKNESS

A. M. Pashaev [1], O. I. Davarashvili [2], M. I. Enukashvili [2],
Z. G. Akhvlediani [2, 3], R. G. Gulyaev [2], L. P. Bychkova [2], V. P. Zlomanov [4]

[1] National Aviation Academy of Azerbaijan
Baku, Azerbaijan
[2] I. Javakhishvili Tbilisi State University
Tbilisi, Georgia
omardavar@yahoo.com
[3] E. Andronikashvili Institute of Physics
I. Javakhishvili Tbilisi State University
Tbilisi, Georgia
zairaak@yahoo.com
[4] M. Lomonosov Moscow State University
Moscow, Russia

Accepted May 29, 2013

1. Introduction

Doping of the materials like PbTe and PbSe, and their solid solutions with the impurities with varying valence such as Cr, In, Yb, Ga, etc. is an interesting and promising problem in semiconductor materials science [1]. At a high degree of doping, the impurities of this kind compensate each other and electrically active nonstoichiometric defects. In a certain composition, the balanced impurity level is located in the middle of the forbidden gap, and the quasi-dielectric state is attained, in particular, for creation of high-sensitivity and high-temperature IR photodetectors. However, it turned out that such a state was realized generally at $T < 40$ K and for a limited number of solid solutions. If the variations in the composition used to be the factor of changing the forbidden gap width and the level of impurity location, pressure could play the same role [2]. In this case, under "negative" pressure the forbidden gap width of IV–VI semiconductors increases, and the impurity level shifts rapidly into the depth of the forbidden gap. This allows realizing the dielectric state for a wider range of compositions and at higher temperatures. This work deals with two important issues of this problem: creation of effective "negative" pressure and determination of the forbidden gap width of PbSe nanolayers.

2. Experimental methods

The PbSe layers were grown on the KCl substrate by the method of molecular epitaxy with a "hot wall". The growth rate of the layers was varied over the range of 0.5 – 25 nm / s by varying the temperature of the epitaxy source (polycrystalline PbSe) from 450 to 510 °C, through the change in the distance between the open end of the quartz ampoule with the

epitaxy source and the substrate from 1 to 12 mm, and also by varying of the substrate temperature from 240 to 320 °C [3].

The thickness of layers d and the tangential lattice constant a_τ were determined by the method of X-ray diffraction. The thickness of layers was determined through the relationship between the intensity of radiation reflected from a pure substrate and that reflected from the substrate with deposited layer at multiple planes (200) and (400). The lattice constant was determined at reflection from these planes (200) and (400) also by a symmetric scheme by the relationships $a_\tau = \lambda / \sin\theta$ and $a_\tau = 2\lambda / \sin\theta$, respectively, where λ is the radiation wavelength, 1.7889 Å, and θ is the diffraction angle.

The deformation ε was determined via the tangential lattice constant a_τ : $\varepsilon = (a_\tau - a_{PbSe}) / a_{PbSe}$, where a_{PbSe} is the lattice constant of the PbSe monocrystal (6.126 Å).

The forbidden gap width was determined by optical transmission spectra recorded in the wavelength range from 2.5 to 25.0 μm by means of prism – diffraction spectrophotometer SPECORD–75–IR.

3. Results and discussion

Thus, a new resource in the nanolayers of IV–VI semiconductors can be revealed when studying three important issues: the realization of "negative" pressure, the determination of the rate of changes in the forbidden gap width with the changing pressure and the shift of impurity levels into the depth of the forbidden gap. In this work the first and the second issues are mainly discussed. According to present views, in order to achieve a high level of the strained state, the layers should be grown at as low temperature as possible and in a short time (at high growth rate). In this case, it is possible for the layer growth to be ahead relative to the penetration of dislocations into the layer and their concentration at the heteroboundary when just begins fast relaxation of strains. Hence, at the first stage, the processes of growth of the nanolayers at 240 °C were studied.

The layers ≤ 200 nm thick were mainly investigated. In **Figure 1** is shown the growth rate dependence of the tangential lattice constant of layers. The central point is the layer grown at the rate of 6 nm / s and having the tangential lattice constant $a_\tau = 6.150$ Å. It divides the dependence into two areas. As the growth rate increases up to 25 nm / s, the lattice constant to the right of this point decreases to $a_\tau = 6.130$ Å. To the left of this point, the curve has two extensions. At the layer thickness < 100 nm, the tangential lattice constant increases with the decreasing growth rate and makes up $a_\tau = 6.180$ Å at the rate of ~ 1 nm / s. At the layer thickness of ~ 200 nm, the tangential lattice constant decreases with the decreasing growth rate. The high tangential lattice constant at the layer thickness of < 100 nm can be referred to the location of nonstoichiometric defects ($n \approx 10^{19}$ cm^{-3}) in the nuclei of dislocations and a complex character of their movement from sliding to "creeping" with a high diffusion coefficient. As the growth rate of layers increases, the disordered state is "frozen" in thin layers, at the interface of subgrains-crystallites high disorientation takes place, and, along with the relaxation at the layer-substrate interface, additional relaxation of strains is observed. In the layers ~ 200 nm thick, the increase in the tangential lattice constant with the increasing growth rate up to 6 nm / s correlates with the abovementioned views about the situation when the layer growth rate is ahead the dislocation movement and formation of the disordered state.

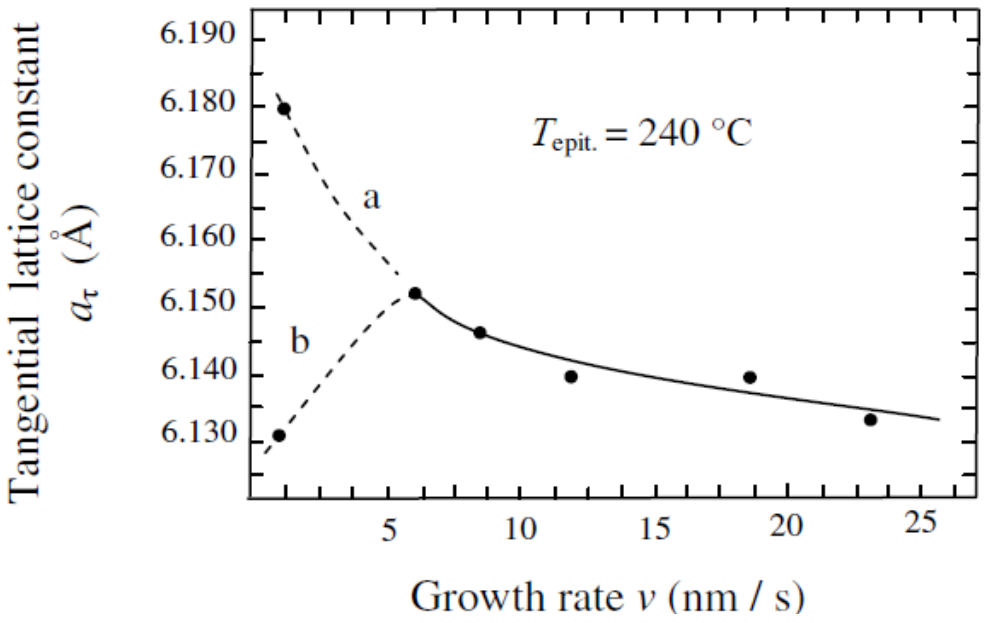

Figure 1. Dependence of the tangential lattice constant on the growth rate of layers at the thickness: (a) $d \leq 100$ nm, (b) $d \sim 200$ nm.

The half-width of the X-ray diffraction line, reaching 33′ at the increasing growth rate, can be taken as a measure of formation of high disorientation. In the layers ~ 200 nm thick, their elastic energy is already so high that location of nonstoichiometric defects in the nuclei of dislocations cannot cause their retardation.

For revealing the effect of the growth temperature on the tangential lattice constant, the layers were grown at the substrate temperature of 300 °C.

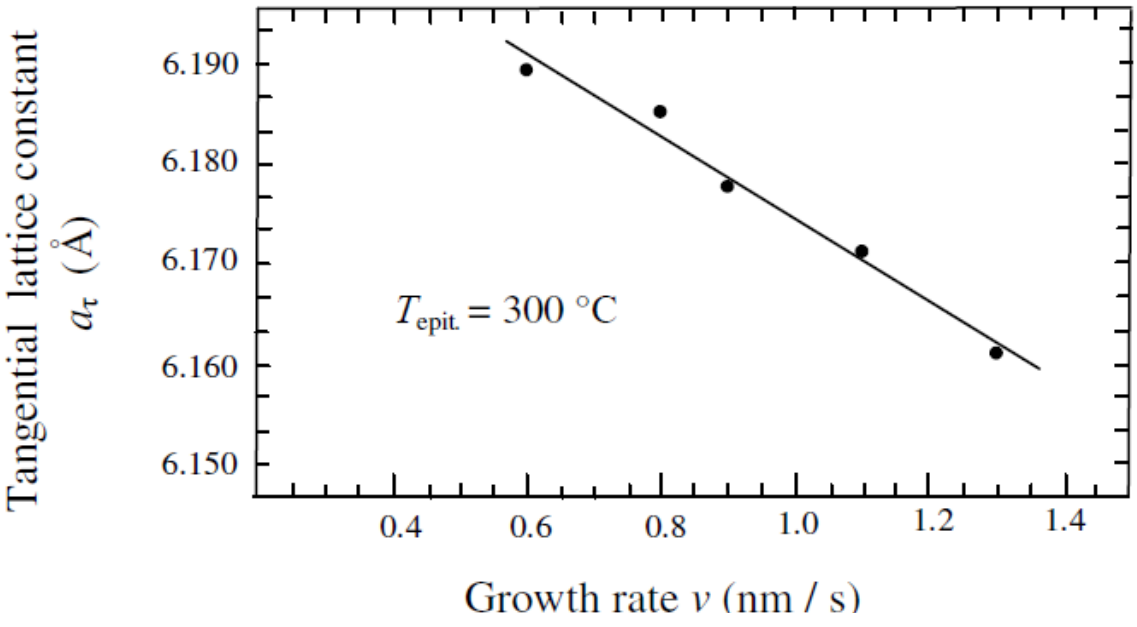

Figure 2. Dependence of the tangential lattice constant on the growth rate of layers.

It turned out that, for layers < 100 nm thick, as the growth rate decreased from 1.3 to 0.6 nm / s, the lattice constant increased by 0.030 Å and made up $a_\tau = 6.190$ Å (**Figure 2**). At the initial mismatch between PbSe ($a = 6.126$ Å) and KCl ($a = 6.290$ Å), deformation was $\varepsilon = 0.026$, at the obtained lattice constant of 6.190 Å – $\varepsilon = 0.01$; at a_τ of the layer equal to 6.208 Å, the value of ε was 0.013 (half as much), while the layer thickness was < 40 nm. The layers with such a lattice constant were grown with heating up of the KCl substrate from the rear by a filament lamp.

Despite the strained state, the layers grow monocrystalline, and, in this case, the half-width of the X-ray diffraction line makes up 18 – 20′.

We have elaborated the methods of determination of the forbidden gap width of the layers of different thickness, including nanolayers, by optical transmission [4]. By optical characterization of the layers – by sequential determination of the refractive index and the reflection and absorption coefficients, and their spectrum, straightening of squared absorption coefficients in accordance with the relationship for direct band-to-band transitions $\alpha^2 \sim h\nu - E_g$ was performed. It should be noted that the straightening of $(\alpha h\nu)^2 \sim f(h\nu)$ for the IV–VI semiconductors yields the same value of the forbidden gap width E_g within the accuracy of determination 5 – 6 meV.

The spectra of epitaxial layers < 700 nm thick generally showed a monotonic increase with a small slope as the wavelength increased. In this case, as well as in the case of thick layers in the spectra of which interference peaks were revealed, such spectra were processed by a model of the Fabry–Perot interferometer. Taking the epitaxial PbSe layer as a resonator the ends of which are the boundaries with the substrate and the air, the model considers the interference as the one damping in the wave layer under multiple reflection from the resonator boundaries. The magnitude of the transmission coefficient through the layer is the following:

$$T = \frac{(1-r_1^2)(1-r_2^2)\exp(2\beta_i d)}{(1-R)^2 + 4R\sin^2(\beta d)}, \qquad (1)$$

where $r_1 = (N_{PbSe} - N_{air})/(N_{PbSe} - N_{air})$ is the amplitude value of reflection coefficient at the PbSe / air interface; $r_2 = (N_{PbSe} - N_{KCl})/(N_{PbSe} - N_{KCl})$ is the amplitude value of reflection coefficient at the PbSe (layer) / KCl (substrate) interface, $R = r_1 r_2 \exp(2\beta_i d)$, $\beta = 2\pi N/\lambda$, and $\beta_i = -\alpha/2$ is the absorption coefficient.

Extrapolating the values of the refractive index determined by interference peaks, for instance, for layer SL-69 1.83 μm thick, the values r_1 and r_2 in the short-wavelength region were obtained [4 – 6]. The obtained values of r_1 and r_2 were substituted into the equation for determination of the absorption coefficient α through $y = \exp(-\alpha d)$:

$$T(r_1 r_2)y^2 - \left((1-r_1^2)(1-r_2^2) + 2Tr_1 r_2 - 4Tr_1 r_2 \sin^2\frac{2\pi N d}{\lambda}\right)y + T = 0. \qquad (2)$$

Because of the high concentration of current carriers (~ 10^{19} cm^{-3}) in the epitaxial layers, the absorption by free carriers is high, and it could be quite significant in the region of eigenabsorption as well. Hence the straightening of squared absorption coefficients is performed by the relationship $(\alpha - \alpha_{fr.car})^2 = f(h\nu)$. The quantity $\alpha - \alpha_{fr.car}$ corresponds to interband absorption and characterizes its edge, especially in thin layers where, along with the high concentration of current carriers, a significant decrease in the relaxation time is observed.

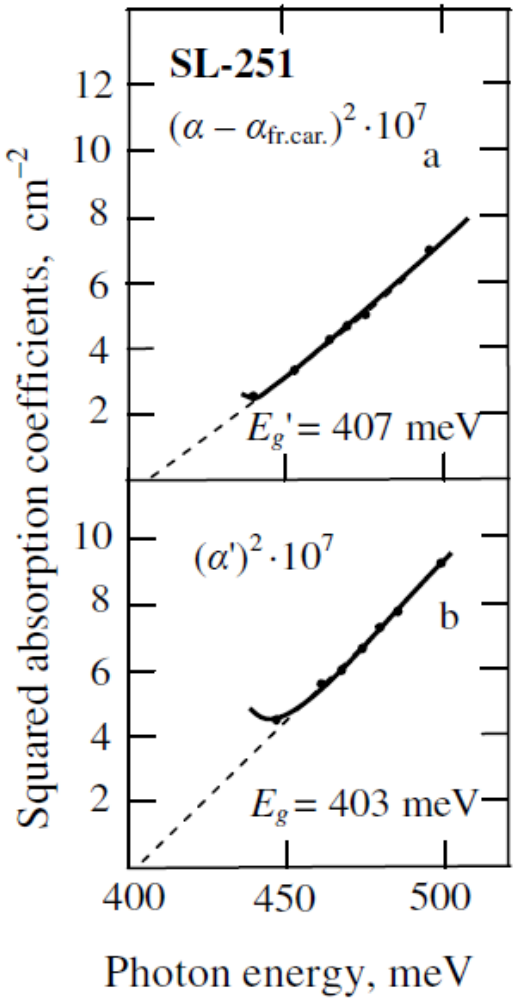

Figure 3. Dependence of the squared absorption coefficients in strained layer SL-251 on the photon energy: (a) in the degenerate case, (b) in the nondegenerate case.

As at high concentrations of current carriers the transitions between band edges are impossible because of the Burstein effect, for determination of the forbidden gap width, the straightening of function $((\alpha - \alpha_{fr.car})/\gamma)^2 = f(h\nu)$ is performed. In the last expression, $1/\gamma$ accounts for degeneration, and the dependence of this factor on the forbidden gap width and the Fermi level E_F is given in Ref. [7]. Thus the straightening of $(\alpha - \alpha_{Cb.H})^2 = f(h\nu)$ determines the absorption edge, while the one of $(\alpha')^2 = ((\alpha - \alpha_{fr.car})/\gamma)^2 = f(h\nu)$ – determines the forbidden gap width in the pure, nondegenerate semiconductor. It is noteworthy that, for straightening of both functions, the range of squared total absorption coefficients made up $10^7 - 10^8$ cm^{-2}, and in particular, α was less than 9000 cm^{-1} at 496 meV. This means that, for direct band-to-band transitions, the absorption has not reached saturation at this energy yet. As is seen from **Figure 3**, at the straightening of squared absorption coefficients, the forbidden gap width makes up 403 meV and the absorption edge – 407 meV at $T = 300$ K. The obtained value is closed to the forbidden gap width of PbS – 410 meV, for which the absorption coefficient α makes up 8000 cm^{-1} at 496 meV. This fact is an additional indicator of correct straightening of the squared absorption coefficients.

The data on layer SL-251 are typical at the layer thickness < 100 nm, and these data are presented in the **Table 1**. As the layers thickness decreases, the tangential lattice constant, deformations – strains and hence the forbidden gap width of the layers increases. With the decreasing of the layers thickness their color changed from silvery and dark brown to transparent [8], which correlated also with the increasing of the forbidden gap width [9].

Table 1. Data for the tangential lattice constants, deformations (strains) and corresponding forbidden gap width in PbSe layers.

#	Layer	Layer thickness d, nm	Tangential lattice constant a_τ, Å	Relative mismatch-deformation $\varepsilon = \frac{a_\tau - a_{PbSe}}{a_{PbSe}}$	Strain $\sigma = \frac{E}{1-\nu}\varepsilon$, kbar	E_g, meV
1	SL-69	1830	6.126(4)	0	0	286
2	SL-277	181	6.149(0)	0.0038	3.1	340
3	SL-304	119	6.154(8)	0.0047	3.8	355
4	SL-251	72	6.175(4)	0.0081	6.5	403
5	SL-262	52	6.188(2)	0.0100	8.1	421

At the tangential lattice constants equal to 6.149(0) and 6.175(4) Å and with account for Young's modulus $E = 5 \cdot 10^{11}$ dyne / cm^2, the "negative" pressure in the layers made up 3.1 and 6.5 kbar, respectively. When the forbidden gap width of strained layers increased by 54 and 117 meV, respectively (for unstrained PbSe $E_g = 286$ meV) the rate of changing of E_g was 18 – 19 meV / kbar.

According to our estimates, if we manage to shift the Cr impurity level lower than the conductivity band edge only by 30 meV, the concentration of carriers will decrease by four orders of magnitude.

4. Conclusions

Under the conditions of "negative" pressure and increasing forbidden gap width, at their appropriate doping, the lead selenide nanolayers can show new resources for designing high-sensitivity and high-temperature IR photodetectors. Such resources will be on high demand when the "negative" pressure increases at the layers thickness > 50 nm. As the elastic energy of layers increases with their thickness, it reflects the degree of relaxation of strains. At the layers thickness < 100 nm, the nonstoichiometric defects located in the nuclei of dislocations cause the retardation of dislocations, and maximum deformations and strains are reached. High temperature and low growth rates can enhance such retardation. At "negative" pressure, the forbidden gap width increases, and the rate of its built-up depends on the elastic properties of layers. In particular, at the modulus of elasticity $E = 5 \cdot 10^{11}$ dyne / cm^2, it makes up ~ 19 meV / kbar.

References

1. B. A. Volkov, L. I. Ryabova, D. R. Khokhlov. Impurities with varying valence in solid solutions based on lead telluride. Phys. – Uspekhi 152 (2002) 1.
2. A. M. Pashaev, O. I. Davarashvili, V. A. Aliyev, M. I. Enukashvili, V. P. Zlomanov. The effect of deformations on the change in the forbidden gap width in the epitaxial layers of $A^{IV}B^{VI}$ semiconductors. Georg. Eng. News 3 (2008) 53.
3. A. M. Pashaev, O. I. Davarashvili, Z. G. Akhvlediani, M. I. Enukashvili, R. G. Gulyaev, V. P. Zlomanov. Growth and properties of strained epitaxial nanolayers of lead selenide. In: Abs. Int. Confe. Functional Mater. & Nanotechnol. 2012, Riga, 198.
4. A. M. Pashaev, O. I. Davarashvili, Z. G. Akhvlediani, M. I. Enukashvili, R. G. Gulyaev, V. P. Zlomanov. Unrelaxed state in epitaxial heterostructures based on lead selenide. J. Mod. Phys. 3 (2012) 502.
5. A. M. Pashaev, O. I. Davarashvili, M. I. Enukashvili, L. P. Bychkova, V. P. Zlomanov. Analysis of the optical properties of epitaxial lead selenide layers. Trans. Natl. Aviation Acad. Sci. Azer. 13 (2011) 3.
6. Y. V. Mal'tsev, E. D. Nensberg, A. V. Petrov, S. A. Semiletov, Y. I. Yukhanov. Electrical and optical studies on PbS. Phys. Solid State 8 (1966) 2154.
7. Y. I. Ravich, B. A. Efimova, I. A. Smirnov. Methods of investigation of semiconductors as applied to lead chalcogenides PbTe, PbSe and PbS. 1968, Moscow: Nauka.

8. A. M. Pashaev, O. I. Davarashvili, M. I. Enukashvili, Z. G. Akhvlediani, R. G. Gulyaev, L. P. Bychkova. Epitaxial lead selenide layers over a wide range of their thickness on dielectric substrates. J. Mater. Sci. & Eng. 3 (2013), 97.
9. A. M. Pashaev, O. I. Davarashvili, M. I. Enukashvili, Z. G. Akhvlediani, R. G. Gulyaev, M. A. Dzagania. Supercritical epitaxial nanolayers of lead selenide. In: Abs. 3rd Inte. Conf. Phys. Opt. Mater. & Dev. 2012, Belgrade, 217.

К ТЕОРИИ ФАЗОВЫХ ПРЕВРАЩЕНИЙ В $PrAlO_3$

З. Б. Чачхиани, Л. К. Дарчиашвили, Э. М. Зерагия

Грузинский технический университет
Тбилиси, Грузия

Принята 3 июня 2013 года

Среди огромного семейства перовскитов $PrAlO_3$ занимает особое место в связи с большим числом структурных превращений, которые наблюдаются в этом кристалле: известно пять кристаллических фаз. При высоких температурах ($T > 1320$ К) симметрия кристалла с одной формульной единицей в примитивной ячейке – O_n^1. В интервале температур 205 – 1320 °К устойчива самая изученная фаза кристалла с симметрией D_{3d}^6 и двумя формульными единицами в ячейке. Обозначим ее через $D_{3d}^6(2)$. Структуру этой фазы легко получить, если в качестве параметра порядка выбрать вращение кислородного октаэдра вокруг иона Al. Переходы, описываемые таким параметров, называются переходами типа смятия и очень широко распространены в семействе перовскита. Так, аналогичный переход $O_n^1(1)$ (I) – $D_{3d}^6(2)$ наблюдается в $LaAlO_3$, $CeAlO_3$ и $NdAlO_3$; другой типичный пример перехода типа смятия $O_n^1(1)$ (I) – $D_{4n}^{18}(2)$ наблюдается в $KMnF_3$ и $SrTiO_3$. Алюминат празеодима отличается от перечисленных кристаллов тем, что в нем наблюдаются обе известные в семействе перовскитов фазы смятия; причем тетрагональная фаза устойчива при низких температурах $T < 99$ К [1]. На промежуточных температурах существуют еще две фазы: орторомбическая при 146 К $< T <$ 196 К и моноклинная при 99 К $< T <$ 146 К [1]. При интерпретации рентгенограмм орторомбической фазы в [2] было предложено, что в этой фазе имеется дополнительное смещение по Pr^{3+} и соответственно, была предложена моноклинная группа симметрии C_{2n}^3. Однако моноклинных искажений угла между элементарными трансляциями не обнаружено [2]. Аналогично было предложено, что в моноклинной фазе есть понижающие симметрию до триклинной смещения ионов празеодима, но углы между элементарными трансляциями говорят об отсутствии дополнительного понижения симметрии. Более того, предположение о дополнительном смещении ионов Pr^{3+} не согласуется с другими макроскопическими измерениями, которые утверждают, что переход между орторомбической и моноклинной, также как и переход между моноклинной и тетрагональной модификациями – второго рода. Действительно, смещения празеодима, предложенные в [2] соответствуют подключению второго параметра порядка. Переходы в фазы, описываемые двумя параметрами порядка – это довольно частое явление, но они непременно первого рода [3, 4]. Поэтому в [5] фактически поставлена задача определить структуру фаз орторомбической и моноклинной, не противоречащую известным экспериментальным результатам. Это и будет одной из целей данной работы.

Вторая цель работы состоит в описании всей серии фазовых переходов в кристалле алюмината празеодима. Раньше делалась попытка провести такое описание на основе

феноменологической модели Томаса и Мюллера [6]. Эта модель, как теперь очевидно, идентична первой феноменологической модели Гинзбурга для титаната бария и, как было показано, недостаточна, чтобы описать, например, орторомбическую фазу. Чтобы описать моноклинную фазу, нужна еще более полная модель [7, 8]. Именно эта более полная модель и будет рассмотрена в данной работе.

Третья цель работы состоит в построении адекватной феноменологической модели, описывающей расщепление уровней Pr^{3+} в разных фазах кристалла. Модели, которые до сих пор обсуждались [1], явно недостаточны. Попутно будет проиллюстрировано применение метода [7] к задачам ЭПР. Метод рассмотрения пространства представлений ε и целого рационального базиса векторных инвариантов в этом пространстве позволяет получить некоторые точные результаты относительно температурной зависимости расщепления уровней Pr^{3+} в низкосимметричных фазах $PrAlO_3$.

1. Термодинамика фазовых переходов в $PrAlO_3$

В высокосимметричной фазе $PrAlO_3$ имеет симметрию O_n^1 ; причем ионы празеодима расположены по правильной системе точек $\vec{a}\,(0,0,0)$, ионы алюминия по $\vec{b}\,(1/2,1/2,1/2)$, а ионы кислорода занимают трехкратную позицию $\vec{c}\,(0,1/2,1/2)$, $(1/2,0,1/2)$ и $(1/2,1/2,0)$. Параметр порядка, описывающий переход в D_{3d}^6 преобразуется по представлению Γ_{25} точки R зоны Бриллюэна (или по представлению $\tau_\delta(k_{13})$ по таблицам Ковалева [9]. Представление $\Gamma_{25}(R)$ – трехмерное. Рассмотрим трехмерное Эвклидово пространство ε_1 и в нем декартовую систему координат, на осях которой отложены компоненты параметра порядка. Все операции из бесконечной группы O_n^1 в этом пространстве будут иметь вид операций из точечной группы O_n. Следовательно [9], неравновесный потенциал Ландау $\phi(\eta_1,\eta_2,\eta_3)$, описывающий переходы в низкосимметричные фазы с таким параметром порядка, является целой рациональной функцией трех однородных полиномов, составленных из компонент параметра

$$I_1=\eta_1^2+\eta_2^2+\eta_3^2 \qquad I_2=\eta_1^4+\eta_2^4+\eta_3^4 \qquad I_3=\eta_1^2\eta_2^2\eta_3^2 . \tag{1}$$

Минимизация $F(I_1,I_2,I_3)=\phi(\eta_1,\eta_2,\eta_3)$ приводит к выводу, что таким параметром порядка можно описать шесть низкосимметричные фазы [7, 8]:

$$\begin{array}{lll}(\eta_1,\eta_2,\eta_3)-D_{3d}^6 & (\eta,0,0)-D_{4n}^{18} & (\eta,\eta,0)-D_{2n}^{28}\\ (\eta_1,\eta_2,0)-C_{2n}^3 & (\eta_1,\eta_1,-\eta_2)-C_{2n}^6 & (\eta_1,\eta_2,\eta_3)-C_n^1 .\end{array} \tag{2}$$

Поскольку среди фаз (2) есть и орторомбическая и моноклинная и триклинная фазы, то ограничимся предположением, что один параметр порядка, который описывает переход O_n^1 – D_{3d}^6 , описывает и другие фазы кристалла. Поскольку переходы в $PrAlO_3$ либо обладают малой скрытой теплотой (переходы в ромбоэдрическую фазу и орторомбическую фазу), либо – второго рода, то предположим, что все фазы $PrAlO_3$ описываются малым решением уравнений состояния. В этом случае потенциал Ландау можно записать в виде ограниченного ряда полиномов (1):

$$F=a_1I_1+a_2I_1^2+a_3I_1^3+a_4I_1^4+b_1I_2+b_2I_2^2+c_1I_3+\sigma_{12}I_1I_2+\sigma_{112}I_1^2L_2+\sigma_{13}I_1I_3 . \tag{3}$$

Потенциал (3) – это модельное предположение в феноменологической теории и оправданием для такого предположения будет только правильное описание экспериментальных фактов. Предположение о том, что все переходы в $PrAlO_3$ описываются одним неприводимым представлением уже обсуждалось в [1], но принятая в [1] модель потенциала четвертой степени описывала только тетрагональную и ромбоэдрическую фазы. Потенциал (3) совместно с предположением о том, что фазы описываются малыми решениями уравнений состояния, позволяет получить полное решение задачи о взаимном расположении фаз на фазовой диаграмме [8]. Вид фазовой диаграммы дается на плоскости (a_1, b_1) в предположении, что $c_1 > 0$ и $\Delta = 4a_2b_2 - c_{12}^2 > 0$

В фазовой диаграмме можно выбрать путь, например,

$$a_1 = -\alpha_0 + \gamma b_1 \qquad b_2 = \beta(I - I_0), \tag{4}$$

при котором будет наблюдаться последовательность фазовых переходов O_n^1 – D_{3d}^6 – D_{2n}^{28} – C_{2n}^3 – D_{4n}^{18}, что говорит в пользу принятой модели (3) для описания фазовых переходов в $PrAlO_3$.

Фазовый переход D_{3d}^6 – D_{2n}^{28} как следует из модели (3), всегда первого рода, а переходы D_{2n}^{28} – C_{2n}^3 и C_{2n}^3 – D_{4n}^{18} – всегда второго рода. Вывод о роде перехода D_{3d}^6 – D_{2n}^{28} можно сделать и из более простых соображений: группы не связаны соподчинением и поэтому переход всегда первого рода. Вывод о том, что переходы D_{2n}^{28} – C_{2n}^3 – D_{4n}^{18} всегда непременно второго рода, является прямым следствием предположения о том, что фазы описываются малыми решениями уравнений состояния. Теоретико-групповые соображения только не запрещают возможность перехода второго рода. Существует экспериментальное подтверждение этого вывода. В твердом растворе $Pr_{1-x}Nd_xAlO_3$ линия переходов, идущая из точки T_3 на оси от $x = 0$ вплоть до $x = 1/4$, остается линией перехода второго рода [10].

Изученная экспериментально еще одна точка $x = 1/2$, при которой второй переход $Pr_{1/2}Nd_{1/2}AlO_3$ первого рода, возможно, соответствует прямому переходу D_{2n}^{28} – D_{4n}^{18}. Параметры реального термодинамического пути, соответствующего понижению температуры при $p = 1$ атм, проще всего определить по температурам фазовых переходов. Обозначим $\delta \equiv 2a_2\sigma_{12} - 3a_3\sigma_{12}$; тогда четыре уравнения для определения четырех параметров (4) имеют вид:

$$\begin{aligned}
&\alpha_0 = \gamma\beta(T_1 - T_0)\\
&T_2 - T_0 = \left(\sigma_{12} - \frac{2c_1}{9}\right)(T_2 - T_1)\\
&\gamma(T_3 - T_1) = \frac{2a_2}{\sigma_{12}}(T_3 - T_0) + \left(\frac{\delta}{\sigma_{12}^3} + \frac{\Delta}{2\sigma_{12}^3}\right)\beta(T_3 - T_0)^2\\
&\gamma(T_4 - T_1) = \frac{2a_2}{\sigma_{12}}(T_4 - T_0) + \left(\frac{\delta}{\sigma_{12}^3} + \frac{\Delta}{2\sigma_{12}^3}\right)\beta(T_4 - T_0)^2 .
\end{aligned} \tag{5}$$

Здесь $T_1 = 1320$, $T_2 = 205$, $T_3 = 146$ и $T_4 = 99$ К.

Зная выражения параметров α_0, γ, β и T_0, через температуры перехода и параметры модели (2), легко получить и температурную зависимость параметра порядка на термодинамическом пути и зависимость аномальной части термодинамического

потенциала от температуры. Для полноты приведем зависимость параметра порядка от a_1 и b_1 в фазах $PrAlO_3$:

$$D_{3d}^6 \eta_1^2 = \eta_2^2 = \eta_3^2 = -\frac{a_1}{6a_2} + \frac{a_1 b_1}{18a_2^2} - \frac{27a_3 + 9\sigma_{12} + c_1}{8a_2^3} a_1^2, \tag{6}$$

$$D_{2n}^{28} \eta_3 = 0 \qquad \eta_1 = \eta_2 = -\frac{a_1}{2a_2} + \frac{a_1 b_1}{8a_2^2} - \frac{3(2a_3 + c_{12})}{32a_2^3} a_1^2, \tag{7}$$

$$c_{2n}^3 \begin{cases} \eta_3 = 0 \qquad \eta_1^2 = \eta_2^2 = \dfrac{\sigma_{12} b_1 - 2b_2 a_1}{\Delta} + \dfrac{\sigma_{12} c_1 - 6a_3 b_2}{\Delta^3} (c_{12} b_1 + 2b_2 a_1)^2 \\ \eta_1^4 + \eta_2^4 = \dfrac{\sigma_{12} a_1 + 2a_2 b_1}{\Delta} + \dfrac{3a_3 \sigma_{12} - 2a_2 c_1}{\Delta^3} (c_{12} b_1 - 2b_2 a_1)^2 \end{cases}, \tag{8}$$

$$D_{4n}^{18} \eta_2 = \eta_3 = 0 \qquad \eta_1^2 = -\frac{a_1}{2a_2} + \frac{a_1 b_1}{2a_2^2} - \frac{3(a_3 + \sigma_{12})}{8a_2^3} a_1^2. \tag{9}$$

Феноменологические параметры модели (2) можно в соответствии с (6 – 9) определять из разных экспериментов. Так, скачок энтропии при фазовом переходе из фазы D_{3d}^6 в фазу D_{2n}^{28} равен

$$\Delta S = \frac{a_1^3(T_2)}{24a_2^2} \left(\frac{9\sigma_{12} - 2c_1}{18a_2} \gamma\beta - \beta \right). \tag{10}$$

Для вычисления скачка энтропии (10) нужно по (6) и (7) определить потенциал орторомбической и ромбоэдрической фаз, найти линию равенства этих потенциалов и вычислить производные по температуре вдоль (4). Аналогично легко вычисляются аномалии теплоемкости на границах фаз $D_{2n}^{28} - C_{2n}^3$ и $C_{2n}^3 - D_{4n}^{18}$.

Однако существенный интерес представляет непосредственное определение зависимости параметра порядка от внешних условий, в частности, температуры. Поэтому перейдем к обсуждению микроскопических проявлений фазовых переходов в $PrAlO_3$.

2. Искажения структуры при фазовых переходах

Представление $\Gamma_{25}(R)$ группы O_n^1 можно построить, если в качестве базисных функций взять бесконечно малые повороты кислородного октаэдра вокруг осей четвертого порядка, проходящих через ион Al. Следовательно, малые углы поворота октаэдра, которые наблюдаются в низкосимметричных фазах, в первом приближении пропорциональны компонентам параметра порядка. Углы поворота октаэдров можно получить из рентгенограмм, однако интерпретация такого эксперимента достаточно затруднена и имеет смысл обсудить другие возможности косвенного измерения углов поворота октаэдра φ_1, φ_2 и φ_3. Смещения всех шести разных в низкосимметричных фазах ионов кислорода соответственно в фазах D_{4n}^{18} и D_{3d}^6, ион Pr^{3+} в этих фазах занимает беспараметрическую позицию, в фазе с симметрией D_{2n}^{28} симметрия положения иона Pr^{3+} – C_{2v} и, следовательно, в этой фазе ион смещен вдоль оси второго порядка.

Из приведенных чисто геометрических соображений нельзя сказать ни как эти смещения зависят от углов поворота октаэдра, ни какое относительное смещение двух ионов в примитивной ячейке кристалла. Для ответа на эти вопросы необходимо

определить явный вид нелинейных взаимодействий между смещениями ионов празеодима и поворотами у кислородного октаэдра [11]. Для этого необходимо построить целый рациональный базис инвариантов относительно O_n^1, составленный из компонент параметра порядка η_1 , η_2 , η_3 и смещений Pr^{3+} с $K=0\,(\xi_1,\xi_2,\xi_3)$ и $K=1/2\,(b_1+b_2+b_3)\,(\Psi_1,\Psi_2,\Psi_3)$. Приведем только ответ. Нелинейные взаимодействия между $\{\eta_i\}$ и $\{\xi_i\}$ не приводят к необходимости возникновения ξ, если $\{\eta_i\neq 0\}$. Напротив, два типа нелинейных взаимодействий, описываемых инвариантами

$$(\eta_1^2-\eta_3^2)\eta_2\psi_2+(\eta_3^2-\eta_2^2)\eta_1\psi_1+(\eta_2^2-\eta_1^2)\eta_3\psi_3$$
$$(\eta_1^2-\eta_2^2)\eta_3^3\psi_3+(\eta_2^2-\eta_3^2)\eta_1^3\psi_1+(\eta_1^2-\eta_3^2)\eta_2^3\psi_2 \qquad (11)$$

приводят к необходимости смещений, описываемых $\{\Psi_i\}$ в орторомбической, моноклинной и триклинной фазах $PrAlO_3$. Таким образом ионы празеодима смещаются в этих фазах в противоположные стороны и это смещение в первом приближении пропорционально кубу угла поворота октаэдра. Абсолютно аналогично можно исследовать изменение форм-фактора иона Pr^{3+}. В поле сферической симметрии основное состояние этого иона – $^3H_4$. В электрическом поле кубической симметрии (в высокосимметричной фазе) это состояние расщепляется на два триплета симметрии T_{2g} и T_{1g}, синглет A_{1g} и дублет E_g. Основное состояние – дублет, первое возбужденное – триплет T_{2g} с энергией около 150 $см^{-1}$. Будем считать, что только эти два уровня и заполнены в интересном для исследований температурном интервале. Часть форм-фактора ионов Pr, обусловленная электронной плотностью, на E_g уровне изменится в низкосимметричных фазах: уровень расщепится. Обозначим соответствующие новым уровням функции e_1 и e_2 для случая расщепления с $K=0$, и f_1 и f_2 для $K=1/2\,(b_1+b_2+b_3)$. Построив целый рациональный базис инвариантов из η_1 , η_2 , η_3 и e_1 , e_2 , получим, что из-за взаимодействий вида

$$(2\eta_3^2-\eta_1^2-\eta_2^2)e_1+\sqrt{3}(\eta_1^2-\eta_2^2)e_2 \qquad (12)$$

уровень E_g непременно расщепляется в низкосимметричных фазах (кроме ромбоэдрической). Это расщепление на обоих ионах празеодима одинаковое, так как линейных по f_1 и f_2 инвариантов из η_1 , η_2 , η_3 и e_1 , e_2 построить нельзя. Аналогично получаем, что одинаково расщепляется терм T_{2g}. Этот результат позволяет строить теорию расщепления термов Pr^{3+} при изменении симметрии положения для одного иона, расщепление уровней на втором ионе будет таким же, как и на первом.

3. Влияние электронной подсистемы ионов Pr^{3+} на фазовый переход

Поскольку фазовые переходы в $PrAlO_3$ второго рода или близки к переходам второго рода (фазы описываются малыми решениями уравнений состояния), то энергии фаз разнятся мало. В связи с этим в [1] высказано предположение, что подсистема *f*-электронов празеодима может сильно повлиять на переход в том же числе, стабилизировать некоторые фазы.

Перед обсуждением этого предположения заметим, что взаимодействие незаполненной оболочки празеодима с кислородом определяется теми же интегралами переноса, которые определяют косвенное обменное взаимодействие. Поскольку в

интересном для обсуждения интервале температур $PrAlO_3$ немагнитен, то взаимодействие между подсистемами слабое и его можно рассматривать по теории возмущений, т.е. считать, что термодинамические потенциалы подсистем в первом приближении аддитивны.

Разберем вопрос: может ли учет подсистемы *f*-электронов изменить результаты, полученные в рамках модели (2), и каким образом? Термодинамический потенциал системы *f*-электронов определяется по статистической сумме $Z = \sum_i \exp(\beta\varepsilon_i)$, где ε_i – уровни энергии электронной подсистемы. В принятом приближении, когда заселены только два нижних уровня T_{2g} и E_g, уровни энергии в низкосимметричных фазах определяется в первом приближении из решения следующего секулярного уравнения, которое получают приравнивая к нулю определитель симметричной матрицы, элементы которой равны:

$$M_{11} = \Delta - \lambda + c(2\eta_1^2 - \eta_2^2 - \eta_3^2) \qquad M_{22} = \Delta - \lambda + c(-\eta_1^2 + 2\eta_2^2 - \eta_3^2)$$

$$M_{33} = \Delta - \lambda + c(-\eta_1^2 - \eta_2^2 + 2\eta_3^2) \qquad M_{44} = -\lambda + \frac{A}{\sqrt{c}}(2\eta_3^2 - \eta_1^2 - \eta_2^2)$$

$$M_{55} = -\lambda - \frac{A}{\sqrt{c}}(2\eta_3^2 - \eta_1^2 - \eta_2^2) \qquad M_{12} = B\eta_1\eta_2; M_{13} = B\eta_1\eta_3$$

$$M_{23} = B\eta_2\eta_3 \qquad M_{14} = \frac{D}{2}(-1+\sqrt{3})\eta_2\eta_3 \qquad M_{15} = \frac{D}{2}(1+\sqrt{3})\eta_2\eta_3$$

$$M_{24} = \frac{D}{2}(-1+\sqrt{3})\eta_1\eta_3 \qquad M_{25} = \frac{D}{2}(1-\sqrt{3})\eta_1\eta_3$$

$$M_{34} = D\eta_1\eta_2 = -M_{35} \qquad M_{45} = \frac{A}{\sqrt{2}}(\eta_1^2 - \eta_2^2). \qquad (13)$$

Здесь Δ – параметр, который характеризует расщепление T_{2g} и E_g уровней в кубическом поле, C – интеграл, пропорциональный квадрату волновой функции T_{2g} уровня, B – матричный элемент взаимодействия между двумя состояниями, описываемыми двумя разными функциями T_{2g} уровня, D – матричный элемент, характеризующий перемешивание E_g и T_{2g} уровней за счет поворота кислородного октаэдра, A – матричный элемент взаимодействия, приводящий к расщеплению E_g уровня и пропорциональный произведению волновых функций E_g уровня. Матрица оператора возмущений выписана в приближении первого порядка теории возмущений.

Легко записать эту матрицу и с учетом следующих порядков теории возмущений; однако во всех случаях сохранится самое важное свойство этой матрицы: в пространстве волновых функций - это тензор второго ранга, совместимый с симметрией гамильтониана нулевого приближения. В данном случае эта симметрия определяется кубической группой преобразований в обычном пространстве, трансформационными свойствами волновых функций T_{2g} и E_g уровня и трансформационными свойствами $\{\eta_i\}$. Из факта инвариантности тензора следует основной для нас вывод: коэффициенты векового уравнения, определяющего уровня энергии электронной подсистемы, будут зависеть от $\{\eta_i\}$ только как функции набора инвариантов (1). Следовательно, и сами уровни энергии будут зависеть только от набора инвариантов (1), и только от них будет зависеть и свободная энергия электронной подсистемы. Следовательно, электронная подсистема невзаимодействующих ионов Pr^{3+} не может качественно изменить наших выводов о симметрии и структуре низкосимметричных фаз. Вопрос о количественном направлении

некоторых ответов в рамках чисто феноменологической теории решить нельзя. Поэтому остается только обсудить зависимость расщепления энергии ионов празеодима от величины поворота октаэдров в низкосимметричных фазах.

4. Зависимость спектра Pr^{3+} от симметрии фаз

В матрице, определяющей влияние смещений кислорода на изменение структуры спектра, интегралы B, C и A одного порядка, и вообще говоря, больше чем D. Поэтому для простоты ограничимся моделью, в которой $D=0$. В этой модели согласно (13) вековое уравнение для E_g и T_{2g} термов распадается на уравнения второго и третьего порядка. Расщепление E_g терма определится условием

$$\lambda_{1,2} = -A\sqrt{I_2 - \frac{I_1^2}{3}}\,. \tag{14}$$

Это решение обсуждалось ранее в [1] и принятая там модель в этом случае достаточно полна, так как не приводит к случайным вырождениям в спектре в тех фазах, в которых вырождение должно быть снято.

Для T_{2g} уровня вековое уравнение имеет вид

$$(\Delta-\lambda)^3 + (\Delta-\lambda)\left(\frac{3}{2}c^2(I_1^2-3I_2) - \frac{B}{2}(I_1-I_2)\right) +$$

$$+ (3c-B)^2(3c+2B)I_3 + \frac{1}{2}c(B^2-5c^2)I_1^3 + \frac{1}{2}c((3c)^2-B^2)I_1I_2 = 0\,. \tag{15}$$

Из (15) следует, что расщепление уровней в ромбоэдрической фазе определится параметром B:

$$(\lambda_{1,2})_R = \Delta - B\eta_0^2 \qquad (\lambda_3)_R = \Delta + 2B\eta_0^2\,. \tag{16}$$

Расщепление же уровней в тетрагональной фазе определится феноменологическим параметром теории C:

$$(\lambda_{1,2})_T = \Delta - C\eta_0^2 \qquad (\lambda_3)_T = \Delta + 2C\eta_0^2\,. \tag{17}$$

Если эти два параметра удается измерить, то поведение термов в орторомбической и моноклинной фазе можно использовать для измерения поворотов кислородного октаэдра (или наоборот, зная поведение возбужденных уровней иона празеодима в орторомбической и моноклинной фазе).

Для полноты приведем значения уровней энергии в орторомбической

$$(\lambda_1)_C = \Delta - 2C\eta_0^2 \qquad (\lambda_2)_C = \Delta + (C-B)\eta_0^2 \qquad (\lambda_3)_C = \Delta + (C+B)\eta_0^2 \tag{18}$$

и моноклинной фазе

$$(\lambda_1)_M = \Delta - C(\eta_1^2+\eta_2^2) \qquad (\lambda_{2,3})_M = \Delta + \frac{C(\eta_1^2+\eta_2^2)}{2} \mp \sqrt{9C^2(\eta_1^2-\eta_2^2)^2 + 4B^2\eta_1^2+\eta_2^2}\,. \tag{19}$$

Следует заметить, что принятая выше модель – минимальная из полных моделей. Модель ($B=0$), предложенная в [1], такой полнотой не обладает и приводит к случайному вырождению T_{2g} уровней в фазе с симметрией D_{3d}^6.

Ссылки

1. R. T. Harley, W. Hayes, A. M. Perry, S. R. P. Smith. The phase transition of $PrAlO_3$. J. Phys. C 6 (1973) 2382-2400.
2. R. D. Burbant. A qualitative X-ray difraction study of the 205 K and 151 K phase transitions in praseodium aluminates. Acta Cryst. A 25 (1969) 5227-5228.
3. D. L. Benard, W. C. Walher. Birefringence of $PrAlO_3$ in the vicinity of 118 K. Solid State Commun. 18 (1976) 717-719.
4. Ю. М. Гуфан, Е. С. Ларин. К теории фазовых переходов, описываемых двумя параметрами порядка. ФТТ 22 (1980) 463-471.
5. Ю. М. Гуфан, В. И. Торгашев. К феноменологической теории смены многокомпонентных параметров порядка. ФТТ 22 (1980) 1629-1636.
6 H. Thomas, K. A. Muller. Structural phase transitions in perovskite-type crystals. Phys. Rev. Lett. 21 (1968) 1256-1259.
7. Ю. М. Гуфан. К феноменологической теории фазовых переходов, описываемых многокомпонентным параметром порядка. ФТТ 13 (1971) 1225.
8. Ю. М. Гуфан, В. П. Сахненко. Термодинамическое описание кристаллов при фазовых переходах второго рода вблизи *N*-фазной точки. ЖЭТФ 69 (1975) 1428.
9. О. В. Ковалев. Неприводимые представления пространственных групп. 1961, Киев: Изд. АН УССР.
10. W. A. Narolland, L. G. van Vitert. Anomalies in the dielectric constant of the $Pr_{1-x}Nd_xAlO_3$ system. J. Phys. & Chem. Solids 31 (1976) 1257-1262.
11. Ю. М. Гуфан, В. П. Дмитриев. К теории фазовых переходов, описываемых двумя параметрами порядка. Кристаллография 25 (19801) 14-20.

ЭМИССИОННЫЕ МАТЕРИАЛЫ ДЛЯ ПРЕОБРАЗОВАНИЯ СОЛНЕЧНОЙ ЭНЕРГИИ В ЭЛЕКТРИЧЕСКУЮ

М. М. Нищенко [1], Н. А. Шевченко [1],
Е. А. Цапко [1], Г. А. Фролов [2], Л. Л. Сартинская [2]

[1] Институт физики металлов им. Г. В. Курдюмова
Национальная академия наук Украины
Киев, Украина
[2] Институт проблем материаловедения им. И. Н. Францевича
Национальная академия наук Украины
Киев, Украина
sart@ipms.kiev.ua

Принята 23 июля 2013 года

1. Введение

Солнечная энергия является наиболее перспективной из-за ее экологической чистоты, безопасности и возможности возобновления. Среди прямых тепловых преобразователей энергии термоэмиссионные преобразователи (ТЕП) демонстрируют наиболее высокую удельную мощность (вплоть до 30 Вт / см^2) по сравнению с солнечными элементами, которые имеют мощность на 3 порядка ниже (0.05 Вт / см^2). Тем не менее, существенным недостатком существующих ТЕП, одновременно с высокотемпературными электродами, является высокая рабочая температура (около 2000 °C). Предварительные исследования показали, что нанотрубки, нанопровода, наноусы могут служить концентраторами электрического поля и могут быть эффективно использованы в электродах для термоэмиссионных преобразователей, потому что электронные процессы и явления имеют квантовую природу в этих наноструктурных материалах. Кроме того, положение энергетических уровней зависит от расстояния между слоями и от структурных дефектов [1 – 6].

На основании вышеупомянутого следующие принципы и подходы были предложены для использования наноструктур, в частности, нанотрубок и нанокомпозитов, в качестве электродных пар в ТЕП. Тонкие края нанотрубок с радиусом кривизны $r \sim 1-10$ нм в электрическом поле положительных ионов или в контактном поле увеличивают напряженность своего поля на несколько порядков $E \sim U / r$, что снижает потенциальный барьер для электрона (эффект Шоттки) и уменьшает потери мощности.

2. Методика проведения эксперимента

Образцы многослойных углеродных нанотрубок были синтезированы каталитическим пиролизом этилена на катализаторах состава $Al_3FeMo_{0.21}$ и $Al_3FeMo_{0.07}$. Синтез катализаторов (железосодержащая смесь гидроксидов металлов) проводили после

совместного осаждения солей металлов из водных растворов с добавлением стехиометрического количества гидроксида аммония. Осадок соосажденных гидроксидов металлов промывался водой, высушивался при 200 °C и измельчался в вибрационной мельнице в течение 30 – 40 мин. Катализатор смешивали с высокодисперсным пирогенным кремнеземом (А–300) в течение 5 мин в смесителе. Синтез многослойных углеродных нанотрубок проводили в цилиндрическом кварцевом реакторе объемом 2.1 дм^3 при перемешивании катализатора со скоростью 60 – 90 мин$^{-1}$. Наклон оси вращения составлял 8 ° к горизонту.

Для очистки от минеральных примесей полученные нанотрубки обрабатывали раствором бифторида аммония в смеси с соляной кислотой. В результате были получены два вида углеродных нанотрубок: бездефектные нанотрубки и нанотрубки с дислокациями. Многостенные углеродные нанотрубки (УНТ) имели средний диаметр 11 нм и среднее расстояние между слоями 3.5 нм. УНТ состоят, в среднем, из 10 слоев.

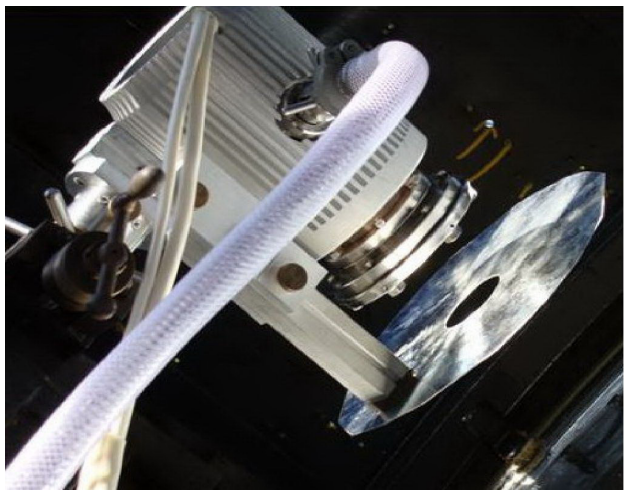

Рисунок 1. Система для преобразования солнечной энергии.
Вакуумная камера (вид сбоку) в ходе исследовательской работы.

Была исследована электронная эмиссия образцов из механической смеси гиперэластичных многостенных УНТ и пластичного терморасширенного графита (ТРГ) под действием концентрированного солнечного излучения (в режиме короткого замыкания и в режиме холостого хода). Эмиссионные свойства образцов были исследованы в вакууме ~ 0.1 Па. Была так же разработана система для преобразования солнечной энергии (**рисунок 1**), позволяющая исследовать эмиссионные свойства наноструктурных материалов.

3. Результаты и обсуждение

Методом углового распределения аннигилированных фотонов было установлено, что дефекты с поперечным размером (0.5 – 0.6 нм) равным удвоенному значению межстенного интервала захватывают позитроны в многостенных УНТ. Такой размер свободного объема может дать ядро краевой дислокации [7]. Уровни основного и возбужденного состояний в дислокации будут находиться ниже положения соответствующих уровней бездефектной области. Это означает, что электроны будут

захвачены ядром краевой дислокации. Так, по данным электроно–позитронной аннигиляции, в нанотрубках с дислокациями происходит перераспределение электронов и увеличение концентрации свободных электронов в ядре дислокации [7].

Были проведены исследования зависимости тока эмисси I в режиме короткого замыкания от температуры T. При самом высоком значении достигнутой температуры наибольшее значение тока катода из УНТ + ТРГ может достигать 450 мкА (**рисунок 2**).

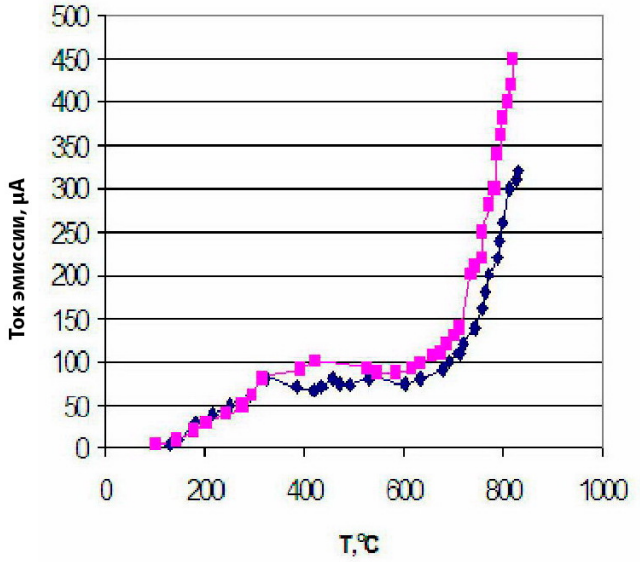

Рисунок 2. Зависимость тока эмиссии с поверхности катода на основе УНТ + ТРГ от температуры катода, нагреваемого концентрированным солнечным излучением при давлении в камере: ■ – 0.13 Па и ♦ – 0.10 Па.

На обеих кривых $I = f(T)$ можно выбрать три характерные области, которые показывают, что процесс многоступенчатый. На первом этапе в диапазоне температур 300 – 350 °C происходит увеличение тока до 90 мкА, которое было обусловлено увеличением концентрации носителей заряда (электронов и ионов) в результате увеличения интенсивности солнечного излучения. На втором этапе в диапазоне температур от 350 до 650 °C на зависимости $I = f(T)$ есть горизонтальный участок, который представляет постоянное значение анодного тока (80 – 90 μA) для обеих кривых зависимости. При температуре, после 700 °C происходит увеличение тока, который достигает 450 мкА. Рост концентрации носителей заряда в межэлектродном пространстве приводит к образованию минимума кривой, полученной при давлении 0.13 Па.

Основываясь на вышеупомянутых результатах можно предложить следующий механизм электронной эмиссии из углеродных нанотрубок под действием солнечного излучения. Под действием концентрированного солнечного излучения происходит поглощение фотонов молекулами остаточной атмосферы в камере. Энергия фотонов приводит к диссоциации молекул с образованием двух частиц. Каждая из них может быть или в возбужденном или в ионизированном состоянии. Механизмы фотопоглощения способствуют уменьшению энергии фотонов до значений энергии видимой области солнечного спектра.

Следующим механизмом повышения концентрации носителей заряда и эмиссионного тока является фотоэлектронная эмиссия с поверхности углеродных нанотрубок под воздействием солнечного излучения.

Углеродные нанотрубки по сравнению с металлами:

- более эффективно поглощают солнечное излучение;
- электроны нанотрубок легче переходят в возбужденное состояние, поскольку они локализованы в направлении размерного квантования;
- электроны нанотрубок легче преодолевают путь от места поглощения фотона к поверхности, поскольку между слоями нанотрубок они перемещаются как в волноводе.

Были также определены основные физические принципы преобразования солнечной энергии в электрическую при помощи многостенных УНТ (МСУНТ). Основными возможными факторами, которые определяют преобразования солнечной энергии в электрическую на многостенных УНТ являются:

1) эффективное поглощение солнечного излучения МСУНТ, возбуждение их электронной подсистемы с переходом электронов на уровни, положение которых определяется значением квантования.
2) усиление электрического поля катиона на концах углеродных нанотрубок.

Таким образом, процесс преобразования солнечной энергии в электрическую можно представить в следующем виде.

Катионы и электроны возникают в результате ионизации газа между электродами под действием концентрированного солнечного излучения. В электрическом поле положительно заряженные частицы движутся к катоду, а электроны – к аноду. Приближение катиона к поверхности катода из нанотрубок приводит к усилению воздействия электрического поля катиона и увеличению электрического поля на концах нанотрубок. Поле уменьшает высоту потенциального барьера (эффект Шоттки) до значения равного длине волны де-Бройля ($\lambda \approx h / p$). Начинает работать механизм туннелирования электронов с поверхности катода, к которой катион приближения. Это приводит к их нейтрализации и к исчезновению контактного электрического поля. После этого появляются слабые силы ван дер Ваальса.

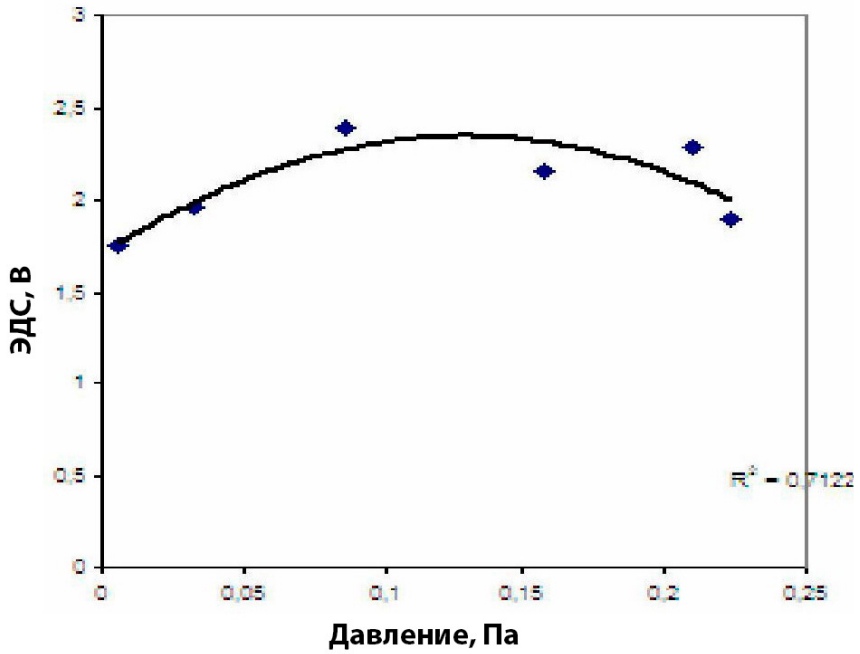

Рисунок 3. Зависимость электродвижущей силы, возникающей на катоде от давления при нагреве под воздействием концентрированного солнечного излучения.

При $T > 600$ °C начинается десорбция нейтральных частиц с поверхности в межэлектродном пространстве. Ток эмиссии растет. Напряжение между электродами определяется разностью работ выхода катода и анода. Под действием температуры и ультрафиолета процесс повторяется и определяет протекание анодного тока в электрической цепи.

Было также обнаружено появление электродвижущей силы на электродах под воздействием концентрированного солнечного излучения (**рисунок 3**). Линейная зависимость ЭДС имеет максимум 2.3 В при давлении в камере 10 – 20 Па.

Следует отметить, что даже при атмосферном давлении (10^5 Па) значение ЭДС достигает 0.5 В для Al–Li анода. Ток эмиссии при таком давлении настолько мал, что не фиксируется обычными электроизмерительными приборами в режиме короткого замыкания (**рисунок 4**).

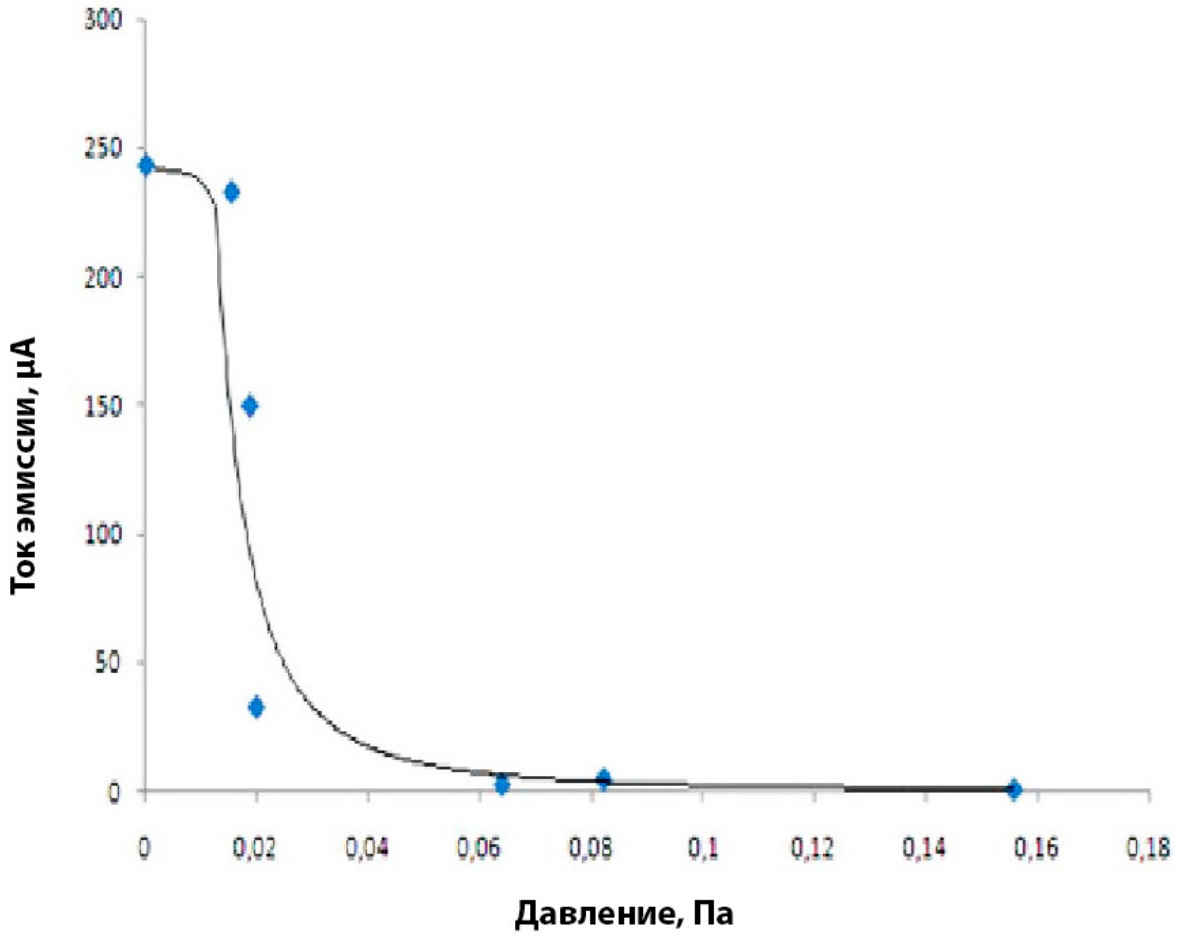

Рисунок 4. Зависимость тока эмиссии от давления в вакуумной камере.

Ход изменения тока эмиссии от давления остаточной атмосферы в вакуумной камере представлен на **рисунке 4**. При уменьшении давления в камере увеличивается генерация тока под действием концентрированного солнечного излучения в режиме короткого замыкания. Максимальное значение тока эмиссии для катодов с многослойными углеродными нанотрубками с дислокациями составило около 8 мА. Это максимальное значение тока, которое удалось достичь на электродах. Учитывая площадь катода, сила такого преобразования достигает 20 мВт / см^2.

4. Заключение

Были разработана и исследована механическая смесь сверхэластичных углеродных нанотрубок и пластичного терморасширенного графита для электродов преобразователей солнечной энергии в электрическую. Были установлены механизмы электронной эмиссии наноструктурных электродов, процесс ионизации газа под действием солнечного излучения различной интенсивности, температуры и вакуума а, также, механизм термоэмиссинного преобразования тепловой энергии в электрическую при нагреве катодов солнечным излучением. Сила преобразования достигает 20 мВт / см^2.

Благодарность

Авторы благодарят за поддержку УНТЦ и CRDF. Эта работа выполнялась в рамках проекта УНТЦ № 4133 и CRDF № UKE2–7034–KV–11.

Ссылки

1. S. Iijima. TEM characterization of graphitic structures. In: Proc. 13th Int. Cong. Electron Microscopy. 1994, Paris, 295.
2. R. T. Collins, F. M. Fauchet, M. A. Tischler. Porous silicon: From luminescence to LEDs. Physics Today, 1997, 50, 1, 24-31.
3. А. П. Шпак, Ю. А. Куницький, О. О. Коротченков, С. Ю. Смик. Квантові низькорозмірні системи. 2003, Київ: Академперіодика.
4. П. Харрис.Углеродные нанотрубки и родственные структуры. Новые материалы XX1 века. 2003, Москва: Техносфера.
5. П. Н. Дьячков. Углеродные нанотрубки, строение, свойства, применение. 2006, Москва: БИНОМ.
6. С. В. Гапоненко. Испускание и рассеяние света в наноструктурах: Роль плотности фотонных состояний. Изв. АН. РФ (Сер. физ.), 2004, 68, 1, 115-118.
7. М. М. Нищенко, С. П. Лихторович. Позитронная спектроскопия пористых материалов. В сб.: Наносистеми, наноматериали, Наносистеми, наноматериали, нанотехнології, 1-1. 2003, Київ: Академперіодика, 193-259.

SYNTHESIS OF GOLD NANOPARTICLES BY NEW STRAINS OF THERMOPHILIC ACTINOMYCETES

T. Kalabegishvili [1, 2], E. Kirkesali [1], E. Ginturi [1], A. Rcheulishvili [1], I. Murusidze [2], D. Pataraya [3], M. Gurielidze [3], N. Bagdavadze [1], N. Kuchava [1], D. Gvarjaladze [2], L. Lomidze [2]

[1] E. Andronikashvili Institute of Physics
I. Javakhishvili Tbilisi State University
Tbilisi, Georgia
kalabegi@yahoo.com
[2] Institute of Applied Physics
Ilia State University
Tbilisi, Georgia
[3] S. Durmishidze Institute of Biochemistry and Biotechnology
Agricultural University of Georgia
Tbilisi, Georgia

Accepted July 26, 2013

Introduction

The actinomycetes are a widespread group of Gram-positive bacteria. They are distinguished from other bacteria by their morphology and genome [1]. The actinomycetes are classified as prockaryotes and can be easily manipulated genetically to control sizes and polydispersity of nanoparticles produced by actinobacteria [2, 3].

Actinomycetes-mediated chemistry has many advantages for the synthesis of gold and silver nanoparticles [4 – 7]. Terrestrial actinobacteria are rich sources of biologically active products and are being extensively used for industrial production of pharmaceuticals. Numerous actinomycetes have been isolated from different environments – soils, compost, marine sediments, rocks, water, etc.

The actinomycetes are widely used in drugs delivery. Two-third of microbial-produced antibiotics belongs to actinomycetes. Antibiotics produced by actinobacteria are also widely used in medicine.

Gold nanoparticles are characterized by stability, oxidation resistance and biocompatibility. Due to their optical and chemical properties and high infrared phototherapy potential they can be used for early diagnosis and treatment of cancer. The use of precisely engineered gold nanoparticles as anticancer agents allows direct treatment of diseased cells with reduced damage to healthy cells [8, 9].

Thus, it is important to screen new classes of actinomycetes to synthesize gold nanoparticles with technologically important properties such as the resistance to high temperature.

Among many geographical regions of our planet, the South Caucasus has attracted much attention of bioprospectors. There are fourteen different soil-climatic zones on the southern

slopes of the Caucasus with an average annual temperature in the interval of 5 – 25 °C. This area is characterized by extreme microbial and plant biodiversity. Special interest is focused on the adaptation mechanisms of living organisms to extreme environment.

In earlier works the results of the studies of several new strains of actinomycetes for developing methods of producing gold and silver nanoparticles have been presented [10 – 12]. Some *Actinomycetes* genera have been studied for the development of clean and nontoxic methods of the synthesis of gold and silver nanoparticles.

Several analytical and spectral methods have been used for examining gold and silver nanoparticles [11, 12]. The obtained results are discussed to evaluate the ability of the studied strains to produce gold and silver nanoparticles.

In the present work two new strains of thermophilic actinomycetes – *Thermoactinomycete spp*. 44 Th, isolated from the red soil of Adjara region, and *Thermomonospora spp*. 67 Th, isolated from the cinnamonic calcareous soil of Tetritskaro region at high temperature were studied to use them in the synthesis of gold nanoparticles. The gold nanoparticles obtained in biomass of thermophilic actinomycetes were characterized using various optical and analytic methods.

Materials and methods

The first isolation of thermophilic actinomycetes cells from soils was carried out on solid medium with TSA (Tryptic Soy Agar) nutrient solution ((g / l): Tryptone – 15.0, Soytone – 5.0, Sodium chloride – 5.0, Agar – 15.0, pH 7.3 ± 0.2) in the thermostat at 55 °C for 24 h. Then the culture was placed into 500 ml Erlenmeyer flasks with 100 ml nutrient medium TSB solution (Tryptic Soy Broth) ((g / l): Tryptone – 17.0, Soytone – 3.0, Glucose – 2.5, Sodium chloride – 5.0, Dipotassium phosphate – 2.5, pH 7.3 ± 0.2) and incubated in thermostat at temperature 55 °C for 36 h. The biomass obtained was isolated by centrifugation and washed thrice with distilled water.

The cultivation of *Thermoactinomycete spp*. 44 Th and *Thermomonospora spp*. 67 Th for preparation of samples containing Au nanoparticles was carried out using $HAuCl_4$ 10^{-3} M water solutions by the method described elsewhere [10 – 12]. As in the previous studies, for producing gold nanoparticles 2 g biomass with 100 ml 10^{-3} M concentration aqueous solution of $HAuCl_4$ was placed in 250 ml Erlenmeyer flasks under aerobic conditions at the temperature of 28 – 30 °C and permanent shaking of suspension. The formation of nanoparticles was observed for different time intervals (1 – 10 days).

ACS-reagent grade was purchased from Sigma (St. Louis, MO, USA).

For spectrophotometric study by the UV–Vis method suspensions obtained after centrifugation (20 min at 12 000 g) were used. The suspensions were also studied by transmission electron microscopy.

After lyophilization the biomasses of both types were studied by atomic absorption spectrometry (AAS) and by the X-ray diffraction (XRD) method.

The UV–Vis measurements was carried out on a spectrophotometer Cintra 10e (GBC Scientific Equipment Pty Ltd, Australia), XRD – on a Dron–2 diffractometer.

Transmition eletron microscopy (TEM) was performed using the JEOL SX–100 equipment (Japan). For AA) of bacterial samples the flame spectrometer Beckman–495 was used.

Results and discussion

The study of UV–Vis spectra of *Thermoactinomycete spp*. 44 Th and *Thermomonospora spp*. 67 Th after reaction of $HAuCl_4$ 10^{-3} M water solution showed that Au nanoparticles were formed in both cases, which was proved by the appearance of a peak at 530 nm in the spectra typical for the absorption by surface plasmons (**Figures 1 a** and **b**).

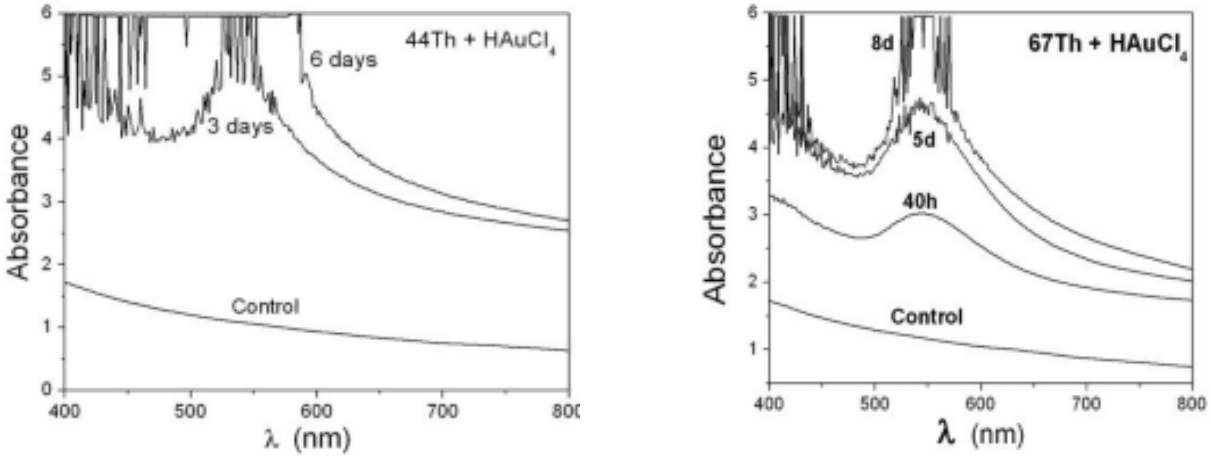

a **b**

Figure 1. UV–Vis spectra of *Thermoactinomycete spp*. 44 Th and *Thermomonospora spp*. 67 Th biomass with gold nanoparticles after reaction with $HAuCl_4$ for different time.

The UV–Vis spectra for *Thermoactinomycete spp*. 44 Th indicate the gold nanoparticles intensive production after 3 – 6 days of reaction and for *Thermomonospora spp*. 67 Th – at 40 h – 8 days. The shapes of peaks correspond to spherical gold nanoparticles.

The TEM pictures which show gold nanoparticles in the studied samples of the thermophilic actinomycetes are given in **Figures 2 a** and **b**.

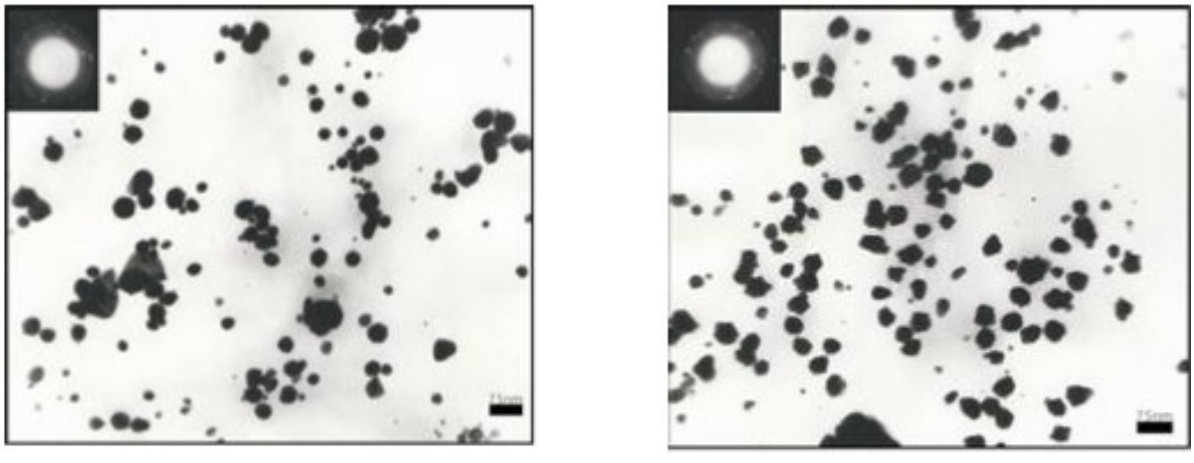

a **b**

Figure 2. TEM micrographs recorded from drop-cast films of gold nanoparticles formed by the reaction of the $HAuCl_4$ solution with biomass *Thermoactinomycete spp.* 44 Th after 6 days (a) and *Thermomonospora spp.* 67 Th after 8 days (b) as well as diffraction patterns recorded from the gold nanoparticles in selected areas.

In **Figure 3** the nanoparticles sizes distributions for TEM micrograms of *Thermoactinomycete spp.* 44 Th (a) and *Thermomonospora spp.* 67 Th (b), respectively, are given. This distributions show that for *Thermoactinomycete spp.* 44 Th the sizes of Au nanoparticles are within the interval of 5 – 60 nm with an average 20 nm and for *Thermomonospora spp.* 67 Th – within the interval of 15 – 55 nm with an average 30 nm.

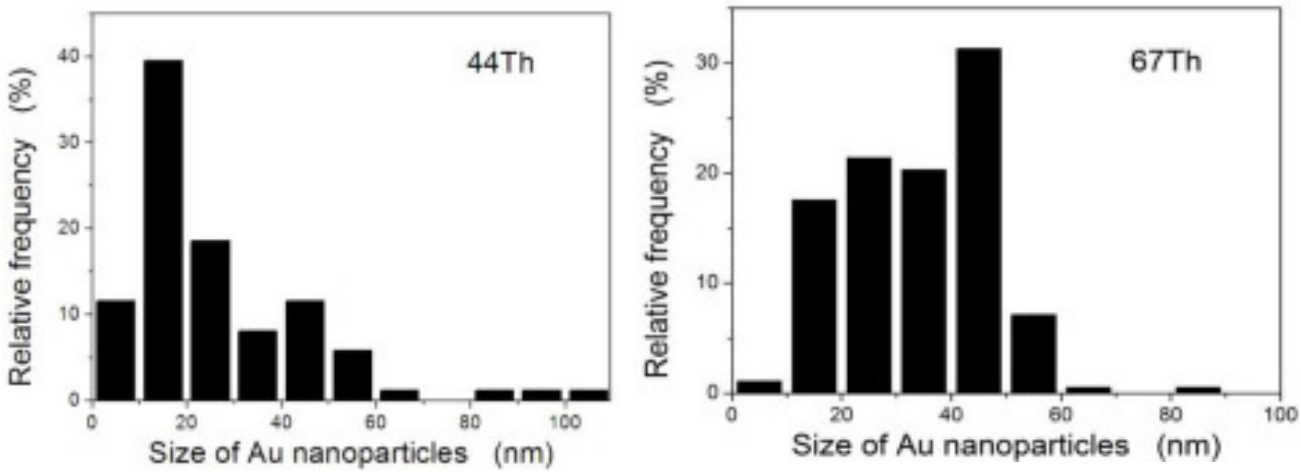

a **b**

Figure 3. The nanoparticles sizes distributions for TEM micrograms of *Thermoactinomycete spp.* 44 Th (a) and *Thermomonospora spp.* 67 Th (b).

The thermophilic actinomycetes *Thermoactinomycete spp.* 44 Th and *Thermomonospora spp.* 67 Th were also studied by the XRD method. **Figures 4 a** and **b** show the XRD diffraction patterns of the *Thermoactinomycete spp.* 44 Th and *Thermomonospora spp.* 67 Th biomass, respectively, after their exposure to the $HAuCl_4$ water solutions for 6 days. As is obvious, the peaks indicate the crystal structure of the produced nanoparticles.

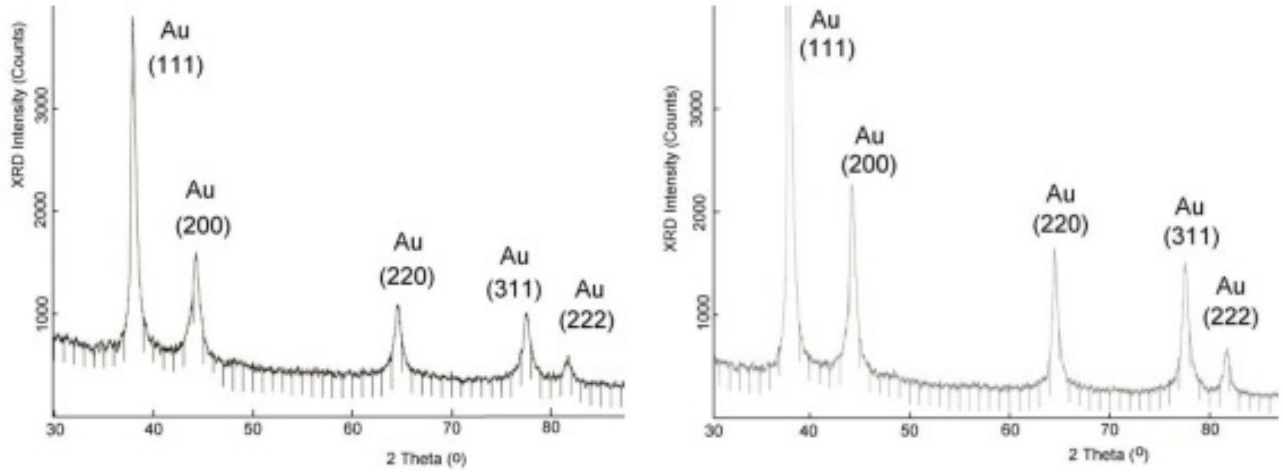

a **b**

Figure 4. Diffraction patterns of the *Thermoactinomycete spp.* 44 Th biomass (a) and *Thermomonospora spp.* 67 Th biomass (b) after their exposure to the $HAuCl_4$ water solutions for 6 days.

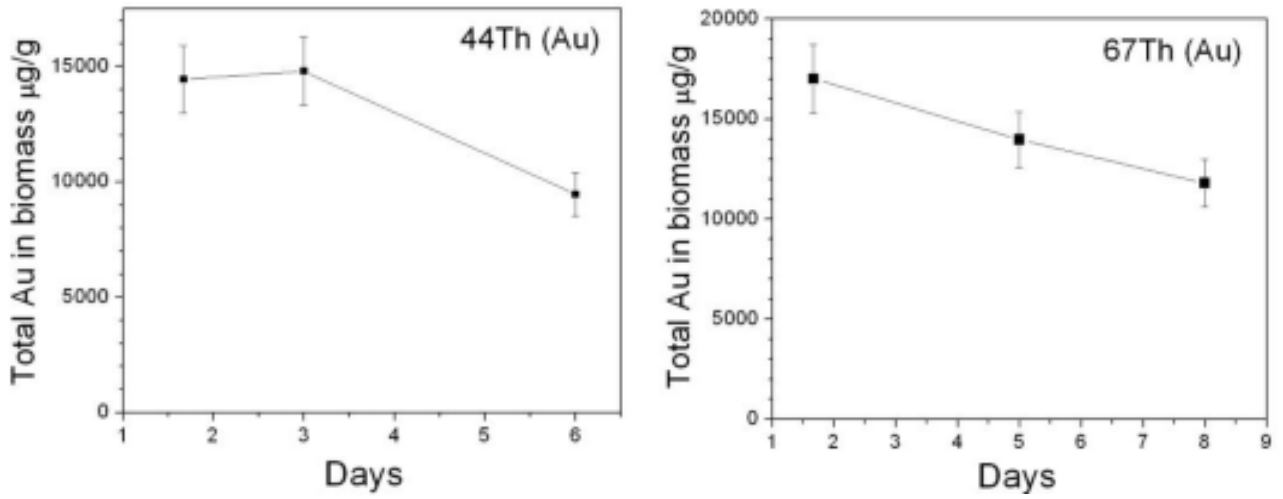

a **b**

Figure 5. The total gold concentrations determined by AAS in biomass of *Thermoactinomycete spp.* 44 Th and *Thermomonospora spp*. 67 Th versus of reaction time with $HAuCl_4$.

The data obtained by AAS for total gold concentrations in *Thermoactinomycete spp*. 44 Th and *Thermomonospora spp*. 67 Th biomass (**Figures 5 a** and **b**) illustrate that at first day the metal concentration increases rapidly and then decreases very slightly for the next few days. It may suggest that in the first 'rapid' phase the metal ions are mainly adsorbed on the surface of microorganisms by the functional amino, carboxylic, sulfydryl, phosphate and thiol groups that are able to bind metal ions. The synthesis of nanoparticles takes place extracellularly. In the second 'slow' phase, the metal ions are transported across the cell membrane into the cytoplasm and accumulated intracellularly.

Conclusions

The results of this study show that the new strains of thermofilic actinomycetes *Thermoactinomycete spp*. 44 Th and *Thermomonospora spp*. 67 Th can be used for extracellular production of gold nanoparticles with mainly spherical shapes and with sizes in the range of 5 – 60 nm with the average size of 20 – 30 nm. The developed methods of nanoparticle biosynthesis using actinomycetes are innovative, simple, non toxic and applicable in many areas of science and industry. The gold nanoparticles produced by the strains of the tested actinomycetes may have great potential especially in medicine and pharmacology for drugs delivery

Acknowledgements

The authors acknowledge the Ukrainian Science and Technology Centre (STCU) Grants # 4744 and # 5002.

References

1. M. Sastry, A. Ahmad, M. I. Khan, R. Kumar. Biosynthesis of metal nanoparticles using fungi and actinomycete. Curr. Sci. 85 (2003) 162-170.

2. D. Mandal, M. E. Bolander, D. Mukhopadhyay, G. Sarkar, P. Mukherjee. The use of microorganisms for the formation of metal nanoparticles and their application. Appl. Microbiol. & Biotechnol. 69 (2006) 485-492.
3. T. J. Beverige. Ultrastructure, chemistry and function of the bacterial wall. Int. Rev. Cytology 72 (1981) 229-317.
4. A. Ahmad, S. Senapati, M. I Khan, R. Kumar, M. Sastry. Extracellular biosynthesis of monodisperse gold nanoparticles by a novel extremophilic actinomycete *Thermomonospora spp*. Langmuir 19 (2003) 3550-3553.
5. A. Ahmad, S. Senapati, M. I. Khan, R. Kumar, M. Sastry. Intracellular synthesis of gold nanoparticles by a novel alkalotolerant actinomycete *Rhodococcus* species. Nanotechnol. 14 (2003) 824-828.
6. L. V. Kalakutskii, N. S. Agre. Comparative aspects of development and differentiation in actinomycetes. Bacteriolog. Rev. 40 (1976) 469-524.
7. A. Ahmad, S. Senapati, M. I. Khan, R. Kumar, R. Ramani, V. Srinivas, M. Sastry. Intracellular synthesis of gold nanoparticles by a novel *alkalotolerant actinomycete*, *Rhodococcus species*. Nanotechnol. 14 (2003) 824-828.
8. S. K. Das, E. Marsilli. A green chemical approach for synthesis of gold nanoparticles: Characterization and mechanistic aspect. Rev. Environ. Sci. & Biotechnol. 9 (2010) 199-204.
9. L. R. Hirsh, R. J. Stafford, J. A. Bankson, S. R. Sershen, B. Rivera, R. E. Price. Nanoshell-mediated near-infrared thermal therapy of tumor under magnetic resonance guidance. Proc. Natl. Acad. Sci. USA 100 (2003) 13549-13554.
10. N. Y. Tsibakhashvili, E. I. Kirkesali, D. T. Pataraya, M. A. Gurielidze, T. L. Kalabegishvili, D. N. Gvarjaladze, G. T. Tsertsvadze, M. V. Frontasyeva, I. I. Zinicovscaia, M. S. Wakstein, S. N. Khakhanov, N. V. Shvindina, V. Y. Shklover. Microbial synthezis of silver nanoparticles by *Streptomyces glaucus* and *Spirulina platensis*. Int. J. Adv. Sci. Lett. 4 (2011) 3408-3417.
11. T. L. Kalabegishvili, E. I. Kirkesali, A. Rcheulishvili, E. N. Ginturi, I. G. Murusidze, D. T. Pataraya, M. A. Gurielidze, G. I. Tsertsvadze, V. N. Gabunia, L. G. Lomidze, D. N. Gvarjaladze, M. V. Frontasyeva, S. S. Pavlov, I. I. Zinicovscaia, M. J. Raven, N. M. F. Seaga, A. Faanhof. Synthesis of gold nanoparticles by some strains of *Arthrobacter* genera. J. Mater. Sci. Eng. A 2 (2012) 164-173.
12. T. L. Kalabegishvili, I. G. Murusidze, E. I. Kirkesali, A. N. Rcheulishvili, E. N. Ginturi, E. S. Gelagutashvili, N. E. Kuchava, N. V. Bagdavadze, D. T. Pataraya, M. A. Gurielidze, H.-Y. Holman, M. V. Frontasyeva, I. I. Zinicovscaia, S. S. Pavlov, V. T. Gritsyna. Development of biotechnology for microbial synthesis of gold and silver nanoparticles. J. Life Sci. 7 (2013) 110-122.

PHOTOCHROMIC LIQUID-CRYSTAL MULTIFUNCTIONAL NANOMATERIALS

K. Japaridze, L. Devadze, J. Maisuradze, G. Petriashvili,
Ts. Zurabishvili, I. Mzhavanadze, N. Sepashvili

V. Chavchanidze Institute of Cybernetics
Georgian Technical University
Tbilisi, Georgia
devadze2005@yahoo.com

Accepted August 14, 2013

Introduction

Spiropyrans (SP) are an important class of organic photochromic, bistable compounds. Bistable molecules and molecule ensembles can exist in two thermodynamic stable states divided by a certain energy barrier. Switching from one state to another occurs via external stimulation (light, heat, mechanical stress, electric and magnetic fields, etc.). An uncolored spiropyran molecule with a bulky structure by the influence of ultraviolet light (UV) is transformed into a coplanar, colored merocyanine (MC) form with a high dipole moment. Such bipolar molecules under certain circumstances easily selforganize, i.e. create nanoparticles.

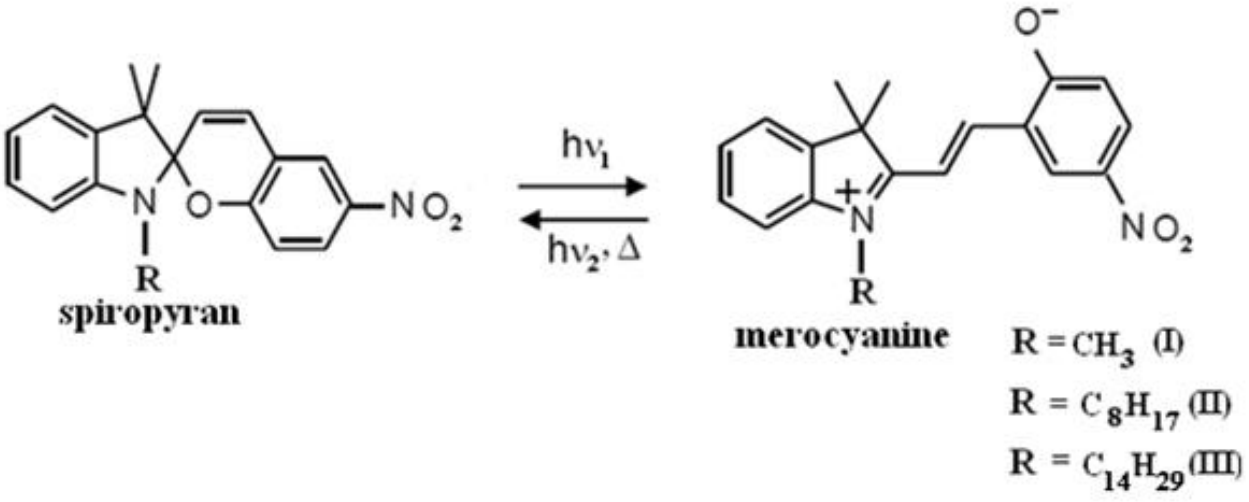

Spiropyrans are practically used in such lightcontrolled devices, as information-recording (including three-dimensional), memorizing and processing systems, nonlinear optical materials, molecular computers, filters with regulated optical density, optical switches, different types of sensors, medical instruments, ecology etc. Spiropyran among other parameters (stability, cyclicity, large cross section of two-photon absorption), must have high photosensitivity. Many scientific centers and companies worldwide carry out studies to increase the photosensitivity of spiropyrans what is evidenced by a large number of published works and patents in the field.

Photosensitivity of the compositions doped with spiropyrans

The photosensitivity of spiropyrans is possible to increase by modification of a molecule: (1) by varying the substitutes of different electronic natures (eletrodonor and electroacceptor) in the indoline and chromen parts and their position in the molecule, and (2) by changing the molecule skeleton. By using this kind of approach, we have synthesized and studied several hundreds of spiropyrans. For instance, the changing the indoline ring by azaindoline allowed us to gain the spiropyrans with increased photosensitivity to the UV light as compared with the known analogues [1], and introduction of the additional fragment in the indoline part of the molecule (tetrahydrochinoline products) increased the photosensitivity to the visible light [2]. The spiropyrans gained on the basis of pyridoxal have demonstrated interesting photochromic properties [3].

The zwitterionic MC form obtained in the result of photochemical isomerization of SP, in the presence of long alkyl radical at the nitrogen atom, is an amphiphilic molecule. This molecule consists of two parts: the lyophilic molecule head, readily soluble in the liquid, and the unsoluble tail. The head (in our case zwitterion) is polar alkyl radical, while the tail (anchor) is a nonpolar. The molecules of this kind are surfactants and they self- organize into micelles under certain conditions. It is well known that micellization is characteristic of such surfactants that have the optimal lyophilic–lyophobic balance. It was revealed experimentally that the surfactants containing the $C_8 - C_{18}$ radical and the zwiterionic head exhibit the capability of micellization [4 – 6].

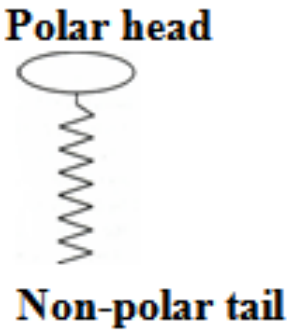

The physical-chemical properties of micelles, i.e. nanoparticles, differ dramatically from those of both separate atoms and molecules, and solid bodies. Separate molecules associated into stable super-molecular structures – supramolecules by means of intramolecular forces function as nanoreactors. In solution, they generate intrinsic micropseudophase the properties of which differ from the characteristics of the main solution. Because of the increased concentration of the solution the character of interaction with light in the nanoreactors changes. The nanoractor-containing systems are one-phase and homogeneous at the macrolevel, and two-phase and microheterogeneous – at the nanolevel. Hence, based on the investigation of nanostructures, it is possible to compose and fabricate the nanomaterials with desired properties, better than the properties of natural materials. For instance, we can increase the efficient photosensitivity of the spiropyran-containing composition.

It is well known that, under certain conditions, amphiphilic molecules form lyotropic liquid crystals (LC). Thus, the investigation of the process of micellization of spiropyrans in the

liquid crystalline medium is of interest. Our choice of the liquid-crystal solvent was determined by the capability of self-organization, i.e. nanostructuring of the studied nematic-chiral LC systems doped with spiropyrans. The latter is observed by the anomalies of Bragg's selective reflection band [7, 8]. We chose the liquid crystal as a solvent, because living organism cells and intracellular organelles are covered with a thin high-order membrane. The membranes, in turn, represent lyotropic LC l structures. The size of spiropyran micelles in the LC decreases nearly by half under UV photoinduction. This fact gives the opportunity of purposeful delivery of medicines in the human organism. The delivered medicine is released with the help of visible light [9].

Experiment

We studied the process of micellization in the composition that represented a nematic-chiral LC matrix doped with R-3,3-dimethylindolino-6'-nitrobenzopyrylospiran's following analogs: R = CH_3 (I), C_8H_{17} (II), and $C_{14}H_{29}$ (III), synthesized by us. The nematic-chiral matrix consisted of Merck's certified components: nematic substance ZLI–1939, containing the cyanic biphenyl group, and optically active substance MLC–4572 or MLC–4571. The experimental sample was made in the following way: the equimolar solutions of the composition under study were placed between flat-parallel glass plates. The sample thickness was determined by the teflon bedding. The samples were placed into a thermostatic chamber. They were irradiated with the same dose of energy by using interference filter ($\lambda = 365$ nm) under the condition of constant temperature. The electron absorption spectra were detected by means of fiber optics spectrometer Avantes 2048.

We studied three compositions: 1 – doped with compound I, 2 – doped with compound II, and 3 – doped with compound III of equimolar concentration. The absorption spectra of the samples were detected prior to the irradiation and after the irradiation with the same dose of UV radiation under the condition of constant temperature (**Figure 1**).

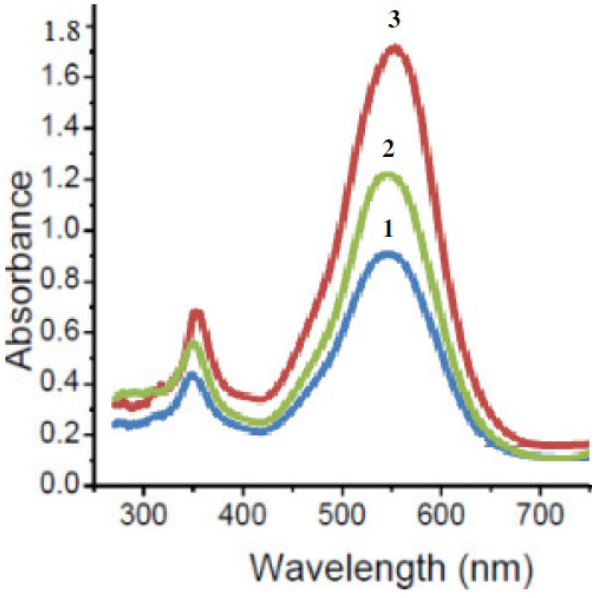

Figure 1. Absorption spectra of the compositions doped with spiropyrans doped with: **1** (blue) –compound I, **2** (green) – compound II, and **3** (red) – doped with compound III.

From **Figure 1** it is evident that along with the radical length, the absorption peak height increases. A hypsochromic shift of peak **2** in respect to peaks **1** and **3** was observed. A similar shift was observed in the ethanol solutions of those substances [10].

For practical application the spiropyran-doped compositions were integrated into the polymer matrix with the improved method of microcapsulation developed by us [11, 12]. The use of the microcapsulation method and icy acetic acid as suitable emulsifying agent allowed us to obtain a stable dispersive system in the polyvinyl alcohol matrix. The obtained system contained a dispersed phase – separated compositions, aggregates in the form of capsules in the dispersive medium of the polymer solution, which preserved at most the initial properties of the dispersive composition doped with spiropyran and conditioned the production of polymer films with high photosensitivity. By controlling all stages of microcapsulation we obtained process-perfect uniform, elastic films meeting the requirements of practical application.

The microscopic investigation of the films confirmed that the polymer matrix consisted of microcapsules. **Figure 2** demonstrates the UV-irradiated and non-irradiated sections of the film, which show that the disperse phase of the polymer matrix in the form of microcapsules did not suffer disintegration in the result of irradiation, and hence the properties of spiropyran-doped compositions did not change.

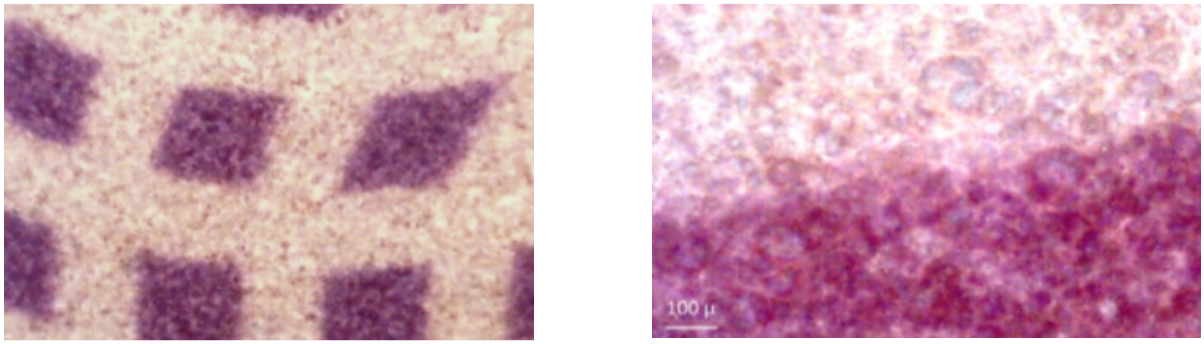

a **b**

Figure 2. Recorded images on the polymer films with (a) 60 × and (b) 200 × magnifications, respetively.

The optical investigation of the films showed that, in the films the same correlation we observed as in the compositions, i.e. along with the SP radical length, the absorption peak height increased. This pointed to the fact that, in the result of microcapsulation of the polymer matrix, the composition retained its initial properties.

Results and discussion

We suppose that the correlation of the efficient photosensitivity of long-radical spiropyran-doped nematic-chiral LC with the radical length is associated with the fact that the MC form of the spiropyran molecule with a zwitterionic lyophilic head and lyophobic alkyl radical at the nitrogen atom represents a surfactant amphiphilic molecule. The so-called Gordon parameter of the nematic-chiral LC of the polar solvent satisfies the conditions of micellization. Therefore, the micellization must occur in spiropyran-doped LC, under certain conditions.

The trigger (switch) of micelle or nanoreactors origination in this case is the UV light ($\lambda = 365\,\text{nm}$). At the given temperature, prior to irradiation, the solution is made up of the

matrix and spiropyran and merocyanine-form molecules, which are in thermodynamic equilibrium with spiropyran. The constant of thermodynamic equilibrium K_T is less than the constant of photochemical equilibrium K_{PH} ($K_T < K_{PH}$). In case of exposition with the UV light, the thermodynamic equilibrium of the composition is disturbed and shifts to the merocyanine-form molecules, and the color of solution gets more intensive. In the process of irradiation, the origination of merocyanine form molecules and growth of their concentration is followed by their structuring as micelle. The critical concentration of micellzation is low for the substances containing the long alkyl radical $C_8H_{17} – C_{14}H_{29}$. The processes of photoinduction and micelle formation are noninertial, i.e. they are initiated as soon as the trigger is started. There is one more pseudophase - the micelle originated at the microlevel in the base solution. In the process of micelle formation, the base solution is depleted with merocyanine molecules and the spiropyran molecules start to transform to the merocyanine ones to restore the thermodynamic equilibrium. To the MC molecules formed photochemically, the MC molecules formed for restoring the thermodynamic equilibrium are added. The given process increases the number of absorbing centers in the composition what in the final account increases the effective photosensitivity of the system. We observed this process experimentally by the increase in the $R = C_8H_{17} – C_{14}H_{29}$ absorption peak in respect to C_1.

The increase in the 3 peak in respect to the 2 peak in both the composition and the films on their base (**Figure 1**) can be attributed to the increase in the micelle radius with increasing alkyl radical length. Accordingly the surface area of micelles increased and the number of molecules arranged on them. For restoring the thermodynamic equilibrium, the edditional quantity of SP molecules converted into the MC form, and then the absorption peak height increased.

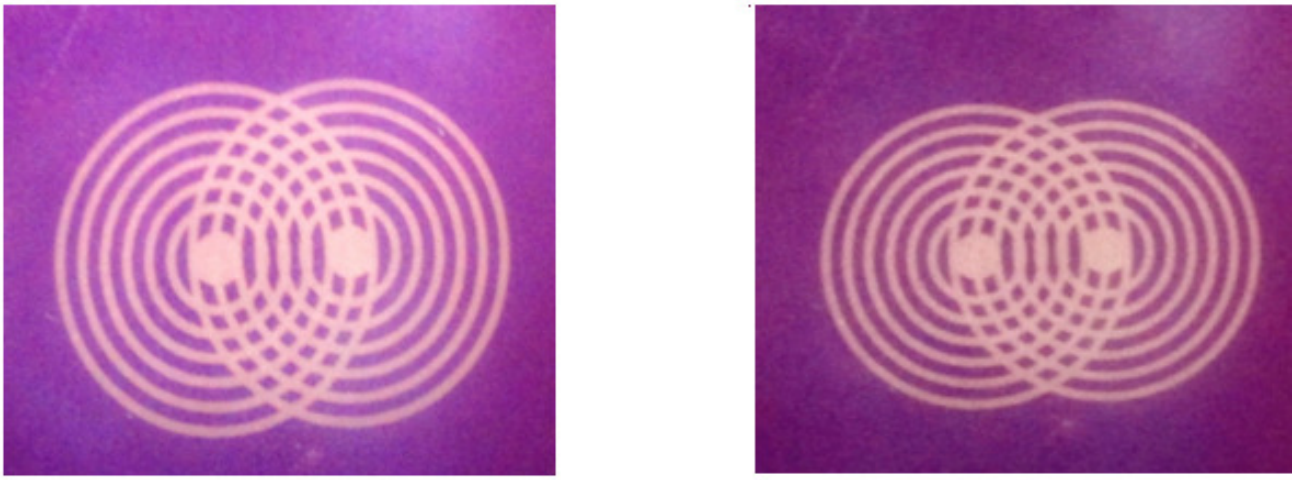

Figure 3. Photo-imprinted images on the polymer films using the mask with two partially intercrossed concentrated rings: (a) doped with compound I and (b) doped with compound II.

The increase of photosensitivity, along with the radical length, is well defined upon information recording in the polymer films (**Figure 3**). The violet (dark) and white colors correspond respectively to irrediated and nonirradiated parts of the films. The contrast strengthening between irradiated and nonirradiated areas of the film (b), shows the increase of photosensitivity.

Thus, we may conclude that as a result of UV light induction of liquid crystal compositions doped with spiropyran, the merocyanine molecules similar to the surfactant molecules are originated, which are structured as micelle (nanoreactors). In the process of micelle origination, in order to restore the thermodynamic equilibrium, the spiropyran molecules transform to merocyanine molecules increasing the effective photosensitivity of the material. In case of further increase of spiropyran concentration the concentration of micelle will be increased in the solution as a result of photoinduction and the pseudophase may become liquid crystal.

Conclusion

By choosing the nematic-chiral liquid-crystal solvent possessing the properties contributing to the micellization allowed us to improve the efficient photosensitivity of long-radical spiropyrans. We observed this process in both the composition and the films obtained on their base by microcapsulation.

Acknowledgements

This work was supported by the Shota Rustaveli National Science Foundation (SRNSF), project number No. 11/12.

References

1. J. P. Maisuradze, Sh. A. Akhobadze, L. V. Devadze, K. G. Japaridze. KhGS 10 (1982) 1367. – in Russian.
2. J. P. Maisuradze, N. I. Makhashvili, L. V. Devadze, N. O. Sepashvili, L. P. Shishkin, K. G. Japaridze. Proc. Acad. Sci. Georg. SSR (Chem. Ser.) 15 (1989) 44 – in Georgian
3. K. Japaridze, L. Devadze, J. Maisuradze, I. Mzhavanadze, N. Sepashvili. Bull. Georg. Natl. Acad. Sci. 4 (2010) 67.
4. A. V. Shibaev, O. A. Korabelskaya. Priroda 2 (2010) 9.
5. J. N. Israelachvili. Intermolecular and Surface Forces: With Application to Colloidal and Biological Systems. 1992.
6. J. N. Israelachvili, D. J. Mitchell, B. W. Ninham. J. Chem. Soc. Faraday Trans. A 72 (1976) 1525.
7. K. G. Japaridze, Z. M. Elashvili, L. V. Devadze, N. O. Sepashvili, M. R. Katsiashvili. Crystallog. Rep. 51 (2006) 497.
8. K. Japaridze, L. Devadze, J. Maisuradze, N. Sepashvili. High Energy Chem. 43 (2009) 527.
9. R. Tong, H. D. Hemmati, R. Langer, D. S. Kohane. J. Am. Chem. Soc. 134 (2012) 8848.
10. K. G. Japaridze. Spirokhromeny. 1979, Tbilisi. – in Russian
11. Ts. Zurabishvili, K. Japaridze, Z. Elashvili, G. Chelidze. Georg. Patent # 2683. – Sakpatenti Bull. 8 (2002).
12. K. Japaridze, Ts. Zurabishvili, G. Petriashvili. Georgi. Patent # 5232. Publ. – Sakpatenti Bull. 1 (2011).

CREATION, RESEARCH AND SUBSEQUENT USAGE OF NANOPARTICLES FLUIDS FOR ELECTRONIC COMPONENTS COOLING

J. J. Avaliani [1], I. M. Avaliani [1], T. I. Khachidze [2], S. V. Dolidze [1]

[1] Institute "Optics"
Tbilisi, Georgia
[2] Georgian Technical University
Tbilisi, Georgia
txachidze@gmail.com

Accepted August 15, 2013

Electronic devices consume electrical energy which is partly transformed into heat energy. As a result, their temperature rises. Temperature rise above the allowable has the negative impact on the parameters and in most cases it can damage them. Semiconductor devices (hereinafter referred to as chips) are especially temperature sensitive. In this case the physics is powerless and it is difficult even theoretically to create semiconductor chip, which will be long-term stable over 100 °C temperature.

The heat removal, allocated in electronic devices and systems has especial value. Thermal streams in powerful electronic systems, for example, in transferring and receiving modules of radars, in powerful laser diodes, in processors of powerful computers and servers, etc. reach values 5 – 10 MW / m^2. In the future thermal streams will even more increase and will reach 20 – 30 MW / m^2. Nowdays, the density of power integrated circuits and micro processors are increasing very intensively and in the future will continue.

In order to settle the problem of heat scattering and removal, there is a need to create new types of heat conductors and to prove that they can successfully remove and scatter powerful heat flows from heating surfaces.

The presented research is dedicated to this problem – so-called thermic siphon method is used to cool modern nanoelectronic devices and equipment.

Thermic siphon is a locked in a cycle of heat exchanger that works through joint action of heat convection and gravity and does not require additional energy. Nowdays thermic siphon heat exchangers are created for Intel Corporation's 45 nm processor's individual structural elements cooling and for the AMD processor's 30 nm transistors cooling. In this or similar types of nanoelements heat removal is the main problem and objective [1].

Apart from thermic siphon principle, in nanotechnology so-called heat pipes method is used. Mass and heat transfer is managed by convection and capillary forces caused by temperature differences. In heat transfer, heat transfer via heat pipes was first demonstrated in the United States – in Los Alamos's Laboratory [2, 3]. Heat pipes are irreplaceable in space technology. Important and interesting as well ares porous materials, which are actually nanostructures because pores' transverse dimensions are changing from 10^{-9} – 10^{-6} m range.

Research of liquids consisted of nanoparticles (further nanoliquids) is a separate section of nanotechnology. Nanoliquids are described as fluids which are engineered as colloidal

suspensions of nanoparticles in a basic fluid. The nanoparticles used in nanoliquids are typically made of metals, oxides, carbides or carbon nanotubes.

One of the most common types of nanoliquids is surface-active substances (SASs) aqueous solutions and suspensions. SASs can cause liquids to reduce the surface tension coefficient, which increases the liquid fluctuation, i.e. their ability to penetrate into nano porous as well as in a liquid during phase transformations. Therefore, the use of nanoliquids in heat exchanger is highly practical. This effect can be observed during even very low concentrations (**Figure 1**), e.g. 5 – 50 ppm, of SAS [3].

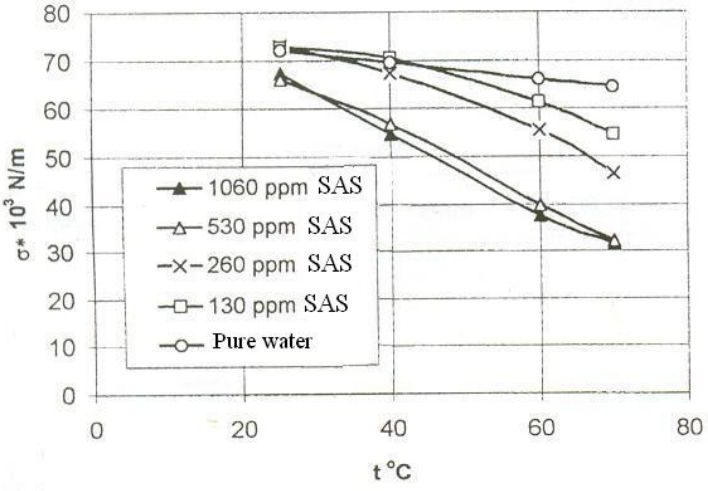

Figure 1. Surface tension as a function of temperature at various concentrations of surface-active substances.

In the electronic cooling systems critical thermal load is a very important value. During this vapor is blanketing with low heat transfer coefficient and often high surface temperature and limiting in industrial and electronic systems large volume boiling application.

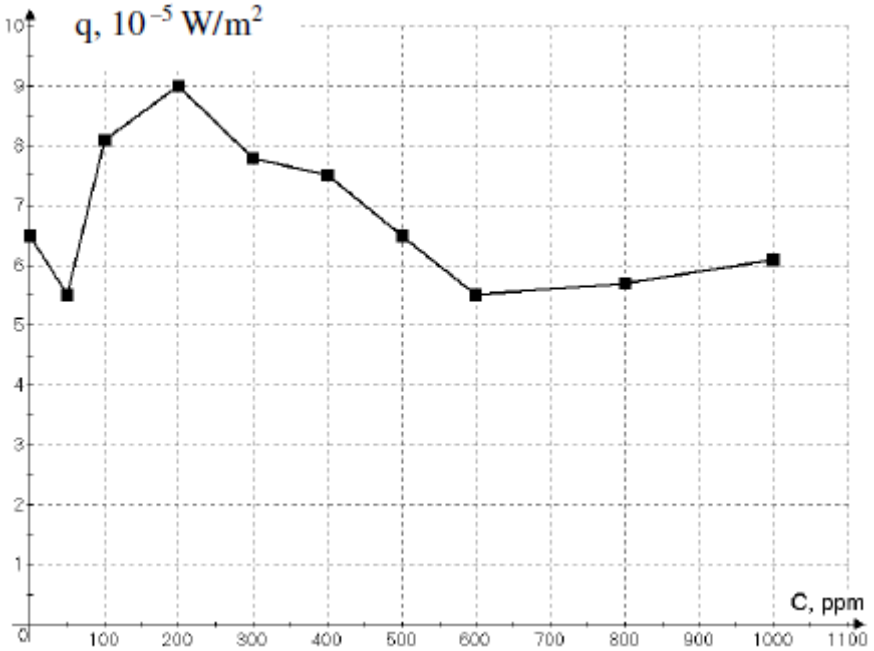

Figure 2. Dependence of nichrome surface critical thermal loads on concentration of natrium dodecyl sulfate.

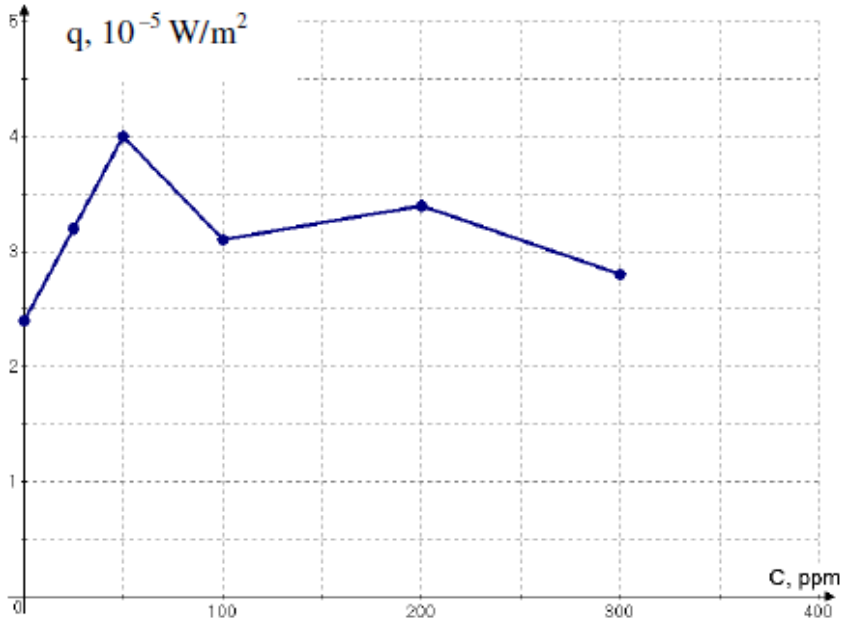

Figure 3. Dependence of nichrome surface critical termal loads on concentration of natrium dodecyl sulfate in freon 113.

Very few studies have been reported related to the critical heat loads in boiling with addition of surfactants. Only Yang & Ma [4] have researched the critical thermal load during large volume boiling water solution with SAS on a horizontal 0.116 mm wire. Results of these experiments are shown in **Figure 2** and **3**. When surfactant concentration in the water increases, the critical thermal load also increases. Because of the experimental wire surface was of very small size, we can not extend it for other cases as long as critical thermal load is dependent on geometrical characteristics.

Nanoliquids are defined as fluids confined in nanopores or as fluids with colloidal suspension of nanoparticles [5].

There are two fundamental methods to obtain nanoliquids:

1. Single step direct evaporation method – the dispersion of nanoparticles is obtained by direct evaporation of the nanoparticle metal and condensation of the nanoparticles in the base liquid; and
2. Double-step method – first the nanoparticles are obtained by different methods and then dispersed into the base liquid.

In order to setlle our research objectives, the special experimental test bench (**Figure 4**) as to be created where possible values of critical thermal loads on the surface of the two-component nanoliquids can be measured during boiling.

The main parts of the device are large and small vessels. Large vessel with water is designed to stabilize temperature in small vessel. A small vessel is placed at the bottom of the metal plate, which is heated by means of a variable transformer. Here nanoliquids critical thermal loads are formed. Advanced automatic measuring stand is used for automatic experimental measuring.

This experimental stand should be used to research nanofluids critical thermal load during boiling, which consists of the main fluid (distilled water, methyl and ethyl alcohol), surfactant (SAS) from the various solid nanoparticiples with the following concentrations: 50, 100, 200, 300, 400, 500, and 1000 ppm.

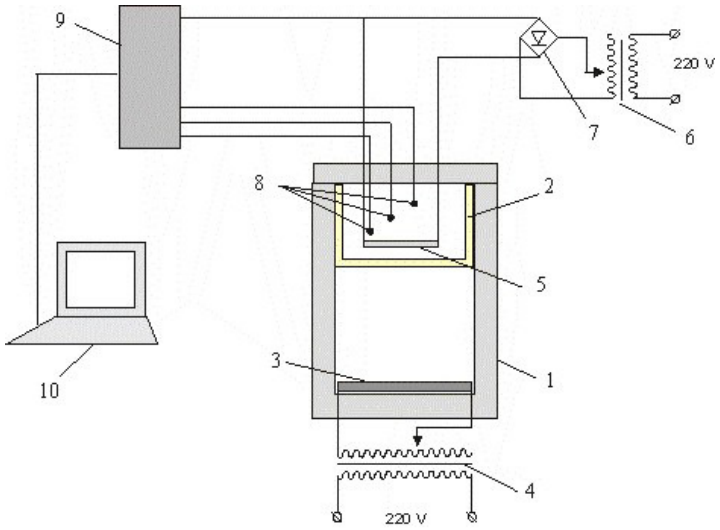

Figure 4. Experimental scheme for researching critical values of thermal loads:
1 – large vessel, 2 – small vessel, 3 – heater, 4 – variable transformer,
5 – heating surface, 6 – variable transformer, 7 – rectifier, 8 – thermocouples,
9 – automatic measuring stand, and 10 – personal computer.

Figure 4 presents the experimental scheme for researching critical values of thermal loads. The results of conducted experiments are shown in above **Figures 2** and **3**. They show the dependence of nichrome surface critical thermal loads on the concentration of natrium dodecyl sulfatewith and without freon, respectively. As it shows the **Figure 2**, if the concentration changes from 0 up to 1000 ppm, the maximum critical load can be obtained during 150 – 250 ppm. While according to the **Figure 3**, if the concentration changes from 0 up to 300 ppm, the maximum critical load can be obtained during 160 – 230 ppm.

Based on the results obtained, we can conclude that:

1. By mixing of refrigeration agents and SAS, it is possible to set up a new refrigeration nanofluids; and
2. It is possible to set up an experimental nanotechnological heat exchanger plant for electronic elements (including the solar energy photoelectronic transformer) cooling.

References

1. J. H. Kralick. Cooling method and apparatus for use with a fuel cell stack. Patent USA, # 6 355 368 B1 (2002).
2. S. D. Garner Heat Pipes for Electronic Cooling Applications. 1996, Lancaster: Thermocore Inc.
3. G. Hestroni, J. L. Zakin, Z. Lin, A. Mosyak, E. A. Pancallo, R. Rozenblit The effect of surfactants on bubble grouth, wall thermal patterns and heat transfer in pool boiling. Int. J. Heat & Mass Transfer 44 (2001) 485-497.
4. Y. Yang, J. Ma. Pool boiling of dilute surfactant solutions. J. Heat Transfer 105 (1983) 190-192.
5. Z. Han. Natural convective heat transfer of water-in-FC72 nanoemulsion fluids, ASME Micro- & Nanoscale Heat Transfer Int. Conf. 2008, Tainan.

ნანომედიცინა და ფოტონები

მ. დოლიძე[1], ნ. დოლიძე[2], ნ. ჭამიაშვილი[3], ზ. ჯიბუტი[3], ლ. ჯიბუტი[4]

[1] პ. შოთაძის სახ. თბილისის სამედიცინო აკადემია
თბილისი, საქართველო
[2] საქართველოს ტექნიკური უნივერსიტეტი
თბილისი, საქართველო
nugzardolidze@gmail.com
[3] საქართველოს აგრარული უნივერსიტეტი
თბილისი, საქართველო
[4] ი. ჯავახიშვილის სახ. თბილისის სახელმწიფო უნივერსიტეტი
თბილისი, საქართველო

მიღებულია 2013 წლის 19 სექტემბერს

ძნელად თუ მოიძებნება ადამიანის მოღვაწეობის ისეთი სფერო, სადაც არ ცდილობს მოსინჯოს თავისი შესაძლებლობები ნანომეცნიერებამ. მისი გამოყენების არეალი ფართოა და მოიცავს როგორც ტექნიკურ დარგებს (ელექტრონიკა, წიაღისეულის მოპოვება და სხვ.), ასევე სიცოცხლის შემსწავლელ მეცნიერებებს. განსაკუთრებით დიდი პერსპექტივები იშლება მისი დანერგვისათვის სამედიცინო სფეროში. მეცნიერები უაღრესად დიდ მნიშვნელობას ანიჭებენ ნანომედიცინის განვითარებას.

ბიოლოგიურ დაავადებათა გამომწვევი ობიექტები ნანოზომებით ხასიათდება და მათთან ბრძოლა სწორედ თანაზომადი და კიდევ უფრო მცირე ნანონაწილაკებით, ნანორობოტებითა და ნანოხელსაწყოებით მიმდინარეობს, რაც მკურნალობის მეთოდების ეფექტურობას მნიშვნელოვნად ზრდის. ნანორობოტების მთავარ დანიშნულებად განისაზღვრება წამლის მიტანა უშუალოდ დაზიანებულ, ავადმყოფ უჯრედებთან, რათა თავიდან იქნას აცილებული ჯანმრთელი უჯრედების დაზიანება.

სწორედ ასეთი სელექტიური, ანუ ამომრჩევლობითი ზემოქმედების უნარი გააჩნია ფოტონოთერაპიასაც. სინათლის კვანტების (ფოტონების) – ელექტრომაგნიტური რხევების ტალღის სიგრძეებიც ნანო- და მიკროზომებისაა და აღმოჩნდა, რომ დაავადებათა გამომწვევი ობიექტებიც ფოტონების შთანთქმის მიხედვით სელექტიურობით ხასიათდება – იგი შთანთქავს მხოლოდ მისი მაქსიმალური იონიზაციის შესაბამისი ფერის (ტალღის სიგრძის) ფოტონებს, და ამავე დროს არ მოქმედებს ჯანმრთელ უჯრადებზე. აქედან გამომდინარე, ფოტონოთერაპიაც ნანომედიცინის ერთერთ მიმართულებად უნდა განვიხილოთ.

ფოტონების (სინათლის ფერების) მოქმედება ადამიანზე დიდი ხანია შემჩნეულია: სინათლე მოქმედებს მის ფიზიოლოგიურ სისტემებზე, ახდენს რა მათი მოქმედების აქტივაციას ან ჩახშობას. ფოტონოთერაპიის (ფერების თერაპია, ქრომოთერაპია) მოქმედება ეფუძნება იმ ფაქტებს, რომ ორგანიზმის თითოეული ბიოლოგიურად აქტიური ზონა რეაგირებს ერთ-ერთ რომელიმე ფერზე

(ელექტრომაგნიტური ტალღების გარკვეულ დიაპაზონზე ან, რაც იგივეა, გარკვეული ენერგიების მქონე ფოტონებზე). ფოტონი, აღწევს რა ცოცხალ ორგანიზმში, იწვევს ქსოვილებში გარკვეულ ბიოქიმიურ რეაქციებს, ახდენს ნივთიერებათა ცვლის რეგულირებას. წინამდებარე ნაშრომში მოყვანილია სხვადასხვა დაავადებების სინათლის კვანტებით (ფოტონებით) მკურნალობის მეთოდები და ფიზიკური მექანიზმები.

ექიმთა შორის გავრცელებულია აზრი, რომ მხოლოდ ხისტი გამა-გამოსხივება, რენტგენული და ულტრაიისფერი სხივები მოქმედებს ეფექტურად ორგანიზმზე. ამიტომაცაა, რომ უფრო ხშირად ეს სხივები გამოიყენება სამედიცინო მიზნებისთვის. მაგრამ სწორედ ზემოთ ჩამოთვლილი გამოსხივებები შთაინთქმება უჯრედის თხევადი ნაწილის მიერ, რაც იწვევს გარემოს იონიზაციას, წარმოქმნის ელექტრონების ნაკადს, რაც, თავის მხრივ, ახდენს ქაოტური ქიმიური რეაქციების კასკადის პროვოცირებას და იწვევს ბიოლოგიური პროცესების რეგულირებას. საპირისპირო ფუნქცია აქვს ხილული დიაპაზონის სინათლის კვანტებს იგი ფოტოსინთეზთან ერთად წარმოადგენს ფოტომორფოგენეტიკური პროცესების რეგულატორს.

ბოლო წლებში, ფოტონოთერაპია ანუ თერაპია ხილული სინათლის ფოტონების საშუალებით განვითარდა, როგორც მკურნალობის ეფექტური მეთოდი. მაგრამ, ცნობილი გამოთქმისა არ იყოს – "ყველაფერი ახალი კარგად დავიწყებული ძველიაო" – სინათლის საშუალებით მკურნალობაც უძველესი დროიდან იყო ცნობილი. მაგრამ ფიზიკის, ქიმიის და ფარმაკოლოგიის განვითარებამ მოიტანა ახალი სამკურნალო საშუალებები, წამლები და სხვ., რის გამოც მკურნალობის ეს უძველესი მეთოდი დროებით დავიწყებას მიეცა. სინათლის სამედიცინო მიზნებით გამოყენების ისტორია ასეთია [1, 2].

ადამიანი სინათლეს სამკურნალოდ ოდითგანვე იყენებდა. ჯერ კიდევ ძველ ეგვიპტეში სინათლეს "ყოვლისშემძლე ღვთიურ მკურნალს" უწოდებდნენ. არქეოლოგებმა აღმოაჩინეს სათავსოები, რომლებიც ისეთნაირად იყო აშენებული, რომ მზის სხივები გარკვეული მიმართულებით გარდატეხილიყვნენ.

ძველი რომაელები ყოველდღიურად ასრულებდნენ ე.წ. "მზის სხივების შესმის" რიტუალს – ისინი მზის აბაზანებს იღებდნენ ან სახლების სწორ ბანებზე, ან სპეციალურად ამ მიზნებისთვის სახლზე მიშენებულ ფართზე, რომელთაც სოლარიუმებს უწოდებდნენ.

ძველ ჩინეთში ექიმები ავადმყოფებს, დაავადების მიხედვით, ურჩევდნენ ეტარებინათ გარკვეული ფერის ტანისამოსი და / ან საცხოვრებელი ოთახის კედლები შეეღებათ შესაბამისი ფერით.

შუა საუკუნეების ევროპაში ექიმები წითელი სინათლის დახმარებით ყვავილის ეპიდემიის მოსპობას ცდილობდნენ. ამისათვის ლაზარეთებში ფანჯრებზე წითელ ფარდებს ჰკიდებდნენ, ხოლო პაციენტებს წითელი ფერის "თეთრეულში" აწვენდნენ. შორს რომ არ წავიდეთ, დღესაც კი საქართველოში, როდესაც ადამიანს, ძირითადად ბავშვებს, ე.წ. "წითელი ბატონები" ანუ "წითელა" შეეყრება, ავადმყოფის ოთახს წითლად მორთავენ: ფარდები, "თეთრეული" და სათამაშოებიც კი ძირითადად წითელი ფერის უნდა იყოს. ასე რომ, სინათლით მკურნალობა დღემდე გამოიყენება, როგორც ზოგი დაავადების მკურნალობის რადიკალური საშუალება.

XIX საუკუნის 70-ანი წლების ბოლოდან მრავალი მეცნიერის ყურადღება მიიპყრო სხვადასხვა მიკროორგანიზმებზე სინათლის გავლენის პრობლემის შესწავლამ. დაიწყო სპეციალური კვლევები შემდეგი სინათლის გავლენის დასადგენად:

- ჩირქოვან სითხეზე
- დუღილის ბაცილასა და სოკოზე
- ციმბირის წყლულის ჩხირებზე და სპორებზე
- ჩირქმბად კოკებზე, სტაფილოკოკებზე
- მუცლის ტიფის ჩხირებზე
- ობისა და საფუარის სპორებზე
- ტუბერკულოზის, დიფტერიის და ტეტანუსის ჩხირებზე
- ქოლერის ვიბრიონებზე
- პათოგენურ ბაქტერიებზე და სხვ.

როგორც ვხედავთ, XIX საუკუნის ბოლოს სინათლის ბიოლოგიურ ობიექტებზე ზეგავლენის კვლევებმა საკმაოდ ფართო ხასიათი მიიღო.

შემდგომში უკვე ფუნდამენტური კვლევების მთელი რიგი შესრულდა და ჩატარდა საერთო ხასიათის სამუშაოები: სინათლის, მათ შორის მონოქრომატული სხივების ბაქტერიოციდული თვისებების, მთელ რიგ ბაქტერიებზე და მიკროორგანიზმებზე ზემოქმედების შესწავლა.

კვლევების შედეგად დადგენილ იქნა არა მხოლოდ სინათლის უბრალოდ ზემოქმედება მიკროორგანიზმებზე, არამედ ისიც, რომ კონცენტრირებული სინათლე დამთრგუნველად მოქმედებს მიკროორგანიზმებზე და სოკოებზე – სინათლის ხანგრძლივი ზემოქმედება იწვევს მათ დაღუპვას და დაშლას (გახრწნას). ამასთან აღმოჩნდა, რომ განათებულობის ერთნაირი ინტენსივობის დროს, სინათლის სპექტრის სხვადასხვა უბნის ზემოქმედება ბიოლოგიურ ობიექტებზე სხვადასხვანაირია. ასე მაგალითად, ბაქტერიებისა და მიკროორგანიზმებისთვის ყველაზე დამღუპველი აღმოჩნდა ე.წ. "ქიმიური" სხივები ანუ სინათლის სპექტრის იისფერი და ულტრაიისფერი უბანი. ხოლო "ოპტიკური" (ყვითელი, მწვანე) და "სითბური" (წითელი და ინფრაწითელი) სხივები – უფრო ნაკლებმოქმედი.

1883 წელს დანიელმა მეცნიერმა ნილს ფინზენმა დაიწყო წითელი სხივებით ყვავილის მკურნალობა. ყვავილით დაავადებულთა სამკურნალოდ სპეციალურად მოეწყო პალატები, რომელთა ფანჯრები დაფარული იყო სქელი წითელი ფარდებით. ასეთ პალატებში ყვავილით დაავადებულთა მკურნალობა წარმატებით მიმდინარეობდა – ყვავილის ბუშტუკები არ გადადიოდა დაჩირქების სტადიაში, არ აღინიშნებოდა მეორეული დაჩირქებები, პირიქით, ბუშტუკები შრებოდა და ხორცდებოდა ნაწიბურის დატოვების გარეშე.

მრავალრიცხოვანი შემდგომი ცდებთ ნ. ფინზენმა დაამტკიცა "ქიმიური" სხივების ძლიერი მოქმედება ნერვულ სისტემაზე, განსაკუთრებით, უმდაბლესი ცხოველებისა და ჩანასახების ნერვულ სისტემაზე. მან გამოიკვლია "ქიმიური" სხივების უნარი მოძრაობაში მოიყვანოს ბაყაყის და სალამანდრას, და ასევე, ჭიებისა და მწერების ემბრიონები.

1886 წელს ნ. ფინზენმა კოპენჰაგენში დააარსა "სინათლით სამკურნალო ინსტიტუტი", რომელიც, როგორც ფინზენი წერს, მოწოდებული იყო "... შეესწავლა ცოცხალ ორგანიზმზე სინათლის გავლენა მიღებული შედეგების პრაქტიკული გამოყენების მიზნით, უპირატესად დაავადებათა სამკურნალოდ". 1887 წლიდან ახლად დაარსებულ ინსტიტუტში ფართოდ გაიშალა კვლევები ბაქტერიებზე სინათლის ზემოქმედების შესწავლის მიზნით. კვლევებმა აჩვენა, რომ სინათლე აფერხებს ბაქტერიების ზრდას, ხოლო სინათლის ძალის მაღალი მნიშვნელობები და ხანგრძლივი დროები კლავს კიდეც მათ. ბაქტერიებზე განსაკუთრებით მოქმედებს

კონცენტრირებული სინათლე. თუკი გაბნეული მზის სხივი ბაქტერიებს 5 წუთში კლავს, 900 ვატიანი რკალური ნათურა – 8 საათში და ვარვარების ნათურა – 11 საათში, კონცენტრირებული სინათლე ასუსტებს ბაქტერიებს 1 წუთში, და კლავს 5 – 7 წუთში. ამასთან, ხაზგასმულია, რომ დამტკიცდა – ბაქტერიებზე ზემოქმედებს არა სითბო,არამედ – სწორედ სინათლე (ცდები ჩატარდა ტიფის, ციმბირის წყლულის და სხვა ბაქტერიებზე).

კვლევებმა აჩვენა, რომ ბაცილების ზრდას აფერხებს სინათლის სპექტრის ყველა უბანი, მაგრამ განსაკუთრებით ძლიერად მოქმედებს იისფერი და ულტრაიისფერი სხივები (ანუ ტალღის სიგრძეები 200 ნმ-დან ქვევით). ინსტიტუტში სინათლის მეტი კონცენტრაციის მიღწევის მიზნით შეიქმნა სპეციალური აპარატურა, რომლის საშუალებით შემცირდა ბაქტერიების დაღუპვის დრო 2 წამამდე. სინათლის მეტი კონცენტრაციის მისაღებად ნ. ფინზენი იყენებდა რკალურ ნათურებს (ნათურები ორი ნახშირის ელექტროდით, რომელთა შორის ინთება ვოლტას რკალი), დიდი ზომის ლინზებს და ჩაზნექილ სარკეებს. გამოსხივების სითბური ნაწილის მოსაშორებლად (დამწვრობის პროფილაქტიკის მიზნით) ნ. ფინზენი სხივებს ობიექტზე დაცემამდე ატარებდა სპეციალურ ოპტიკურ ფილტრებში: შაბიამნის და ამიაკის ხსნარით, ან წყლით მეთილის ლილასთან ერთად. ლინზების მასალად ხმარობდა მთის ბროლს (კვარცისლინზებს). ნ. ფინზენის მიერ შემოთავაზებული მეთოდი გამოიყენეს კანის დაავადებების და, პირველ რიგში. ე.წ. “მგლურას” (რუს.: волчанка, ლათ.: lupus vulgaris) სამკურნალოდ, რომელიც იმ დროისთვის განუკურნელ სნეულებების რიცხვს განეკუთვნებოდა. ფინზენმა თავის ინსტიტუტში 500-მდე ამ სნეულებით დაავადებული განკურნა. მათ დაზიანებული ჰქონდათ სახის ნაწილი, ტუჩები, ცხვირი, ლორწოვანი გარსი და კიდურებიც კი. შედეგები იმდენად შთამბეჭდავი აღმოჩნდა, რომ “მგლურა” მაშინვე მიაკუთვნეს განკურნებად დაავადებათა რიცხვს.

ავადმყოფს გარკვეულ პერიოდში ასხივებდნენ ყოველდღე ან დღეგამოშვებით 1 – 2 საათის განმავლობაში, ამასთან, ასხივებდნენ კანის 2.5 – 3 სმ-იან უბანს. შემდგომ, რამდენიმე თვე ასვენებდნენ და აკვირდებოდნენ შედეგებს. ძლიერად კონცენტრირებული სინათლე ყოველთვის აწითლებდა დასხივებულ ადგილს, ზოგჯერ წარმოიქმნებოდა წყლიანი ბუშტუკები შემდგომი აქერცვლით. ეს ხდებოდა, როცა დასასხივებელ უბანს ცუდად იცავდნენ ძლიერ მაღალი სიცხისგან.

მკურნალობა, დაავადების სტადიის მიხედვით, რამდენიმე თვიდან 1 წლამდე და უფრო მეტიც გრძელდებოდა. 15 – 20 წლის განმავლობაში “მგლურით” დაავადებული ზოგიერთი ავადმყოფი, ინკურნებოდა ამ მეთოდით, მაშინ როცა ტრადიციული მეთოდები – მოწვა, მოკვეთა და მოფხეკა გამოჯანმრთელებას არ იძლეოდა.

ნ. ფინზენის მიერ შემოთავაზებული მეთოდი სრულიად უვნებელი და ამბულატორიული მკურნალობისთვის სრულიად მისაღები აღმოჩნდა. ნ. ფინზენის აზრით, “ქიმიური” სხივების სამკურნალო თვისებებს განსაზღვრავს სამი ფაქტორი:

- ბაქტერიების დახოცვის უნარი (იგი თვლიდა, რომ სინათლე კლავს ყველა პათოგენური ფორმის ბაქტერიებს, ვეგეტატიური ფორმები ადვილად იღუპება, ვიდრე სპორები, ხოლო კოკები უფრო ადვილად, ვიდრე ბაცილები);
- სინათლეს უნარი აქვს გამოიწვიოს ქსოვილის სასარგებლო აღგზნება (ანთება);
- სინათლეს უნარი აქვს შეაღწიოს ქსოვილის სიღრმეში.

მესამე ფაქტორი ანუ ქსოვილის სიღრმეში შეღწევის უნარი, სასარგებლოა არა თავისთავად, არამედ იმით, რომ პირველი ორი ფაქტორის მოქმედებას ქსოვილის დიდ მოცულობებში ავრცელებს. მაგრამ არსებობს კიდევ მეოთხე, ძალიან მნიშვნელოვანი

ფაქტორიც, რომელსაც იმ პერიოდისთვის არ აქცევდნენ ყურადღებას – ქსოვილებში მიმდინარე ყველა პროცესის სტიმულირება გარეგანი დასხივების ენერგიის გადაცემის ხარჯზე (იონიზაციის მაღალი ხარისხი).

მეცნიერულად მეტ-ნაკლები დასაბუთებული სხვადასხვა ფერის სინათლის თერაპიული მეთოდები გამოჩნდა XX საუკუნის დასაწყისში. მაგრამ, ამ მეთოდებით, ძირითადად ორ ფერს – ლურჯს და წითელს იყენებდნენ: ლურჯი ფერით ასხივებდნენ სიყვითლიან ბავშვებს, რაც შემდგომი სისხლის გადასხმის აუცილებლობას ხსნიდა – ლურჯი სინათლე კანის გავლით აღწევს რა ორგანიზმში შლის ბილირუბინს, რასაც ბავშვის ღვიძლი დამოუკიდებლად ვერ ახერხებს.

რუსეთში სინათლით მკურნალობის პრაქტიკა 1899 წლიდან იწყება, როცა პროფესორ კ. პ. სერაპინის ხელმძღვანელობით ქ. სანკტ-პეტერბურგში, პროფესორ ნ. ა. ველიამინოვის აკადემიურ ქირურგიულ კლინიკასთან შეიქმნა სინათლით მკურნალობის განყოფილება. კლინიკაში გაიმეორეს ფინზენის ცდები, გამოიყენეს მისი გამოცდილება და სინათლით უმკურნალეს 200-ზე მეტ სხვადასხვა პაციენტს. შემთხვევების საერთო პროცენტმა, როცა სინათლის მოქმედება დადებითი აღმოჩნდა, შეადგინა 87.5 %, ხოლო სადაც სინათლის მოქმედება სუსტი იყო ან საერთოდ არ იმოქმედა – 12.5 %. მაგრამ, სამწუხაროდ, ამ განყოფილებამ იარსება მხოლოდ 1917 წლამდე, როდესაც კლინიკა გადაკეთდა სამხედრო-სამედიცინო აკადემიად და მის შემადგენლობაში აღნიშნული განყოფილებისთვის არ აღმოჩნდა ადგილი. ამიტომ, ყოფილ საბჭოთა კავშირში (და, აქედან გამომდინარე, საქართველოშიც) სინათლით მკურნალობა თითქმის მივიწყებული იყო და ამგვარი მკურნალობის პრაქტიკა არ არსებობდა.

განსაკუთრებით აღნიშვნას მოითხოვს XX საუკუნის ყველაზე დიდი მიღწევა ელექტრომაგნიტური ტალღების (სინათლის) საშუალებით მკურნალობის საქმეში: ამერიკელი ექიმის, მკვლევარის და მეცნიერის როიალ რაიმონდ რაიფის (1888 – 1971) ექსპერიმენტები [3]. მან 1930-იან წლებში შექმნა, ე.წ. რაიფის უნივერსალური მიკროსკოპი – ოპტიკური ხელსაწყო, რომელშიც გამოიყენა კვარცის ლინზების არაჩვეულებრივი კომბინაცია. მიკროსკოპს შეეძლო, იმ დროისათვის წარმოუდგენელი, 30000-ჯერ გადიდებული გამოსახულების მიღება, ასე, რომ შესაძლებელი გახდა ცოცხალი უჯრედების, ბაქტერიების და ვირუსებისაც კი, დანახვა.

სურათი 1. რაიფის უნივერსალური მიკროსკოპი და რაიფის სხივთა კონა (მარცხნივ როიალ რაიმონდ რაიფი).

ამ უნიკალურ ხელსაწყოში ნიმუშები ნათდებოდა პოლარიზებული სხივებით. კვლევებმა აჩვენა, რომ ყველა ცალკეული მიკროორგანიზმი ანათებდა უნიკალური, მხოლოდ მისთვის დამახასიათებელი ფერით. ფერების მიკროორგანიზმებთან იდენტიფიცირება უმარტივესად ხერხდებოდა.

მეცნიერის მეორე უმნიშვნელოვანესი აღმოჩენა იყო ის, რომ ნებისმიერ ორგანიზმს გააჩნია საკუთარი (სელექტიური) რეზონანსული სიხშირე – რაიფმა მას ვიბრაციის სასიკვდილო სიხშირე უწოდა (mortal oscillatory rate – MOR). რაიფი, მოათავსებდა რა მიკროსკოპში ცოცხალი ბაქტერიების კულტურას, რთავდა მის მიერვე შექმნილ გენერატორს, ე.წ. რაიფის სხივთა კონა (Rife beam ray – RBR), და სიხშირის ცვლილებით ადგენდა მოცემული ბაქტერიების შესაბამის MOR-ს. ეს იყო სიშირე, როდესაც ყველა ბაქტერია წყვეტდა მოძრაობას და კვდებოდა. რაიფმა აღმოაჩინა, რომ შესაძლებელია RBR-ის გამოყენება ადამიანების სამკურნალოდ – სხვადასხვა ინფექციური დაავადების წინააღმდეგ, რაც პრაქტიკაში განახორციელა კიდეც. რეზონანსის მარტივი პრინციპის გამოყენებით, ურჩევდა ვირუსებს და ბაქტერიებს შესაბამის MOR-ს და პოულობდა კიდეც. მრავალი წლის ექსპერიმენტული კვლევების შედეგად მან შეადგინა ამა თუ იმ დაავადების გამომწვევთათვის დამღუპველი სიხშირეების ცხრილი.

მაგრამ ყველაზე გასაოცარი აღმოჩნდა, რომ ეს სხივები წარმატებით ებრძვის კიბოს. რაიფმა შექმნა თეორია, რომ კიბოს იწვევს ვირუსები და მიკროორგანიზმები. თავისივე მიკროსკოპში კიბოს უჯრედებზე პირდაპირი დაკვირვებით, რაიფმა არაერთხელ შესძლო გამოეყო აღნიშნული ვირუსი, რითაც დაამტკიცა თავისივე ჰიპითეზა კიბოს ვირუსული ეთიოლოგიის შესახებ. რადგან ვირუსი აღმოაჩინა, მან გადაწყვიტა მოეძებნა მისი შესაბამისი MOR და იპოვა კიდეც.

ყველაფერი ზემოთ აღნიშნული აღმოჩნდა აშშ-ის სამედიცინო ასოციაციისთვის ძნელად მისაღები. 1934 წელს, გარკვეული დებატების შემდეგ, შეიქმნა რაიფის მეთოდების შემსწავლელი სახელმწიფო კომისია და ჩატარდა ექსპერიმენტი: რაიფი RBR-ის გამოყენებით ყოველდღიურად ასხივებდა 16 კიბოთი დაავადებულ უიმედო, მომაკვდავ პაციენტს. სამი თვის შემდეგ, მედიცის დოქტორებით დაკომპლექტებულმა სახელმწიფო კომისიამ მათგან 14 პაციენტი ჯანმრთელებად გამოაცხადა, ანუ დადებითმა შედეგმა 90 %-ს გადააჭარბა. დარჩენილი 2 პაციენტი უახლოესი 4 კვირის შემდეგ ასევე ჯანმრთელად იყო ცნობილი. გამოჯანმრთელების ასეთი კოეფიციენტი ონკოლოგიურ დაავადების მკურნალობაში დღესაც კი მიუღწეველია.

ისმის კითხვა: თუ კი კაცობრიობამ აღმოაჩინა კიბოს საწინააღმდეგო (და არა მარტო კიბოს) რადიკალური მეთოდი, რა მოხდა შემდეგ, რატომ არ გავრცელდა იგი?

სამწუხაროდ, როგორც ხშირად ხდება, კიბოს მკუნალობის ახალმა თეორიამ და მეთოდიკამ უარყოფითი სოციალური შედეგი გამოიღო – მან ეჭვს ქვეშ დააყენა მრავალი მეცნიერისა და ექიმის კომპენტენტურობა და საფრთხე შეუქმნა ფარმაცევტული მრეწველობის ფინანსურ ინტერესებს. დაიწყო ამ მიღწევის დისკრედიტაციის კამპანია. ახალი ტექნოლოგიის მიმდევარი მეცნიერები იძულებული გახდნენ შეეწყვიტათ აღნიშნული პრაქტიკა. დაიწყო რ. რაისის დევნა, თვალთვალი, მუქარა ტელეფონით და ერთხელ მანქანით მიმავალი უშედეგოდ დაცხრილეს კიდეც. შეწყდა პუბლიკაციები აღნიშნულ თემაზე, ვინაიდან სამედიცინო ჟურნალები მკაცრ ცენზურას დაუქვემდებარეს. ცნობილი მეცნიერები და ექიმები, რომლებიც მხარს უჭერდნენ ახალ ტექნოლოგიას და მის ბაქტერიოლოგიურ მეცნიერულ ბაზას, დაცინვის ობიექტები ხდებოდნენ და მათ საჯაროდ ცრუ მეცნიერებს უწოდებდნენ.

საბოლოოდ, კიბოს მკურნალობის ახალ ტექნოლოგიას ათწლეულობით დაედო სიჩუმის დაღი. კიბოს ამგვარი მკურნალობა მითად იქცა, რომელიც არასოდეს ყოფილა. საბედნიეროდ დარჩა დოკუმენტები, რომლებიც ამტკიცებს, რომ აღნიშნული მეთოდით კიბოს განკურნება ნამდვილად შესაძლებელია. ახალმა ტექნოლოგიამ წარმატებით გაიარა კლინიკური ყველა გამოცდა და სინამდვილეში ფარულად აგრძელებს არსებობას დღემდე.

ასეთია, მოკლედ, ელექტრომაგნიტური ტალღების (სინათლის) საშუალებით მკურნალობის ისტორია, რომელსაც, როგორც ვნახეთ, კაცობრიობა ოდითგანვე იყენებდა.

როიალ რაიფის კვლევებმა აჩვენა, რომ სინათლეს, როგორც ელექტრომაგნიტურ ტალღებს, აქვს უნარი დამღუპველად იმოქმედოს ბიოლოგიური დაავადების გამომწვევ ბაქტერიებზე, მიკროორგანიზმებზე, ვირუსებზე. შემდგომში მეცნიერები შეუდგნენ იმის კვლევას, თუ რა მექანიზმით შეიძლებოდა ემოქმედა რაიფის გენერატორს და როგორ შეიძლებოდა მისი გაუმჯობესება.

1960 წელს რუსმა მეცნიერებმა ნ. გ. ბასოვმა და ა. მ. პროხოროვმა, ამერიკელ მეცნიერ ჩ. თაუნსთან ერთად, შექმნეს სინათლის ოპტიკური გენერატორი – ლაზერი, რისთვისაც 1964 წელს მიიღეს ნობელის პრემია.

ლაზერის შექმნასთან ერთად დაიწყო მედიცინაში სინათლის გამოყენების ახალი ერა – ლაზეროთერაპიისა და ლაზეროქირურგიის სახით. მძლავრი ლაზერები გამოიყენებოდა ქირურგების მიერ, როგორც უსისხლო, მჭრელი, სტერილური ლანცეტი. ხოლო, დაბალი სიმძლავრის ლაზერები (ძირითადად ნარინჯისფერ-წითელი და ახლო ინფრაწითელ არეში) ფოტონური თერაპიის მიზნით [1, 2].

ლაზერები მედიცინაში გამოიყენება, ასევე, ოფთოლმოლოგიაში (კატარაქტა, ბადურის აცლა, მხედველობის ლაზერული კორექცია და სხვ.). მან ფართო გამოყენება ჰპოვა, აგრეთვე, კოსმეტოლოგიაში (ლაზერული ეპილაცია, კანის პიგმენტური და სისხლძარღვთა დეფექტები, ლაზერული პილინგი, ტატუირების და პიგმენტური ლაქების მოცლა).

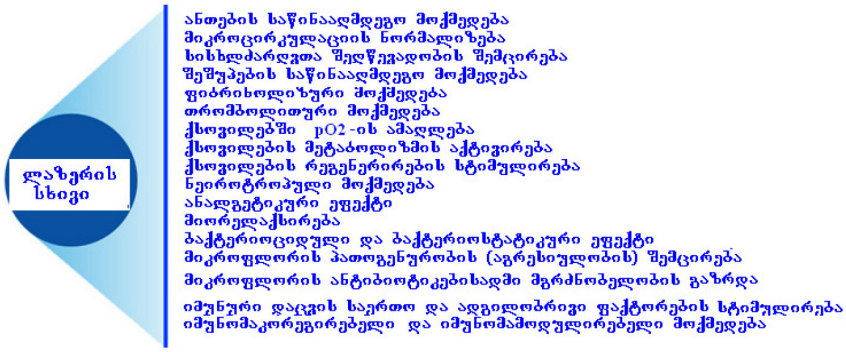

სურათი 2. იმპულსური ლაზერის ($\lambda = 0.85 – 0.95$ მკმ) მრავალ-ფაქტორული პათოგენეტიკური სამკურნალო მოქმედების სქემა.

ლაზერული მკურნალობის მეთოდების ძირითადი განმასხვავებელი თვისებაა პროფილაქტიკური და სამკურნალო მოქმედების ფართო დიაპაზონი, რომელიც განპირობებულია დაბალი ინტენსივობის ლაზერის სხივის მრავალფაქტორიანი პათოგენეტიკური მოქმედების უნიკალური მექანიზმებით. ისინი უზრუველყოფენ მაღალ პროფილაქტიკურ და სამკურნალო ეფექტს, რაც ნათლად არის წარმოდგენილი **სურათზე 2**.

როგორც ვხედავთ, სხვადასხვა სამკურნალო საშუალებების ფართო კომპლექსებთან შედარებით, ლაზერის სხივს გააჩნია უპირატესობები, რომლებიც უნიკალურია. შემდგომმა კვლევებმა აჩვენა, რომ მაღალეფექტური სამკურნალო თვისებები აქვს დაბალი ინტენსივობი სიმპულსური ლაზერების მუდმივ მაგნიტურ ველთან (დაძაბულობები 35 – 50 მტლ) შეთავსებას. ეს მეთოდი, თავისი ხარისხით, არა უბრალოდ ორი ფიზიკური ფაქტორის სუპერპოზიციაა, არამედ იგი პროფილაქტიკისა და მკურნალობის ახალი სახეცაა, რომელიც უზრუნველყოფს უფრო მაღალ ეფექტურობას, ვიდრე მისი ცალკეული შემადგენლის მოქმედება (**სურათი 3**).

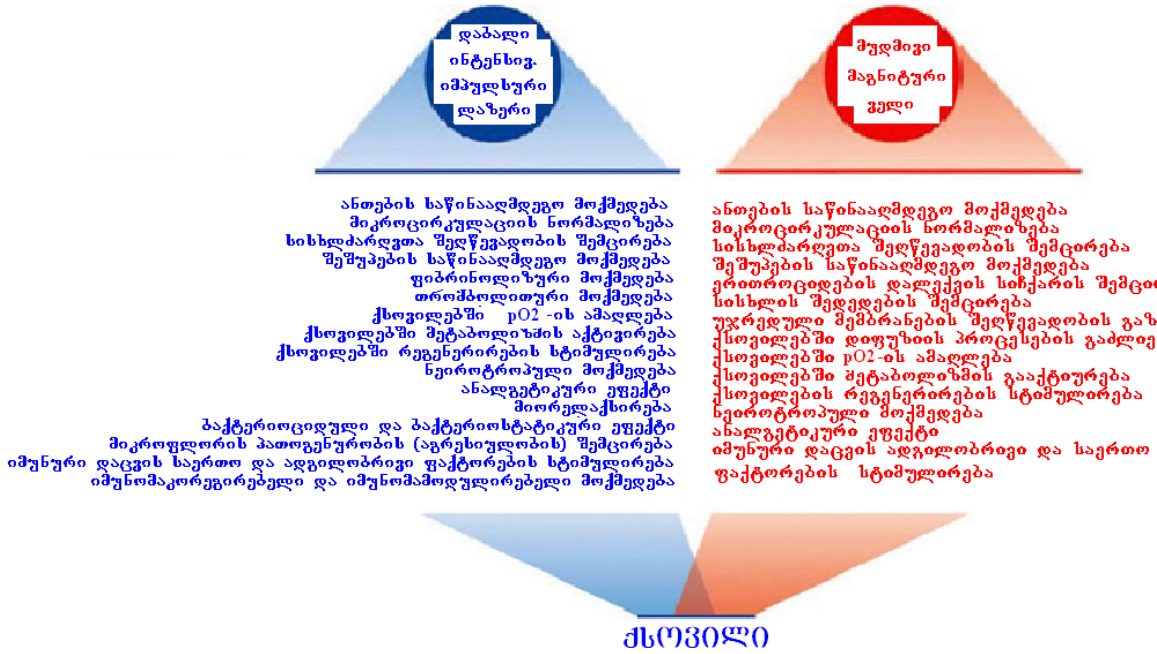

სურათი 3. შეთავსებული დაბალინტენსიური იმპულსური ლაზერისა და მუდმივი მაგნიტური ველის პროფილაქტიკური და სამკურნალო მექანიზმების სამუშაო სქემა.

გასული საუკუნის მეორე ნახევარში სამედიცინო პრაქტიკაში ლაზერების გამოყენებამ ფართო ხასიათი მიიღო. სპეციალური ტერმინიც კი გაჩნდა – კვანტური მედიცინა. კვანტური მედიცინა ეფუძნება მცირე დოზების ელექტრომაგნიტური გამოსხივების (კვანტების) მიზანმიმართულ ზემოქმედებას პაციენტების პროფილაქტიკის, დიაგნოსტიკის, მკურნალობის და რეაბილიტაციისთვის. ამასთან, იგულისხმება ბუნებრივი და ბუნებრივ ფაქტორებთან ახლო ელექტრომაგნიტური ზემოქმედება, რომელიც კეთილისმყოფელ გავლენას ახდენს უჯრედის, ორგანოს და მთელი ორგანიზმის სიცოცხლისუნარიანობაზე. კვანტურ მედიცინაში გამოყენებული ენერგეტიკული ზემოქმედების მცირე სიმძლავრეები აბსოლუტურად უვნებელია. გამოყენებული მეთოდები საშუალებას იძლევა ორგანიზმში წარმოქმნილი ანომალური პროცესი, ანუ დაავადება, გადავიყვანოთ ჯანმრთელ მდგომარეობაში. ეს ფაქტი იმით აიხსნება, რომ კვანტების ზემოქმედება, როგორც ცალკეული უჯრედის, ასევე მთელი ბიოლოგიური სისტემის დონეზე, აამოქმედებს ორგანიზმის დამალულ ადაპტაციურ შესაძლებლობებს. ამ დროს მკვეთრად იზრდება იმუნიტეტი და წარმოებს ორგანიზმის დამცველი ძალების მობილიზება ფუნქციონირებაში წარმოქმნილ გადახრებთან აქტიური წინააღმდეგობისთვის.

კვანტური მედიცინა იყენებს იმ ფაქტს, რომ ყველა ბიოლოგიურ პროცესს, რომელიც თან ახლავს ორგანიზმის ცხოველქმედებას, აქვს თავისი ცალსახა ასახვა ელექტრომაგნიტურ საინფორმაციო ველის სტრუქტურაში, რომელიც გარშემო ერტყმის ორგანიზმს და არსებობს მის შიგნით.

კვანტური ზემოქმედება გამოიყენება 200-ზე მეტი დაავადების სამკურნალოდ: ანგინა, არტრიტები და არტროზები, ბრონქიალური ასტმა, ბრონქიტი, ჰაიმორიტი, გასტრიტი, ბუასილი, ჰერპესი, ჰიპერტონული დაავადებები, ნაწლავების დისბაქტერიოზი, გულის იშემიური დაავადებები, კარდიონევროზი, კოლიტი, ლარინგიტი, მიოზიტები, ნევრიტები, ნევროზები, რადიკულიტი, პროსტატიტი, რინიტი, სტომატიტი, ტონზილიტი, ფარინგიტი, კუჭისა და თორმეტგოჯა ნაწლავის წყლულოვანი დაავადებები და სხვ. ლაზეროთერაპიის რეჟიმები ინდივიდუალურია და ინიშნება ექიმის მიერ, მაგრამ ყველა შემთხვევაში, ექსპოზიციის ერთი სეანსის დრო წუთებს არ აღემატება. **ცხრილში 1** მოცემულია კვანტური მედიცინის შესაძლებლობების შედარებითი მონაცემები ზოგიერთი დაავადებების მკურნალობისას.

ცხრილი 1. ზოგიერთი დაავადების, წამლებზე მოთხოვნილებისა და მკურნალობის ვადების შედარებითი მონაცემები მედიკამენტოზური და კვანტური თერაპიისას.

დაავადების სახე	წამლებზე მოთხოვნილების შემცირება	მკურნალობის ვადების შემცირება
• გულის იშემიური დაავადება • მიოკარდის ინფარქტი • რევმოკარდიტი	2 – 3-ჯერ	8 – 12 დღით
• პროსტატიტი	უწამლოდ	2.5-ჯერ
• რადიკულიტი • ოსტეოქონდროზი	მედიკამენტების გარეშე	1.7 – 2.2-ჯერ
• პნევმონია	1.9-ჯერ	5 – 8 დღით
• ჭრილობები • დამწვრობები	2.4-ჯერ	2 – 3-ჯერ
• კუჭისა და თორმეტგოჯა ნაწლავის წყლული	2.7-ჯერ შემთხვევათა 60 %-ში შეიძლება მედიკამენტებზე მთლიანად უარის თქმა	
• ჰიპერტონიული დაავადება	I და II სტადია უწამლოდ	3 – 5 დღით
• ყელ-ყურ-ცხვირის დაავადებების პროფილაქტიკა	უწამლოდ	დაავადების ალბათობა მცირდება 89 %-ით
• ბრონქიალური ასთმისა და ბრონქიტის პროფილაქტიკა	უწამლოდ	დაავადების ალბათობა მცირდება 76 %-ით

როგორც ვხედავთ, ლაზერის სხივები (ფოტონები) ფართოდ გამოიყენება კლინიკურ და ექსპერიმენტულ მედიცინაში. თანამედროვე ეტაპზე კვანტური მედიცინა ანუ ფოტონური მედიცინა, ძლიერი განვითარების სტადიაშია და მიმდინარე საუკუნის მედიცინის მეტად პერსპექტიულ მიმართულებად ითვლება. ასევე ვიცით, რომ მედიცინაში აპრობირებული, გამოყენებული და დანერგილი ლაზერები საკმაოდ ძვირადღირებულია, ასხივებენ სხვადასხვა ინტენსივობის მონოქრომატულ, კოჰერენტულ და ძლიერად დაფოკუსირებულ სინათლის სხივებს. ამასთან, ყოველმხრივი და დეტალური შესწავლის შედეგად დადგენილია, რომ ლაზეროთერაპიის გამოყენების ათეულობით წლების განმავლობაში არცერთი უარყოფითი შედეგი არ დაფიქსირებულა. მთელი რიგი კვლევებით გამოვლენილია, აგრეთვე, რომ თერაპიის მიზნით ორგანიზმის დასხივებისას, სინათლის სპექტრის ინფრაწითელი, წითელი, ნარინჯისფერ-წითელი დიაპაზონი სავსებით უვნებელია.

სისხლის დასხივებისას ყველაზე ეფექტური აღმოჩნდა ფოტონები, რომელთა ტალღის სიგრძე 0.6-დან 1.1 მკმ-მდე ფარგლებშია, სადაც სისხლის ოპტიკური შთანთქმის კოეფიციენტი მცირეა (**სურათი 4**) [4, 5]. სურათიდან ჩანს, რომ როგორც არტერიული, ასევე ვენური სისხლისთვის შთანთქმა სპექტრის აღნიშნულ უბანში თითქმის სამი რიგით მეტია, ვიდრე 0.3 – 0.6 მკმ-ის დიაპაზონში. აქედან, თუკი ულტრაიისფერი და ლურჯ-მწვანე სხივები სისხლში პრაქტიკულად მთლიანად შთაინთქმება რამდენიმე მკმ-ის სისქეში, მოყვითალო-წითელი და, განსაკუთრებით, ახლო ინფრაწითელი სხივები ($\lambda = 1.1$ მკმ-მდე) თავისუფლად აღწევს ორგანიზმის რამდენიმე სანტიმეტრის სიღრმეში. ეს კი საშუალებას იძლევა სისხლის დიდი მოცულობები გასხივდეს.

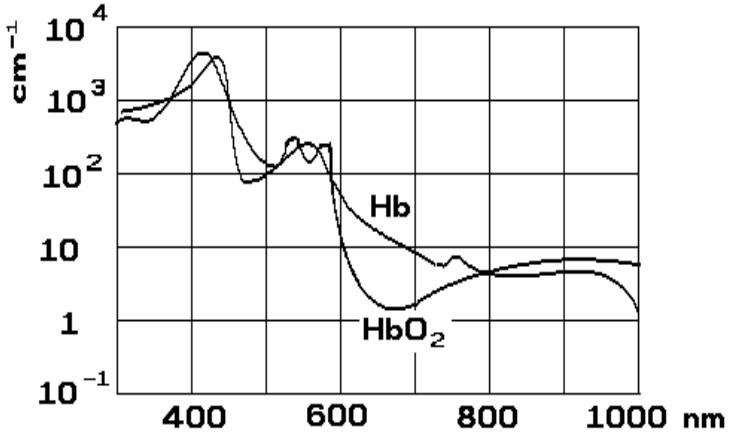

სურათი 4. სისხლის ოპტიკური შთანთქმის სპექტრი:
HbO_2 – არტერიული სისხლი და Hb – ვენური სისხლი.

He – Ne-ის ლაზერი, რომელიც ფართოდ გამოიყენება მედიცინაში, როგორც სამკურნალო ფოტონების წყარო, გამოასხივებს წითელ ($\lambda = 0.6328$ მკმ), მონოქრომატულ, კოჰერენტულ, დაფოკუსირებულ სხივებს. ამასთან, ლაზერის სხივის კოჰერენტულობას და ფოკუსირებას არავითარი მნიშვნელობა არ აქვს ბიოლოგიურ ობიექტთან სინათლის ფოტონის ურთიერთქმედებისას. ვინაიდან, ცოცხალ ორგანიზმზე ზემოქმედებისას, კანის თხელი ფენის გავლისას, ლაზერის სხივი კარგავს კოჰერენტულობას, ფოკუსირებას, იქცევა ჩვეულებრივ სხივად და ასე აღწევს ორგანიზმში, ხოლო პოლიქრომატულობა სამკურნალოდ უფრო უკეთესი აღმოჩნდა.

უკანასკნელ წლებში, თეორიული და კლინიკური კვლევის ანალიზით დადგინდა, რომ ლაზერის სხივების ანალოგიური ეფექტი შესაძლებელია მიღებულ იქნეს ორგანიზმის არაკოჰერენტული, და გარკვეულ დიაპაზონში პოლიქრომატული სხივებით დასხივებისას. უფრო მეტიც, დადგინდა, რომ კვანტური თერაპია ფოტონების საშუალებით, უმჯობესია ჩატარდეს არაკოჰერენტული, დაუფოკუსირებელი, პოლიქრომატული სხივებით ახლო ინფრაწითელ და ხილული დიაპაზონის მოყვითალო-წითელ უბანში [4, 5]. ასეთი სხივების წყარო არის ნახევარგამტარული მაშუქი დიოდები GaAlAs(Zn)-ის ბაზაზე, რომლებიც როგორც წითელი ($\lambda = 0.675$ მკმ), ასევე ახლო ინფრაწითელი სხივების პოლიქრომატულ სპექტრს იძლევა (**სურათი 5**).

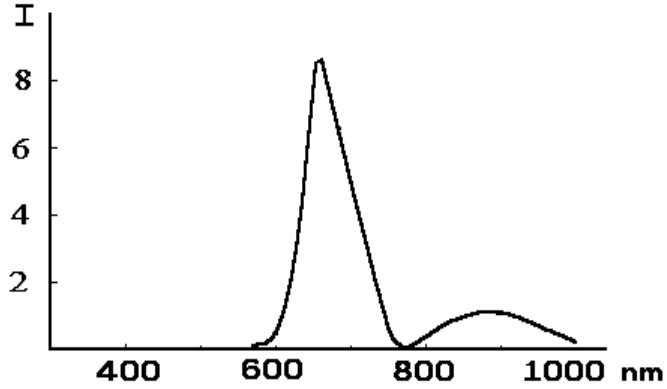

სურათი 5. GaAlAs(Zn)-ის კრისტალებზე
შექმნილი მაშუქი დიოდის გამოსხივების სპექტრი.

სადღეისოდ უკვე შესწავლილი და დადგენილია, რომ ამა თუ იმ პათოლოგიების დროს ორგანიზმის ტემპერატურა იზრდება რამდენიმე გრადუსით და სწორედ ტემპერატურის აწევა იწვევს ბიოქიმიური რეაქციების სიჩქარეების საკმაოდ მკვეთრ გაზრდას. ეს უკანასკნელი კი, სწრაფი გამოჯანმრთელების საფუძველია. ამ პრინციპით მოქმედებს ქიმიური პრეპარატების დიდი უმრავლესობა, რომლებიც სწორედ ამ რეაქციების კატალიზატორის როლს ასრულებს.

დადგენილია, ასევე, რომ ქიმიური რეაქციების სიჩქარე საგრძნობლად მატულობს მასში მონაწილე იონების რაოდენობის გაზრდით. როგორც ვიცით, ამა თუ იმ ნივთიერების ტემპერატურის გაზრდა იწვევს ატომებში ელექტრონების მაღალენერგეტიკულ დონეზე გადასვლას. ეს ელექტრონები ადვილად შორდება ატომებს, ანუ ადგილი აქვს იონიზაციას (ატომები გადაიქცევა იონებად) და მათი კონცენტრაციის მატება ქიმიური რეაქციების ინტენსივობის მკვეთრ გაზრდას იწვევს. ამავე დროს, ცნობილია ისიც, რომ ცოცხალ ორგანიზმს ტემპერატურის გაზრდა შეუძლია მხოლოდ 3 – 4 გრადუსით. და მიუხედავად ტემპერატურის ასეთი მცირე ცვლილებისა ქიმიური რეაქციების სიჩქარე რამდენიმეჯერ ძლიერდება. აქედან გამომდინარე, თუ როგორმე მოხერხდება ორგანიზმში მაღალი ტემპერატურის შესატყვისი პირობების შექმნა, ნათელია, რომ გამოჯანმრთელების პროცესი მეტად ინტენსიური გახდება. რეალურად ასეთ შესაძლებლობას იძლევა გარკვეული ტალღის სიგრძის მქონე სინათლის კვანტები – ფოტონები.

რა ხდება ცოცხალი ორგანიზმების ფოტონებით დასხივების პროცესში?

როგორც აღვნიშნეთ, ბიოლოგიური ობიექტების ორგანოებში და ქსოვილებში, ისევე როგორც ნებისმიერ მატერიალურ გარემოში, ფოტონებით დასხივებისას,

ენერგიის შთანთქმის შედეგად მიმდინარეობს იონიზაციისა და ატომების აღგზნების პროცესები [4 – 7]. სწორედ ეს პროცესებია დასხივების ბიოლოგიური ზემოქმედების საფუძველი. მისი ზომა – ეს არის ორგანიზმის მიერ შთანთქმული ენერგიის რაოდენობა. ნებისმიერ მაიონებელ დასხივებაზე (მათ შორის რადიაციაზეც) ორგანიზმის რეაქცია მიმდინარეობს ოთხ ფაზაში. ამათგან, საკვლევი ფოტონების ენერგიებს შეესაბამება მხოლოდ პირველი სამი ფაზა, რომელთა ხანგრძლივობა არ აღემატება მიკროწამებს, და რომლის განმავლობაშიც სხვადასხვანაირი მოლეკულური ცვლილებები მიმდინარეობს. მეოთხე, ნელ ფაზაში (რადიაციის ზემოქმედებისას) ეს ცვლილებები გადადის ორგანოებში და მთელს ორგანიზმში, უჯრედების ფუნქციური და სტრუქტურული დარღვევების სახით. მეოთხე ფაზა შეიძლება წლებიც გაგრძელდეს. მაგრამ, ამჟამად, ჩვენ ამ ფაზას არ განვიხილავთ.

პირველი ორი ფაზის შედეგად წარმოიქმნება ქიმიური თვალსაზრისით მაღალაქტიური რადიკალები. ეს რადიკალები, ურთიერთქმედებს რა სხვადასხვა ნაერთთან, იძლევა მეორად რადიკალებს, რომლებიც პირველად რადიკალებთან შედარებით მეტი სიცოცხლის ხანგრძლივობით ხასიათდება. მესამე, ქიმიურ ფაზაში უკვე წარმოქმნილი რადიკალები შედის რეაქციაში ორგანული უჯრედების მოლეკულებთან.

აღნიშნული პროცესების შედეგად, რომლებიც 10^{-6} წმ-ის განმავლობაში მიმდინარეობს, მკვეთრად იზრდება იონებისა და თავისუფალი რადიკალების რაოდენობა. ლოკალურად იქმნება მაღალი ტემპერატურის შესაბამისი სიტუაცია. ეს კი, თავის მხრივ, მკვეთრად ზრდის ორგანიზმში მიმდინარე ბიოქიმიური რეაქციების სიჩქარეს, მათ შორის, იმ რეაქციების სიჩქარეს, რომელთა საშუალებითაც ორგანიზმი პათოლოგიას ებრძვის. საყურადღებოა, რომ ამ პროცესში ლოკალურად ორგანიზმის ელექტრონულმა (ეფექტურმა) ტემპერატურამ შეიძლება მიაღწიოს ასეულობით გრადუსს (**სურათი 6**), და ამ დროს ჩვეულებრივი (რეალური) ტემპერატურა პრაქტიკულად უცვლელი რჩება.

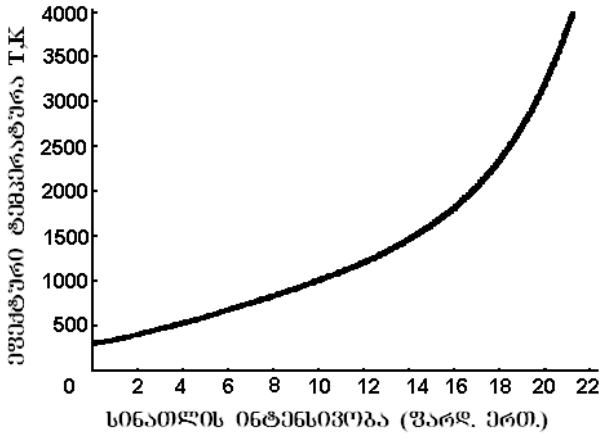

სურათი 6. ეფექტური ტემპერატურის დამოკიდებულება სინათლის ინტენსივობაზე.

ამავე დროს, აღსანიშნავია, რომ სხვაობა ელექტრონულ და რეალურ ტემპერატურებს შორის არსებობს მხოლოდ ბიოლოგიური ობიექტის ფოტონებით დასხივების პროცესში. ამ ზემოქმედების შეწყვეტისთანავე ეფექტური ტემპერატურა სწრაფად ეცემა ნორმალურამდე და ბიოლოგიური რეაქციებიც ჩვეულებრივი სიჩქარით

გრძელდება. აღნიშნულიდან გამომდინარე, სხივის პოლიქრომატულობა უფრო მეტი მოლეკულებისა და ატომების იონიზაციის საშუალებას იძლევა და ლაზერთან შედარებით მცირე სინათლით შესაძლებელი ხდება ლაზერის სხივის იდენტური და კიდევ უკეთესი სამკურნალო ეფექტის მიღება. აქედან გამომდინარე, პოლიქრომატული ფოტონების ნაკადის საშუალებით, ლაზერთან შედარებით, უფრო მცირე სიმძლავრეებით შესაძლებელია იგივე ეფექტის მიღება.

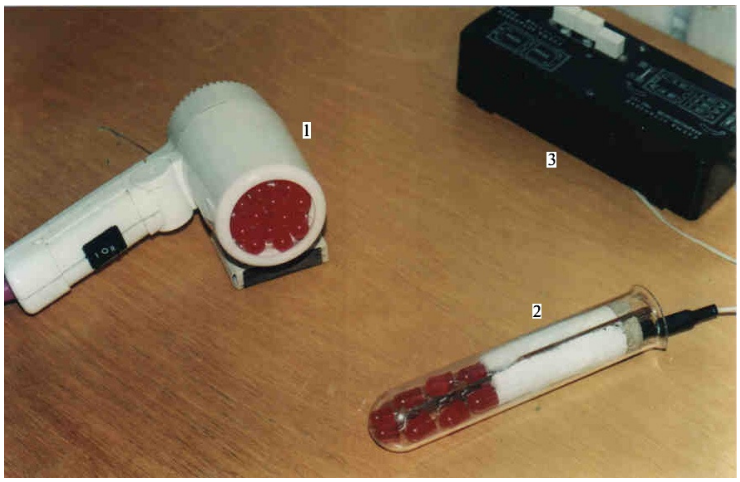

სურათი 7. “ფაზერის“ ორი ვარიანტი: 1 – დისტანციურ-კონტაქტური ზედაპირული დასხივებისთვის და 2 – დისტანციურ-კონტაქტური ღრმულებისა და ფოსოებისთვის; 3 – მეორე ვარიანტის კვების ბლოკი.

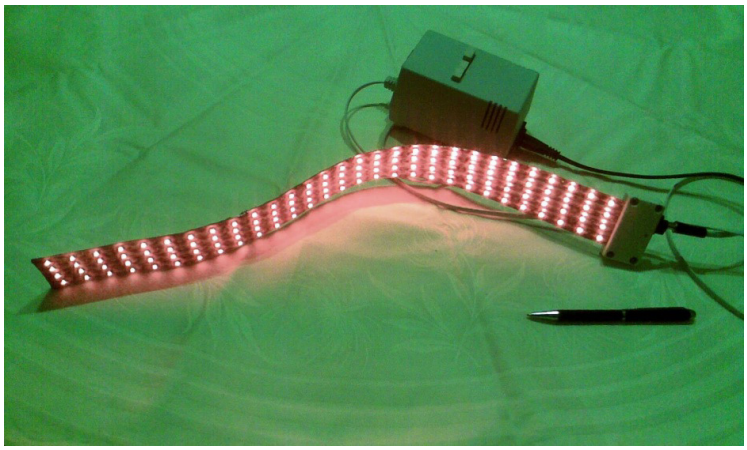

სურათი 8. “ფაზერი” მოქნილი გამომსხივებლით, დამწვრობისა და პლასტიკური ქირურგიის ცენტრისთვის.

წითელი გამოსხივების მაშუქი დიოდების ბაზაზე შექმნილია არაერთი ხელსაწყო, როგორც ჩვენთან, ასევე საზღვარგარეთ, რომელთა საშუალებით წარმატებით ტარდება სამკურნალო პროცედურები. საქართველოში, ი. ჯავახიშვილის სახ. თბილისის სახელმწიფო უნივერსიტეტის კვანტური ელექტრონიკის ლაბორატორიაში, ნახევარგამტარული მაშუქი დიოდების ბაზაზე შეიქმნა საცდელი ხელსაწყო “ფაზერი” (**სურათები 7** და **8**), რომელიც გამოიცადა ქ. თბილისის რამდენიმე კლინიკაში, ისეთებში, როგორიცაა ჯანმრთელობის სამინისტროს უროლოგიის ინსტიტუტი, დამწვრობის

სამეცნიერო-პრაქტიკული ცენტრი, თბილისის სამედიცინო აკადემიის ოტოლარინგოლოგიის კლინიკა, მეანობა-გინეკოლოგიის კათედრის ბაზა – ექსპერიმენტული სამშობიარო სახლი, შპს "ოქროს საწმისი – XXI საუკუნე" ჯანმრთელობის სახლი და სხვ.

გამოცდებმა აჩვენა მკურნალობის მაღალიეფექტიანობა, ამასთან, არავითარი უარყოფითი შედეგი არ გამოვლენილა. გამოცდების შედეგად განისაზღვრა პოლიქრომატული ფოტონების ნაკადის ეფექტურობა:

- სისხლის მიკროცირკულაციის მნიშვნელოვანი გაუმჯობესება
- ფერმენტების აქტივობის გაზრდა
- ბიოქიმიური რეაქციების დაჩქარება
- ანთების საწინააღმდეგო ეფექტი
- ტკივილგამაყუჩებელი ეფექტი
- იმუნური პროცესების კორექცია
- სისხლის შემადედებელი პროცესების კორექცია და სხვ.

მკურნალობის ეფექტიანობა მნიშვნელოვნად იზრდება ტრადიციული მედიკამენტოზური მკურნალობის ფონზე. მაღალთერაპიულ ეფექტს განაპირობებს სისხლის მნიშვნელოვანი გააქტიურება და ორგანიზმის იმუნური სისტემის ამაღლება სისხლისა და ორგანიზმის უჯრედების განსაზღვრული სიხშირის სინათლის სხივით დანათების დროს. ეს მნიშვნელოვნად აჩქარებს ადამიანის ორგანიზმში მიმდინარე ბიოქიმიურ რეაქციებს და ხელსუწყობს გამოჯანმრთელების პროცესის დაჩქარებას.

დადგენილია, რომ ორგანიზმზე განსაკუთრებული დადებითი თერაპიული ეფექტი აქვს მაღალი ინტენსივობის ხანმოკლე სინათლის იმპულსებს. საჭიროებამ მოითხოვა ისეთი ფოტონური გამომსხივებლების სერიის შექმნა და კლინიკური აპრობაცია, რომელიც ასხივებს პერიოდულ მაღალი სიმძლავრის მცირე ხანგრძლივობის იმპულსების სერიას 0.6 – 1 მკმ დიაპაზონში. ამჟამად შექმნილია "ფაზერის" სხვადასხვა ვარიანტი (კონტაქტური, დისტანციური, გამომსხივებელი ზედაპირის განსხვავებული გეომეტრიის), რომლებიც კლინიკების მოთხოვნის მიხედვით მორგებულია ცალკეული დაავადებისთვის.

ფოტონებით მკურნალობა მოიცავს დაავადებათა თითქმის მთელ სპექტრს, რომლებიც ლაზერული თერაპიის ჩვენებები, მათ შორის:

1. თერაპიაში:
- გულსისხლძარღვთა პათოლოგია (კორონაროგენული დაავადებები, ჰიპერტონული დაავადებები, ენდარტერიტი, ფლებიტი და სხვ.)
- გასტროენტეროლოგია (წყლულოვანი დაავადებები, პანკრეატიტი, ქოლეცისტიტი, ჰეპატიტი და სხვ.)
- პულმონოლოგია (პნევმონია, ბრონქიტი, ბრონქიალური ასთმა)
- რევმატიული დაავადებები
2. ქირურგიაში:
- თერმულ დაზიანებათა და აღდგენითი პლასტიკური ქირურგია
- ანთებითი და ჩირქოვანი გართულებების პროფილაქტიკა და თერაპია
- დამწვრობა, შეხორცების პროცესების დაჩქარება
3. ოტორინოლარინგოლოგიაში (ტონზილიტი, რინიტი, ჰაიმორიტი და სხვ.)
4. მეანობასა და გინეკოლოგიაში (ეროზიები, ანთებითი დაავადებები, ოპორტუნისტული ინფექციები, პათოლოგიური პრელიმინარული პერიოდი, ფიტოპლაცენტარული უკმარისობა და სხვ.)

სურათი 9. მკურნალობა სტაციონარში.

სურათი 10. ოპტიკური შხაპი, სადაც სინათლის ჭავლის ჰიდროდინამიკურ წნევასა და ტემპერატურასთან ერთად ადამიანზე მოქმედებს ოპტიკური გამოსხივებაც.

სურათი 11. მაწოვარა და საბავშვო ბოთლი, რომლებშიც ჩამონტაჟებულია ნათებადი დიოდი და გამოიყენება მწვავე ინფექციური ვირუსების სამკურნალოდ.

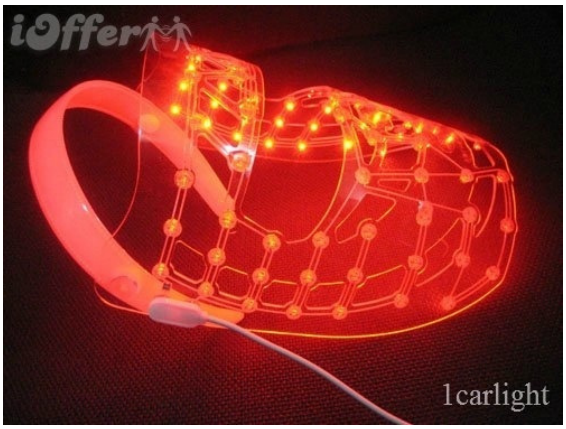

სურათი 12. ქოშები, წითელი ნათებით.
გამოიყენება სისხლძარღვების მკურნალობისთვის.

როგორც აღვნიშნეთ, შექმნილია ფოტონოთერაპიისთვის განკუთვნილი არაერთი ხელსაწყო. დღეისათვის არსებობს სხვადასხვა მოწყობილობა, რომლებიც საშუალებას იძლევა სტაციონარსა და საყოფაცხოვრებო პირობებში განვახორციელოთ ადამიანის ორგანიზმზე ჯანმრთელობისთვის სასარგებლო ფოტონური ზემოქმედებები. სურეთებზე 9 – 12 მოყვანილია ფოტონებით მკურნალობის ზოგი მაგალითი.

მითითებები

1. ნ. დოლიძე, ქ. კოტეტიშვილი, გ. ჩიხლაძე. მაიონიზებელი გამოსხივება მედიცინაში. ნაწ. I: დიაგნოსტიკა. 2012, თბილისი: ტექნიკური უნივერსიტეტი.
2. ნ. დოლიძე, ქ. კოტეტიშვილი, გ. ჩიხლაძე. მაიონიზებელი გამოსხივება მედიცინაში. ნაწ. II: მკურნალობა. 2012, თბილისი: ტექნიკურიუნივერსიტეტი.
3. Б. Лайнз. Лечение рака, которое работало – Раймонд Райф. http://m-l-m.info/?p=478
4. М. И. Джибладзе. Физические основы светотерапии. 2011, Тбилиси: Знание.
5. მ. ნ. დოლიძე, ნ. დ. დოლიძე, მ. ი. ჯიბლაძე. ფოტოთერაპიის ფიზიკური საფუძვლები. საერთაშორისო სამეცნიერო კონფერენციის “გამოყენებითი ფიზიკის აქტუალური საკითხები” მოხსენებათა კრებულში. 2011, თბილისი: ტექნიკური უნივერსიტეტი, 67-70.
6. G. Gverdtsiteli, Z. V. Jibuti, M. G. Pkhakadze. Photons and living cells. Bull. Georg. Acad. Sci.,1996, 153, 1, 99-101.
7. Z. V. Jibuti. Color therapy in modern medicine. In: Proc. Int. Sci. Conf. “Phys. Res. Meth. Med.”. 2011, Tbilisi: Technical Univ., 137- 139.

ФОРМИРОВАНИЕ И ИССЛЕДОВАНИЕ ТОНКИХ ОКСИДНЫХ ПЛЕНОК ДЛЯ НАНОЭЛЕКТРОНИКИ

А. П. Бибилашвили, З. В. Джибути, Н. Д. Долидзе, Г. А. Схиладзе

Институт микро- и наноэлектроники
Тбилисский государственный университет им. И. Джавахишвили
Тбилиси, Грузия
amiran.bibilashvili@tsu.ge

Принята 8 октября 2013 года

Введение

Развитие современной нанотехнологии, в основном, определяется постоянным совершенствованием методов изготовления полупроводниковых приборов и интегральных микросхем (ИМС) с целью уменьшения размеров составляющих их элементов. В этом направлении основным двигателем прогресса является создание новых материалов и тонких структур с уникальными свойствами, созданных по нанотехнологиям. При этом нанотехнологические приемы постоянно совершенствуются, появляются все новые и новые методы формирования наноматериалов.

Основным элементом большинства наноэлектронных приборов является диэлектрик, к которому предъявляются особые требования: он должен быть сверхтонким (5 – 80 нм), с большой диэлектрической проницаемостью при больших значениях напряжения кулонивской блокады (без уменьшения напряжения пробоя диэлектрика), однородным, сплошным, бездефектным, беспримесным для ограничения тунелирования, стабильным к внешним факторам [1]. В отличие от микроприборов, где толщины диэлектрических слоев гораздо больше (> 150 нм) и требования не такие жесткие, для формирования диэлектрических слоев наноприборов стандартная высокотемпературная (1400 K) технология непригодна – при высоких температурах в сверхтонких слоях происходит диффузия нежелательных примесей, увеличение пористости, ухудшение адгезии с подложкой, возникновение термодефектов и т.д. Поэтому, вышеперечисленные требования к тонким диэлектрикам не выполняются. Отсюда, стало необходимостью поиск, не только типа приемлемых диэлектриков, но и путей уменьшения температуры их получения.

Ряд методов формирования тонких оксидных пленок, первоначально разработанных для технологии микроэлектроники, нашли широкое применение при создании наноэлектронных приборов и ИМС на их основе. Таким методом является и рассматриваемый ниже технологический метод формирования тонких оксидных пленок металлов и полупроводников низкотемпературным каталитическим плазменным анодированием. Этот метод удачно был применен для формирования микроэлектронных металл–оксид–полупроводник (МОП) структур и элементов ИМС на их основе [2].

Целью данной работы является формирование тонких оксидных пленок металлов и полупроводников низкотемпературным каталитическим плазменным анодированием для наноэлектроники и исследование их свойств, а также выяснение механизма каталитического плазменного анодирования.

Методика эксперимента

На сегодняшний день, в наноприборах основным материалом подложки все еще остается Si и сформированная на нем МОП-структура. Одним из путей уменьшения температуры формирования тонких оксидов является процесс анодирования. Основное преимущество данного метода, по сравнению с традиционным, заключается в возможности проведения процесса оксидирования при комнатной температуре. При этом метод отличается большой локализованностью. Низкотемпературные процессы анодирования проводятся, как электрохимическим (в растворе), так и плазменным (в вакууме) методами.

Метод плазменного анодирования сухой, хорошо согласуется с другими технологическими процессами создания наноприборов. Оксидные пленки, полученные плазменным анодированием, не содержат примесей, ни в объеме, ни на поверхности (в отличие от электрохимического анодирования). Метод позволяет непосредственно перед началом процесса анодирования, с помощью ионной бомбардировкив вакууме, на месте очистить поверхность оксидируемого материала от “естественного” окисла. Однако, метод не получил широкого применения из-за малой эффективности процесса и повреждения поверхности окисляемого материала, вызванного бомбардировкой ионами плазмы [3].

Разработанный нами усовершенствованный метод – каталитическое плазменное анодирование (КПА) исключает все вышеперечисленные недостатки. Суть метода в том, что на поверхности окисляемого материала в вакууме, перед окислением, напыляется тонкий слой редкоземельного элемента (РЗЭ). В процессе плазменного анодирования такой структуры, быстро окисляется тонкий слой РЗЭ и находящиеся под ним окисляемый материал [2, 4]. В это время на порядок увеличивается скорость окисления и почти на два порядка увеличивается эффективность процесса, улучшаются электрофизические свойства структуры. После окончания процесса, без повреждения поверхности оксида, химически снимается РЗЭ. Поверхность оксида получается идеально чистой, поскольку находящиеся на поверхности РЗЭ защищает оксид от бомбардировки ионами плазмы в процессе окисления.

Экспериментальные результаты и их обсуждение

Указанный метод был применен для получения высококачественных тонких оксидных слоев (собственный окисел SiO_2, TiO_2,, Ta_2O_5 и Al_2O_3) на Si. Пластины Si n-типа, с удельным сопротивлением 4.5 и 0.3 Ом · см, имели поверхностную ориентацию (100).

Для полученния оксидной пленки (ОП) TiO_2, Ta_2O_5 и Al_2O_3 на кремниевые подложки предворительно напылялся слой металлов Ti, Ta или Al, соответственно. Тугоплавкие металлы напылялись методом реактивного магнитронного распыления, а Al-резистивным испарением в вакууме при давлении ~ $1.3 \cdot 10^{-4}$ Па и температурах ~ 423 K. Напыление тонкого сплошного слоя катализатора иттрия (Y) проводилось методом

электронно-лучевого испарения в вакууме при давлении ~ $1.3 \cdot 10^{-4}$ Па и температуре ~ 373 K. Перед напылением металлов Ti, Ta, Al и Y поверхности подложек кремния обрабатывались химическим способом по общеизвестной технологии.

Процессы плазменного анодирования структур РЗЭ–окисляемый материал (ОМ), осуществлялись на вакуумной установке трехэлектродного типа с генерируемой кислородосодержащей плазмой постоянного тока (**рисунок 1**). Процессы анодирования проводились в гальваностатическом (ГСТ) режиме. В этом случае увеличение падения напряжения на формируемой ОП указывает на приращение ее толщины.

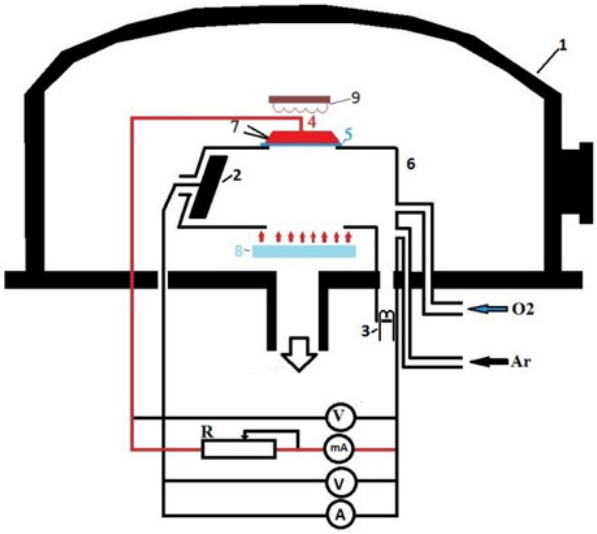

Рисунок 1. Схема установки плазменного анодирования: 1 – колпак, 2 – анод, 3 – катод, 4 – контакт мишени, 5 – образец, 6 – удерживатель плазмы, 7 – вывод термопары, 8 – источник ультрафиолетового облучения, 9 – нагреватель образца.

Для усовершествования структуры полученных оксидов на части образцов проводился термический отжиг в атмосфере азота при температуре 773 K в течение 15 мин, а на другой части – импульсный фотонный отжиг (ИФО), где источниками фотонов служили 19 гологенных ламп мощностью 1000 Вт каждый. Режимы ИФО: 1 – 3 импульса длительностью 1 с со скважностью 1 с.

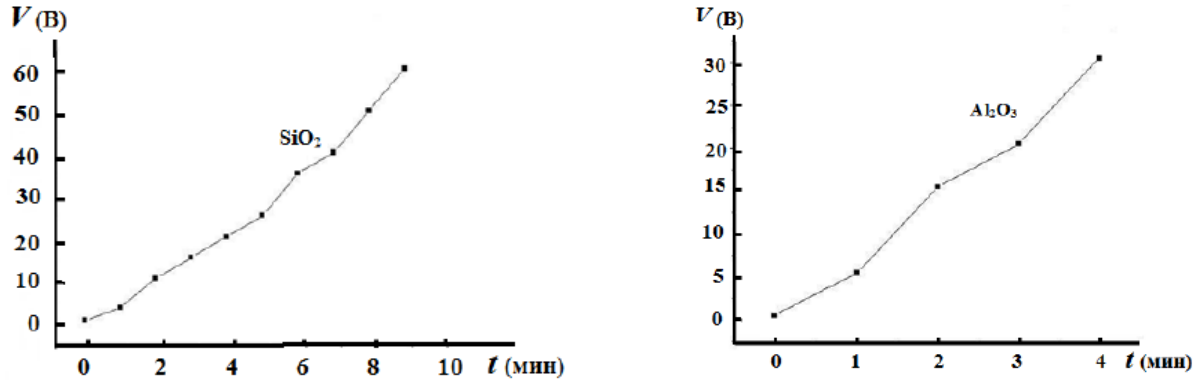

Рисунок 2. Изменения напряжения формовки оксидов SiO_2 и Al_2O_3 от времени КПА при I_f = 0.5 мА / см^2 и T = 473 K.

На **рисунках 2** и **3** приведены экспериментальные зависимости изменения напряжения формовки оксидов от времени КПА при разных токах формовки (I_f) и

температурах (T). Везде давление в вакуумной камере $P = 2.7$ Па и отношение концентрации газов кислорода и аргона 3 : 1. Следует отметить, что в этих условиях без применения катализатора оксиды не формируются.

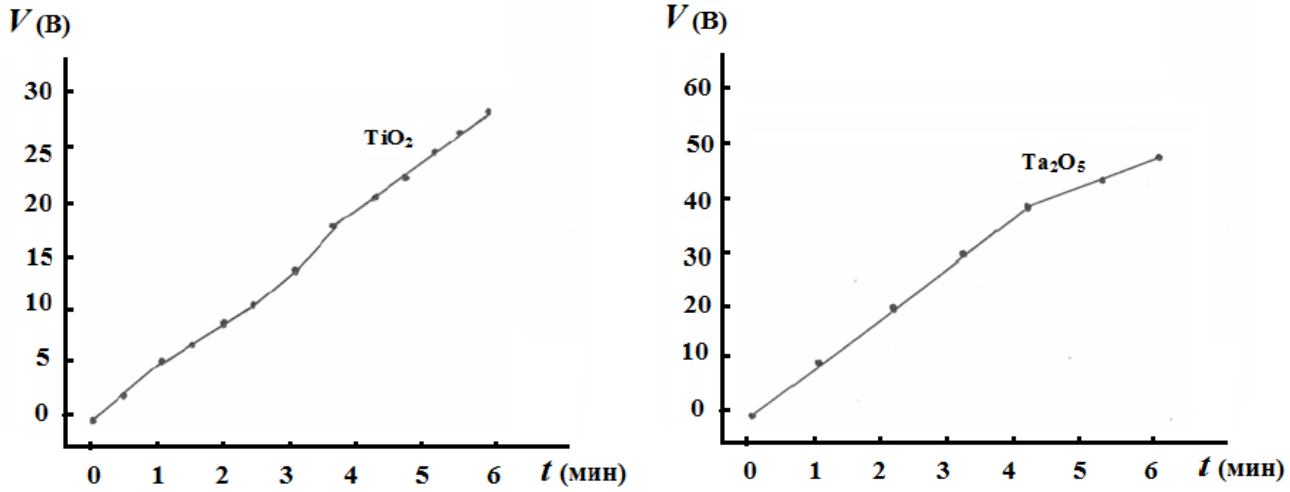

Рисунок 3. Изменения напряжения формовки оксидов TiO_2 и Ta_2O_5 от времени КПА при $I_f = 1.0$ мА / см^2 и $T = 673$ К.

Как показывают рисунки, эти зависимости квазилинейны и из них можно определить скорости роста полученных оксидов.

Для определения заряда в оксиде и плотностей поверхностных состояный на границе раздела кремный-оксид снимались ВЧ вольт–фарадные характерастики. Как пример, на **рисунке 4** приведены эти характерастики для структур Si–SiO_2–Al и Si–Al_2O_3–Al.

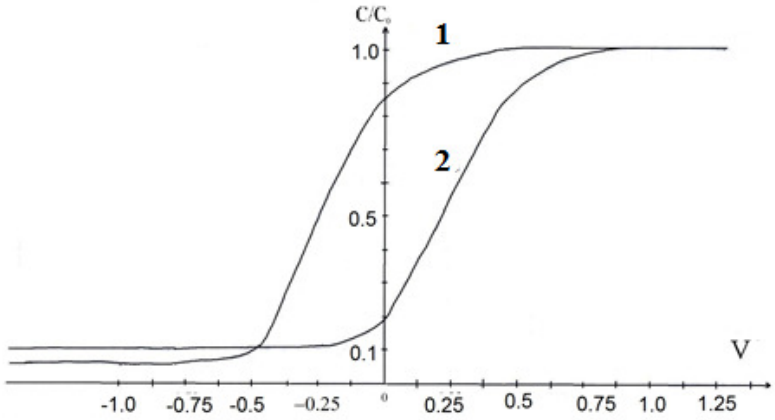

Рисунок 4. Нормированные вольт–фарадные характерастики МОП структур на основе SiO_2 (1) и Al_2O_3 (2).

У всех оксидов, за исключнием Al_2O_3, наблюдается накопление в объеме положительного заряда, а у Al_2O_3 – отрицательное (**рисунок 4**, кривая 2).

Шероховатость поверхности полученных оксидов измерялись на установке ALPHASTEP–200 PROFILOMETER, где игла, диаметром 12 мкм и весом на нее 8 мг, сканировалась по поверхности ОП. Результаты измерения приведены на **рисунках 5** и **6**. Как видно расстояние от верхней точки вершины поверхности до нижней точки глубины

(R_a) составляет для Si – 20, SiO_2 – 12, Al_2O_3 – 19 и TiO_2 – 9 Å. Видно, что после оксидирования кремния ее поверхность становится более гладкой, а вид поверхности остальных оксидов зависит от материла металла и процесса их осаждения.

Измерения толщин ОП проводились на установках NANOSPEC 180, оптических микроскопах фирмы Leitz и ЛЭМ–2 именялись в пределах 35 – 85 нм.

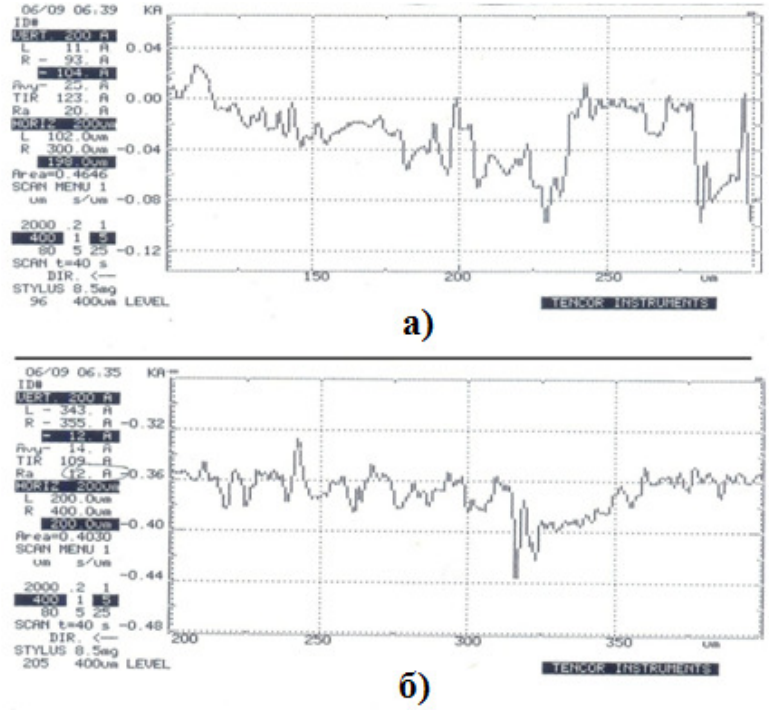

Рисунок 5. Профилограмы Si (а) и SiO_2 (б).

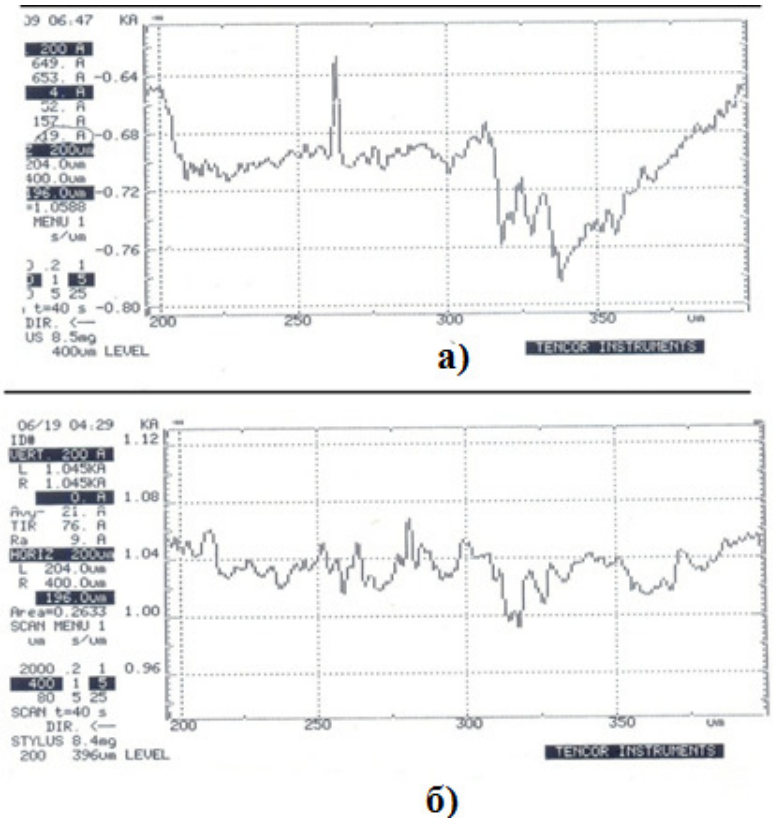

Рисунок 6. Профилограмы Al_2O_3 (а) и TiO_2 (б).

Рентгеноструктурный анализ полученных оксидов проводился на дифрактометре ДРОН–4, где источником рентгеновского излучения использовался Co (напряжение 21 кВ, ток 12 мА). Результаты измерения приведены на **рисунках 7** и **8**. Измерения показали, что все полученные ОП имеют аморфную структуру.

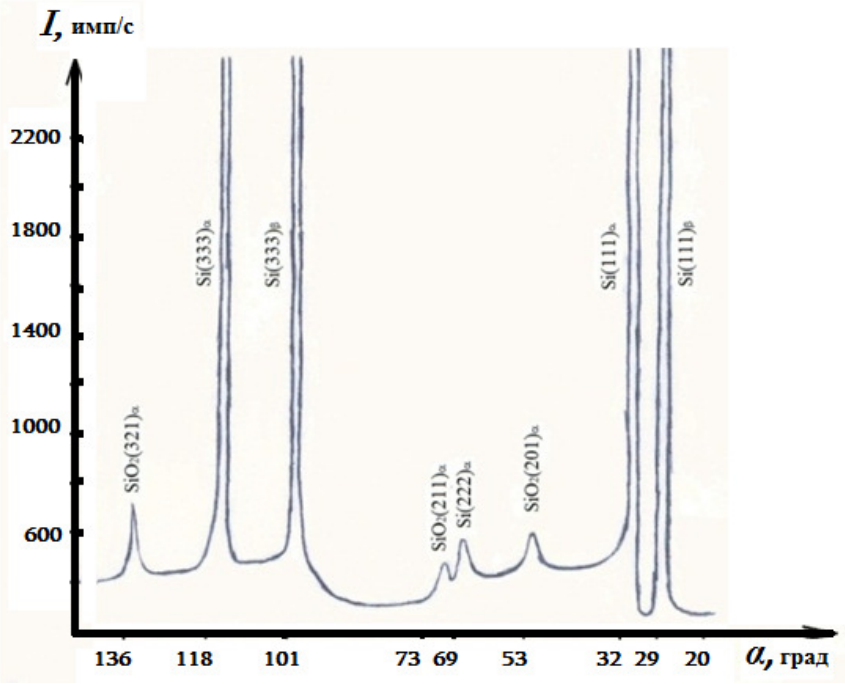

Рисунок 7. Рентгенодифракционные пики на структуре Si + SiO_2.

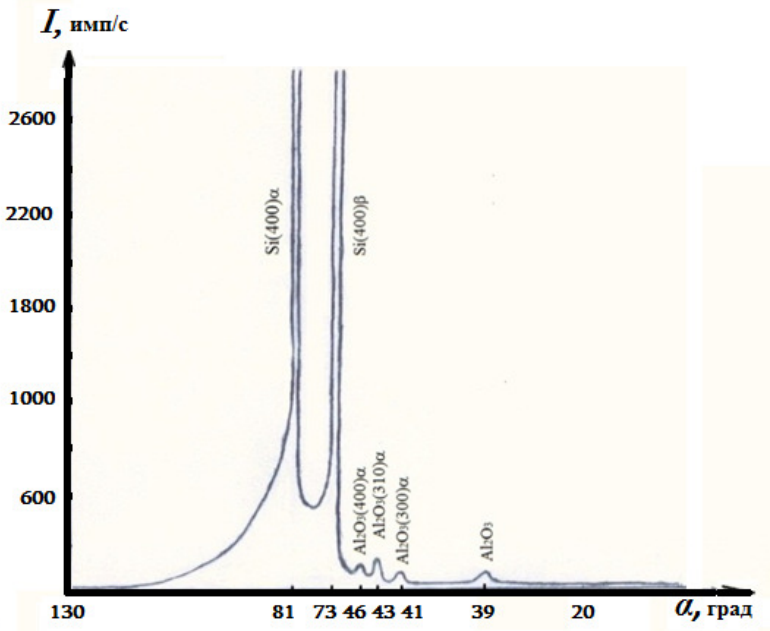

Рисунок 8. Рентгенодифракционные пики на структуре Si + Al + Al_2O_3.

Основные электрофизические и диэлектрические параметры полученных каталитических плазменных ОП на Si приведены в **Таблице 1**.

Таблица 1.

№	Параметры	SiO_2	Al_2O_3	TiO_2	Ta_2O_5
1	Толщина *d*, нм	35–75	40–85	35–80	35–70
2	Скорость роста оксидов, В / мин	5.8	6.7	5.2	10.0
3	Заряд в окисле Q_{ss}, $см^{-2}$	3E11	–2E11	2E11	3E11
4	Плотность поверхностных состояний *Nss*, $см^2 \cdot эВ^{-1}$	2E11	8E10	4E10	2.5E11
5	Шероховатость R_a, Å	12	19	9	15
6	Диэлектрическая постояннная ε	4.5	6.0	23.0	16.8
7	Напряжение пробоя $E_{пр}$, В / см	4E6	6E6	5E6	7E6

Механизм процесса

При создании механизма каталитического плазменного анодирования надо учитывать ту особенность, которую вносит сам катализатор. Она, в основном, заключается в том, что РЗЭ (Y) имеют незаполненные *d*- или *f*-орбитали [5] и их электроотрицательности (ЭО) меньше, чем ЭО анодируемых материалов (АМ) [6].

В начале процесса первичная окисная пленка иттрия образуется быстро за счет хемодсорбции кислорода на его поверхности, так как у него высокая адсорбционная способность [7]. Дальнейшее увеличение толщины оксида Y происходит путем диффузии и дрейфа иона кислорода сквозь окисную пленку. Этот процесс тоже проходит быстро, так как коэффициент диффузии иона кислорода в Y_2O_3 очень высок [5]. При приложении внешнего положительного поля в Y_2O_3 входят и электроны. Эти инжектированные электроны, с одной стороны, являются антисвязывающими и ослабевают химическую связь между Y и кислородом, облегчающей отрыв связьей Y–O, а с другой стороны, они попадают в незаполненную зону *d*-орбиталей, где эффективная масса электронов больше и, соответственно, их подвижность меньше [8]. Следовательно, большинство инжектированных электронов задерживаются в катализаторе и они почти не участвуют в электропроводности. Поэтому под катализатором ток формовки для анодируемого материала состоит в основном из ионной составляющей.

Рисунок 9. Энергия активации реагирующей системы кислород – анодируемый материал с использованием Y (1) и без него (2).

Поскольку ЭО анодируемого материала и кислорода больше ЭО иттрия, атомы кислорода перетягиваются из Y_2O_3 в анодируемый материал, что стимулируется приложенным положительным внешним полем и отрицательным эффективным зарядом кислорода. Вакансии кислорода на поверхности катализатора легко заполняются кислородом из плазмы. Известно [9], что в присутствии катализатора возникают промежуточные комплексы с меньшей энергией активации, чем образуемые без катализатора, в нашем случае Y–O, что вызывает изменение формы (уменьшение) потенциального барьера (**рисунок 9**).

Таким образом, Y окисляется очень быстро, удерживает в себе электроны, передает кислород АМ и сам снова его легко берет из плазмы – является эффективным поставщиком ионов кислорода для АМ – т.е. катализатором в формировании оксидов металлов и полупроводников.

Выводы

Проведенные исследования позволяют сделать следующие заключения:

1. Разработан метод низкотемпературного каталитичекого анодирования с применением иттрия для получения окидов металлов и полупроводников;
2. Разработан механизм процесса низкотемпературного каталитичекого анодирования, который основан на свойства незаполненных внутренных орбит и низкой электроотрицательности катализатора и на переходы электронов из связывающей зоны в антисвязывающую зону;
3. Как показали измерения параметров, полученные пленки высокого качества;
4. Показано, что разработанная технология и полученные этой технологией оксидные пленки могут быть использованы в наноэлектронной технологии.

Ссылки

1. В. Е. Борисенко, А. И. Воробьева, Е. А. Уткина. Наноэлектроника – теория и практика. 2013, Москва: БИНОМ.
2. А. П. Бибилашвили. Физ. и хим. обр. матер. 5 (2001) 40.
3. В. П. Пархутик, В. А. Лабунов. Плазменное анодирование (физика, техника, применение в микроелектронике). 1990, Минск: Навука і Тэхніка.
4. А. П. Бибилашвили, А. Б. Герасимов, Г. Б. Чахунашвили. Способ получения диэлектрических покрытий. Авт. свид. № 551972HO1L21, 29.11.1976.
5. К. Тейлор, Н. Дарби. Физика редкоземельных соединении. 1978, Москва: Мир.
6. Л. Полинг, П. Полинг. Химия. 1978, Москва: Мир.
7. В. М. Фистуль. Физика и химия твердого тела, Том 2. 1995, Москва: Металлургия.
8. А. Н. Кочарян, Д. И. Хомский. Журн. ВХО им. Д. И. Менделеева 26 (1981) 39.
9. О. С. Зайцев. Состояние веществ и химические реакции. 1990, Москва: Химия.

NEW ROTATION-CORROSION DISPERGATION METHOD FOR OBTAINING OF IRON-OXYGEN NANOPARTICLES

O. M. Lavrynenko, V. I. Kovalchuk, S. V. Netreba, Z. R. Ulberg

F. D. Ovcharenko Institute of Bio-Colloid Chemistry
NAS of Ukraine
Kyiv, Ukraine
alena-lavry@yandex.ru

Accepted October 9, 2013

Introduction

Among the first problems that classical colloid chemistry solves conditions of the formation and properties of the disperse particles, structuring and properties of the disperse systems stand out [1]. Colloid chemistry of disperse minerals chooses among various objects of colloid chemistry investigation. It combines the studies of separate mineral properties and the main problems of disperse state. So, the formation, destruction and the properties of disperse systems play a determinative role in the genesis of rocks and soils, in the development of living organisms, in technological processes and in different branches of productive industry [1]. The basis of colloid mineralogy was formed in the monograph [2], where the most important colloid-chemical processes in the Earth's crust were shown and where the general information about colloidal mineralogy and the characteristic of the primary colloidal and metal-colloidal minerals, in particular the iron oxide group, were laid out. The following development of that science direction was orientated on the studying of disperse iron–oxygen minerals and their phase transformation under hypergenesis condition [3].

Rapid development of the modern science and the barest necessity in materials with nanosized structural units led to appearance of new investigation methods and evolution of disperse system technologies [4, 5]. It helped to generalize and rethink the progress of colloid chemistry and physics of colloid systems [6], it gave the powerful impulse to disperse mineral studying and founded the basis for a new section of science – nanomineralogy [7]. Among the monographs devoted to the study of natural disperse iron–oxygen minerals; their synthesis under the laboratory conditions as well as their structure, physicochemical and colloid-chemical properties, the most determinative place belongs to the works [8, 9]. Numerous publications are devoted to obtaining nanosized iron–oxygen species and studying their structure and properties, for example [10, 11]. The practical usage of disperse iron–oxygen particles is closely connected with medical-biological investigations, therefore the studying of biological activity and interaction of such species with biological objects and systems are directed on the creation of new kind of functional materials used in diagnostics and therapy of different diseases and pathological states [12 – 15].

The search of a new way for the obtaining of material with nanometer particles size and unique physicochemical and colloid-chemical properties attracts attention of scientists to

formation of synthetic analogs of the disperse iron containing minerals. Due to high sorption, catalytic, biochemical and biological activity of iron–oxide and iron–hydroxide minerals obtained in the laboratory they can be effective raw materials for creating new products of the medical-biological precipitation [13]. The practical value such particles raise due to the presence of magnetic properties, for example, by vector drug delivery in the magnetic field, by creating hyperthermia areas, diagnostics and therapy of different diseases etc. [12].

Among disperse minerals that correspond to such condition the particular attention belongs to nanosized natural minerals – ferrihydrite [16, 17] and Fe(II)–Fe(III) layered double hydroxides (LDH) that can be precursors for purposeful formation of the numerous disperse iron–oxygen particles, especially iron oxides and oxyhydroxides, spinel ferrites and core & shell composites formed on their basis.

The principle of rotation-corrosion dispergation method (the RCD method) is based on the obtaining of iron–oxygen nanoparticles during iron (steel) electrode corrosion when it contacts with air and water dispersion medium. The metered oxygen delivery and the agglomeration of ferrous iron on the steel – dispersion medium – air interface and permanent change of the physicochemical condition when the iron–oxygen seed structures are formed take place due to creating of interrupted contact of the steel surface with air and water solution. Variable particles contact with thin film saturated by hydroxyl, ferrous iron and other disperse medium species and provide for controlled component delivery into the reaction area and create the specific condition for heterogeneous growth of the Green Rust seed particles and the products of it phase transformation, namely iron oxides and oxyhydroxides. Such condition helps to form mineral particle layers on the electrode surface and in the near electrode layer (the NEL) as well as on the interface water medium – air and the iron–oxygen phase repeatability in every specie layer.

Realization of the rotation-corrosion dispergation method provides for the entrance of iron–oxygen nanoparticles from the reaction area into dispersion medium and their phase transformation in other mineral particles and their agglomeration in the form of weak concentrated sol. The particle size and phase composition of iron–oxygen minerals have a clear dependence on the time of their formation. It allows obtaining the polymorph particles of nanometer size as well as their micrometer analogs.

The main parameters that influence the process of particle formation, their structure and properties are chemical composition and pH value of disperse medium, the oxidant condition and temperature. As an additional factor different surface-active reagents can be named. When such species are added into the system the sedimentative and aggregative stability of sols will be grown. Moreover, the process of the disperse iron–oxygen mineral formation could be changed to the direction of the formation of a particular mineral or stopped on any stage of phase formation.

The characteristic of the corrosion process when the rotation-corrosion dispergation method of the nanoparticle formation is applied

At first look the process of the primary crystals (the seed structures) formation in the systems based on the iron (steel) contacting with water dispersion medium and air oxygen is determined by simple electrochemical reactions on the metal surface. To make an electrode we used steel 3 (St 3) and ultra-pure iron $^{57}Fe^{0}$.

Steel 3 belongs to iron–carbon alloys and it contains apart from iron other chemical components, namely, %: C 0.14 – 0.22, Si 0.05 – 0.15, Mn 0.40 – 0.65; Cr 0.30, Ni 0.30, P 0.04, S 0.05, N 0.01 [18]. The phases of iron, spinel ferrites, in particular magnetite $FeFe_2O_4$; graphite C; iron carbide or cementite $(Fe,Ni,Co)_3C$ and other species are present in the steel structure. As a result the numerous galvanic couples are formed in the steel, for example spinel ferrite – graphite, spinel ferrite – cementite. At the same time the steel surface could be perceived as a heterogeneous system with local anodic and cathodes areas [19].

The influence of chemical additive agents on the process of anodic steel dissolution is shown in the special literature source such as [20]. We did not determine any significant influence of trace contaminants on the phase composition of disperse iron–oxygen minerals. According to XRD-data in the phase composition other minerals except the iron oxides and hydroxides are absent. Only ferrous and ferric iron are found in the disperse medium when the process of phase formation was finished [21].

We think that when iron and manganese are dissolved from the steel surface the latter is enriched by mineral phases that contain chromium, nickel, phosphorus, sulfur and other. The complex investigation of the sediments removed from the steel surface after chemical and mechanical treatment showed the presence of insoluble basic ferric salts according to XRD-data and 100 % content of iron according to X-ray fluorescence spectroscopy. So, it is possible to admit that the trace contaminants from steel 3 do not influence chemical and phase composition of iron–oxygen minerals formed in the systems based on the iron (steel).

Another electrode used for the modeling process of phase formation was made from ultra-pure iron ^{57}Fe. An iron foil was enriched by ^{57}Fe to 96 %. The electrode surface is characterized by the considerable reduction of cathode areas in comparison with the steel 3 surface. It leads to cathodes polarization of electrochemical (corrosion) process [22]. In spite of the fact that the phase composition in both cases was similar and the iron-oxygen minerals such as ferrous hydroxide (amakinite) $Fe(OH)_2$ → ferroxyhyte δ-FeOOH or lepidocrocite γ-FeOOH → magnetite $FeFe_2O_4$ were being identified on the ^{57}Fe electrode surface during six months.

When additional cathodes components were present in the system the reaction area enriched by hydroxyl and the phases such as lepidocrocite γ-FeOOH and maghemite γ-Fe_2O_3 were formed mainly on the steel surface [23].

In general the electrochemical process includes the spatial separated half reactions of iron ionization in the anodic sections with supply of ferrous iron into the system and oxygen depolarization on cathodes sections [24] according to the reaction:

$$Fe^0 + O_2 + 2H_2O + 2e^- = Fe^{2+} + 4OH^-. \quad (1)$$

While the anodes process controls the quantity of the reactionary-capable iron that got to the system, the cathodes process changes pH value on the steel (iron) surface and in the reaction area. The pH value of dispersion medium is determined by the cathode process [25], that is accompanied by the proton binding in the water molecules at initial pH value 2.0 – 6.0:

$$O_2 + 4H^+ + 4e^- = 2H_2O, \quad (2)$$

or it leads to entrance of hydroxyl into the system at initial pH value 6.0 – 10.0:

$$O_2 + 2H_2O + 4e^- = 4OH^-. \quad (3)$$

Such flexibility of the chemistry of the cathode process leads to the spontaneous change of the pH value to neutral in the water layer near the electrode surface. The specific chemical condition provided by anode and cathode processes and species microcirculation between anode and cathode sections [26] we determine as a reaction area (**Figure 1**). The reaction area

width was determined on the assumption that the structure element size on the steel surface was ~ 10^{-6} m and the typical diffusion constant for oxygen was $2 \cdot 10^{-9}$ m^2 / s. The typical time t of the rearrangement of the electrode process products between structural elements (grains) makes up:

$$t = \frac{d^2}{D} = \frac{(10^{-6} m)^2}{2 \cdot 10^{-9} m^2 / s} = 0.5 \cdot 10^{-3} s .$$

So, during one disk electrode rotation the products of the electrode process diffuse on the distance that is much bigger than the grain size.

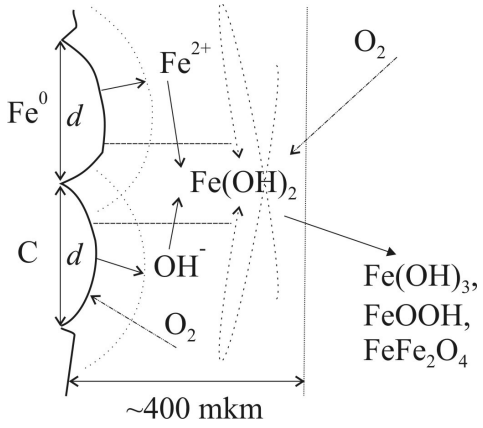

Figure 1. The schematic image of the reaction area, where d Is the grain size of the structural elements on the steel surface.

The velocity of the disk electrode rotation is 2 rpm. In such condition the time t_1 of the electrode contact with air or dispersion medium is on average 60 s. The layer thickness where the products of electrode process are distributed during determined time is ~ 400 μm:

$$\delta = \sqrt{\pi D t_1} = \sqrt{3 \cdot 10^{-9} m^2 / s \cdot 60 s} = \sqrt{18 \cdot 10^{-8} m} = 4 \cdot 10^{-4} m \approx 400 \mu m .$$

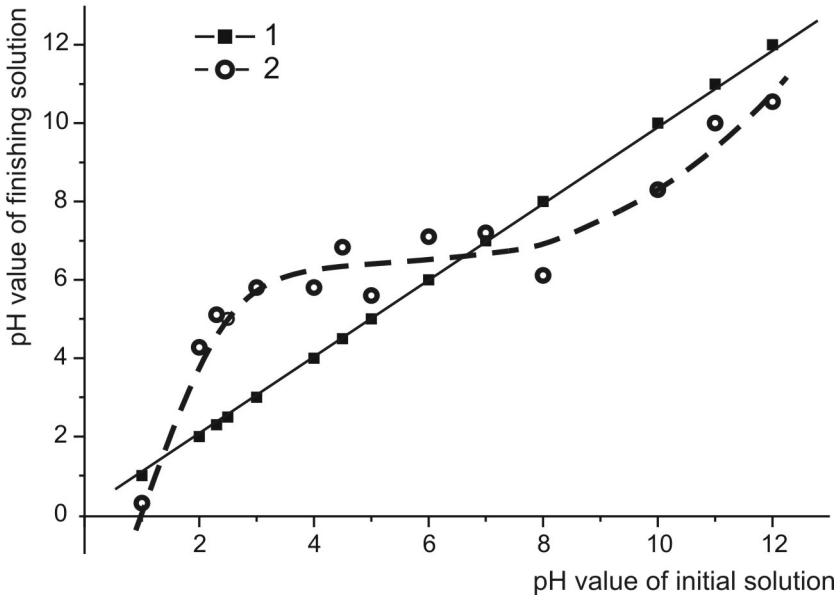

Figure 2. The changes of the pH value in the reaction area during the contact of the steel surface with water dispersion medium. The numbers correspond to: 1 – pH value of the initial solution; 2 – pH value of the solution after finishing the process of phase formation [27].

According to our investigation [23] the pH value after finishing of the phase formation process at the wide range of the initial pH values (from 2.5 to 11.5) is on average 7.0 – 9.0 in the narrow water layer on the steel surface and in the reaction area (**Figure 2**). Such pH values were confirmed by an indicator test (nitrasin yellow and phenolic red) when the rotated disk electrode contacted with air [28].

The narrow range of the pH value in the reaction area leads to limit of ferric and ferrous aquahydroxoforms that are capable to take part in the process of iron–oxygen disperse mineral formation. So, in the reaction area a few ferrous and ferric iron forms could be present, namely $Fe(OH)_3$, Fe^{2+}, $FeOH^+$ and $Fe(OH)_2$. Hydroxyl or protons presented in the reaction area act as other active components in the process of phase formation. Oxygen and carbon–oxygen species get in the system from air and they interact with steel surface by adsorption [29, 30]. It is possible only in the open-air system.

Under the mentioned conditions the carbon-oxygen species could be present in the form of CO_2, H_2CO_3, HCO_3^-, CO_3^{2-}, or they are able to form the soluble complexes, for example $FeHCO_3^+$, $Fe(HCO_3)_2$, $Fe(CO_3)_2^{2-}$ [31]. The other oxygen source is the water molecules that interact with the steel surface or the mineral phases localized on the steel surface.

The compromise potential of the steel electrode is positioned in the range from – 0.6 to – 0.3 V. Such condition is suitable for formation of iron–oxygen seed particles, especially Green Rust, on the steel surface [32].

The main processes and principles of the iron–oxygen particle formation when the rotation-corrosion dispergation method is applied

The purposeful iron–oxygen particles formation by the rotation-corrosion dispergation method requires solving a few problems, namely:

– the control of the particle formation by the regulation of pH value: $a < \text{pH} < b$; oxygen concentration C_{O2}: $c < C_{O2} < d$; the concentration of other components in the reaction area C_i; temperature in the reaction area;

– the choice of the equipment type and the velocity of the disk electrode rotation;

– the determination of the component ingress mechanisms in the reaction area including diffusion and convection (Figure 3) that are provided with the electrode rotation;

– the determination of the colloid-chemical mechanism of the particle formation on the steel surface, in the near electrode layer of the water solution and in the disperse medium;

– the definition of the probability of particle flushing from the surface due to the electrode rotation.

The estimate of the liquid layer thickness remaining on the disk electrode surface when it rotates was carried out according to the equation [33, 34]:

$$h_0 = \frac{k(\mu\nu)^{2/3}}{(\rho g)^{1/2}\sigma^{1/6}} \approx 3.5 \cdot 10^{-5} m = 35 \mu m ,$$

where $\rho = 10^3$ kg / m^3, $g = 10$ N / kg, $\sigma = 0.04$ N / m, $\mu = 10^{-3}$ Pa · s, $V = 0.1$ m / s, $k = 0.94$. Depending on the rotation velocity of the interface water / solution the k-value can be changed from 0.94 to 1.88. So, the film thickness averages to 35 – 70 μm.

Figure 4 shows the stationary film profile including the thicknesses of the surface structures δ_1, the liquid layer δ_2 and the near surface layer δ_3. We will calculate the time of the oxygen transfer through them.

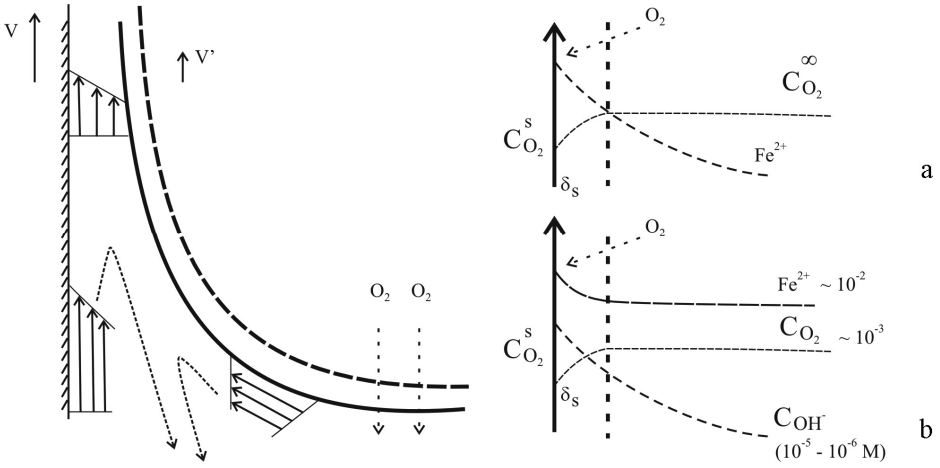

Figure 3. The convection scheme rotating electrode when the variable surface contact with air oxygen and water medium is made. The components receive profiles in the system: a – distilled water, b – ferrous iron solution.

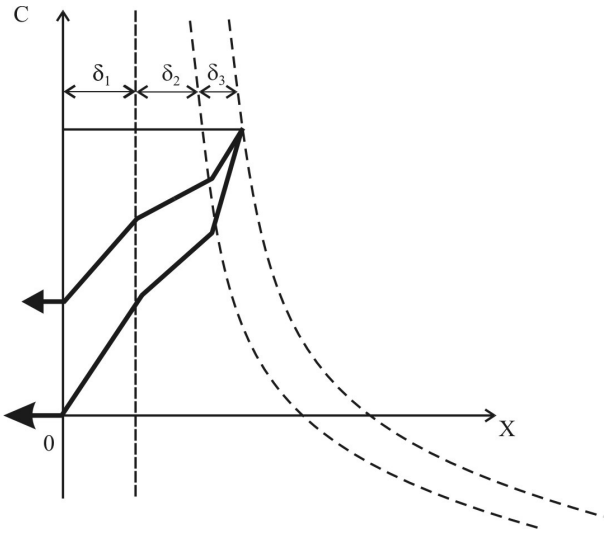

Figure 4. The stationary diffusion oxygen profile when the particles are formed by applying the rotation-corrosion dispergation method.

Time of the oxygen passing through the solution layer is calculated according to the equation:

$$t_2 \approx \frac{\delta_2^2}{D} = \frac{(50 \cdot 10^{-6} m)^2}{2 \cdot 10^{-9} m^2 / s} = \frac{12{,}5 \cdot 10^{-10}}{10^{-9}} s = 1.25 s,$$

where D – the oxygen diffusion coefficient averages to ~ $2 \cdot 10^{-9}$ m² / s, δ_2 the thickness of the liquid layer is ~ $50 \cdot 10^{-6}$ m = 50 μm.

Probably, $D_1 < D_2$ and their ratio can be about 0.1, at the same time $(\delta_1 / \delta_2)^2 \approx 10^{-4}$. So, the diffusion time through liquid layer significantly exceeds the time of diffusion through the surface structure layer.

We think that $D_3 < D_2$ and $\delta_3 \geq \delta_2$. According to our experimental result the thickness of the near electrode layer is $\delta_3 \cong 0.5$ mm = $5 \cdot 10^{-4}$ m. The smaller diffusion coefficient (10^{-9} m² / s) was chosen for calculation of diffusion velocity through the porous structure of the near surface layer.

$$t_3 > \frac{(5\cdot 10^{-4} m)^2}{2\cdot 10^{-9} m^2/s} = 1.25\cdot 10^2 s = 150s \approx 2\,\text{min}\,.$$

The velocity of the electrode rotation is 2 rpm, and during one rotation it contacts with air for 1 min. So, oxygen does not have time for penetration into whole thickness of the near surface layer. Probably that is the cause for the two mineral layer formations.

During the contact of the disk electrode with air the diffusion front makes the progress to increase the near surface layer due to the concentration of the reaction products and it is changed on the inner side of the film. During another half-turn the near surface layer localized on the liquid surface is enriched by oxygen. Consequently the near surface layer (film) periodically becomes saturated by the products of the electrode process or oxygen. In exactly the same way the oxygen concentration in the liquid layer on the electrode surface is changed. These processes influence the localization of the iron–oxygen phase formation, the velocity of the separate reactions and the particle size of the individual disperse mineral formed in the system.

The localization of the iron–oxygen mineral particle formation in rotation-corrosion dispergation process

Air oxygen plays the oxidant role in the rotation-corrosion dispergation process and it influences the structure and properties of iron–oxygen particles.

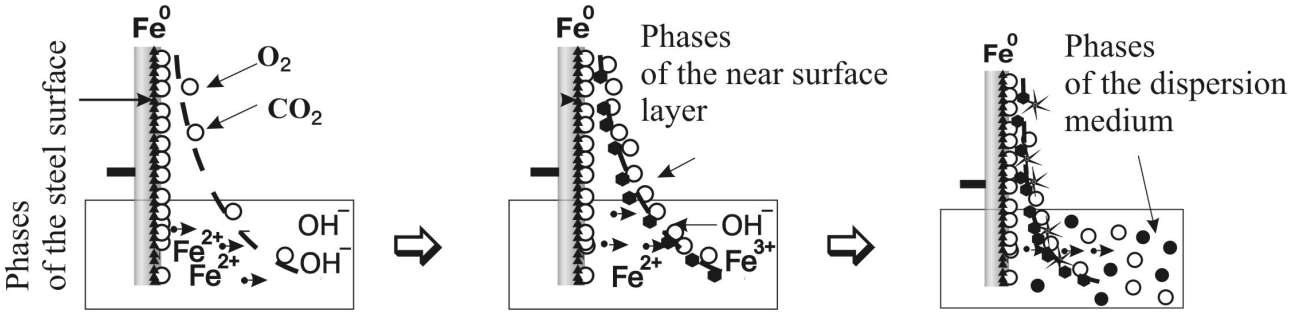

Figure 5. The localization of the phase formation process in the system $Fe^0 – H_2O – O_2$ [35].

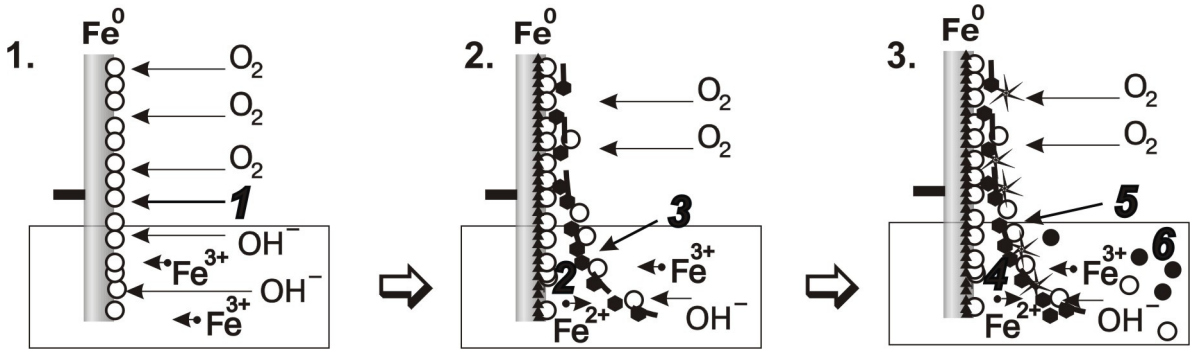

Figure 6. The physical-chemical conditions of the iron–oxygen mineral phase formation in the system $Fe^0 – H_2O – O_2$: 1 – on the surface; 2 – on the surface under the monolayer of the near surface film; 3 – in the monolayer of the near surface film; 4 – on the surface and on the inner side of the near surface film; 5 – on the outer side of the near surface film; 6 – in dispersion medium [36].

The peculiarity of the oxidizing condition that is typical for the $Fe^0 – H_2O – O_2$ system gave us the reason firstly to determine three local areas of the phase formation, exactly the steel surface, the near surface film and dispersion medium (**Figure 5**) [35], and later such distribution was expanded to six characterized conditions of the seed structure formation, mineral phase formation and their transformation (**Figure 6**) [36]. So different conditions were marked out: 1) directly on the steel surface when the near surface film was not formed; 2) on the steel surface after the monolayer of a near surface film was formed 3) in the monolayer of a near surface film; 4) on the steel surface and on the inner side of the near surface film; 5 – on the outer side of the near surface film; 6 – in dispersion medium.

The formation of seed structure particles on the iron (steel) surface, their structure and properties

The formation of the iron–oxygen mineral particles on the iron (steel) surface after its previous physicochemical treatment starts during the first minutes of contact with water dispersion medium. **Figure 7** shows the electron micro photos of the steel 3 surface during first minutes of the phase formation process, where the beginning of the metal destruction (chemical dissolution) and the origin of iron-oxygen seed structures Green Rust and ferrihydrite are presented. **Figure 8** shows the XRD-data in situ of the steel surface: straight away after the chemical activation process (**Figure 8a**); after 1 h of contact with water solution $FeSO_4$ (C_{Fe} = 10 mg / dm^3) (**Figure 8b**) and after 2 h of contact with water solution $Fe_2(SO_4)_3$ ($C_{Fe(III)}$ = 10 mg / dm^3) (**Figure 8c**). Whereas on the first picture the single pick of Fe^0, is presented that corresponds to iron component of steel, on the second picture the weak reflexes of hydroxycarbonate Green Rust GR(CO_3^{2-}) and lepidocrocite γ-FeOOH are registered, on the third picture we can see the 6-lines ferrihydrite $Fe_5O_3(OH)_9$ reflexes and the single peak of goethite α-FeOOH. The obtained data are evidence of the fact that the seed iron–oxygen particles appear even during the first hours of iron (steel) contact with water dispersion medium and their quantity is enough for XRD-investigation.

The primary mineral phases clearly registered on the iron (steel) surface by XRD in situ and scanning electron microscopy are Fe(II)–Fe(III) layered double hydroxides (Green Rust, GR) and ferrihydrite (Fh). The principal factors determining chemical composition and structure of the primary mineral particles are the oxidizing condition (the oxidant entrance into the reaction area) or the presence of ferric and ferrous iron aquahydroxoforms in the dispersion medium.

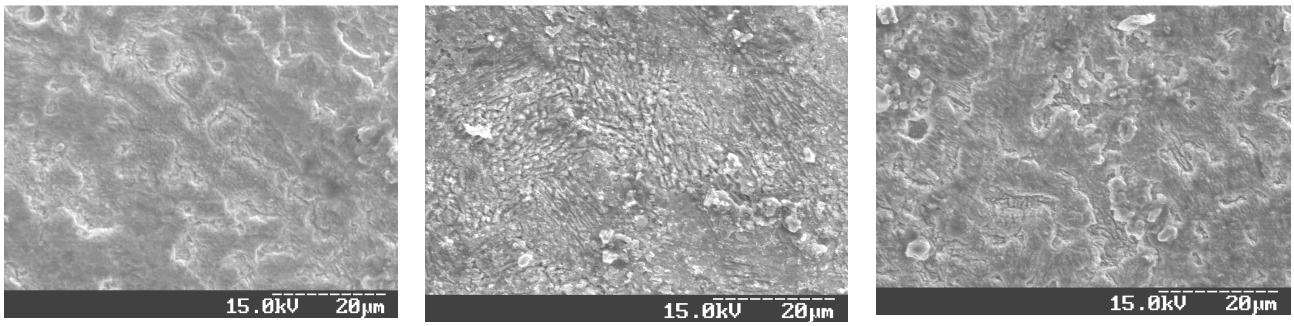

a **b** **c**

Figure 7. The steel surface after its contact with water dispersion medium during 1 (a), 2 (b), and 5 min (c).

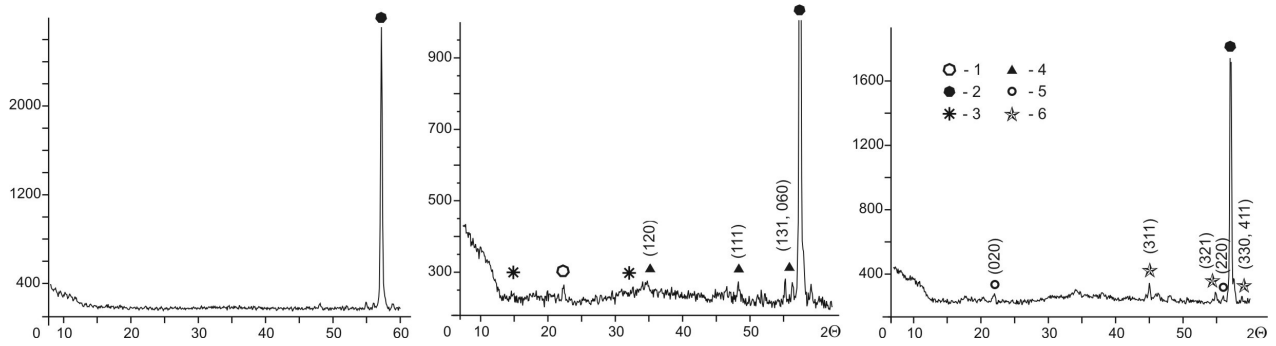

Figure 8. XRD-data in situ of the steel surface: a – after the activation process; b – after 1 h of contact with water solution $FeSO_4$; c – after 2 h of contact with water solution $Fe_2(SO_4)_3$. The numbers correspond to: 1 – fluorocarbon polymer; 2 – Fe^0 (the steel surface) and the mineral phases: 3 – Green Rust $GR(CO_3^{2-})$, 4 – lepidocrocite γ-FeOOH, 5 – ferrihydrite $Fe_5O_3(OH)_9$, 6 – goethite α-FeOOH.

The typical specimens of Fe(II)–Fe(III) layered double hydroxides (LDH) formed in the system based on iron are hydroxycarbonate (**Figure 9**) and hydroxysulphate (**Figure 10**) Green Rust that correspond to the first and the second types of the lattice. According to the literature source, their chemical formulas are the following $Fe^{II}_4Fe^{III}_2(OH)_{12}CO_3{\cdot}2H_2O$ [32, 37] or $Fe^{II}_4Fe^{III}_2(OH)_{12}CO_3{\cdot}3H_2O$ [38] and $Fe^{II}_4Fe^{III}_2(OH)_{12}SO_4 \cdot \sim 8H_2O$ [39]. In abbreviated form they are denoted as $GR(CO_3^{2-})$ and $GR(SO_4^{2-})$, respectively. The formation of Fe(II)–Fe(III) LDH structures takes place when ferrous iron aquahydroxoforms including $Fe(OH)_2$ are present in the reaction area. Other components necessary for the particle formation are hydroxyl, carbon oxygen species and anions (SO_4^{2-} or O^{2-}). Under such condition the original micelle structures can form in water film adjacent to electrode surface. They may be represented as when ferrous iron is presented in solution: $((m\mathrm{Fe(OH)_2})\cdot n\mathrm{FeOH^+}\cdot(n–x)\mathrm{OH^-})^{x+}\cdot x\mathrm{OH^-}$ and $((m\mathrm{Fe(OH)_2})\cdot n\mathrm{Fe^{2+}}\cdot 2(n–x)\mathrm{OH^-})^{2x+}\cdot 2x\,\mathrm{OH^-}$; when both ferrous and ferric iron are presented in solution: $((m\mathrm{Fe(OH)_3})\cdot 2n\mathrm{FeOH^+}\cdot(n–x)\mathrm{A^{2-}})^{2x+}\cdot x\mathrm{A^{2-}}$, and $((m\mathrm{Fe(OH)_3})\cdot n\mathrm{Fe^{2+}}\cdot(n–x)\mathrm{A^{2-}})^{2x+}\cdot x\mathrm{A^{2-}}$, where A^{2-} – dyad anions SO_4^{2-}, CO_3^{2-}.

We think such structures can be precursor-species of Green Rust formed on the steel surface. This supposition agrees with electrochemical data according to the primary formation of gellike phase $Fe(OH)_2$ on the steel surface in the corrosion process [40, 41].

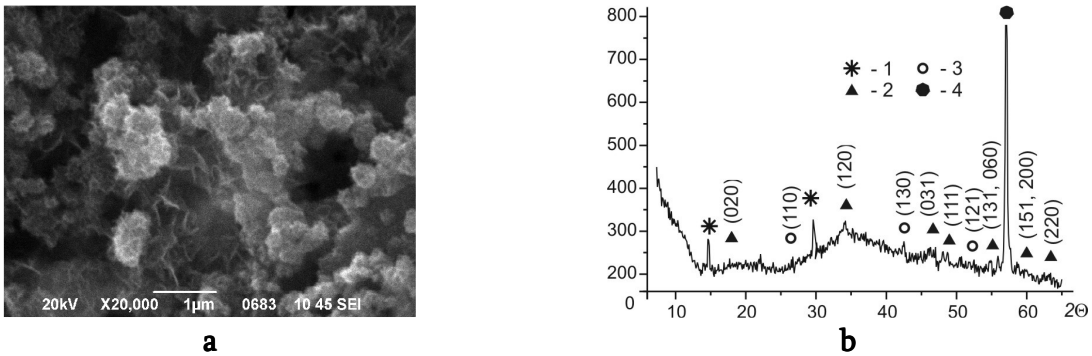

Figure 9. Hydroxycarbonate Green Rust I ($GR(CO_3^{2-})$) formed on the steel surface contacting with water disperse medium and air oxygen: a – SEM-image, b – XRD-data. The numbers correspond to phases: 1 – $GR(CO_3^{2-})$, 2 – γ-FeOOH, 3 – α-FeOOH, 4 – iron from steel surface (Fe^0).

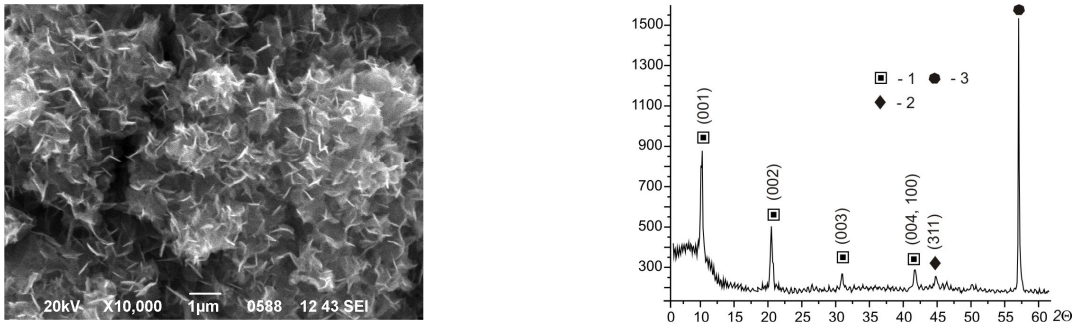

Figure 10. Hydroxysulphate Green Rust II ($GR(SO_4^{2-})$) formed on the steel surface contacting with water disperse medium and air oxygen: a – SEM-image, b – XRD-data. The numbers correspond to phases: 1 – $GR(SO_4^{2-})$, 2 – $FeFe_2O_4$, 3 – (Fe^0) from steel surface.

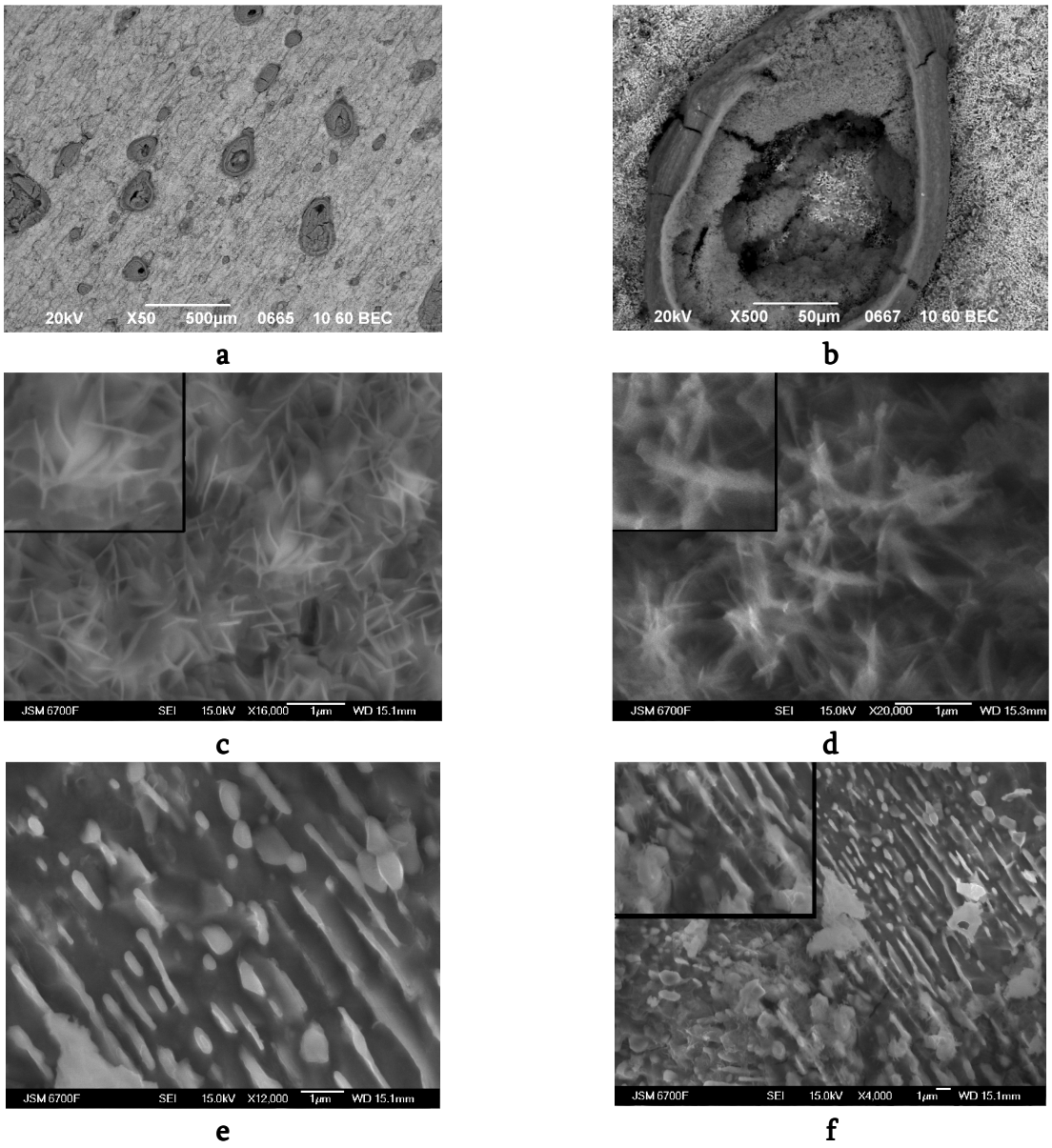

Figure 11. The stages of the Green Rust particles development on the steel surface: a, b – the localization of the seed formation process on defects of the steel surface; c, d – disordering of the GR particles on the steel surface; e, f – the orientation of GR plates perpendicular to the steel surface and their separation from it.

The formation of Green Rust particles starts on the structural defect on the steel surface (in pit corrosion) (**Figure 11a**); further they cover whole electrode area and form the porous film (layer). The obtained data show that during the rotation of disk electrode and the electrochemical reaction the primary (seed) Green Rust particles oriented parallel to the surface rotate and become the chaotically distributed (**Figures 11c** and **d**). That permits to form one porous layer. Probably, every Green Rust particle transforms to the separate iron oxide or hydroxide particle (**Figures 11e** and **f**), which may develop on the surface as well as in dispersion medium. So, the seed Green Rust phase spontaneously disperses and the other part of the rotation-corrosion dispergation process realize. The scheme of the particle development during rotation-corrosion process is presented on the **Figure 12**.

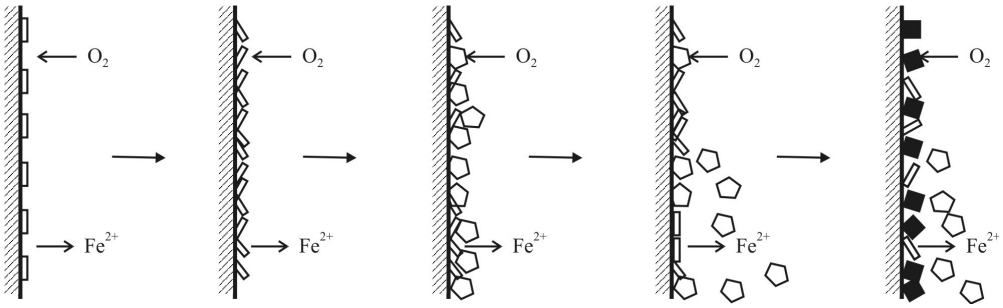

Figure 12. The scheme of the Green Rust particle formation and their transformation in magnetite.

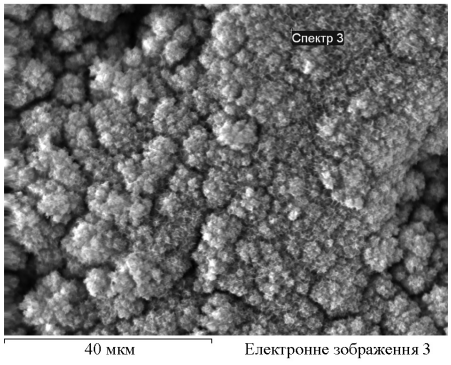

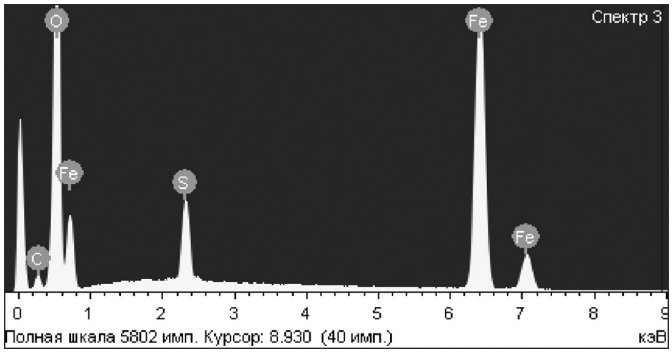

a **b**

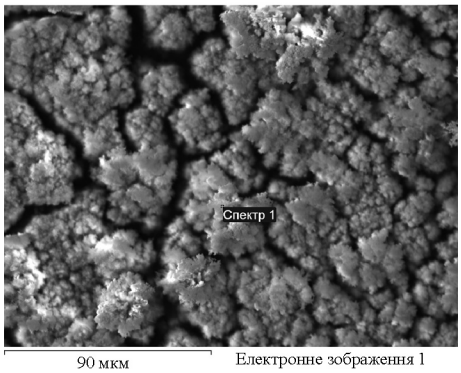

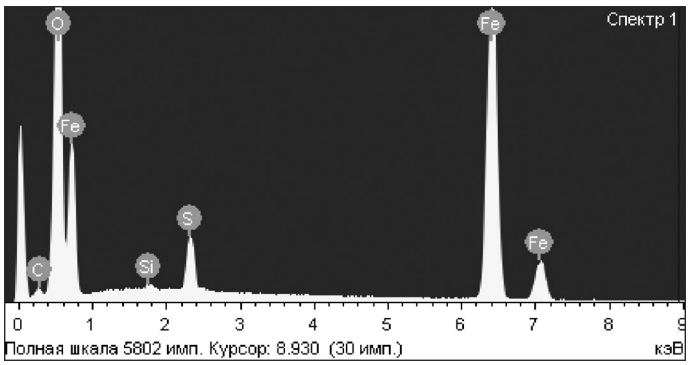

c **d**

Figure 13. Electron pictures (a, c) and EDX-data (b, d) of hydroxysulphate Green Rust containing ferrous and ferric iron respectively.

EDX-data show the presence of Fe 37.41, O 56.29, S 6.29, C 0.01 at. % in the GR(SO_4^{2-}) structure formed when the steel surface was contacting with $FeSO_4$ water solution ($C_{Fe(II)}$ = 1000 mg / dm³). Another chemical composition was GR(SO_4^{2-}) obtained when the steel surface was contacting with $Fe_2(SO_4)_3$. In such condition the element composition of Green Rust was Fe 36.94, O 56.52, S 6.51, both C and Si on average ~ 0.03 at. %. EDX and electron picture of GR(SO_4^{2-}) are presented on the **Figure 13**.

Considering the colloid-chemical mechanism of the GR(CO_3^{2-}) formation we think that the ferric and ferrous hydroxide micelles can be their precursor species. The process of phase formation has been realized when carbon–oxygen species, oxygen and ferrous aquahydroxoforms are present in reaction area. The similar process was described for oxidizing condition in work [40], where Green Rust formation on the steel surface took place in the atmosphere enriched by CO_2. Schematically the reaction of hydroxycarbonate Green Rust formation by rotation-corrosion dispergation method can be represented as:

$$3Fe(OH)_2 + 3(Fe(OH)_{(x)})^{(2-x)+} + H_y(CO_3)^{(2-y)-} + (8-3x)H_2O + ½O_2 =$$
$$= Fe_4^{II}Fe_2^{III}(OH)_{12}CO_3 \cdot 3H_2O + (4-3x+y)H^+, \quad (4)$$

where $x = 0, 1$ and $y = 0, 1, 2$;

$$2Fe(OH)_3 + 4(Fe(OH)_{(x)})^{(2-x)+} + (H_yCO_3)^{(2-y)-} + (9-4x)H_2O =$$
$$= Fe_4^{II}Fe_2^{III}(OH)_{12}CO_3 \cdot 3H_2O + (6-4x+y)H^+, \quad (5)$$

where $x = 0, 1$ and $y = 0, 1, 2$;

$$2Fe(OH)_3 + 4Fe(OH)_2 + H_y(CO_3)^{(2-y)-} + (3-y)H_2O =$$
$$= Fe_4^{II}Fe_2^{III}(OH)_{12}CO_3 \cdot 3H_2O + (2-y)OH^-, \quad (6)$$

where $y = 0, 1, 2$.

While the carbon–oxygen species indispensable for the GR(CO_3^{2-}) formation entered into the reaction area from air spontaneously, the sulphate anions present in the GR(SO_4^{2-}) structure are added into the system from the outside. Probably, the formation of $Fe_4^{II}Fe_2^{III}(OH)_{12}SO_4 \cdot \sim 8H_2O$ can be described by schematic reactions that are similar to reactions (4 – 6) if the water molecule quantity increased to eight.

When the $Fe(OH)_2$ particles are oxidized in presence of ferrous iron and SO_4^{2-} or CO_3^{2-} to the formation Fe(II)–Fe(III) layered double hydroxides GR(SO_4^{2-}) or GR(CO_3^{2-}) respectively the phase transformation has topotactic character and can appear in the lines of the structural iron–oxygen mineral γ-row [3, 42]. Another way of the iron-oxygen mineral particle development can be realized due to transformation of "green complexes" as it was shown in our previous investigation [43].

The further development of the iron–oxygen surface structures during the rotation-corrosion dispergation process is connected with the magnetite particle formation. While the formation of the cubic particles takes place under unfettered condition and the excess of hydroxyl due to direct crystal growth that is a typical process for sols, the magnetite particles formed on the steel surface are usually characterized by a spherical form and coagulation type of the structure. The coagulation of magnetite seed is a result of combined magnetic and van der Waals's forces and it takes place when repulsion of the particles is weak.

The seed particles $FeFe_2O_4$ are formed in the gel $Fe(OH)_2$ or, more likely, in Green Rust layer, they form small aggregates and then grow into bigger particles. We believe the mechanism of the magnetite particle formation is contact–recrystallization [44]. The essence of such process lies in the accumulation of the primary magnetite particles on the surface of ferrous hydroxide $Fe(OH)_2$ or Fe(II)–Fe(III) LDH, where they form aggregates and prove the

recrystallization process. The big magnetite particles enter into phase-precursor gel (Green Rust) and grow with surrounding primary particles included into their structure. At the same time the big particles prevent the small particle growth and lead to the formation of new clusters. So, we can observe the competition between the growth of big particle due to adhesion of the primary (small) particles that usually form aggregates and the aggregation of the big particles. When the system reaches the stationary state the particle size averages out.

Figure 14 shows TEM-images of the primary magnetite particles adsorbed on the Fe(II)–Fe(III) LDH surface (a, b); the magnetite particles collected on the surface (c), and magnetite aggregates whose particle form the structure with the fragile contacts (d). Such contacts broke when the magnetite phase is removed from the surface and the particles get unbound state.

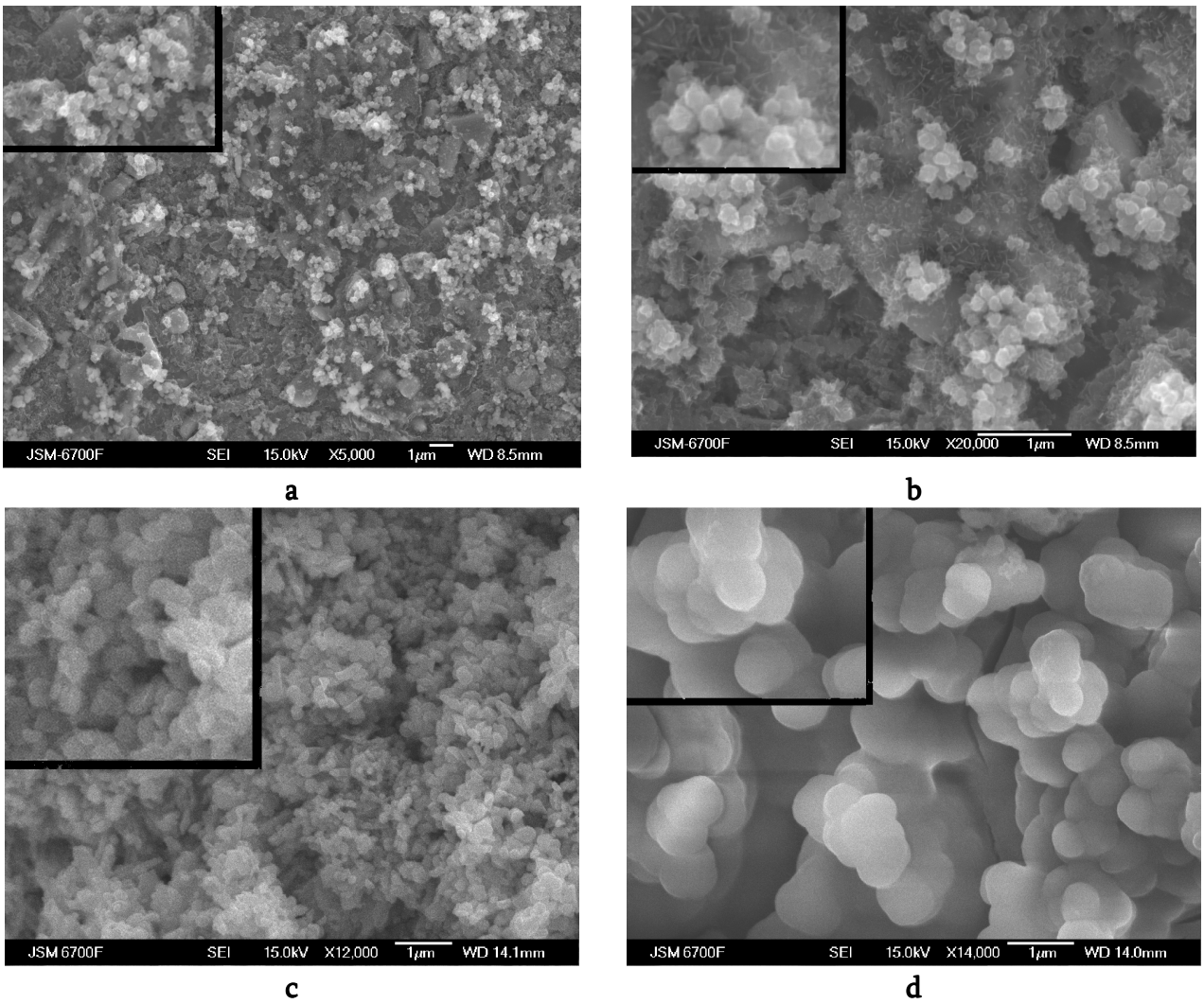

Figure 14. Magnetite formed on the steel surface during the rotation-corrosion dispergation process: a, b – adsorption of the seed (primary) particles on the Fe(II)–Fe(III) LDH surface, c – the particle collection on the Fe(II)–Fe(III) LDH surface, d – the formation of the fragile magnetite aggregates.

The near surface layer (film) formation

When the disk electrode rotates the near electrode water film on the interface air – the steel surface is formed. The formation of such film is determined by the system peculiarity and

physicochemical conditions in the reaction area due to electrochemical (corrosion) processes on the steel surface. So, in the first seconds of the contact of the steel surface with water dispersion medium the primary products of the electrochemical process (ferrous iron and hydroxyl) begin to flow into the reaction area with the $(Fe(OH)_{(x)})^{(2-x)+}$ complex formation. The electrode rotation provides for saturation of the reaction area by air oxygen that passes through water layer during 2.5 s. So, the full oxidation of ferrous iron takes place in the reaction area. We admit the formation of ferric iron micelles in the reaction area. In experimental conditions and alkalescent medium (pH value 7 – 9) the mechanism of the $Fe(OH)_3$ ionization is acidic and micelle formula could be written as [45]: $((m Fe(OH)_3) n Fe(OH)_2O^-(n-x)H^+) x H^+$.

Obviously the species quantity will be growing in the reaction area and the density gradient will appear between the reaction area and the amount of the solution. At the same time the electrode rotation permits the species diffusion into disperse medium from the reaction medium and it causes the accumulation of the substance on the interface water film on the steel surface. So, the profitable condition for the particle formation and structuring in near surface film is created.

According to XRD-data and TEM images ferrihydrite particles $Fe_5O_3(OH)_9$ form the primary near electrode film. The process of the ferrihydrite aggregate formation, their coagulation and polycondensation is shown on the **Figure 15**.

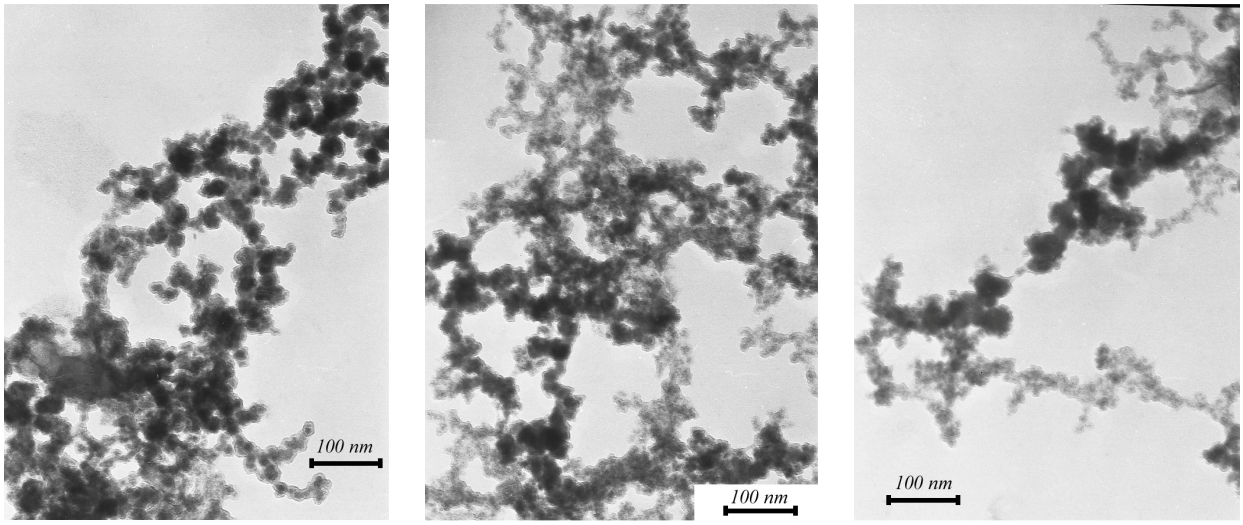

Figure 15. The process of the ferryhydrite structuring onto the primary near electrode film: a – 1, b – 2, c – 4 h.

Schematically the equation that describes the process of the amorphous ferric hydroxide formation in the reaction area and its transformation in the near surface film to ferrihydrite particles could be presented as:

$$(Fe_{3x}(OH)_y)^{(3x-y)+} + (3x-y)OH^- \rightarrow x(Fe(OH)_3), \quad (7)$$

where x, $y = 1, 2$;

$$5(Fe(OH)_3) \rightarrow Fe_5O_3(OH)_9 + 3H_2O. \quad (8)$$

Generalized schematically equation is:

$$5(Fe_x(OH)_y]^{(3x-y)+} + (9x-5y)OH^- + {}^3/_2xO_2 + 6xe^- \rightarrow x(Fe_5O_3(OH)_9), \quad (9)$$

where x, $y = 1, 2$.

At the same time the ferrihydrite particle formation on the steel surface could take place due to the phase transformation of Fe(II)–Fe(III) LDH under limited oxidation [46].

The Fe(II)–Fe(III) LDH oxidation in the presence of ferrous iron, hydroxyl and oxygen can be described according to the equation:

$$(Fe_4^{II}Fe_2^{III}(OH)_{12}CO_3 \cdot 3H_2O) + 4Fe^{2+} + 2O_2 + 8OH^- \rightarrow 2(Fe_5O_3(OH)_9) + H_2CO_3 + 3H_2O. \quad (10)$$

The formation of the structured ferrihydrite film screens the electrode surface and the reaction area against the contact with air and complicates the oxidant (air oxygen) transfer into the system. So, it considerably influences the future process of iron–oxygen mineral particle formation.

When the primary ferrihydrite film forms in the near surface layer the Green Rust particle phase transformation onto magnetite starts on the steel surface. Ferric and ferrous aquahydroxoforms appeared in the reaction area take part in the formation of ferric oxyhydroxides in the near surface layer. The phase transformation into NSL leads to formation of needle like lepidocrocite γ-FeOOH particles on its inner side and goethite α-FeOOH particles on its outer side.

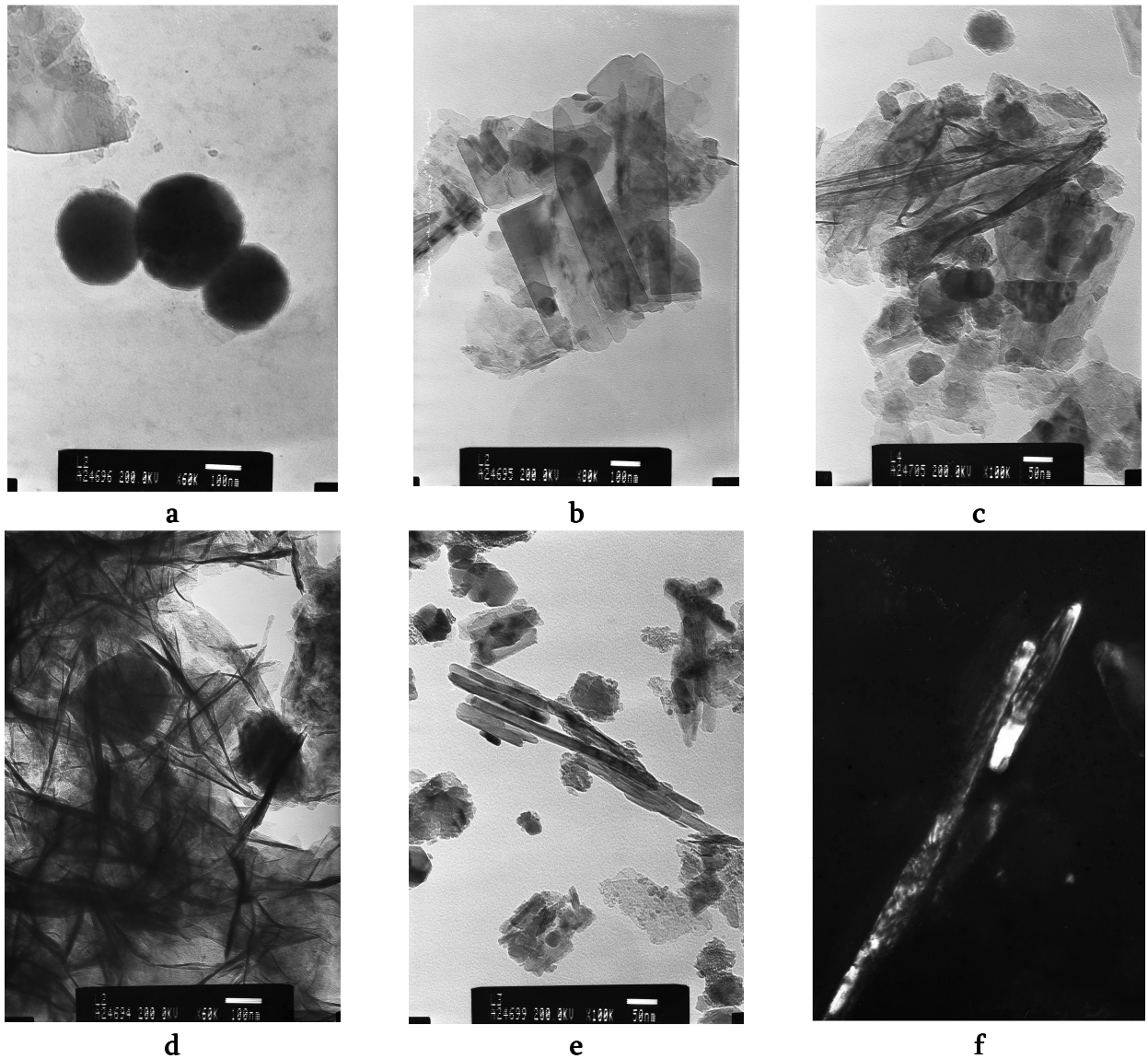

Figure 16. Particles formed in the near surface film: a – ferrihydrite, b – Green Rust, c – Green Rust particle and lepidocrocite needles, d – lepidocrocite, e, f – goethite needles.

Figure 16 shows TEM-images of the iron-oxygen particles from the NSL. The size difference between the primary particles of ferrihydrite and Green Rust and its transformation products attract our attention. The length of oxyhydroxide crystals reaches microns. The probable mechanism of the well crystallized α-FeOOH and γ-FeOOH micro particles formation is the solution–reprecipitation [46] or reconstructive transformation [47]. According to such mechanism the phase transformation of Fe(II)–Fe(III) LDH in water medium has two stages: 1. The ferrous oxidation into Green Rust lattice with partial solution (destruction) of their nanosized particles and 2. The second precipitation of the well-ordered micro sized lepidocrocite γ-FeOOH particles [48]. The similar process was studied in water medium under condition of Fe(II)–Fe(III) LDH oxidation by dissolved oxygen. It leads to formation of well-crystallized goethite α-FeOOH particles [49].

The phase transformation of ferrihydrite precipitated in water medium from ferric salts into goethite α-FeOOH leads to the solution–reprecipitation mechanism [47], when weak crystallized ferrihydrite particles dissolve and the dissolution products precipitate as well-crystallized goethite particles. Ferrous iron catalyzes such process due to its adsorption on the ferrihydrite surface when it reduces ferric iron to ferrous iron in ferrihydrite lattice that desorbs from particle surface into dispersion medium. Ferrous species oxidize in water medium to ferric species and precipitate as new goethite phase [9].

The acceleration of such process is determined by the lowering of the reaction activation barrier from 56 to 38 kJ / mole due to the presence of ferrous iron [50]. The phase transformation of Fh on α-FeOOH passes through the stages of the ferrihydrite dissolution with $Fe(OH)^{2+}$ and / or $Fe(OH)_2^{+}$ formation, their polymerization and α-FeOOH sedimentation. At the same time, the α-FeOOH formation in water medium can occur only in the presence of aquahydroxoforms $Fe(OH)(H_2O)_5^{2+}$, $Fe(OH)_2(H_2O)_4^{+}$, $Fe(OH)_4(H_2O)_2^{-}$, $Fe(OH)_5(H_2O)^{2-}$, $Fe(OH)_6^{3-}$ [50]. On the contrary, $Fe(H_2O)_6^{3+}$ prevents phase transformation of ferrihydrite into goethite and as a product of phase transformation under such condition hematite α-Fe_2O_3 is formed. The optimum condition for the phase transformation of Fh into lepidocrocite γ-FeOOH in the presence of trace ferrous iron by dissolution – reprecipitation corresponds to $T \leq 40$ °C and pH value ~ 7.0, when ~ 50 % Fe(II) is in the form of $FeOH^{+}$. Such species is determined as a catalyst of the ferrihydrite dissolution and lepidocrocite re-precipitation [50].

When we consider the process of the microsized lepidocrocite and goethite particle formation in the near surface film under rotation-corrosion dispergation, its conformity with the processes described above is obvious. So, pH value in the NSL and in the reaction area in average is 7 – 9, and it is favorable for hydration as well as ferrous iron hydrolyzes. The free entrance of air oxygen leads to generation of ferric iron species. Probably, the primary ferrihydrite and Fe(II)–Fe(III) LDH particles dissolve in the near surface film, interact with each other and with other components located in the near surface film and then we obtain species sediments in the form of well-crystallized micro particles of iron oxyhydroxides. According to [51], the ferric and ferrous iron concentrations influence the iron-oxygen particle morphology: high content needle-like crystals are formed in the sediment.

The complete near surface film holds on the steel surface due to adhesion and when the steel electrode plunges into solution it proceeds to the solution interface due to viscous forces and it shows the hydrophobic properties.

Figure 17 shows TEM-images of the near surface film structuring. Probably, iron oxyhydroxide forms big aggregates that unite into island structures (**Figure 17a**) that gradually

increase due to joining of the neighbor islands (**Figure 17b**) and grow due to entrance of the initial components from the reaction area. The formation of NSF stops when the equilibrium complete layer of iron-oxygen structures is formed (**Figure 17c**) [52].

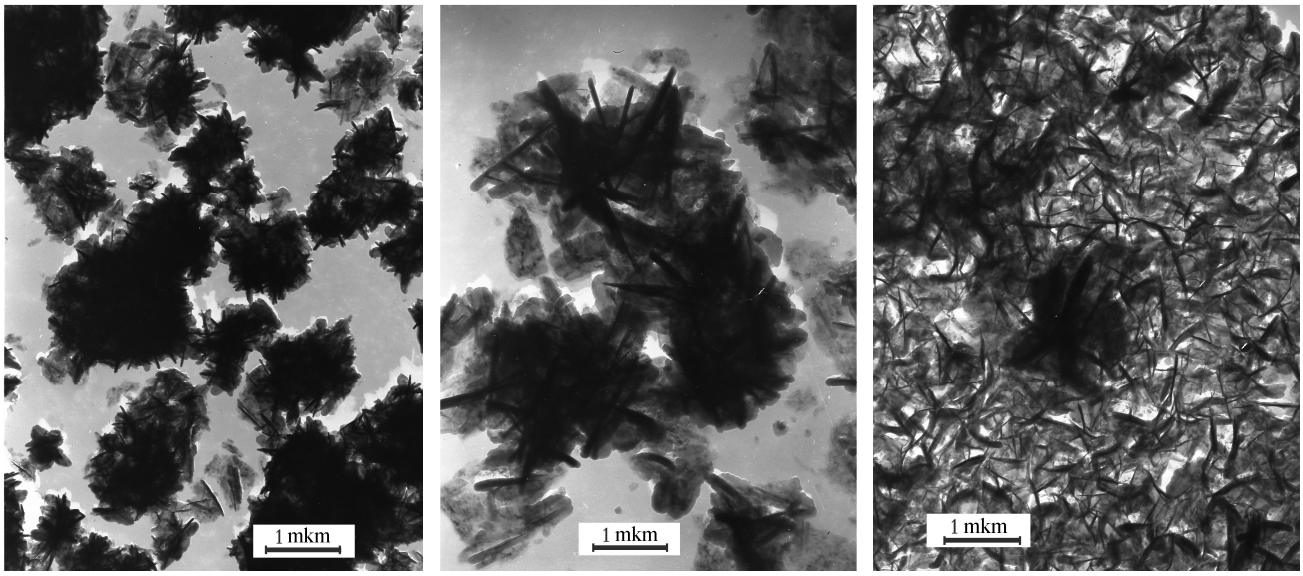

Figure 17. The stages of the near surface film formation: a – the island structure formation, b – the island growth, c – the formation of the complete film [52].

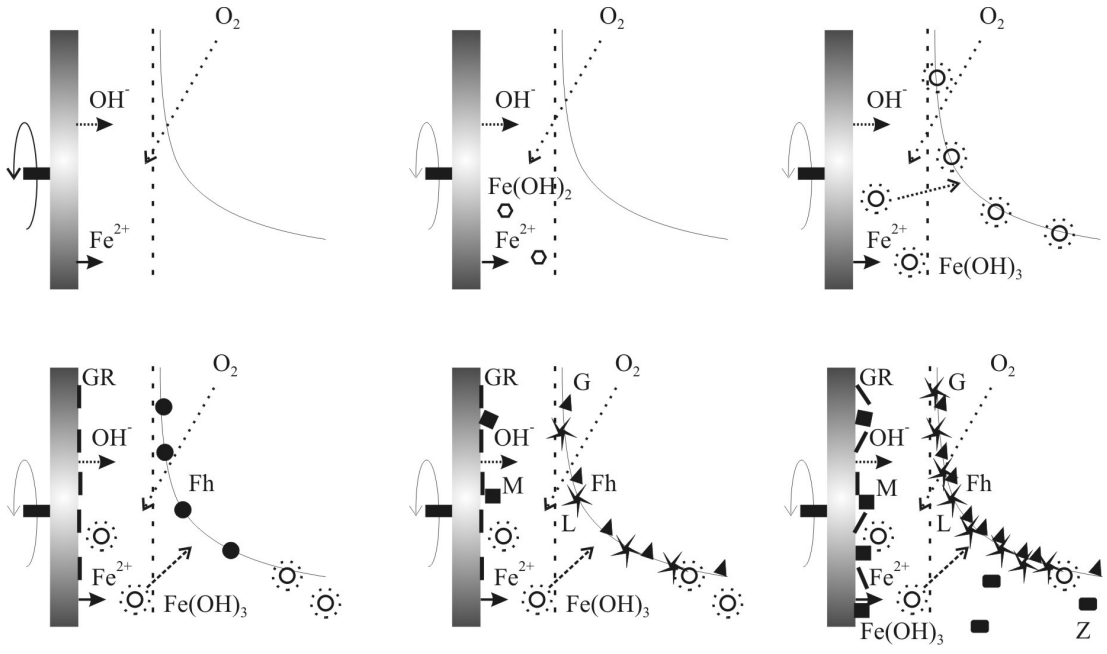

Figure 18. The scheme phase formation during rotation-corrosion dispergation. Letters correspond to the particles: GR – Green Rust, Fh – ferrihydrite, G – goethite, L – lepidocrocite, M – magnetite, Z – sol (magnetite, iron oxyhydroxides, spinel ferrite, core & shell composite).

Due to the peculiarity of the oxidizing conditions the particles of the near surface film form the coagulation structures on the inner side and condensation-coagulation structures on its outer side. The formation of the inner layer near surface film is realized under following condition: hydroxyl, ferrous and ferric iron excess and oxidant (air oxygen) deficiency. This

allows forming lepidocrocite γ-FeOOH particles as well as maghemite γ-Fe_2O_3 or magnetite $FeFe_2O_4$. It is indicative that the iron–oxygen particles formed on the inner side of NSF are characterized by imperfect structure and presence of the lattice defects. The outer side of NSF is formed by oxidant excess. So, microsized flake-like goethite α-FeOOH particles and needle-like lepidocrocite γ-FeOOH particles have perfect structure. When the NSF stops contacting with water medium the oxyhydroxides particles will dehydrate and NSF lose elastic properties and it will spontaneously separate from the surface mineral phases. The scheme of the near surface film formation and development of the mineral particles on the steel surface is shown in **Figure 18**.

The iron–oxygen particle formation in water dispersion medium

When the mineral phases are formed on iron (steel) surface and in its near electrode layer the iron–oxygen nanoparticles entered in water medium from the reaction area spontaneously form weak-concentrated sols. The sol concentration growth lasts during system development from formation of the primary seed particles to their stationary state. The presence of ferrous iron or other cations leads to ion-stabilization of the sols, but the steadiness of such sols is insignificant [53] and it could be broken due to sol carrying over into the other flaks. So, in the investigation of the mineral particles in dispersion medium obtained by the rotation-corrosion dispergation we used the additional treatments to increase sol aggregative and sedimentative stability.

The formation of the primary particles in sols starts in the reaction area during interaction of ferrous iron aquahydroxoforms with $Fe(OH)_3$ micelles, Fe(II)–Fe(III) LDH and ferrihydrite particles, oxygen, hydroxyl, carbon–oxygen species and other components added into dispersion medium from the outside.

Usually water sols formed during rotation-corrosion dispergation are characterized as weak-concentrated sols (1.5 – 12.0 mg / dm^3 of disperse phase into 1 dm^3 dispersion medium) with nanometer particle size.

The most colloid sol stability we noticed when aquahydroxoforms of precious metals were present in the dispersion medium [54]. Under such condition the nanosized particles of core & shell composites with magnetite or maghemite core and silver, gold, platinum or palladium shell are formed in the sol. The presence of free argentums cations in dispersion medium prevents from their aggregation and sedimentation of the particles during more than six months. Similar properties are typical for core & shell composites of other chemical composition, for example, iron oxide core and gold shell obtained in water solution in the presence of hydroxylamine [55].

Figure 19a shows the core & shell composite γ-Fe_2O_3&Ag^0 formed during rotation-corrosion dispergation process when water solution of $AgNO_3$ ($C_{Ag(I)}$ = 1 mg / dm^3) was added in the system. We can see that the γ-Fe_2O_3&Ag^0 particles do not form aggregates as well as maghemite particles (**Figure 19b**).

The nephelometric estimation shows that the most stable sols were obtained after 24 h of their formation. Moreover, the sedimentation process for all sols carried into glass flaks stopped after 24 h too. Equilibrium in such systems kept more than 600 h.

The investigation of the influence of sol concentration degree on the mineral composition and particle properties shows that such parameters do not change even by the

1 – 25 times evaporation by 50 °C. The obtained data prove that the weak concentrated water sols of iron-oxygen mineral particles formed by rotation-corrosion dispergation method could be concentrated by evaporation without the loss of their properties. It can give a good ground for their practical usage in biology and medicine.

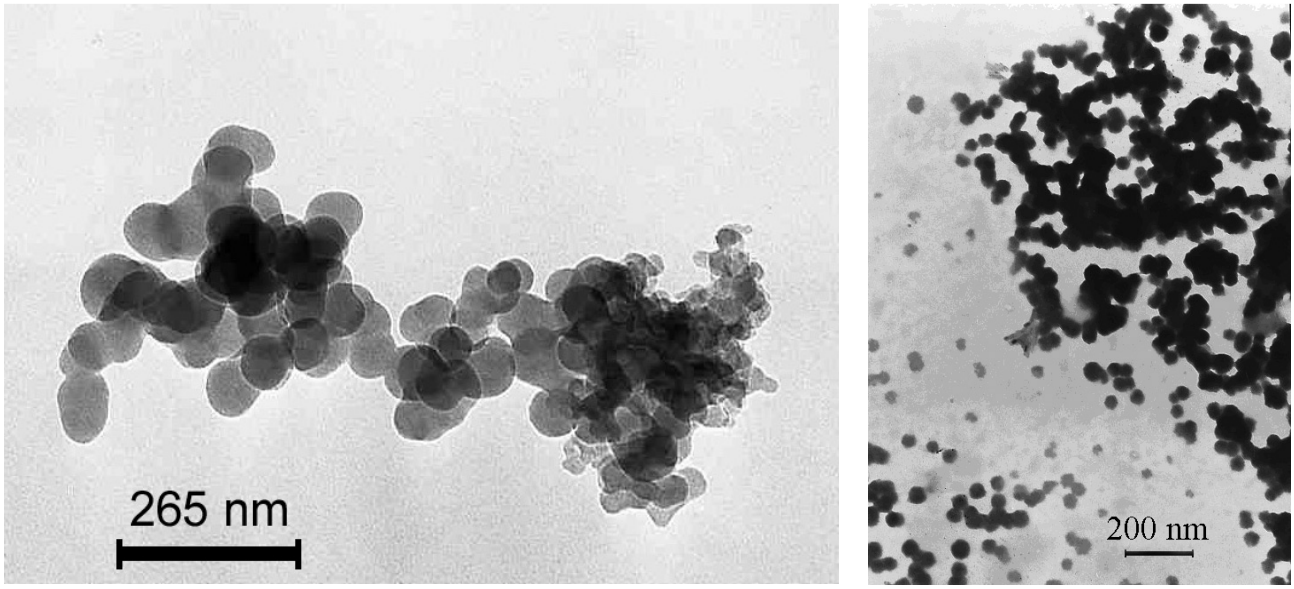

a b

Figure 19. Sol particles: a – nanocomposite γ-Fe_2O_3&Ag^0 after 600 h precipitation, b – maghemite.

At the same time, iron–oxygen nanoparticles used for medical-biological investigation must be characterized by height colloidal stability, magnetic susceptibility, size and content homogeny as well as compatibility with biological objects and availability of surface activity. The active centers on the particle surface are able to interact with organic polymers, precious metals or oxides [14]. The iron–oxygen nanoparticles must keep their physicochemical properties during further treatment, for example by covering of bioactive molecules including medicines.

We studied the influence of different admixes, such as EDTA: $C_{10}H_{16}N_2O_8$ ($C = 6.8 \cdot 10^{-7} – 1.7 \cdot 10^{-4}$ M / dm³), NaH_2PO_4 ($C = 0.8 \cdot 10^{-3} – 0.42$ M / dm³) and humic acid (molecular weight 1300, $C = 1.5 \cdot 10^{-7} – 3.75 \cdot 10^{-5}$ M / dm³), on aggregative and sedimentative stability of iron–oxygen nanoparticles obtained by rotation-corrosion dispergation method [57]. We are guided by the choice of reagents in their reaction capability for iron–oxygen mineral particles [9] and compatibility with biological objects and systems [57].

The application of chemical admixes could be used for obtaining of separate particles and aggregates of ferric oxyhydroxides. So, when EDTA $3.4 \cdot 10^{-5}$ M / dm³ solution was added into water medium the lepidocrocite sol was formed in the system. The similar effect was reached when the $0.8 \cdot 10^{-2}$ M / dm³ water solution was used for the nanoparticles obtaining. In the presence of humic acid solution ($7.6 \cdot 10^{-6}$ M / dm³) goethite globule was formed at the rotation-corrosion dispergation. **Figure 20** shows the lepidocrocite particles, where we can see their morphological difference (aggregates formed in the presence of EDTA and needle-like crystals formed in the presence of NaH_2PO_4). **Figure 21** shows 5 – 7 nm goethite globules that formed the 40 – 50 nm aggregates.

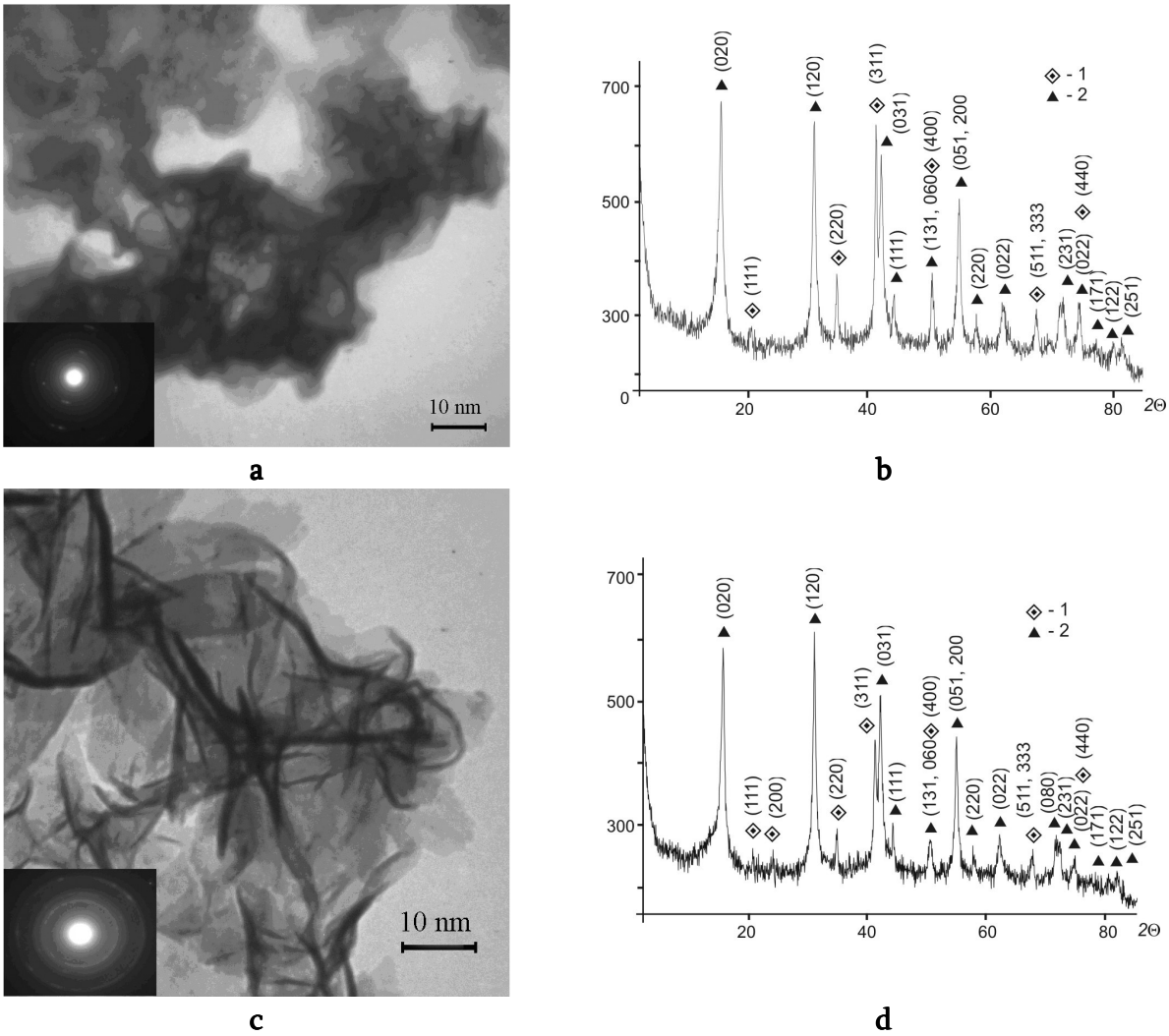

Figure 20. TEM-images (a, c) and XRD-data (b, d) of lepidocrocite γ-FeOOH with maghemite γ -Fe_2O_3 admixture obtained by applying RCD-method in the presence of EDTA and NaH_2PO_4 respectively. Numbers correspond to the phases: 1 – maghemite γ-Fe_2O_3, 2 – lepidocrocite γ-FeOOH.

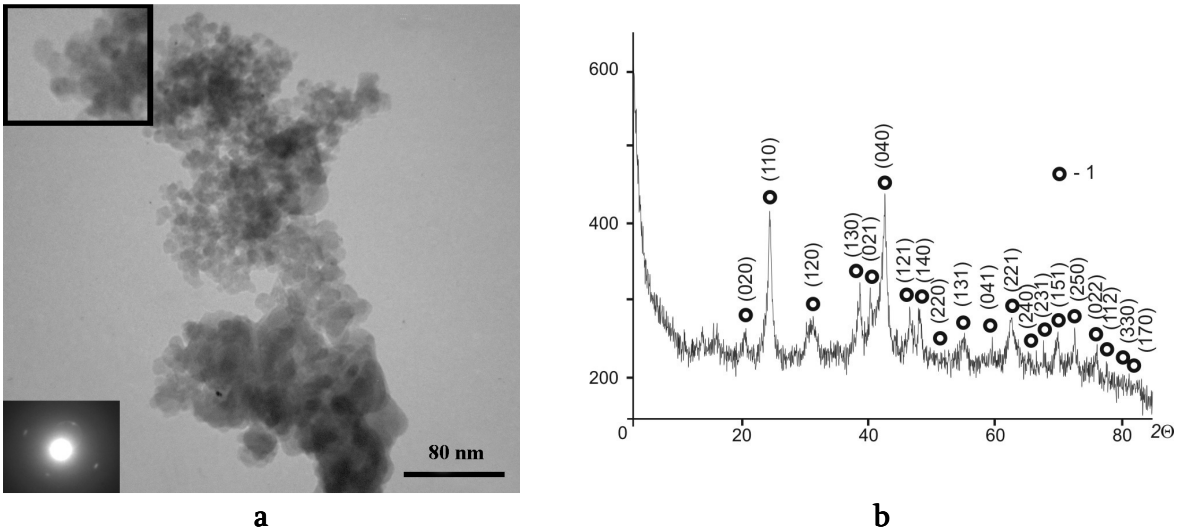

Figure 21. TEM-image (a) and XRD-data (b) of goethite α-FeOOH obtained by applyin the

RCD-method in the presence of humic acid. Number 1 corresponds to goethite α-FeOOH.

So, the usage of stabilizer species when the RCD method of the iron-oxygen nanoparticles obtaining is applied can change sedimentative and aggregative stability of water sols as well as help iron oxyhydroxide mineral particles and aggregates formation.

Obtaining of nanosized iron–oxygen mineral phases when the rotation-corrosion dispergation method is applied

One of the main peculiarities of the iron–oxygen nanoparticles formation applying RCD method is the sequential development of mineral phases with the structural rows. During the definite time the precursor species passes through the individual stages of development and it characterized by fixed lattice, particle size, its form and morphology.

During the process of the particle formation applying RCD method their size, content and structure do not remain constant (permanent) due to phase transformation that continuously take place in the system. We picked out the following stages of the particle development, namely: the formation of the primary nanoparticles ferrihydrite and Fe(II)–Fe(III) LDH (protolepidocrocite), their transformation in nano- or microsized particles and aggregates of iron oxyhydroxides (monohydrates) and oxides, further phase transformation of iron oxyhydroxides in oxides and iron oxide destruction up oxyhydroxides due to oxidation [52].

In general the initial phase transformation of ferrihydrite $Fe_5O_3(OH)_9$ in goethite α-FeOOH and Fe(II)–Fe(III) LDH in lepidocrocite γ-FeOOH gives rise to formation of the mineral particles that belong to α- and γ-structural rows. Their development passes through the chain of phase transformation in "goethite" and "lepidocrocite" direction. Physicochemical condition in the system determine of the primary particle type, development way in structural rows, the reaction products and change in phases of different rows. General scheme of phase transformation is present on **Figure 22**. It shows the phase bonds in the every structural row but does not include the transformation between phases of different structural rows.

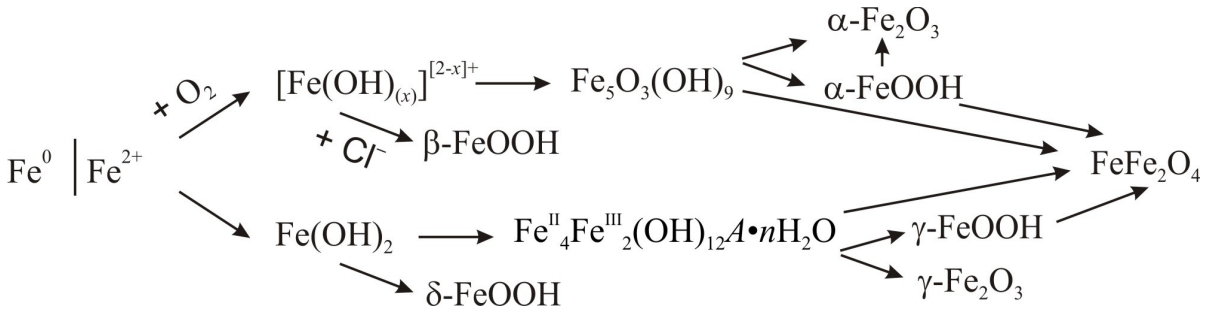

Figure 22. The scheme of phase transformation in α- and γ-structural rows (the $Fe^0 – H_2O – O_2$ system).

Our experimental investigation gives opportunity to determine the optimum condition for the individual mineral phases obtained by application of the rotation-corrosion dispergation method.

The most important parameters influencing on the mineral composition and phase transformation on the interfaces steel surface – water solution and water solution – air during rotation-corrosion dispergation process are chemical composition and pH value of dispersion

medium, temperature and oxidation condition. The control over the listed parameters gives us the opportunity to find out the optimum physicochemical conditions for obtaining of mineral particles that belong to separate structural rows and crystallographic modifications. Moreover, if the above parameters of the process will be changed we could influence colloid-chemical, physicochemical, mineralogical properties of iron–oxygen phases including the type of the structure, crystalline as well as the shape, size and morphology of particles. Separately the biological activity of the iron-oxygen minerals could be pointed for their high importance for perspective of medical-biological usage obtained material.

Figure 23 shows the diagrams where the optimal conditions of the formation and existence of lepidocrocite, goethite, magnetite and spinel ferrite as typical products of RCD process are determined.

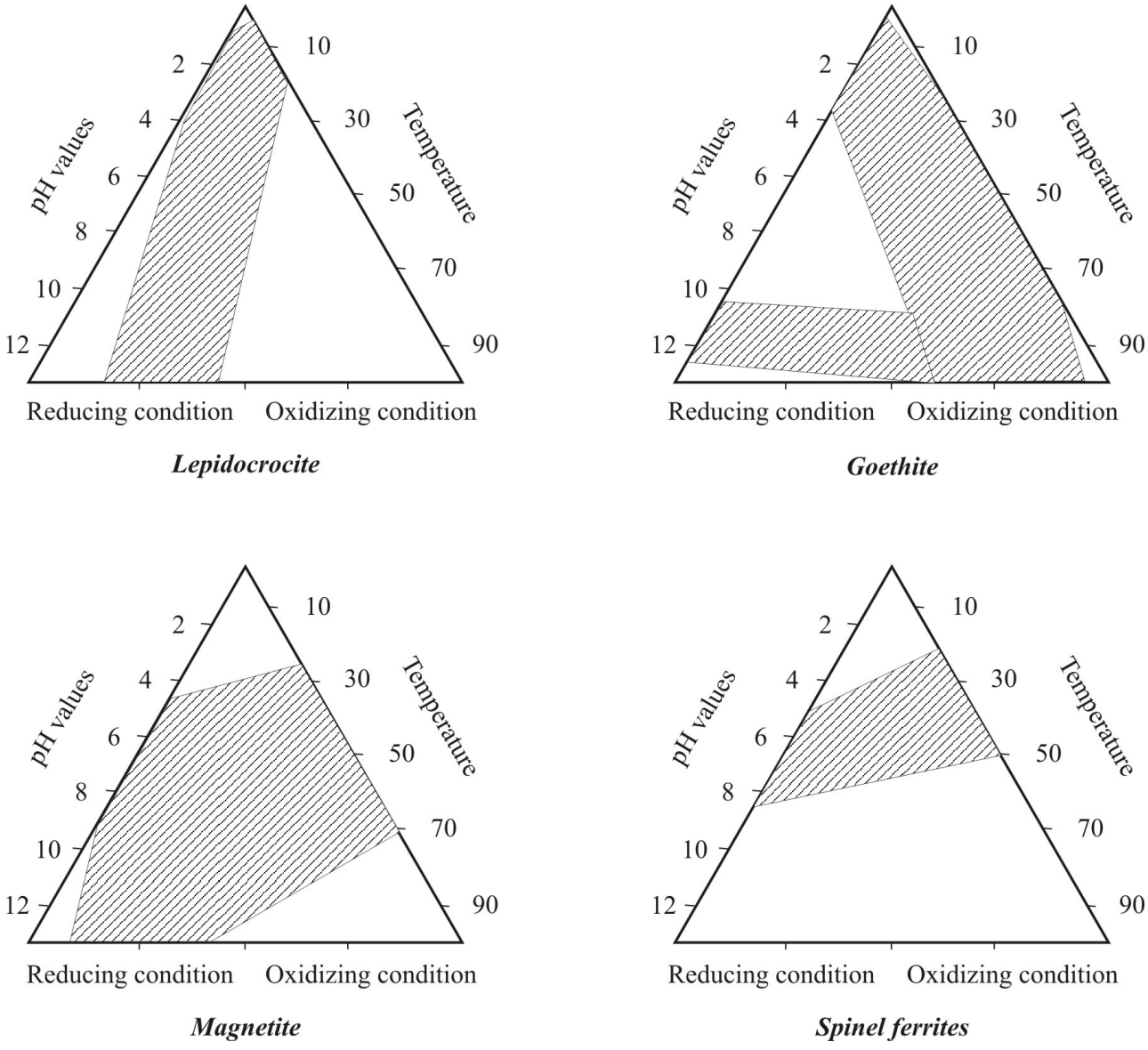

Figure 23. Diagrams of disperse iron–oxygen mineral stability obtained when the rotation-corrosion dispergation process is applied.

So, for the formation of separate lepidocrocite γ-FeOOH particles it is necessary to provide low pH value (1.5 – 4.0), low temperature (3 – 10 °C) and slow oxidation of the system. **Figure 24** shows the process of lepidocrocite structuring in the near surface layer.

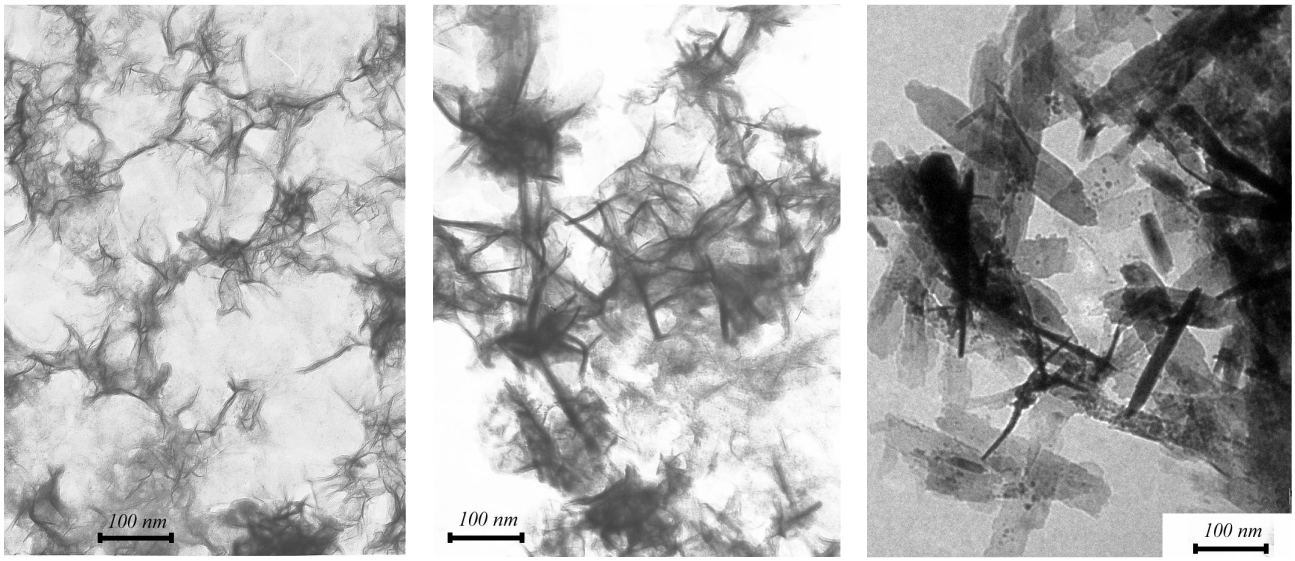

a **b** **c**

Figure 24. TEM-images of lepidocrocite in near surface film: a – formation of the primary particles, b – formation the aggregates, c – phase transformation of aggregates.

On the contrary, forced oxidation and presence ferric aquahydroxoforms in the reaction area is necessary for obtaining of goethite α-FeOOH particles. It is typical for low pH value (< 4.0). In such condition it is possible to obtain well crystallized needle-like goethite particles of condensation-crystallization structure with needle length < 100 nm (**Figure 25**).

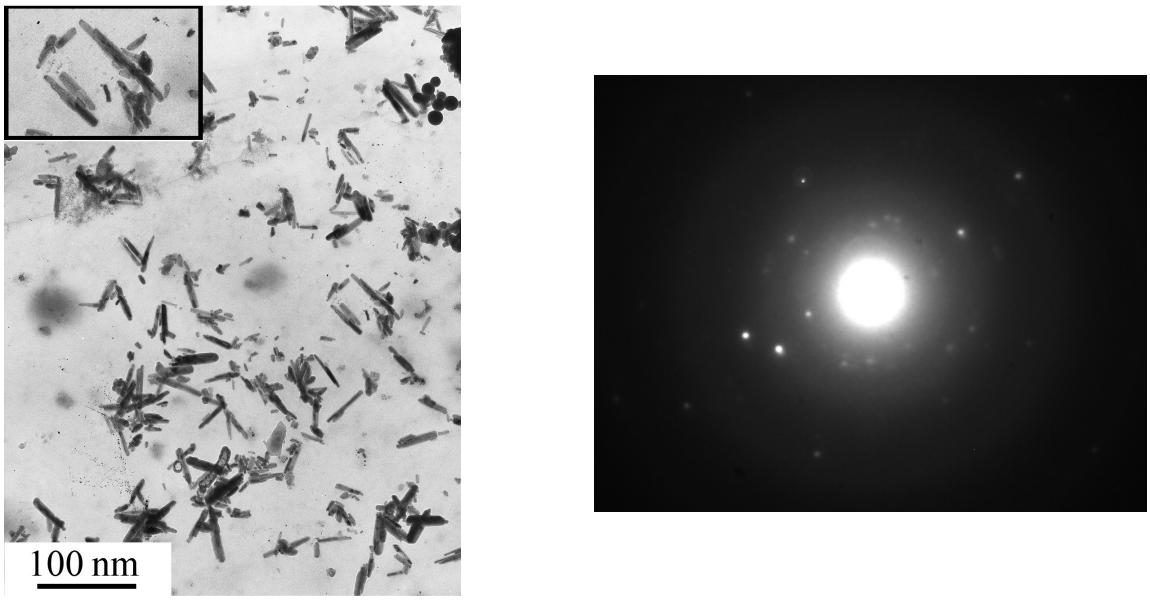

a **b**

Figure 25. TEM-image of goethite α-FeOOH particles (a), XRD-data (b).

The principal condition for the maghemite γ-Fe_2O_3 (**Figures 26a – c**) particle and aggregate formation applying the RCD method are saturation by hydroxyl of the reaction area

and limitation the presence of ferrous iron in it. We realized such condition in the galvanic couple iron (steel) – carbon system [23]. On the contrary, magnetite $FeFe_2O_4$ belongs to mineral phases that formed in the wide range of initial physicochemical conditions (**Figure 26d**). At the same time the ferrous iron concentration in the reaction area influences on the magnetite particles development. While at $C_{Fe(II)} > 300$ mg / dm³ Fe(II)–Fe(III) LDH particles remain stable during 24 h, at $C_{Fe(II)} = 10$ mg / dm³ they go through the phase transformation chain to the formation of magnetite $FeFe_2O_4$ during 4 – 5 h [58]. Probably, the change of the chemical composition of dispersion medium when the particles are formed can be not only particle stabilization but also the process stopping on every stage of the phase formation. **Figure 26e** shows XRD-data of magnetite. The presence of goethite reflexes (020) and (120) is the evidence of oxidizing process on the surface due to nanometer size of the particles. The attention should be paid to the differences in XRD-data of magnetite and maghemite (**Figure 26f**). These structures can be distinguished only by the comparative pick (440) intensity, that amounts for magnetite on average up to 45 and for maghemite it amounts on average up to 79 units in relation to 100 unit for reflection (311).

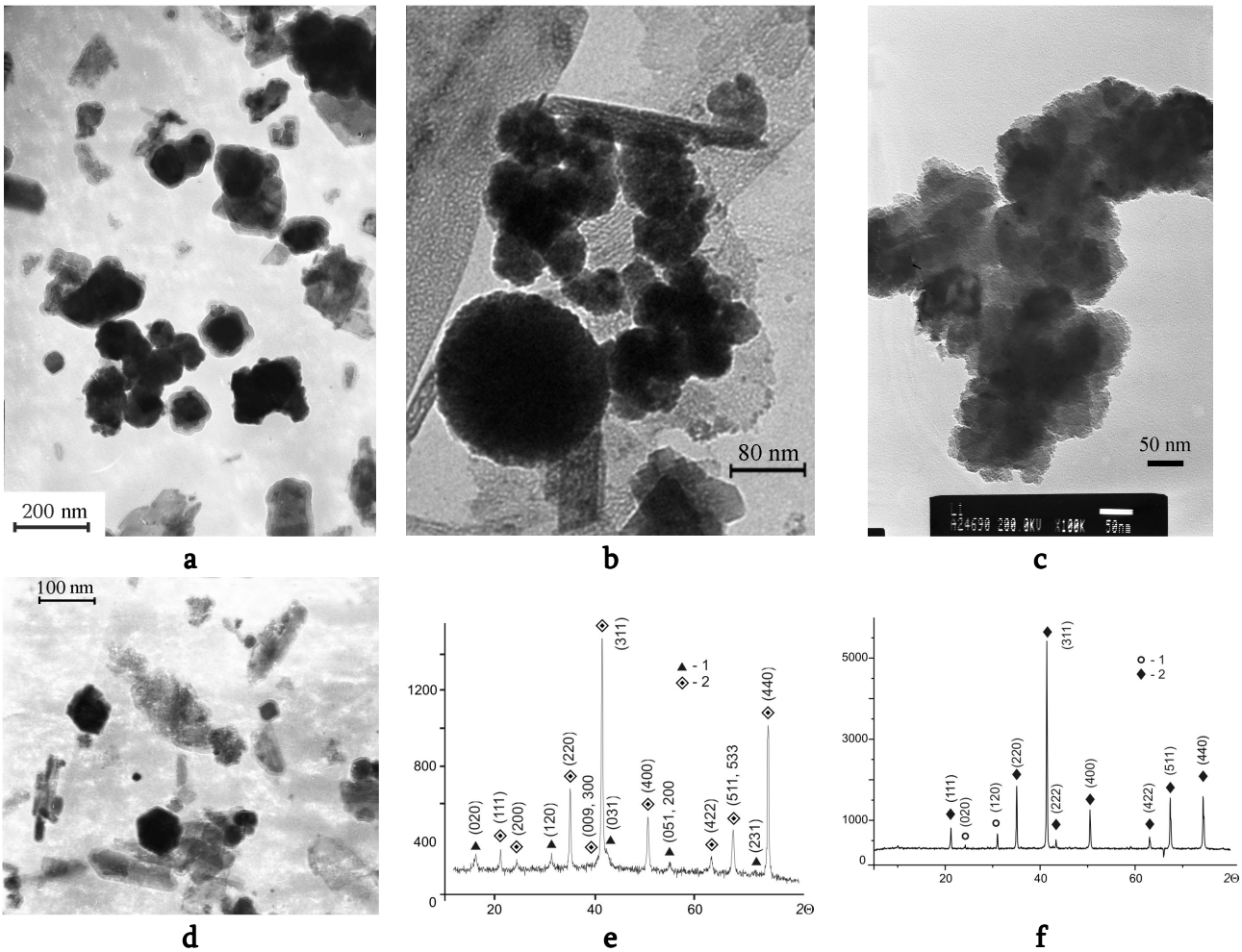

Figure 26. Iron oxides formed with the application of the rotation-corrosion dispergation method. TEM-images of maghemite (a, b, c) and magnetite (d); XRD-data of maghemite (e) and maghemite (f).

Hematite α-Fe_2O_3 does not belong to the typical product formed by applying the RCD method. Usually it forms admixture in the phase composition. Hematite could be obtained when ferrihydrite or goethite are dehydrated at high temperature [59] as well as due to transformation of weak crystalline (amorphous) phase of ferric iron hydroxide in the presence of "trace" amount of ferrous iron in the system [60].

At the time of the work with iron–oxygen nanoparticles formed when the RCD method was used it is required to keep in mind their chemical activity and ability for aggregation, coagulation and phase transformation. Therefore immediately after the formation of the particle layer on the steel surface they could be removed from the reaction area, flushed by distilled water, centrifuged and transferred in other dispersion medium (organic or inorganic including water) that contain surfactants for sol stability.

Conclusions

1. New rotation-corrosion dispergation method for the obtaining of iron–oxygen particles bases on the simple electrochemical process of iron dissolution and oxygen depolarization. The metered oxygen delivery and the agglomeration of ferrous iron on the steel – dispersion medium – air interface and permanent change of the physicochemical condition when the iron–oxygen seed-structures are formed take place due to creating of interrupted contact of the steel surface with air and water solution. Variable particles contact with thin film saturated by hydroxyl, ferrous iron and other disperse medium species and provide for controlled component delivery into the reaction area and create the specific condition for heterogeneous growth of the Green Rust seed particles and the products of it phase transformation.
2. As primary particles registered on the steel surface are Fe(II)–Fe(III) layered double hydroxides and ferrihydrite. The peculiar micelle species are formed in the reaction area and they take place in the formation of Fe(II)–Fe(III) LDH layer on steel surface. Such structures transform in magnetite particles by contact-recrystallization mechanism. The essence of such process lies in the accumulation of the primary magnetite particles on the surface of Fe(II)–Fe(III) LDH, where they form aggregates and prove the recrystallization process.
3. The primary ferrihydrite particles form the structured film of near surface layer. Ferric and ferrous aquahydroxoforms from the reaction area take part in the formation of ferric oxyhydroxides in the near surface layer. The phase transformation into NSL leads to formation of needle like lepidocrocite γ-FeOOH particles on its inner side and goethite α-FeOOH particles on its outer side. The probable mechanism of the well crystallized α-FeOOH and γ-FeOOH micro particles formation are the solution-reprecipitation or reconstructive transformation. According to such mechanism the phase transformation of Fe(II)–Fe(III) LDH in water medium occurs in two stages: the ferrous oxidation into Green Rust lattice with partial solution (destruction) of its nanosized particles and the second precipitation of the well-ordered microsized oxyhydroxide particles.
4. When the mineral phases are formed on iron (steel) surface and in its near electrode layer the iron–oxygen nanoparticles entered in water medium from the reaction area spontaneously form weak-concentrated sols. Usage of stabilizer species applying the RCD method of the iron–oxygen nanoparticles obtaining could change of sedimentative

and aggregative stability of water sols as well as iron oxyhydroxide mineral particles and aggregates formation.

5. According to experimental investigation we found the optimum physicochemical condition for the formation of nanosized iron–oxygen particle such as lepidocrocite, goethite, magnetite, spinel ferrites. As the most important parameters for obtaining nanoparticles during rotation-corrosion dispergation process chemical composition and pH value of dispersion medium, temperature and oxidation condition were pointed out.

References

1. П. А. Ребиндер. Поверхностные явления в дисперсных системах. Коллоидная химия. Избранные труды. 1978, Москва: Наука.
2. В. Ф. Чухров. Коллоиды в земной коре. 1955, Москва: Изд-во АН СССР.
3. Ф. В. Чухров, Л. П. Ермилова, А. И. Горшков. Гипергенные окислы железа в геологических процессах. 1975, Москва: Наука.
4. Н. А. Шабанова, В. В. Попов, П. Д. Саркисов. Химия и технология нанодисперсных оксидов. 2006, Москва: ИКЦ «Академкнига».
5. С. В. Волков, Є. П. Ковальчук, В. М. Огенко, О. В. Решетняк. Нанохімія, наносистеми, наноматеріали. 2008, Киев: Наукова думка.
6. Ред. А. П. Шпака, З. Р. Ульберг. Коллоидно-химические основы нанонауки.. 2005, Киев: Академперіодика.
7. Наноминералогия. Ультра- и микродисперсное состояние минерального вещества. 2005, Санкт Петербург: Наука.
8. U. Schwertmann, R. M. Cornell. Iron Oxides in the Laboratory. Preparation and Characterization. 2000, Wienheim: Wiley–VCH.
9. R. M. Cornell, U. Schwertmann. The Iron Oxides. Structure, Properties, Reactions, Occurrence and Uses. 2003, Weinheim: Wiley–VCH.
10. И. П. Суздалев, Ю. В. Максимов, В. К. Имшенник. Росс. нанотехнол. 2 (2007) 73.
11. J. L. Jambor, J. E. Dutrizac. Chem. Rev. 98 (1998) 2549.
12. Q. A. Pankhurst, J. Connolly, S. K. Jones, J. Dobson. J. Phys. D 36 (2003) R167.
13. P. S. Haddad, T. M. Martins, L. d'Souza–Li, L. M. Li, K. Metze, R. L. Adam, M. Knobel, D. Zanchet. Mater. Sci. & Eng. 28 (2008) 489.
14. A. K. Gupta, M. Gupta. Biomater. 26 (2005) 3995.
15. П. П. Горбик, А. Л. Петрановская, М. П. Турелик. В сб.: Наноматериалы и нанокомпозиты в медицине, биологии и экологии (Сост. П. П. Горбик, В. В. Туров). 2011, Киев: Наукова думка, 188.
16. C. E. Cabello, M. P. Morales, C. J. Serna, V. Barrón, J. Torrent. Clays & Clay Miner. 57 (2009) 46.
17. M. J. W. de Baar, J. T. M. de Jong. In: The Biogeochemistry of Iron in Seawater (Eds. D. R. Turner, K. A. Hunter). 2001, New York: Wiley, 123.
18. Стали и сплавы высоколегированные, коррозионностойкие, жаростойкие и жаропрочные (деформируемые). Марки: ГОСТ 5632–61. 1962, Москва: Стандартгиз.
19. Н. П. Жук. Курс теории коррозии и защиты металлов. 2006, Москва: Альянс.
20. Л. Киш. Кинетика электрохимического растворения металлов. 1990, Москва: Мир.

21. Е. Н. Лавриненко. Наносистеми, наноматеріали, нанотехнології 6 (2008) 529.
22. О. Н. Разумов, В. А. Прокопенко, Е. Н. Лавриненко, С. В. Мамуня, А. П. Скоблик. Наносистеми, наноматеріали, нанотехнології 5 (2007) 217.
23. О. М. Лавриненко. Процеси утворення дисперсних фаз у системі гальваноконтакту залізо-вуглець (кокс) у водному середовищі (Дисс. на соис. уч. ст. канд. хім. наук). 2002, Киев: ИБКХ.
24. Л. И. Антропов. Теоретическая электрохимия. 1984, Москва: Высшая школа.
25. В. В. Зозуля, Е. Н. Лавриненко, В. А. Прокопенко, Н. В. Перцов. Укр. хім. журн. 66 (2000) 48.
26. Т. Е. Корочкова, Н. Г. Шкода, А. А. Чернова, В. М. Розенбаум. Поверхность 4 (2012) 19.
27. В. А. Прокопенко, Е. Н. Лавриненко, С. В. Мамуня, С. Н. Буданкова. Наноструктур. материаловед. 1 (2008) 59.
28. O. M. Lavrynenko, S. V. Netreba, V. A. Prokopenko, Ya. D. Korol. Хімія, фізика та технологія поверхні 2 (2011) 93.
29. Л. Юнг. Анодные оксидные пленки. 1967, Ленинград: Энергия.
30. П. Д. Данков, Д. В. Игнатов, Н. А. Шишаков. Электронографические исследования окисных и гидроокисных пленок на металлах. 1953, Москва: Изд-во АН СССР.
31. L. Legrand, S. Savoye, A. Chausse, R. Messina. Electrochem. Acta 46 (2000) 111.
32. S. Peulon, H. Antony, L. Legrand, A. Chausse. Electrochem. Acta 49 (2004) 2891.
33. Б. В. Дерягин, Н. В. Чупаев, В. М. Муллер. Поверхностные силы. 1985, Москва: Наука.
34. K. J. Mysels, K. Shinoda, S. Frankel. Soap films. Studies of Their Thinning. 1959, London: Pergamon Press.
35. В. А. Прокопенко, Е. Н. Лавриненко, С. В. Мамуня. Наносистеми, наноматеріали, нанотехнології 3 (2005) 513.
36. В. А. Прокопенко, Е. Н. Лавриненко, С. В. Мамуня. Коллоидный журнал 68 (2006) 821.
37. B. C. Christiansen, T. Balic–Zunic, K. Dideriksen, S. L. S. Stipp. In: Proc. 19th Goldschmidt Conf. 2009, Davos, 223.
38. J.-M. R. Genin, M. Abdelmoula, Ch. Ruby, Ch. Upadhyay. C. R. Geosci. 338 (2006) 402.
39. J.-M. R. Genin, A. A. Olowe, Ph. Refait, L. Simon. Corros. Sci. 38 (1996)1751.
40. H. Tamura. Corros. Sci. 50 (2008) 1872.
41. J.-M. R. Genin, Ch. Ruby, A. Gehin, Ph. Refait. C. R. Geosci. 338 (2006) 433.
42. A. L. Mackay. In: Reactivity of Solids. 1960, Amsterdam, 571.
43. Е. Н. Лавриненко, В. А. Прокопенко, Н. И. Лебовка, С. В. Мамуня. Коллоидный журнал 70 (2008) 336.
44. T Sugimoto, E. Matijevic. J. Coll. Interface Sci. 74 (1980) 227.
45. В. В. Манк, О. М. Мірошников, О. В. Подобій, Н. О. Стеценко. Колоїдна хімія: Практикум. 2008, Киев: НУХТ.
46. Ph. Refait, O. Benali, M. Abdelmoula, J.-M. R. Genin. Corros. Sci. 45 (2003) 2435.
47. E. Tronc, P. Belleville, J. P. Jolivet, J. Livage. Langmuir 8 (1992) 313.
48. R. Srinivasan, R. Lin, R. L. Spicer, B. H. Davis. Coll. Surf. A 113 (1996) 97.
49. Ph. Refait, A. Gehin, M. Abdelmoula, J.-M. R. Genin. Corros. Sci. 45 (2003) 659.
50. N. Yee, S. Shaw, L. G. Benning, T. H. Nguyen. Am. Mineral. 91 (2006) 92.

51. М. Д. Глинчук, А. В. Рагуля. Наноферроики. 2010, Киев: Наукова думка.
52. В. А. Прокопенко, Е. Н. Лавриненко, С. В. Мамуня. Наносистеми, наноматеріали, нанотехнології 6 (2008) 385.
53. Е. А. Щукин, А. В. Перцов, Е. А. Амелина. Коллоидная химия. 2004, Москва: Высшая школа.
54. Е. Н. Лавриненко, С. В. Нетреба. Нанострук. материаловед. 2 (2009) 9.
55. J. L. Lyon, D. A. Fleming, M. B. Stone, P. Schiffer, M. E. Williams. Nano Lett. 4 (2004) 719.
56. Е. Н. Лавриненко, В. И. Шостик, И. М. Астрелин, В. А. Прокопенко, Е. А. Маслова. Нанострук. материаловед. 2 (2010) 3.
57. Г. А. Долинский, Е. Н. Лавриненко, И. Н. Тодор, Н. Ю. Лукьянова, В. А. Прокопенко, В. Ф. Чехун. Нанострук. материаловед. 1 (2010) 59.
58. О. М. Лавриненко, В. А. Прокопенко, С. В. Мамуня. Наукові вісті Національного технічного університету України «КПІ» 6 (2005) 143.
59. Y. Cudennec, A. Lecerf. J. Solid Sate Chem. 179 (2006) 716.
60. H. Liu, Y. Wei, P. Li, Y. Zhang, Y. Sun. Mater. Chem. & Phys. 102 (2007) 1.

THE INDUSTRIAL REVOLUTION

F. Habashi

Laval University
Québec City, Canada
Fathi.Habashi@arul.ulaval.ca

Accepted December 22, 2012

Introduction

The 18th century was the century of the Industrial Revolution in England as well as the Chemical Revolution in France by Lavoisier. It was also the century of the beginning of mining and metallurgical education when Schools of Mines were created in Saxony, in Russia, and in the Austrian Empire to give instruction for future miners, metallurgists, geologists, and other technicians needed for the industry. Education was for a long time in the hands of the clergy and there was general apathy for introducing engineering disciplines in universities. Military activities especially after the introduction of gunpowder necessitated the distinction between a military and a civil engineer. The education of the civil engineer grew slowly from an apprentice system to a highly specialized academic discipline. Architects became a distinct group from civil engineers in the Middle Ages during the construction of the great cathedrals.

When the steam engine was introduced in the 18th century, mechanical engineers were organized in a separate group. When mechanical engineers drained water from coal mines and the exploitation of these mines started, the profession of mining engineers was created followed by that of the metallurgical engineers who transformed the coal into coke for iron production in blast furnaces, and iron into steel. The processing of coal tar, produced as a by-product of the coke industry, created the profession of the chemical engineer in the 19th century. This was later developed further, particularly in North America, when the petroleum industry was founded. At nearly the same epoch electrical engineers became organized to deal effectively with the numerous power stations generating electricity to serve industry as well as other human needs.

British engineering education took a form different from that in continental Europe. In England the aspiring engineer began as an apprentice with a working engineer. The explanation for this difference is partly to be found in the early success of British industry where the leading figures of the Industrial Revolution were not formally trained engineers. This had shown that people with no theoretical training could develop new technologies, which eventually transformed society.

Important books dealing with economic problems were published in England, e.g., *The Wealth of Nations* in 1776. In this work, Adam Smith argued in favour of free trade, among other things. The eighteenth century was also the century of systematisation. In Sweden, Carl Linnaues (1707–1778) proposed a system for flora and fauna, Axel Fredrik Cronstedt (1722–1765) classified minerals according to their chemical composition, and Denis Dedirot (1713–

1784) published the *Encyclopedia* in Paris between1751 and 1777 documenting the technology of his time.

Iron and steel

The primitive furnace

The reduction of iron ore to produce metallic iron took place in ancient times in a small furnace 2 to 3 meters high, charged with lumps of iron ore mixed with pieces of charcoal prepared from timber. Air required for burning of charcoal to supply the necessary heat for reduction was supplied by small bellows (**Fig. 1**). The ore lumps were reduced to iron but not melted because the air draft was not strong enough to generate the high temperature needed for melting. When the furnace was cooled, the lump of metallic iron mixed with partially melted gangue minerals and slag, was then removed from the furnace, heated and hammered to get a consolidated metallic product known as "wrought iron". A furnace of this type would produce 1 or 2 kilograms of malleable iron per day, which was enough to supply the need of that time.

Figure 1. A typical furnace located in a forest for producing iron during the Roman Empire. The worker is operating bellows using his feet to blow air in the furnace. On the left hand is a kiln for producing charcoal from wood.

Large charcoal furnace

To increase productivity, larger furnaces were built with larger air bellows mechanically operated by large water wheels (**Fig. 2**). Furnaces were constructed next to large rivers to make use of the flowing water for operating the water wheel. As a result of blowing large amounts of air, the temperature in the furnace increased and the iron produced melted in the furnace. Some iron was tapped directly into moulds in the casting house and the remaining was collected by allowing it to drain into sand moulds (called "pigs") prepared in the immediate vicinity. The product contained much dissolved carbon and was suitable for casting many items because of its high fluidity. A furnace of this period would be 5 to 10 meters high and would produce 10 or 20 tons of iron per day. The maximum size of the furnace was limited by the mechanical strength of the charcoal.

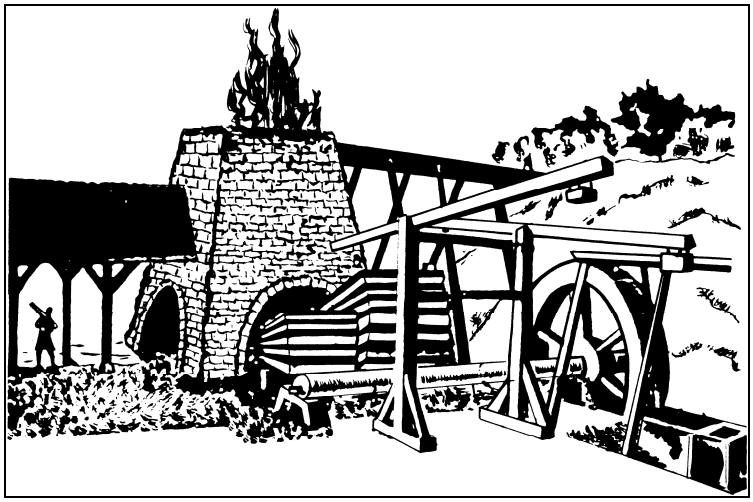

Figure 2. Production of cast iron in a charcoal furnace with large air bellows operated by a water wheel.

Charcoal

Charcoal, the backbone of the iron and gunpowder industries, was produced in piles (**Fig. 3**). An area of 9 – 12 m diameter flat surface of the forest floor was cleared on which center a pole about 5.5 m long was erected. Wood then stacked in four layers around the pole to form a cone shaped pile. The pole then removed, wood chips and kindling were placed down the central chimney hole that was formed. The pile was then covered by a layer of leaves and finally a layer of soil. The charring process started by lighting the wood chips and kindling in the chimney from the top of the mound. To allow air into the pit to drive out the moisture and burn the volatile matter without burning the remaining charcoal, holes were poked through the soil layer. The charring process starts from the top down and requires 10 – 14 days to complete. The soil layer was then slowly raked from the top of the pit to the ground and piled for future use. The remaining charcoal was about one third the original pile of wood. It was allowed to cool then transported to the iron making site.

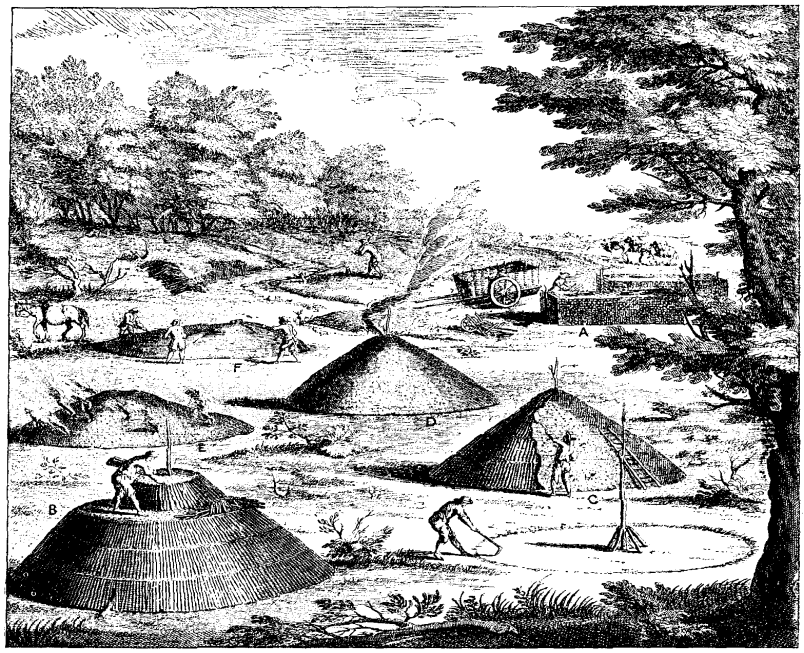

Figure 3. An early method for producing charcoal.

Charcoal was later made in brick kilns, either rectangular or conical in shape. These had a manhole on the top for charging the wood, a door at ground level for raking out the finished charcoal, and several holes around the circumference of the kiln to control the air inlet. Operation of kilns was similar to that of the pits. The problem with this technology was, however, that it led to deforestation and gradually increased cost of production. A furnace producing 20 tons / day of pig iron consumed about 200 tons of charcoal which were obtained from 0.8 acres of forest / day, or 292 per year. Once all the local trees were cut down, wood or charcoal would have to be transported from far away, usually by wagons drawn by horses which meant additional cost.

The Industrial Revolution

The Industrial Revolution started in England in the 18th century and took place in two stages: the first when coke replaced charcoal in 1709 and the second when the steam engine became widespread in 1780s. As a result, pig iron was produced in increacing quantitiies for machinery and constructional purposes. Today, iron production in one year exceeds that of all other metals combined in ten years. It is a huge industry that started from a modest furnace producing 1 – 2 kilograms metal per day to a gignatic reactor producing 10000 tons per day.

The use of coke

When coal mining became safe, many unsuccessful attempts were made to replace charcoal by coal until the solution was found by first transforming coal into coke. The industrial revolution started in England in 1709 by Abraham Darby I (1677 – 1717) of Coalbrookdale near Birmingham (**Fig. 4**) when he substituted charcoal by coke. Coke is produced from coal by baking — it is porous and can withstand high mechanical pressures. Hence larger furnaces could be built which resulted in a further increase in production. Coal cannot be used because it contains appreciable amount of objectionable sulfur impurities and also because it softens during heating and renders the charge impermeable.

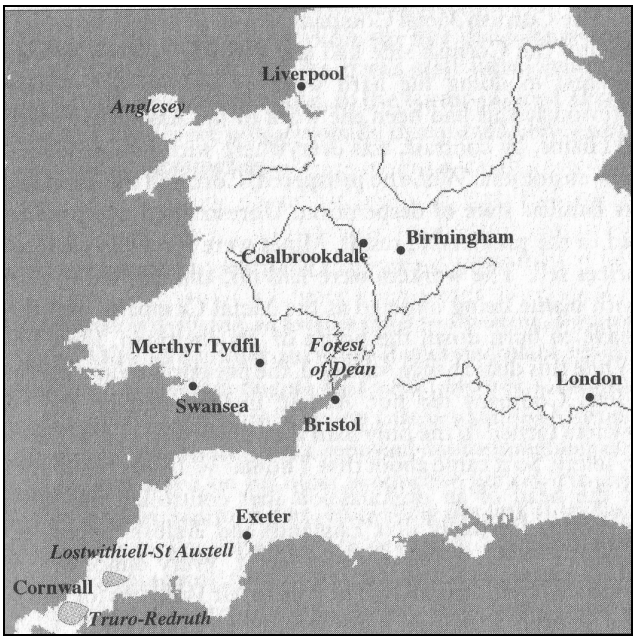

Figure 4 . Location of Coalbrookdale near Birmingham.

Coal mining was also unsafe because of the natural gas explosions until Humphry Davy introduced the miner's safety lamp. Further, a great effort was needed to pump out the water flooding the mines. Using coal solved the problem of cutting trees from the forests which were needed to build ships and homes.

Coke became available at a much lower cost than charcoal, but iron produced using coke was of inferior quality because of the large amount of impuritites. Coke was first produced by piling coal in mounds and partially burning it in the open air in the same way charcoal was made. Beehive ovens replaced the open air method in 1763 in which the volatile matter was burned to supply heat for carbonization. The first attempt to recover the volatile matter was in the horizontal retorts system. The gas collected was known as coal-gas and was first used for illumination and later as a fuel. Ammonia was also recovered during coke making and this was an important source of this chemical before the invention of the synthetic method. Now large batteries of vertical retorts are used. Volatile matter collected proved to be an important source of chemicals. The distillation of the tar and the separation of its different components became the basis of the organic chemical industry in the 19th century. Today, a coke manufacturing plant is a battery of hundreds of vertical retorts assembled together.

Cast iron

To obtain an iron of better quality that can be cast into shapes of thin thickness, a small shaft furnace known as "cupola" (Fig. 5) was invented in 1795 by William Wilkinson from Shropshire. By melting pig iron in the cupola and blending it with other material, he was able to produce "cast iron" of exact composition and of equal quality to the cast iron produced from a charcoal furnace. Consequently, England produced high-quality cannons for the navy and this was one of the basis on which the British Empire was founded.

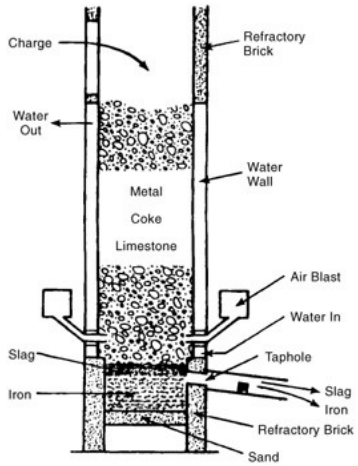

Figure 5. Cupola.

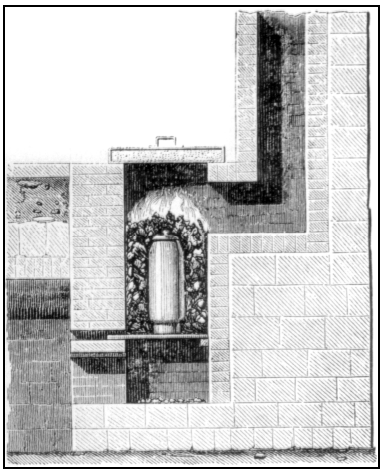

Figure 6. Production of cast steel in cementation furnace.

Steel

To produce a high quality iron for tools and knives, it was necessary to refine this iron in what was known as a "finery". Small pieces of the iron were re-melted in an oxidizing atmosphere to remove as much as possible of the carbon to produce a malleable product equivalent to wrought iron. Mathias Meysey and William Ellyott in Birmingham invented in 1614 the "cementation process" to make a high quality product known as "blister steel". In this process bars of wrought

iron were embedded in charcoal and sealed in chests which were maintained at red heat for ten days. The iron absorbed carbon, but the steel was more highly carburized near the surface than at the core (**Figs. 6 – 9**).

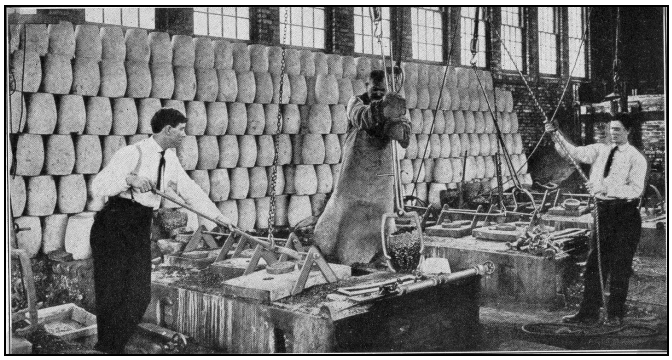

Figure 7. Production of cast steel: cementation furnace and crucibles.

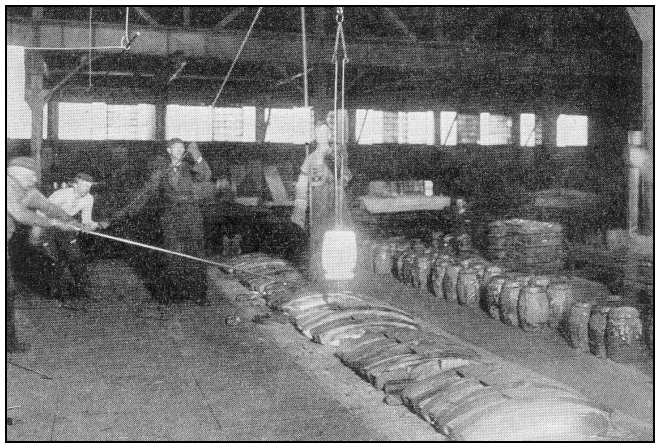

Figure 8. Production of cast steel: removing of crucible from cementation furnace.

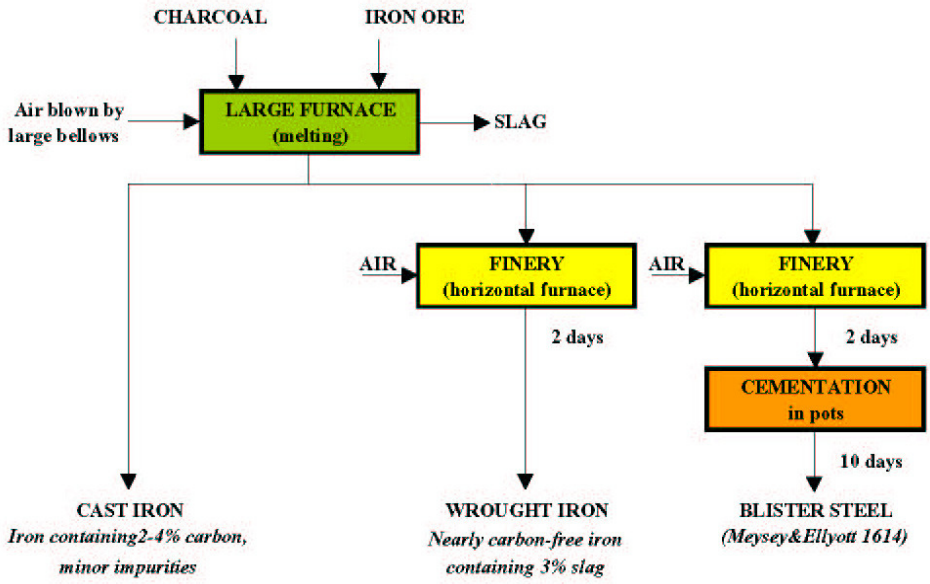

Figure 9. Production of cast iron in a charcoal furnace with large air bellows and the introduction of the "cementaton" process.

Pig iron produced from the blast furnace can be readily cast. However because of the presence of large amount of carbon and a number of other impurities it is brittle and hence cannot be forged to shape. To render it malleable, the carbon content was lowered by melting the pigs in a "fining" furnace to oxidize the carbon and produce wrought iron containing less than 1 % carbon. It was used for the production of nails, small arms, agricultural implements, horseshoes, wire, locks, and bolts. Benjamin Huntsman (1704 – 1776) in Sheffield in 1740 produced an improved steel by re-melting bars of blister steel produced by the cementation process in closed crucibles to produce a "cast steel" of uniform carbon content and much better quality.

Pig iron

Pig iron produced in the coke blast furnace contained 3 – 5 % carbon and other impurities which were not present in the iron produced in the charcoal furnace. It was hard and brittle, of inconsistant composition, but cheap and of high fluidity which simplifiied casting. It was used for making pots and pans, fire grates, some machine parts especially for steam engines, anchors, cannons and cannon balls. This was particularly important in warfare, because before the arrival of pig iron, cannons were made of bronze or brass which were more expensive. Once the blast furnace technology using coke was established, efforts were made to economize coke consumption and to cope with increased productivity. This took place, however, in the first half of the 19th century.

The availablity of large deposits of iron ore and coal, and the undesirability of reliance on charcoal for iron smelting, were stimuli for technical development. The production of large amounts of iron made possible the casting of large number of cannons as well as the production of armour plates for battle ships. As well, it permitted the construction in 1779 of the first bridge in the world made of iron (**Fig. 10**), across the Severn River near Coalbrookdale. The importance of this bridge lies in the fact that although iron had been used for thousands of years it had not been a major construction material because there was not enough of it. Outside Britain the adoption of coke furnaces proceeded very slowly.

Figure 10. The first iron bridge at Coalbrookdale across the River Severn.

Steel by the puddling furnace

Henry Cort (1740 – 1800) from Lancater in England in 1784 invented the "puddling process" in which by a careful control of air and time of heating in the furnace, it was possible to transform directly pig iron into cast steel (Figs. 11 – 13). The aim of this process was to retain a sufficient carbon content in the product to render it hard but not brittle. The correct conditions for this were determined by experience since the role of carbon in steel was not yet known. The process was tedious and expensive; it took 3 to 4 days at high temperature to produce a few hundred kilograms of the product, but this was the price to pay for a high quality steel. Naturally steel produced by the puddling process was an expensive alloy. It was used for making special tools, knives, springs, etc., but was not a material of construction. Many puddling furnaces were constructed, the process was mechanised, and the material became very popular that Gustave Eiffel used it for constructing his tower in 1889 on the occasion of hundredth anniverary of the French Revolution. But, it was tedious and expensive. **Fig. 14** gives a summary of processes for producing the first steel.

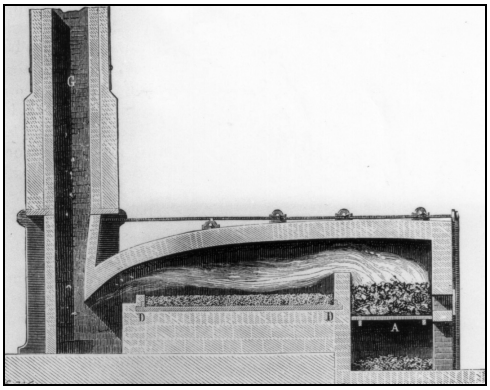

Figure 11. Puddling furnace.

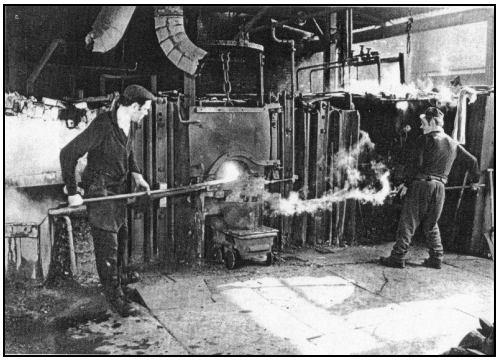

Figure 12. Workers operating a puddling furnace.

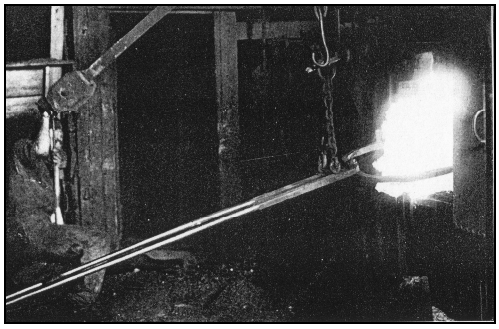

Figure 13. A lump of few kilograms of steel produced in the puddling furnace.

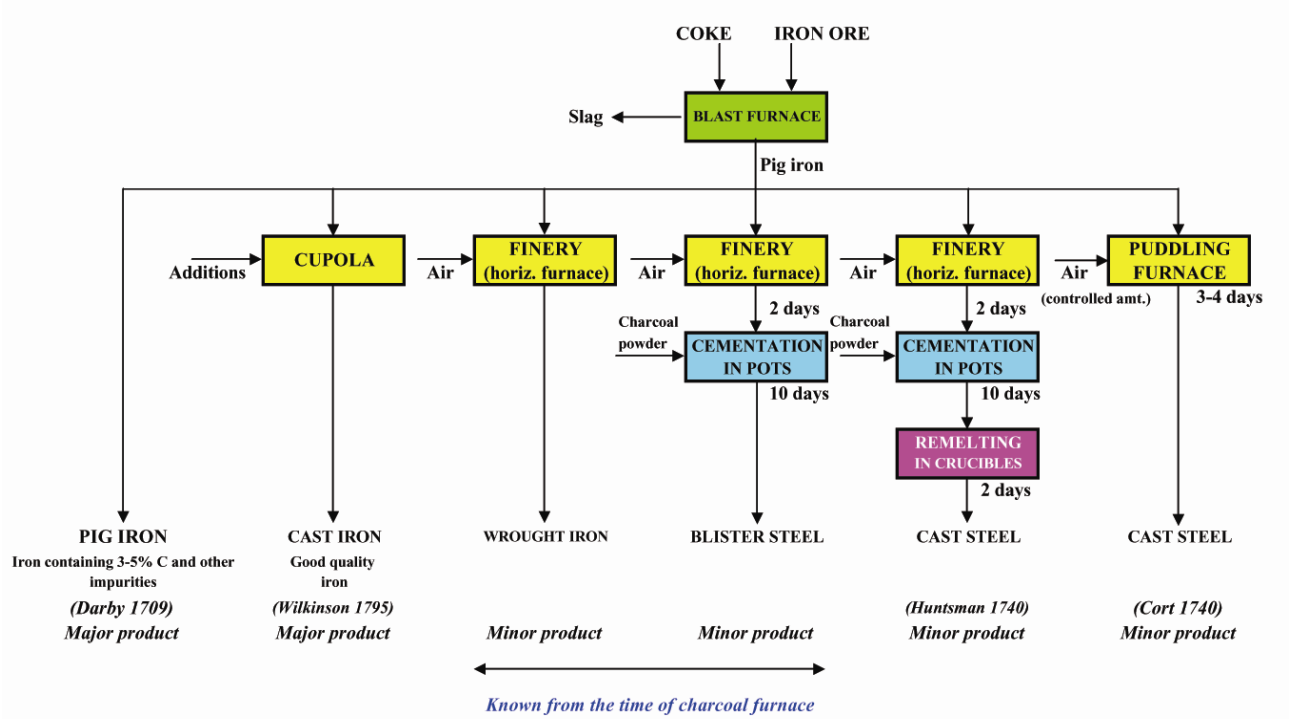

Figure 14. The first stage of the Industrial Revolution. Production of Cast iron in a coke blast furnace and the different varieties of steel.

The steam engine

The steam engine came at a time when wood was the main fuel for industry and household. Wood was also needed for the building industry and for ship building. The steam engine required a huge demand for fuel which could not be satisfied by the shrinking forests. As a result, attention was directed towards the exploitaion of coal. Once the safety lamp was invented by Humphry Day (1778 – 1829) in England and coal mining became relatively safe, the industry started to shift from wood burning to coal burning economy. The steam engine was responsible for solving the problems in the iron industry. The growth of the industry suffered from the following:

- Water power was neither abundant nor reliable. Power was needed for operating the pumps to drain water from coal mines, the bellows to blow air in the blast furnace, the hammers for forging, and the rolling mills.
- The use of coke necessited a more powerful blast than that obtained from water-driven bellows because of its higher ignition temperature.
- A cheap way to transport coal in bulk to the coke making plant which is located near the blast furnace.

The steam engine was invented to fulfil these needs. The idea of using steam for doing work goes back to 1695 when Denis Papin (1647 – 1712), a French Huguenot who found refuge in England in 1675, demonstrated this principle in a simple model. Newcomen's machine invented in 1712 was the first attempt to solve the problems associated with this idea. But it used large amounts of coal to boil water to generate steam which was then condensed by cold water spray to create the vacuum needed to operate the machine. It was James Watt (1736 – 1819) (**Fig. 15**) who in 1770s successfully built a machine that economized greatly on the coal needed, by introducing a separate condensing chamber for the steam so that the cylinder could

remain hot throughout every stroke. However, it was not until 1784 that the steam engine became a reality and started to replace the water wheel. The bellows were no longer needed and air could be blown in the furnace through tuyeres. George Stepheson (1781 – 1848) (**Fig. 16**) from Northumberland in 1820s solved the problem of coal transportation by inventing the steam locomotive.

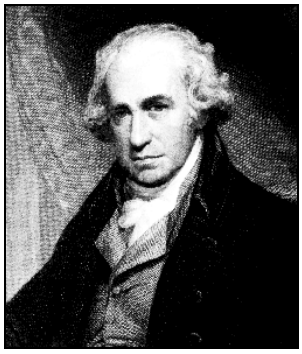

Figure 15. James Watt (1736 – 1819).

Figure 16. George Stepheson (1781 – 1848).

The steam engine made possible the utilization of ample power. This had tremendous impact on industry and commerce, and was responsible also for the second stage of the Industrial Revolution which can be summarized, as follows:

- Work once performed by hand could now be done on machines powered by steam engines.
- The manufacturers were freed from depending on the water wheel or the windmill for their source of energy.
- Large cotton mills were established in Lancashire where cotton was imported from the colonies and the textile products were exported back to them.
- Steam ships replaced sailing boats which meant faster transportation at sea.
- A system of canals was created in England for the cheap transportation of coal by water. This was later replaced by trains moved by steam locomotives. Trains also replaced horse-driven wagons which meant faster transportation on land.
- The food industry greatly benefitted from the steam engine. Improved technique for rolling wrought iron plates favorably affected the manufacture of tin plate for food containers and utensils needed for the navy.

The British machine economy incited many foreigners to visit Britain for the purpose of studying the bew technology. One of these was the French government official Gabriel Jars (1732–1769) who visited England in 1764 – 1765 and wrote his observations in his book *Voyages Metallurgiques* published in 1774, five years after his early death.

Further development

The Industrial Revolution continued further in England when steel was produced in greater amounts, faster, and much cheaper in the 19th century when Henry Bessemer (1813 – 1898) (**Fig. 17**) from Hertfordshire invented his process in 1856. The tedious and expensive "puddling process" could now be replaced by a fast process that did not use a fuel — heat required to keep the metal molten was generated by the oxidation of the impurities themselves present in the iron. Tons of pig iron could be transformed in less than half an hour by simply blowing air through the molten metal (**Fig. 18**). The product became known as "mild steel".

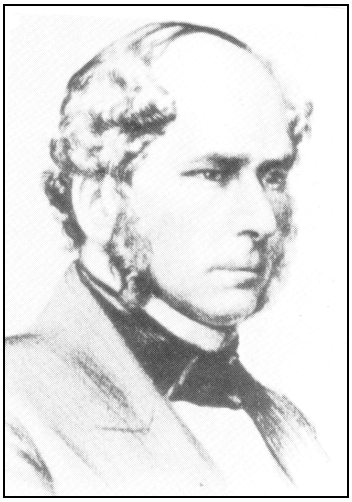

Figure 17. Henry Bessemer (1813 – 1898).

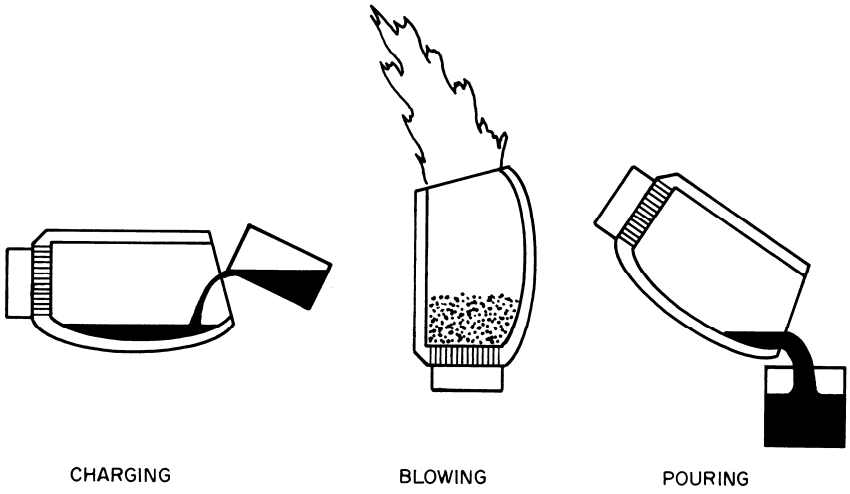

Figure 18. Bessemer process.

This made England the master of the world. She was at least fifty years in advance to other European powers in iron and steel making. In addition to steelmaking, Britain was the center for copper, zinc, tin, and platinum metals production. Copper matte was shipped from as far away countries as Chile and Montana to be refined in Swansea in Wales. Nehemial Champion in Bristol was the first in Europe to produce metallic zinc from calamine and zinc blende in 1702. Bristol was also a center for brass manufacture while Cornwall was a center for the production of tin. Innovation in spinning and weaving also took place in England as part of the Industrial Revolution.

The transition from wood to coal economy

When wood was used as the basic fuel, as charcoal in blast furnaces, as a major component in gunpowder, and as a basic material for ship building, there was also a chemical industry based on wood by-products. Wood was the source of tar, pitch, and resin needed as a presevative, particularly for timber for ship building. Potash was recovered by leaching the wood ash with water and was used for making soap and glass. Turpentine was used as a solvent and for making lamp black for inks. Acetic acid was also obtained as a by-product of wood distillation in form of calcium acetate from which acetone was made by dry distillation. All these were widely used material.

When coal replaced wood, other industries came into existance, especially when the volatile matter was collected during the carbonization process. Coal gas in the earlier years of the industry was used almost entirely as an illuminant. Later gases became a source of ammonia, elemental sulfur (from H_2S), and gaseous fuel. The coal tar was distilled to produce a varitey of organic compounds like benzene, toluene, phenol, naphthalene, anthracene, etc., as well as pitch. This baceme the basis of the organic industry for manufacturing dyestuffs, explosives, pharmaceuticals, etc.

The blast furnace

The blast furnace gradually increased in size as a result of using air blowers operating by the steam engine (**Figs. 19** and **20**) hence increased productivity.

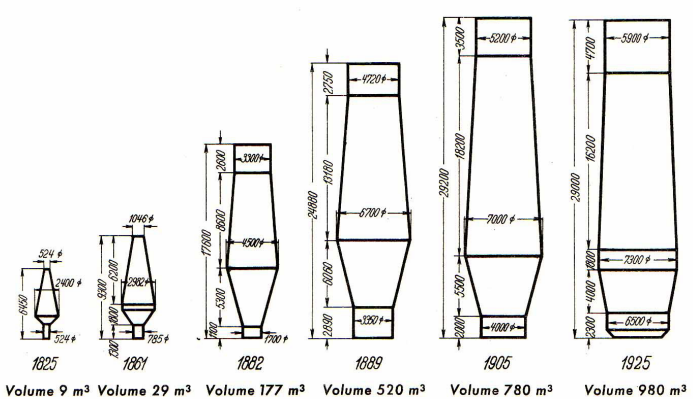

Figure 19. Developments in the construction of blast furnace.

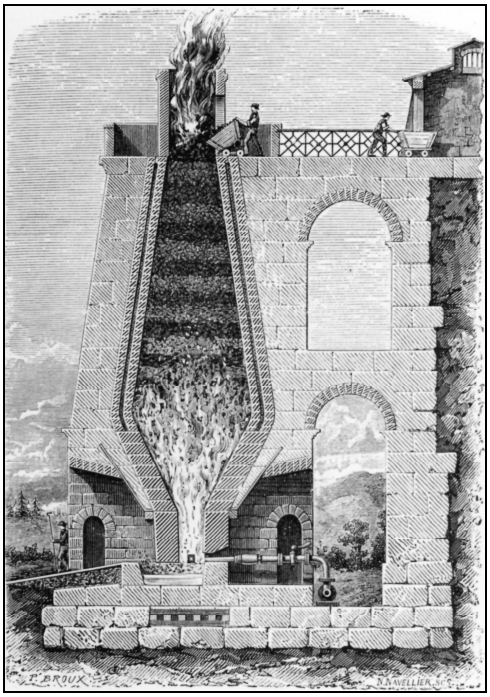

Figure 20. An 18thcentury blast furnace in which air is blown by a steam engine.

Capitalism and colonialism

The beginning of capitalism was a direct result of the Industrial Revolution. As a consequence there was an over supply of products and a need for markets as well as for raw materials. Colonization was the solution to this problem. Iron and coal continued to be the core of industry, but once petroleum was discovered in North America, the centre of gravity of imperialism shifted from Britain to USA. This coincided with the invention of motor cars and aeroplanes. The shift became complete after World War II and the New Industrial Revolution became based on petroleum and aluminum.

Suggested reading

1. F. Habashi. Readings in Historical Metallurgy. Volume 1: Changing Technology in Extractive Metallurgy. 2006, Québec City" Métallurgie Extractive Québec. – Distributed by Laval University Bookstore, www.zone.ul.ca.

მასკანირებელი გვირაბული ელექტრონული მიკროსკოპი – მოწყობილობა, რომლითაც შეიძლება ცალკეული ატომების და მოლეკულების დანახვა

ც. რამიშვილი

პ. მელიქიშვილის ფიზიკური და ორგანული ქიმიის ინსტიტუტი
ი. ჯავახიშვილის სახელობის თბილისის სახელმწიფო უნივერსიტეტი
rtsiuri@yahoo.com

მიღებულია 2013 წლის 20 აგვისტოს

“ჩვენ ჭეშმარიტად გვჯერა, რომ ატომური სტრუქტურების სილამაზე სტიმული გახდება ამ მეთოდის გამოყენებისთვის იმ ამოცანების გადაჭრისთვის, რითაც მას შეუძლია ყველაზე მეტი სარგებლობა მოუტანოს კაცობრიობას.”

გ. ბინიგი, ჰ. რორერი, 1986 წ.

სტატია ეძღვნება ნობელის პრემიის ლაურეატს, ნანოტექნოლოგიის ერთ-ერთ ფუძემდებელს შვეიცარიელ ფიზიკოსს ჰაინრიხ რორერს (Heinrich Rohrer, 1933.06.06, Buchs, შვეიცარია), რომელიც ხანგრძლივი ავადმყოფობის შემდეგ სულ ახლახანს გარდაიცვალა 79 წლის ასაკში (2013.16.05, Wollerau, შვეიცარია).

ჰაინრიხ რორერი სკოლის დამთავრების შემდეგ 1951 წ. მოეწყო შვეიცარიის სახელმწიფო ტექნოლოგიურ ინსიტუტში (ETH) ფიზიკის განყოფილებაზე. 1960 წ. ის იქვე გახდა დოქტორი (PhD). მისი მასწავლებლები იყვნენ ცნობილი ფიზიკოსები ვოლფგანგ პაული (ნობელიანტი, 1945) და პაულ შერერი. შემდეგ ჰ. რორერი მუშაობდა რატგერსის (აშშ) უნივერსიტეტში. 1963 წ. რიუშლიკონში (Rüschlikon, ციურიხის კანტონი, შვეიცარია) ის შეუერთდა IBM-ს (IBM – International Business Machines Corporations, მსოფლიოში უდიდესი აპარატურული და პროგრამული უზრუნველყოფის ტრანსნაციონალური კომპანია, აშშ) სამეცნიერო-კვლევით ჯგუფს; თავდაპირველად ის სწავლობდა სხვადასხვა მასალებსა და შენადნობებზე მაგნიტური ველის მოქმედებას; მან აქვე მომუშავე გერმანელ ახალგაზრდა ფიზიკოსთან გერდ კარლ ბინიგთან (Binnig, Gerd Carl) ერთად 1979 წ. დააპატენტა, შემდეგ კი (1981 წ.) დააპროექტა და ააგო მსოფლიოში პირველი მასკანირებელი (რასტრული) გვირაბული მიკროსკოპი (Scanning Tunneling Microscope – STM); მათ გერმანელ ელექტროინჟინერ და გამოგონებელ ერნსტ რუსკასთან (Ernst Ruska, 1906 – 1988) ერთად 1986 წ. მიენიჭათ ნობელის პრემია ფიზიკაში; პრემიის ნახევარი გადაეცათ გ. ბინიგს და ჰ. რორერს მასკანირებელი გვირაბული მიკროსკოპის შექმნისთვის და მეორე ნახევარი – ე. რუსკას ფუნდამენტური სამუშაოებისთვის ელექტრონულ ოპტიკაში და ელექტრონული მიკროსკოპის შექმნისთვის.

ჰაინრიხ რორერი, შვეიცარია, IBM.
ნობელის პრემიის ლაურეატი, 1986.

ერნსტ რუსკა, გფრ,
ფრიტც–ჰაბერის ინსტიტუტი,
ნობელის პრემიის ლაურეატი, 1986.

ნობელის პრემიის საორგანიზაციო კომიტეტის გადაწყვეტილებაში აღნიშნული იყო: "1986 წლის პრემია ფიზიკაში – მასკანირებელი გვირაბული მიკროსკოპის შექმნისთვის, რომელიც ეფუძნება ვაკუუმში მყარი სხეულის ზედაპირის სკანირებას (მოსინჯვას) ნემსის წვრილი ბოლოთი. ეს ტექნიკა გამოიყენება ნახევრადგამტარების ფიზიკაში და მიკროელექტრონიკაში, დნმ მოლეკულის კვლევაში. ლაურეატების უდიდესი მიღწევაა ის, რომ, დაეყრდნენ რა ისინი თავიანთ ადრინდელ სამუშაოებს და იდეებს, მათ შესძლეს გადაელახათ წარმოქმნილი უდიდესი ექსპერიმენტული სიძნელეები საჭირო სიზუსტისა და სტაბილობის ხელსაწყოს შექმნისას."

ოპტიკური და ელექტრონული მიკროსკოპებისაგან განსხვავებით, სადაც მიიღება ბრტყელი გამოსახულება, მასკანირებელი ზონდური გვირაბული მიკროსკოპი არის მოწყობილობა, რომელიც იძლევა შესაძლებლობას დავინახოთ ცალკეული ატომების და მოლეკულების სამგანზომილებიანი გამოსახულება.

ცხადია, კალმის წვერზე მასკანირებელი გვირაბული მიკროსკოპის შექმნის პროექტი დიდი ხნით ადრე იყო მოფიქრებული, მაგრამ STM-ის აგებიდან მხოლოდ ორი წლის შემდეგ, 1982 წელს მოახსენეს გ. ბინიგმა და ჰ. რორერმა პირველი ინფორმაცია მის შესახებ; პირველად მათ მიიღეს ოქროსა და $CaIrSn_4$-ის ზედაპირების ატომური სტრუქტურების სურათი (Surface studies by scanning tunneling microscopy. Phys. Rev. Lett., 1982, 49, 1, 57-61) და შემდგომ – უფრო დახვეწილი ატომური სტრუქტურის სურათი Si (111) ზედაპირისთვის (7 × 7 reconstruction on Si (111) resolved in real space. Phys. Rev. Lett., 1983, 50, 2, 120-123). STM-ის გამოგონებაში არსებითი როლი ითამაშა ჰ. რორერმა, როგორც ამას აღნიშნავენ IBM-ში. ნობელის პრემიის გარდა, იგი დაჯილდოვეს გერმანელ ფიზიკოსთა პრემიით, ოტო კლუნგის პრემიით, ჰევლეტ პაკარდის ევროპელ ფიზიკოსთა პრემიით, საუდის არაბეთის მეფის ფაიზალის საერთაშორისო პრემიით, კრესონის მედლით და ის ჩაირიცხა აშშ ნაციონალურ გამომგონებელთა დიდების დარბაზში; მას მიანიჭეს IBM-ის საპატიო თანამშრომლის ტიტული (IBM Fellow).

ჰ. რორერის კარიერა მთლიანად იყო დაკავშირებული IBM-თან, მხოლოდ ერთი წლით, 1970 წელს იმყოფებოდა ის აშშ-ში, სანტა ბარბარაში, კალიფორნიის უნივერსიტეტში. 1986 – 1988 წლებში ის იყო ციურიხში IBM-ის ლაბორატორიის ფიზიკურ მეცნიერებათა დეპარტამენტის ხელმძღვანელი. პენსიაზე გასვლის შემდეგაც – 1997 წლიდან აგრძელებდა სამეცნიერო საქმიანობას მსოფლიოს სხვადასხვა

სამეცნიერო ცენტრებში ნანოტექნოლოგიის მიმართულებით. მისი ბოლო სამუშაო ადგილი იყო ესპანეთში აკუსტიკის ინსტიტუტში მცირე სისტემების ფიზიკისა და ნანოტექნოლოგიების ლაბორატორია.

1986 წ. ნობელიანტების პატივსაცემად გამართულ ბანკეტზე სტოკჰოლმში წარმოთქმულ სიტყვაში ნობელიანტმა ერნსტ რუსკამ აღნიშნა, რომ მის მიერ ელექტრონული მიკროსკოპის გამოგონება არ იყო მისი მიზანდასახული ამოცანის შედეგი, მაშინ ის მუშაობდა კათოდური სხივების ოსცილოგრაფის სრულყოფაზე და შემთხვევით მივიდა ელექტრონების ნაკადით ვიზუალიზაციის შესაძლებლობასთან; ხოლო ჩემ კოლეგებს – გ. ბინიგს და ჰ. როერს, აღნიშნავდა ე. რუსკა, თავიდანვე ჰქონდათ დასახული ამოცანა და თავიანთი საოცარი იდეის მეშვეობით წარმატებით შეძლეს წმინდა მექანიკური საშუალებებით ატომურ ზომებამდე წინსვლა. გ. ბინიგმა და ჰ. როერმა არსებითად გააუმჯობესეს ელექტრონული მიკროსკოპის კონსტრუქცია და შექმნეს ზონდი, რომლის წვეროზე არის ერთადერთი ატომი; 1981 წელს მათ მიერ შექმნილი გვირაბული მასკანირებელი ზონდური მიკროსკოპით მათ აჩვენეს მთელი რიგი კრისტალების, დნმ-ის ჯაჭვების ზედაპირის სტრუქტურები და პირველად შეძლეს პატრონი-უჯრედისგან ვირუსის მოცილებისთვის თვალის დევნება.

როგორ აკვირდებიან ნანოობიექტებს?
მასკანირებელი გვირაბული მიკროსკოპი

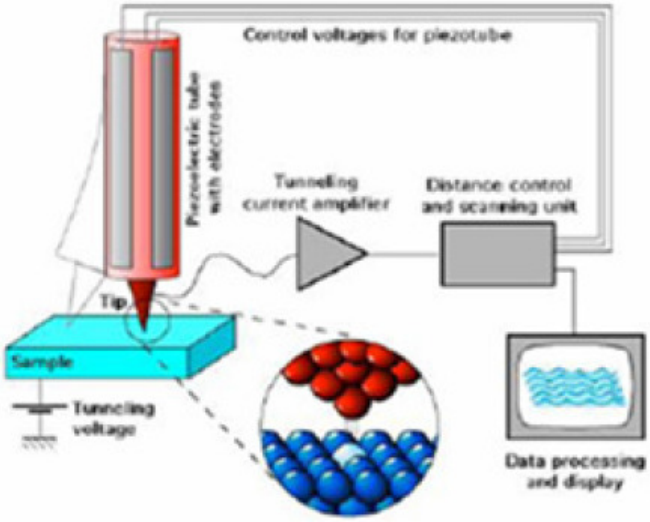

გერდ ბინგი და ჰაინრიხ როერი, IBM-ის ლაბორატორია ციურიხში, 1981 წ. (ნობელის პრემია 1986 წ. გაიყვეს გვირაბული ელექტრონული მიკროსკოპის გამომგონებელ ერნსტ რუსკასთან).	მასკანირებელი გვირაბული მიკროსკოპი (ინგლ. STM – scanning tunneling microscope), მასკანირებელი ზონდური მიკროსკოპის ვარიანტი, რომელიც განკუთვნილია გამტარი ზედაპირების რელიეფის გაზომვებისათვის მაღალი სივრცითი გარჩევადობით (0.06 ნმ).

აღსანიშნავია, რომ გ. ბინიგმა თავის კოლეგასთან IBM-ის საკვლევი ცენტრიდან ციურიხში ქრისტოფ გერბერთან (Christoph Gerber) და სტენფორდის უნივერსიტეტის პროფესორ კალვინ კვეიტთან (Calvin Quate) ერთად 1986 წ. შექმნა ატომურ ძალური მიკროსკოპი, რომლითაც, განსხვავებით STM-გან, შეიძლება არა მარტო ლითონებისა და ნახევრადგამტარების, არამედ დიელექტრული მასალების კვლევაც.

ნანოსტრუქტურების და აფსკური მასალების კვლევის ძირითადი მეთოდი დღეისათვის არის გვირაბული მასკანირებელი მიკროსკოპია, რომელსაც საფუძვლად უდევს მეოცე საუკუნის ოცდაათიან წლებში რამდენიმე მეცნიერის (E. Schrödinger, F. Hund, G. Gamow, R. Gurnay, E. Condon) თეორიული მოსაზრებების საფუძველზე გაკეთებული დასკვნა, ნაწილაკის მიერ ენერგეტიკული ბარიერის გადალახვის შესაძლებლობაზე (ნულისგან განსხვავებულ ალბათობაზე) იმ შემთხვევაში, როდესაც მისი სრული ენერგია მნიშვნელოვნად ნაკლებია პოტენციალური ბარიერის სიმაღლეზე. ამ ეფექტს ნახევარი საუკუნის შემდეგ, 1981 წელს ეწოდა გვირაბული ეფექტი. ქვანტური გვირაბირების ამ ეფექტით აიხსნა მრავალი ექსპერიმენტული ფაქტი და მის საფუძველზე შეიქმნა გვირაბული დიოდები იაპონელი მეცნიერის ლეონა ესაკის (Leona Esaki) მიერ, რაც აღინიშნა ნობელის პრემიით 1973 წელს. ეს ეფექტი უდევს საფუძვლად 1981 წელს გ. ბინიგის და ჰ. რორერის მიერ მასკანირებელი გვირაბული მიკროსკოპის და შემდგომ 1986 წელს გ. ბინიგის, ჰ. ჰერბერის და ს. კვაიტის მიერ ატომურ-ძალური მიკროსკოპის (AFM) შექმნას; აგრეთვე – ტექნოლოგიებს, რომლებითაც შეიძლება ნანომეტრის რიგის ზემცირე ზომის ნაწილაკებით ოპერირება.

ნებისმიერი მასკანირებელი ზონდური მიკროსკოპიის საფუძველია ზონდის მოქმედება საკვლევ ზედაპირთან მექანიკური, ელექტრული ან მაგნიტური ძალების საფუძველზე. კერძოდ, მასკანირებელ გვირაბულ მიკროსკოპიაში სისტემის "გამოძახილია" გვირაბული დენი ზონდსა და მასკანირებელ ზედაპირს შორის, ატომურ ძალურ მიკროსკოპიაში – ზონდის ზედაპირთან ურთიერთქმედების ვან დერ ვაალსის ძალები, ხოლო მაგნიტურ-ძალური მიკროსკოპიის შემთხვევაში ზონდი რეაგირებს ზედაპირის ზემოთ მაგნიტური ველის ცვლილებაზე; ახლო ველის მასკანირებელ ოპტიკურ მიკროსკოპიაში (near-field scanning optical microscope, NSOM) ნიმუშის ოპტკური თვისებები დეტექტირდება დიაფრაგმით, რომელიც მოთავსებულია საკვლევი ზედაპირის უახლოეს ზონაში.

გვირაბული მასკანირებელი ზონდური მიკროსკოპის ძირითადი ელემენტია მინიატურული, ძალიან წვრილი, ლითონის (Au, W, Pt–Ir) ზონდი (probe); ხანდახან მას უწოდებენ სასინჯს ან უბრალოდ ნემსს, რომლის წვეროში ზღვრულ შემთხვევაში შეიძლება იყოს მხოლოდ ერთი ატომი. ატომური ზომების წვეროს მქონე ნემსის მოსამზადებლად წინასწარ აღნიშნული ლითონის ნემსებს ამუშავებენ *ex situ* (მექანიკური გაპრიალება, გახლეჩა ან ელექტროქიმიური ამოჭმა) და შემდეგ ახდენენ *in situ* დამუშავებას ზემაღალი ვაკუუმის კამერაში. ზონდების სიმაღლეა 3 – 15 მკმ, სიმრუდის რადიუსი – 10 ნმ-ის რიგისაა.

ზონდი ზედაპირის გასწვრივ მოძრაობს დაახლოებით 0.5 – 1 ნმ მანძილზე, ე.ი. ის არ ეხება მას, რაც აუცილებელი პირობაა გვირაბული დენის არსებობისთვის (უფრო მცირე მანძილებზე ჩნდება ძლიერი, ჩვეულებრივი ელექტრული დენი, უფრო დიდ მანძილებზე კი – გვირაბული დენი ხდება მინელებადი, მცირე). ზონდსა და ზედაპირს შორის მოდებულია რამდენადმე ნაკლები ელექტრული ძაბვა (მაგ., 0.1 – 1 ვ), ვიდრე ეს საკმარისია ზედაპირიდან ელექტრონების მოხლეჩისთვის; ნემსის ზედაპირზე წარმოიქმნება მცირე დადებითი მუხტი, ამიტომ ზედაპირიდან ელექტრონები იწყებენ

ზონდზე შეუფერხებლად გადასვლას (გვირაბირებას) პოტენციალური ბარიერის (ღრეჩოს) გავლით ზონდისკენ და სისტემაში ზედაპირი–ზონდი აღიძვრება გვირაბული დენი.

მასკანირებელი გვირაბული მიკროსკოპის (STM) მოქმედების პრინციპი ემყარება წარმოქმნილი გვირაბული დენის ძალის გაზომვას; დენის გავლისთვის აუცილებელია, რომ ნიმუშიც და ნემსის წვეროც იყოს დენის გამტარი ან ნახევრადგამტარი. დიელექტრიკების გამოსახულებას STM ვერ მოგვცემს. ელექტრონების გვირაბირება ხდება ნემსისა და ზედაპირის ატომთა ტალღური ფუნქციების გადაფარვით. გვირაბული დენის მთავარი განსაკუთრებულებაა მისი ექსპონენციალური დამოკიდებულება ნიმუშის ზედაპირსა და ზონდს შორის მანძილისაგან. მაგალითად, ნიმუშსა და ნემსს შორის 1 ვ ძაბვისას და ზონდის მიახლოებისას ზედაპირთან 1.5-დან 0.8 ნმ-მდე (მანძილის დაახლოებით ორჯერ შემცირებით) დენის ძალა იცვლება 1 პა-დან ათეულ ნა-მდე (ე.ი. 10 000-ჯერ). თუ ასეთ ზემგრძნობიარე ზონდს ზედაპირზე გავატარებთ, მაშინ გვირაბული დენის ძალის ცვლილება იქნება ზედაპირის პროფილის შესაბამისი გარჩევადობით ნანომეტრის მეათედი და მეასედიც კი ვერტიკალური მიმართულებით და ატომების ზომების რიგის ჰორიზონტალურად. ე.ი. მისი სიდიდე განისაზღვრება ატომური ზომების ზედაპირის სტრუქტურული თავისებურებებით, რის გამოც სკანირებისას გვირაბული დენის ცვლილებით შეიძლება აიგოს ზედაპირის შესაბამისი გამოსახულება.

ზონდით, რომელიც გადაადგილდება ზედაპირის გასწვრივ პიეზოელექტრული ძრავის მეშვეობით და ახდენს მის სკანირებას ყოველ წერტილში, ზედაპირის სურათი ფორმირდება კომპიუტერულად; ზონდის მოძრაობა ზედაპირის გასწვრივ რეგისტრირდება და კონტროლირდება განსაკუთრებით მაღალი, ატომური, სიზუსტით. დღევანდელ გვირაბულ მასკანირებელ ზონდურ მიკროსკოპებში ზონდის გადაადგილება დაპროგრამებულია კომპიუტერით და მისი ბიჯი შეადგენს 0.01 ნმ-ს.

გამოსახულება მიიღება ზონდის მექანიკური გადაადგილებით რასტრის სახის (სტრიქონ-სტრიქონ) ტრაექტორიით და შემდგომ ზონდსა და ზედაპირს შორის ურთიერთქმედების, როგორც ზონდის მდებარეობის (კოორდინატის) ფუნქციის, რეგისტრაციით. ზონდით ზედაპირის “მოსინჯვის” სურათი ჰგავს ლითონის ნემსის რხევებს ედისონის მიერ გამოგონებულ გრამოფონში, რომელიც გრამოფონის ფირფიტაზე იმეორებს ბგერითი ბილიკის ამობურცულობებს და ჩაღრმავებებს და ამგვარად ახდენს გრამფირფიტის ჩანაწერის აღწარმოებას.

ნემსის ზედაპირთან შეხების ან მისი გვირაბული დენის გავლის არედან გასვლის თავიდან ასაცილებლად იყენებენ უკუკავშირის სისტემას; ეს სისტემა მუდმივად არეგისტრირებს გვირაბულ დენს, აკორექტირებს რა ზონდის ჩამოკიდების სიმაღლეს ნიმუშის ზემოთ სკანირების ყველა წერტილში გვირაბული დენის მოცემული სიდიდის შესაბამისად. ამ დროს ზონდი რჩება ერთ და იგივე მანძილზე ზედაპირიდან, რაც იძლევა შესაძლებლობას განისაზღვროს ნიმუშში ელექტრონული ღრუბლების განაწილება, ხოლო ზონდის ტრაექტორია ნიმუშის რელიეფს ასახავს. ამგვარად, ზედაპირის სკანირებით შეიძლება ატომური პოტენციალის განაწილების განსაზღვრა, აგრეთვე ინფორმაციის მიღება ატომური გარჩევადობის სტრუქტურაში ატომების განლაგების შესახებ. ამ მეთოდის პრეციზიულობა, ცხადია, დიდ მოთხოვნებს უყენებს შესასწავლი ზედაპირის სისუფთავეს. დღეისათვის STM მიკროსკოპები მოთავსებულია ზემაღალი ვაკუუმის კამერებში წყლის, ჟანგბადის, ჰაერის აზოტის და ნახშირორჟანგის ადსორბციის თავიდან ასაცილებლად.

ცხრილი. სხვადასხვა სახის მიკროსკოპიის
ზღვრული გარჩევითი შესაძლებლობები.

მიკროსკოპიის სახე	ზღვრული გარჩევადობა, ნმ	გარემო	ზემოქმედება
ტრადიციული ოპტიკური	~ 200	ჰაერი, თხევადი	არადაშლადი
ფლუორესცენტული ნანოსკოპია	100 – 10	ჰაერი, თხევადი	არადაშლადი
ნელი ელექტრონების (LEEM)	10-მდე	ვაკუუმი	შესაძლებელია ნაწილობრივ დაშლა
მასკანირებელი ელექტრონული (SEM)	1-მდე	ვაკუუმი	დაშლადი
გაშუქებითი ელექტრონული (TEM)	0.05 (ცალკეული ატომები)	ვაკუუმი	დაშლადი
მასკანირებელი გვირაბული (STM)	0.2-მდე (ცალკეული ატომები)	ვაკუუმი, ჰაერი, თხევადი	არადაშლადი
ატომურ-ძალური (AFM)	0.2-მდე (ცალკეული ატომები)	ვაკუუმი, ჰაერი, სხვა აირები, თხევადი	არადაშლადი
ველის იონური (FIM)	0.2-მდე (ცალკეული ატომები)	ვაკუუმი	დაშლადი
ველის ემისიური (FEM)	0.2–მდე (ცალკეული ატომები)	ვაკუუმი	დაშლადი

რადგანაც მასკანირებელ ზონდურ მიკროსკოპიაში ზედაპირის გამოსახულება მიიღება ზონდის, რომელიც ახდენს ობიექტის ზედაპირის სკანირებას, მექანიკური გადაადგილებისას, გარჩევადობას განსაზღვრავს ზონდის ზომა და მისი ურთიერთქმედების ხასიათი ობიექტთან. **ცხრილში** შედარებულია სხვადასხვა სახის მიკროსკოპიის ზღვრული გარჩევითი შესაძლებლობები და, მათ შორის, მასკანირებელი ზონდური გვირაბული მიკროსკოპიის (STM). ტრადიციულ ელექტრონულ მიკროსკოპიასთან შედარებით მასკანირებელ გვირაბულ მიკროსკოპიას აქვს ერთი მნიშვნელოვანი უპირატესობა – გვირაბირებადი ელექტრონების ენერგია მნიშვნელოვნად ნაკლებია ქიმიური ბმის ენერგიაზე, ის სულ რამდენიმე ევ-ია; ეს კი იძლევა შესაძლებლობას, რომ ნიმუშების შესწავლა ამ მეთოდით მოხდეს მათი დესტრუქციის გარეშე. მაღალი გარჩევადობის ელექტრონულ მიკროსკოპიაში კი დაცემული ელექტრონების ენერგია რამდენიმე ათეული კევ ან მეგაევ-ია და აქ ნიმუშების დაშლა გარდაუვალია.

მასკანირებელი ზონდური გვირაბული მიკროსკოპის (STM) შექმნისას გადაჭრილი იქნა ურთულესი ტექნიკური ამოცანები:

– აკუსტიკური და მექანიკური ვიბრაციის პრობლემა; ამისთვის გამოიყენეს ზეგამტარი მაგნიტური საკიდი ნიმუშებისა და მასკანირებელი კვანძისთვის; შემდგომში ეს ამოცანა გადაიჭრა მთელი მიკროსკოპის გრძელ ზამბარებზე ჩამოკიდებით და მასკანირებელი კვანძის ვიბროსაიზოლაციო მაგიდაზე მოთავსებით;

– სწრაფმოქმედი და უხმაურო ელექტრონიკის შექმნა, რომლითაც გაიზომებოდა ზემცირე სიდიდის გვირაბული დენები და შესაძლებელი იქნებოდა ნიმუშზე სხვადასხვა მანიპულაციები;

– ხელსაწყოს უნდა ემუშავა ზედაბალ ტემპერატურებზე და კარგი თერმოსტატირების პირობებში, რადგანაც ტემპერატურის 0.01 °C-ით ცვლილებისას მექანიკური დეტალების სიგრძის ცვლილება 0.1 ნმ-ია, რაც განსასაზღვრი ობიექტის ზომების რიგისაა;

– ატომური "სიმახვილის" წვრილი ზონდების დამზადება და მათი დიაგნოსტიკა.

ყველა ეს პრობლემა წარმატებით გადაჭრა გ. ბინიგის და ჰ. რორერის გუნდმა (Ch. Gerber და E. Weibel) ორი წლის განმავლობაში.

ნაპოვნი და გამოყენებული ტექნიკური გადაწყვეტილებების მიხედვით, მასკანირებელი ზონდური გვირაბული მიკროსკოპი არის ადამიანის გონების გამორჩეული შემოქმედების პროდუქტი, რომელიც შეიძლება შევადაროთ ორბიტალური კოსმოსური სადგურის, ტელესკოპის "ჰაბლი" და კომპიუტერის შექმნას.

მასკანირებელი ზონდური გვირაბული მიკროსკოპი არის არა მარტო კვლევის ინსტრუმენტი ატომური სტრუქტურების ვიზუალიზაციაში, არამედ ის არის, აგრეთვე, ინსტრუმენტი ნანოობიექტების შექმნაში; თუ ზედაპირს და ზონდს შორის იმაზე მეტ ძაბვას მოვდებთ, ვიდრე სკანირებისას, მაშინ შეიძლება მივაღწიოთ იმას, რომ ზონდით მიიზიდება ზედაპირის ერთი ან რამდენიმე ატომი, რომელიც შეიძლება მაღლა ავწიოთ და სხვა ადგილას გადავიტანოთ (ნანოგადაადგილება); შესაძლებელია აგრეთვე ატომები ვაიძულოთ გადაადგილდნენ ზედაპირის გასწვრივ ან რამდენიმე ატომი მოვაცილოთ მოლეკულას; ანუ STM-ით იქმნება შესაძლებლობა თითოეული ატომის თანდათან დამატებით ავაგოთ ნებისმიერი მოლეკულა და ნანოსტრუქტურა, პერსპექტივაში კი – ვაწარმოოთ ისინი მაკროსკოპული მოცულობებით. პირველად ატომებით მანიპულირება STM-ით დემონსტრირებული იყო 1989 წ. ამერიკელი ფიზიკოსის დონ ეიგლერის (Don Eigler, IBM, აშშ) ჯგუფის მიერ კალიფორნიის შტატში, სან ხოსეში IBM-ის ალმადენის სამეცნიერო-კვლევით ლაბორატორიაში; მათ ნიკელის მონოკრისტალის ზედაპირზე ქსენონის 35 ატომით გამოსახეს აბრევიატურა "IBM" და გადაუღეს მას სურათი.

გ. ბინინგის და ჰ. რორერის მიერ შექმნილ მასკანირებელი გვირაბული მიკროსკოპი (STM) გახდა ამოსავალი მომენტი მიკროსკოპიის მთელი რიგი მასკანირებელი და ზონდური მეთოდებისთვის. ამ ტიპის უახლესი ხელსაწყოებია მასკანირებელი ატომურ ძალური მიკროსკოპი (AFM) და ახლო ველის მასკანირებელი ოპტიკური მიკროსკოპი (near-field scanning optical microscope, NSOM), აგრეთვე ნანოობიექტის რეალური სამგანზომილებიანი გამოსახულების მისაღები ლაზერული მასკანირებელი კონფოკალური მიკროსკოპი (laser scanning confocal microscope, LSCM), რომელშიც გამოიყენება ლაზერით შექმნილი ულტრაიისფერი სინათლე და მასკანირებელი სარკეები.

აღსანიშნავია, რომ ნიჭიერმა ფიზიკოსებმა გ. ბინიგმა და ჰ. რორერმა არა მარტო უნიკალური სამეცნიერო აპარატურა შექმნეს, არამედ ფილოსოფიურადაც გაიაზრეს ადამიანური შემოქმედების საწყისები და როლი ბუნებაში; გერდ ბინიგმა 1989 წელს

დაწერა ძალზედ საინტერსო წიგნი “Aus dem Nichts. Űber die Kreativität von Natur und Mensch”. Gerd Binnig. München; Zürich: Piper. 1989 (“არაფრისაგან. ბუნებისა და ადამიანის შემოქმედების შესახებ”). წიგნში გატარებულია შემოქმედების ქაოსთან კავშირის იდეა. 1994 წ. გ. ბინიგმა დაარსა კომპანია “Delphi Creative Technologies GmbH”, რომელიც ორიენტირებულია ანალიზზე სხვადასხვა მასშტაბის გამოსახულებებისა – მიკროფოტოგრაფიიდან თანამგზავრულ რუკებამდე.

ჰ. როერი იყო არა მარტო ნიჭიერი ფიზიკოსი-ექსპერიმენტატორი; როგორც მისი კოლეგები აღნიშნავენ, მას გააჩნდა ლიდერული თვისებები, ის ოპტიმიზმს უნერგავდა ადამიანებს; გერდ ბინიგმა ჰ. როერის სამგლოვიარო ცერემონიაზე განაცხადა: “ჰაინი ჩემი მამა იყო, მისაბაძი პიროვნება, ემოციური და სულიერი მასწავლებელი და საუკეთესო მეგობარი – ყველაფერი ეს იყო ერთ პიროვნებაში. ის იყო არაჩვეულებრივად დიდი პიროვნება შეუდარებელი სიყვარულით და ადამიანური სახით”.

უდიდესია მეცნიერებაში გ. ბინიგისა და ჰ. როერის წვლილი: გვირაბული ელექტრონული მიკროსკოპის სიძვირის მიუხედავად (ულტრათანამედროვე მაღალი გარჩევადობის ხელსაწყოს ღირებულება 4 მილიონი ევროა), პრაქტიკულად ნებისმიერი თანამედროვე კვლევა ფიზიკში, ქიმიაში, ბიოლოგიში, მასალათმცოდნეობასა და, განსაკუთრებით, ნანოტექნოლოგიებში საჭიროებს ელექტრონული მიკროსკოპიის მეთოდით მიღებულ მონაცემებს.

ნანოტექნოლოგია – გარღვევა თანამედროვე ტექნოლოგიაში

2012 წელს გამომცემლობაში აი-ჯი-აი გლობალი, ნ. ეკეკვესა და ნ. ისლამის რედაქციით, დაიბეჭდა კოლექტიური მონოგრაფია "გამრღვევი ტექნოლოგიები, ინოვაცია და გლობალური რედიზაინი: მზარდი გავლენა". წიგნის ავტორები შესაბამისი სფეროს აღიარებული სპეციალისტებია მსოფლიოს 14 ქვეყნიდან (ავსტრია, ამერიკის შეერთებული შტატები, ბანგლადეში, დიდი ბრიტანეთი, ინდოეთი, იტალია, კანადა, მაროკო, ნიგერია, ნიდერლანდები, სამხრეთ აფრიკის რესპუბლიკა, საქართველო, ტაივანი და ჩინეთი).

ამ წიგნის თემტიკაა და დანიშნულება ასე იხსნება. ესა თუ ის ახალი საწარმოო ტექნოლოგია მიჩნეულია გამრღვევ ტექნოლოგიად, თუ იგი გარკვეული დანიშნულების პროდუქციას ადრინდელთან შედარებით ბევრად უფრო ხელმისაწვდომად გადააქცევს და, იმავდროულად, მაქსიმალურ სამომხმარებლო მოგებას უზრუნველყოფს. სწორედ ამგვარი ტექნოლოგიური ინოვაციები იყო და რჩება საზოგადოების მიერ ახალი ცოდნის მოპოვების პროცესის მთავარ მამოძრავებელ ძალად. წიგნის ცალკეულ თავებში თეორიული ანალიზით, ლიტერატურულ მიმოხილვებზე დაყრდნობით, კონკრეტული შემთხვევების გამოკვლევით, საწარმოო პრაქტიკიდან აღებული ცალკეული მაგალითებით და ა.შ. ნაჩვენებია, თუ როგორ ცვლიან გამრღვევი ტექნოლოგიები მსოფლიოს – მარკეტინგული წარმატებით და არსებულის ჩანაცვლების გზით, გაუმჯობესებული ხარისხის პროდუქტებისა და მომსახურების შეთავაზებით.

Eds. N. Ekekwe, N. Islam. Disruptive Technologies, Innovation and Global Redesign: Emerging Implications. 2012, Hershey: IGI Global

წიგნი საკმაოდ სქელტანიანია – იგი 28 თავისაგან შედგება, რომლებიც 4 განყოფილებად არის განაწილებული:

განყოფილება 1
გამრღვევი ტექნოლოგიები (თავები 1 – 7)
განყოფილება 2
ინოვაცია (თავები 8 – 15)
განყოფილება 3
გლობალური რედიზაინი (თავები 16 – 22)
განყოფილება 4
მზარდი ბიძგი და გავლენა (თავები 23 – 28)

თავი 1 “გამრღვევი ტექნოლოგიები, ინოვაცია და გლობალური რედიზაინი” (გვ. 1 – 11), რომელიც ფაქტობრივად შესავალს წარმოადგენს, დაწერილია კოლექტიური მონოგრაფიის შემდგენელი რედაქტორების ნასრულ ისლამის (დიდი ბრიტანეთი) და ნდუბუისი ეკეკვეს (აშშ / ნიგერია) მიერ. აქ დეტალურადაა დახასიათებული ეკონომიკის ის სექტორები, სადაც ახლახან შეაღწია გამრღვევმა ტექნოლოგიებმა და, აგრეთვე, მთელი რიგი კულტურული, სოციალური და ეკონომიკური ცვლილებებისა, რომელიც ამ პროცესთანაა დაკავშირებული.

ზოგადად ნანოტექნოლოგიებს ეძღვნება თავი 7 “ნანომეცნიერება და ნანოტექნოლოგიები: ევოლუციის ტრაექტორიები და ამგვარი გარღვევის თავისებურებანი” (გვ. 107 – 126). ავტორი – უგო ფინარდი (იტალია) – დარგის ბევრი სხვა ექსპერტის მსგავსად, მიუთითებს, რომ ნანომეცნიერება და ნანოტექნოლოგია თანამედროვე მეცნიერებისა და ტექნოლოგიის მთლიან პანორამაში ორ ყველაზე უფრო მნიშვნელოვან სიახლეს წარმოადგენს. ნაჩვენებია მათი ევოლუციის გზა და არსებითი თავისებურებანი, ხელმისაწვდომი ფართო სოციალ-ეკონომიკური ბიბლიოგრაფიიდან ამოკრებილ ექსპერიმენტულ მონაცემებზე დაყრდნობით გაანალიზებულია ნანოტექნოლოგიის, როგორც გამრღვევი ტექნოლოგიის, როლი საზოგადოებასა და ეკონომიკაში.

თამარ ჩაჩიბაიას (საქართველო) მიერ დაწერილი თავი 9 “სამედიცინო განათლებაში ნანოტექნოლოგიური ინოვაციების შემოტანის სტრატეგიისა და პოლიტიკის საკითხები” (გვ. 147 – 172) ეძღვნება ერთ-ერთ კონკრეტულ ნანოტექნოლოგიურ ინოვაციას – სამედიცინო განათლებაში ამგვარი ტექნოლოგიების სწავლებას. ამ ინოვაციის აუცილებლობა იმითაა ახსნილია, რომ ბევრი თანამედროვე სამედიცინო ტექნოლოგია (მაგალითად, სამკურნალო საშუალებების სელექტიური მიწოდება პაციენტის სხვადასხვა ორგანოებისათვის) არსებითად ნანოტექნოლოგიას წარმოადგენს.

იმისათვის, რომ უფრო ნათლად წარმოვიდგინოთ, თუ რა კონტექსტში განიხილება ნანოტექნოლოგია თანამედროვეობის ერთ-ერთ მთავარ გამრღვევ ტექნოლოგიად, ქვემოთ ჩამოვთვლით წიგნის შემადგენელი თავების სათაურებს:

თავი 1

გამრღვევი ტექნოლოგიები, ინოვაცია და გლობალური რედიზაინი

თავი 2

ინოვაციური რისკის შეფასების გზა ახალი მეცნიერებებისა და ტექნოლოგიებისათვის: ილუსტრირება შეფერვით სინთეზირებული მზის ბატარეების მაგალითით

თავი 3

გამრღვევი პროდუქციის შემოტანის სტრატეგია: პორტატული ციფრული მუსიკალური ფლეიერის შემთხვევა

თავი 4

წარმოადგენს მობილური ტელეფონი გამრღვევ ტექნოლოგიას? განვითარებადი ეკონომიკების მონაცემების ნაწილობრივი მიმოხილვა

თავი 5

გამრღვევი პროდუქციის შემოტანის სტრატეგია თავდაპირველი წარმოების წამომწყებისათვის: შემოტანის მცირე დანახარჯებიანი ქვემოდან–ზემოთ მოდელი

თავი 6

ტექნოლოგიური გარღვევისა და ცვალებადობის მენეჯმენტი: გამრღვევი ინოვაციით შეღწევა ბაზარზე

თავი 7

ნანომეცნიერება და ნანოტექნოლოგიები: ევოლუციის ტრაექტორიები და ამგვარი გარღვევის თავისებურებანი

თავი 8

როგორ მოქმედებენ ფირმები პროდუქციის წყვეტილი შემოტანისას: ემპირიული ანალიზი

თავი 9

სამედიცინო განათლებაში ნანოტექნოლოგიური ინოვაციების შემოტანის სტრატეგიისა და პოლიტიკის საკითხები

თავი 10

ნიკელის ფიტოგადამუშავება: მექანიზმები, გამოყენება და მენეჯმენტი

თავი 11

ინოვაცია ინფორმაციული და კომუნიკაციური ტექნოლოგიების (ICT) დაფინანსების მექანიზმში

თავი 12

ახლებურად ბრენდირება: თურქეთის შემთხვევის კვლევა

თავი 13

ტექნოლოგიური განათლება და ინოვაციები ნიგერიის ადგილობრივ შრომით ჯგუფებში: დღევანდელი მდგომარეობა და პოლიტიკის მიმართულებანი

თავი 14

სოციალური ქსელები, ონლაინ-ტექნოლოგიები, და სწავლა ვირტუალურად: (რე)სტრუქტურირების დაწოლა და იერარქიები აკადემიურ წრეში

თავი 15

VoIP- თუ GSM-ტექნოლოგია: კომუნიკაციის სამომავლო გზა

თავი 16

ტექნოლოგიის გადაცემის საშუალებები და პროცესები: დახმარების მიმღებ განვითარებად ქვეყნებში მეცნიერული ცოდნისა და ნოუ-ჰაუ-ის გადატანის სისტემის გაუმჯობესება

თავი 17

საგანმანათლებლო ტექნოლოგიის დაგეგმვა და დიზაინი დაბალი შემოსავლის მქონე ჯგუფებისათვის: ერთიანი პროფილაქტიკური მიდგომა

თავი 18

ტექნოლოგია და მრავალპოლუსიანი გლობალური ეკონომიკა: შედეგები ევროპის კონკურენტუნარიანობისათვის

თავი 19

კომუნიკაციის მასობრივ საშუალებათა თეორიების გადააზრება ინტერნეტის ერაში

თავი 20

ოცნება და რეალობა: “ციფრული კონცეფციის” ათვისება წარმოქმნის პროცესში მყოფი ქვეყანის მიერ

თავი 21

განვითარებად ეკონომიკაში ჯანმრთელობის დაცვაში ახალი ტექნოლოგიების დანერგვასთან დაკავშირებული მარკეტინგული შეცდომები

თავი 22

დანახარჯები და ექსპონირება: ხვალინდელი ვირტუალური გლობალური განათლება

თავი 23

გენეტიკური ტესტირებისა და გენეტიკური ინფორმაციის გავლენა ეთიკურ, იურიდიულ და სოციალურ საკითხებზე ჩრდილო ამერიკაში: ზოგადი ჩარჩო

თავი 24

ტექნოლოგიის გავრცელება და ეკონომიკური პროგრესი აფრიკაში: გამოწვევები და შესაძლებლობები

თავი 25

გამრღვევი ტექნოლოგიის თანმდევი შედეგები: მენეჯმენტის ახალი პრაქტიკის მიმოხილვა და ადამიანური შესაძლებლობები

თავი 26

ტელეფონები ორი SIM-ბარათით: გამრღვევი ტექნოლოგიაა?

თავი 27

პოლიტიკის გავლენა მზის PV-ბატარეების ჩართვაზე ნიგერიული სოფლის ენერგეტიკულ ბალანსში

თავი 28

ნიგერიაში ტექნოლოგიის ინკუბატორების კოორდინირება, მონიტორინგი და გავლენის შეფასება

ლევან ჩხარტიშვილი

2012 წლის 1 ოქტომბერი

არაორგანული მასალათმცოდნეობა / ფერდინანდ თავაძე – 100

2012 წლის 4 – 6 ივნისს საქართველოში ჩატარდა საერთაშორისო კონფერენცია “არაორგანული მასალათმცოდნეობის თანამედროვე ტექნოლოგიები და მეთოდები”, მიძღვნილი გამოჩენილი ქართველი მეცნიერ-მეტალურგისა და საზოგადო მოღვაწის აკად. ფერდინანდ თავაძის დაბადებიდან 100 წლისთავისადმი, რომელიც 2012 წლის 21 მაისს შესრულდა.

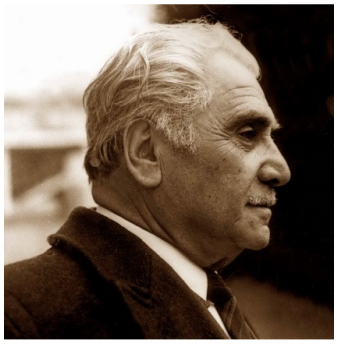

აკად. ფერდინანდ თავაძე – 100

კონფერენციაში ქართველ მეცნიერებთან ერთად მონაწილეობა მიიღეს აშშ-ის, ისრაელის, რუსეთის, სომხეთისა და უკრაინის ცნობილმა სპეციალისტებმა – მეტალურგებმა და მასალათმცოდნეებმა.

კონფერენციის ორგანიზატორები ფერდინანდ თავაძის მეტალურგიისა და მასალათმცოდნეობის ინსტიტუტთან (ფთმმი) ერთად იყვნენ საქართველოს მეცნიერებათა ეროვნული აკადემია, საქართველოს თავდაცვის სამინისტრო და საქართველოს სახელმწიფო სამხედრო სამეცნიერო-ტექნიკური ცენტრი “დელტა”. საერთაშორისო კონფერენცია “არაორგანული მასალათმცოდნეობის თანამედროვე ტექნოლოგიები და მეთოდები” ფინანსურად მხარდაჭერილი იყო შოთა რუსთაველის ეროვნული სამეცნიერო ფონდის გრანტით. კონფერენციის ჩასატარებლად შეიქმნა საერთაშორისო სამეცნიერო კომიტეტი გიორგი თავაძის (საქართველო) თავმჯდომარეობით და შემდეგი წევრებით: თამარ ბაძოშვილი (საქართველი), ალექსი ბერნერი (ისრაელი), ალექსანდრე მერჟანოვი (რუსეთი), გიორგი ონიაშვილი (საქართველო), ბორის პატონი (უკრაინა), ირაკლი ჟორდანია (საქართველო), ვალერი სკოროხოდი (უკრაინა), არჩილ ფრანგიშვილი (საქართველო), გივი ცინცაძე (საქართველო), ალექსანდრე შტეინბერგი (აშშ), ჯუმბერ ხანთაძე (საქართველო), ავთანდილ ხვადაგიანი (საქართველო).

კონფერენცია მიმდინარეობდა თბილისში, სასტუმრო “ვერე პალასში”. იგი გახსნა ფერდინანდ თავაძის მეტალურგიისა და მასალათმცოდნეობის ინსტიტუტის დირექტორმა, საერთაშორისო საორგანიზაციო კომიტეტის თავმჯდომარემ, აკად. წევრ-კორ. გიორგი თავაძემ. გახსნის სხდომაზე მონაწილეებს მიესალმნენ საქართველოს პარლამენტის ვიცე-სპიკერი, საქართველოს მეცნიერებათა ეროვნული აკადემიის პირველი ვიცე-პრეზიდენტი, აკად. ფრიდონ თოდუა და საქართველოს ტექნიკური უნივერსიტეტის რექტორი, აკად. წევრ-კორ. არჩილ ფრანგიშვილი.

მთლიანობაში წარმოდგენილი იქნა 23 ზეპირი და 9 სასტენდო მოხსენება. მათში გაშუქებული იყო ისეთი აქტუალური თემები, როგორიცაა მასალების ელექტრონული მიკროსკოპია, მათი თერმოდინამიკური თვისებები, ლითონებისა და შენადნობების

მეტალურგია, თვითგავრცელებადი მაღალტემპერატურული სინთეზი, მეტალოკერამიკები და სხვა კომპოზიტები, რადიაციულად მდგრადი მასალები, საწარმოო ნარჩენების რეგენერაციისა და გაუვნებელყოფის ტექნოლოგიები, აგრეთვე – ისტორიული მეტალურგია. აღსანიშნავია, რომ კონფერენცია გაიხსნა დოქტორ ირინე ღამბაშიძის მოხსენებით მსოფლიოში უძველესი მეტალურგიული კერების უახლეს არქეოლოგიურ აღმოჩენებს საქართველოში.

ფთმმი-ის დირექტორი, საერთაშორისო საორგანიზაციო კომიტეტის თავმჯდომარე, აკად. წევრ-კორ. გიორგი თავაძე

საიუბილეო სხდომის პრეზიდიუმში

საიუბილეო სხდომის დარბაზში

4 ივნისს, გახსნის სხდომის შემდეგ, საქართველოს მეცნიერებათა ეროვნულ აკადემიაში გაიმართა აკად. ფერდინანდ თავაძის დაბადებიდან 100 წლისთავისადმი მიძღვნილი საიუბილეო სხდომა. სხდომა გახსნა აკადემიის პრეზიდენტმა, აკად. თამაზ გამყრელიძემ. შემდეგ კონფერენციის მონაწილეებისა და სტუმრებისათვის გაიმართა აკად. ფერდინანდ თავაძის შესახებ მომზადებული ახალი დოკუმენტური ფილმის პრეზენტაცია. ფერდინანდ თავაძის მეცნიერულ მოღვაწეობაზე და მის მიერ გავლილ ცხოვრების გზაზე ისაუბრა თავის მოხსენებაში საქართველოს საწარმოო ძალებისა და ბუნებრივი რესურსების შემსწავლელი ცენტრის დირექტორმა, აკად. ირაკლი ჟორდანიამ. აკად. ფერდინანდ თავაძე გაიხსენეს მისმა კოლეგებმა და მოსწავლეებმა – ჯუმბერ ხანთაძემ (ფთმმი), იოსებ ციცაძემ (ფთმმი), ვლადიმერ იუხვიდმა (სტრუქტურული მაკროკინეტიკისა და მასალათმცოდნეობის ინსტიტუტი, მოსკოვი, რუსეთი), ვიქტორ შაპოვალოვმა (ე. პატონის სახ. ელექტროშედუღების ინსტიტუტი, კიევი, უკრაინა) და ალექსანდრე შტეინბერგმა (ბერკლის უნივერსიტეტი, ბერკლი, აშშ). ლეონიდ ჩერნიშოვმა ი. ნ. ფრანცევიჩის სახ. მასალათმცოდნეობის პრობლემათა

ინსტიტუტიდან (ინფმმპი, კიევი, უკრაინა) ამ ინსტიტუტის სახელით აკად. წევრ-კორ. გიორგი თავაძეს გადასცა აკადემიკოს გრიგორი სამსონოვის მედალი; ნაჩვენები იყო ინფმმპი-ის დირექტორის აკად. ვალერი სკოროხოდის ვიდეომისალმება. უკრაინის ეროვნული მეცნიერებათა აკადემიის პრეზიდენტის აკად. ბორის პატონის მისალმება დამსწრე საზოგადოებას გააცნო ვიქტორ შაპოვალოვმა (ე. ო. პატონის სახ. ელექტროშედუღების ინსტიტუტი, კიევი, უკრაინა).

ი. ჟორდანია

ჯ. ხანთაძე

ი. ცინცაძე

ა. შტეინბერგი

ვ. იუხვიდი

ლ. ჩარნიშოვი გ. სამსონოვის მედალს გადასცემს გ. თავაძეს

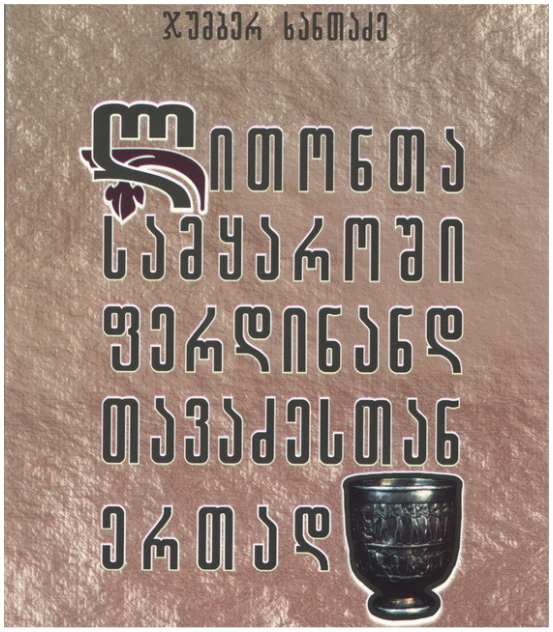

ჯ. ხანთაძის წიგნი “ლითონთა სამყაროში ფერდინანდ თავაძესთან ერთად”

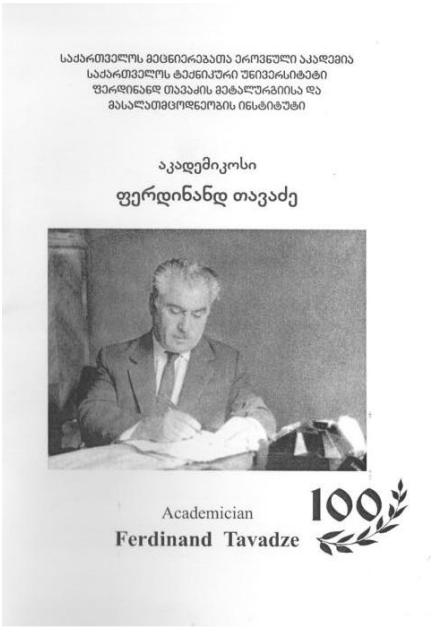

ჯ. ხანთაძის ბროშურა “აკადემიკოსი ფერდინანდ თავაძე – 100”

ამავე იუბილეს მიეძღვნა ჯუმბერ ხანთაძის წიგნის “ლითონთა სამყაროში ფერდინანდ თავაძესთან ერთად” გადამუშავებული ვარიანტის გამოცემა 2012 წელს. იგი მკითხველს აცნობს მკვლევარის ცხოვრებისა და მოღვაწეობის ცალკეულ მნიშვნელოვან ფრაგმენტებს და დიდ მეცნიერულ მემკვიდრეობას. წიგნი უხვად არის ილუსტრირებული და დიდი ინტერესით იკითხება. ამიტომ იგი საშუალებას მისცემს ახალგაზრდა თაობას, ფერდინანდ თავაძის მოღვაწეობის მაგალითზე, ძალდაუტანებლად ეზიაროს მეცნიერებას ლითონების შესახებ. ჯ. ხანთაძემ აგრეთვე გამოსცა ბოიგრაფიული ხასიათის ბროშურა “აკადემიკოსი ფერდინანდ თავაძე – 100” სამ ენაზე – ქართულად, ინგლისურად, რუსულად და გამოაქვეყნა (ი. ჟორდანიასთან ერთად) სტატია გაზეთში “საქართველოს რესპუბლიკა”.

გამოიცა კონფერენციაზე წარმოდგენილ მოხსენებათა სრული ტექსტების კრებული (მთავარი რედაქტორი – ჯუმბერ ხანთაძე, რედკოლეგიის წევრები – დომენტი გაბუნია, დალი რამაზაშვილი, ლევან ჩხარტიშვილი).

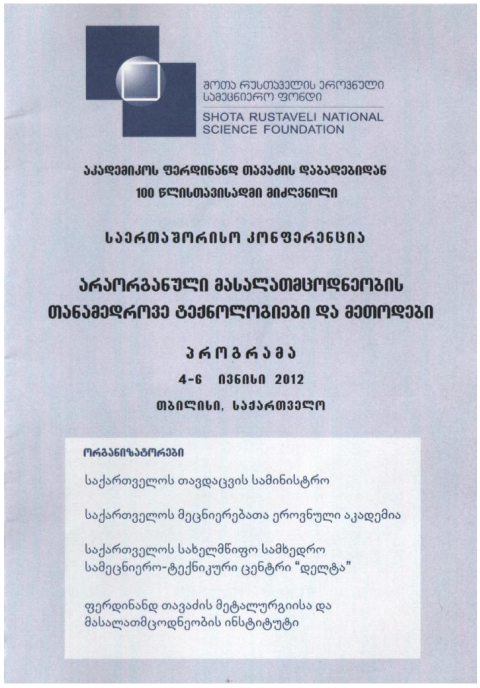

კონფერენციის პროგრამა

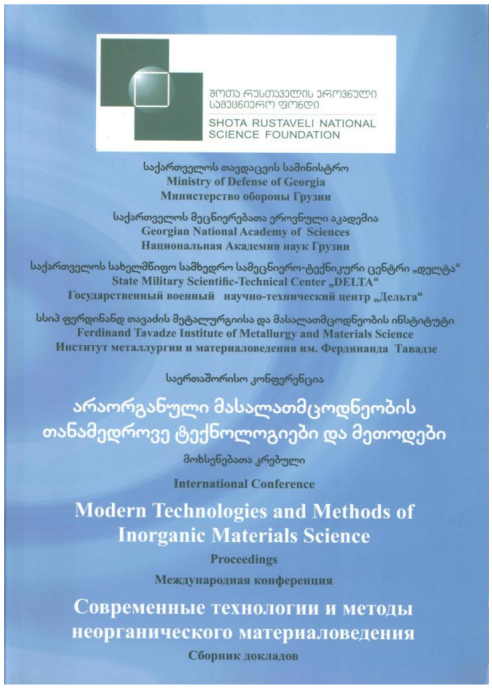

კონფერენციის მოხსენებათა კრებული

საიუბილეო კონფერენციის სოციალური პროგრამის მიხედვით, მისი მონაწილეთათვის გაიმართა ბანკეტი და მოეწყო ექსკურსია თბილისის ისტორიულ უბნებში და საქართველოს ძველ დედაქალქ მცხეთაში.

კონფერენციის დასკვნით სხდომაზე გაიმართა შემაჯამებელი დისკუსია. მონაწილეები ერთსულოვნად აღნიშნავდნენ, რომ ის იყო უაღრესად ნაყოფიერი ღონისძიება როგორც მეტალურგიისა და არაორგანული მასალათმცოდნეობის დარგში მიღებული ახალი შედეგების სპეციალისტების მიერ ურთიერთგაცნობისათვის, ასევე ამ სფეროებში სამეცნიერო თანამშრომლობის შემდგომი განვითარებისთვის. გადაწყდა, რომ არაორგანული მასალათმცოდნეობის ტექნოლოგიებისა და მეთოდებისადმი მიძღვნილი საერთაშორისო კონფერენციები რეგულარულად, ორ წელიწადში ერთხელ გაიმართოს თბილისში, საქართველოში.

ოთარ ცაგარეიშვილი

2012 წლის 18 ივნისი

ინტერნეტ-კონფერენცია ნანოტექნოლოგიაში

2013 წლის 22 მაისს გაიმართა 1-ლი სრულიად რუსეთის სამეცნიერო-პრაქტიკული ინტერნეტ-კონფერენცია საერთაშორისო თანამონაწილეობით "ნანოტექნოლოგია თეორიასა და პრაქტიკაში". კონფერენცია მიზნად ისახავდა, რომ ხელი შეეწყო თანამედროვე მეცნიერებატევადი ტექნოლოგიებისათვის აუცილებელი ახალი ნანომასშტაბური მეთოდებისა და ნანომასალების შექმნის, განვითარებისა და გავრცელებისათვის.

კონფერენციის ძირითადი თემები იყო:

- ნანომასალების სტრუქტურისა და თვისებების მოდელირება
- ნანოტექნოლოგიები და ნანოკომპოზიტები კოსმოსური დარგისათვის
- ნანოტოქსიკოლოგია
- ნანოსტრუქტურების თვისებები
- ნანომასალები
- ნანონაწილაკების გამოკვლევის მეთოდები
- ახალი ნანოსტრუქტურირებული მასალების სინთეზი

PAX GRID
scientific conferencing in virtual reality

რამდენადაც ვირტუალური ფორუმები ქართველი მეცნიერებისათვის შედარებით სიახლეს წარმოადგენს, მოკლედ შევჩერდეთ ამ ღონისძიების ორგანიზაციაზე. კონფერენცია "ნანოტექნოლოგია თეორიასა და პრაქტიკაში" ჩაატარა ელექტრონულმა ქსელმა Pax Grid. ამიტომ მონაწილეებმა რეგისტრაცია გაიარეს აღნიშნული ქსელის შესაბამის საიტზე. დარეგისტრირებულ მონაწილეს საშუალება ჰქონდა ელექტრონულად შესულიყო "პირად კაბინეტში" და იქიდან აეტვირთა თავისი მოხსენების ტექსტი და საილუსტრაციო მასალები. შესაძლებელი იყო მოხსენების:

- ზეპირი პრეზენტაცია
- სტენდური წარმოდგენა ვირტუალურ დარბაზში
- მხოლოდ პუბლიკაცია

ინტერნეტ-კონფერენციები "იმართება" ვირტუალურ დარბაზებში და ვირტუალურ სტენდებთან.

ვირტუალური კონფერენციის მსვლელობისას მონაწილეებს ერთმანეთთან კომუნიკაციისათვის სჭირდებათ ინტერნეტში ჩართული კომპიუტერი, მიკროფონი და საყურისები (ანდა ბგერითი სვეტები).

კონფერენციის დასრულების შემდეგ მისი მასალების კრებული ელექტრონულ ფორმაში ხელმისაწვდომია ინტერნეტით. კრებული გამოიცა ბეჭდურადაც და დარეგისტრირდა რუსეთის წიგნის პალატაში. იგი დაეგზავნა არა მარტო ავტორებს, არამედ მთელ რიგ წამყვან ბიბლიოთეკებსაც.

კონფერენციაზე წარმოდგენილი
მოხსენებების კრებულის გარეკანი.

თავად რუსეთის ჩათვლით, 1-ლ სრულიად რუსეთის სამეცნიერო-პრაქტიკულ ინტერნეტ-კონფერენციაში "ნანოტექნოლოგია თეორიასა და პრაქტიკაში" სულ 6 ქვეყნის (რუსეთი, საფრანგეთი, საქართველო, სლოვაკეთი, უკრაინა და ყაზახეთი) მეცნიერებმა მიიღეს მონაწილეობა. საქართველოს ტექნიკური უნივერსიტეტის საინჟინრო ფიზიკის ფაკულტეტის პროფესორმა ლევან ჩხარტიშვილმა წარმოადგინა მოხსენება თემაზე: "ბორის ნიტრიდის ნანოტუბულარული და ფულერენული ზედაპირების სიმრუდე".

იმისათვის, რომ მკითხველს შეექმნას უფრო კონკრეტული წარმოდგენა კონფერენციით მოცული თემატიკის მრავალფეროვნებაზე, ქვემოთ მოვიტანთ წარმოდგენილი მოხსენებების სათაურებს:

- ალუმინშემცველი კომპოზიტები მარსზე პილოტირებადი ექსპედიციისათვის.
- ნახშირბადის ნანომილაკების ტოქსიკური ეფექტების შეფასება ბიოლუმინესცენციური ანალიზის მეთოდებით.
- სპილენძის ანტიბაქტერიული მოქმედების შესწავლა *in vitro* და *in vivo* ცდებით.
- ნახშირბადისა და სილიციუმის ფუძეზე შექმნილი ნანომასალების დრეკადი თვისებების მოდელირების შედეგები.

- სარანპაულსკის საბადოს ცეოლითების სორბციულობის უნარის ამაღლების მექანო-ქიმიური ტექნოლოგია.
- Ni – Al – Zr-ის სისტემის ნანოსტრუქტურული მასალების მიღება თვითგავრცელებადი მაღალტემპერატურული სინთეზით ნავთობის თანმდევი გაზების კატალიზური კონვერსიისათვის.
- წყალბადითა და ფტორით დოპირებულ გრაფენში პიეზოეფექტის მათემატიკური მოდელირება.
- ნახშირბადის სუპერკრისტალური ნანომილაკების სითბოგამტარობის მათემატიკური მოდელირება.
- პიეზოელექტრიკებისა და რკინაშემცველი ნატრიუმ-კალიუმ-ბორსილიკატური მინების დიელექტრული მახასიათებლების შესწავლა გიგაჰერცულ დიაპაზონში.
- C_{60} ფულერენისა და მისი ნანოკომპოზიტების ცხოველებისა და ადამიანის იმუნიტეტსა და ჰემოსტაზის სისტემაზე გავლენის შესწავლა.
- ბინარული სისტემის ფხვნილი–ნანოფხვნილი მოდელირება.
- ქიტოზანისა და გარდამავალი ლითონების ნანონაწილაკების ფუძეზე შექმნილი კომპლექსური პრეპარატის გავლენა ინფიცირებული ჭრილობის რეგენერაციაზე.
- მრავალფენიანი გრაფენის გამოყენება სორბენტად.
- დამუშავებები დეტალების რეცხვის დაბალსიხშირული კავიტაციური მოწყობილობებისა და მაღალეფექტური ფირფიტოვან-ელასტომერული ამორტიზატორების ნანოტექნოლოგიათა ტრიბოტექნიკაში გამოყენების თაობაზე.
- არაორგანული ნაერთების და მიკრო- და ნანომილაკების მიღების ახალი ხერხი, დაფუძნებული გამყოფ საზღვარზე ხსნარი–ჰაერი სინთეზირებული ფენების “დახვევაზე”.
- ნანოსტრუქტურების ფორმირება სუსპენზიებისა და ხსნარების პრეკურსორების პლაზმური დაფრქვევისას.
- ველიანი ეფექტი ოქროს ნანონაწილაკების ელექტრონულ სპექტრებში.
- ძლიერი სპინ–ორბიტალური ურთიერთქმედების მქონე კვანტური ნანოსტრუქტურების ელექტრონული სპექტრები.
- ტიტანსილიკატური ნანოკონსტრუქტორი დეკათიონიზებული კუკისვუმიტის ფუძეზე, როგორც პერსპექტიული მასალა თანამედროვე მასალათმცოდნეობის მიზნებისათვის.
- Nb – Ti-ის შენადნობის ფუძეზე შექმნილი მრავალძარღვა ზეგამტარის სტრუქტურებზე ცივი ადიდვით დეფორმირების გავლენა.
- ექსპერიმენტის პირობებში ლითონების ნანონაწილაკების ანტიბაქტერიული მოქმედება.
- ხრტილოვანი ქსოვილების ლაზერული ინჟინერიისათვის ბიოფუნქციური ნანონაწილაკების შექმნის ფიზიკურ-ქიმიური ასპექტები.
- მოცულობითი ნანოსტრუქტურული თერმოელექტრული მასალა $(Bi, Sb)_2Te_3$-ის ფუძეზე.
- სამედიცინო ტექნიკის ნაკეთობათა პლაზმურად დაფრქვეული მრავალფენიანი დანაფარების იონურ-სხივური მოდიფიცირება.
- ნახევრად ურთიერთშეღწევადი პოლიმერული ბადის ფორმირებისათვის ეპოქსიდური მატრიცის სივრცული სტრუქტურის მოდიფიცირება ლითონის / ნახშირბადის ნანოკომპოზიტებით.

- ნახშირბადის ნანომილაკების შემცველი ცემენტის ჰიდრირებისას სითბოს გამოყოფის ხასიათი.
- ზედაპირული პლაზმური რეზონანსის გრძელ- და მოკლეტალღოვანი მოდების დამზერა ნანოზომის ოქროს ფირში.
- ადამიანის ორგანიზმზე ნანომასალების არხელსაყრელი ზემოქმედების რისკები.
- ბიოაქტიური სუბსტანციების გადასატანად მოდიფიცირებული ნანონაწილაკები.
- ნახშირბადოვან შაბლონზე სინთეზირებული ZrO_2 / TiO_2 / SiO_2-ის ნანოკომპოზიტების მორფოლოგია და სტრუქტურა.
- სტრონციუმის ფტორიდის ფუძეზე შექმნილი და იშვიათმიწა ელემენტებით თანააქტივირებული ლუმინოფორების ნანოფხვნილების მიღება და გამოკვლევა.
- ფოსფორული დენდრიმერების რხევების დინამიკა და სტრუქტურა.
- მიკრონული სისხოს ფხვნილებისა და ნანოფხვნილების შერევის თავისებურებანი.
- ბორის ნიტრიდის ნანოტუბულარული და ფულერენული ზედაპირების სიმრუდე.
- კლასტერების ზომების შესწავლა ხისტი ანიზოტროპული დისკო-მართკუთხედებისა და იზოტროპული დისკოების 2D ნარევებში.
- შრობადი სითხეების კომპონენტების მოლეკულური თვითაწყობის დინამიკა ინფორმაციას იძლევა მათ შემადგენლობაზე და სტრუქტურაზე. ფენომენის შესაძლო გამოყენება.
- კომპოზიციები ადვილდნობადი შენადნობების ფუძეზე.
- საწვავ–აირული ჭავლის ნანოდისპერსიული სტრუქტურის ოპტიკური დიაგნოსტიკა.
- ლითიუმის ტერაბორატის კრისტალების სტრუქტურული და რხევითი თვისებები.

ლევან ჩხარტიშვილი

2013 წლის 23 ივლისი

ISSN 1987-8826